Schriftenreihe

**DES INSTITUTES FÜR
GRUNDBAU UND BODENMECHANIK
DER RUHR-UNIVERSITÄT BOCHUM**

Herausgeber: Th. Triantafyllidis

Heft 38

Explicit accumulation model for non-cohesive soils under cyclic loading

by
Torsten Wichtmann

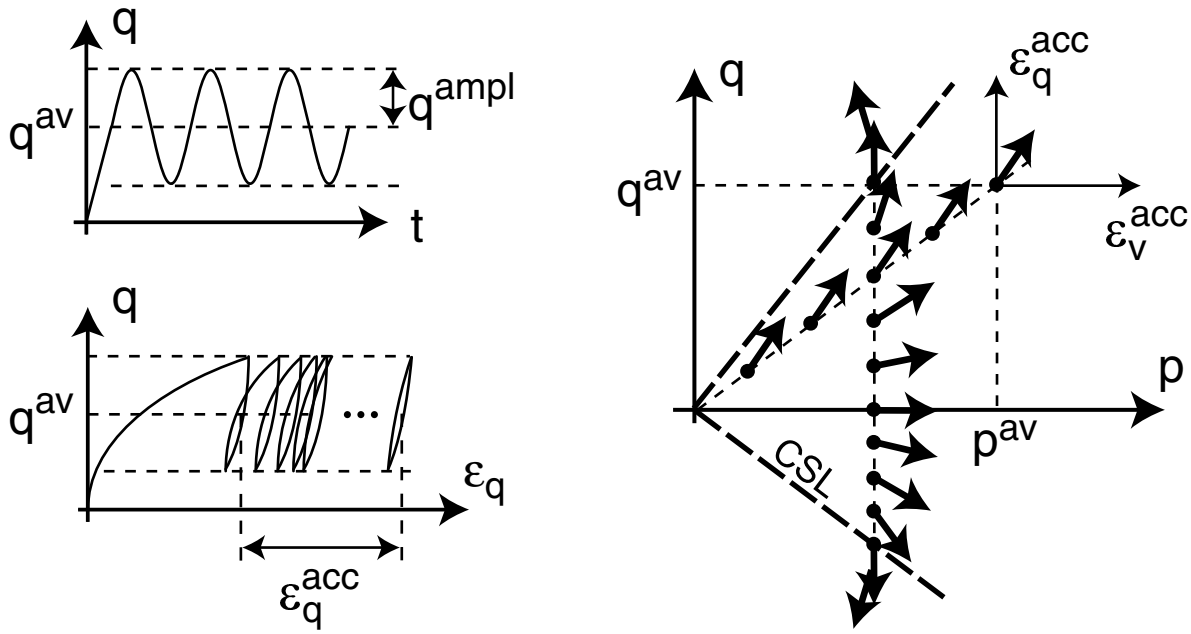

ISSN 1439-9342

Bochum 2005

Von der Fakultät für Bauingenieurwesen
der Ruhr-Universität Bochum genehmigte

DISSERTATION

von
Dipl.-Ing. Torsten Wichtmann
aus Finnentrop-Ostentrop

Wisssenschaftlicher Mitarbeiter am
Lehrstuhl für Grundbau und Bodenmechanik
der Ruhr-Universität Bochum

Tag der mündlichen Prüfung:
15. November 2005

Referenten

Univ.-Prof. Dr.-Ing. habil. Th. Triantafyllidis
o. Prof. Dr.-Ing. Dr. hc. G. Gudehus
Univ.-Prof. Dr.-Ing. R. Breitenbücher

Editor's preface

The application of cyclic loading on non-cohesive soils even with small amplitudes but with a large number of cycles leads to significant plastic deformations. This phenomenon is well known over 60 years in soil mechanics but up to now neither objective models nor reliable methods have been developed for the solution of the respective engineering problems. For the newly developed systems of high speed railway tracks, magnetic levitation trains, wind power generation plants, watergates, storage tanks etc. which in their design life are subjected to a large amount of loading cycles, design tools for the estimation of their serviceability are required. The foundation of these structures has to be designed for polycyclic non-linear soil-structure interaction effects and therefore the demand for reliable and objective models in this area is quite high.

In the past empirical formulas for the accumulation behaviour of foundation elements due to cyclic loading have been developed based on model tests. These approximations were not accurate enough for a polycyclic loading: they were only applicable for a specific boundary value problem without the possibility of extension of their validity to similar other problems and most of them were not objective. In addition, numerical algorithms of implicit nature using either elasto-plastic or elasto-hypoplastic constitutive relations for the soil have not been able to calculate the long-term behaviour of structures subjected to polycyclic loading due to the accumulation of numerical errors caused by the time integration techniques or procedures.

In this thesis of Wichtmann a very comprehensive literature review is presented which can be regarded as a state-of-the-art for the up to date knowledge in the field of cyclic accumulation in non-cohesive soils. The experiments have been performed with a very high accuracy and in a very careful manner so that the findings, which partially disprove findings of other researchers, are used for the formulation of an explicit accumulation model considering effects of the barotropy, pyknotropy, historiotropy, change of strain polarization, stress ratio, etc. This explicit model has been implemented in a combined numerical strategy consisting of implicit and explicit schemes for the solution of accumulation problems in the engineering practise. In the thesis some numerical results for the behaviour of strip footings and piles due to a vertical cyclic loading have been presented as well as the validation of model tests carried out at our institute. In the meantime this model is implemented for the numerical solution of more complex problems like the serviceability of reinforced earth embankments due to cyclic loading and the simulation of deep vibratory compaction techniques.

The basic outcome of this study is the determination or validation of the cyclic flow rule and the simple formula for the accumulation intensity as a scalar function. The advantages

of the accumulation model in comparison to the existing approaches in the literature are clearly demonstrated as well as the prediction accuracy of the model by comparison with respective laboratory tests.

This work opens a large area of scientific work for the coming years and offers in the meantime a simple tool for the solution of engineering problems, which deal with high numbers of loading cycles.

The present work has been financially supported by the DFG (German Research Council) with the partial project A8 within the frame of the collaborative research centre SFB 398 "Life time oriented design concepts", which is gratefully acknowledged herewith.

Theodoros Triantafyllidis

Author's preface

The present thesis summarizes my work at the Institute of Foundation Engineering and Soil Mechanics of Ruhr-University Bochum in the period 2001 - 2005. It presents the results of numerous cyclic laboratory tests on sand and describes an explicit accumulation model which is based on these experiments. The accumulation model is capable to predict settlements or changes of stress in the soil under cyclic loading with many cycles and low amplitudes.

I am deeply indebted to many persons who were involved in this work. First, I want to thank my first supervisor Prof. Th. Triantafyllidis for his guidance during my research, for his continuous interest in my work and for many valuable discussions. He provided the financial and consultant support to arrange our high-standard laboratory for cyclic and dynamic testing of soils here in Bochum.

I am also grateful to my colleague and friend Dr. A. Niemunis with whom I worked closely together during my research. Due to his large experience and knowledge on the field of constitutive modelling of soils, he contributed many good ideas, both for novel testing devices and improvements of the accumulation model.

My thanks are also dedicated to Prof. G. Gudehus for his interest in my work, for being the second supervisor of my thesis and for giving many valuable hints which helped to improve the manuscript. I would like to thank Prof. R. Breitenbücher for being the third examiner and Prof. R. Höffer for being the chairman of my examination.

Next, I would like to thank the staff of our workshop (R. Schudy, B. Schmidt, M. Becker, T. Vogel and B. Dapprich). For the studies presented in this thesis, they manufactured five cyclic triaxial devices, the resonant column apparatus, the multidimensional simple shear device, two large-scale oedometer devices and numerous other laboratory tools necessary to prepare samples and perform tests. They gave many valuable hints how to improve the construction of the devices. In this context, I also want to thank Dr. D. König for many good ideas. Furthermore, I thank Dr. H. Nawir for several helpful discussions on the measurement technique.

I am indebted to R. Rammelkamp who installed numerous electrical components in the laboratory and calibrated the sensors. In particular, I am much obliged to the laboratory assistants D. Lüpckes and M. Skubisch who prepared a large number of high-quality sand samples and performed the tests with much patience and care. I appreciate also the contribution of R. Mosinski who took care for the computers in the laboratory.

My thanks are also dedicated to my student co-workers A. Hammami and B. Schwarz as well as to my diploma thesis students F. Schanzmann, K. Güc, M. Poblete, M. Hammami,

S. Keßler and H. Canbolat. Furthermore, I would like to thank all my current and former colleagues for a friendly and familiar working atmosphere.

The present English version of the manuscript is a translation of the original German thesis. In this context, I want to thank D. Triantafyllidis for a careful reading and corrections of the English text. If required, the German version can be obtained as a pdf-file from the author (moreover, some of our papers mentioned in the bibliography may be downloaded from `www.gub.rub.de/mitarbeiter/torsten_wichtmann.htm`).

The financial support of this research was given by "Deutsche Forschungsgemeinschaft (DFG)" in the framework of SFB 398 (project A8) which is gratefully acknowledged herewith.

Last but not least, I would like to thank my family for their continuous support.

Finally, I want to emphasise that an extensive experimental study like the one presented in this thesis can only be realized by teamwork. Thus, all persons mentioned above have part in its success. I hope that during the next years, the accumulation model presented in this thesis will be continuously developed, that its range of applicability will be extended (e.g. to cohesive and gravelly soils) and that it can serve as a means for solving many interesting boundary value problems with cyclic loading of soils.

Torsten Wichtmann

Contents

Chapter 1

Introduction

1.1 Theme and objective of this work

If a foundation passes cyclic loads into a soil, the residual settlement increases with the number of cycles (Figure 1.1). This is due to the fact that the nearly closed stress loops, resulting from external loading, lead to not perfectly closed strain loops. Thus, with each cycle an irreversible deformation remains in the soil. The extent of accumulation of residual settlements depends on the loading of the foundation (average load, load amplitude) and on the current state of the soil. In the case of non-cohesive soils especially the soil density and the fabric of the grain skeleton are of importance. Even small amplitudes can cause significant settlements if the number of cycles is high (e.g. $N > 10^3$, so-called *poly-* or *high-cyclic* loading).

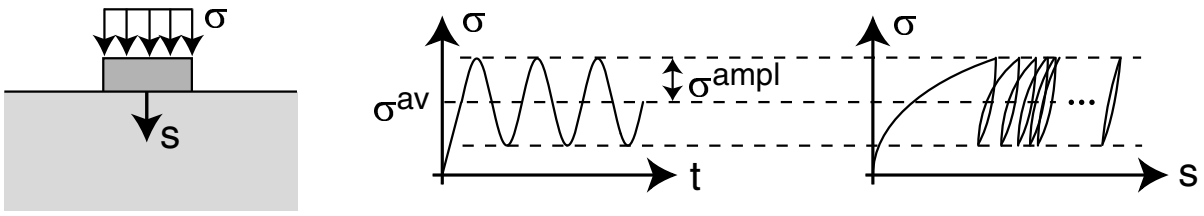

Figure 1.1: *Settlements of a foundation under cyclic loading*

A cyclic loading of a foundation may be caused by crossing vehicles (e.g. railways, magnetic levitation trains, cars, crane rails), by wind (e.g. wind power plants on-shore as well as off-shore), by waves (e.g. coastal structures), by changing water levels or fillings (e.g. watergates, tanks, silos) or rotating unbalances (e.g. machine foundations). The cyclic loading can be of a deterministic or a random nature. Also the installation of sheet pile

walls or piles using vibratory drivers leads to a cyclic shearing of the surrounding soil. Some densification techniques (deep vibratory compaction, vibratory compaction at the soil surface) make use of cyclic loading in order to improve the mechanical properties of the soil (shear strength, stiffness, liquefaction resistance).

The residual deformations due to cyclic loading concentrate much stronger in the vicinity of the foundation than those due to monotonic loading (see Section 8.4). Thus, there are larger differential settlements, due to the spatial fluctuation of the state variables, occuring for cyclic loading than for monotonic loading.

In the literature, one may find several reports on damages in buildings in connection with cyclic loading of their foundations. Damages in structures (bridge, hall, apartment houses) near railways due to differential settlements were documented e.g. by Heller [47]. The non-uniform deformations of the sandy subsoil induced by cyclic loading led to cracks in walls and ceilings. Due to the damages parts of the hall even had to be teared down. Some years later Heller [48] reported on settlements of foundations on sand below the piers of a crane rail (Figure 1.2). After a few years of operation differential settlements resulted in a tilting of the crane rail. They could be attributed to the non-uniform loading of the piers due to the running of the trolley. Wolffersdorff & Schwab [173] described damages at the concrete structure of watergate "Uelzen I" (waterway "Elbe-Seitenkanal") due to a large number of operations. The watergate had to be repaired several times, because the soil-structure interaction under cyclic loading with large deformations was not sufficiently taken into account during the design. On settlements of oil and water storage tanks and silos on predominantly non-cohesive soils under cyclic loading was reported by Sweeney & Lambson [155]. They summarized measurements of several authors. After a small number of cycles ($N < 100$) the residual settlement reached twice the settlement after the first filling (Figure 1.3). The tanks suffered no damage since the settlements were uniform. Problems concerning connection pipes could arise from differential settlements, e.g. if a group of tanks is unequally used.

It is desirable to estimate the settlements and differential settlements of a cyclically loaded foundation already during the design phase. If tolerances for the differential settlements were exceeded, counteractive measures (e.g. change of the foundation or soil improvement) could be applied. For this purpose simple engineering models using laboratory tests and settlement laws of the shape $s(N, ...)$, based on small-scale 1g-model tests and centrifuge model tests, were developed. However, their application is restricted to simple foundation geometries. More complex boundary value problems with cyclic loading can be studied numerically by means of the finite element method (FEM). The so-called *implicit* method, wherein each cycle is calculated with a $\dot{\boldsymbol{\sigma}}$-$\dot{\boldsymbol{\varepsilon}}$ constitutive model and many strain increments, is not applicable for a number of cycles $N > 50$ because of the accumulation of numerical

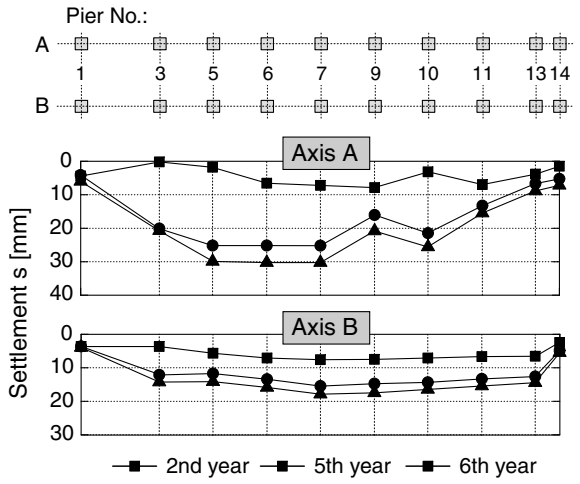

Figure 1.2: *Differential settlements of single foundations under the columns of a crane rail during six years of operation, after Heller [48]*

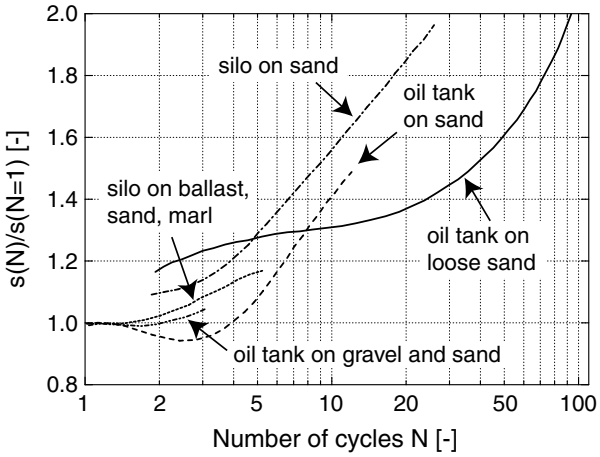

Figure 1.3: *Settlements of storage tanks and silos due to repeated filling and emptying, after Sweeney & Lambson [155]*

errors and the huge calculation effort. In this case the so-called *explicit* method is superior to the *implicit* one. An explicit model treats the accumulation of residual strains under cyclic loading similar to the problem of creep under constant loads.

In the literature one may find several explicit models, which are summarized and discussed in Chapter 6. Most of these models describe the material behaviour in a very simplified manner, i.e. they ignore important influences (e.g. the influence of the shape of the stress or strain loop or the average stress) or they describe only a portion of accumulation (e.g. only the volumetric one). Some models were developed for special cases only, e.g. for an isotropic stress superposed by uniaxial vertical stress cycles.

The experimental basis of many explicit models is thin. Most studies with drained cyclic laboratory tests are restricted to the examination of a few influencing parameters (e.g. only the strain amplitude and the void ratio are varied) or only a single effect of cyclic loading (e.g. the flow rule or the volumetric portion of accumulation) is studied.

The aim of this work was the development and inspection of an explicit accumulation model (so-called "Bochum accumulation model") for the FE-prognosis of residual settlements in non-cohesive soils under cyclic loading. This model should describe the evolution of the full strain tensor (i.e. the evolution of the volumetric as well as of the deviatoric portion) and should consider all essential influencing parameters. An extensive laboratory program with drained cyclic tests was planned to serve as the basis of the model. All influencing parameters should be studied on a single sand. With the accumulation model

shallow foundations and piles under cyclic loading had to be analyzed using FE calculations. Special attention was payed to the problem of the determination of the initial fabric of the grain skeleton or the cyclic loading history (so-called "*cyclic preloading*" or "*historiotropy*") in situ.

1.2 Strain vs. stress accumulation

Within this work the term "accumulation" is used in such way that it can stand for an increase as well as a decrease of the value of a variable. The above-mentioned accumulation of strain in the case of (nearly) closed stress loops (Figure 1.4a) is a special case of the *accumulation* phenomenon under cyclic loading. The stress-controlled drained cyclic triaxial test conforms with this case. Depending on the boundary conditions a cyclic loading can lead to residual strains and/or a change of stress. If the strain loops are closed, the material reacts with not perfectly closed stress loops (Figure 1.4b) and thus the stress accumulates, which mostly manifests itself in relaxation. An example is the displacement-controlled undrained cyclic triaxial test on fully water-saturated specimens (deformation with constant volume). Also a simultaneous accumulation of stress and strain is possible (Figure 1.4c). This material response is obtained e.g. in an undrained cyclic triaxial test on fully water-saturated specimens with a control of the deviatoric stress.

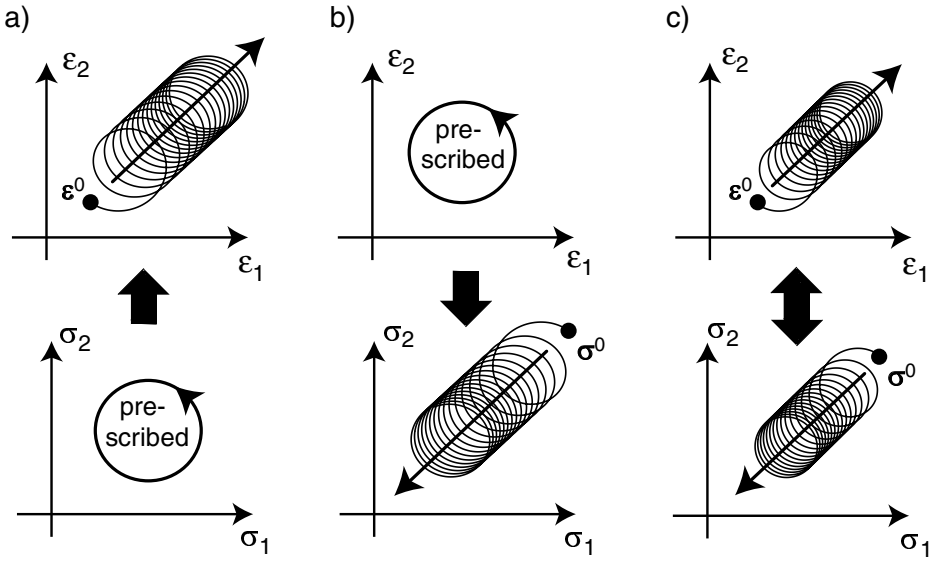

Figure 1.4: *Accumulation of stress or strain, illustrated for the two-dimensional case*

The accumulation of stress under cyclic loading is important e.g. in the case of fully water-saturated soils and poor or insufficient drainage conditions (e.g. if the permeability is small and the loading frequency is high). In this case the cyclic shearing does not lead to compaction but to a build-up of excess pore water pressures u. These excess pore water pressures cause a reduction of the effective stress $\sigma' = \sigma - u$ (at konstant total stress σ) and thus a decrease of shear strength and stiffness. In the case $\sigma = u$, i.e. $\sigma' = 0$ the soil looses any shear strength and "liquefies". In dependence on the amount of the accumulated excess pore water pressures the serviceability or even the load capacity of a foundation may be endangered. The described problem is of importance e.g. for coastal or off-shore structures. Also in the case of earthquakes seismic shear waves cause a cyclic loading of the soil and thus often a build-up of excess pore water pressures. However, in that case in contrast to the examples given above, the number of cycles is low (usually $N < 20$) and the strain amplitudes are large ($\varepsilon^{\mathrm{ampl}} > 10^{-3}$).

The accumulation model presented in Chapter 7 predicts strain or stress accumulation depending on the boundary conditions.

1.3 Quasi-static vs. dynamic loading

If the cycles are applied with a low loading frequency f_B, the inertia forces are not considered or are negligible and it is spoken of a *quasi-static* cyclic loading. If the loading frequency is large, inertia forces are relevant and the loading is *dynamic*. The border between quasi-static and dynamic loading depends also on the amplitude of the cycles. A harmonic excitation with the displacement $u = u^{\mathrm{ampl}} \cos(\omega t)$ and the acceleration $\ddot{u} = -u^{\mathrm{ampl}} \omega^2 \cos(\omega t)$ is quasi-static, if $u^{\mathrm{ampl}} \omega^2 \ll g$ holds with g being the acceleration of gravity. Often this amplitude dependence is ignored and the border between quasi-static and dynamic loading is said to lay at $f_B \approx 5$ Hz. At a certain strain amplitude tests up to $f_B = 30$ Hz in the literature (Section 3.2.2.8) and also the own tests (Section 5.2.5) showed no influence of the loading frequency f_B on the secant stiffness (elastic portion of strain) and on the accumulation rate of residual strain. The accumulation model presented in Chapter 7 uses the strain amplitude as a basic variable. The strain amplitude is evaluated from the strain loop within a cycle. For the model it is irrelevant if this strain loop results from quasi-static or dynamic loading. The explicit model is thus applicable independently of the loading frequency. Therefore, in the following a distinction between quasi-static and dynamic loading is set beside and the general denotation *cyclic* loading is used.

1.4 Explicit vs. implicit method

In FE calculations of the accumulation due to cyclic loading two different numerical strategies can be considered: the *implicit* and the *explicit* method.

In the implicit procedure each cycle is calculated with a $\dot{\boldsymbol{\sigma}}$-$\dot{\boldsymbol{\varepsilon}}$ constitutive model. The accumulation results as a by-product due to the not perfectly closed stress or strain loops. Elastoplastic multi-surface models (Mróz et al. [97], Chaboche [18, 19]), endochronic models (Valanis & Fee [170]) or the hypoplastic model with intergranular strain (Kolymbas [78], Gudehus [38], von Wolffersdorff [172], Niemunis & Herle [106]) can be used. The applicability of the implicit method is restricted to a low number of cycles ($N < 50$) because with each increment an accumulation of systematic errors of the constitutive model or the integration scheme takes place (Niemunis [104]). Even small errors accumulate significantly (e.g. with a factor 10^6, if 10^4 cycles are calculated each with 100 increments). Thus, a constitutive model of an unreachable perfection would be necessary. Also the large calculation effort sets boundaries to the application of the implicit method. Wolffersdorff & Schwab [173] had to restrict their implicit FE calculation of watergate "Uelzen I" to less than 25 cycles.

For high-cyclic loading in general *explicit* models are the better choice. They treat the process of accumulation under cyclic loading similar to a process governed by viscosity. The number of cycles N replaces the time t. First, two cycles are calculated *implicitly* with strain increments (Figure 1.5) using a $\dot{\boldsymbol{\sigma}}$-$\dot{\boldsymbol{\varepsilon}}$ constitutive model (e.g. the hypoplastic model with intergranular strain as in this work). This implicit calculation can be performed quasi-static or dynamic. During the second cycle in each integration point the strain loop is recorded as a series of discrete strain points. The recording follows some predefined criteria (e.g. a change of the direction of the strain path and a minimum distance to the last recorded point). The strain amplitude $\varepsilon^{\mathrm{ampl}}$ is determined from this strain loop (see Figure 1.5 and the definition in Section 7.2.1). The first cycle is not suitable for the determination of $\varepsilon^{\mathrm{ampl}}$, since the deformations in the first cycle can significantly differ from those in the subsequent cycles (Figure 1.5, the first quarter of the first cycle up to the maximum load is a first loading). The amplitude of the second cycle is more representative for the amplitudes in the following cycles.

The accumulation starting from the second cycle is calculated directly by means of an equation of the shape

$$\mathring{\mathbf{T}} = \mathsf{E} : (\mathbf{D} - \mathbf{D}^{\mathrm{acc}}) \tag{1.1}$$

($\mathring{\mathbf{T}}$: Jaumann stress rate, $\mathbf{D}$: strain rate, $\mathbf{D}^{\mathrm{acc}}$: given accumulation rate, E: elastic stiffness), without following the strain path during the particular cycles, i.e. Equation (1.1)

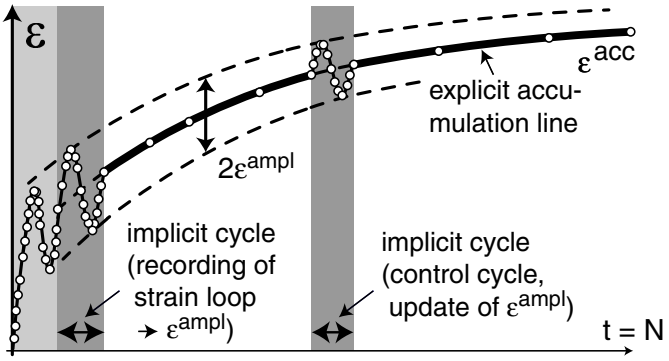

Figure 1.5: *Procedure of a explicit calculation of accumulation*

delivers the increment of residual strain or of stress due to a package of ΔN (e.g. 20) cycles directly. Depending on the boundary conditions Equation (1.1) leads to an accumulation of stress (e.g. $\mathring{\mathbf{T}} = -\mathsf{E} : \mathbf{D}^{\mathrm{acc}}$ at $\mathbf{D} = \mathbf{0}$) and/or strain ($\mathbf{D} = \mathbf{D}^{\mathrm{acc}}$ at $\mathring{\mathbf{T}} = \mathbf{0}$). In the case $\mathring{\mathbf{T}} = \mathbf{0}$ the strain follows the average accumulation curve $\boldsymbol{\varepsilon}^{\mathrm{acc}}(N)$ given in Figure 1.5.

For this explicit calculation the strain amplitude $\varepsilon^{\mathrm{ampl}}$ is assumed constant. Due to a compaction and a re-distribution of stress the stiffness and thus the strain amplitude may change. The explicit calculation can be interrupted after definite numbers of cycles and $\varepsilon^{\mathrm{ampl}}$ can be updated in an implicit so-called *control cycle* (Figure 1.5). In a control cycle also the static admissibility of the state of stress and the overall stability can be checked. The latter one can get lost e.g. in the undrained case due to excess pore water pressures.

1.5 Outline of this thesis

In Chapter 2 the essential definitions used within this thesis are summarized.

Chapter 3 gives an overview about experimental studies on non-cohesive soils in the literature. First different methods to study cyclic loading and varying types of laboratory tests are mentioned. Then the influence of several parameters on the residual strains is discussed. Also the main dependencies of the hysteretic stiffness are summarized. In the following model tests and settlement laws for shallow foundations and piles are reviewed.

In Chapter 4 the testing devices used in this work (cyclic triaxial device, cyclic multi-dimensional simple shear device, resonant column device, triaxial cell with piezoelectric elements) are introduced. The characteristics of the tested grain size distributions and the material behaviour under monotonic loading (drained and undrained monotonic triaxial

tests, oedometric compression tests) are presented. The problem of membrane penetration in the case of a cyclic variation of the cell pressure σ_3 is discussed.

Chapter 5 presents the results of the cyclic laboratory tests. Different amplitudes (the span, shape and polarization were varied), average stresses (the average mean pressure p^{av} and the average stress ratio $\eta^{av} = q^{av}/p^{av}$ were varied), initial void ratios, loading frequencies, monotonic preloadings and grain size distribution curves were tested. Also changes of the direction of cyclic shearing and of the amplitude (packages of cycles) were studied. In Section 5.1 the test results are analyzed concerning the direction of accumulation ("flow rule", ratio of the volumetric and the deviatoric accumulation rate). In Section 5.2 they are discussed with respect to the intensity of accumulation. The own test results are compared to those documented in the literature.

Chapter 6 presents several explicit accumulation models in the literature and discusses their advantages and deficits. The need for a more general model, which considers all influencing parameters, is emphasised.

The explicit accumulation model developed on the basis of the laboratory tests is presented in Chapter 7. Several elements of the model are discussed in detail. The explanation of the tensorial amplitude definition and a new state variable for considering polarization changes is restricted to the two-dimensional case. The full tensor notation of the model is given in Appendix III. The accumulation model is validated by the re-calculation of element tests. In Chapter 7 also a description of the hypoplastic model with intergranular strain is given. This model was used in the implicit calculation steps. Its performance (deformations under monotonic loading, strain amplitudes) is discussed.

In Chapter 8 first the re-calculation of a centrifuge model test from the literature with a cyclically loaded strip foundation is presented. Then, parameter studies of shallow foundations under cyclic loading are shown. The state variables of the soil, the foundation geometry and the loading was varied. Also some technical aspects of FE calculations with an explicit accumulation model are addressed. Finally, FE calculations of a pile cyclically loaded in the axial direction and other applications of the accumulation model are presented.

In Chapter 9 the issue is broached to the determination of the initial fabric of the soil skeleton or the historiotropy (cyclic preloading), respectively of the in situ soil. A correlation of the historiotropy with both the dynamic soil properties and the so-called "liquefaction resistance" was studied in laboratory tests. Possible alternative methods for the determination of the historiotropy are mentioned.

Finally, in Chapter 10 the main results of this work are summarized and an outlook on further research activities is given.

Chapter 2

Definitions

The notation of scalar and tensorial quantities used in this thesis is given in Appendix I. In Chapter 7, presenting the description of the explicit accumulation model, the sign convention of mechanics (tension stress and elongation are positive) is used. In all other chapters the sign convention of soil mechanics (compression stress and compression strain are positive) is applied. This choice has been made since most publications on experiments use the sign convention of soil mechanics whereas in the literature on constitutive modelling the sign convention of mechanics is commonly adopted. In this chapter the definitions are introduced for the case of an axisymmetric loading. The tensorial generalization is given in Appendix II.

2.1 Stress

The effective state of stress at a point in the three-dimensional space is described by the Cauchy stress tensor $\boldsymbol{\sigma}$. The axial stress component is denoted by σ_1 and the lateral one by $\sigma_2 = \sigma_3$ (Figure 2.1). With the exception of the sections 4.3.3, 4.4 and 9.2 the designation of effective stress components by a superposed $\sqcup'$ is set beside (in the respective sections the deviating notation is explicitly mentioned). The Roscoe invariants p (mean pressure) and q (deviatoric stress) are used as well as the Lode angle θ:

$$p = \frac{1}{3}\ (\sigma_1 + 2\ \sigma_3) \tag{2.1}$$

$$q = \sigma_1 - \sigma_3 \tag{2.2}$$

$$\theta = \frac{1}{3}\ \arccos\left(-\frac{3\sqrt{3}J_3}{2{J_2}^{3/2}}\right) \tag{2.3}$$

In Equation (2.3) J_2 and J_3 are basic invariants of the stress deviator (see also Appendix II). An alternative to p and q are the so-called "isomorphic" variables

$$P \;=\; \sqrt{3}\,p \quad \text{and} \quad Q \;=\; \sqrt{2/3}\,q. \tag{2.4}$$

Using isomorphic variables two vectors, which are orthogonal to each other in the three-dimensional σ_1-σ_2-σ_3-principal stress coordinate system, preserve their orthogonality in the P-Q-plane. This does not apply to the p-q-coordinate system (Niemunis [105]).

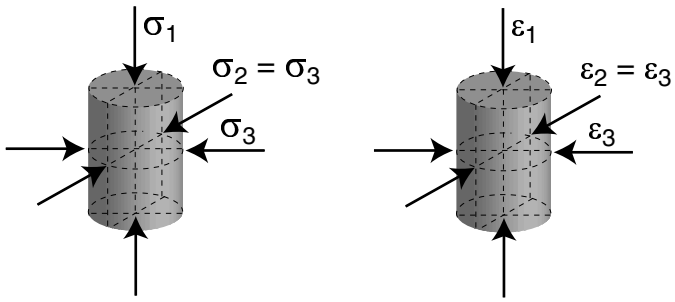

Figure 2.1: *Definiton of stress and strain components in the triaxial test*

In the p-q-plane the state of stress (Figure 2.2) can be described by the stress ratio

$$\eta \;=\; q/p \tag{2.5}$$

or alternatively by $\bar{Y}$:

$$\bar{Y} \;=\; \frac{Y - Y_i}{Y_c - Y_i} \;=\; \frac{Y - 9}{Y_c - 9} \quad , \quad Y \;=\; -\frac{I_1 I_2}{I_3} \quad , \quad Y_c \;=\; \frac{9 - \sin^2\varphi_c}{1 - \sin^2\varphi_c} \tag{2.6}$$

The function Y of Matsuoka & Nakai [95] is related to η as follows:

$$Y \;=\; \frac{27(3+\eta)}{(3+2\eta)(3-\eta)} \quad , \quad \eta \;=\; \frac{3Y-27}{4Y} \pm \sqrt{\left(\frac{3Y-27}{4Y}\right)^2 + \frac{9Y-81}{2Y}} \tag{2.7}$$

The I_i in Equation (2.6) are the basic invariants of the stress $\boldsymbol{\sigma}$ (see also Appendix II). In Equation (2.6), φ_c is the critical friction angle (critical state = progressive deformation without change of stress and volume). The state variable $\bar{Y}$ takes the value 0 for isotropic stresses ($\eta = 0$, $Y = Y_i = 9$) and is 1 for a critical stress ratio ($\eta = M_c(\varphi_c)$ or $\eta = M_e(\varphi_c)$, $Y = Y_c$). The inclinations M_c and M_e of the borderlines in the p-q-plane (Figure 2.2) can be calculated from:

$$M_c \;=\; \frac{6\,\sin\varphi}{3-\sin\varphi} \quad \text{and} \quad M_e \;=\; -\frac{6\,\sin\varphi}{3+\sin\varphi}. \tag{2.8}$$

Therein $\varphi = \varphi_c$ has to be chosen for the critical state line (CSL) and $\varphi = \varphi_p$ for the maximum shear strength (φ_p = peak friction angle). The inclinations in the P-Q-plane are $M_{cPQ} = 2/\sqrt{18}\ M_c$ and $M_{ePQ} = 2/\sqrt{18}\ M_e$. In the triaxial case the stress ratios $K = \sigma_3/\sigma_1$ and η are connected via

$$\eta \;=\; \frac{3(1-K)}{2K+1} \tag{2.9}$$

For $K = 0.5$ one obtains $\eta = 0.75$ and $\bar{Y} = 0.341$.

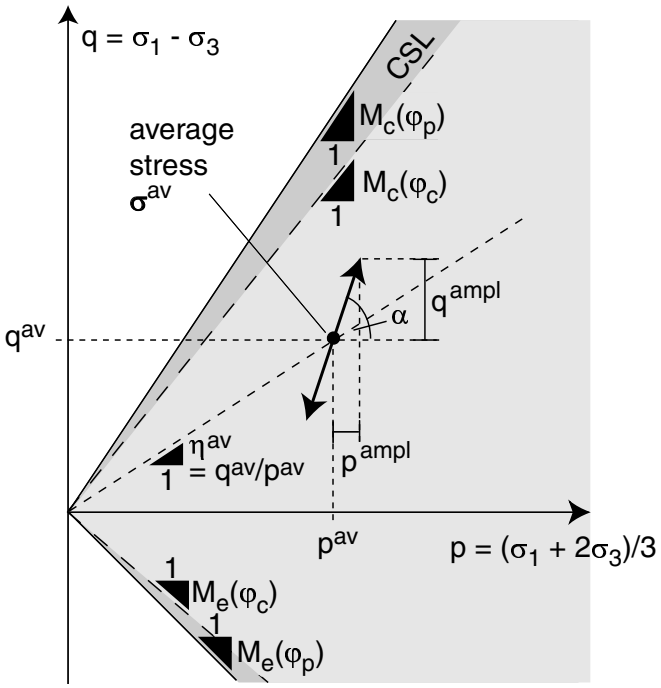

Figure 2.2: *Cyclic stress path in the p-q-plane*

Figure 2.2 shows a stress path in the p-q-plane, which is typical for a cyclic triaxial test. An average stress $\boldsymbol{\sigma}^{\mathrm{av}}$ (described by p^{av} and q^{av} or η^{av} or $\bar{Y}^{\mathrm{av}}$) is superposed by a cyclic portion. An oscillation of the axial and the lateral stresses $\sigma_1(t)$ and $\sigma_3(t)$ without a phase-shift in time (*in-phase*-cycles, see Section 2.4) results in stress cycles along a straight line with a certain inclination $\tan\alpha = q^{\mathrm{ampl}}/p^{\mathrm{ampl}}$ in the p-q-plane (Figure 2.2). For the special case of constant lateral stresses ($\sigma_3^{\mathrm{ampl}} = 0$) $\tan\alpha = 3$ holds and the amplitude ratio

$$\zeta \;=\; \frac{\sigma_1^{\mathrm{ampl}}}{p^{\mathrm{av}}} \;=\; \frac{q^{\mathrm{ampl}}}{p^{\mathrm{av}}} \tag{2.10}$$

is used. More complex stress paths, e.g. ellipses in the p-q-plane, can be tested, if the stress components $\sigma_1(t)$ and $\sigma_3(t)$ are applied with a phase-shift in time (*out-of-phase*-cycles, see Section 2.4).

2.2 Strain

The definitions are explained for the strain $\boldsymbol{\varepsilon}$, although they are also valid for its rate $\dot{\boldsymbol{\varepsilon}}$ In the context of cyclic loading "rate" means a derivative with respect to the number of cycles N, i.e. $\dot{\sqcup} = \partial \sqcup / \partial N$ instead of $\dot{\sqcup} = \partial \sqcup / \partial t$ (in which the discrete number of cycles N is treated as a "smoothed" continuous variable). The strain in the axial direction is denoted with ε_1 and the one in the lateral direction with $\varepsilon_2 = \varepsilon_3$. The strain invariants

$$\varepsilon_v = \varepsilon_1 + 2\,\varepsilon_3 \tag{2.11}$$

$$\varepsilon_q = \frac{2}{3}\,(\varepsilon_1 - \varepsilon_3) \tag{2.12}$$

are used. The rates of the volumetric strain $\dot{\varepsilon}_v$ and the deviatoric strain $\dot{\varepsilon}_q$ are work-conjugated to the Roscoe invariants p and q. The isomorphic strain invariants are

$$\varepsilon_P = 1/\sqrt{3}\,\varepsilon_v \quad \text{and} \quad \varepsilon_Q = \sqrt{3/2}\,\varepsilon_q. \tag{2.13}$$

The total strain is

$$\varepsilon = \sqrt{(\varepsilon_1)^2 + 2(\varepsilon_3)^2} = \sqrt{(\varepsilon_P)^2 + (\varepsilon_Q)^2}. \tag{2.14}$$

As an alternative to ε_q the shear strain

$$\gamma = \varepsilon_1 - \varepsilon_3 \tag{2.15}$$

is used. In the case of cyclic loading the strain $\boldsymbol{\varepsilon}$ is composed of an accumulated, residual portion ($\boldsymbol{\varepsilon}^{\mathrm{acc}}$) and an elastic, resilient portion ($\boldsymbol{\varepsilon}^{\mathrm{ampl}}$). In Figure 2.3 this is illustrated for the total strain ε. The rate of strain accumulation $\dot{\boldsymbol{\varepsilon}}^{\mathrm{acc}}$ can be completely described by the rate of the total strain $\dot{\varepsilon}^{\mathrm{acc}}$ ("intensity of accumulation") and the ratio of the rates of the volumetric and the deviatoric strain ("direction of accumulation, flow rule")

$$\Omega = \frac{\dot{\varepsilon}_v^{\mathrm{acc}}}{\dot{\varepsilon}_q^{\mathrm{acc}}} \quad , \quad \omega = \frac{\varepsilon_v^{\mathrm{acc}}}{\varepsilon_q^{\mathrm{acc}}} \tag{2.16}$$

In the case of *in-phase*-cycles (Section 2.4) the strain amplitude can be described by the amplitude of the total strain $\varepsilon^{\mathrm{ampl}}$ or by the volumetric and deviatoric components $\varepsilon_v^{\mathrm{ampl}}$ and $\varepsilon_q^{\mathrm{ampl}}$, respectively. The shear strain amplitude γ^{ampl} can be used as an alternative to $\varepsilon_q^{\mathrm{ampl}}$. For strain loops, which enclose some strain space (*out-of-phase*-cycles, e.g. due to elliptic stress loops in the p-q-plane), a more complex amplitude definition is needed. Such a definition is explained in Section 7.2.1.

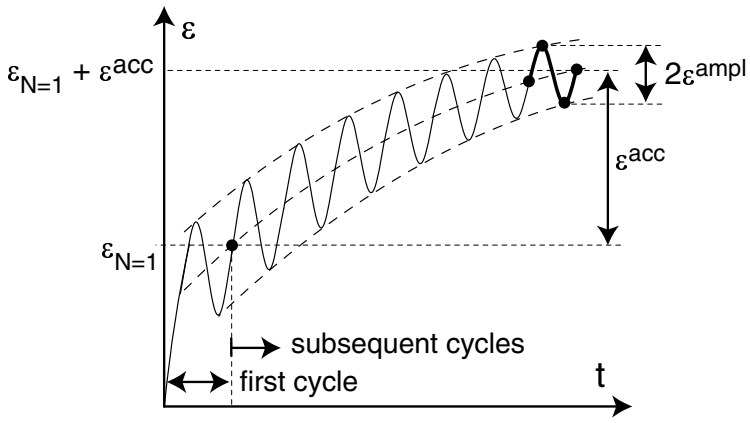

Figure 2.3: *Evolution of total strain ε in a cyclic triaxial test*

2.3 Pore volume

The magnitude of pore volume is described by the void ratio e or the porosity n. The density index I_D is calculated from the void ratios $e_{\min}$ and $e_{\max}$ or the dry densities $\varrho_{d,\max}$ and $\varrho_{d,\min}$ in the densest and loosest condition of the grain skeleton (determined according to DIN 18126) and void ratio e or dry density ϱ_d as follows:

$$I_D = \frac{e_{\max} - e}{e_{\max} - e_{\min}} = \frac{\varrho_{d,\max}}{\varrho_d} D_r = \frac{\varrho_{d,\max}}{\varrho_d} \frac{\varrho_d - \varrho_{d,\min}}{\varrho_{d,\max} - \varrho_{d,\min}} \tag{2.17}$$

The initial value of the density index at the beginning of a test is denoted by I_{D0}. Alternatively, the relative density D_r is often used in the literature.

2.4 Shape of the cycles

It is distinguished between so-called *in-phase (IP)* and *out-of-phase (OOP)* - cycles. The definitions are explained by means of the strain $\boldsymbol{\varepsilon}$ (Figure 2.4).

In the case of IP-cycles all components of $\boldsymbol{\varepsilon}$ oscillate with the same scalar, periodical function $-1 \leq f(t) \leq 1$ in the time t (e.g. $f(t) = \sin(t)$), i.e. $\boldsymbol{\varepsilon} = \boldsymbol{\varepsilon}^{\mathrm{av}} + \boldsymbol{\varepsilon}^{\mathrm{ampl}} f(t)$. These cycles are also addressed as "one-dimensional". A special case of the IP-cycles are the *uniaxial* cycles (Figure 2.4a), where only one component varies with time, e.g.:

$$\boldsymbol{\varepsilon} = \boldsymbol{\varepsilon}^{\mathrm{av}} + \begin{pmatrix} \varepsilon_1^{\mathrm{ampl}} & & \\ & 0 & \\ & & 0 \end{pmatrix} f(t) \tag{2.18}$$

In all other cases one speaks of *multiaxial* IP-cycles (Figure 2.4b):

$$\boldsymbol{\varepsilon} = \boldsymbol{\varepsilon}^{\mathrm{av}} + \begin{pmatrix} \varepsilon_1^{\mathrm{ampl}} & & \\ & \varepsilon_3^{\mathrm{ampl}} & \\ & & \varepsilon_3^{\mathrm{ampl}} \end{pmatrix} f(t) \tag{2.19}$$

In the case of OOP-cycles (Figure 2.4c) the components oscillate with a phase-shift θ in time:

$$\boldsymbol{\varepsilon} = \boldsymbol{\varepsilon}^{\mathrm{av}} + \begin{pmatrix} \varepsilon_1^{\mathrm{ampl}}\, f(t) & & \\ & \varepsilon_3^{\mathrm{ampl}}\, f(t+\theta) & \\ & & \varepsilon_3^{\mathrm{ampl}}\, f(t+\theta) \end{pmatrix} \tag{2.20}$$

In the cyclic triaxial test with $\sigma_3 =$ constant uniaxial IP-stress cycles are applied, because only the axial component σ_1 varies with time. If $\sigma_3 \neq$ constant and σ_1 and σ_3 oscillate without a phase-shift multiaxial IP-stress cycles are obtained. An oscillation *with* a phase-shift results in OOP-stress cycles.

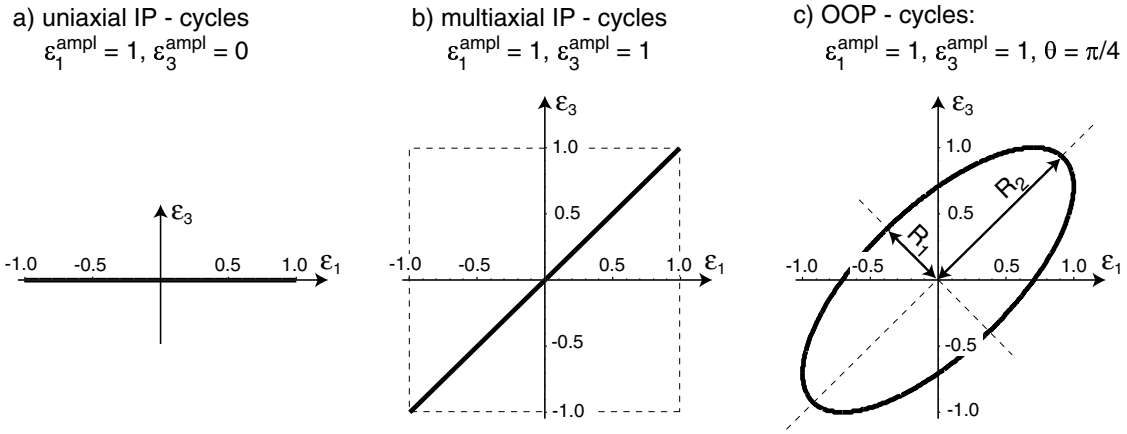

Figure 2.4: *Distinction between uniaxial IP-, multiaxial IP- and OOP-cycles*

Chapter 3

State of the art: element and model tests with cyclic loading

3.1 General remarks

The behaviour of soil or foundations under cyclic loading was studied in different ways:

- element tests in the laboratory
- small-scale model tests
- model tests with increased gravitation (in particular centrifuge model tests)
- large-scale model tests
- in-situ tests and measurements at real buildings

In element tests with cyclic loading the residual and the elastic (secant stiffness of the stress-strain-hysteresis) portions of deformation were studied. Different types of test devices were used. They are illustrated in Figure 3.1:

a) triaxial test on cylindrical specimens

b) true triaxial test on cubical specimens

c) torsional shear test on hollow cylinder specimens

d) simple shear test

e) direct shear test

f) shaking table test

g) resonant column test

h) measurement of wave velocities in specimens by means of piezoelectric elements

In most test devices two types of control are possible: a control of the stresses (or loads) induced at the specimen boundaries on one hand and a control of the boundary displacements on the other hand. The tests are briefly explained for a stress control in the following.

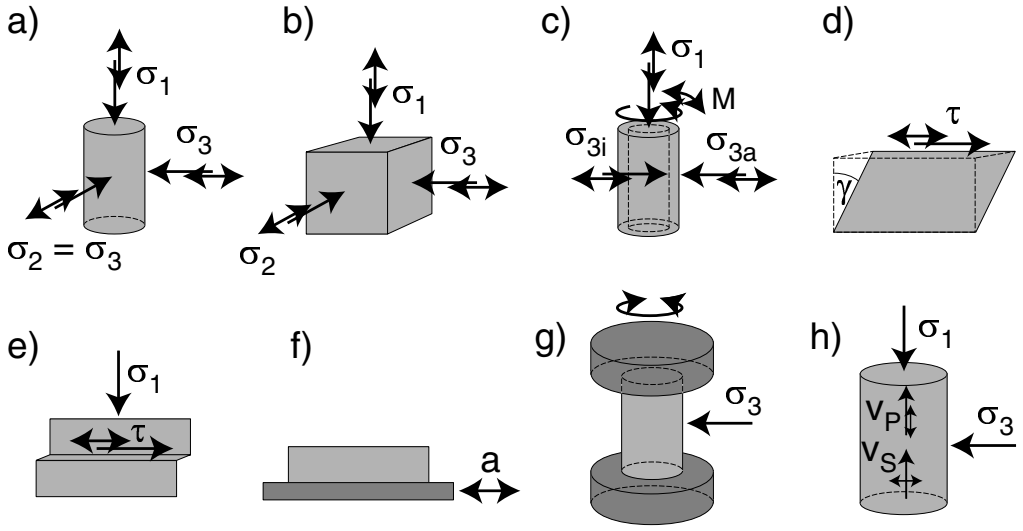

Figure 3.1: *Types of laboratory tests for the material behaviour under cyclic loading*

In most triaxial tests on cylindrical specimens (Figure 3.1a), the axial stress σ_1 is cyclically varied, whereas the lateral stress $\sigma_2 = \sigma_3$ is kept constant. Therefore, only uniaxial stress cycles with an inclination of 1:3 in the p-q-plane are tested. Sometimes also σ_3 is oscillating (see e.g. Sections 5.2.1.3 and 5.2.1.4 of this thesis) and therefore different inclinations of the stress cycles and elliptic cycles in the p-q-plane can be studied. The triaxial devices used in this work are discussed in Section 4.1.1.

The stress cycles in the triaxial test on cylindrical specimens are at most two-dimensional since in the σ_1-σ_2-σ_3-principal stress space they lay within a plane. Three-dimensional stress cycles can be tested in a true triaxial test (Figure 3.1b, cyclic variation of all three principal stresses) and in the torsional shear test on hollow cylinder specimens (Figure 3.1c, cyclic variation of inner pressure σ_{3i}, outer pressure σ_{3a}, axial stress σ_1 and torsional moment M).

In a simple shear test (Figure 3.1d) a shear stress or a displacement is induced at the upper boundary and the lateral boundaries are forced to a linear displacement over the

specimen height. The lateral stresses are rarely measured. Thus, the accumulation of stress in the horizontal direction caused by cyclic loading is not known. The problem of the inhomogeneous stress and strain fields within a specimen in a simple shear test is addressed in Section 4.1.2. Simple shear devices can be modified in order to allow a circular cyclic shearing. Such a device was used within this work. It is presented in Section 4.1.2.

In contrary to the triaxial test, a shear band in a direct shear device (Figure 3.1e) cannot freely develop. Due to the mutual shearing of the upper and the lower half of the specimen, its location is enforced near the middle of the specimen. The applicability of this type of test for studies of the material behaviour under cyclic loading is limited. Direct shear tests were used to examine changes of the granulometry in the shear band during cyclic loading (Helm et al. [49]). This type of test was also chosen to study the contact between soil and foundation under cyclic loading (z.B. Malkus [92]).

Shaking table tests (Bild 3.1f) are applied in "liquefaction" studies of sand layers under earthquake loading. At the base of the shaking table definite accelerations are induced. In some studies several shaking tables were mounted in orthogonal directions onto each other. In this case a multidimensional cyclic loading could be tested (Section 3.2.2.5).

Resonant Column (RC) tests (Figure 3.1g) were rarely used to study residual deformations (e.g. for the determination of the so-called threshold shear strain, see Vucetic [174] or own tests in [180]). Their main field of application is the determination of the secant stiffness of the stress-strain-hysteresis. The strain amplitudes measured in the RC device are mostly smaller than those in the cyclic triaxial tests (Figure 3.2). The system of the RC test consists of a cylindrical specimen, the base mass and the top mass. In dependence of the bearing of these masses the RC devices are further distinguished (e.g. type "fixed-free" for a fixed support at the base and a freely movable top mass). The system is dynamically excited by a torsional moment (frequencies $f > 20$ Hz). The secant shear stiffness is determined from the resonant frequency of the system. Some RC devices allow for an excitation of the specimens in the axial direction. In that case secant Young moduli in the axial direction can be measured. Also the material damping can be obtained from RC tests. The RC device used in this work (type "free-free') is explained in detail in Section 4.1.3.

Compression or shear waves generated by piezoelectric elements propagate with strain amplitudes $< 10^{-6}$ within a soil specimen. The secant stiffness at small strains (= dynamic stiffness) can be calculated from the wave velocities (Section 3.3). In the range of very small strain amplitudes the measurement of wave velocities in soil specimens is thus an alternative to RC tests. A testing device with piezoelectric elements and the measurement

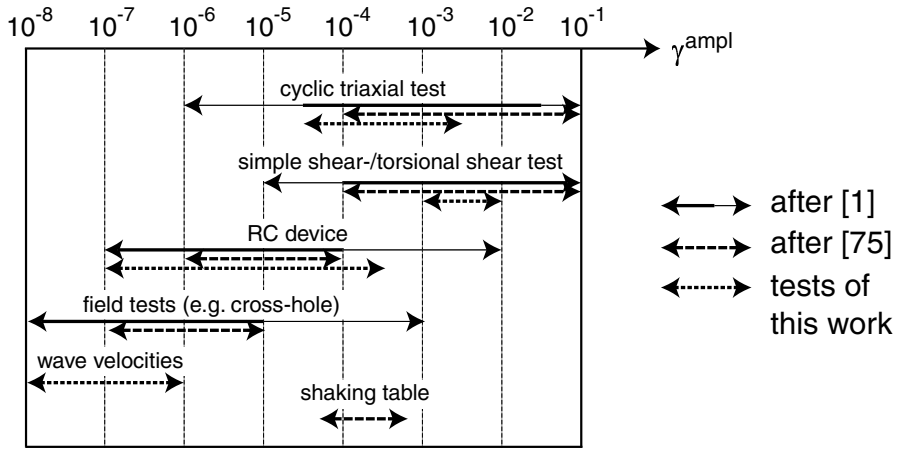

Figure 3.2: *Typical ranges of shear strain amplitude γ^{ampl} for different types of tests*

of wave velocities are discussed in Section 4.1.4.

Beside the type of the test device and the type of control (load, displacement), the tests can be further distinguished concerning the drainage conditions (fully drained, partly drained, undrained) and the frequency of loading (quasi-static, dynamic). In shaking table tests, RC tests and measurements of the wave velocities the excitation is per se dynamic.

The following Section 3.2 gives an overview about element tests with cyclic loading in the literature. It summarizes their essential results concerning the residual deformations (direction and intensity of accumulation). With respect to the intensity of accumulation the following influences or parameters are discussed:

- number of cycles
- strain or stress amplitude
- polarization (direction) of the cycles
- polarization changes
- shape of the cycles
- average stress
- void ratio / relative density
- loading frequency
- fabric of the grain skeleton / historiotropy (cyclic preloading)
- random cyclic loading / packages of cycles
- grain size distribution curve

If possible the influencing parameters are discussed using drained tests. However, there is much more literature on undrained tests, because a substantial research was done on this theme in regions with a frequent occurrence of earthquakes. Furthermore, some influencing parameters were studied solely in undrained tests. Thus, in the following also results of undrained cyclic tests are reported.

The literature on experimental work concerning the elastic portion of strain (secant stiffness of the stress-strain-loop) under cyclic loading is not less voluminous. Mostly RC tests or measurements of wave velocities in soil specimens were performed. This thesis concentrates on the residual deformations. However, they cannot be discussed separately from the elastic portion of strain. Section 3.3 therefore summarizes some fundamental dependencies of the secant stiffness on several parameters. These dependencies are necessary for the interpretation of the own test results in Chapter 5.

In the literature shallow foundations and piles under cyclic loading were tested. Section 3.4 summarizes model and in-situ tests. The derived settlement laws and engineering models are presented. While Section 3.4.1 deals with shallow foundations, Section 3.4.2 addresses to piles.

3.2 Element tests on accumulation under cyclic loading

3.2.1 Direction of accumulation

In a drained cyclic triaxial test Luong [91] observed, that it depends on the average stress if a sand shows a contractive or dilative behaviour under cyclic loading. He applied packages each with 20 cycles in succession at different average deviatoric stresses q^{av}. The right part of Figure 3.3 shows the measured q-ε_v-loops. Below a certain value of q^{av} the material behaviour was contractive while it was dilative at larger average deviatoric stresses. Luong defined a borderline in the p-q-plane (the so-called "characteristic threshold (CT) line") separating the contractive ($\boldsymbol{\sigma}^{\mathrm{av}}$ below the CT-line) and the dilative ($\boldsymbol{\sigma}^{\mathrm{av}}$ above the CT-line) material behaviour. This borderline was shown to be independent of the soil density.

A second important study on the direction of accumulation was conducted by Chang & Whitman [21]. In a series of cyclic triaxial tests on medium coarse to coarse sand the average mean pressure p^{av} was kept constant, while the stress ratio η^{av} varied from test to test. Four tests were performed on loose and four other ones on dense samples. In Figure 3.4a the residual volumetric strain after 100 cycles is shown as a function of the

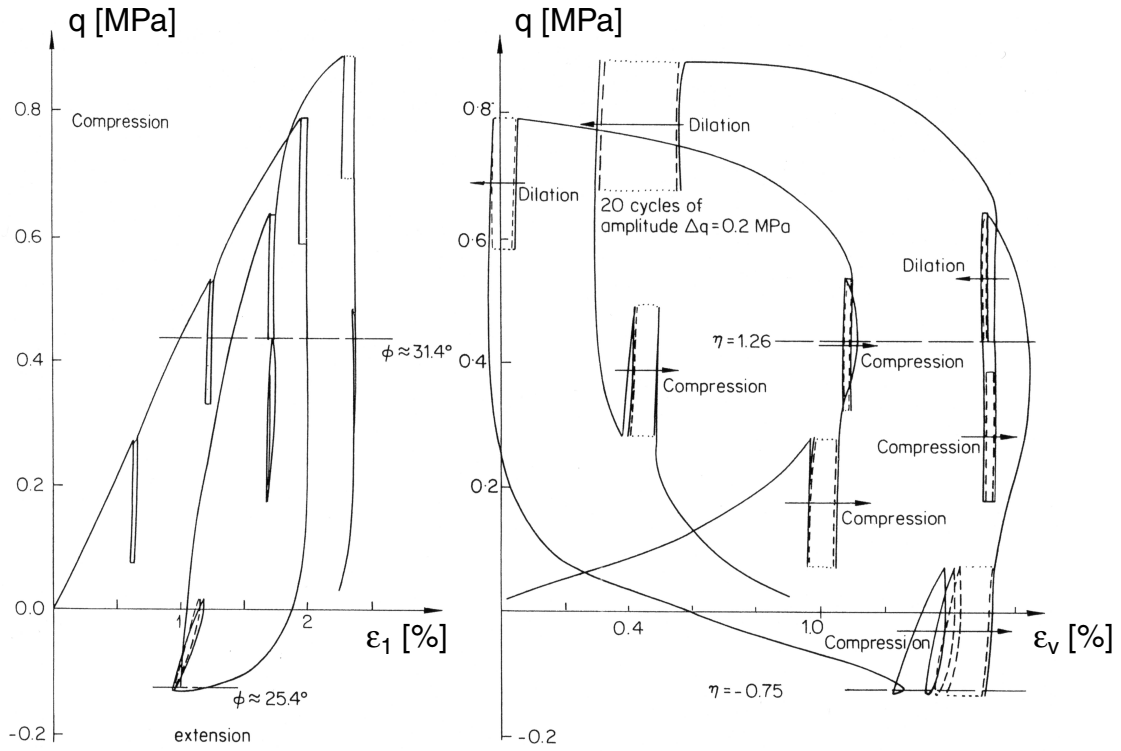

Figure 3.3: *Contractive or dilative behaviour of sand under cyclic loading in dependence of the average stress after Luong [91]: a) q-ε_1-loops, b) q-ε_v-loops*

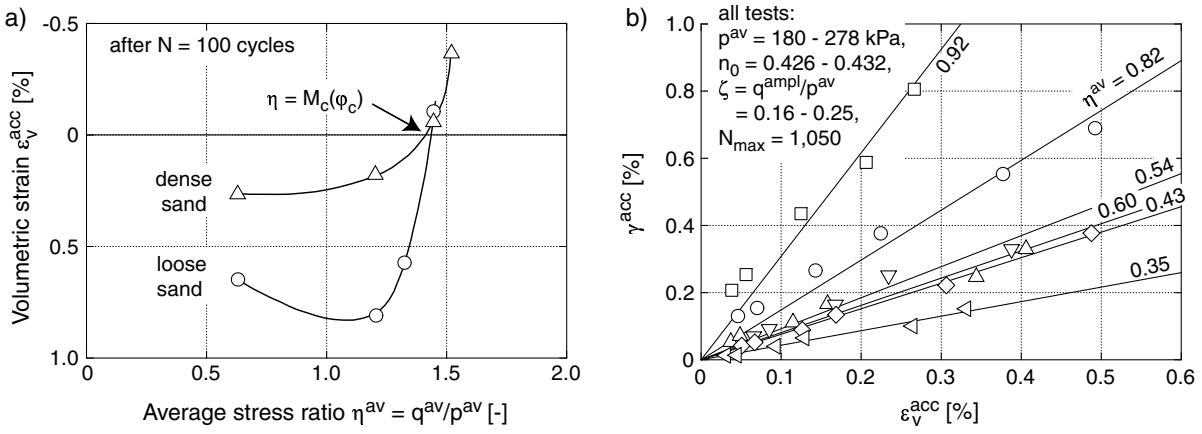

Figure 3.4: *Studies on the direction of accumulation of Chang & Whitman [21]: a) residual volumetric strain ε_v^{acc} as a function of the average stress ratio η^{av}, b) residual shear strain γ^{acc} as a function of ε_v^{acc} for different values of η^{av}*

average stress ratio $\eta^{av} = q^{av}/p^{av}$. Independently of the density of the sand, a vanishing accumulation rate of the volumetric strain was observed for $\eta^{av} \approx M_c(\varphi_c)$. Thus, Chang & Whitman [21] assumed the CT-line of Luong [91] to be identical with the critical state line. For $\eta^{av} < M_c(\varphi_c)$ a compaction and for $\eta^{av} > M_c(\varphi_c)$ a dilative material behaviour was measured.

In further tests Chang & Whitman [21] observed, that the ratio $\gamma^{acc}/\varepsilon_v^{acc}$ increases with increasing values of η^{av} (Figure 3.4b). A good approximation of the measured direction of accumulation by the flow rule of the modified Cam Clay model $\omega = ({M_c}^2 - (\eta^{av})^2)/(2\eta^{av})$ could be demonstrated for different sands (see the illustration in the p-q-plane in Figure 3.5a). An influence of the average mean pressure p^{av} and the amplitude ratio $\zeta = q^{ampl}/p^{av}$ on the inclination of the γ^{acc}-ε_v^{acc}-paths could not be detected (Figure 3.5b). In [21] also the influence of the number of cycles is reported to be negligible. However, Chang & Whitman [21] tested only 1,050 cycles. It is therefore not clear if the test results can be extrapolated to larger numbers of cycles.

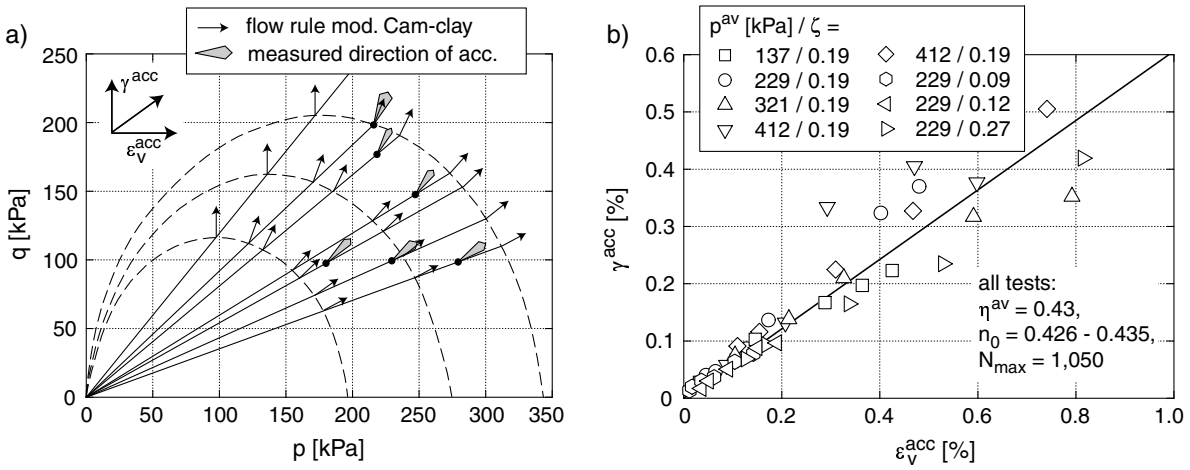

Figure 3.5: *Studies on the direction of accumulation of Chang & Whitman [21]: a) measured directions of accumulation in the p-q-plane compared to the flow rule of the modified Cam Clay model, b)* γ^{acc} *as a function of* ε_v^{acc} *for different average mean pressures* p^{av} *and stress amplitudes* $\zeta = q^{ampl}/p^{av}$

3.2.2 Intensity of accumulation

3.2.2.1 Influence of the number of cycles

Concerning the evolution of the residual strain or deformation with the number of cycles N, it is distinguished between a *stepwise failure*, a *shakedown* and an *abation* (Figure 3.6). These definitions were introduced by Goldscheider & Gudehus [34] and refer originally to foundations subjected to cyclic loading. However, they can also be applied to element tests. In the case of a *stepwise failure* (Figure 3.6a) the residual strain increases linearly or even over-linearly with the number of cycles N. In the case of a *skakedown* (Figure 3.6b) the rate of residual strain vanishes completely after a few load cycles and only the elastic strains have to be considered in the following cycles. In the case of an *abation*, the rate $\dot{\varepsilon}^{\mathrm{acc}} = \partial\varepsilon^{\mathrm{acc}}/\partial N$ decreases with each cycle, but it never vanishes completely (e.g. $\varepsilon^{\mathrm{acc}} \sim \ln(N)$, Figure 3.6c). Explicit accumulation models are developed for the case of an *abation*. Thus the following remarks concentrate on this case.

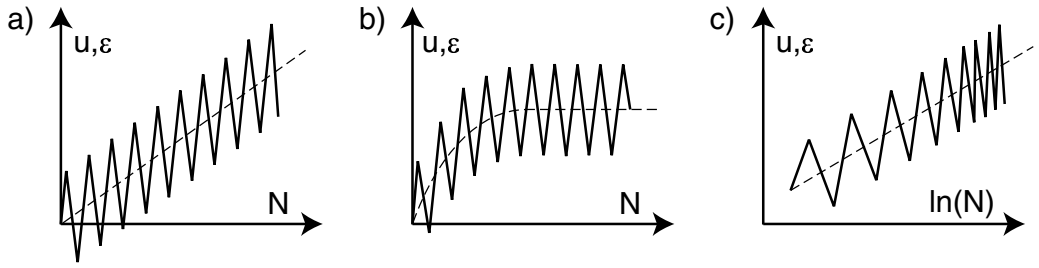

Figure 3.6: *Distinction of the deformation behaviour of a foundation (displacement u) or a soil specimen (strain ε) under cyclic loading: a) stepwise failure, b) shakedown, c) abation [34]*

In the literature, different shapes of the curves $\varepsilon^{\mathrm{acc}}(N)$ were reported. In drained cyclic triaxial tests on sand Lentz & Baladi [85] observed an increase of the residual axial strain $\varepsilon_1^{\mathrm{acc}}$ proportional to the logarithm of the number of cycles N (Figure 3.7). In the tests starting from an isotropic stress the axial stress was cyclically varied between $\sigma_1 = \sigma_3$ and $\sigma_1 = \sigma_3 + 2\sigma_1^{\mathrm{ampl}}$.

Also Suiker [153] worked with stress cycles with $q^{\min} \approx 0$ and different maximum stress ratios $\eta^{\max}/M_c(\varphi_p)$ in a triaxial cell. The tests were performed on unsaturated ballast and well-graded sand. The specimens were prepared with 95 % of the proctor density ($I_D \approx 0.85 \div 0.90$) and with the optimum water content w_{Pr}. The drained cyclic loading was applied with a frequency of 5 Hz. Figure 3.8 presents the increase of the deviatoric strain with the number of cycles. In a diagram with a semi-logarithmic scale a reduction

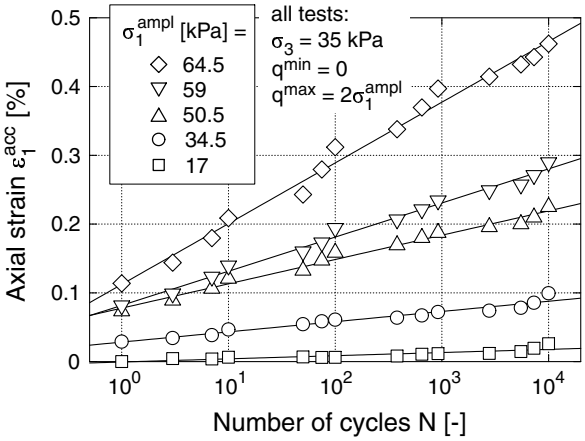

Figure 3.7: *Accumulation curves $\varepsilon_1^{acc}(N)$ after Lentz & Baladi [85]*

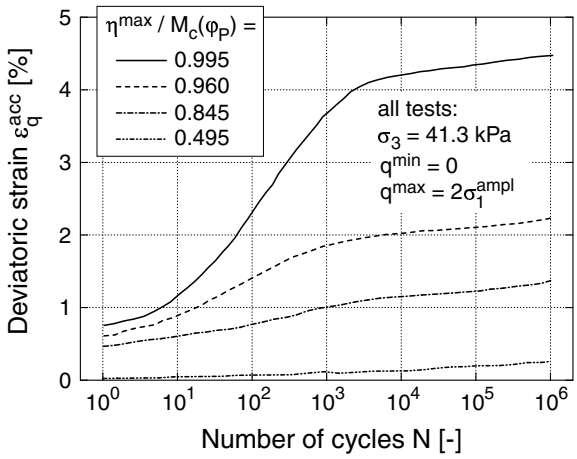

Figure 3.8: *Accumulation curves $\varepsilon_q^{acc}(N)$ for a well-graded sand after Suiker [153]*

of the inclination of the curves $\varepsilon_q^{\mathrm{acc}}(N)$ after approx. 1,000 cycles was observed (even in the test with $\eta^{\max} \approx M_c(\varphi_P)$). Suiker chose the denotation "conditioning phase" for $N < 10^3$ and "densification phase" for $N > 10^3$. However, in a test with $N_{\max} = 5 \cdot 10^6$ a re-increase of the inclination at higher numbers of cycles was measured.

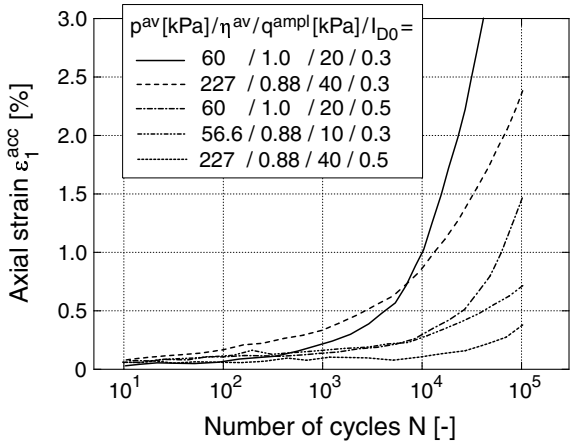

Figure 3.9: *Accumulation curves $\varepsilon_1^{acc}(N)$ for a medium coarse sand after Helm [49]*

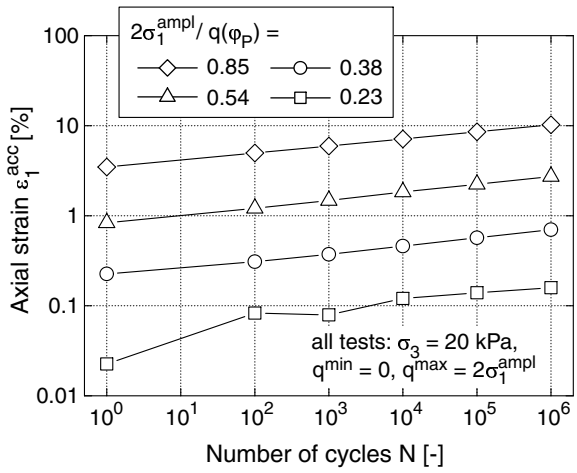

Figure 3.10: *Accumulation curves $\varepsilon_1^{acc}(N) \sim N^{\alpha}$ for ballast 22.4/63 after Gotschol [35]*

Helm et al. [49] studied two cohesive (silt, marl) and two non-cohesive soils (fine sand, medium coarse sand) in drained cyclic triaxial tests. While the lateral stress σ_3 was constant, the axial stress was oscillating with an amplitude σ_1^{ampl} around the average value σ_1^{av}, but in contrary to Lentz & Baladi [85] and Suiker [153] the stress at minimum

σ_1 was not isotropic. The development of the axial strain with N for the medium coarse sand is illustrated in Figure 3.9. In the diagram with semi-logarithmic scale a significant increase of the inclination of the curves $\varepsilon_1^{\mathrm{acc}}(N)$ with increasing number of cycles can be detected. Helm et al. [49] proposed a bilinear approximation of the curves in the semi-logarithmic scale.

Accumulation curves $\varepsilon^{\mathrm{acc}}(N)$ which were over-proportional to $\ln(N)$ were also measured by Marr & Christian [94] on a poorly graded fine sand. Figure 3.10 shows the results of large-scale cyclic triaxial tests on ballast performed by Gotschol [35]. The illustration includes also the residual strain in the first cycle. In the $\varepsilon_1^{\mathrm{acc}}$-$N$-diagram with double-logarithmic scale, one obtains straight lines. Thus, the accumulation curves can be described by a power law $\varepsilon_1^{\mathrm{acc}} \sim N^{\alpha}$ with a constant α. This approach was also frequently used in explicit accumulation models (see Chapter 6). However, the curves of the volumetric strain $\varepsilon_v^{\mathrm{acc}}(N)$ shown by Gotschol [35] contradict the cyclic flow rule reported by Luong [91] and Chang & Whitman [21] (Section 3.2.1).

3.2.2.2 Influence of the strain or stress amplitude

In Figures 3.7 up to 3.10 an increase of the accumulation rate with the stress amplitude is obvious. In cyclic simple shear tests, Youd [188] also detected a strong increase of the rate of densification with increasing shear strain amplitude γ^{ampl} (Figure 3.11). Amplitudes less than a threshold shear strain $\gamma^{\mathrm{ampl}} = 10^{-4}$ did not cause any residual strains. Silver & Seed [151, 150] drew similar conclusions from their cyclic simple shear tests (Figure 3.12). In the diagrams in Figures 3.11 and 3.12 with semi-logarithmic (!) scale, one can see an approximately quadratic increase of the accumulation rate with γ^{ampl}.

Sawicki & Świdziński [133, 134] performed cyclic simple shear tests on a fine sand with different amplitudes γ^{ampl}. Figure 3.13a shows again, that larger amplitudes can cause a faster densification. If $\varepsilon_v^{\mathrm{acc}}$ or the state variable "compaction" $\Phi = \Delta n/n_0$, defined by Sawicki & Świdziński, is plotted versus $\tilde{N} = \frac{1}{4} N (\gamma^{\mathrm{ampl}})^2$, the curves $\Phi(\tilde{N})$ fall together into a single curve (Figure 3.13b). Sawicki & Świdziński called this curve "common compaction curve". It was approximated by

$$\Phi(\tilde{N}) \;=\; C_1 \, \ln\left(1 + C_2 \, \tilde{N}\right) \tag{3.1}$$

with the material constants C_1 and C_2. The curves $\Phi(\tilde{N})$ in Figure 3.13b slightly diverge. Thus, Equation (3.1) presumably does not fit for larger numbers of cycles $N > 50$. This is also demonstrated in Section 5.2.6.

In simple shear tests with large shear strain amplitudes in the first cycles exclusively densification takes place. If a certain density is achieved at each shear stress reversal first

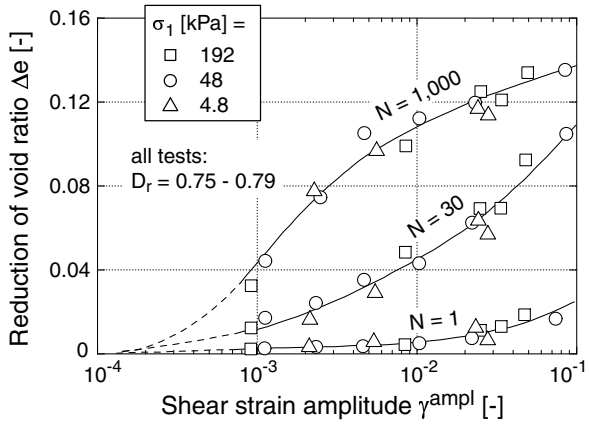

Figure 3.11: *Increase of the residual compaction Δe with the shear strain amplitude γ^{ampl} after Youd [188]*

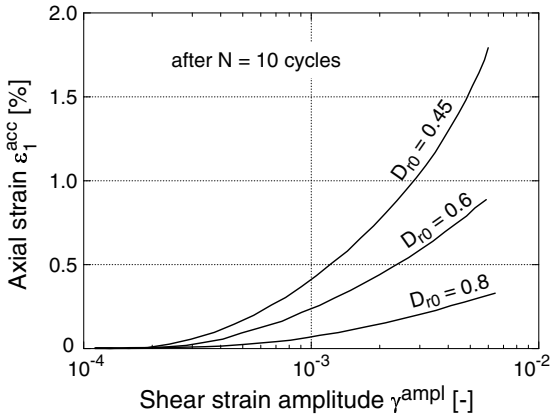

Figure 3.12: *Residual axial strain ε_1^{acc} as a function of the shear strain amplitude γ^{ampl} after Silver & Seed [151, 150]*

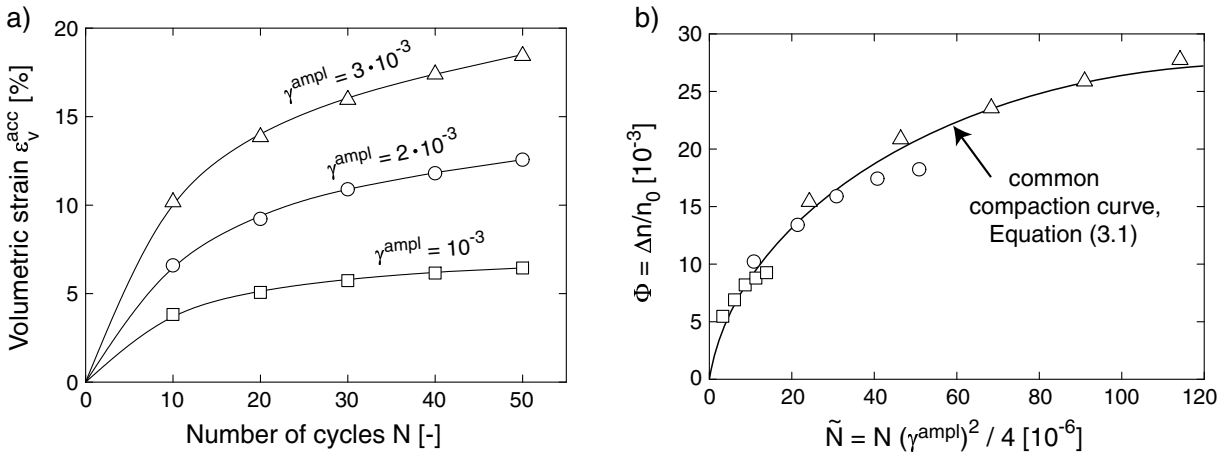

Figure 3.13: *Curves a) $\varepsilon_v^{acc}(N)$ and b) $\Phi(\tilde{N})$ for different shear strain amplitudes γ^{ampl} after Sawicki & Świdziński [133, 134]*

a contractive material behaviour followed by a dilative material behaviour is observed (Figure 3.14, Gudehus [39] or also Pradhan et al. [121] and Triantafyllidis [162]). Thus, in the case of shear waves the frequency of the accompanying longitudinal waves is doubled (Gudehus et al. [40]).

In general it is debatable if quantitative conclusions can be drawn from cyclic simple shear tests, since the strain field is inhomogeneous over the specimen volume and the lateral stresses are usually not measured. Cyclic triaxial tests and also cyclic torsional shear tests on hollow cylinder specimens are thought to be more meaningful and reliable. A series of cyclic triaxial tests on the influence of the amplitude was undertaken by Marr & Christian [94]. The average stress and the initial density were kept konstant while the

amplitude ratio $\zeta = \sigma_1^{\text{ampl}}/p^{\text{av}}$ was varied from test to test. Figure 3.15 presents curves $\varepsilon^{\text{acc}}(\zeta)$ which were derived from the data of Marr & Christian [94]. Curves of the shape $\varepsilon^{\text{acc}} \sim \zeta^{\alpha}$ with $1.9 \leq \alpha \leq 2.3$ could be fitted to the data for different numbers of cycles.

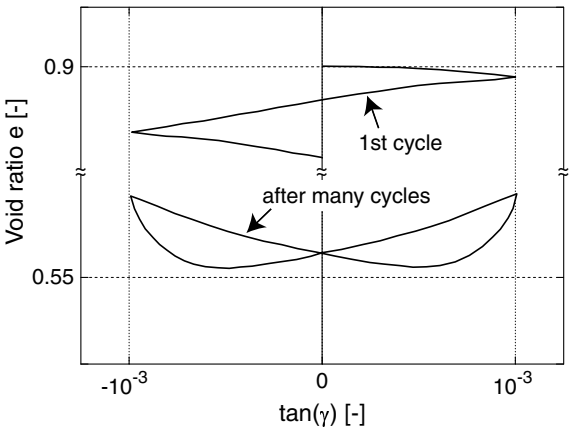

Figure 3.14: *e*-tan(γ)-*hysteresis: Doubling of frequency of the curves of void ratio versus time* $e(t)$ *in the case of large amplitudes after many cycles, after Gudehus [39]*

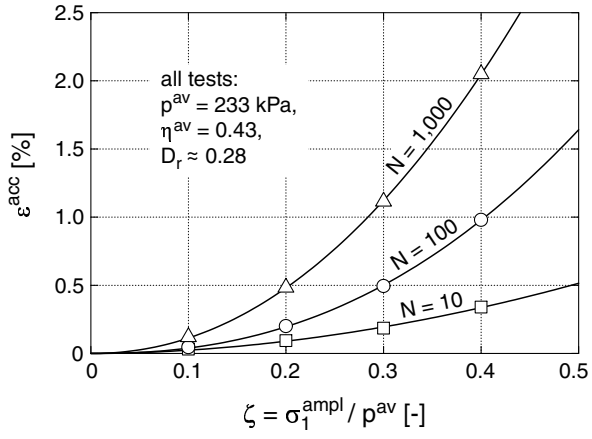

Figure 3.15: *Residual strain* ε^{acc} *as a function of the amplitude ratio* ζ *after Marr & Christian [94]*

3.2.2.3 Influence of the polarization of the cycles

The influence of the polarization, i.e. the direction of the cycles in the stress or strain space was rarely studied until now. Mostly a pure deviatoric shearing in the simple shear test or predominant deviatoric cycles in the triaxial test with $\sigma_3 =$ constant were investigated. Ko & Scott [76] tested the effect of repeated cycles with hydrostatic compression on the accumulation of strains in cubical specimens. The tests showed a small compression of the specimens during the first cycles while no further strain accumulation could be observed during the following cycles. However, the tests of Ko & Scott [76] were restricted to very few cycles.

Choi & Arduino [23] performed undrained true triaxial tests on gravel (cubical specimens, length of edge 24.1 cm). At an initial effective pressure of $p_0 = 138$ kPa stress cycles with different directions in the deviatoric plane were tested. No dependence of the liquefaction resistance on the polarization of the cycles in the deviatoric plane could be detected (Figure 3.16).

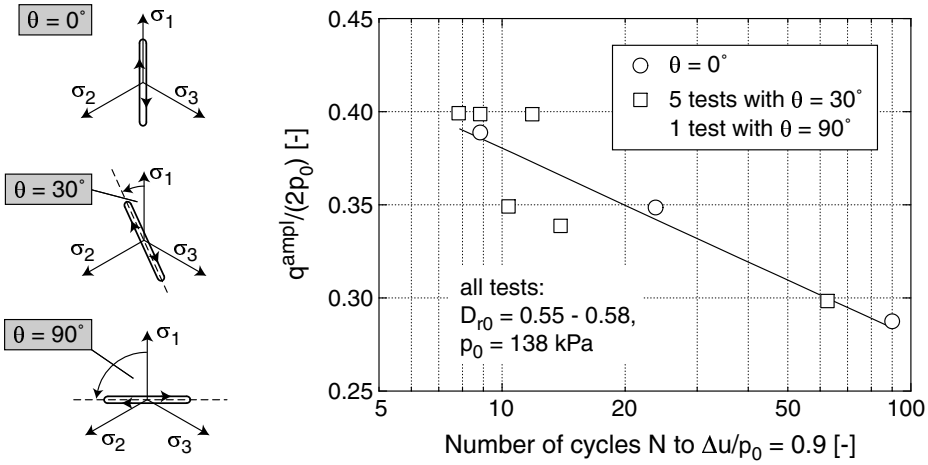

Figure 3.16: *Liquefaction resistance of gravel specimens in true triaxial tests: Influence of the direction of the cycles θ in the deviatoric plane after Choi & Arduino [23] (p_0 = effective consolidation pressure, Δu = excess pore water pressure)*

3.2.2.4 Influence of polarization changes

Yamada & Ishihara [187] studied the influence of a change of the polarization of the stress cycles in drained and undrained tests on loose saturated sand in true triaxial tests. After consolidation under an isotropic stress four cycles were applied. In the first cycle, the vertical stress was increased until a certain octahedral shear stress τ_{oct} (see definition in Appendix II) was reached. Subsequently, it was reduced again to $\tau_{\mathrm{oct}} = 0$. The two horizontal stress components were varied in such way, that the mean pressure p remained konstant during the cycle. After that, the direction of loading was rotated by a certain angle θ in the octahedral plane and the second cycle was applied with the same amplitude in this new direction. The polarization of the third cycle was identical with that of the first one, but $\tau_{\mathrm{oct}}^{\mathrm{ampl}}$ was larger. In the fourth cycle, the specimen was sheared in the direction of the second cycle with an amplitude $\tau_{\mathrm{oct}}^{\mathrm{ampl}}$ being identical to that in the third cycle.

In the drained tests Yamada & Ishihara observed, that the residual volumetric and deviatoric strains after the second and the fourth cycle increased with increasing angle θ, i.e. with an increasing deflection of the shearing direction in the second and the fourth cycle from the direction in the first and the third cycle (Figure 3.17). Similar conclusions could be drawn concerning the build-up of excess pore pressure in the undrained tests. Yamada & Ishihara concluded, that the material (at least partly) "forgets" its loading history, if the actual direction of loading deflects significantly from the previous polarization. This lost of memory grows with increasing angle between the two subsequent polarizations.

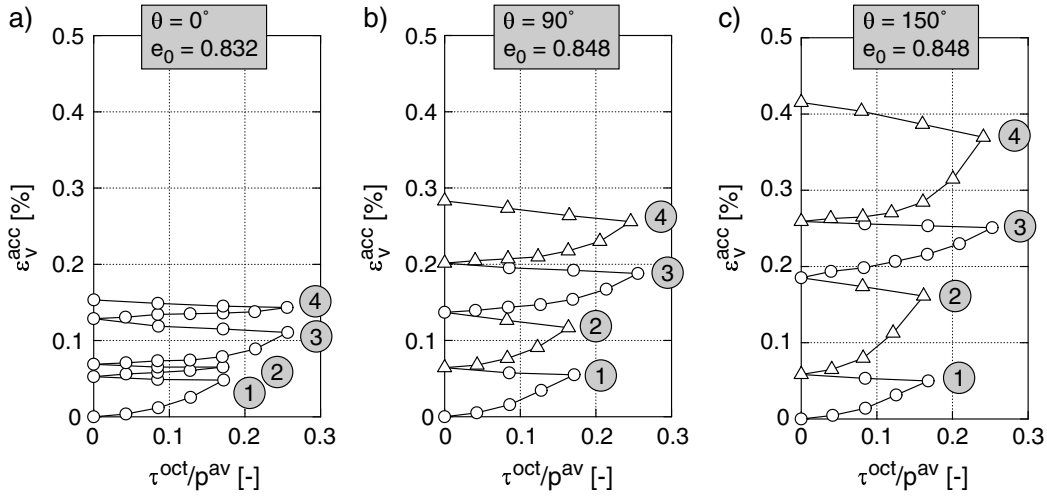

Figure 3.17: *Influence of a change of the polarization of the cycles in the octahedral plane by a) $\theta = 0°$, b) $\theta = 90°$ and c) $\theta = 150°$ on the accumulation of volumetric strain after Yamada & Ishihara [187]*

3.2.2.5 Influence of the shape of the cycles

Pyke et al. [122] subjected a dry sand layer (diameter $d = 91.4$ cm, height $h = 7.6$ cm) to a multiaxial cyclic loading. Two shaking tables were used. One was mounted transversely on the other one, allowing for 2-D shearing. If approximately circular stress cycles were applied, the settlements were twice larger than for uniaxial stress cycles with the same maximum shear stress (Figure 3.18a). Furthermore, if two stochastically generated loadings $\tau_1(t)$ and $\tau_2(t)$ with $\tau_1^{\text{ampl}} \approx \tau_2^{\text{ampl}}$ were applied simultaneously, the resulting settlement was twice larger than in the case where the sand layer was sheared only with $\tau_1(t)$ or only with $\tau_2(t)$ (Figure 3.18b). Thus, concerning the accumulation rate the maximum values of shear stress in the directions of both axes seem to be more important than the shape of the path between the extrema. If additionally to the horizontal loading with $\tau_1(t)$ and $\tau_2(t)$ the shaking tables were accelerated in the third, vertical direction, the accumulation rate was even larger (Figure 3.18b). The conclusion of the test results was that if sand is cyclically sheared simultaneously in several orthogonal directions, the resulting settlement is identical with the sum of the settlements which would result from an uniaxial cyclic shearing in the individual directions.

Ishihara & Yamazaki [65] performed undrained simple shear tests with a stress-controlled shearing in two mutually perpendicular directions. In a first series elliptic stress cycles were tested. The amplitude τ_1^{ampl} was kept constant and the amplitude in the orthogonal direction was varied in the range $0 \leq \tau_2^{\text{ampl}} \leq \tau_1^{\text{ampl}}$ (Figure 3.19a). The liquefaction resistance decreased with an increasing ovality of the stress loops. With increasing ratio

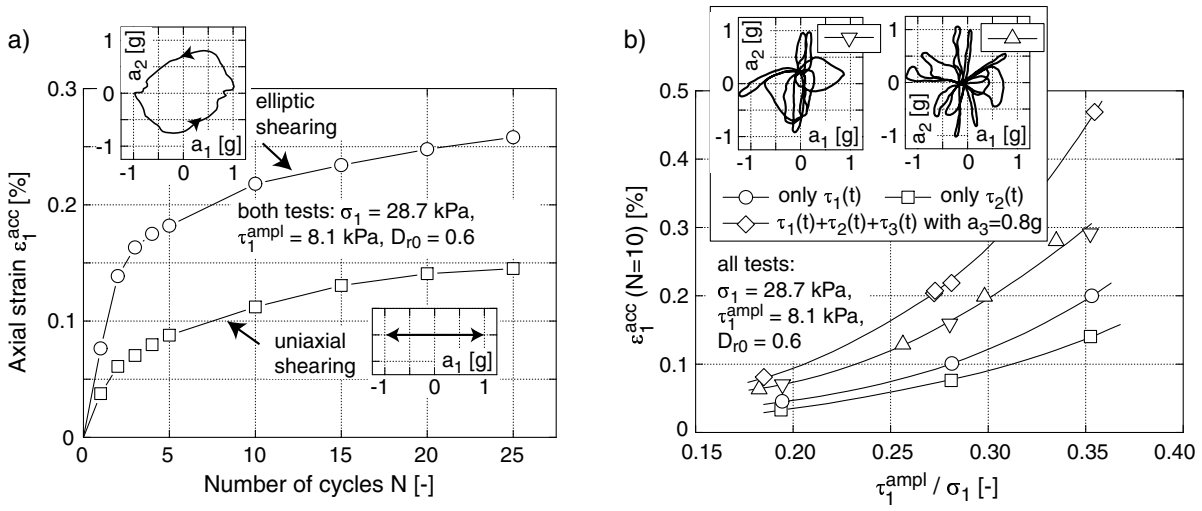

Figure 3.18: *Shaking table tests of Pyke et al. [122]: a) Comparison of uniaxial and circular stress cycles, b) effect of stochastically generated cycles*

$\tau_2^{\mathrm{ampl}}/\tau_1^{\mathrm{ampl}}$, the accumulation of excess pore water pressure was accelerated and the liquefaction (defined as the time at which $\gamma^{\mathrm{ampl}} = 3$ % was reached) was achieved in less cycles (Figure 3.19a). Let us consider the amplitude ratio $\tau_1^{\mathrm{ampl}}/\sigma_{1,0} = 0.1$ ($\sigma_{1,0}$ = effective vertical stress prior to cyclic loading). The liquefaction was reached after approx. 45 cycles of uniaxial shearing ($\tau_2^{\mathrm{ampl}}/\tau_1^{\mathrm{ampl}} = 0$), whereas only 8 cycles were necessary in the case of a circular shearing ($\tau_2^{\mathrm{ampl}}/\tau_1^{\mathrm{ampl}} = 1$). In a second series of tests, the specimens were sheared alternatingly in the τ_1- and the τ_2-direction (Figure 3.19b). A cycle was completed when both shearing directions were passed. Also in these tests, the liquefaction resistance decreased with an increasing ratio $\tau_2^{\mathrm{ampl}}/\tau_1^{\mathrm{ampl}}$. For an amplitude ratio $\tau_1^{\mathrm{ampl}}/\sigma_{1,0} = 0.1$ approx. 11 cycles were necessary to reach liquefaction in the case of an amplitude ratio $\tau_2^{\mathrm{ampl}}/\tau_1^{\mathrm{ampl}} = 1$. Thus, the accumulation of excess pore water pressure was slightly slower than for circular cycles (Figure 3.19a).

3.2.2.6 Influence of the average stress

Several experimental studies with cyclic simple shear tests (Youd [188], Silver & Seed [151, 150], Sawicki & Świdziński [133, 134]) came to the conclusion, that the axial stress σ_1 does not affect the strain accumulation. This can be also seen from Figure 3.11. However, in the test series only few cycles with large amplitudes ($\gamma^{\mathrm{ampl}} > 10^{-3}$) were applied. The disadvantages of cyclic simple shear tests were already mentioned.

Timmerman & Wu [160] performed cyclic triaxial tests with $\eta^{\mathrm{av}} = q^{\mathrm{av}}/p^{\mathrm{av}} =$ constant. They compared the strain accumulation for two different lateral stresses $\sigma_3 = 48$ kPa and

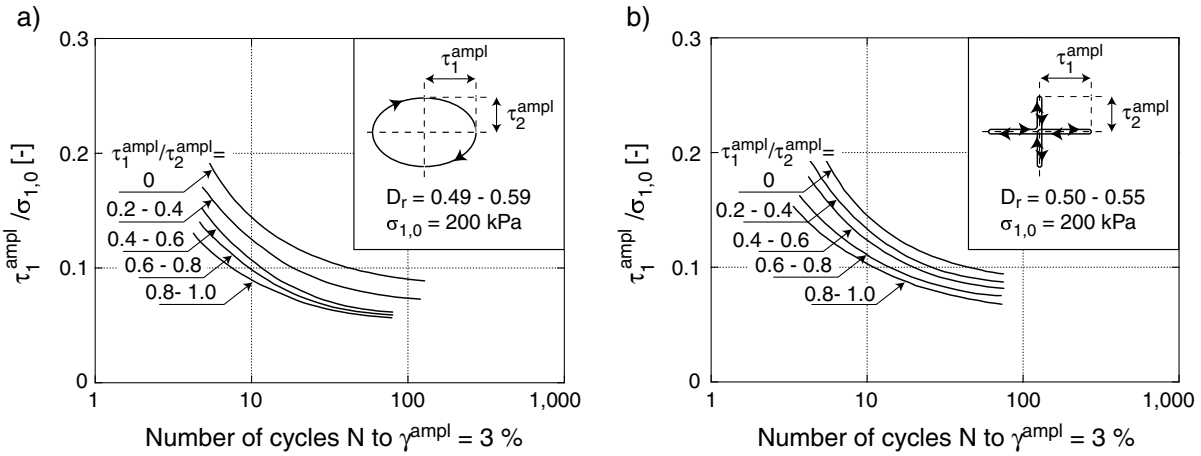

Figure 3.19: *Influence of the shape of the stress cycles on the liquefaction resistance after Ishihara & Yamazaki [65]: a) elliptic cycles, b) alternating cycles*

$\sigma_3 = 138$ kPa. In the tests with the smaller σ_3, smaller stress amplitudes were sufficient to cause the same residual strain after 10^4 cycles as in the tests with the larger σ_3. However, the pressure-dependence of stiffness was not taken into account by Timmerman & Wu. Probably the increase of the accumulation rate with decreasing average mean pressure p^{av} for $q^{\mathrm{ampl}} =$ constant results mainly from the simultaneous increase of the strain amplitude.

Marr & Christian [94] studied different average stresses $p^{*\mathrm{av}} = (\sigma_1^{\mathrm{av}} + \sigma_3^{\mathrm{av}})/2$, $q^{*\mathrm{av}} = (\sigma_1^{\mathrm{av}} - \sigma_3^{\mathrm{av}})/2$, $\eta^{*\mathrm{av}} = q^{*\mathrm{av}}/p^{*\mathrm{av}}$ in cyclic triaxial tests with $\zeta^* = \sigma_1^{\mathrm{ampl}}/p^{*\mathrm{av}} =$ constant. Curves of identical residual strains ($\varepsilon_1 =$ constant or $\varepsilon_v =$ constant, respectively) in a $\eta^{*\mathrm{av}}$-N- or $p^{*\mathrm{av}}$-N-diagram are presented in Figure 3.20. Marr & Christian observed a significant increase of the accumulation rate of the axial strain with the stress ratio $\eta^{*\mathrm{av}}$ (Figure 3.20a). Initially, the rate of volumetric strain (Figure 3.20c) became slower with increasing $\eta^{*\mathrm{av}}$. However, at larger stress ratios it increased again. These observations are in contradiction with the results of Luong [91] and Chang & Whitman [21], who found that the volumetric rate vanishes on the critical state line. The accumulation of the axial (Figure 3.20c) and the volumetric strain (Figure 3.20d) became faster with increasing average mean pressure. However, also Marr & Christian did not consider the increase of the strain amplitude with pressure for $\zeta^* =$ constant. The larger strain amplitudes $\varepsilon^{\mathrm{ampl}}$ (not given in [94]) at higher pressures may have caused the larger accumulation rates.

An extrapolation of the own test data (Section 5.2.4) predicts an accumulation rate $\dot{\varepsilon}^{\mathrm{acc}} \neq 0$ for the case of zero effective average stress. $\boldsymbol{\sigma}^{\mathrm{av}} = \mathbf{0}$ occurs e.g. in an undrained cyclic test after the liquefaction of the specimen. Shamoto et al. [147] performed such tests with a subsequent re-consolidation of the specimens. Figure 3.21a presents the relationship between the generated excess pore water pressure Δu and the volumetric strain $\varepsilon_{v,RC}$

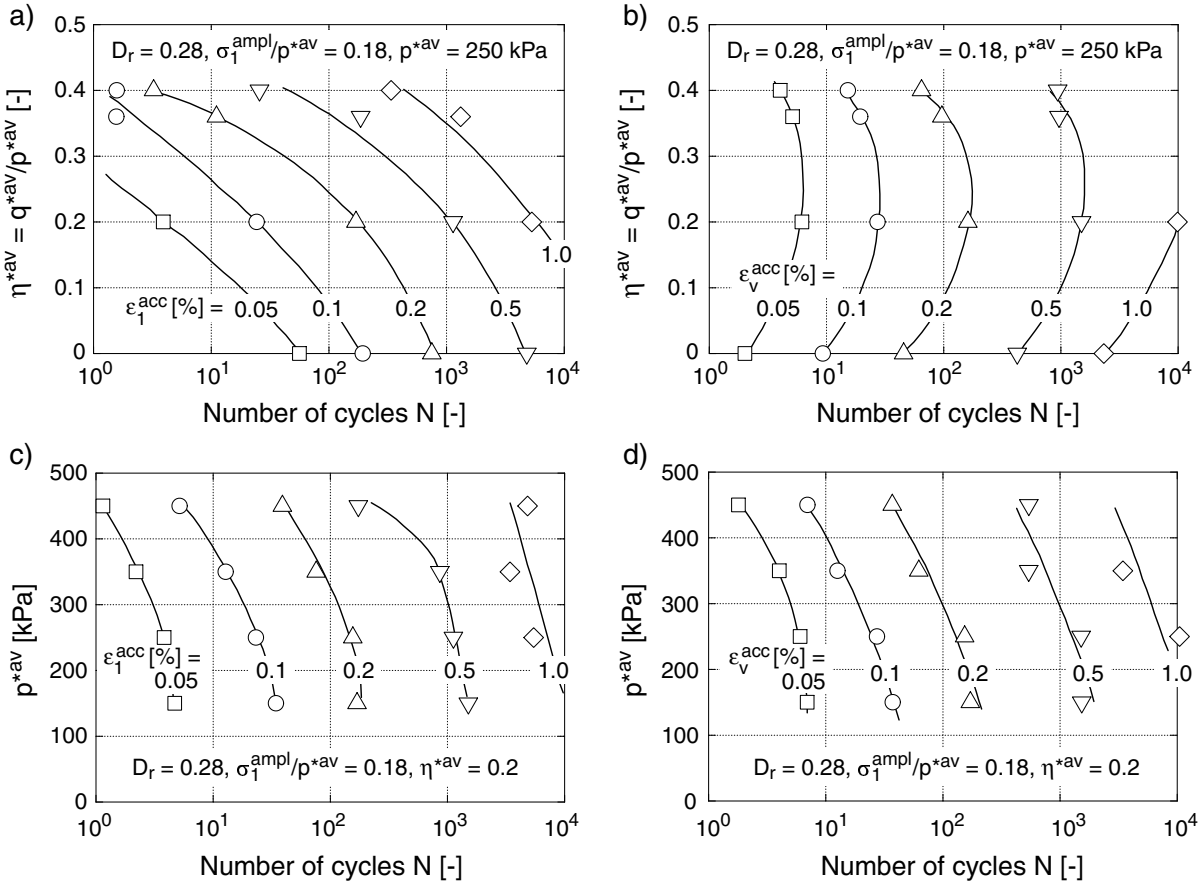

Figure 3.20: *Influence of the average stress on strain accumulation after Marr & Christian [94]: effect of η^{*av} on a) ε_1^{acc} and b) ε_v^{acc}, effect of p^{*av} on c) ε_1^{acc} and d) ε_v^{acc}*

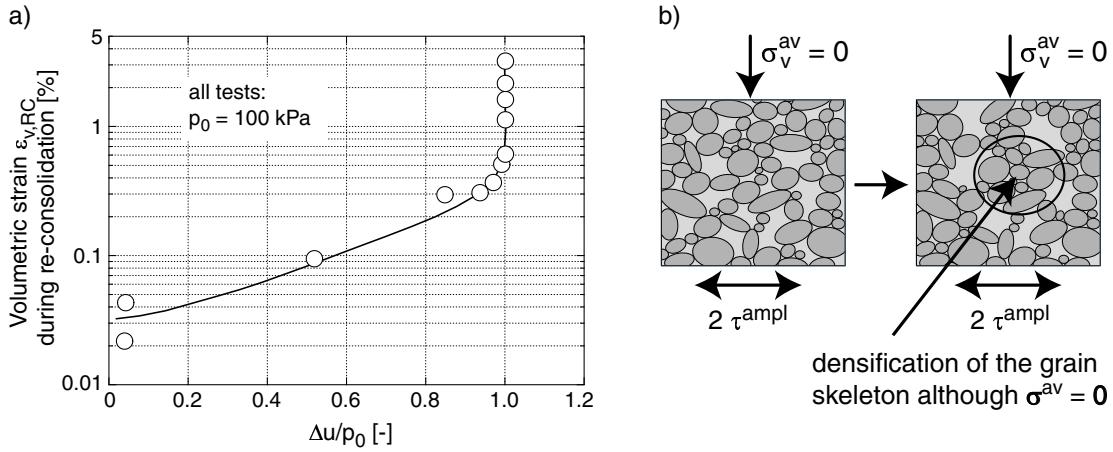

Figure 3.21: *Densification of the grain skeleton although $\boldsymbol{\sigma}^{av} = \mathbf{0}$: a) Undrained cyclic triaxial tests with re-consolidation after Shamoto et al. [147], b) Scheme of the densification at $\boldsymbol{\sigma}^{av} = \mathbf{0}$*

during re-consolidation due to the dissipation of the pore water. A clear correlation between $\varepsilon_{v,RC}$ and Δu exists for those specimens, which did not "liquefy" during the undrained cyclic loading ($\Delta u/p_0 < 1$ with the isotropic effective consolidation pressure p_0). For the "liquefied" specimens ($\Delta u/p_c = 1$) a significant scatter of the values $\varepsilon_{v,RC}$ was observed (the logarithmic scale of the ordinate has to be considered). This may be probably attributed to a different cyclic shearing at $\boldsymbol{\sigma}^{\mathrm{av}} = \mathbf{0}$. Thus, a latent accumulation in the soil skeleton goes on, even at $\boldsymbol{\sigma}^{\mathrm{av}} = \mathbf{0}$ (Figure 3.21b). It may be explained as a local densification which gets visible during re-consolidation. This correlates with the practical observations, that settlements after an earthquake are often larger than it could be expected from the generated excess pore water pressures.

3.2.2.7 Influence of void ratio / relative density

From Figure 3.12 after Silver & Seed [151, 150] it could already be seen, that the accumulation rate strongly depends on the initial density. In simple shear tests with an initial density of $D_{r0} = 0.45$ the residual strains were twice as large as for $D_{r0} = 0.6$ and six times larger than for $D_r = 0.8$. Youd [188] observed, that cyclic loading can cause the void ratio to fall significantly below the minimum void ratio $e_{\min}$ from standard procedures. For different test parameters, (σ_1, γ^{ampl}) Youd [188] found a compaction up to $I_D = 1.27$.

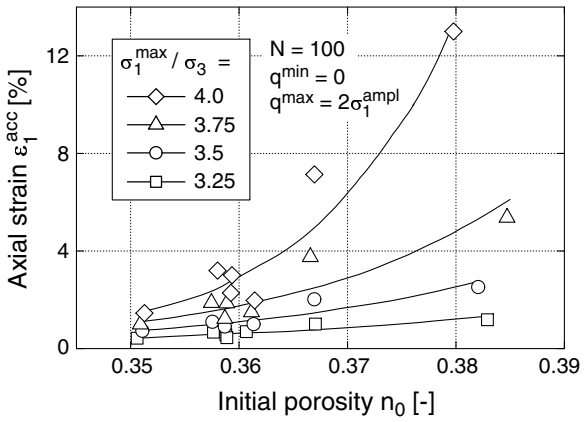

Figure 3.22: *Accumulated axial strain ε_1^{acc} as a function of initial porosity n_0 after Hain [42]*

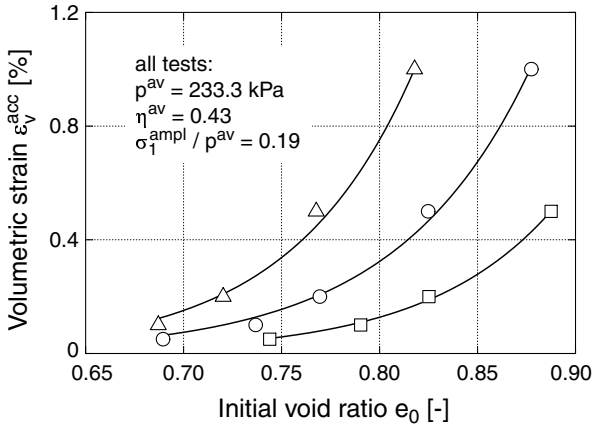

Figure 3.23: *Accumulated volumetric strain ε_v^{acc} in dependence of the initial void ratio e_0 after Marr & Christian [94]*

In cyclic triaxial tests, Hain [42] studied a fine-grained dry sand with different initial porosities n_0. The axial stress was oscillating between $\sigma_1 = \sigma_3$ and $\sigma_1 = \sigma_1^{\max}$. For peak stress ratios $\sigma_1^{\max}/\sigma_3 \leq 3$, the curves $\varepsilon_1^{\mathrm{acc}}(n_0)$ for a certain number of cycles N were linear.

For larger stress ratios at peak over-linear curves were measured (Figure 3.22). An over-proportional increase of the residual volumetric (Figure 3.23) and axial strains with the initial void ratio e_0 was reported also by Marr & Christian [94].

3.2.2.8 Influence of the loading frequency

In the literature one may find contradictory reports on the influence of the loading frequency on strain accumulation. In drained cyclic simple shear tests Youd [188] could not detect a dependence of the accumulation rate on the frequency within the tested range 0.2 Hz $\leq f_B \leq$ 1.9 Hz (Figure 3.24). Shenton [149] documented results of drained cyclic triaxial tests on ballast with loading frequencies 0.1 Hz $\leq f_B \leq$ 30 Hz. He also could not find an influence of the loading frequency on the residual strains. Similar conclusions were drawn by Kokusho et al. [77] from undrained cyclic triaxial tests. Also Sasaki & Yamada (after Tatsuoka et al. [158]) measured the same liquefaction resistance for different loading frequencies ($f_B = 0.05$ Hz and $f_B = 0.5$ Hz).

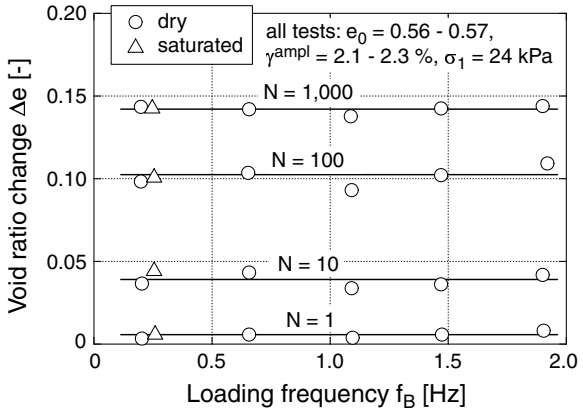

Figure 3.24: *Compaction Δe in dependence on the loading frequency after Youd [188]*

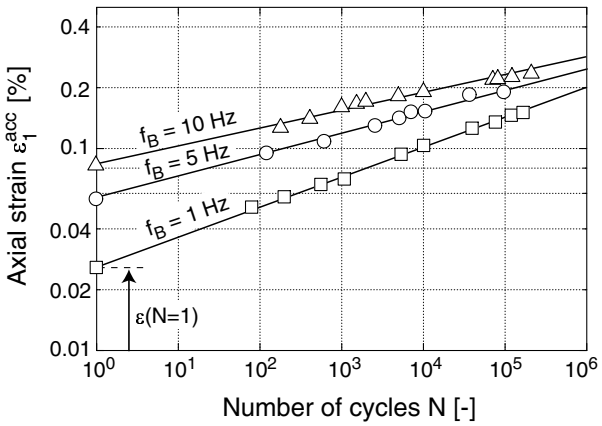

Figure 3.25: *Accumulation curves $\varepsilon_1^{acc}(N)$ for different loading frequencies after Kempfert et al. [71]*

Contrary to these results, Kempfert et al. [71] reported on a non-negligible influence of the loading frequency on the accumulation of deformations in cyclic triaxial tests on ballast. The deformation due to the first cycle grew with increasing loading frequency, whereas higher frequencies f_B caused a lower accumulation rate during the subsequent cycles. It should be annotated, that at least for the higher loading frequencies $f_B \geq 5$ Hz identical stress amplitudes lead to smaller strain amplitudes due to inertia forces. The decrease of the accumulation rate in the subsequent cycles with increasing f_B may possibly be

attributed to the decrease of $\varepsilon^{\mathrm{ampl}}$.

3.2.2.9 Influence of the fabric of the grain skeleton and the historiotropy

The accumulation rate depends strongly on the fabric of the grain skeleton and the spatial distribution of the contact forces. The initial fabric results from sedimentation or in the case of laboratory specimens from the method of sample preparation (*inherent* anisotropy). It is changed by monotonic and cyclic loading (*induced* anisotropy). The influence of the fabric or the historiotropy (history dependence) on the accumulation rate was mainly studied in tests without drainage.

Different preparation methods lead to different initial fabrics of the grain skeleton. If dry sand is pluviated, oblong grains tend to lay flat, whereas a random orientation is achieved by tamping of moist sand (Nemat-Nasser & Takahashi [100]). Several authors have demonstrated with undrained tests that different preparation techniques lead to different accumulation rates of excess pore pressure and thus to different liquefaction resistances. Exemplary undrained cyclic triaxial tests on three different sands performed by Ladd [81] are shown in Figure 3.26. Ladd observed, that specimens which were prepared by dry pluviation and compacted by vibration liquefied at four times lower numbers of cycles than specimens which were prepared by moist tamping. Similar test results were obtained by Mulilis et al. [98, 99]. Porcino et al. [117] reported that pluviation through air leads to a significantly lower liquefaction resistance than pluviation through water. Oda et al. [116] pointed out the significance of the direction of deposition compared to the polarization of cyclic loading. Specimens which were cyclically loaded perpendicular to the direction of deposition exhibited a higher liquefaction resistance than those loaded parallelly. Many authors found the sensitivity to liquefy of high-quality, undisturbed specimens to be significantly lower than the one of re-constituted specimens, irrespectively of the method of preparation (Mulilis et al. [98, 99], Tokimatsu & Hosaka [161], Hatanaka et al. [46], Porcino et al. [117]). This can probably be attributed to the historiotropy of the in-situ soil or to aging effects (see Section 3.2.2.11).

Several publications (Finn et al. [31], Seed et al. [144], Seed et al. [146], Teachavoransinskun et al. [159], Ishihara & Okada [63, 64], Suzuki & Toki [154]) deal with the influence of a cyclic history on the liquefaction resistance. The results of these test series were summarized by Wichtmann et al. [178]. The tests of Seed et al. [144] are discussed here as an example. Seed et al. [144] performed shaking table tests on fully water-saturated sand under undrained simple shear conditions. Packages with a small number of cycles N (smaller than N causing liquefaction) were applied in succession to the saturated sand, each simulating an earthquake of low intensity. After each package the drainage was

opened and the sand layer was re-consolidated. Figure 3.27 shows that the pore water pressure rise became slower with each succeeding package, i.e. with increasing cyclic preloading.

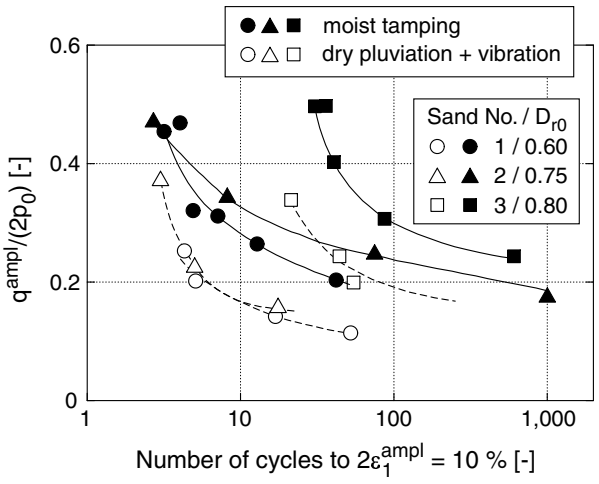

Figure 3.26: *Different liquefaction resistances due to different sample preparation techniques for three sands after Ladd [81]*

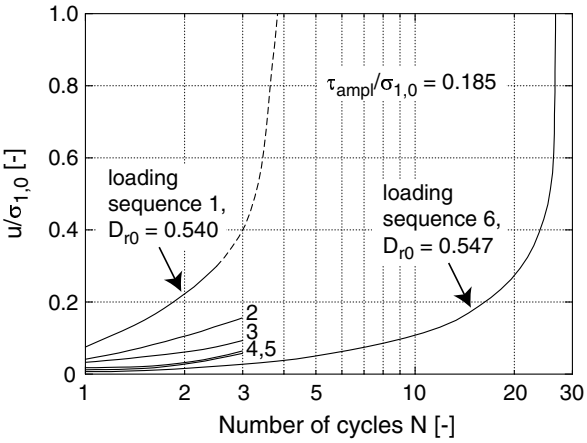

Figure 3.27: *Decrease of the rate of pore water pressure $\dot{u} = \partial u/\partial N$ with increasing cyclic preloading, shaking table tests after Seed et al. [144]*

3.2.2.10 Random cyclic loading and packages of cycles

In many practical problems (traffic loads, wind, waves), the amplitude is not constant but varies from cycle to cycle. In the field of fatigue of metals under cyclic loading the Miner's rule [96] is used in order to consider varying amplitudes. If N_{fi} is the number of cycles which is necessary to cause failure with a constant amplitude σ_i, a failure during cyclic loading with varying amplitudes can be expected if

$$\sum_{i=1}^{n} \frac{N_i}{N_{fi}} = 1 \tag{3.2}$$

holds, wherein N_i is the number of cycles applied with the amplitude σ_i. Accordingly, the sequence of the packages of cycles does not play a role concerning the time of failure.

Also the stress amplitudes during an earthquake vary strongly with time. Random cyclic loading histories were tested e.g. by Ishihara & Yasuda [66] and Tatsuoka et al. [158]. In order to estimate the risk of liquefaction, an irregular loading is replaced by an equivalent number of regular cycles with a constant amplitude (Seed et al. [142, 141]). In this context

"equivalent" means that the irregular and the regular cyclic loading cause the same build-up of excess pore water pressure. The constant amplitude of the regular cycles is chosen as a certain fraction (mostly 65 %) of the maximum amplitude of the irregular cycles.

Packages of cycles (so-called "multistage cyclic loading") were studied on a calcareous sand in drained triaxial tests by Kaggwa et al. [69]. At a constant average stress (p^{av} = 266.7 kPa, q^{av} = 200 kPa), three packages, each with 50 cycles, were applied in succession. The amplitudes q^{ampl} = 100, 150 and 200 kPa were tested in different sequences. The residual shear and volumetric strains are illustrated in Figure 3.28. While the course of the curves with N depends on the sequence of the packages, the sequence hardly influences the residual strains at the end of the third package. The concept of an equivalent number of cycles proposed by Kaggwa et al. [69] is able to describe the development of the residual strains under packages of cycles (see the solid curves in Figure 3.28 and also Chapter 6).

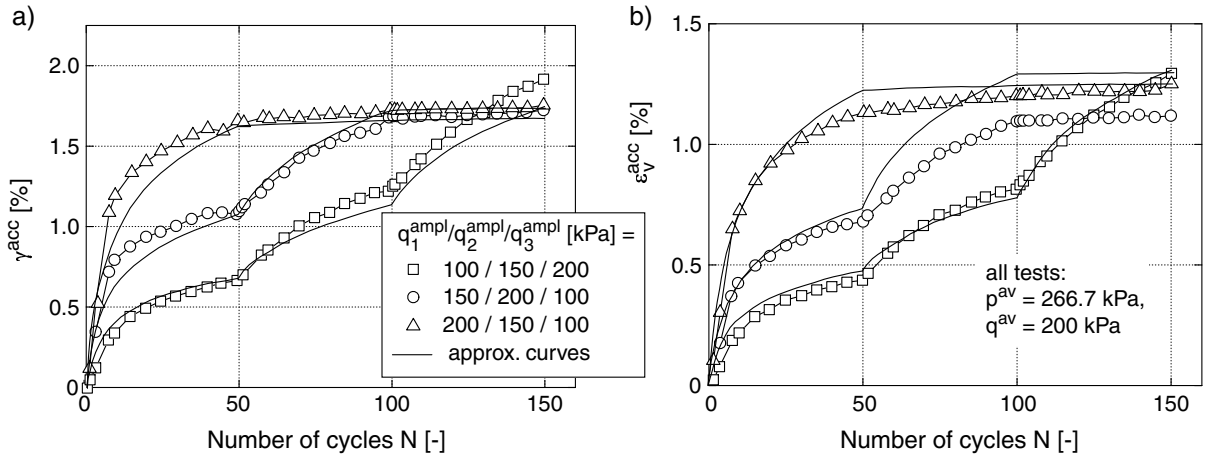

Figure 3.28: *Residual a) shear and b) volumetric strains in tests with packages of cycles after Kaggwa et al. [69]*

3.2.2.11 Aging effects

The term "aging" describes a change of the mechanical properties of a soil with time t under constant external stress. An increase of stiffness and shear strength with t was reported. Aging effects result e.g. from cementation of the grain contacts or an improvement of their micro- or macro-interlocking due to very small relative movements. A detailed study on the cause of aging effects (which could also not answer all questions) was undertaken by Baxter [8]. Aging effects also lead to a reduction of the accumulation rate under cyclic loading. Figure 3.29 presents undrained laboratory tests of Seed [139]. The specimens were cyclically loaded directly after preparation or after a certain period

(1 day $\leq t \leq$ 100 days) under constant stresses. The liquefaction resistance of a specimen which stood 100 days under constant stresses was 25 % higher than the respective value of a freshly pluviated sample. Seed [139] extrapolated his test results to larger periods t and could therewith explain the higher liquefaction resistances in situ compared to re-constituted laboratory specimens of the same material (Figure 3.29).

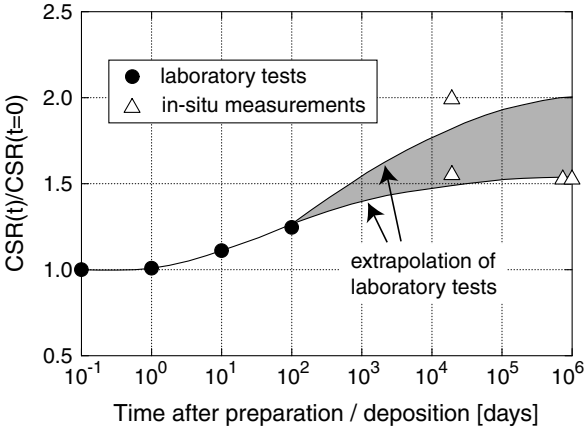

Figure 3.29: *Increase of the liquefaction resistance due to aging of the soil after Seed [139] (CSR = "cyclic stress ratio" = amplitude ratio q^{ampl}/p_0 which is necessary to cause liquefaction after a certain number of cycles)*

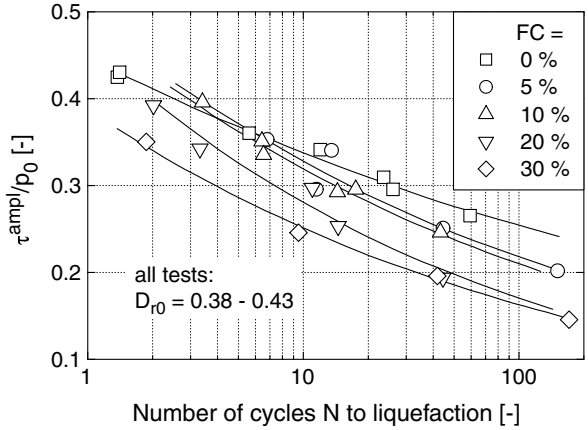

Figure 3.30: *Reduction of the liquefaction resistance with increasing content of fines FC (grains with $d < 0.075$ mm) after Chien et al. [22]*

3.2.2.12 Influence of the grain size distribution curve

Up to the present the influence of the grain size distribution curve of non-cohesive soils on the accumulation rate was rarely studied in drained cyclic tests. Helm et al. [49] observed smaller residual deformations in tests on a fine sand ($d_{50} = 0.13$ mm, $U = d_{60}/d_{10} = 1.75$) compared to a medium coarse sand ($d_{50} = 0.31$ mm, $U = 2.12$). This was explained with the larger non-uniformity index U and the larger maximum grain size of the medium coarse sand. From the results of undrained cyclic tests, Castro & Poulos [17] concluded that the influence of the grain size distribution curve on the liquefaction resistance is as high as the effect of the initial density. Contrary to Helm et al. [49] a faster build-up of excess pore water pressures was observed for soils with a smaller d_{10}. Similar conclusions were drawn by Lee & Fitton [84].

Chien et al. [22] (see Figure 3.30) and Kokusho et al. [77] reported a reduction of the

liquefaction resistance with an increasing content of fines. Elsewhere (Wong et al. [185], Evans & Zhou [30]) one may read, that in undrained tests the accumulation of pore water pressure is slower for gravel or gravelly sand in comparison to sand. Apart from the observations of Helm et al. [49], the test results documented in the literature support an increase of the accumulation rate with decreasing grain size.

3.3 Element tests on the secant stiffness of the stress-strain-hysteresis

Most experimental studies on the secant stiffness of the stress-strain-hysteresis under cyclic loading were performed by means of RC tests. Thus, they examine the dependence of the secant shear modulus G_{hyst} on several influencing parameters.

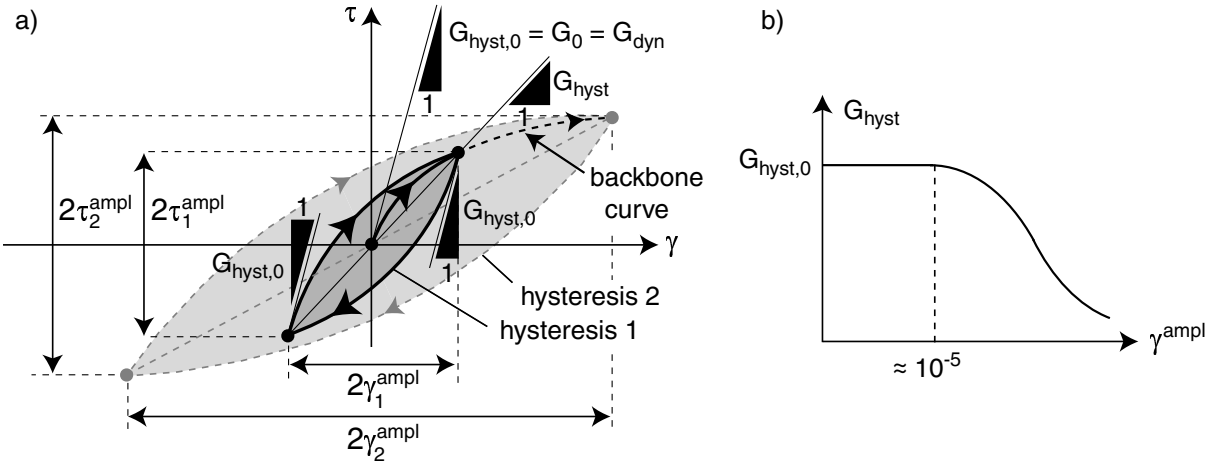

Figure 3.31: *a) τ-γ-hysteresis and definition of secant shear stiffness G_{hyst}, b) Decrease of G_{hyst} with shear strain amplitude γ^{ampl}*

A schematic illustration of a shear stress-shear strain-hysteresis during a cycle is given in Figure 3.31a. Usually the loop is (in contrary to Figure 3.31a, see e.g. Figure 1.4) not perfectly closed. A residual strain or change of stress remains in the material. If one follows the curve of first loading $\tau(\gamma)$, starting from $(\tau, \gamma) = (0, 0)$, the shear stiffness G declines with increasing shear strain γ. Due to the increased shear stiffness directly after a reversal of the strain path and the subsequent decrease of G during continued shearing the loading and the unloading branch of the hysteresis loop differ. Thus, the hysteresis encloses some area in the τ-γ-plane. The secant shear modulus $G_{\mathrm{hyst}} = \tau^{\mathrm{ampl}}/\gamma^{\mathrm{ampl}}$ corresponds to the inclination of a straight line in the τ-γ-diagram through both extreme

points of the hysteresis. Below a certain shear strain amplitude (for sand usually below $\gamma^{\text{ampl}} = 10^{-5}$) the secant shear modulus $G_{\text{hyst}} = G_{\text{hyst},0}$ is not influenced by the shear strain amplitude. This maximum value of the secant shear modulus is identical with the stiffness at the beginning of the curve of first loading. It is also identical with the stiffness directly after a reversal of the strain path. In specialized literature $G_{\text{hyst},0}$ is also addressed as "dynamic shear modulus" G_{dyn}, G_{max} or G_0. For $\gamma^{\text{ampl}} > 10^{-5}$, the secant shear modulus G_{hyst} decreases with γ^{ampl} (Figure 3.31b). In the τ-γ-plane the hysteresis thus lays more flat with increasing shear strain amplitude (compare hystereses 1 and 2 in Figure 3.31a with $\gamma_2^{\text{ampl}} > \gamma_1^{\text{ampl}}$). The maximum of the hysteresis follows the so-called "backbone" curve $\tau(\gamma)$.

The curves $G_{\text{hyst}}(\gamma^{\text{ampl}})$ can be approximated e.g. by a formula of Hardin [44]:

$$G_{\text{hyst}} = G_{\text{hyst},0} \frac{1}{1 + \gamma^{\text{ampl}}/\gamma_r} \tag{3.3}$$

Therein the void ratio and pressure-dependence of the curves $G_{\text{hyst}}(\gamma^{\text{ampl}})$ is taken into account by the reference shear strain γ_r, which can be calculated from the failure shear stress with $\tau = \tau_{\text{max}}$:

$$\gamma_r = \frac{\tau_{\text{max}}}{G_{\text{hyst},0}} \quad \tau_{\text{max}} = \sqrt{\left[(1 + K_0)/2\ \sigma_1 \sin\varphi + c\cos\varphi\right]^2 - \left[(1 - K_0)/2\ \sigma_1\right]^2} \tag{3.4}$$

with the effective vertical stress σ_1, the earth pressure coefficient at rest K_0 and the effective shear strength parameters c (cohesion) and φ (friction angle). Own experiments [180] confirmed a good approximation of the test data from RC tests by the equations (3.3) and (3.4).

The maximum value $G_{\text{hyst},0}$ depends mainly on mean pressure p and void ratio e. Figure 3.32 presents the results of the pioneer work of Hardin & Richart [45]. The shear wave velocity plotted on the ordinate is correlated with the secant shear stiffness at small strains via $v_S = \sqrt{G_{\text{hyst},0}/\varrho}$. $G_{\text{hyst},0}$ decreases with increasing void ratio and increases accordingly to $G_{\text{hyst},0} \sim p^n$ with the mean pressure. In general the exponent n is reported between 0.4 and 0.5. However, Iwasaki & Tatsuoka [68] observed an increase of n with the shear strain amplitude. This question is further discussed on the basis of the own tests in Section 5.2.4.1.

For an estimation of $G_{\text{hyst},0}$ a formula of Hardin [45, 43] is often used:

$$G_{\text{hyst},0}[\text{MPa}] = A \frac{(a - e)^2}{1 + e} \left(p[\text{kPa}]\right)^n \tag{3.5}$$

with $A = 6.9$, $a = 2.17$ and $n = 0.5$ for round grains and $A = 3.23$, $a = 2.97$ and $n = 0.5$ for angular grains. For cohesive soils, Equation (3.5) is extended by the influence of the

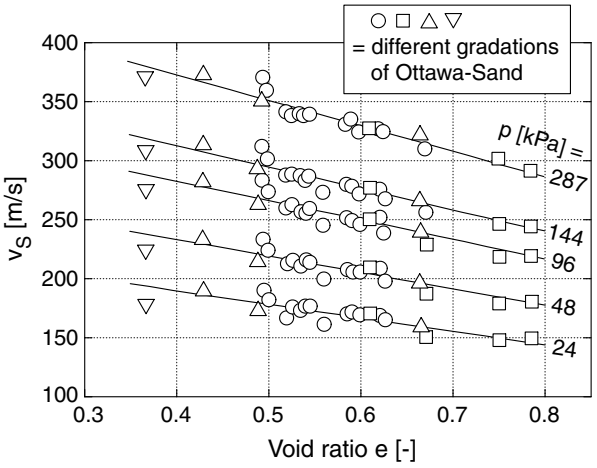

Figure 3.32: *Shear wave velocity* $v_S = \sqrt{G_{hyst,0}/\varrho}$ *as a function of void ratio* e *and mean pressure* p *after Hardin & Richart [45]*

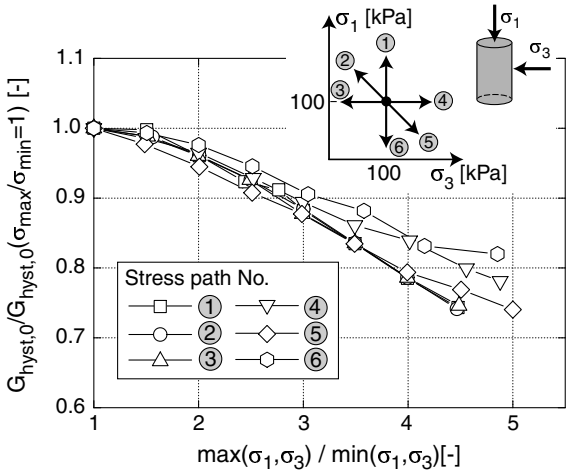

Figure 3.33: *Increase of* $G_{hyst,0}$ *with increasing stress anisotropy after Yu & Richart [189]*

overconsolidation ratio [1]. Equation (3.5) can be made free of dimensions, if the factor $(p_a)^{1-n}$ with the atmospheric pressure $p_a = 100$ kPa is supplemented [43]. In this case, the constant A has to be re-defined. Other authors (e.g. Roesler [130], Bellotti et al. [9]) do not introduce the mean pressure p but the individual stress components into the formula of $G_{\mathrm{hyst},0}$:

$$G_{\mathrm{hyst},0} \quad \sim \quad {p_a}^{1-n-m}\ {\sigma_a}^{n}\ {\sigma_p}^{m} \tag{3.6}$$

Equations of type (3.6) were mostly developed on the basis of measurements of the shear wave velocity in cylindrical or cubical specimens. In Equation (3.6), σ_a and σ_p are the stress components in the direction of shear wave propagation or in the direction of particle movement (polarization), respectively. In the axially symmetric RC test $\sigma_a = \sigma_1$ and $\sigma_p = \sigma_3$ holds. The stress component perpendicular to the plane of wave propagation does not influence $G_{\mathrm{hyst},0}$ (Bellotti et al. [9]). While Roesler [130] determined significantly different values $n = 0.30$ and $m = 0.21$, in later publications (e.g. Bellotti et al. [9], see a summary in Yu & Richart [189]) $n \approx m$ was reported.

An increase of the anisotropy of stress leads to a reduction of $G_{\mathrm{hyst},0}$. This was shown by Yu & Richart [189]. They performed tests, where starting from $\sigma_1/\sigma_3 = 1$ the stress ratio was changed. In Figure 3.33 the shear moduli measured by Yu & Richart [189] at $\sigma_1/\sigma_3 \neq 1$ are divided by the values of the corresponding isotropic stress with the same mean pressure $p = (\sigma_1 + 2\sigma_3)/3$. The decrease of $G_{\mathrm{hyst},0}$ with σ_1/σ_3 is almost linear. For $\sigma_1/\sigma_3 = 2$ the secant shear modulus takes 95 % of the corresponding value at an isotropic

stress.

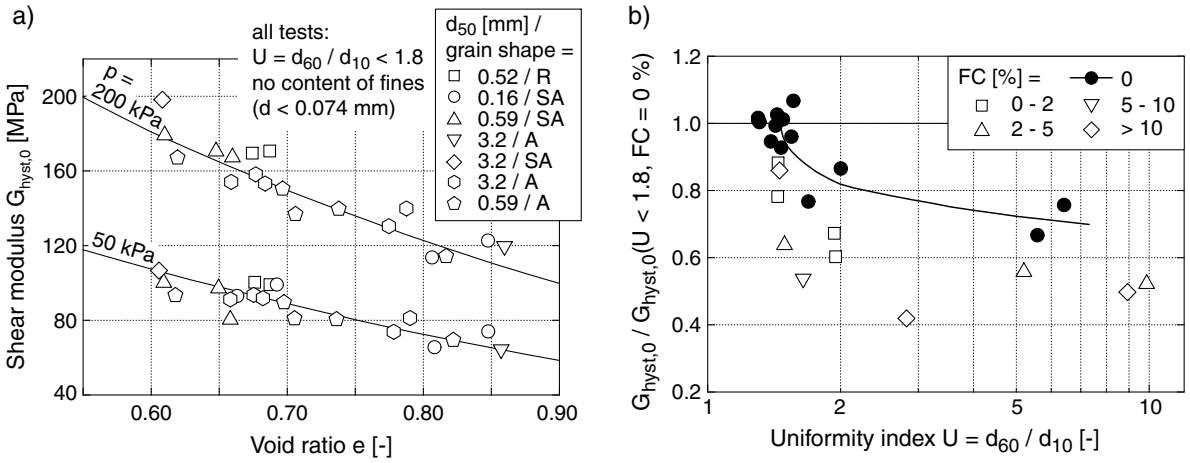

Figure 3.34: *Influence of a) the mean grain diameter d_{50} and the grain shape and b) the uniformity index $U = d_{60}/d_{10}$ and the content of fines FC on $G_{hyst,0}$ after Iwasaki & Tatsuoka [67]*

In partly saturated soils, the capillary pressure causes an increase of the effective stress and thus an increase of the shear stiffness compared to dry or fully saturated soils (Wu et al. [186], Quian et al. [123]). Under constant stresses, $G_{\mathrm{hyst},0}$ increases approximately logarithmically with time (aging, see Afifi & Woods [3], Afifi & Richart [2], Baxter [8] and own experiments in [180]). In geological old deposits, the wave velocities can be significantly higher than in laboratory tests on disturbed specimens. Also the grain size distribution curve influences $G_{\mathrm{hyst},0}$. Iwasaki & Tatsuoka [67] reported a strong reduction of the secant shear stiffness with an increasing content of fines and an increasing uniformity index $U = d_{60}/d_{10}$ (Figure 3.34b). For poorly graded sands, $G_{\mathrm{hyst},0}$ is approximately independent of the mean grain diameter d_{50} and the grain shape (Figure 3.34a, the latter one contradicts Hardin [45]). The influence of the fabric of the grain skeleton or the historiotropy (cyclic preloading) has been discussed controversially in the literature. A detailed survey is given in Section 9.1.1.

The remarks on G_{hyst} made above mostly refer to RC tests or measurements of the shear wave velocity with the direction of propagation along the vertical axis and a polarization in the horizontal direction (wave type $v_{S,vh}$). In the analysis of cyclic triaxial tests, also the secant Young modulus $E_{\mathrm{hyst}} = \sigma_1^{\mathrm{ampl}}/\varepsilon_1^{\mathrm{ampl}}$ is used. Due to pluviation laboratory specimens are transversally isotropic, i.e. they exhibit the same wave velocities in the two horizontal directions but show different wave velocities in the vertical (x_v) and the horizontal (x_h) direction. In that case four independent wave velocities (compression (P-)

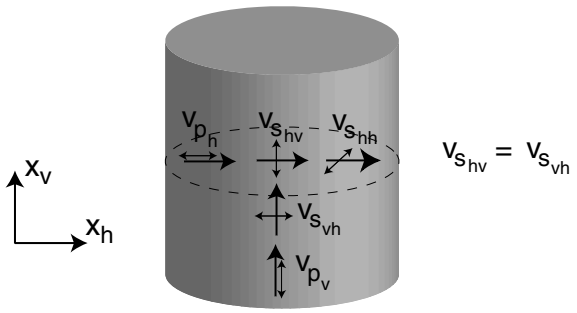

Figure 3.35: *Wave velocities in a transversally isotropic material*

waves v_{Pv}, v_{Ph}, shear (S-) waves $v_{Svh} = v_{Shv}$, v_{Shh}, see Figure 3.35) can be measured (e.g. Bellotti et al. [9], Kuwano et al. [80]). Knowing the soil density ϱ, the secant stiffnesses at small strains can be calculated from the corresponding wave velocities:

$$E_{s,\mathrm{hyst},0} \;=\; \varrho\,(v_P)^2 \quad \text{and} \quad G_{\mathrm{hyst},0} \;=\; \varrho\,(v_S)^2 \tag{3.7}$$

($E_{s,\mathrm{hyst},0}$: secant stiffness for constrained lateral strains). Finally, it should be mentioned, that the area enclosed by the stress-strain-hysteresis (Figure 3.31a) is a measure of the energy dissipated during a cycle. While the secant shear modulus decreases with the shear strain amplitude γ^{ampl}, the material damping increases.

3.4 Model tests, settlement laws and so-called engineering models

3.4.1 Shallow foundations

3.4.1.1 1g - model tests and settlement laws

Holzlöhner [56] performed 1g-model tests on circular foundations (diameter 17.8 cm $\leq d \leq$ 71.4 cm) on a poorly-graded gravelly sand (average, static load F^{av}, load amplitude F^{ampl}, loading frequency 9 Hz $\leq f_B \leq$ 56 Hz). The tests were conducted both in the laboratory and in situ. The soil was deposited in layers and densified to the required initial density (outdoor a vibrator on the soil surface was used). Thus, the soil experienced a cyclic preloading. Figure 3.36 shows the observed linear settlement curves $s(N)$ in a semi-logarithmic scale. In [56] a description of the curves by

$$s(N) \;=\; A\,\ln\left(N/N_a + 1\right) \tag{3.8}$$

with a factor A and a so-called preloading number N_a was proposed. The residual settlement increased with the square of $F^{\mathrm{ampl}}/F^{\mathrm{av}}$ (see also Figure 3.36) and grew with increasing average load F^{av} as well as with decreasing soil density. The influence of the loading frequency was small. Holzlöhner [56] reported, that even in the case of large settlements no densification was observed below the base of the foundation (predominant shear deformations). The soil surface settled only in a small zone around the foundation. For an application in practice, Holzlöhner suggested to perform a model test in situ and to transfer the measured settlement to the prototype.

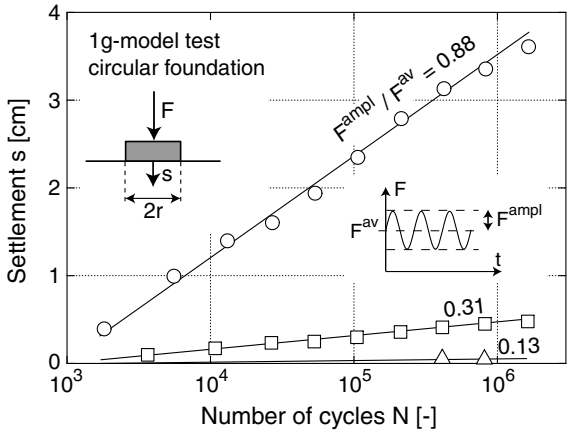

Figure 3.36: *Development of the settlement of a circular foundation under cyclic loading after Holzlöhner [56]*

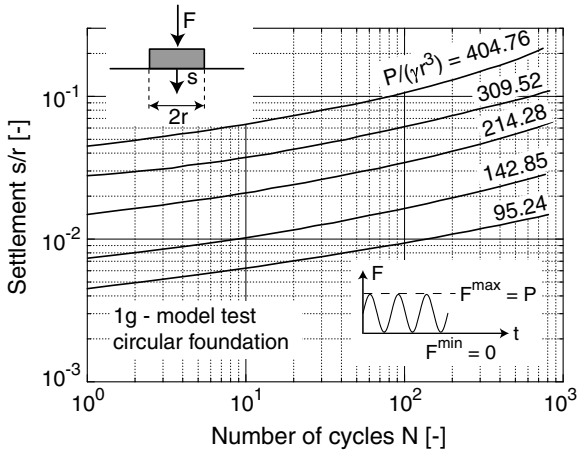

Figure 3.37: *1g-model tests of Hettler [52, 53, 54]: Settlement of a circular foundation under cyclic loading*

Hettler [52, 53, 54] tested circular foundations (radius $r = 5$ cm, embedding $t = 0$) on a dense medium-coarse sand. The axial load was varied within a cycle between the minimum load $F^{\min} = G = 0$ and the maximum load $F^{\max} = G + P = P$. Figure 3.37 shows the settlement curves during 800 cycles for different amplitudes. In the case of the top curve the maximum load $F^{\max}$ corresponds to a fraction of 75 % of the static bearing capacity, for the lowest curve it is 17 % of the bearing capacity. In a diagram with a double-logarithmic scale, Hettler obtained approximately parallel curves. He developed a model law based on the dimensional analysis and a similarity theory. His formula delivers the settlement $s(N)$ of a foundation after N load cycles and considers also the case $G \neq 0$:

$$s(N) \;=\; s_1 \left[1 + f(N) \left(\frac{P}{G+P}\right)^{\alpha}\right] \quad \text{with} \quad s_1 = s(N=1) = f\left(\frac{P}{\gamma\, b^3}, \frac{a}{b}, D_r\right) \tag{3.9}$$

The settlement s_1 after the first cycle depends on the load, the foundation geometry (side lengths $a \times b$ or radius r), the weight γ of the soil and its relative density. The function

$f(N) = C_N \ \ln(N)$ is independent of the load and the soil density, but depends on the geometry of the foundation. For the tested foundations $C_N = 0.55$ was determined. In Equation (3.9), α is another constant. Equation (3.9) with the function $f(N)$ proposed by Hettler reproduces the parallelism of the curves $s(N)$ in the double-logarithmic scale. However, the over-logarithmic course of the settlement curves is not described. The influence of the stress level can be considered by an additional factor [55, 54]. By means of Equation (3.9), Hettler [53] was also able to predict the settlements in a model test with railroad ties under cyclic loading. A major disadvantage of equations of type (3.9) is the extrapolation of the settlement in the subsequent cycles from the settlement in the first cycle. This is further discussed in Section 6.1.4 in connection with the accumulation model of Gotschol [35, 36].

Raymond & El Komos [126] performed 1g-model tests on strip foundations (width 7.5 cm $\leq b \leq$ 22.8 cm). Figure 3.38 presents typical settlement curves $s(N)$ for $F^{\min} = 0$ and different ratios $F^{\max}/F^{\mathrm{BC}}$ (F^{BC}: static bearing capacity). The curves are similar to those of Hettler (if the latter ones are illustrated with a semi-logarithmic scale). In [126] they are approximated by

$$s(N) \quad = \quad \frac{A}{1/\log(N) - B} \qquad \text{with} \qquad A, B = f(F^{\max}, F^{\mathrm{BC}}, b) \tag{3.10}$$

For an identical soil pressure $\sigma = F/b$, smaller residual settlements were measured with increasing width of the foundation (the settlements at $b = 22.8$ cm were only half of the settlements at $b = 7.4$ cm). However, this contradicts observations for monotonic loading (Burland et al. [15], Holzlöhner [57]).

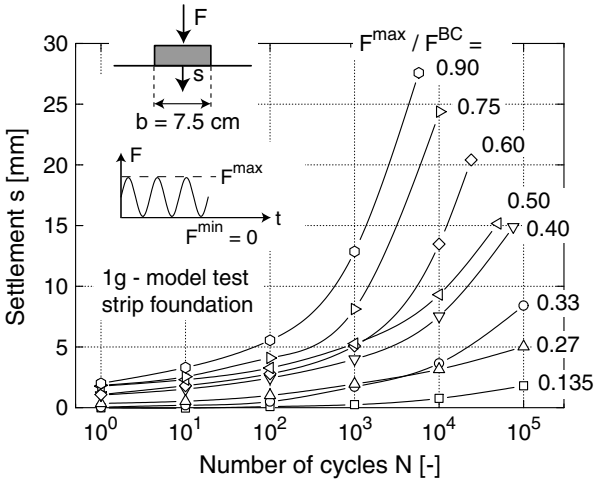

Figure 3.38: *1g-model tests on strip foundations after Raymond & El Komos [126]: Settlement curves $s(N)$ for different load amplitudes*

3.4.1.2 ng - model tests and settlement laws

The own element tests (Section 5.2.4) show, that the accumulation in the soil strongly depends on stress. Therefore, the results of centrifuge model tests, i.e. tests with an increased gravitation, should be closer to reality than small-scale 1g-model tests. Laue [82] performed centrifuge model tests (acceleration level 30 g) on circular foundations (diameter in the prototype $d = 1.68$ m) on a dense fine sand. The average stress σ^{av}, the stress amplitude σ^{ampl} and the depth of embedding t were varied. An increase of the settlement of the foundation proportional to the logarithm of the number of cycles was measured (Bild 3.39a). A lift-up of the soil surface beneath the foundation was observed. Laue [82] proposed a settlement formula, which in contrary to Equation (3.9), decouples the settlements in the first (s_1) and in the subsequent cycles:

$$s(N) \;=\; s_1 + B\ \ln(N) \qquad \text{with} \qquad B = f(t, I_D, \frac{\sigma^{\mathrm{ampl}}}{\sigma^{\mathrm{av}}}, \frac{\sigma^{\mathrm{av}}}{\sigma^{\mathrm{BC}}}) \tag{3.11}$$

The factor B increased with the amplitude σ^{ampl} and with the average load for $\sigma^{\mathrm{ampl}}/\sigma^{\mathrm{av}}$ = constant (Figure 3.39b). It decreased with the depth of embedding. For an application in-situ, Laue [82] recommended to determine B from observations at similar buildings, from test loadings or centrifuge model tests.

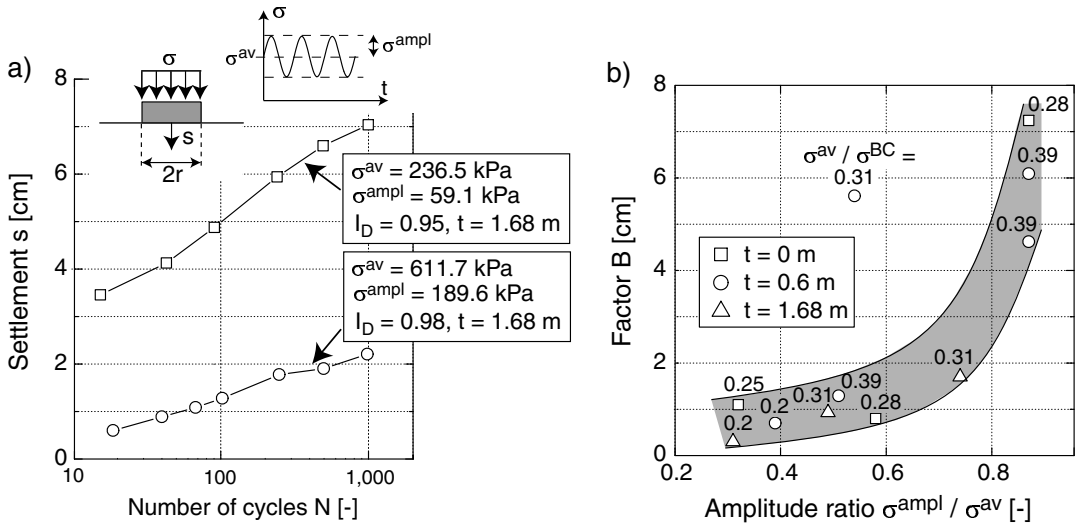

Figure 3.39: *Centrifuge model tests of Laue [82] on circular foundations: a) typical settlement curves $s(N)$, b) factor B of Equation (3.11) in dependence on $\sigma^{ampl}/\sigma^{av}$, σ^{av}/σ^{BC} and the depth of embedding t (derived from data in [82])*

Helm et al. [49] presented a centrifuge model test (acceleration level 30 g), which is recalculated in Section 8.2.1. In this test a strip foundation (width in the prototype b =

1.0 m, Figure 3.40a) was placed without embedding on a freshly pluviated dense fine sand ($I_D \approx 0.9$) and loaded with $N = 10^5$ cycles. Within a cycle, the loading varied with an amplitude $\sigma^{\text{ampl}} = 75.1$ kPa around the average value $\sigma^{\text{av}} = 88.7$ kPa (Figure 3.40a, loading frequency 0.44 Hz in the prototype, static bearing capacity $\sigma^{\text{BC}} = 345$ kPa). Figure 3.40b shows the load-settlement loops for selected numbers of cycles N. With an amplitude of settlement $s^{\text{ampl}} \approx 0.8$ mm the residual settlement after 10^5 cycles was $s(N = 10^5) = 7.3$ cm (including the settlement resulting from the static load and the first cycle). Figure 3.40c presents photos of the marked sand with the strip foundation for $N = 0$ and $N = 70,000$. Both, a slight tilting of the foundation and a bulging of the soil surface beneath the foundation, was observed. Below the foundation, the soil was compacted.

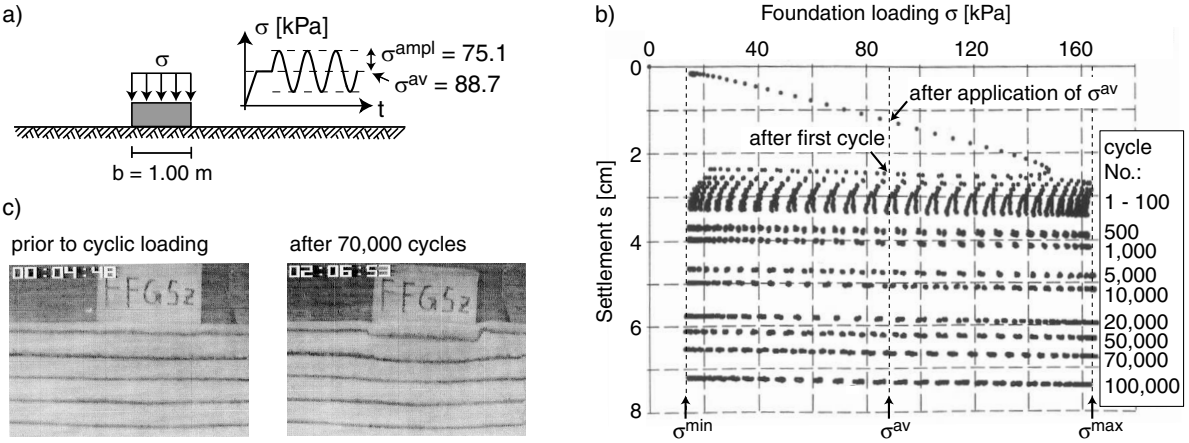

Figure 3.40: *Centrifuge model test of Helm et al. [49] with a strip foundation under cyclic loading: a) prototype, b) load-settlement loops, c) deformation of the half space*

3.4.1.3 So-called engineering models based on laboratory tests

Beside the settlement laws mentioned above so-called engineering models based on laboratory tests were proposed in order to predict the settlements of foundations under cyclic loading.

Mallwitz & Holzlöhner [93] described a procedure to estimate the accumulation of settlements with cyclic oedometric tests. An oedometric compaction of the soil below the foundation up to a depth $z = 2b$ (b = width of foundation) is assumed. For different depths $z \leq 2b$, the static vertical stress $\sigma_1^{\text{av}}(z)$ and the amplitude $\sigma_1^{\text{ampl}}(z)$ (resulting from traffic loads) are determined. With these input parameters, cyclic oedometric tests are performed in order to obtain curves $\varepsilon_1^{\text{acc}}(N, z)$ of the residual vertical strain with the

number of cycles. The settlement of the foundation after N cycles is estimated from an integration of the strains measured in the laboratory over the depth up to $z = 2b$. A similar method using cyclic triaxial tests was described by Diyaljee & Raymond [26].

Sawicki et al. [135] also assume an oedometric compaction of a limited zone below the foundation. The vertical compression of this zone is determined by means of the so-called common compaction curve (Sections 3.2.2.2 and 6.1.1), integrating the residual volumetric strains over the compaction zone. With this method 1g-model tests could be described satisfactorily.

3.4.2 Pile foundations

3.4.2.1 Small-scale 1g-model tests

Chan & Hanna [20] performed 1g-model tests on aluminium piles ($d = 1.9$ cm, $l = 57$ cm) in a medium dense or dense, medium-coarse sand. Prior to cyclic loading the piles were pressed into the dry sand. A pressure of 100 kPa was applied to the soil surface in order to simulate a certain soil depth. In a first series of tests, piles were subjected to a compressive-to-zero repeated loading. At a minimum load of $F^{\min} = 0$, the maximum load $F^{\max}$ was varied between 10 and 50 % of the static ultimate load in compression $Q_{l,c}$. The settlement curves are presented in Figure 3.41a. After a time period with small settlements, which increased with decreasing amplitude, the residual displacements grew over-linearly with N. For larger numbers of cycles Chan & Hanna [20] reported on a re-decrease of the settlement rate. This can also be observed in Figure 3.41a from the settlement curve of the test with $F^{\max} = 0.15\ Q_{l,c}$.

In a second series of tests a compressive-to-tensile (alternating) cyclic loading was performed (Figure 3.41b). The maximum load in compression was kept constant at 15 % of the static ultimate load $Q_{l,c}$, while the minimum load in tension was varied between 0 and 30 % of the ultimate load in tension $Q_{l,t}$. At the beginning of each test, settlements of the piles which developed faster with increasing tensile load, were observed. For $F^{\min} = 0.2Q_{l,t}$ and $F^{\min} = 0.3Q_{l,t}$, a sudden pull-out of the piles after initial settlements was obtained. This may be attributed to the decrease of the normal stress onto the pile shaft due to the densification of the soil and the accompanying reduction of the maximum shear stresses which can be carried by the shaft.

Hettler [54, 52] described 1g-model tests on piles, which were subjected to axial tensile loads. For $P/(\gamma l^3) \geq 0.0059$ (P: double amplitude of tensile load, l: depth of embedding), a step-wise failure occured, i.e. a linear or over-linear increase of the pile lift-up u with

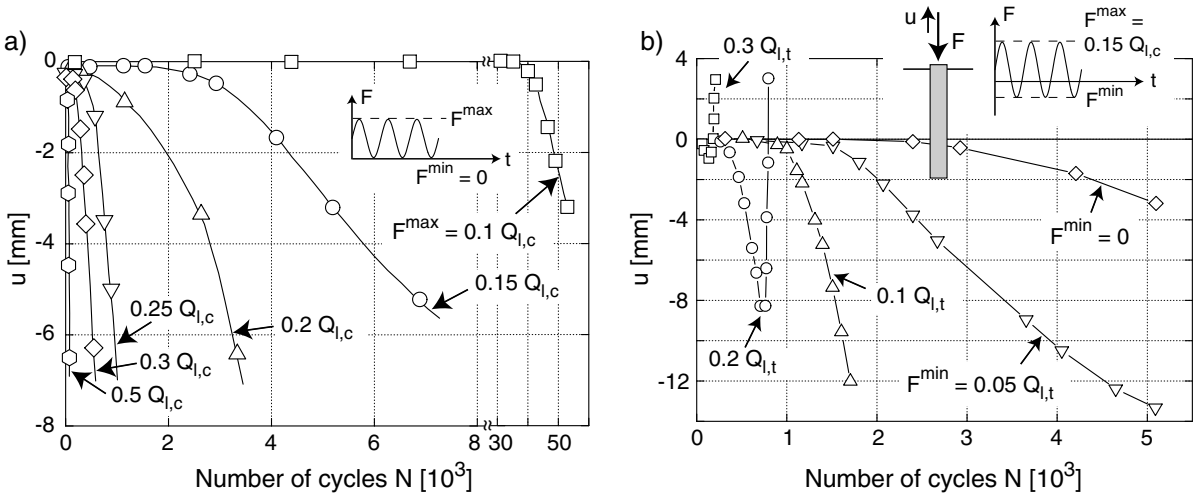

Figure 3.41: *Cyclic 1g-model tests on piles with a) compressive-to-zero cyclic loading and b) compressive-to-tensile cyclic loading after Chan & Hanna [20]*

N (Figure 3.42a) took place. Finally, the pile was pulled out of the soil. Piles which were loaded with amplitudes below the critical value $P/(\gamma l^3) = 0.0059$ exhibited an abation, i.e. an under-linear curve $u(N)$ (Figure 3.42a). Similar curves $u(N)$ for tensile-to-zero cyclic loading were measured by Chan & Hanna [20].

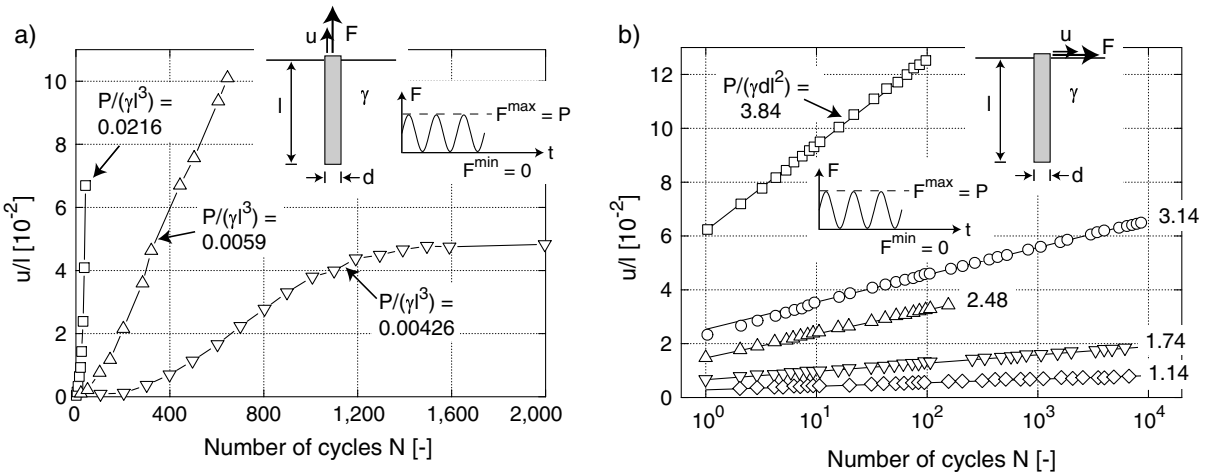

Figure 3.42: *1g-model tests on piles of Hettler [54, 52] with a) cyclic axial tensile loading and b) cyclic horizontal loading*

Figure 3.42b illustrates 1g-model tests of Hettler [54, 52], where piles (l = 18.5 cm, d/l = 0.14) were subjected to a horizontal cyclic loading. For different loads, an increase of the horizontal displacement of the pile top proportional to $\ln(N)$ was measured. The

model law given in Equation (3.9) can be also used for the horizontally loaded pile, if the horizontal displacement u replaces the settlement s. For the tests in Figure 3.42b $C_N = 0.2$ was determined.

The development of the shaft friction and the tip resistance under cyclic loading was studied by Le Kouby et al. [83]. Model piles ($d = 2$ cm, $l = 50$ cm) were tested in a medium dense sand. The tests were performed in a calibration chamber with specified vertical and horizontal stresses. For a model pile which was pressed into the soil, a decrease of the shaft friction (mean value over 20 cm shaft length) and an increase of the tip resistance with N was measured (Figure 3.43a). In contrary to this, if the sand was pluviated around the pile, an increase of the skin friction and a decrease of the tip resistance occured.

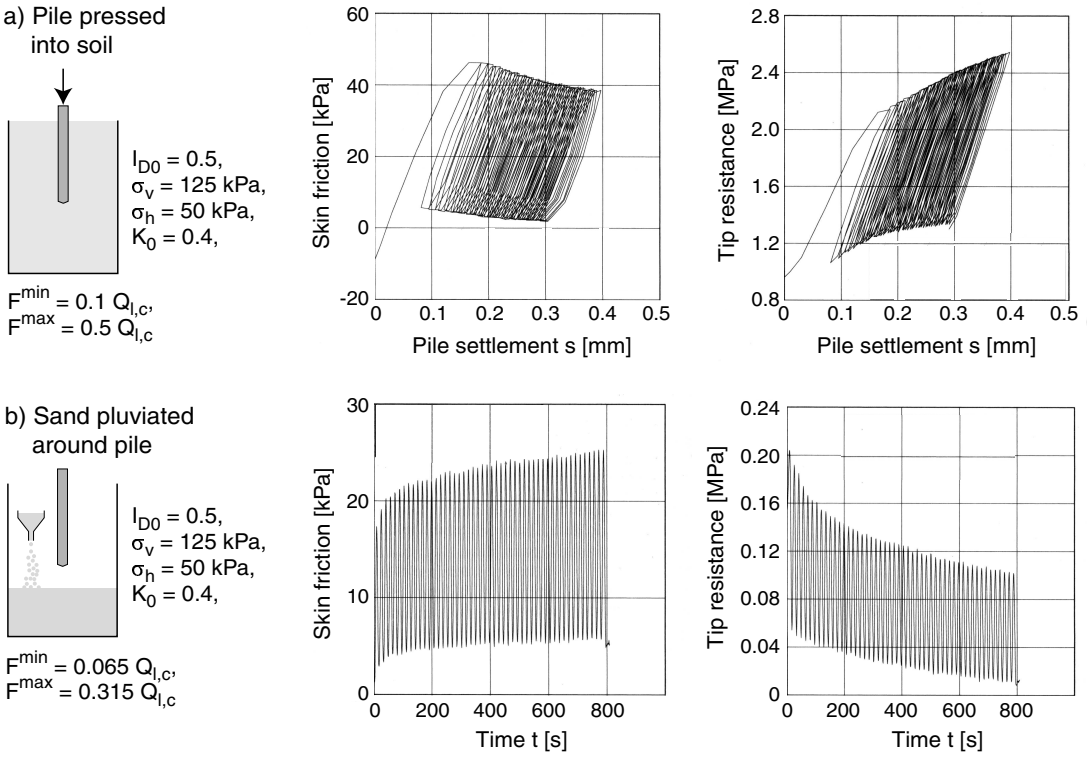

Figure 3.43: *Development of the skin friction and the tip resistance in tests of Le Kouby et al. [83] on model piles, which were embedded into the soil by different methods*

3.4.2.2 Large-scale 1g-model tests and in-situ tests

Gruber et al. [37] and Schwarz [138] tested grouted piles (diameter approx. 13 cm, length approx. 5 m) under cyclic axial loading. A silty fine to medium coarse sand was filled

into a testing pit layer by layer. A vibrator was used to densify the soil to $D_r = 0.42$. The piles were installed under in-situ conditions and afterwards subjected to compressive or to compressive-to-tensile cyclic loading. The settlement curves of two tests with compressive-to-tensile cyclic loading are shown in Figure 3.44a. In both tests the permanent axial displacements remained relatively small up to $N = 10^4$, while the amplitudes of displacement slightly increased with N. Between $N = 10^4$ and $N = 10^5$ in both tests a sudden increase of the displacement amplitude occurred. Both, the lift-up under minimum load and the pull-down under maximum load, increased. The tests were stopped when a lift-up of 10 mm was reached. Thus, the failure of the piles under compressive-to-tensile cyclic loading occurs suddenly and without noticeable warning. This was already demonstrated by the small-scale tests of Chan & Hanna [20] (Figure 3.41). In the case of a compressive cyclic loading (Figure 3.44b) an increase of the pile settlement proportional to $\ln(N)$ was measured up to $N = 10^4$. For larger numbers of cycles an over-logarithmic accumulation was observed.

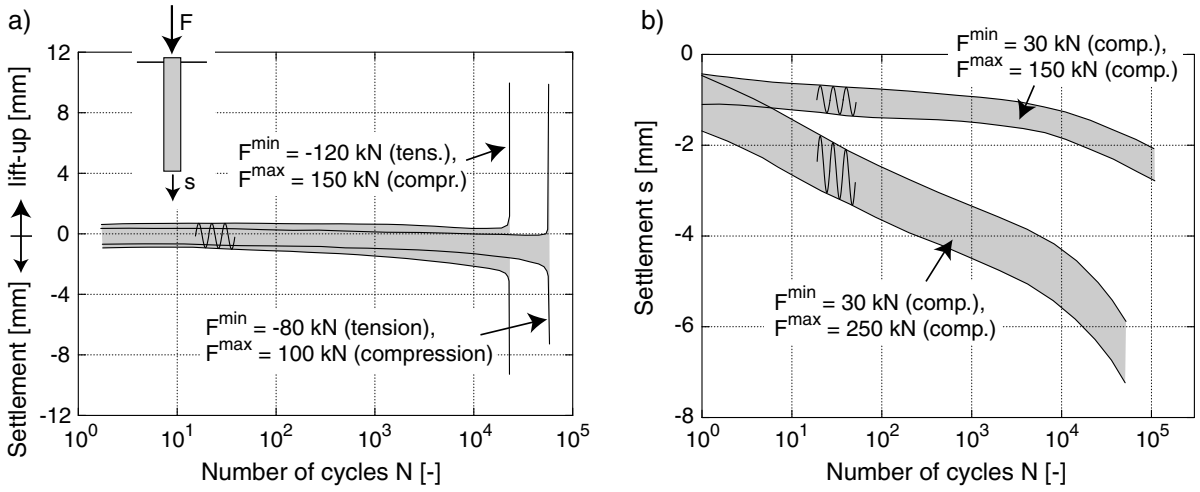

Figure 3.44: *Cyclic axial loading of grouted piles after Gruber et al. [37]: tests with a) compressive-to-tensile cyclic loading and b) compressive cyclic loading*

Schwarz [138] reported that a failure of the piles was commenced much faster, when the sand was flooded. Thus, the capillarity of the moist sand significantly reduces the accumulation of deformation and delays a failure. Figure 3.45 (after Schwarz [138]) illustrates the development of the shear stress, which is transmitted into the soil over the shaft of the grouted piles. While the shear stresses in the upper part of the pile decreased with the number of cycles N, an increase could be observed for larger depths. Gruber et al. [37] also presented an in-situ cyclic loading of a drilled pile. However, the loading scheme was complex and only approx. 100 cycles were tested. Trofimenkov & Mariupolskii [168]

reported on in-situ-tests on screwed piles. Recent test series on a monopile (horizontal cyclic loading of a steel pipe, Savidis et al. [132]) are still at the beginning.

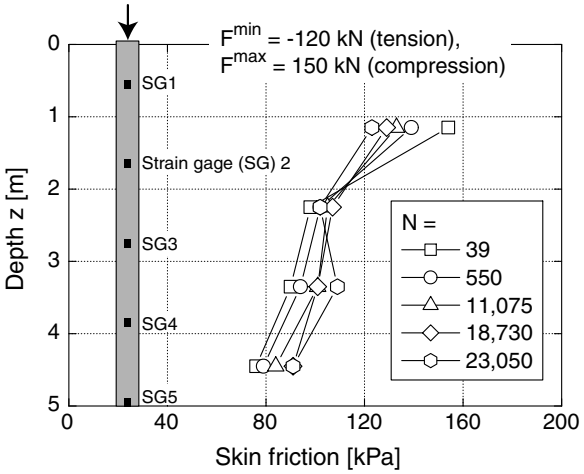

Figure 3.45: *Development of skin friction with the number of cycles in a test of Gruber et al. [37], after Schwarz [138]*

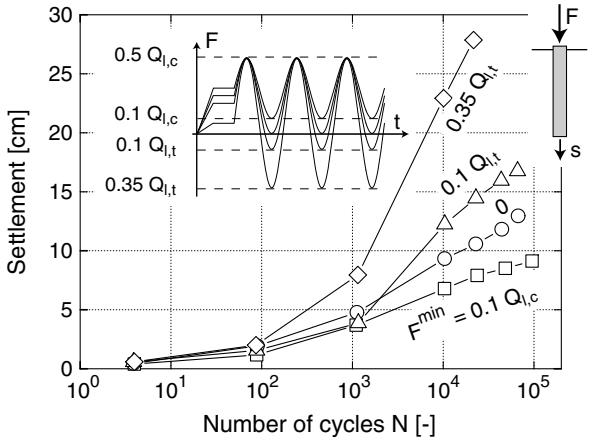

Figure 3.46: *Settlement of a pile in sand under axial cyclic loading, centrifuge model tests of Staupe [152]*

3.4.2.3 Centrifuge model tests

Staupe [152] performed centrifuge model tests (acceleration 30 g). Aluminium piles (diameter $d = 0.45$ m, depth of embedding $t = 4.65$ m in the prototype, surface pasted up with sand) in a dense fine sand ($I_D > 0.9$) were subjected to an axial cyclic loading. The axial load was oscillating with a loading frequency (prototype) of 0.33 or 0.033 Hz, respectively, between $F^{\max} = 0.5Q_{l,c}$ and different minimum loads ($0.35Q_{l,t} \leq F_{\min} \leq 0.1Q_{l,c}$), i.e. both, compressive and compressive-to-tensile cyclic loading, were tested. The axial displacement of the pile with N is presented in Figure 3.46. For the chosen loads always settlements were obtained. The increase of the settlements with increasing number of cycles was over-logarithmic. With increasing amplitude the settlement rate increased.

3.4.2.4 Engineering models

Models for the description of pile displacements were developed amongst others by Poulos [118, 119, 120] and Sawicki & Swinianski [156]. However, the model of Poulos is mainly based on theoretical considerations and many assumptions. The method of Sawicki & Swinianski uses an accumulation model with several disadvantages (Section 6). A detailed description is set aside here.

Chapter 4

Own experimental studies

4.1 Testing devices and specimen preparation

In the studies on the influence of several parameters on the accumulation rate under cyclic loading, several cyclic triaxial devices were used as well as a novel multidimensional simple shear device. In the experiments on the correlation of the historiotropy with dynamic soil properties (Section 9.1), a resonant column device and a triaxial cell with piezoelectric elements were employed. Beside the construction of the test devices, the specimen preparation method and the measurement technique are presented in the following.

4.1.1 Triaxial devices

Two types of triaxial cells (in the following addressed as *type I* and *type II*), which differ concerning their construction, were applied. Four triaxial cells of type I and one of type II were available.

The principal construction of the triaxial cells of type I is illustrated in the scheme in Figure 4.1. The photo in Figure 4.2 shows this type of triaxial cell in a pneumatic loading frame. A special feature of these cells is the location of the load cell for the measurement of the axial load. This load cell is placed under the specimen base plate in a free space sealed against the cell water. The axial load acting onto the base plate is conducted into the load cell via a rod, which is rigidly connected to the base plate and runs into a ball bearing. Thus, the axial load is measured directly at the base of the specimen and a falsification due to friction at the sealing of the load piston is prevented. Moreover, a low-friction sealing ring is used at the lead-through of the load piston. The load piston, which is guided by a ball bearing, and the specimen top cap are rigidly connected in

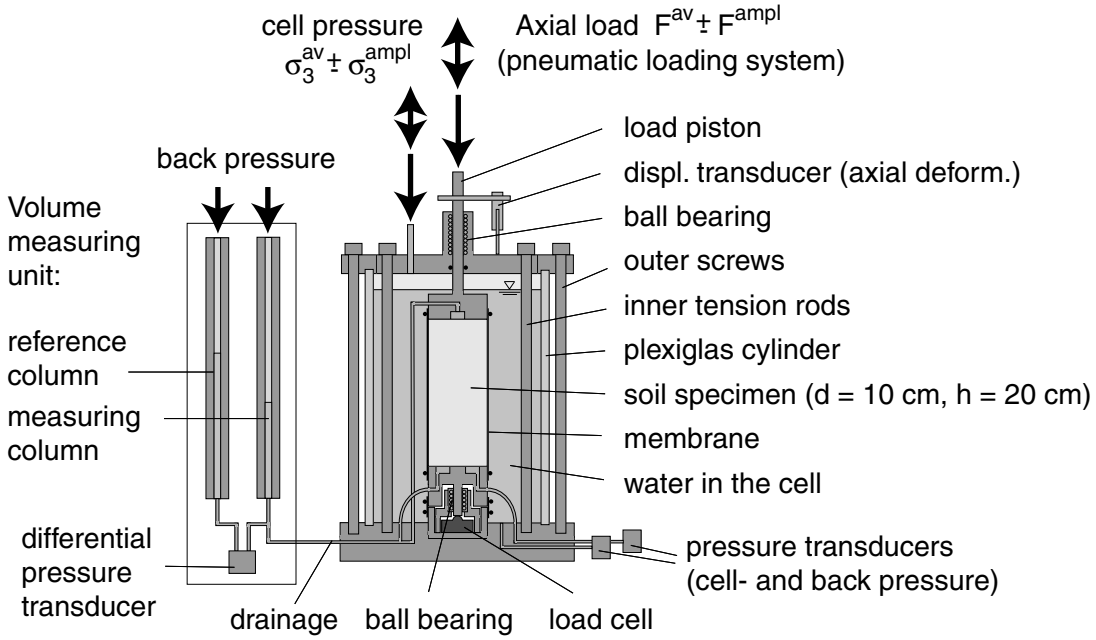

Figure 4.1: *Scheme of the triaxial cell of type I*

order to prevent tilting. The top plate of the triaxial cell consists of two parts, the inner plate (with the ball bearing of the load piston) and an outer ring, which serves for fixing the plexiglas cylinder. This allows specimen preparation, in particular the placement of the specimen top cap onto the soil surface and the measurement of the geometry of the specimen, before the plexiglas cylinder is mounted.

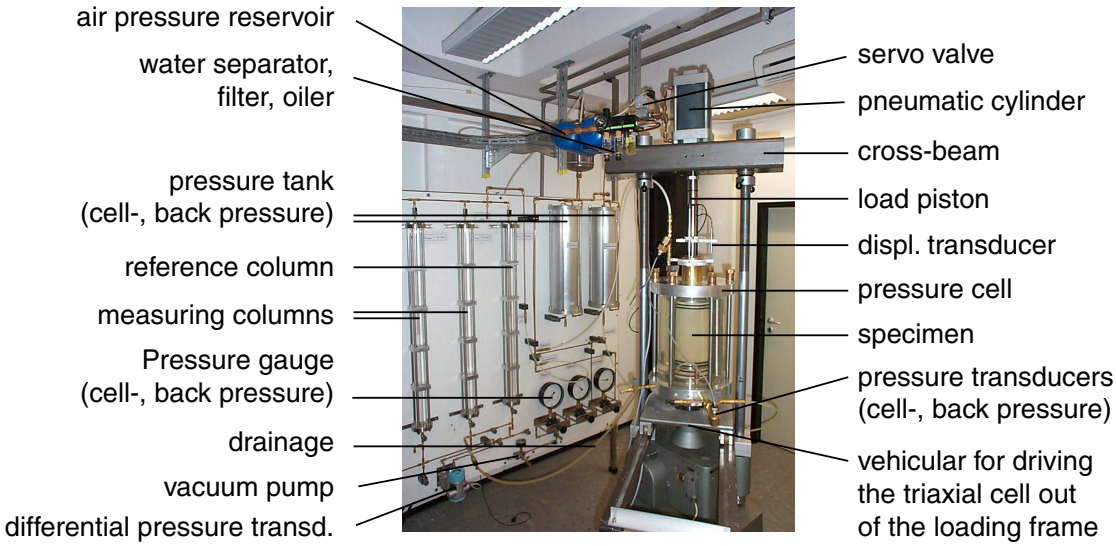

Figure 4.2: *Photo of the triaxial cell of type I in a pneumatic loading frame*

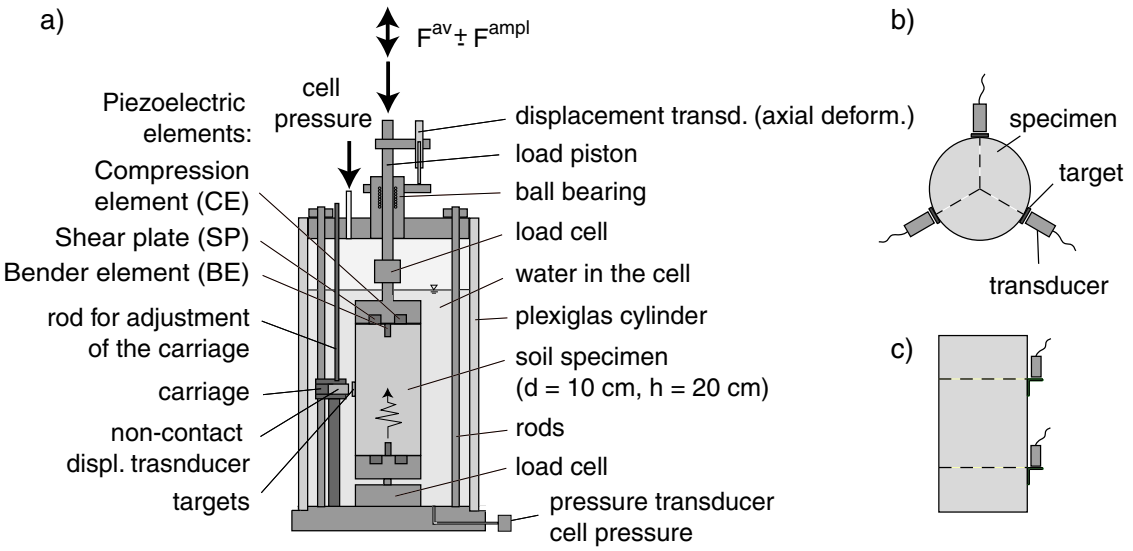

Figure 4.3: *Scheme of the triaxial cell of type II*

The triaxial cell of type II (Figure 4.3a) differs from type I concerning the arrangement of the load cells (one below and one above the specimen). Also the mounting of the plexiglas cylinder is different (Figure 4.3a). The additional equipment of this triaxial cell for the measurement of wave velocities is explained in Section 4.1.4.

For the purpose of specimen preparation (specimen diameter $d = 10$ cm, height $h = 20$ cm), the specimen end plates were lubricated with a thin film of grease and a thin latex membrane was applied. This lubrication reduces the friction at the end plates and supports the generation of a homogeneous stress field in the specimen. In the analysis of the tests, the measured axial strain amplitude $\varepsilon_1^{\text{ampl}}$ was corrected by the elastic deformation of the membranes at the end plates. This so-called "bedding error" was determined in a preliminary test on a steel dummy. After the lubrication of the end plates the latex membrane of the specimen (thickness $t_M = 0.4$ mm) was pulled over the specimen base plate and sealed with O-rings (Figure 4.4b). The mounting of the split moulds (Figure 4.4c) followed and the membrane was sucked to the moulds by means of vacuum. The dry sand was pluviated out of a funnel into the moulds (Figure 4.4d). The funnel was continuously lifted up in order to keep the distance between the outlet of the funnel and the sand surface in the mould constant. Different soil densities were achieved by choosing different fall heights and diameters of the funnel. After having flattened the soil surface (Figure 4.4e), the load piston with the specimen top cap was placed and the membrane was sealed to this top cap with O-rings. The specimen was stabilized by a vacuum of 50 kPa. Afterwards the moulds could be removed (Figure 4.4f). The geometry of the specimen was measured, the plexiglas cylinder was mounted and the cell was filled with

water. An air cushion remained in the upper part of the pressure cell. The cell pressure was applied on this air cushion. The vacuum in the specimen was gradually replaced by the cell pressure keeping the effective stress constant.

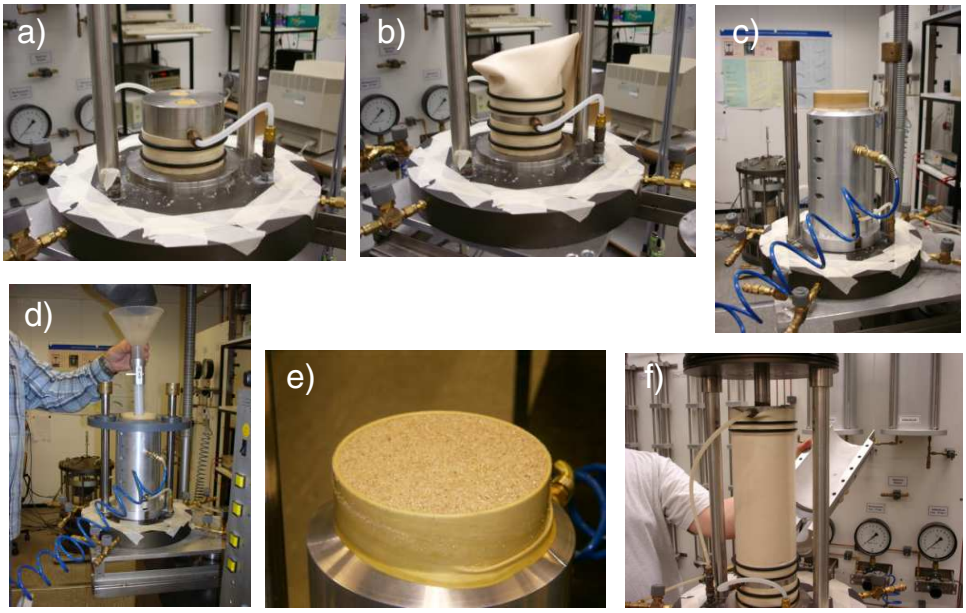

Figure 4.4: *Preparation of a specimen for a triaxial test: a) specimen base plate before lubrication, b) pulling over and sealing of the membrane, c) mounting of the split moulds, d) pluviation of the sand out of a funnel, e) flattened soil surface, f) specimen under vacuum after the removal of the moulds*

Most tests were performed on fully water-saturated specimens. They were first flushed with carbon dioxide (CO_2) and afterwards saturated with de-aired water. The drainage was connected to one pipe of the volume measuring unit (see Figures 4.1 and 4.2). A back pressure of usually 200 kPa was applied via this pipe. The cell pressure was kept always higher than the back pressure. After a period of approximately one day, the saturation of the specimen was checked by means of the B-value of Skempton (criterium for a sufficient saturation: $B \geq 0.95$). The isotropic effective stress was re-increased to $p = 50$ kPa. It was assumed that the procedure of saturation causes no deformation of the specimen (a measurement of all deformations during saturation was not possible). Thus, the geometry of the specimen after saturation and at $p = 50$ kPa was assumed to be identical with the geometry measured in the dry condition under a vacuum of 50 kPa.

Starting from this small effective isotropic stress, the average stress $\boldsymbol{\sigma}^{\mathrm{av}}$ of the individual test was applied. First, the cell pressure was increased and afterwards the axial load was increased (triaxial compression) or reduced (triaxial extension). The deformations of the

specimen during the application of $\boldsymbol{\sigma}^{\mathrm{av}}$ were measured. After a consolidation period of approx. 1 h the average stress was superposed by stress cycles.

For the application of the axial load four pneumatic loading systems (Figure 4.2) and one freely programmable load press were available. In one device also the cell pressure σ_3 could be varied cyclically by means of a pneumatic valve.

Due to the large deformations, the first cycle was applied with a low frequency $f_B = 0.01$ Hz. This way an unintentional build-up of excess pore water pressure and a possible liquefaction of the specimens due to a too fast loading was prevented. The subsequent mostly 10^5 load cycles were applied with a frequency of 1 Hz. In the tests with triaxial extension and in the tests with a cyclic variation of the lateral stress σ_3 smaller frequencies (0.1 Hz or 0.05 Hz, respectively) were chosen, due to technical reasons (adapter for tension loads or application of σ_3 via the air cushion in the upper part of the pressure cell, respectively). In these tests only 10^4 cycles were tested.

The axial deformations of the specimens were measured by means of a displacement transducer which was attached to the load piston outside the pressure cell. The volume changes of fully water-saturated specimens were determined via the squeezed out or absorbed pore water. For this purpose a differential pressure transducer was employed (see Figures 4.1 and 4.2, in Figure 4.3a the volume measuring unit is not illustrated). In the triaxial cell of type II the lateral deformations of dry specimens were determined by means of six non-contact displacement transducers. Flat aluminium targets were glued onto the membrane and the transducers were placed with a certain distance in front of these targets. A carriage system allowed the adjustment of this distance in the case of large deformations of the specimens. A possible arrangement of the transducers is shown in Figure 4.3b. Studies of Niemunis [105] with the PIV-(Particle Image Velocimetry) method (Raffel et al. [124]) revealed, that the strain field within a triaxial specimen under monotonic and cyclic loading is inhomogeneous. These inhomogeneities in the field of the amplitude and in the field of the accumulation rate remain even after a large number of load cycles. Although there may be a loose zone at the top of the specimen stemming from the preparation procedure, the axial strain measured at the whole specimen is thought to be more representative than the local measurement between two points with a short distance (see the possible measurement by means of angular targets in the triaxial cell of type II, Figure 4.3c). The measurement technique was completed by pressure transducers for the control of cell and back pressure.

During cyclic loading, the signals of all transducers were recorded by means of a data acquisition system. In order to reduce the amount of data, five complete cycles were sampled in certain intervals. The distance between these recordings was increased proportional to

$\ln(N)$.

In anticipation of the test results presented in Chapter 5, the good reproducibility of the tests should be mentioned. This is supported by the results of four identical tests which are illustrated in Figure 4.5. Figure 4.5a shows the coincident accumulation curves $\varepsilon^{\mathrm{acc}}(N)$, while the $\varepsilon_q^{\mathrm{acc}}$-$\varepsilon_v^{\mathrm{acc}}$-strain paths, which were only slightly different, are presented in Figure 4.5b.

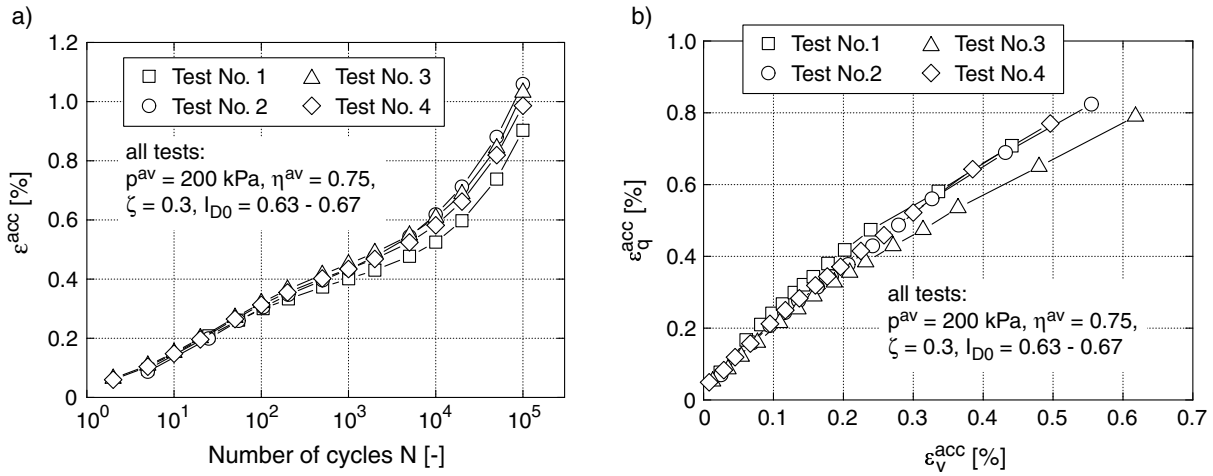

Figure 4.5: *Reproducibility of the cyclic triaxial tests: a) accumulation curves $\varepsilon^{acc}(N)$, b) ε_q^{acc}-ε_v^{acc}-strain paths (direction of accumulation)*

4.1.2 Multidimensional simple shear device (CMDSS device)

In order to compare the accumulation rates due to a circular and a uniaxial cyclic shearing and in order to study polarization changes, i.e. changes of the direction of the cycles in the stress or strain space, a simple shear device was developed. It is called Cyclic MultiDimensional Simple Shear (CMDSS) device or colloquial "hula-hoop"-device. A scheme and a photo of this testing apparatus can be found in Figure 4.6.

The test device is a modified NGI-type (Kjellman [74], Bjerrum & Landva [10]) simple shear device. The specimen base plate is guided by ball bearings in such way, that only horizontal movements in both directions x_1 and x_2 are allowed and vertical ones are prevented. The cyclic movement of the specimen base plate is caused by an electric motor which rotates an eccentric. The eccentric runs in a cut-out of a plate, which is rigidly screwed to the specimen base plate. Different displacement paths in the x_1-x_2-plane (uniaxial and circular cycles, different amplitudes, see a sequence of deformations

in Figure 4.7a) can be tested by using different eccentrics and cut-outs. The specimen top cap is movable only in the vertical direction, since it is guided by three ball bearings.

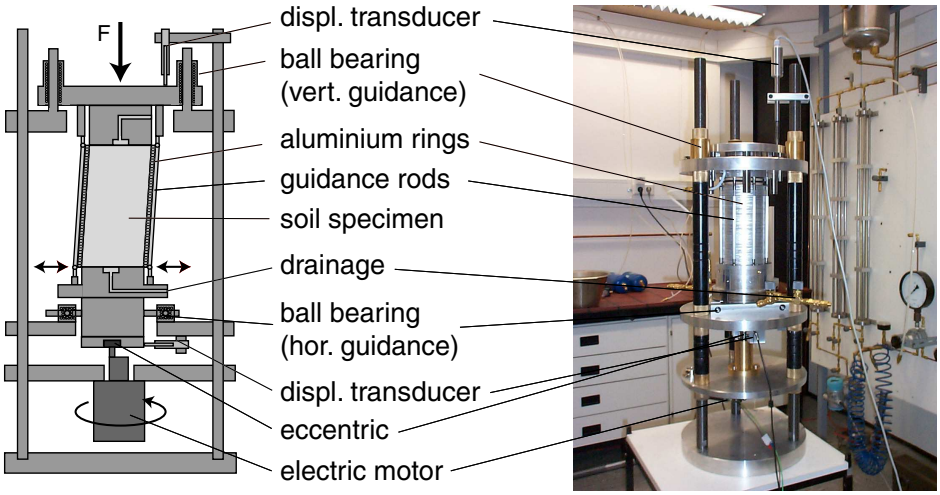

Figure 4.6: *Scheme and photo of the CMDSS device*

A lateral deformation of the specimen (diameter $d = 10$ cm, height $h = 20$ cm) is prevented by means of 200 aluminium rings each of 1 mm thickness, which surround the specimen over the complete height. Sand and aluminium rings are separated by a latex membrane. The aluminum rings are guided by eight vertical rods. The rods are extendable and connected to the specimen end plates with ball joints. In this way a displacement of the lateral boundaries of the specimen, which decreases linearly with the specimen height, is achieved.

In the tests presented in Chapter 5, the axial stress σ_1 was applied by placing weights on the upper specimen end plate. Thus, the tests were performed at relatively small stresses. Since the lateral strain is prevented, a kind of K_0-initial stress state develops. The specimens were prepared by pluviating dry sand out of a funnel. During the procedure of pluviation the split moulds enclose both, the latex membrane and the 200 aluminium rings. The specimens were also tested under dry conditions. All CMDSS tests were performed with a loading frequency of $f_B = 0.5$ Hz. The axial deformation was measured with a displacement transducer. Since no lateral deformations are possible $\varepsilon^{\mathrm{acc}} = \varepsilon_v^{\mathrm{acc}}$ holds. The horizontal movement of the specimen base plate was controlled by two displacement transducers mounted orthogonally to each other. The signals of all transducers were recorded with a data acquisition system.

A major disadvantage of all simple shear devices is the inhomogeneous distribution of strain over the specimen volume (although the displacements of the boundaries increase

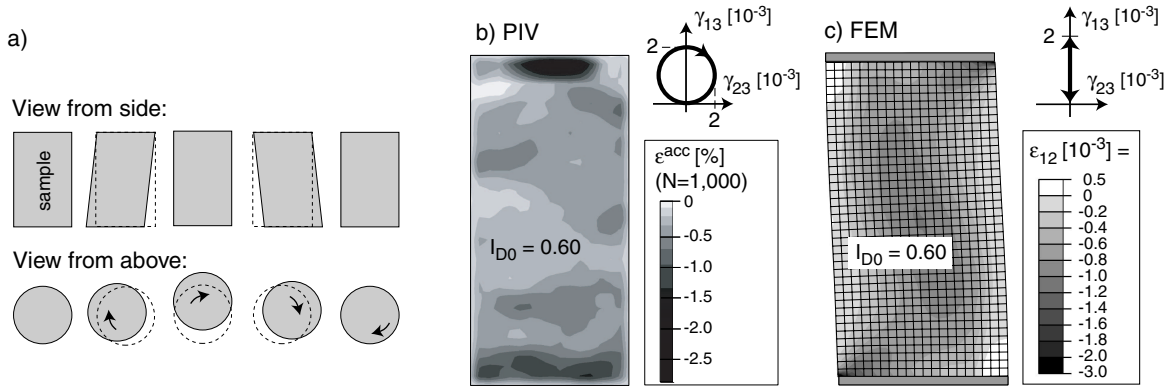

Figure 4.7: a) Sequence of deformations during a circular cyclic shearing, b) Field of ε^{acc} in a CMDSS specimen in a test without aluminium rings (PIV-analysis), c) Distribution of shear strains in a corresponding FE calculation (2-D) with a hypoplastic material

linearly with height, see also Budhu [13, 14]). The inhomogeneities within a specimen in the CMDSS device were studied with a PIV analysis and in FE calculations. Deviating from the usual test procedure, the aluminium rings had to be removed for the PIV analysis. The specimen was stabilized by a vacuum of 15 kPa. The membrane was provided with colour springes. Before and after the application of 1,000 circular strain cycles a photo of the specimen was taken. From a comparison of the photos, i.e. the change of the location of the colour springes, the strain field in the specimen could be obtained. From Figure 4.7b it can be seen, that this field is very inhomogeneous. The accumulated strain concentrates at the ends of the specimen. The strain amplitudes seem to be larger at the ends of the specimen than in its middle. Thus, the middle of the specimen performs a rigid rotation. The corresponding FE calculation of a monotonic uniaxial shearing of the specimen using a hypoplastic material (Figure 4.7c) also exhibited an inhomogeneous strain field and a concentration of the shear strains at the ends of the specimen. The shear strains in the middle of the specimen were less than those at the ends, but they were not as small as it could be expected from the PIV analysis.

In further FE calculations the aluminium rings and thus the linear displacement of the boundary over the specimen height were modelled. Also the friction between the membrane and the aluminium rings was considered (a coefficient of friction $\mu = 0.5$ was assumed, Figure 4.8a). It was expected that this friction leads to a more homogeneous strain field, but also to a reduction of the settlements of the specimen. Figures 4.8b and 4.8c present calculations with shear strains $\gamma = 10^{-3}$ and $\gamma = 10^{-2}$. These shear strains represent the limits of the amplitudes tested. The strain field at $\gamma = 10^{-3}$ is more homogeneous than in the case of the calculation without the aluminium rings (Figure 4.7c). With increasing shear strain γ, the inhomogeneity increases (compare Figures 4.8b and

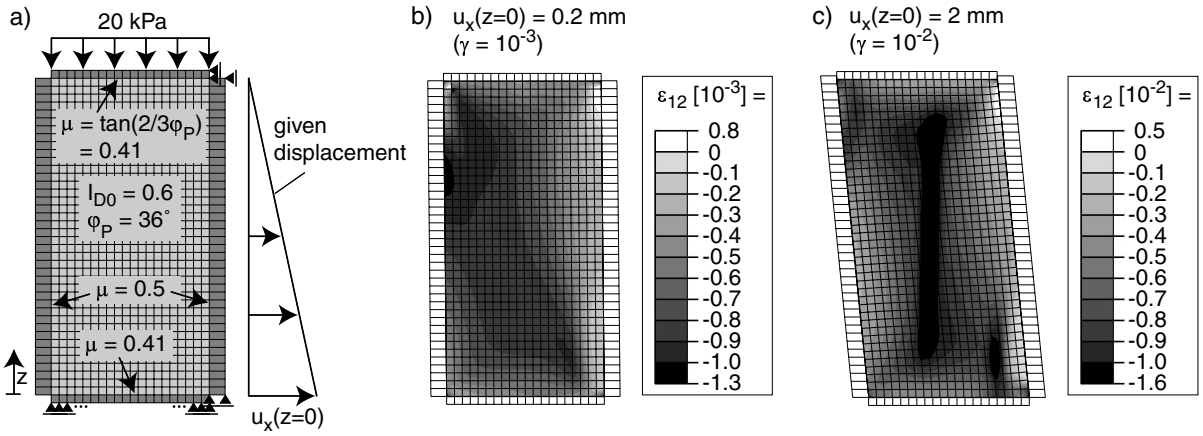

Figure 4.8: FE calculations (2-D) of the CMDSS test with the aluminium rings and a hypoplastic material

4.8c) and a localization occurs (Figure 4.8c).

In contrary to the triaxial test, due to the inhomogeneous strain field the simple shear test cannot be seen as an element test. The test results are of a qualitative nature. However, the influence of the shape of the strain loop and the effect of polarization changes can be demonstrated clearly by means of this test device.

4.1.3 Resonant column (RC) device

The used RC device (Figure 4.9) is of the "free - free" type, i.e. both the top and the base mass are freely rotatable. The cuboidal top mass (so-called *excitation head*) is equipped with two electrodynamic exciters each of them accelerating a small mass. This acceleration is measured with an acceleration transducer. Thus, the driving force $F(t)$ in the axis of the electrodynamic exciter can be determined. The pair of driving forces results in a torsional moment acting on the top of the cylindrical specimen. Other acceleration transducers measure the acceleration of the excitation head. From an integration the twist $\phi(t)$ of the specimen at its top can be calculated. The system composed of the base mass, the specimen and the top mass is enclosed in a pressure cell which can sustain cell pressures σ_3 up to 800 kPa. The state of stress is almost isotropic. A small stress anisotropy results from the weight of the top mass ($m \approx 9$ kg), i.e. the vertical stress σ_1 is slightly higher than the lateral one σ_3. However, for larger cell pressures this anisotropy is of secondary importance.

A sinusoidal electrical signal is generated by a function generator, amplified and applied to the electrodynamic exciters. The frequency of excitation is varied until the resonant

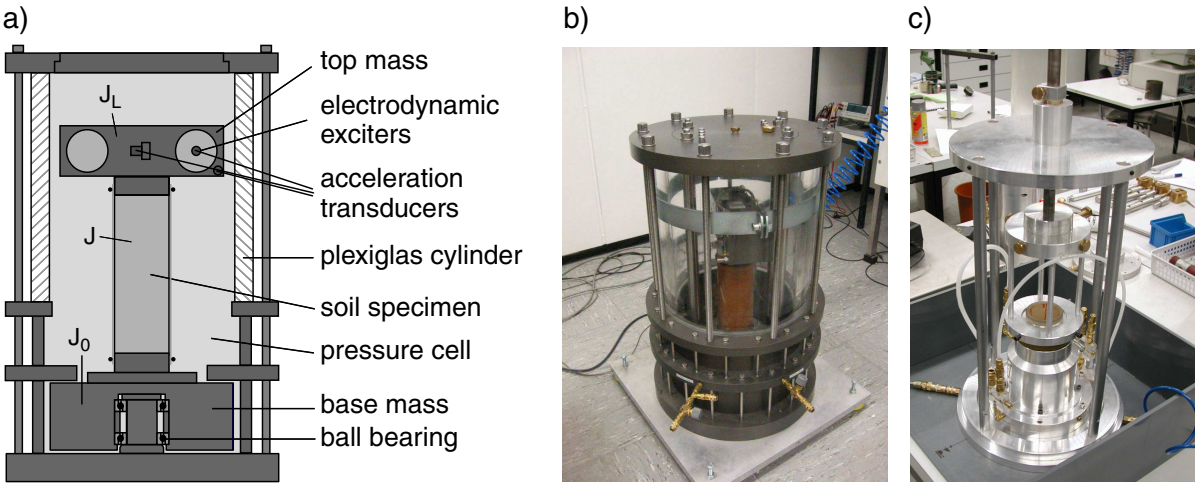

Figure 4.9: *Resonant Column tests: a) scheme of the test device, b) photo of the test device, c) apparatus for placing the specimen top cap*

frequency f_R of the system composed of the two end masses and the specimen has been found. By definition, this is the case when $\phi(t)$ and $F(t)$ have a phase-shift of $\pi/2$ in time t. If the displacement $u(t)$ in the axis of the electrodynamic exciter is plotted versus $F(t)$, one obtains an ellipsoidal *Lissajous* figure. In the resonant case its axes are parallel to the u- and F-axes. The secant shear modulus

$$G_{\text{hyst}} = \left(\frac{2\pi\ h\ f_R}{a}\right)^2 \varrho \tag{4.1}$$

is calculated from the resonant frequency with the height h and the density ϱ of the specimen. The parameter a is obtained from the implicit eigenvalue equation (4.2):

$$a\ \tan(a) - \frac{J^2}{J_0\ J_L}\frac{\tan(a)}{a} = \frac{J}{J_0} + \frac{J}{J_L} \tag{4.2}$$

In Equation (4.2) J, J_0 and J_L are the polar mass moments of inertia of the specimen, the base mass and the top mass, respectively (Figure 4.9a). For cylindrical specimens (diameter d) $J = 1/32\ \pi\ \varrho\ h\ d^4$ holds. The shear strain amplitude γ^{ampl} is calculated as a geometrical mean value over the specimen volume (see Wichtmann et al. [179]). Different shear strain amplitudes can be tested by varying the amplitude of the excitation signal. The damping ratio D is determined as the ratio of the energy W_D, which is dissipated within a cycle, and the elastic energy W_e:

$$D = \frac{1}{4\pi}\frac{W_D}{W_e} \tag{4.3}$$

The dissipated energy W_D is obtained from the area of the Lissajous figure. The elastic energy is calculated from (V: specimen volume):

$$W_e = \frac{1}{2}\ G_{\text{hyst}}\ (\gamma^{\text{ampl}})^2\ V \tag{4.4}$$

The specimens were prepared outside the RC device using the pluviation technique (see Section 4.1.1). The specimen top cap was placed onto the soil surface using a special apparatus (Figure 4.9c) in order to prevent excentricity and tilting. While a vacuum was applied to the grain skeleton the split moulds were removed and the specimens were placed into the RC device. The specimen base plate was screwed to the rotatable base mass of the RC device. The excitation head was placed onto the specimen top plate and screwed. Having mounted the pressure cell, the vacuum in the specimen was gradually replaced by the cell pressure keeping the effective stress constant.

Specimens with a full and such with a hollow cylinder cross section were tested. The specimens with a full cross section measured $d = 10$ cm in diameter and $h = 20$ cm or 30 cm in height. Preliminary tests showed that the specimen height has no influence on the measured stiffness for 20 cm $\leq h \leq$ 30 cm, whereas in the case of the specimens with $h = 10$ cm only 95 % of the value of the higher specimens was obtained. The hollow cylinder specimens (see also Figure 4.9c) had an outer diameter $d_a = 10$ cm, an inner diameter $d_i = 6$ cm (i.e. a wall thickness of 2 cm) and a height $h = 10$ cm. The advantage of the hollow cylinder specimens compared to the full cylinder ones is the more homogeneous distribution of shear strain over their cross section. However, a comparison of the measurements performed on hollow and full cylinder specimens revealed no significant differences in the dynamic soil properties. Thus, the laborious preparation of hollow cylinder specimens (with inner and outer split moulds and inner and outer membranes) seems not to be worthwhile for this purpose.

4.1.4 Measurement of wave propagation with piezoelectric elements

A scheme of the used triaxial cell (type II) was already shown in Figure 4.3. The specimen end plates at the bottom and the top are equipped each with three piezoelectric elements (Figure 4.10). These elements deform, when an electrical voltage is applied. Vice versa they generate an electrical signal when they are deformed mechanically. The *compression element* (CE) deforms in the direction of its thickness. It is used for measuring the compressional wave velocity (P-wave type v_{Pv} referring to Figure 3.35). The *shear plate* (SP) performs shear deformations and sends out shear waves (S-wave type v_{Svh} referring to Figure 3.35) into the soil. The shear wave velocity can also be determined from a measurement with the *bender elements* BE. While CE and SP are fully integrated into the specimen end plates, BE extents approx. 3 mm into the specimen.

The arrangement of the measuring instruments is given in Figure 4.11. A single sinusoidal

Figure 4.10: *Photo of the specimen end plates with piezoelectric elements*

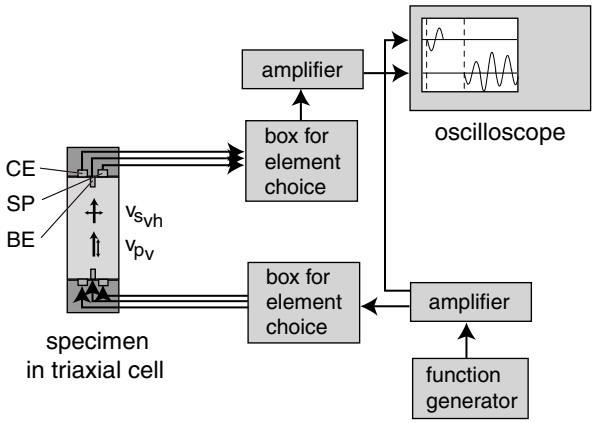

Figure 4.11: *Scheme of the arrangement of the devices for the measurement of wave propagation velocities in triaxial specimens*

electrical impulse is generated by a function generator, amplified and applied to one of the piezoelectric elements in the specimen base plate. The deformation of the element leads to the generation of a wave. The wave propagates in the axial direction of the soil specimen. If the wave reaches the corresponding piezoelectric element in the specimen top plate, the deformation of this element causes the generation of an electrical signal. This signal is amplified and displayed at an oscilloscope. The running time t_t of the wave in the specimen is determined from the transmitted and the received signal (Figure 4.12). In some cases this is difficult, among other things due to reflections of the wave at the specimen boundaries (Sanchez-Salinero et al. [131], Viggiani & Atkinson [171], Brignoli et al. [12], Arulnathan et al. [5]). The running time can be determined from a comparison of the starting points (points A-A' in Figure 4.12), a comparison of corresponding minima, maxima and zero-crossings (points B-B',C-C',D-D' in Figure 4.12) or by means of a cross correlation. The tests in Section 9.1.2.4 were analyzed by comparing the starting points. In either case delay times of the signal in cables or electrical devices have to be determined in a calibration and subtracted from the measured running time. The wave velocity is calculated from

$$v = l_t/t_t. \tag{4.5}$$

In the case of CE and SP l_t is the specimen height. For BE, the distance between the tips of the elements is set into approach (see Viggiani & Atkinson [171], Brignoli et al. [12], Dyvik & Madshus [29]). Using Equation (3.7) the corresponding secant stiffnesses $G_{\mathrm{hyst},0}$ and $E_{s,\mathrm{hyst},0}$ at small strains can be determined from the wave velocities.

The frequency of the transmitted impulse was chosen in the range 10 kHz $\leq f_{\mathrm{TRM}} \leq$ 100 kHz depending on the piezoelectric element and the soil stiffness. Since in this range of

frequencies hardly any dispersion (i.e. a dependence of the wave velocity on the frequency) is present (Triantafyllidis et al. [167]), the frequency can be selected in such way that the received signal is clear and well interpretable with respect to the wave arrival.

The good congruence of the shear moduli $G_{\mathrm{hyst},0}$ from RC tests and from measurements of wave propagation velocities in the triaxial cell is shown in Figure 4.13. In Figure 4.13 an illustration similar to Figure 3.32 was chosen.

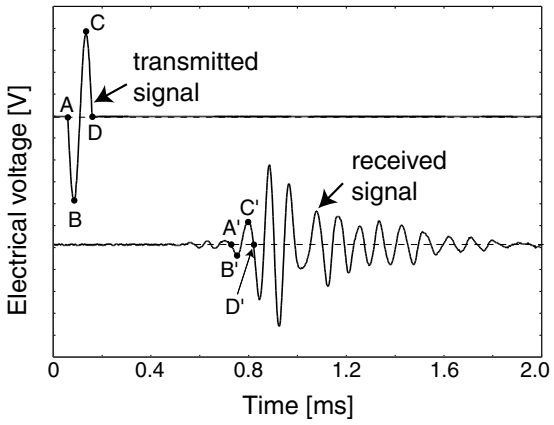

Figure 4.12: *Measurement of wave propagation with piezoelectric elements: transmitted and received signal (here: bender element)*

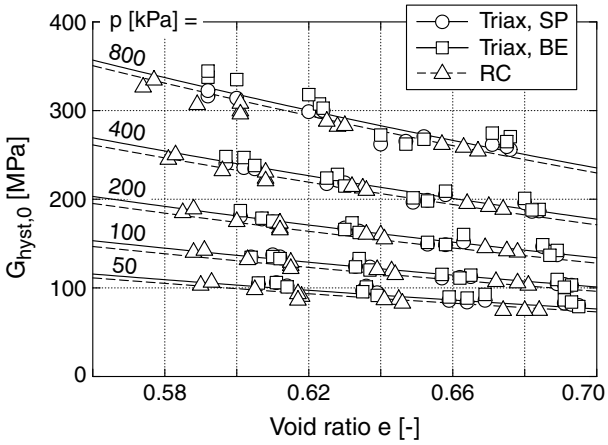

Figure 4.13: *Comparison of the shear moduli from RC tests and from measurements of wave propagation velocities in the triaxial cell*

4.2 Tested material

The tests in this work were performed with a quartz sand with subangular grains. In all tests, except those on the influence of the grain size distribution curve (Section 5.2.9), the grain size distribution curve No. 3 with respect to Figure 4.14 was used, a uniform medium coarse to coarse sand. The characteristics of the grain size distributions (mean grain diameter d_{50}, non-uniformity index $U = d_{60}/d_{10}$, curvature index $C = {d_{30}}^2/(d_{60}\, d_{10})$, the maximum ($e_{\max}$) and minimum ($e_{\min}$) void ratios referring to German standard code DIN 18126, the critical friction angle φ_c (mean value of 10 cone pluviation tests) and photos of the grain size distributions are given in Figure 4.15.

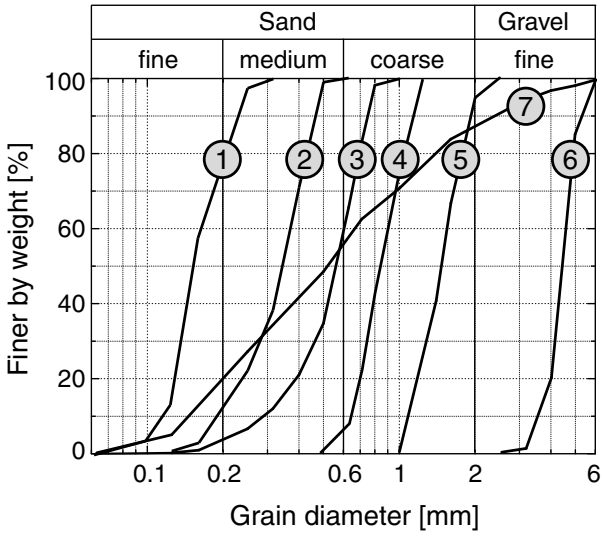

Figure 4.14: *Tested grain size distribution curves of a quartz sand*

Soil	1	2	3	4	5	6	7
d_{50}	0.15 mm	0.35 mm	0.55 mm	0.84 mm	1.45 mm	4.4 mm	0.52 mm
U	1.4	1.9	1.8	1.4	1.4	1.3	4.5
C	0.9	1.2	1.2	1.0	0.9	1.1	0.7
e_{max}	0.992	0.930	0.874	0.878	0.886	0.851	0.691
e_{min}	0.679	0.630	0.577	0.590	0.623	0.669	0.422
φ_c	31.3°	33.3°	31.2°	33.7°	33.9°	35.1°	33.3°
Photo	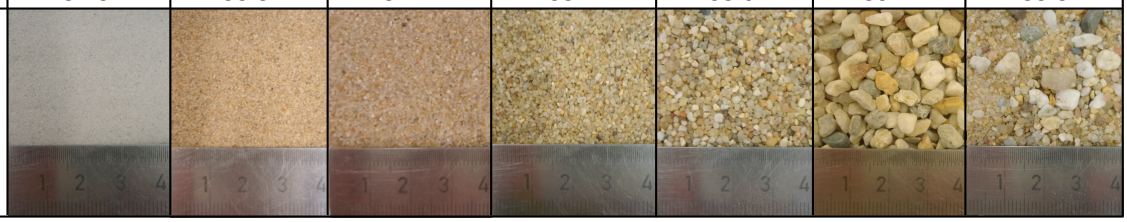						

Figure 4.15: *Mean grain diameter d_{50}, non-uniformity index $U = d_{60}/d_{10}$, maximum ($e_{\max}$) and minimum ($e_{\min}$) void ratios, critical friction angle φ_c and photos of the tested grain size distributions*

4.3 Material behaviour under monotonic loading

Preliminary to the cyclic tests drained monotonic triaxial tests and tests with oedometric compression were performed on grain size distribution curve No. 3. These tests served for a determination of the peak friction angle $\varphi_P(I_D)$ and the constants of the hypoplastic constitutive model (Section 7.3.1.3). For a better interpretation of the undrained cyclic

tests presented in Section 9.2 (correlation of the historiotropy with the liquefaction resistance), undrained monotonic tests were performed in order to determine the lines of phase transformation and failure. The test results are discussed in the following.

4.3.1 Peak friction angle from drained triaxial tests

In order to determine the peak friction angle in dependence on the relative density, drained monotonic triaxial tests with three different initial densities ($0.18 \leq I_{D0} \leq 0.26$, $0.59 \leq I_{D0} \leq 0.67$ and $0.95 \leq I_{D0} \leq 1.02$) were performed. The specimens were compressed in the axial direction with a constant displacement rate $\dot{s} = 0.1$ mm/min. For each density, tests with effective lateral stresses 50 kPa $\leq \sigma_3 \leq$ 200 kPa were performed. Volume changes were measured via the pore water of the saturated specimens.

Figure 4.16 presents the course of the deviatoric stress q and the volumetric strain ε_v with increasing axial strain ε_1 in the tests on initial medium dense specimens. Certainly $q_{\max}$ increased with increasing lateral stress σ_3. For the six tested lateral stresses, the maximum value of q was reached at strains $6\% \leq \varepsilon_1 \leq 8\%$ (Figure 4.16a). Afterwards the deviatoric stress declined, but the residual value was not reached at the maximum tested axial strain of approx. 23 %. The curves $\varepsilon_v(\varepsilon_1)$ (Figure 4.16b) show the initial contractancy followed by a distinct dilatancy. The dilatant phase for the higher lateral stresses (e.g. $\sigma_3 = 200$ kPa) started later than for the smaller pressures (e.g. $\sigma_3 = 50$ kPa).

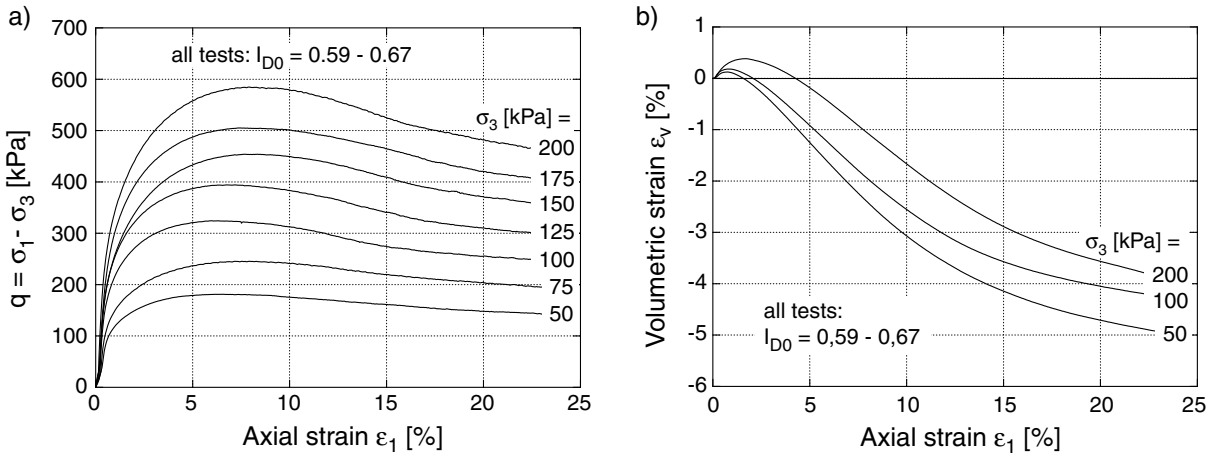

Figure 4.16: *a) Deviatoric stress q and b) volumetric strain ε_v as a function of axial strain ε_1 for $0.59 \leq I_{D0} \leq 0.67$ and different lateral stresses σ_3*

Figure 4.17 compares the curves $q(\varepsilon_1)$ and $\varepsilon_v(\varepsilon_1)$ for the three tested initial densities and $\sigma_3 = 200$ kPa. As is known, $q_{\max}$ increases with increasing initial density (Figure 4.17a), but after having reached $q_{\max}$, the curves $q(\varepsilon_1)$ converge to the same residual value. The initial phase of contractancy becomes shorter with increasing initial density.

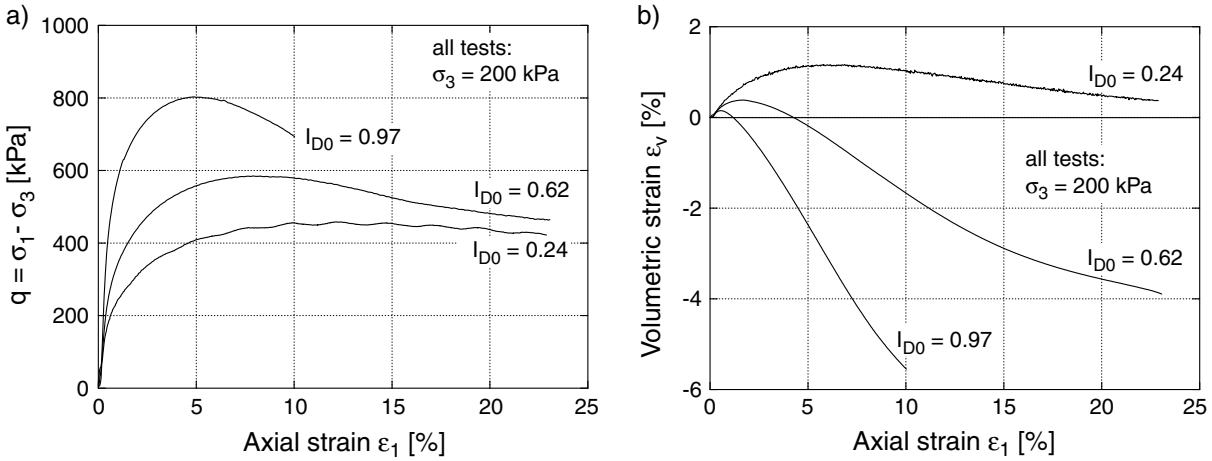

Figure 4.17: *a) Deviatoric stress q and b) volumetric strain ε_v as a function of axial strain ε_1 for $\sigma_3 = 200$ kPa and different initial densities I_{D0}*

Figure 4.18a shows the peak stresses $(p_{\max}, q_{\max})$ of all tests in a p-q-diagram. The inclinations $M_c(\varphi_P)$ of the failure lines which are given in Figure 4.18a result from the fitting of a linear function through the origin (cohesion $c = 0$). From Equation (2.8) the peak friction angle φ_P was calculated. In Figures 4.18b and 4.18c it is illustrated as a function of the density index $I_{D,P}$ at peak and the void ratio e_P at peak. For the given sand the relationships $\varphi_P(I_{D,P})$ and $\varphi_P(e_P)$ can be expressed by

$$\begin{aligned} \varphi_P(I_{D,P}) &= 31.2^\circ \, \exp\left(0.40 \; {I_{D,P}}^{1.41}\right) \\ \text{or} \quad \varphi_P(e_P) &= 31.2^\circ \, \exp\left[2.22 \; (0.874 - e_P)^{1.41}\right] \end{aligned} \tag{4.6}$$

For the loosest possible density ($I_D = 0$) thus $\varphi_P = \varphi_c = 31.2^\circ$ holds.

4.3.2 Oedometric compression

The tests with oedometric compression served primarily for the determination of the hypoplastic material constants (Section 7.3.1.3). Three specimens with a loose initial density ($0.02 \leq I_{D0} \leq 0.03$, preparated by pluviation of a cone and removal of its tip) and three initially dense specimens ($0.88 \leq I_{D0} \leq 0.90$) were tested. Since the reproducibility in tests with small specimens (diameter $d = 7.0$ cm, height $h = 1.9$ cm) of the medium

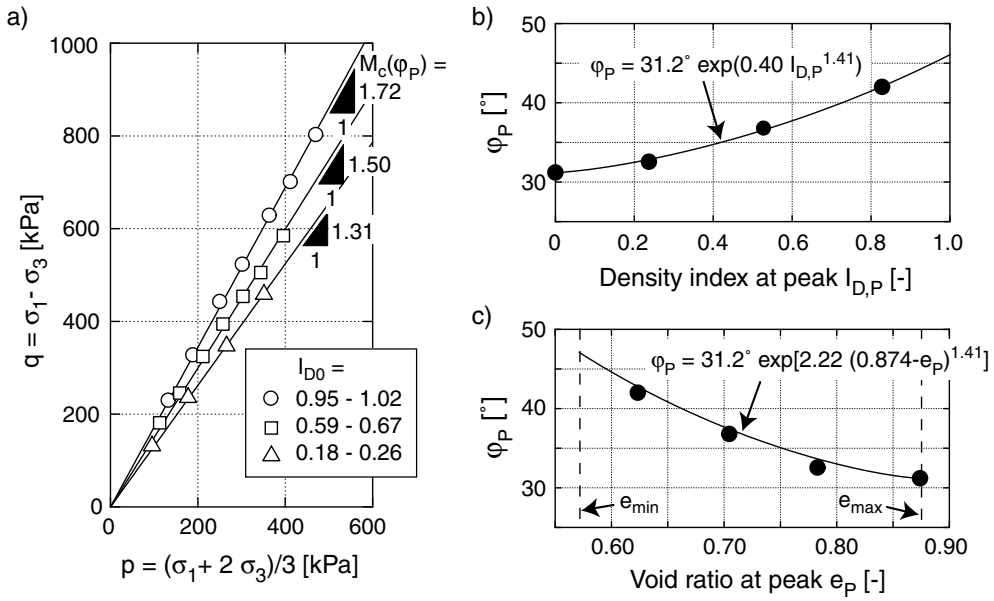

Figure 4.18: *a) Peak stresses in the p-q-diagram, b) peak friction angle φ_P as a function of the density index $I_{D,P}$ at peak and c) as a function of the void ratio e_P at peak*

coarse to coarse sand was not satisfactory, the tests were performed on larger specimens ($d = 28$ cm, $h = 8$ cm). A detailed description of the respective test device is given in [182]. The reduction of void ratio e with mean pressure p is illustrated in Figure 4.19. In the analysis the mean pressure $p = (\sigma_1 + 2\sigma_3)/3$ was calculated with a lateral pressure coefficient of $K_0 = 1 - \sin(\varphi_P)$. The peak friction angle was determined from Equation (4.6).

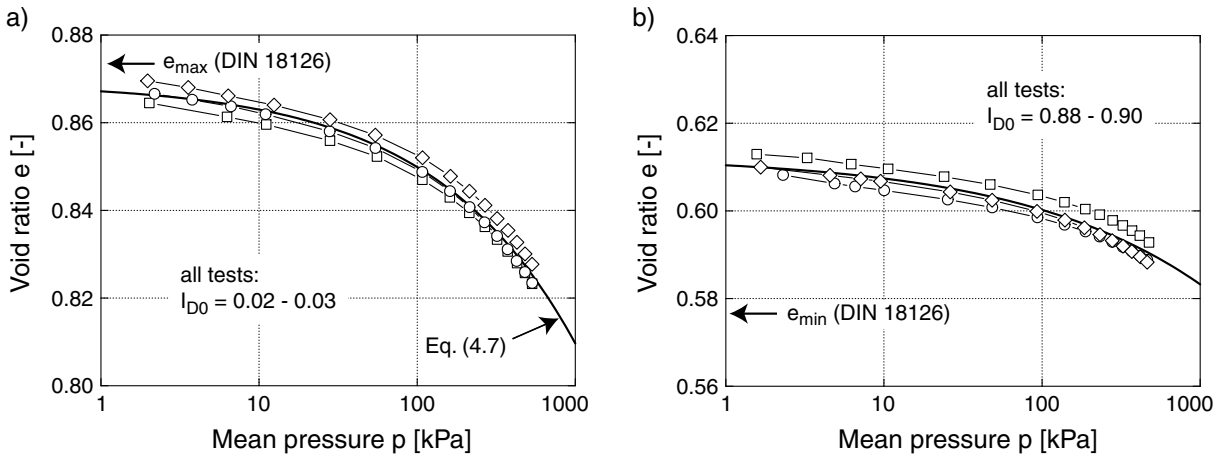

Figure 4.19: *Reduction of void ratio e with mean pressure p in tests with oedometric compression for a) initially loose and b) initially dense specimens*

The curves in Figure 4.19 can be described by the equation of Bauer [7]:

$$\frac{e}{e_0} = \exp\left[-\left(\frac{3p}{h_s}\right)^n\right] \tag{4.7}$$

For the initially loose specimens a curve-fitting (solid lines in Figure 4.19a) resulted into $e_0 = 0.869$, $h_s = 591$ MPa and $n = 0.50$.

4.3.3 Undrained monotonic triaxial tests

Preliminary to the undrained cyclic triaxial tests for the correlation between the historiotropy and the liquefaction resistance, eight undrained monotonic triaxial tests (compression and extension) were performed in order to determine the so-called phase transformation line (PT) and the so-called failure line (FL). The specimens were consolidated under four different isotropic effective stresses 50 kPa $\leq p_0' \leq$ 200 kPa. Having closed the drainage system they were compressed in the axial direction with a displacement rate $\dot{s}$ = 0.1 mm/min. The curves $q(\varepsilon_1)$ and the effective stress paths in the p'-q-plane with the inclinations M_c and M_e of PT and FL are presented in Figure 4.20. Deviating from the notation used so far, the effective stresses in Figure 4.20 and also in the following Section 4.4 are denoted by $\sqcup'$.

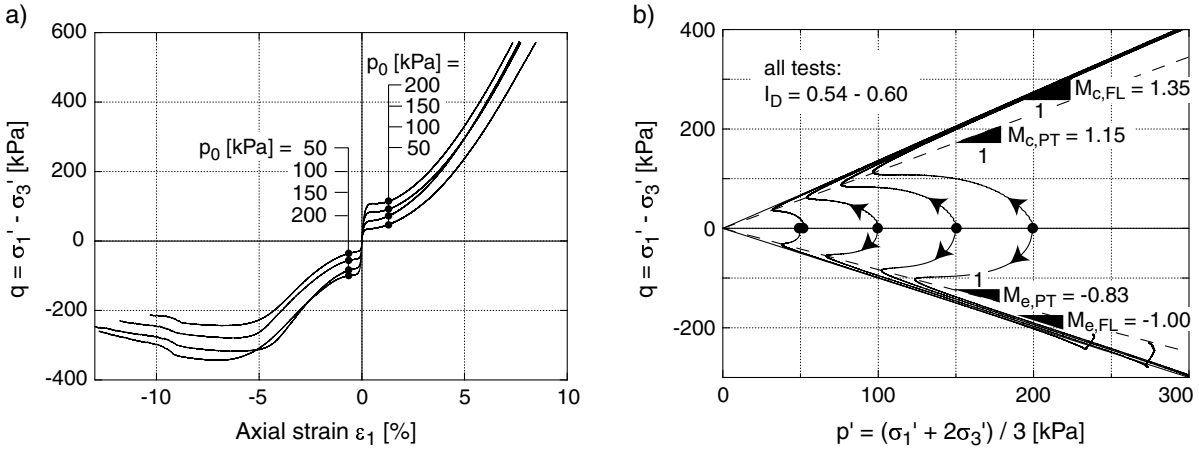

Figure 4.20: *Eight undrained monotonic tests with triaxial compression and extension: a) curves $q(\varepsilon_1)$, b) stress paths in the p-q-plane*

4.4 Membrane penetration due to a variation of the effective lateral stress

In the cyclic triaxial tests which are presented in Sections 5.2.1.3 and 5.2.1.4, the axial stress σ_1 *and* the lateral stress σ_3 were oscillating simultaneously. The volumetric strain was measured via the pore water. However, if in a triaxial test the lateral effective stress σ_3' is varied, the total volumetric strain $\varepsilon_{v,T}$ measured via the pore water is composed of both a portion $\varepsilon_{v,S}$ resulting from the deformation of the soil skeleton and a portion $\varepsilon_{v,\mathrm{MP}}$ originating from membrane penetration:

$$\varepsilon_{v,T} \;=\; \varepsilon_{v,S} + \varepsilon_{v,\mathrm{MP}} \;=\; \varepsilon_{v,S} + \delta V_{\mathrm{MP}} \frac{A_M}{V_0} \tag{4.8}$$

A_M is the area of the membrane which is in contact with the specimen, V_0 is the initial volume of the specimen and δV_{MP} is the membrane penetration per unit area. The portion of membrane penetration results from the fact that due to an increase of the effective lateral stress, the membrane is pressed into the voids between the grains (Figure 4.21). While the residual volumetric strain $\varepsilon_v^{\mathrm{acc}}$ is not afffected by membrane penetration, the amplitude of volumetric strain $\varepsilon_v^{\mathrm{ampl}}$ has to be corrected by this effect.

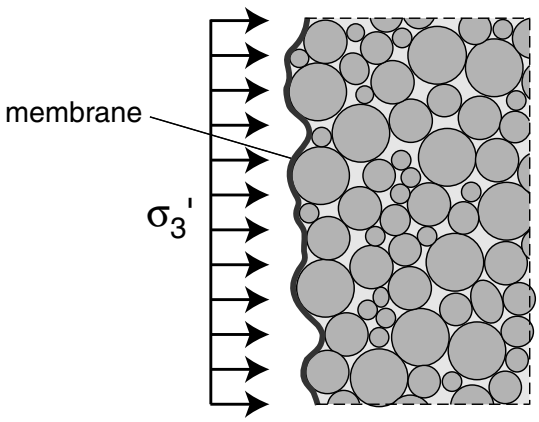

Figure 4.21: *Problem of membrane penetration: Pressing of the membrane into the voids between the grains due to an increase of the effective lateral stress* σ_3'

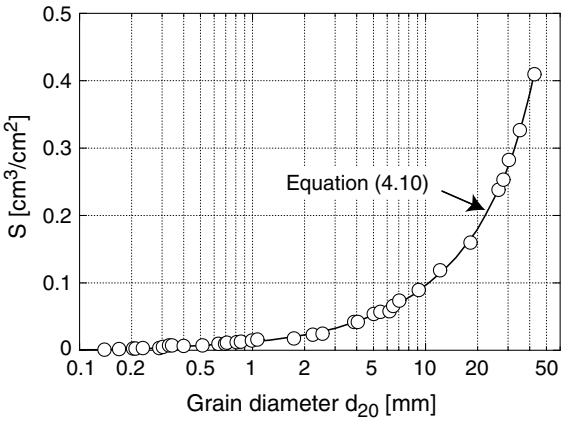

Figure 4.22: *Factor S in Equation (4.9) in dependence on the grain diameter* d_{20} *after Nicholson et al. [103]*

The membrane penetration δV_{MP}, due to an increase of the effective lateral stress from $\sigma_3'^A$ to $\sigma_3'^B$, can be determined from the empirical equation (Nicholson et al. [103])

$$\delta V_{\mathrm{MP}} \;=\; S \;\log(\sigma_3'^B/\sigma_3'^A) \tag{4.9}$$

In the literature, several proposals concerning the determination of the factor S can be found. These methods are based on modified standard laboratory tests or special testing devices (Newland & Allely [101, 102], Frydman et al. [32], Raju & Sadasivian [125], Kiekbusch & Schuppener [73], Vaid [169], Kramer [79], Lo et al. [89], Seed et al. [145]). Nicholson et al. [103] provide a survey and a critical discussion of the proposed methods. They favour the isotropic compression of specimens with different ratios of the membrane area A_M and the initial specimen volume V_0. The ratio A_M/V_0 can be varied e.g. by testing specimens with a full cross section and different specimen diameters or hollow cylinder specimens with different inner diameters. Also dummies within a specimen were used in order to reduce the volume of the grain skeleton. Referring to Nicholson et al. [103], the amount of membrane penetration primarily depends on the grain size distribution curve. A minor influence of the void ratio, the grain shape, the fabric of the grain skeleton and the thickness t_M and the stiffness of the membrane (if "usual" measures of t_M are applied) was reported. On the basis of many laboratory tests (Figure 4.22), Nicholson et al. [103] proposed the following correlation between S and the grain diameter d_{20}:

$$S = 0.0019 + 0.0095\ d_{20} - 0.0000157\ (d_{20})^2 \tag{4.10}$$

with S in the unit [cm^3/cm^2] and d_{20} in [mm]. For the medium coarse to coarse sand used in the own tests (grain size distribution curve No. 3 referring to Figure 4.14) with $d_{20} = 0.4$ mm Equation (4.10) delivers a value $S = 0.0057$ cm^3/cm^2.

In the framework of this thesis the constant S was determined from tests with an isotropic compression of cylindrical specimens with different diameters d. Specimens with the diameters $d = 10$ cm, 7 cm and 3.5 cm were tested. For each diameter the ratio $h/d = 2$ was studied. Because of $A_M/V_0 = (\pi dh)/(\pi d^2 h/4) = 4/d$, the specimen height h should not influence the membrane penetration. In order to control this, a ratio $h/d = 1$ was tested for the largest and the smallest diameter under consideration. Schemes and photos of the tested specimen geometries are shown in Figure 4.23. The thickness of the membrane $t_M = 0.4$ mm was identical to the one in the tests presented in Sections 5.2.1.3 and 5.2.1.4. The isotropic compression was conducted in the triaxial cell of type II (Figure 4.3). Having placed the specimen top cap onto the soil surface, the load piston could be removed. At a back pressure of $u = 200$ kPa, the effective stress was isotropically increased from $p' = \sigma'_3 = 50$ kPa to $p' = \sigma'_3 = 600$ kPa. The volume changes were measured via the pore water of the fully water-saturated specimens. An initial density of $I_{D0} \approx 0.6$ was intended since similar densities were studied in the tests reported in Sections 5.2.1.3 and 5.2.1.4.

The increase of the total volumetric strain $\varepsilon_{v,T}$ with the effective pressure is presented in Figure 4.24a. With increasing ratio A_M/V_0 also $\varepsilon_{v,T}$ increases, due to a larger volumetric

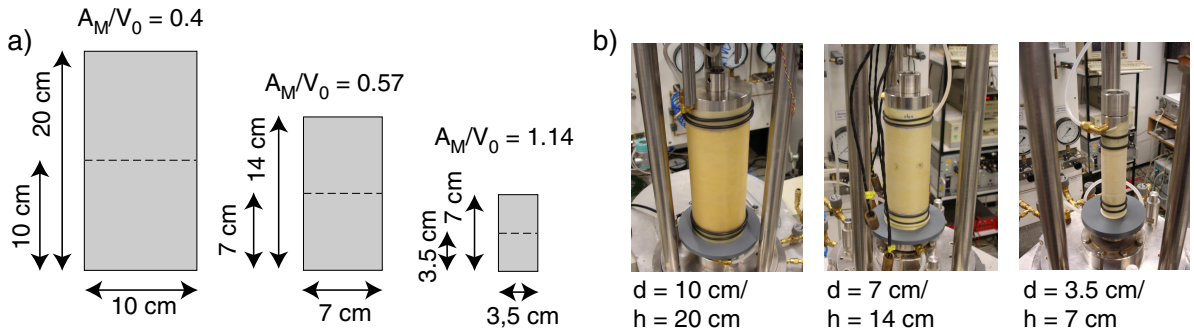

Figure 4.23: *Comparison of tested specimen geometries: a) schemes, b) photos*

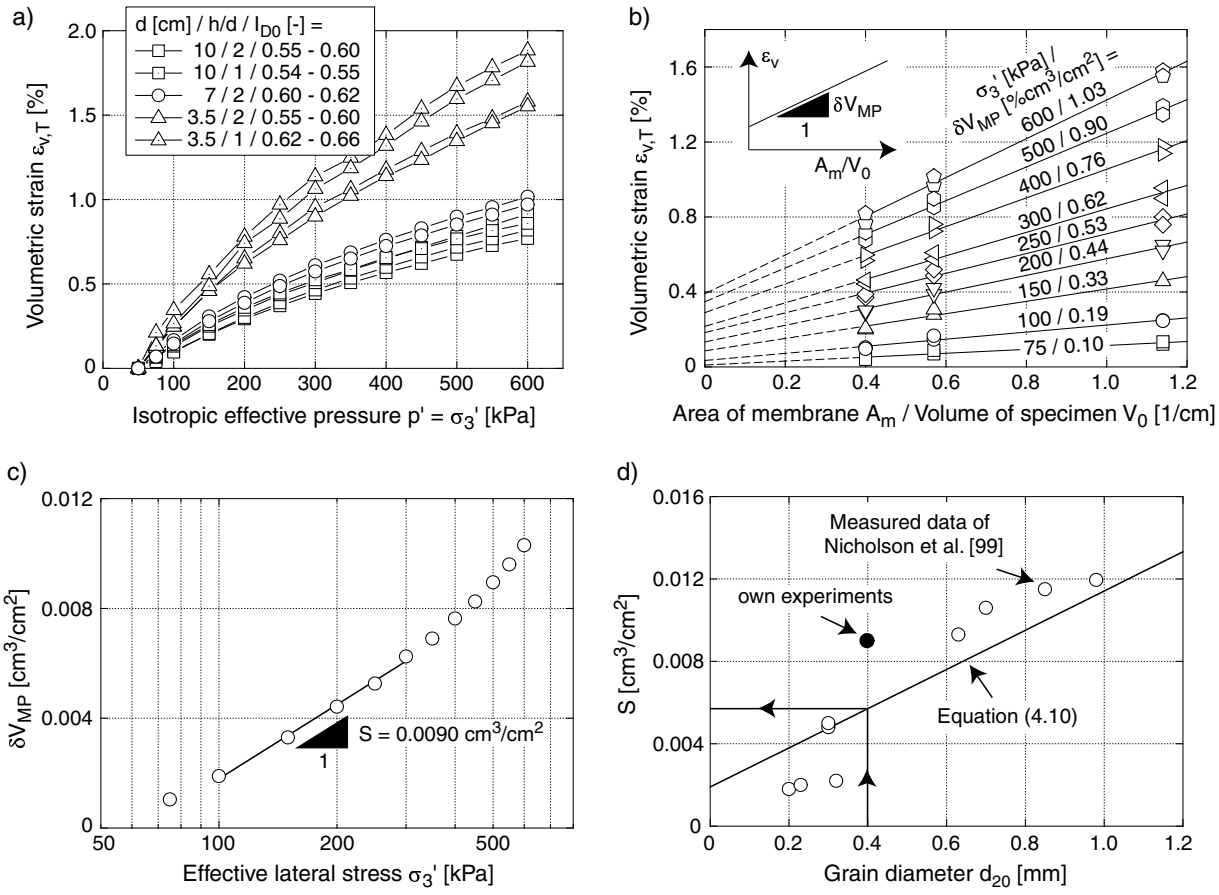

Figure 4.24: *Isotropic compression of specimens with different geometries in order to determine membrane penetration: a) curves $\varepsilon_{v,T}(\sigma_3')$, b) $\varepsilon_{v,T}$ as a function of A_M/V_0, c) curve $\delta V_{MP}(\sigma_3')$ and determination of S for the decisive range of pressures, d) comparison of the experimentally obtained value of S with Equation (4.10) and measured data of Nicholson et al. [103]*

strain $\varepsilon_{v,\mathrm{MP}}$ resulting from membrane penetration. However, the larger volumetric strains for $h/d = 1$ in comparison with $h/d = 2$ were not expected. This observation can only be explained by differences during specimen preparation or inhomogeneities of the specimen (larger influence of the ends of the specimens for smaller heights).

In Figure 4.24b, $\varepsilon_{v,T}$ is plotted versus A_M/V_0 for different effective pressures. Only the tests with $h/d = 2$ were used in Figure 4.24b. For a certain σ'_3, the total volumetric strain $\varepsilon_{v,T}$ increases with A_M/V_0. Referring to Equation (4.8), the volumetric strain for the fictitious ratio $A_M/V_0 = 0$ conforms to the volumetric strain of the grain skeleton $\varepsilon_{v,S}$. The inclination of the linear curves $\varepsilon_{v,T}(A_M/V_0)$ is δV_{MP}. It was assumed, that the curves $\varepsilon_{v,T}(A_M/V_0)$ can be extrapolated linearly to $A_M/V_0 = 0$. The values of δV_{MP} given in Figure 4.24b were plotted versus σ'_3 in Figure 4.24c. Due to the slightly over-logarithmic course of the curves $\delta V_{\mathrm{MP}}(\sigma'_3)$, Equation (4.9) was fitted only to the range 100 kPa $\leq \sigma'_3 \leq$ 300 kPa since these stresses were decisive for this work. A value $S = 0.0090$ cm^3/cm^2 was obtained.

This value is larger than $S = 0.0057$ cm^3/cm^2 determined from Equation (4.10). This can also be seen from the comparison with the measured data of Nicholson et al. [103] in Figure 4.24d (enlarged part of Figure 4.22). However, from the strain loops resulting from isotropic stress cycles on the p-axis (Wichtmann et al. [176]), a smaller value of S than that from Equation (4.10) could be expected. Thus, at the time this thesis is under preparation, the precise value of membrane penetration S is not clear. Further tests are planned for the future. In Sections 5.2.1.3 and 5.2.1.4 the value of S resulting from Equation (4.10) was set into approach.

Chapter 5

Influences on the accumulation rate

In Section 5.1 the results of the performed tests are first discussed exclusively with respect to the direction of accumulation $\dot{\varepsilon}_v^{\mathrm{acc}}/\dot{\varepsilon}_q^{\mathrm{acc}}$. Afterwards Section 5.2 deals with the intensity of accumulation $\dot{\varepsilon}^{\mathrm{acc}}$.

5.1 Direction of accumulation (flow rule)

The test results presented in the following sections demonstrate that the direction of accumulation is governed mainly by the average stress ratio $\eta^{\mathrm{av}} = q^{\mathrm{av}}/p^{\mathrm{av}}$. A slight change of the direction of accumulation with the number of cycles N was observed. The average mean pressure p^{av}, the strain loop (span, shape, polarization), the void ratio, the loading frequency, the static preloading and the grain size distribution curve do not influence the ratio $\dot{\varepsilon}_v^{\mathrm{acc}}/\dot{\varepsilon}_q^{\mathrm{acc}}$.

5.1.1 Influence of the average stress

Tests were performed with in-phase stress cycles (σ_3 = constant) at different average stresses $\boldsymbol{\sigma}^{\mathrm{av}}$. The average mean pressure (50 kPa $\leq p^{\mathrm{av}} \leq$ 300 kPa) and the average stress ratio $-0.88 \leq \eta^{\mathrm{av}} \leq 1.375$ were varied. The considered average stresses cover the case of triaxial compression ($\eta^{\mathrm{av}} > 0$) as well as triaxial extension ($\eta^{\mathrm{av}} < 0$). In Figure 5.1 they are illustrated in the p-q-plane. The specimens were prepared with similar initial densities ($0.57 \leq I_{D0} \leq 0.69$). In the tests with $\eta^{\mathrm{av}} > 0$ amplitude ratios $\zeta = q^{\mathrm{ampl}}/p^{\mathrm{av}} = 0.3$ were applied. In the tests with triaxial extension a smaller ratio $\zeta = 0.2$ was chosen, due to the smaller distance of $\boldsymbol{\sigma}^{\mathrm{av}}$ to the yield surface. For this reason in the tests with η^{av} = -0.75 and η^{av} = -0.88 even amplitude ratios of $\zeta = 0.1$ and $\zeta = 0.05$, respectively, were chosen.

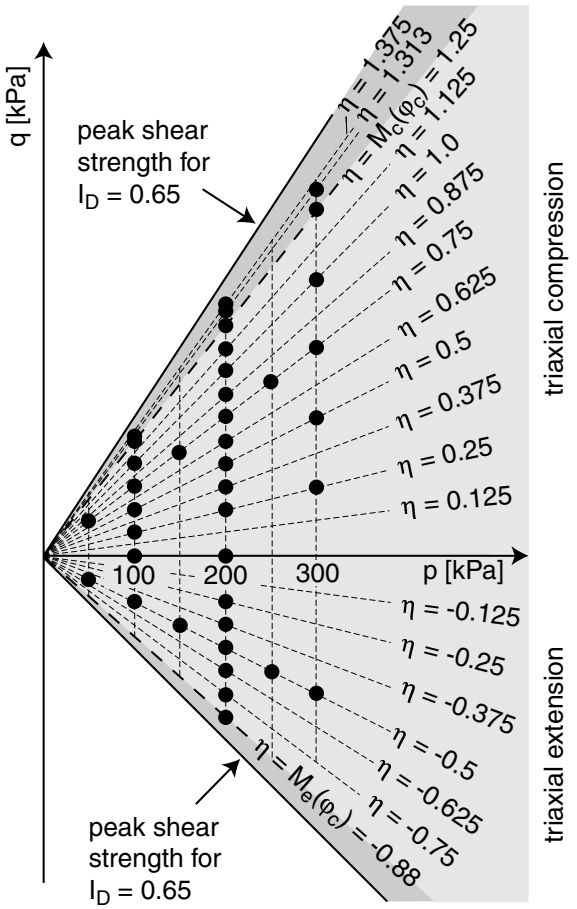

Figure 5.1: *Tested average stresses*

First the tests with $p^{\mathrm{av}} = 200$ kPa are analysed. In Figure 5.2 for selected average stress ratios η^{av}, the residual deviatoric strain $\varepsilon_q^{\mathrm{acc}}$ is plotted versus the accumulated volumetric strain $\varepsilon_v^{\mathrm{acc}}$. The strain in the first cycle is excluded from Figure 5.2 and all other figures of Section 5.1. The data points in Figure 5.2 correspond to the numbers of cycles $N = 2$, 5, 10, 20, 50, 100, ..., $5 \cdot 10^4$ and 10^5. From Figure 5.2 it is apparent that the direction of accumulation significantly depends on the average stress ratio η^{av}. At an isotropic average stress ($\eta^{\mathrm{av}} = 0$), a pure volumetric accumulation (compaction) takes place while the rate of deviatoric strain vanishes ($\dot{\varepsilon}_q^{\mathrm{acc}} = 0$). With increasing absolute value of the average stress ratio $|\eta^{\mathrm{av}}| = |q^{\mathrm{av}}/p^{\mathrm{av}}|$ the deviatoric component of the direction of accumulation increases in comparison to the volumetric portion. At an average stress on the critical state line ($\eta^{\mathrm{av}} = M_c(\varphi_c) = 1.25$ or $\eta^{\mathrm{av}} = M_e(\varphi_c) = -0.88$, respectively), only the deviatoric strain accumulates and a vanishing rate of volumetric strain ($\dot{\varepsilon}_v^{\mathrm{acc}} = 0$) could be observed (at least during the first cycles). The latter conclusion holds although the material is not in the critical density. While average stress ratios $M_e(\varphi_c) < \eta^{\mathrm{av}} < M_c(\varphi_c)$ lead to a densification of the sand, a dilative behaviour was observed in the overcritical regime (see e.g. the test

with $\eta^{av} = 1.375$). The measured dependence of the direction of accumulation on η^{av} agrees well with the results of the experiments of Luong [91] and Chang & Whitman [21] (Section 3.2).

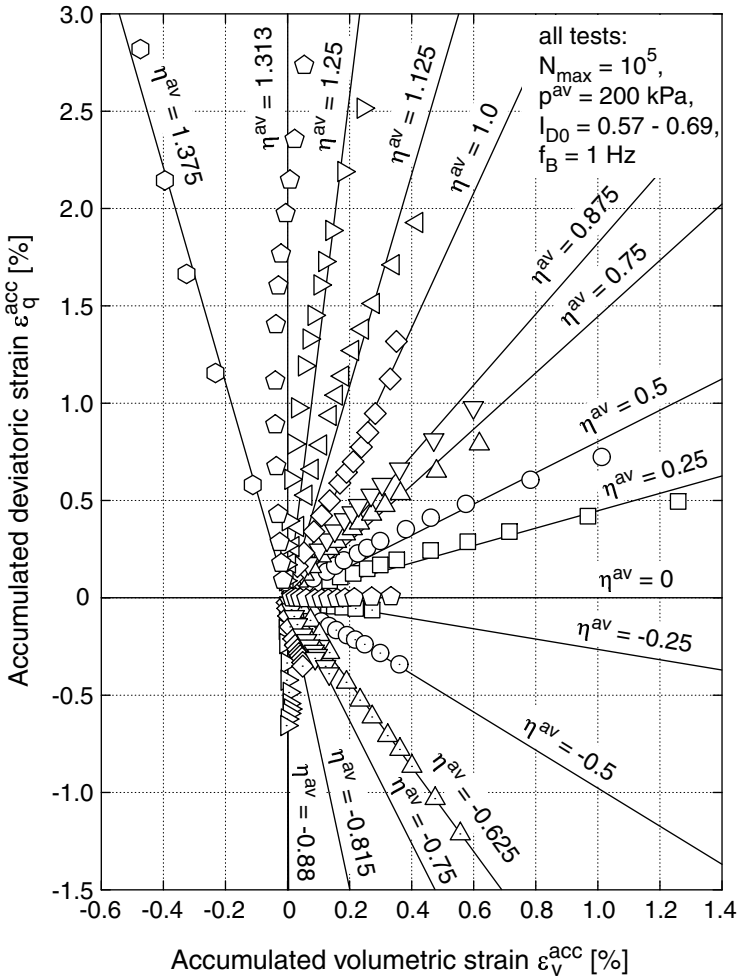

Figure 5.2: ε_q^{acc}-ε_v^{acc}-*strain paths for* $p^{av} = 200$ *kPa and different average stress ratios* $-0.88 \leq \eta^{av} \leq 1.375$

Also conforming with the test results of Chang & Whitman [21] (Figure 3.5b), the average mean pressure p^{av} does not influence the direction of accumulation. This is demonstrated in Figure 5.3 for the tests with $\eta^{av} = 0.75$ (triaxial compression) and in Figure 5.4 for $\eta^{av} = -0.5$ (triaxial extension). The strain paths in the ε_q^{acc}-ε_v^{acc}-diagram coincide for the tests with different average mean pressures p^{av} (Figures 5.3a and 5.4a).

From the illustration of the strain ratio $\omega = \varepsilon_v^{acc}/\varepsilon_q^{acc}$ as a function of p^{av} for different numbers of cycles N (Figures 5.3b and 5.4b), the increase of the volumetric rate compared to the deviatoric rate with N is apparent. In Figure 5.2 this rotation of the direction of

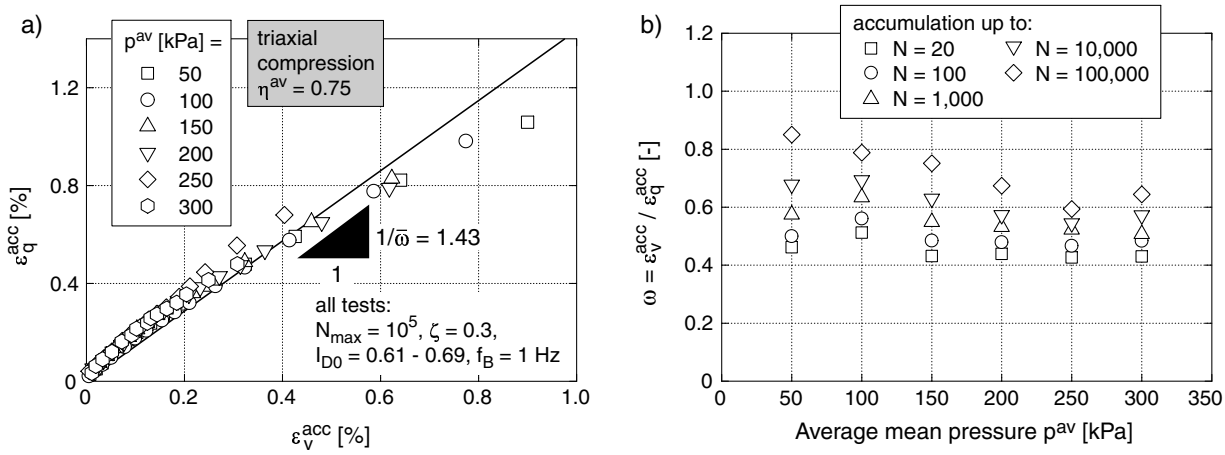

Figure 5.3: *Direction of accumulation for $\eta^{av} = 0.75$ (triaxial compression) and different average mean pressures 50 kPa $\leq p^{av} \leq$ 300 kPa: a) ε_q^{acc}-ε_v^{acc}-strain paths, b) ratio $\omega = \varepsilon_v^{acc}/\varepsilon_q^{acc}$ as a function of p^{av}*

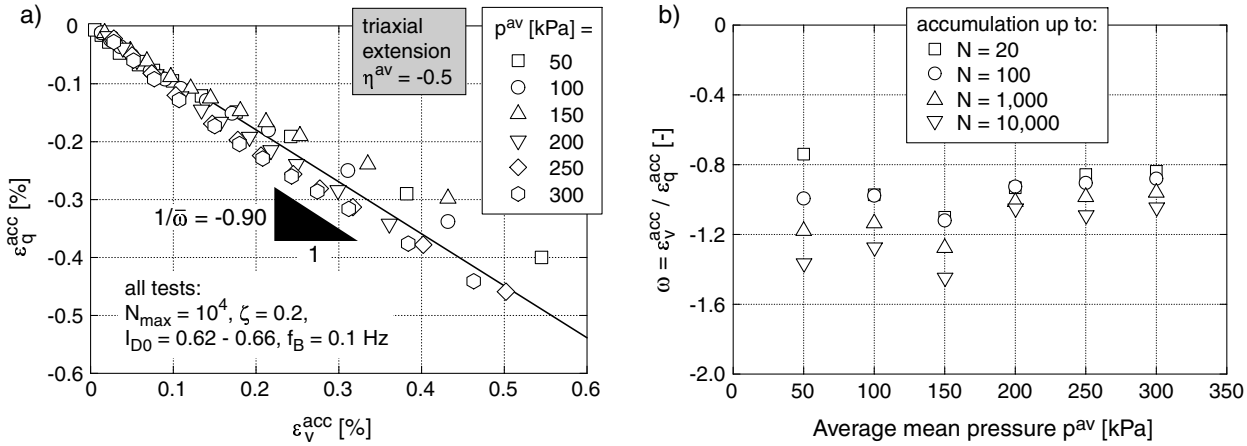

Figure 5.4: *Direction of accumulation for $\eta^{av} = -0.5$ (triaxial extension) and different average mean pressures 50 kPa $\leq p^{av} \leq$ 300 kPa: a) ε_q^{acc}-ε_v^{acc}-strain paths, b) ratio $\omega = \varepsilon_v^{acc}/\varepsilon_q^{acc}$ as a function of p^{av}*

accumulation is also noticeable, e.g. for the test with $\eta^{\mathrm{av}} = M_c(\varphi_c) = 1.25$ as an increasing deflection of the strain path from the vertical.

It is unlikely that the cause of the rotation of the direction of accumulation lies in the measurement technique (e.g. resulting from the measurement of volume changes via the pore water). The same results were obtained on dry specimens (determination of lateral strains from local measurements with non-contact displacement transducers) and independently of the loading frequency, i.e. the duration of a test. An increase of the water level in the measurement pipe due to a densification of the specimen leads to an

increase of the back pressure in the specimen and thus to a reduction of the axial and the lateral effective stresses, i.e. a reduction of p^{av} at q^{av} = constant. However, this cannot be made responsible for the experimental observations since it leads to an increase of the stress ratio η^{av} which should cause a *decrease* of ω with N. Anyway, in the test with $\eta^{\mathrm{av}} = M_c(\varphi_c) = 1.25$, the accumulation of volumetric strain is small and the water level in the measurement pipe rarely changes its height.

Figure 5.5 presents the measured directions of accumulation for all tested average stresses $\boldsymbol{\sigma}^{\mathrm{av}}$ as unit vectors in the p-q-plane. The origin of each vector lies in (p^{av},q^{av}) of the corresponding test. Figure 5.5a was generated using the strain accumulated up to a certain number of cycles N. Thus, the inclination of the vectors to the p-axis is $1/\omega = \varepsilon_q^{\mathrm{acc}}/\varepsilon_v^{\mathrm{acc}}$. In Figure 5.5b, the directions of accumulation were calculated from the rates, i.e. the vectors are inclined by $1/\Omega = \dot{\varepsilon}_q^{\mathrm{acc}}/\dot{\varepsilon}_v^{\mathrm{acc}}$. The rates were calculated from $\dot{\varepsilon}^{\mathrm{acc}} \approx \Delta\varepsilon^{\mathrm{acc}}/\Delta N$ with $\Delta\varepsilon^{\mathrm{acc}}$ being the differential strain accumulated between two subsequent (distance ΔN) data recordings. The vectors in Figure 5.5 are shown for different numbers of cycles which is indicated by the different grayscales. The rotation of the vectors towards the positive p- or $\varepsilon_v^{\mathrm{acc}}$-axis with increasing number of cycles is even more pronounced in the illustration with rates (Figure 5.5b) than in the plot of the total strains (Figure 5.5a).

Let us consider the mathematical description of the direction of accumulation. Chang & Whitman [21] reported, that the flow rule of the modified Cam Clay model, i.e. a model for monotonic loading, approximates the cyclic flow rule in a good manner (Figure 3.5). In the following this is proven for the tests with $p^{\mathrm{av}} = 200$ kPa. Figure 5.6a shows the ratio of the residual strains $\omega = \varepsilon_v^{\mathrm{acc}}/\varepsilon_q^{\mathrm{acc}}$ as a function of η^{av} for the tests with $\eta^{\mathrm{av}} > 0$ (triaxial compression). For stress ratios η^{av} near zero, the cyclic flow rule can be better illustrated in a diagram with the reciprocal value $1/\omega$ on the ordinate (Figure 5.6b). Figures 5.6c and 5.6d analogously present diagrams for the ratio of the rates $\Omega = \dot{\varepsilon}_v^{\mathrm{acc}}/\dot{\varepsilon}_q^{\mathrm{acc}}$ or its reciprocal value $1/\Omega$, respectively. The scatter of data is larger in the diagrams plotted with rates. Figure 5.6 confirms that the deviatoric portion of the accumulation rate vanishes at $\eta^{\mathrm{av}} = 0$, while the volumetric portion vanishes at the critical stress ratio $\eta^{\mathrm{av}} = M_c(\varphi_c)$ (at least for small numbers of cycles $N \leq 100$). Beside the measured directions of accumulation also the flow rules of the modified Cam clay and the hypoplastic model are drawn into Figure 5.6. Both flow rules approximate the direction of accumulation under cyclic loading well. For small stress ratios, the congruence of the monotonic and the cyclic flow rule is best for $N > 10^4$. For stress ratios $\eta^{\mathrm{av}} = M_c(\varphi_c)$, the direction of accumulation is better approximated for $N \leq 100$ than for higher numbers of cycles.

The latter is due to a shift of the limit $\eta^{\mathrm{av}}(\dot{\varepsilon}_v^{\mathrm{acc}} = 0)$ to larger stress ratios with increasing number of cycles. Simultaneously, the volumetric portion of the direction of accumulation

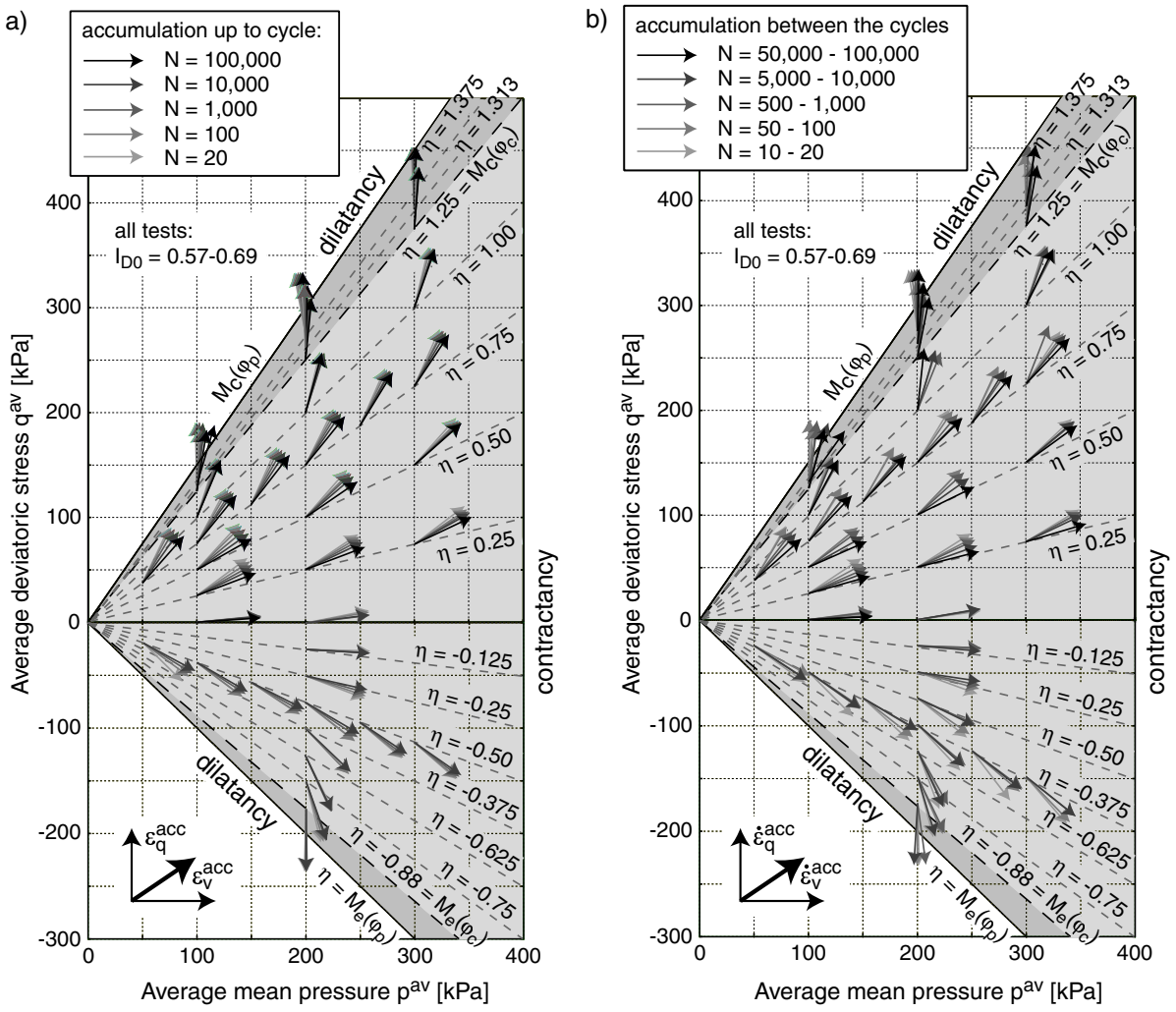

Figure 5.5: *Direction of accumulation for different average stresses* $\boldsymbol{\sigma}^{av}$*, shown as a unit vector in the p-q-plane, a) determined from the total strain accumulated up to a certain number of cycles N, b) determined from the strain increments between two data recordings*

increases for stress ratios $\eta^{av} < M_c(\varphi_c)$. The evolution of the limit $\eta^{av}(\dot{\varepsilon}_v^{acc} = 0)$ is probably related to a hardening of the material under cyclic loading. Also a change of the grain size distribution curve due to abrasion and an accompanying increase of the critical friction angle φ_c may be responsible. Due to the shift of the limit $\eta^{av}(\dot{\varepsilon}_v^{acc} = 0)$, smaller stress ratios η^{av} approach the limit of pure volumetric accumulation $\eta^{av}(\dot{\varepsilon}_q^{acc} = 0) = 0$ for $\boldsymbol{\sigma}^{av} =$ constant. The volumetric portion of the direction of accumulation increases therefore.

Analogously to Figure 5.6, Figure 5.7 contains diagrams for the tests with $p^{av} = 200$ kPa and $\eta^{av} < 0$ (triaxial extension). From Figure 5.7 it can also be seen that the deviatoric portion of the direction of accumulation takes the value zero at $\eta^{av} = 0$ and that the volumetric rate vanishes at $\eta^{av} = M_e(\varphi_c)$. For triaxial extension the volumetric portion

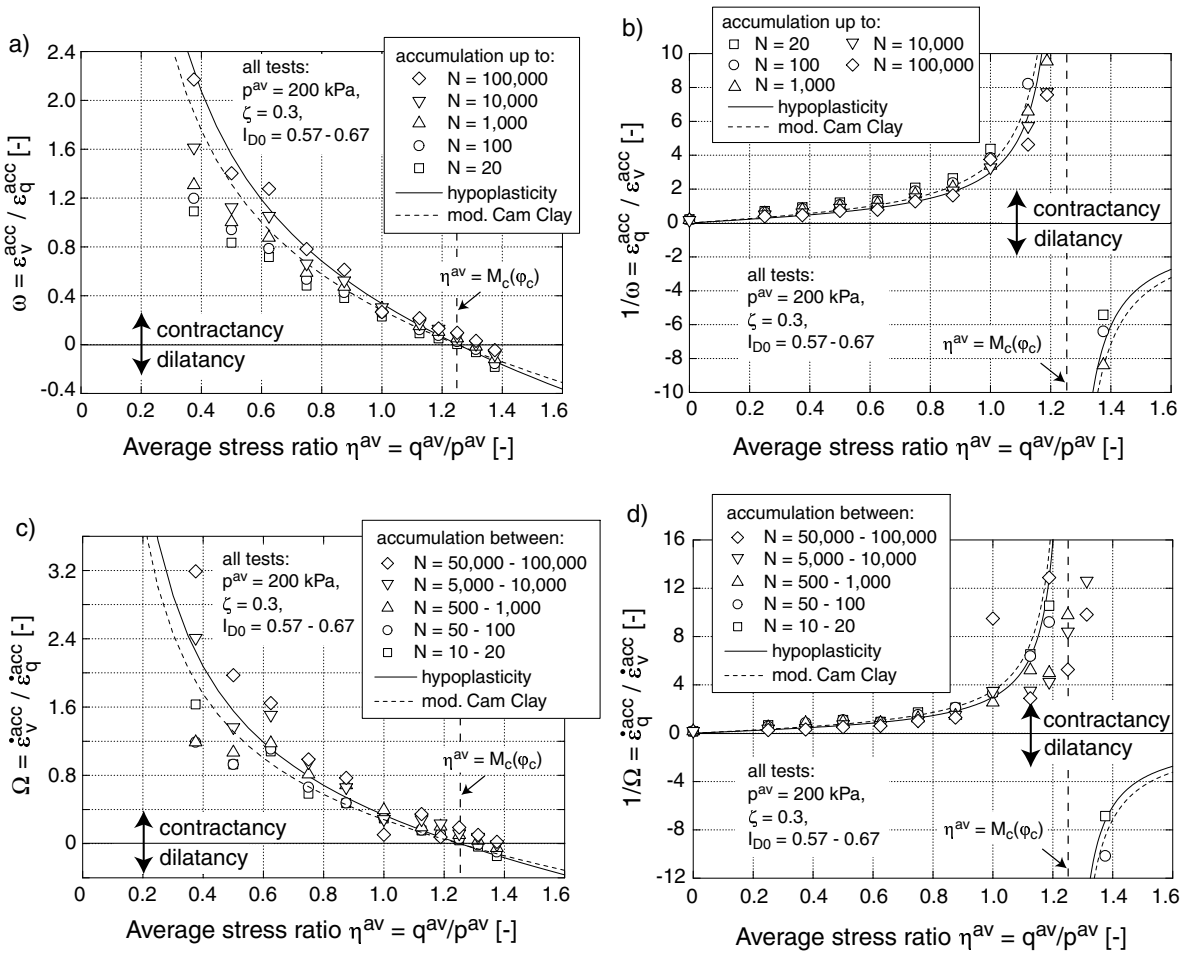

Figure 5.6: *Direction of accumulation in dependence of the stress ratio η^{av} for p^{av} = 200 kPa and triaxial compression: a) strain ratio $\omega = \varepsilon_v^{acc}/\varepsilon_q^{acc}$, b) reciprocal value $1/\omega$, c) strain ratio $\Omega = \dot{\varepsilon}_v^{acc}/\dot{\varepsilon}_q^{acc}$, d) reciprocal value $1/\Omega$*

of the accumulation rate also increases with N and the flow rules of the modified Cam Clay model and the hypoplastic model deliver a good description of the experiments. It is thus justified to use one of these flow rules for the cyclic flow rule of the explicit accumulation model ($\mathbf{m}$ in Equation (7.2)).

5.1.2 Influence of the span, shape and polarization of the loops

First uniaxial stress cycles (σ_3 = constant) with p^{av} = 200 kPa and η^{av} = 0.75 are analyzed. In the tests on initially medium dense sand the stress amplitude was varied within the range 12 kPa $\leq q^{ampl} \leq$ 80 kPa. The illustration of the ε_q^{acc}-ε_v^{acc}-strain paths in Figure 5.8a demonstrates, that the amplitude of the uniaxial cycles does not influence the cyclic flow rule. Figure 5.8b contains a plot of ω versus the strain amplitude $\bar{\varepsilon}^{ampl}$. The bar

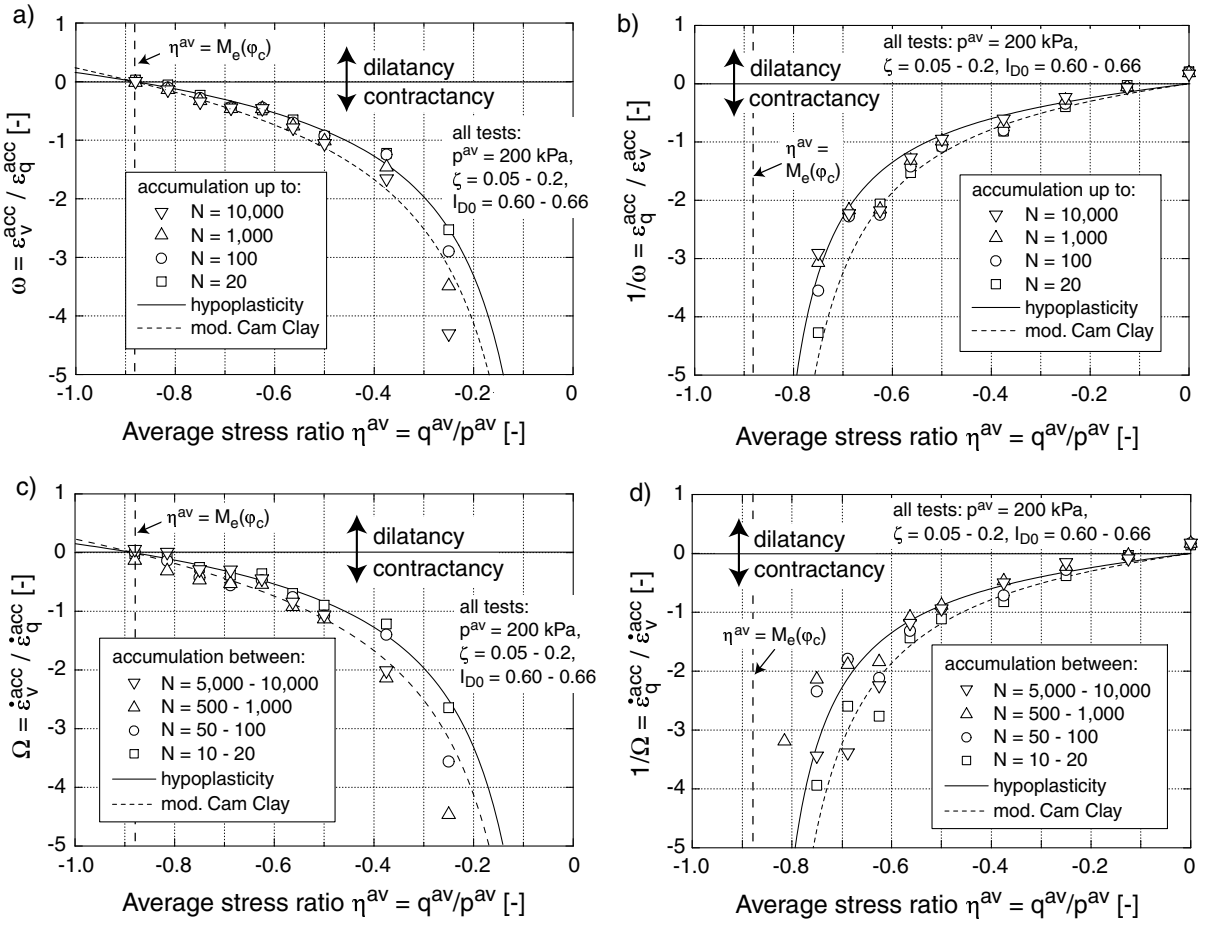

Figure 5.7: *Direction of accumulation in dependence of the stress ratio η^{av} for p^{av} = 200 kPa and triaxial extension: a) strain ratio $\omega = \varepsilon_v^{acc}/\varepsilon_q^{acc}$, b) reciprocal value $1/\omega$, c) strain ratio $\Omega = \dot{\varepsilon}_v^{acc}/\dot{\varepsilon}_q^{acc}$, d) reciprocal value $1/\Omega$*

$\bar{\square}$ over $\varepsilon^{\mathrm{ampl}}$ denotes, that the strain amplitude was calculated as a mean value over N cycles (see details concerning $\varepsilon^{\mathrm{ampl}}(N)$ in Section 5.2.1.1). The increase of ω with N is more pronounced in the tests with larger strain amplitudes and thus larger accumulation rates (Section 5.2.1.1). From Figure 5.8a (and similar diagrams in the following) it can be concluded that the increase of the volumetric portion of the direction of accumulation during cyclic loading is correlated with the residual strain $\varepsilon^{\mathrm{acc}}$ (or the historiotropic variable g^A, see Section 5.2.6) rather than with N. Probably, a significant hardening or a significant change of the grain size distribution curve for larger amplitudes is responsible for these observations.

Similar tests at an average stress ratio η^{av} = -0.5 (triaxial extension, Figure 5.9) confirmed, that the cyclic flow rule is not a function of the stress and strain amplitude of the uniaxial cycles.

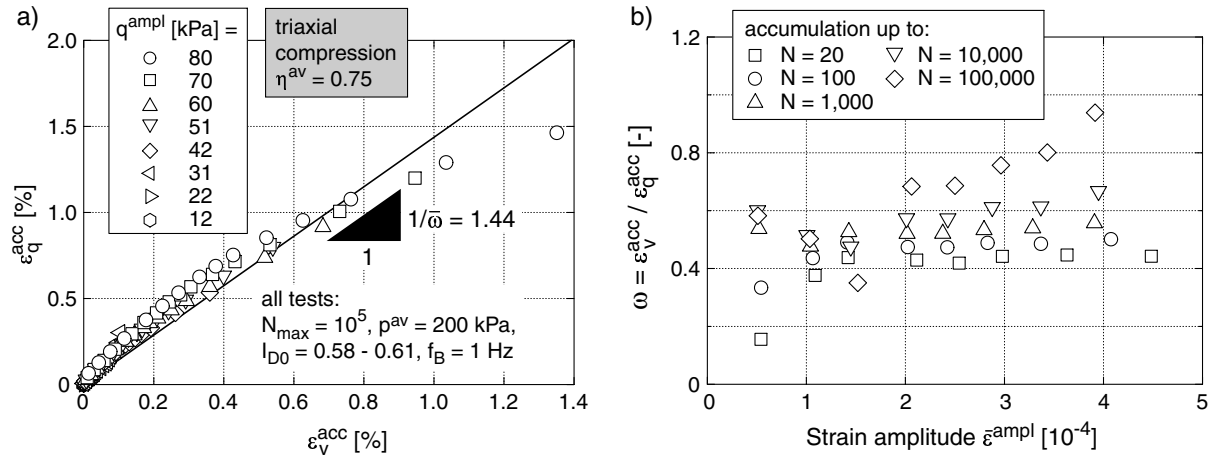

Figure 5.8: *Direction of accumulation for different stress amplitudes at $\eta^{av} = 0.75$ (triaxial compression): a) ε_q^{acc}-ε_v^{acc}-strain paths, b) ratio $\omega = \varepsilon_v^{acc}/\varepsilon_q^{acc}$ as a function of the strain amplitude $\bar{\varepsilon}^{ampl}$*

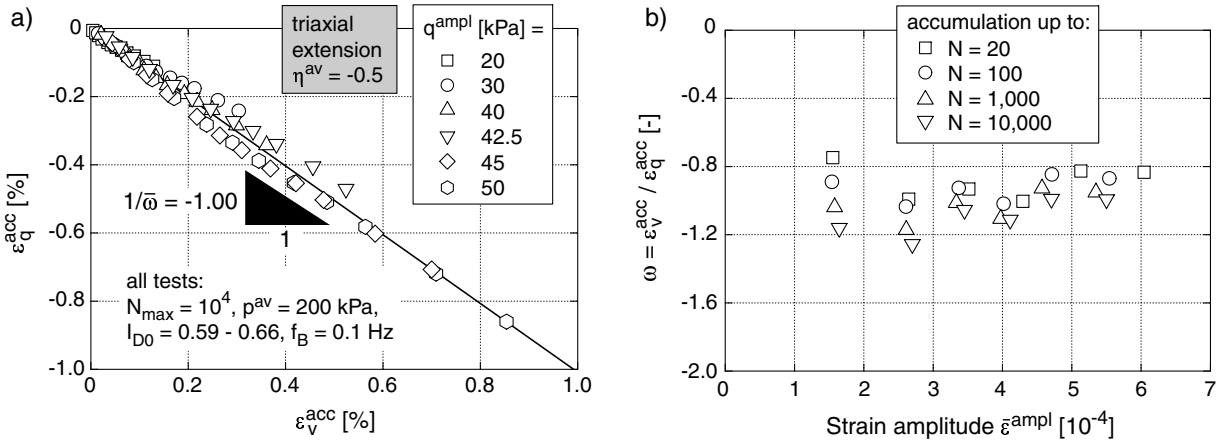

Figure 5.9: *Direction of accumulation for different stress amplitudes at $\eta^{av} = -0.5$ (triaxial extension): a) ε_q^{acc}-ε_v^{acc}-strain paths, b) ratio $\omega = \varepsilon_v^{acc}/\varepsilon_q^{acc}$ as a function of the strain amplitude $\bar{\varepsilon}^{ampl}$*

Also the polarization of the cycles, i.e. their direction in the stress or strain space is of minor importance with respect to the direction of accumulation. At $p^{av} = 200$ kPa and $\eta^{av} = 0.5$ in-phase stress cycles with six different inclinations $0° \leq \alpha_{PQ} \leq 90°$ in the P-Q-plane were tested. For each polarization, four or five stress amplitudes 20 kPa $\leq \sqrt{(P^{ampl})^2 + (Q^{ampl})^2} \leq 100$ kPa were studied. A detailed discussion of the stress and strain loops of this test series is given in Section 5.2.1.3. Figure 5.10 presents the measured ε_q^{acc}-ε_v^{acc}-strain paths. Each diagram contains the paths of the tests with a certain polarization α_{PQ}.

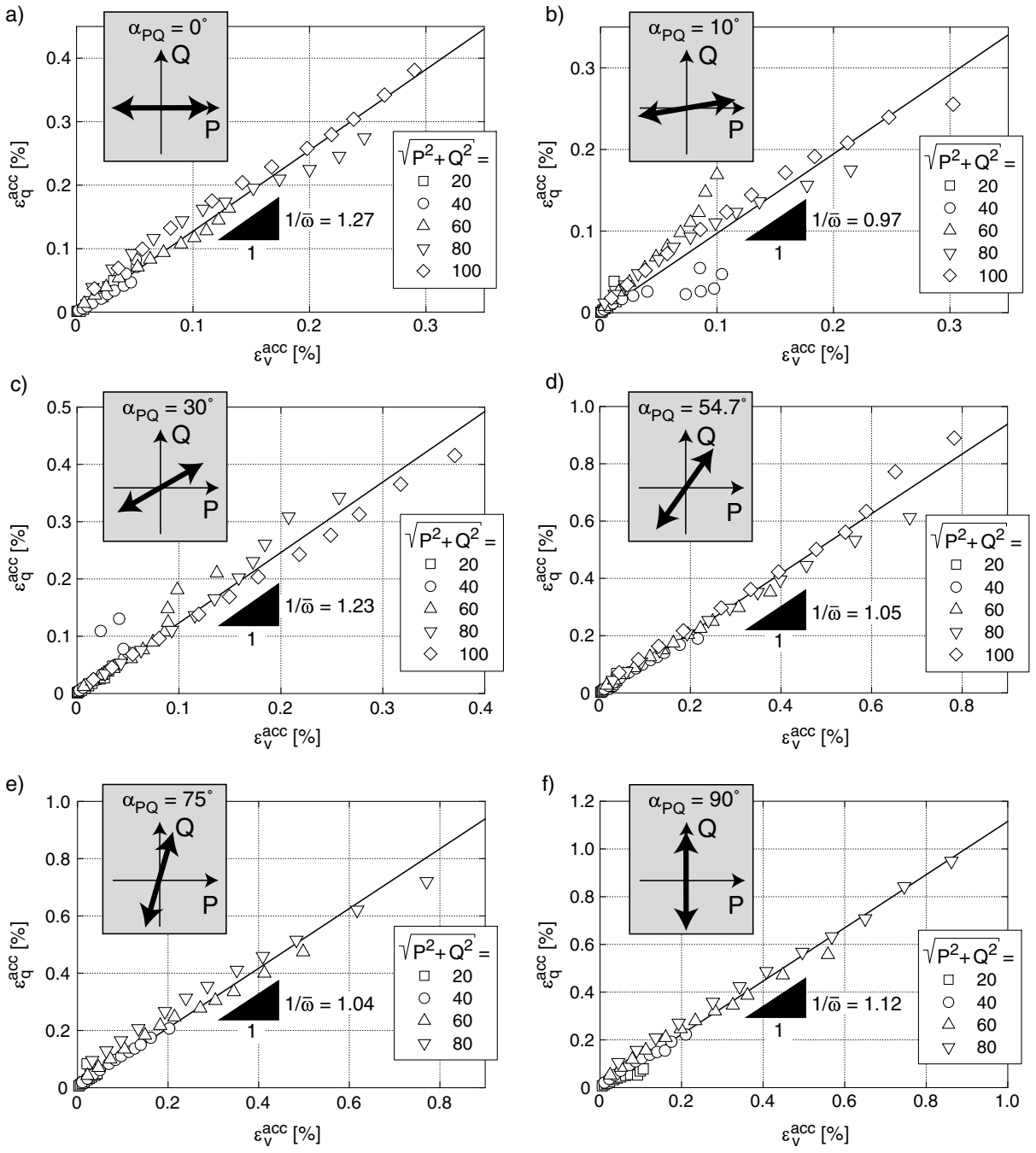

Figure 5.10: ε_q^{acc}-ε_v^{acc}-*strain paths for in-phase stress cycles with different inclinations in the P-Q-plane (all tests:* $N_{\max} = 10^4$, $p^{av} = 200$ *kPa*, $\eta^{av} = 0.5$, $0.56 \leq I_{D0} \leq 0.64$, $f_B = 0.05$ *Hz)*

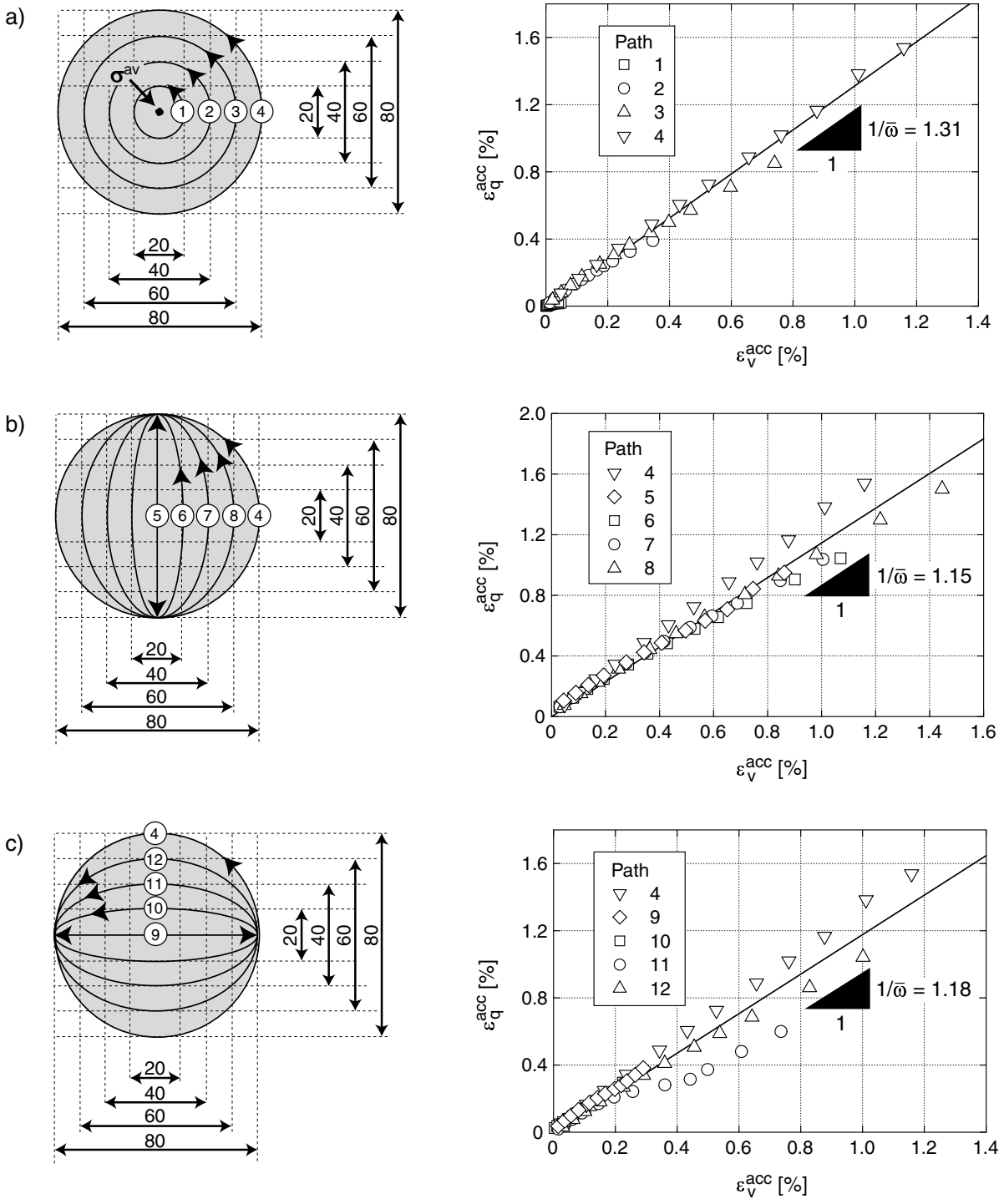

Figure 5.11: ε_q^{acc}-ε_v^{acc}-*strain paths for different elliptic stress paths in the P-Q-plane (all tests:* $N_{\max} = 10^4$, $p^{av} = 200$ *kPa*, $\eta^{av} = 0.5$, $0.58 \leq I_{D0} \leq 0.68$, $f_B = 0.05$ *Hz)*

Although the data for $\alpha_{PQ} = 10°$ scatters, independently of α_{PQ} the direction of accumulation does not depend on the amplitude $\sqrt{(P^{\mathrm{ampl}})^2 + (Q^{\mathrm{ampl}})^2}$ of the cycles. The six diagrams in Figure 5.10 provide the mean value of the inclination $1/\bar{\omega}$ of the strain paths in the $\varepsilon_q^{\mathrm{acc}}$-$\varepsilon_v^{\mathrm{acc}}$-plane. The values lie within $0.97 \leq 1/\bar{\omega} \leq 1.27$. Since no correlation of $1/\bar{\omega}$ with α_{PQ} is noticeable, it can be concluded, that the cyclic flow rule does not depend on the polarization of the cycles.

Also the shape of the stress or strain cycles does not influence the direction of accumulation. Tests were performed with elliptic stress cycles in the P-Q-plane. The average stress was $p^{\mathrm{av}} = 200$ kPa and $\eta^{\mathrm{av}} = 0.5$. Circular cycles with different radii (Figure 5.11a), elliptic cycles with $Q^{\mathrm{ampl}} = 80$ kPa and different spans in the direction of the P-axis (Figure 5.11b) as well as elliptic cycles with $P^{\mathrm{ampl}} = 80$ kPa and different amplitudes along the Q-axis (Figure 5.11c) were tested. A significant dependence of the inclination $1/\bar{\omega}$ of the $\varepsilon_q^{\mathrm{acc}}$-$\varepsilon_v^{\mathrm{acc}}$-strain paths on the shape of the cycles could not be found.

Thus, the cyclic flow rule is exclusively governed by η^{av}. The span, the polarization and the shape of the stress loop (or the resulting strain loop) surrounding $\boldsymbol{\sigma}^{\mathrm{av}}$ have no influence on the direction of accumulation.

5.1.3 Influence of amplitude changes (packages of cycles)

Figure 5.12 presents results of tests, in which four packages of cycles were applied in succession. Each package consisted of $2.5 \cdot 10^4$ cycles. The amplitudes $q^{\mathrm{ampl}} = 20$, 40, 60 and 80 kPa were tested at an average stress with $p^{\mathrm{av}} = 200$ kPa and $\eta^{\mathrm{av}} = 0.75$. The sequence of the amplitudes was varied from test to test. The direction of the strain paths in the $\varepsilon_q^{\mathrm{acc}}$-$\varepsilon_v^{\mathrm{acc}}$-diagram hardly changes due to the change in the amplitude. At the most, a small increase of the ratio $\dot{\varepsilon}_q^{\mathrm{acc}}/\dot{\varepsilon}_v^{\mathrm{acc}}$ was measured at the beginning of a package, when the amplitude q^{ampl} was increased compared to the previous package. However, this was only the case if no larger stress amplitude was previously applied.

5.1.4 Influence of the void ratio / relative density

Tests with different initial void ratios e_0 but identical stresses ($p^{\mathrm{av}} = 200$ kPa, $\eta^{\mathrm{av}} = 0.75$, $q^{\mathrm{ampl}} = 60$ kPa) exhibited that the cyclic flow rule does not depend on the void ratio. Figure 5.13a demonstrates this for some of the tests which are discussed in more detail in Section 5.2.3. The smaller inclination $1/\bar{\omega}$ in Figure 5.13a in comparison to Figures 5.3a and 5.8a can be explained by the larger residual strains in the test with $I_{D0} = 0.24$ and the resulting larger rotation of the direction of accumulation. For high initial densities

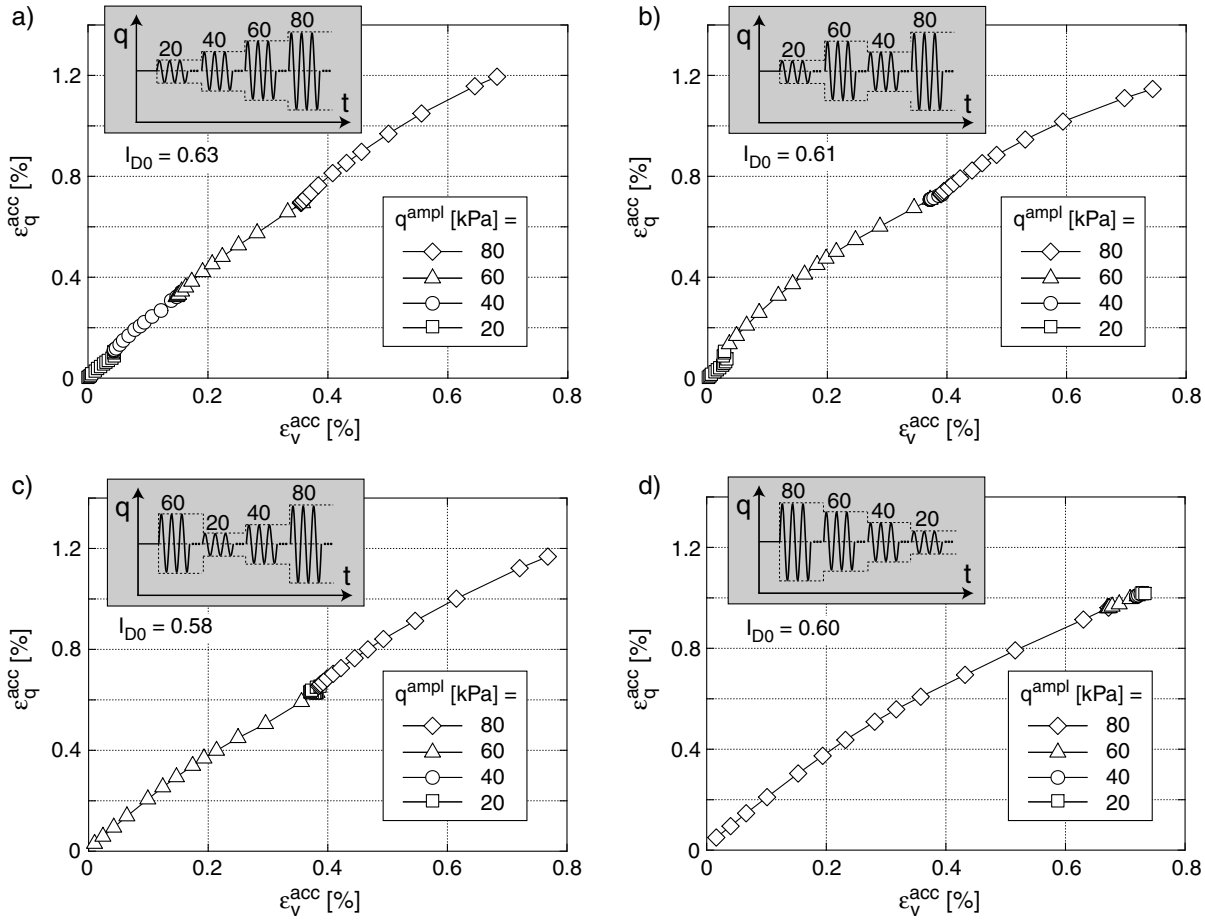

Figure 5.12: ε_q^{acc}-ε_v^{acc}-*strain paths in tests with packages of cycles (all tests:* $N_{\max} = 10^5$, $p^{av} = 200$ *kPa,* $\eta^{av} = 0.75$, $f_B = 0.25$ *Hz)*

($I_D > 0.9$) the values of ω scatter significantly (Figure 5.13b) since the ratio is calculated as the quotient of two relatively small strains. However, a clear tendency of this scattering (i.e. an increase of the deviatoric portion in comparison to the volumetric component with decreasing e) could not be detected. Thus, it is also assumed for high relative densities that the direction of accumulation does not depend on e.

5.1.5 Influence of the loading frequency

Tests with different loading frequencies 0.05 Hz $\leq f_B \leq$ 2 Hz at identical stresses and with similar initial densities are presented in Figure 5.14. A dependence of the cyclic flow rule on f_B could not be found.

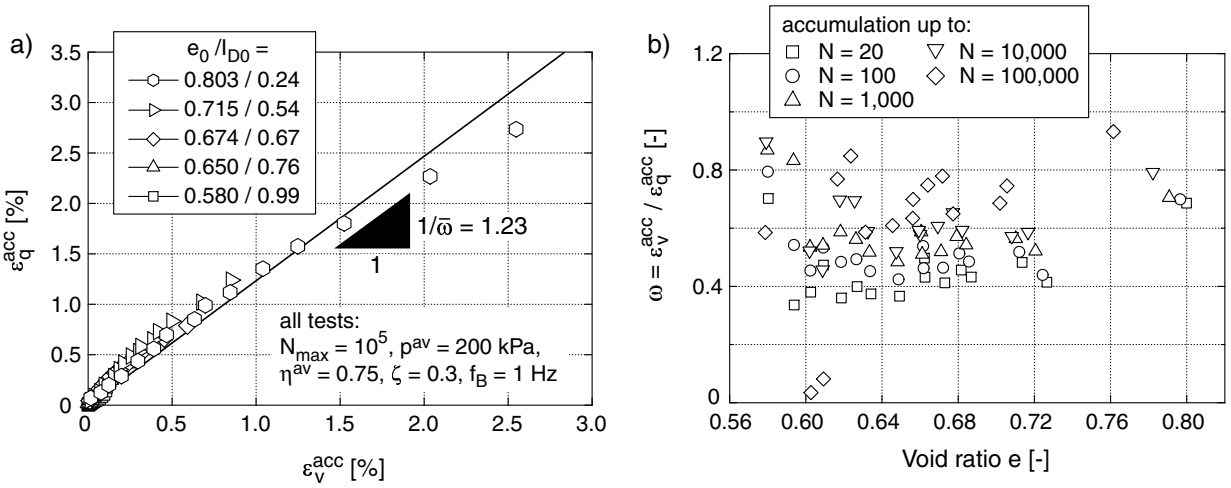

Figure 5.13: *Direction of accumulation in tests with different initial densities I_{D0}: a) ε_q^{acc}-ε_v^{acc}-strain paths, b) ratio $\omega = \varepsilon_v^{acc}/\varepsilon_q^{acc}$ as a function of void ratio e*

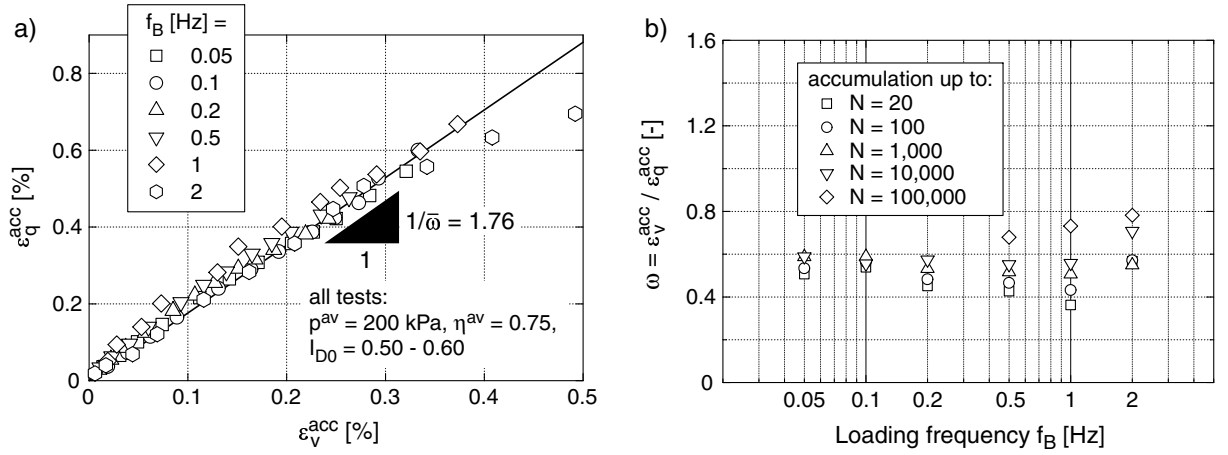

Figure 5.14: *Direction of accumulation for different loading frequencies f_B: a) ε_q^{acc}-ε_v^{acc}-strain paths, b) ratio $\omega = \varepsilon_v^{acc}/\varepsilon_q^{acc}$ as a function of f_B*

5.1.6 Influence of the number of cycles

The increase of the volumetric portion of the direction of accumulation with N was discussed already in the previous sections. The tests presented up to now were restricted to 10^4 or 10^5 load cycles. Figure 5.15 shows the results of two long-time tests, each with $2 \cdot 10^6$ cycles. The increase of ω with N continues also for $N > 10^5$.

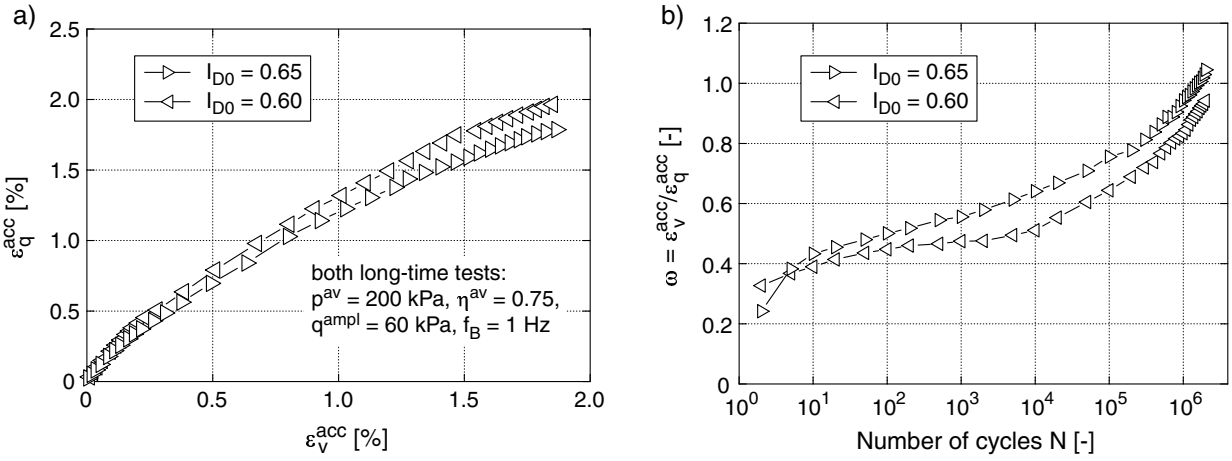

Figure 5.15: *Direction of accumulation in two tests with* $N_{\max} = 2 \cdot 10^6$*: a)* ε_q^{acc}-ε_v^{acc}*-strain paths, b) increase of* $\omega = \varepsilon_v^{acc}/\varepsilon_q^{acc}$ *with* N

5.1.7 Influence of a static (monotonic) preloading

The influence of a monotonic preloading was also tested. Starting from $p = 50$ kPa, the specimens were loaded with stress paths along the p-axis or along a line with an inclination $\eta = 0.75$ (corresponds to $K_0 = 0.5$) up to a certain preloading pressure 100 kPa $\leq p_{\text{preload}} \leq 300$ kPa (Figure 5.16a). This pressure was maintained five minutes, followed by an unloading towards $p^{\text{av}} = 100$ kPa. Subsequently, 10^4 cycles with an amplitude $q^{\text{ampl}} = 50$ kPa were applied at $p^{\text{av}} = 100$ kPa and $\eta^{\text{av}} = 0$ or $\eta^{\text{av}} = 0.75$, respectively. The tests with $p_{\text{preload}} = 100$ kPa correspond to a non-preloaded specimen. Figure 5.16b makes clear, that the $\varepsilon_q^{\text{acc}}$-$\varepsilon_v^{\text{acc}}$-strain paths of the three tests with the K_0-preloading coincide. A similar conclusion can be drawn for the isotropic preloading. Thus, a monotonic preloading does not affect the direction of accumulation.

5.1.8 Influence of the grain size distribution curve

All preceding remarks on the direction of accumulation referred to the grain size distribution curve No. 3 with respect to Figure 4.14. Additionally, the grain size distribution curves No. 2 ($d_{50} = 0.35$ mm, $U = 1.9$), No. 5 ($d_{50} = 1.45$ mm, $U = 1.4$) and No. 7 ($d_{50} = 0.52$ mm, $U = 4.5$) were tested. The critical friction angles of the four grain size distribution curves lay in the range $31.2° \leq \varphi_c \leq 33.9°$. The average stress ($p^{\text{av}} = 200$ kPa, $\eta^{\text{av}} = 0.75$) was kept constant and the stress amplitude 12 kPa $\leq q^{\text{ampl}} \leq 87$ kPa was varied in the tests.

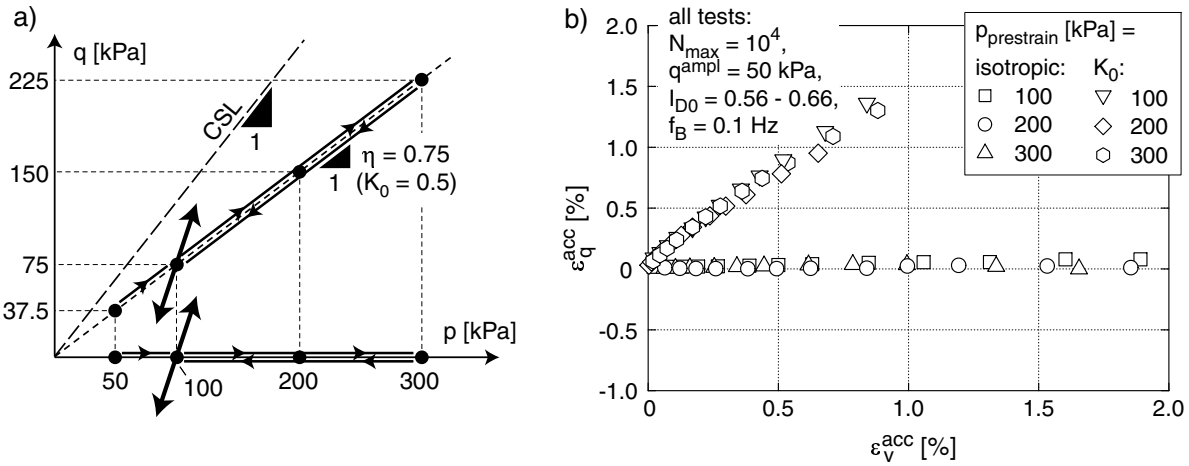

Figure 5.16: ε_q^{acc}-ε_v^{acc}-*strain paths for a cyclic loading after a monotonic (isotropic or* K_0*) preloading*

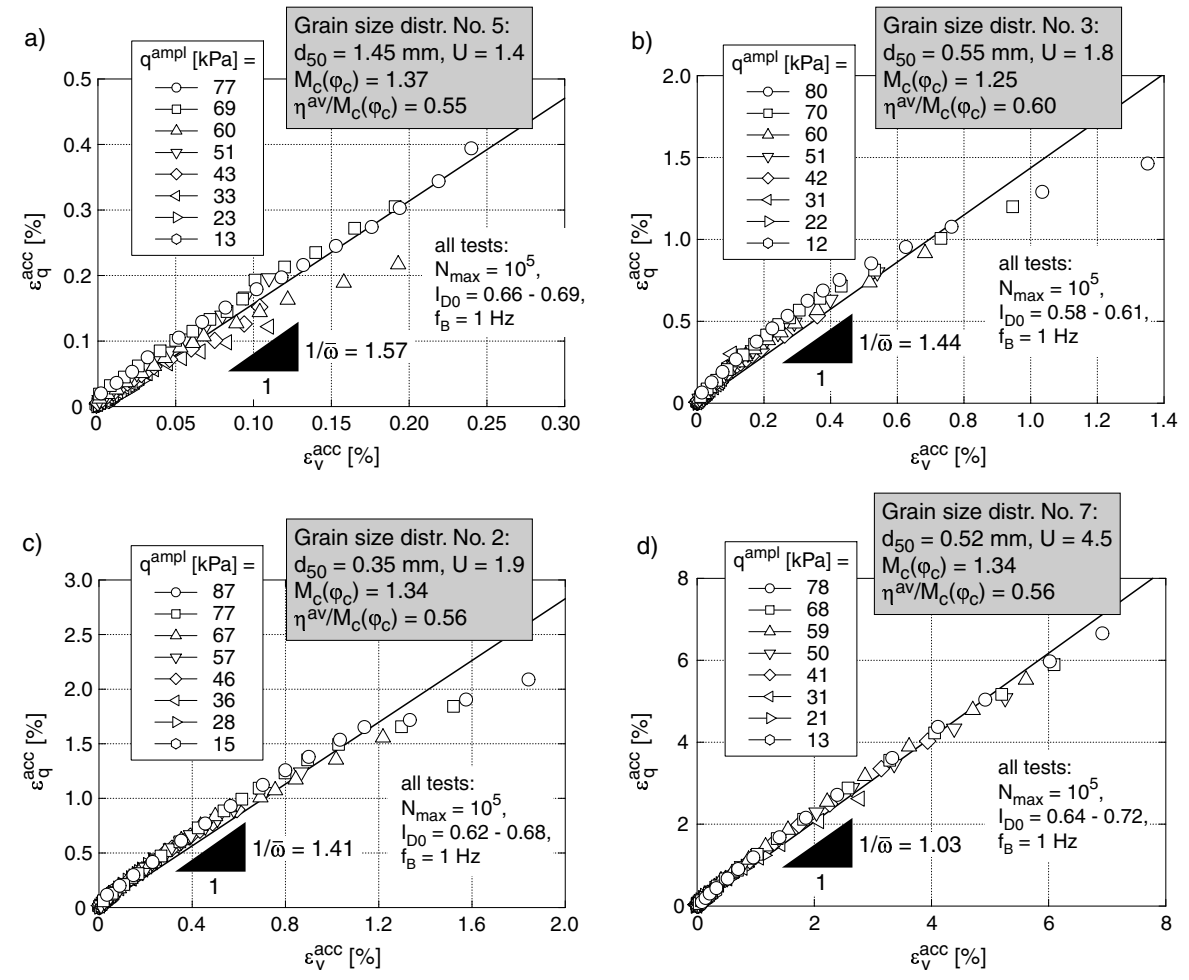

Figure 5.17: ε_q^{acc}-ε_v^{acc}-*strain paths for different grain size distribution curves (all tests:* p^{av} *= 200 kPa,* η^{av} *= 0.75)*

Figure 5.17 presents the ε_q^{acc}-ε_v^{acc}-strain paths for the four tested grain size distribution curves. The diagram 5.17b for sand No. 3 repeats Figure 5.8a in order to facilitate comparison. Also for the three grain size distributions tested additionally, the independence of the cyclic flow rule of the stress or strain amplitude could be confirmed. The mean inclination of the strain paths in the ε_q^{acc}-ε_v^{acc}-diagram of the medium coarse sand No. 2 ($1/\bar{\omega} = 1.41$) is slightly smaller than the one of the medium coarse to coarse sand No. 3 ($1/\bar{\omega} = 1.44$). The coarse sand No. 5 exhibits a larger deviatoric component ($1/\bar{\omega} = 1.57$), the well-graded sand No. 7 a larger volumetric portion ($1/\bar{\omega} = 1.03$). However, these differences are due to the different accumulation rates (see Section 5.2.9) and the resulting different residual strains. The larger the residual strains are, the smaller is the mean inclination $1/\bar{\omega}$. This becomes clear, if the ε_q^{acc}-ε_v^{acc}-strain paths of the four tested grain size distribution curves for $\varepsilon_v^{acc} \leq 2\%$ are plotted into a common diagram (Figure 5.18). A significant difference of the inclinations of the strain paths in Figure 5.18 cannot be detected. Thus, it can be concluded, that the direction of accumulation does not depend on the grain size distribution curve.

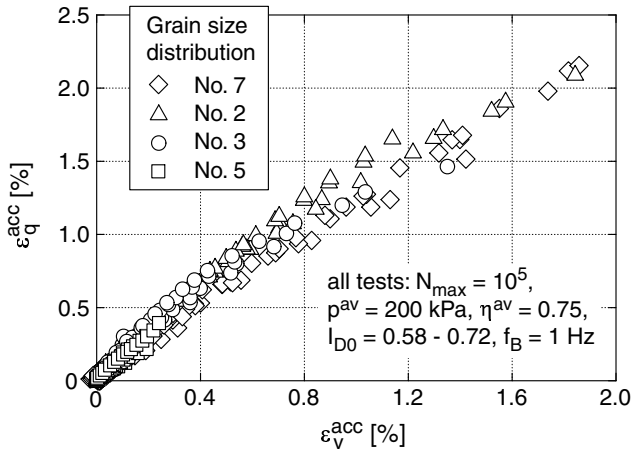

Figure 5.18: *Summary of the ε_q^{acc}-ε_v^{acc}-strain paths of the four tested grain size distribution curves in a common diagram*

5.2 Intensity of accumulation

5.2.1 Influence of the span, shape and polarization of the loops

5.2.1.1 Span of the loop (amplitude of in-phase cycles)

First, *small* cycles are considered, i.e. cycles with stress paths laying between the critical state lines in the p-q-plane. In a first test series, uniaxial stress cycles (σ_3 = constant) were tested with different stress amplitudes 12 kPa $\leq q^{\mathrm{ampl}} \leq$ 80 kPa (see the scheme of the stress cycles in Figure 5.19). The average stress (p^{av} = 200 kPa, η^{av} = 0.75) was identical in all eight tests. The specimens were prepared with similar initial densities $0.58 \leq I_{D0} \leq 0.61$.

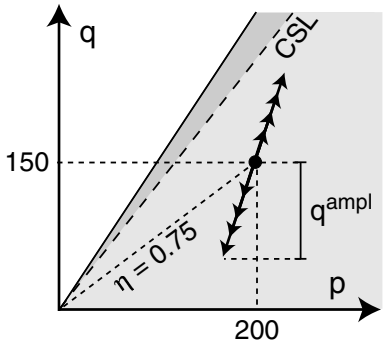

Figure 5.19: *Tests with uniaxial stress cycles and different amplitudes: stress paths in the p-q-plane*

In Figure 5.20 the q-ε_1-hystereses are plotted for the test with q^{ampl} = 80 kPa and selected numbers of cycles. The illustration makes clear, that the first cycle differs significantly from the subsequent ones. The first quarter of the first cycle corresponds to a first loading of the material. The residual strains at the end of the first cycle are much larger than in the subsequent cycles. Also an increased stiffness at the beginning of the first cycle attracts attention. This first cycle was applied after having waited a period of one hour at the average stress $\boldsymbol{\sigma}^{\mathrm{av}}$. The small oscillation of the axial force ($\leq \pm$ 2 N) due to the pneumatic loading system may be responsible for this increase of stiffness. If one tries an interpretation using the concept of intergranular strain (Niemunis & Herle [106]), small cycles lead to a reduction of the intergranular strain although they cause nearly no residual strains. During the subsequent monotonic loading the strain path thus starts from a state with an increased stiffness. In Figure 5.20 also the increase of the residual

strain with the number of cycles is obvious.

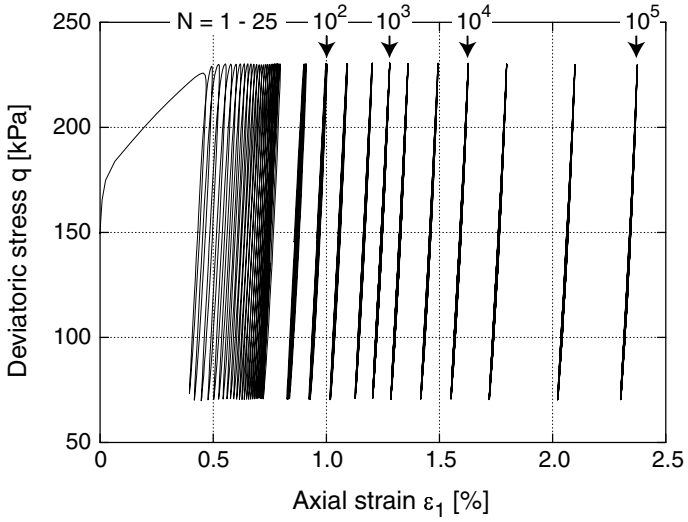

Figure 5.20: *q-ε_1-hystereses in a test with q^{ampl} = 80 kPa*

Figure 5.21 shows the first cycle for the different amplitudes. All *q-ε_q*-hystereses exhibit the increased initial stiffness (Figure 5.21a). As expected, the residual strains after the first cycle increase with increasing stress amplitude q^{ampl} (Figure 5.21b).

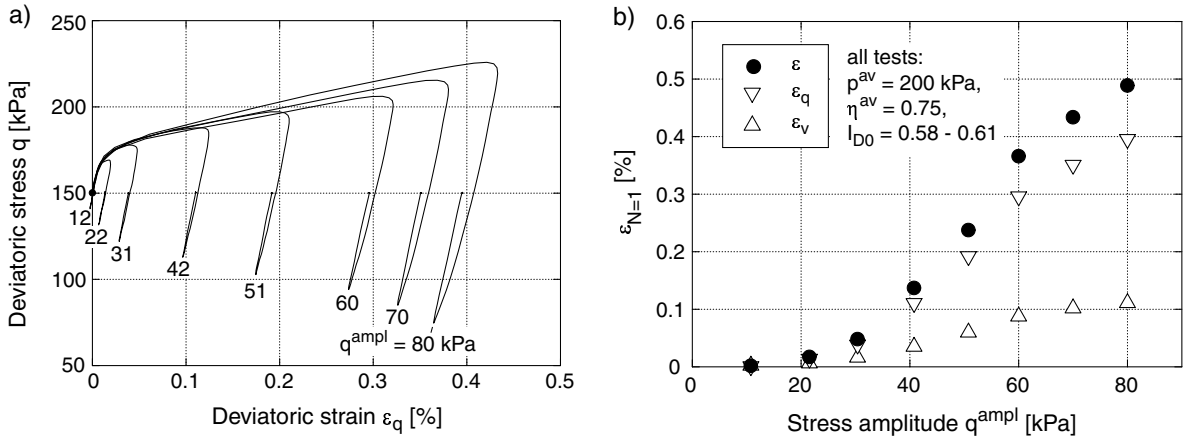

Figure 5.21: *First cycle: a) q-ε_q-hystereses, b) residual strains*

In particular in the case of the larger stress amplitudes $q^{\mathrm{ampl}} \geq 30$ kPa the strain amplitude $\varepsilon^{\mathrm{ampl}}$ (Figure 5.22a) decreased during the first 100 cycles and remained almost constant during the subsequent cycles. In Figure 5.22b the mean values of the strain amplitudes $\varepsilon_v^{\mathrm{ampl}}$, $\varepsilon_q^{\mathrm{ampl}}$, $\varepsilon^{\mathrm{ampl}}$ and γ^{ampl} over 10^5 cycles are plotted versus q^{ampl}. It is obvious that for

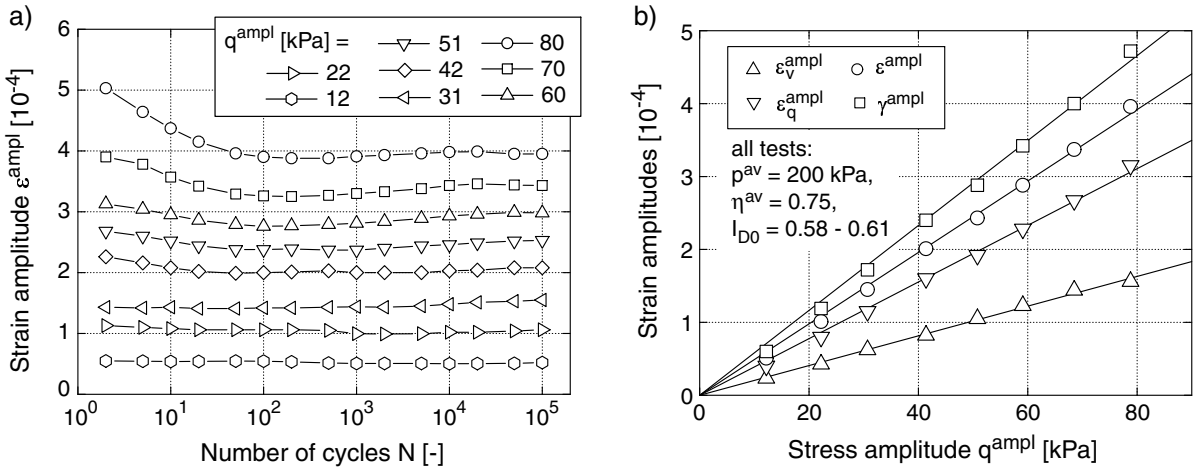

Figure 5.22: *a) Strain amplitude ε^{ampl} as a function of the number of cycles N, b) Mean values of the strain amplitudes over 10^5 cycles as a function of the stress amplitude q^{ampl}*

small amplitudes the strain amplitudes are proportional to the stress amplitudes.

Figure 5.23 depicts the increase of the residual strain ε^{acc} with the number of cycles N during the cycles with $N > 1$. The accumulation rate $\dot{\varepsilon}^{acc} = \partial\varepsilon^{acc}/\partial N$ decreases with N. The shape of the accumulation curves $\varepsilon^{acc}(N)$ (proportional to $\ln(N)$ for $N \leq 10^4$, over-logarithmic for larger numbers of cycles) is discussed in detail in Section 5.2.6. The intensity of accumulation increases with increasing stress or strain amplitude (Figure 5.23).

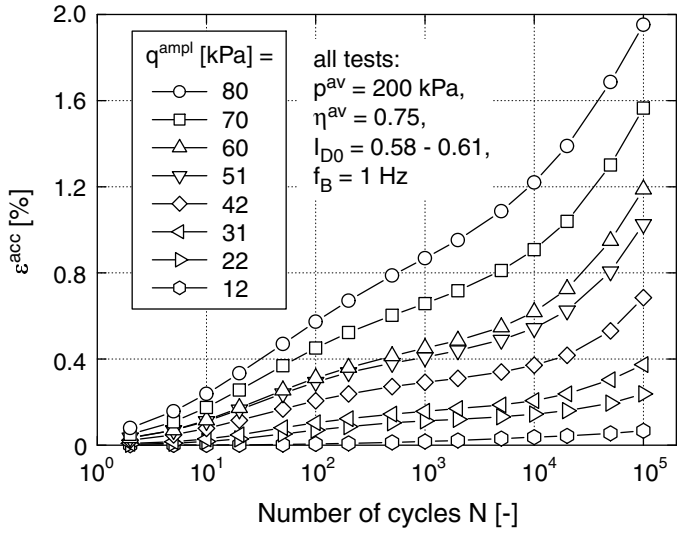

Figure 5.23: *Accumulation curves $\varepsilon^{acc}(N)$ for different stress amplitudes q^{ampl}*

In Figure 5.24 the accumulated strain $\varepsilon^{\mathrm{acc}}$ after different numbers of cycles is plotted versus the square of the strain amplitude $(\bar{\varepsilon}^{\mathrm{ampl}})^2$. Due to the variation of $\varepsilon^{\mathrm{ampl}}$ with N a mean value $\bar{\varepsilon}^{\mathrm{ampl}} = (\int_1^N \varepsilon^{\mathrm{ampl}}(N)\ \mathrm{d}N)/N$, up to the number of cycles N was used in Figure 5.24. For a better orientation also a scale for the amplitude $\bar{\varepsilon}^{\mathrm{ampl}}$ is given at the top of the diagram. The residual strain $\varepsilon^{\mathrm{acc}}$ was normalized with the void ratio function f_e (Section 5.2.3) in order to consider the slightly different initial void ratios and the different compaction in the eight tests. The bar $\bar{\square}$ over f_e indicates, that f_e was calculated with a mean value of the void ratio $\bar{e} = (\int_1^N e(N)\ \mathrm{d}N)/N$. Independently of N, one obtains linear curves in Figure 5.24. Thus, the accumulation rate is proportional to the square of the strain amplitude:

$$\dot{\varepsilon}^{\mathrm{acc}} \quad \sim \quad (\varepsilon^{\mathrm{ampl}})^2 \tag{5.1}$$

The relationship (5.1) is confirmed by the accumulation rates $\dot{\varepsilon}^{\mathrm{acc}}$ shown in Figure 5.25 for different numbers of cycles. In Figure 5.25 the actual strain amplitude $\varepsilon^{\mathrm{ampl}}$ (in the middle of the interval, which is used to evaluate $\dot{\varepsilon}^{\mathrm{acc}}$, $\varepsilon^{\mathrm{ampl}} \neq \bar{\varepsilon}^{\mathrm{ampl}}$) is plotted on the abscissa. Also the function f_e, which was used to normalize $\dot{\varepsilon}^{\mathrm{acc}}$, was calculated with the actual void ratio e (and not with $\bar{e}$).

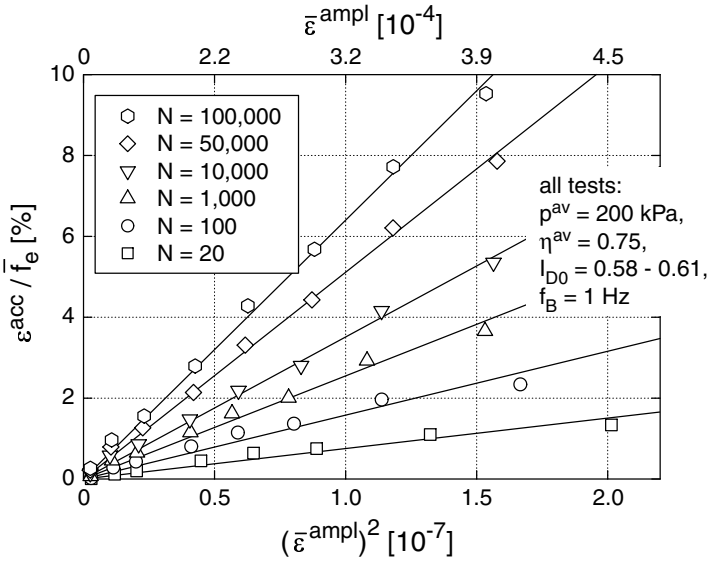

Figure 5.24: *Accumulated strain $\varepsilon^{acc}/\bar{f}_e$ plotted versus the square of the strain amplitude $(\bar{\varepsilon}^{ampl})^2$ with $\bar{\varepsilon}^{ampl} = (\int_1^N \varepsilon^{ampl}(N)\ dN)/N$*

Since a well-defined direction of accumulation exists, which depends solely on the average stress ratio η^{av} (Section 5.1), the intensity of accumulation (except for $\dot{e} = \partial e/\partial N = 0$) can adequately be expressed by the volumetric portion of accumulation, i.e. the densification

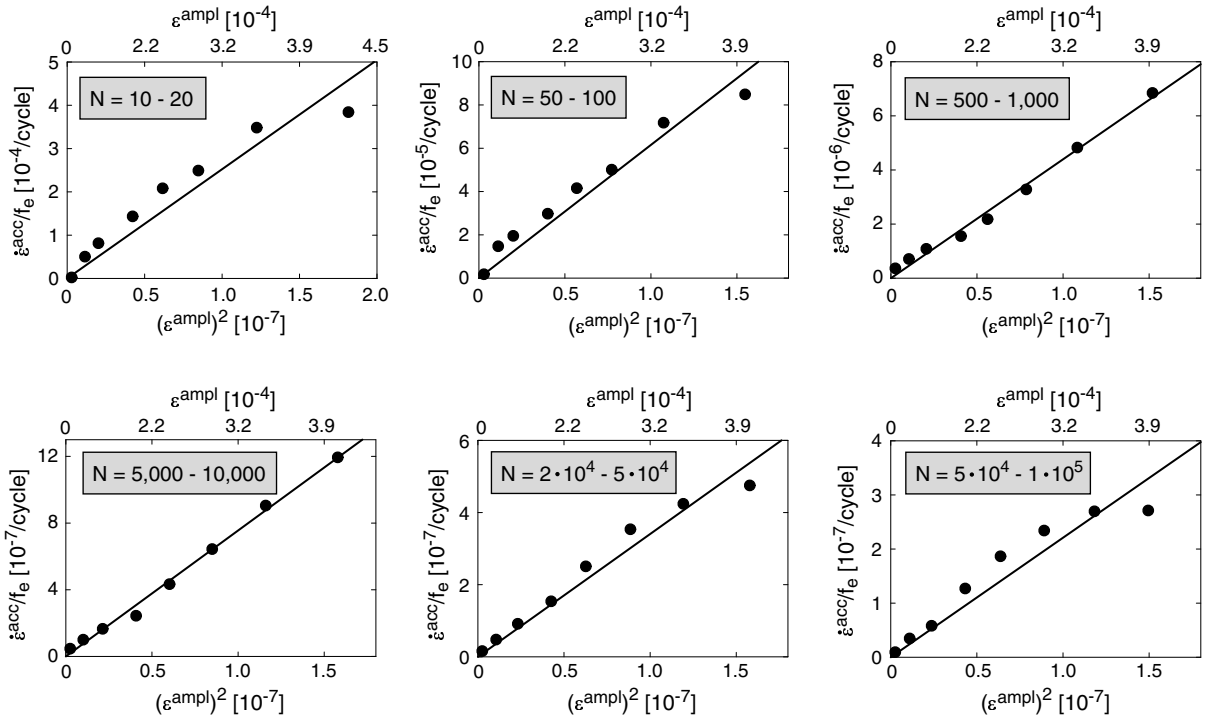

Figure 5.25: *Rate of accumulation* $\dot{\varepsilon}^{acc} \approx \Delta\varepsilon^{acc}/\Delta N$ *in dependence on* $(\varepsilon^{ampl})^2$ *for different numbers of cycles*

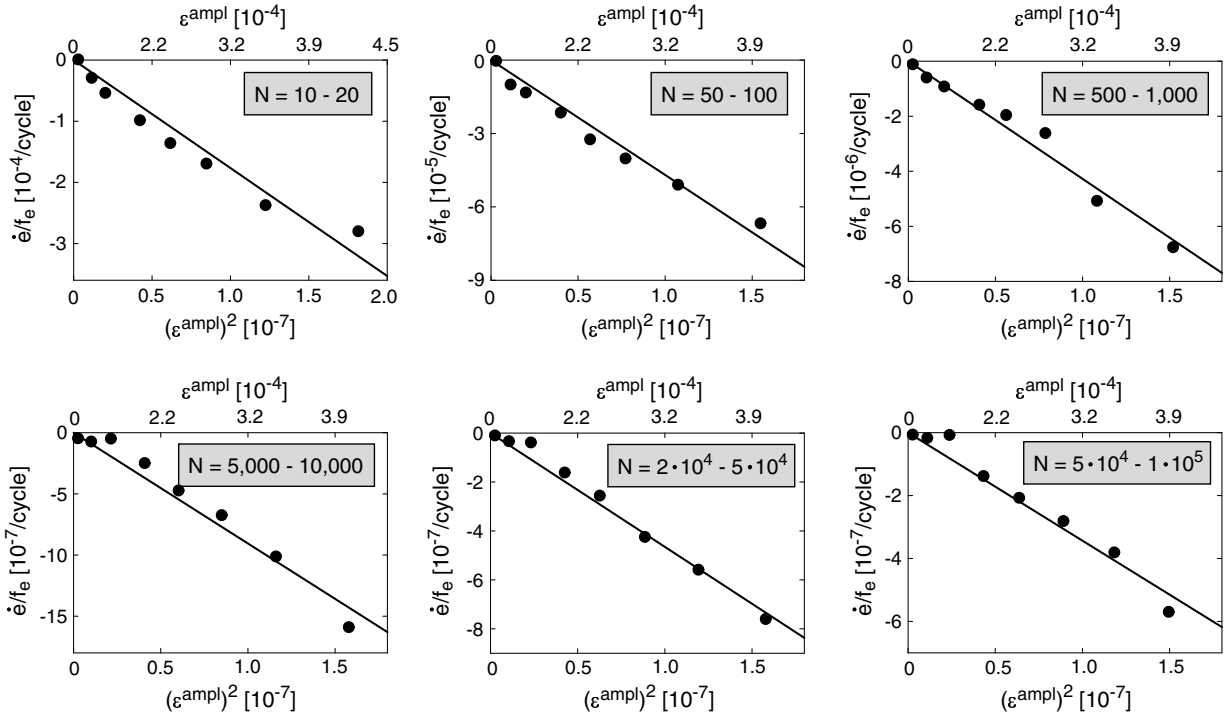

Figure 5.26: *Densification rate* $\dot{e} \approx \Delta e/\Delta N$ *as a function of* $(\varepsilon^{ampl})^2$ *for different numbers of cycles*

rate $\dot{e} = \partial e / \partial N$. Thus, instead of the accumulated strain, the change of the state variable void ratio is considered. Equivalent to Figure 5.25, Figure 5.26 depicts the densification rates for different numbers of cycles. The negative rates mean a reduction of void ratio. As expected, the quadratic relationship $\dot{e} \sim (\varepsilon^{\mathrm{ampl}})^2$ can be seen in Figure 5.26.

The test results coincide with the relationship $\varepsilon^{\mathrm{acc}} \sim \zeta^2$ derived from the tests of Marr & Christian [94] (Section 3.2.2.2, Figure 3.15). The "common compaction curve" proposed by Sawicki & Świdziński [133, 134] is confuted by the own tests in Section 5.2.6.

In the accumulation model (Chapter 7), the influence of the strain amplitude on the intensity of accumulation is captured by the function f_{ampl} with the reference amplitude $\varepsilon^{\mathrm{ampl}}_{\mathrm{ref}} = 10^{-4}$:

$$f_{\mathrm{ampl}} = \left(\frac{\varepsilon^{\mathrm{ampl}}}{\varepsilon^{\mathrm{ampl}}_{\mathrm{ref}}} \right)^2 \tag{5.2}$$

The dependence of the accumulation rate on the strain amplitude was also studied for an average stress with triaxial extension ($p^{\mathrm{av}} = 200$ kPa and $\eta^{\mathrm{av}} = -0.5$). Stress amplitudes 20 kPa $\leq q^{\mathrm{ampl}} \leq$ 50 kPa were tested (see the scheme of the stress paths in Figure 5.27).

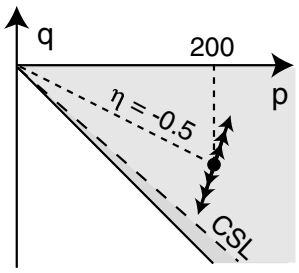

Figure 5.27: *Scheme of the stress paths in the tests on f_{ampl} with triaxial extension*

Figure 5.28a again presents the decrease of the strain amplitude $\varepsilon^{\mathrm{ampl}}$ during the first approx. 100 cycles. For $N > 100$ $\varepsilon^{\mathrm{ampl}}$ remains approximately constant. In Figure 5.28b it can be seen, that the strain amplitudes $\varepsilon^{\mathrm{ampl}}_v$, $\varepsilon^{\mathrm{ampl}}_q$, $\varepsilon^{\mathrm{ampl}}$ and γ^{ampl} are linear proportional to the stress amplitude for $q^{\mathrm{ampl}} \leq 40$ kPa. For larger stress amplitudes the strain amplitudes increased over-proportionally with q^{ampl}.

Figure 5.29a shows the accumulation curves $\varepsilon^{\mathrm{acc}}(N)$ in the six tests. In Figure 5.29b $\varepsilon^{\mathrm{acc}} / \bar{f}_e$ is given as a function of the square of the strain amplitude $(\bar{\varepsilon}^{\mathrm{ampl}})^2$. Independently of N, linear curves are obtained in Figure 5.29b. Thus, the function f_{ampl} could be confirmed also for $\eta^{\mathrm{av}} = -0.5$.

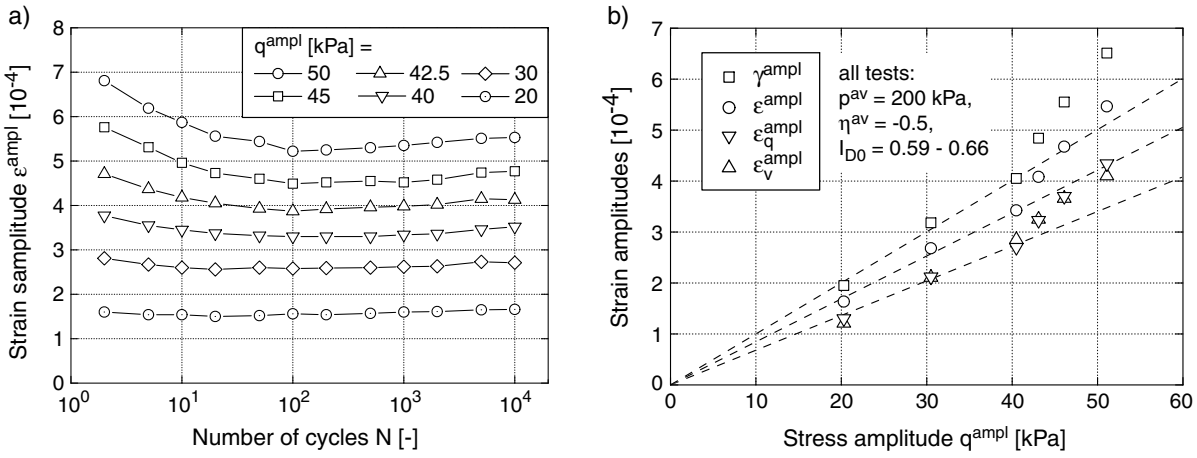

Figure 5.28: *Strain amplitudes in tests on f_{ampl} with an average stress with triaxial extension: a) curves $\varepsilon^{ampl}(N)$, b) mean values of the strain amplitudes over 10^4 cycles as a function of the stress amplitude q^{ampl}*

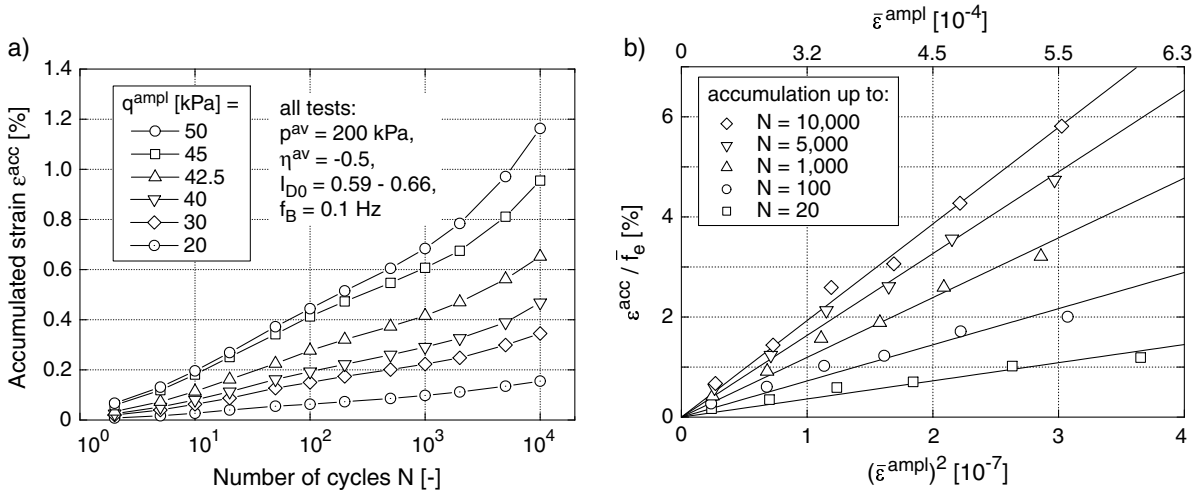

Figure 5.29: *Residual strain in tests on f_{ampl} with an average stress with triaxial extension: a) curves $\varepsilon^{acc}(N)$, b) linear relationship between $\varepsilon^{acc}/\bar{f}_e$ and $(\bar{\varepsilon}^{ampl})^2$*

5.2.1.2 Large strain amplitudes $\varepsilon^{\mathbf{ampl}} \geq 6 \cdot 10^{-4}$

In the tests in Section 5.2.1.1 the strain amplitudes lay below $\varepsilon^{\mathrm{ampl}} = 6 \cdot 10^{-4}$. Larger strain amplitudes were studied in cyclic triaxial tests with a special control. Figure 5.30 presents a scheme of this control. Starting from a stress $\boldsymbol{\sigma}^0$ ($p^0 = 200$ kPa, $q^0 = 150$ kPa), the axial strain was increased by a predefined value $\varepsilon_1^{\mathrm{ampl}}$ ($0 \rightarrow 1$). Afterwards it was reduced by $2\varepsilon_1^{\mathrm{ampl}}$ ($1 \rightarrow 2$). The stress cycle was closed by a return towards the initial stress $\boldsymbol{\sigma}^0$ ($2 \rightarrow 0$). This mixture of displacement and load control allowed us to test predefined strain amplitudes $\varepsilon_1^{\mathrm{ampl}} > 6 \cdot 10^{-4}$ while the accumulation of *strain* (and

not *stress* as in the case of a conventional displacement control) was measured.

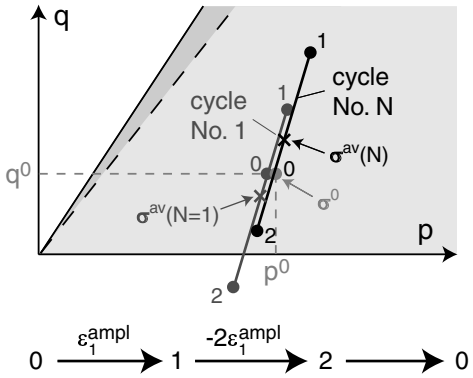

Figure 5.30: *Scheme of the control of the tests with large strain amplitudes* $\varepsilon^{ampl} > 6 \cdot 10^{-4}$

However, the average stress $\boldsymbol{\sigma}^{\mathrm{av}}$ (defined as the mean value of the smallest and the largest stress, $\boldsymbol{\sigma}^{\mathrm{av}} \neq \boldsymbol{\sigma}^{0}$) did not remain constant during cyclic loading. As an example, Figure 5.31 shows the stress path in the p-q-plane and the q-ε_q-loop for different numbers of cycles of a test with a strain amplitude $\bar{\varepsilon}^{\mathrm{ampl}} = 2.3 \cdot 10^{-3}$. While the minimum deviatoric stress q^{min} did hardly change during 1,000 cycles, the maximum value q^{max} increased with N. This is due to an increase of the stiffness caused by cyclic loading. For the larger numbers of cycles the stress path even exceeds the peak shear strength calculated from Equation (4.6) for $e(N)$, i.e. a hardening of the material with increasing N was observed. A comparison of Figures 5.31 and 5.20 reveals, that for the large strain amplitudes tested in this series, the stress-strain loops enclose a significantly larger area in the q-ε_q-plane, i.e. as expected the dissipation of energy increases with $\varepsilon^{\mathrm{ampl}}$. With increasing number of cycles the q-ε_q-hystereses loops become "slimmer".

In Figure 5.32 the residual strain is plotted as a function of the square of the strain amplitude. The values of $\varepsilon^{\mathrm{acc}}$ were normalized with $\bar{f}_e$, $\bar{f}_p$ and $\bar{f}_Y$ (see the discussion of the functions f_p and f_Y in Section 5.2.4) in order to consider the influences of the void ratio and the average stress. Figure 5.32 also contains the tests presented in Section 5.2.1.1. It is obvious that the relationship $\dot{\varepsilon}^{\mathrm{acc}} \sim (\varepsilon^{\mathrm{ampl}})^2$ loses its validity for large strain amplitudes (starting from approx. $\varepsilon^{\mathrm{ampl}} = 10^{-3}$). The accumulation rate is approximately constant for larger strain amplitudes, i.e. it hardly depends on $\varepsilon^{\mathrm{ampl}}$ (see also the accumulation rates in Figure 5.33) Figure 5.33 also shows, that the largest amplitude for which $\dot{\varepsilon}^{\mathrm{acc}} \sim (\varepsilon^{\mathrm{ampl}})^2$ holds, increases with the number of cycles.

Corresponding to the diagram for $50 \leq N \leq 100$ in Figure 5.33, the ε_q-q- and ε_q-ε_v-loops are depicted for $N = 100$ in Figure 5.34. From Figure 5.33 it can be seen, that $\dot{\varepsilon}^{\mathrm{acc}} \sim (\varepsilon^{\mathrm{ampl}})^2$ is not valid for the tests with the three largest amplitudes. The cyclic stress

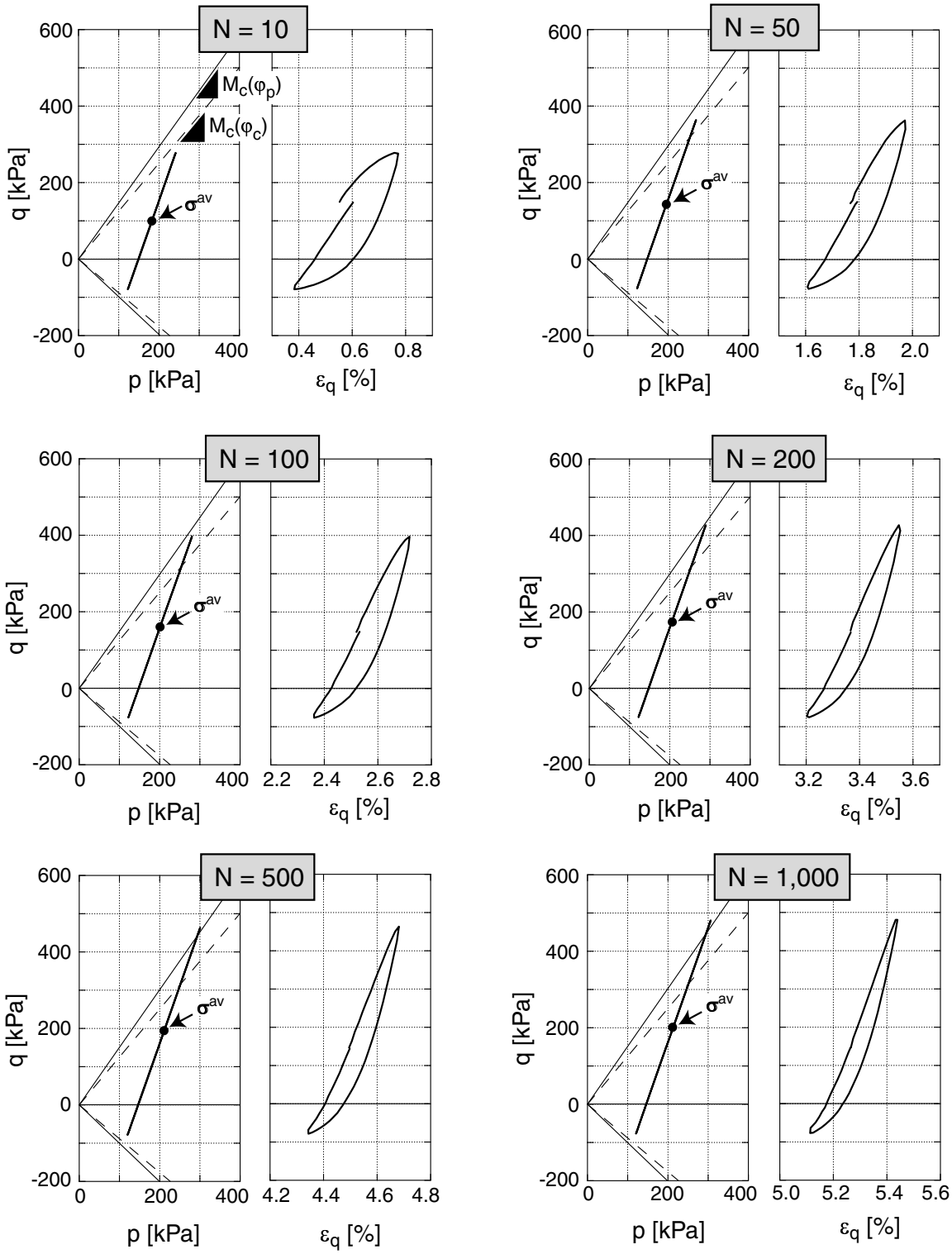

Figure 5.31: *Stress paths in the p-q-plane and ε_q-q-loops for different numbers of cycles*

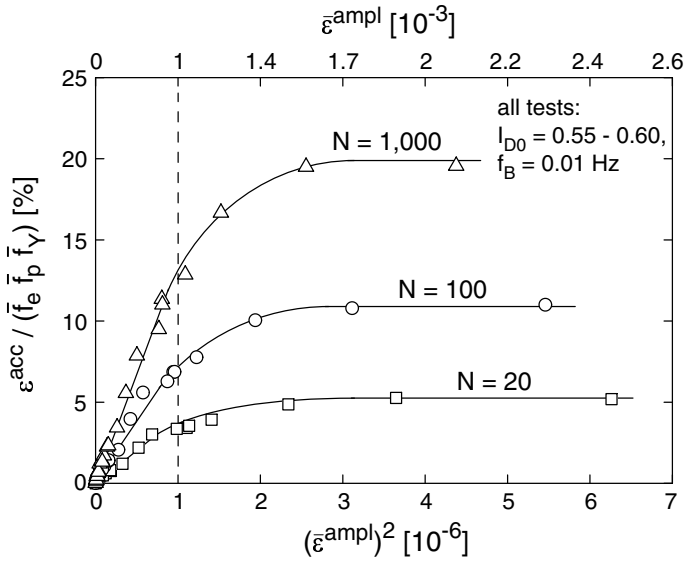

Figure 5.32: *Accumulated strain* $\varepsilon^{acc}/(\bar{f}_e\bar{f}_p\bar{f}_Y)$ *in dependence on the strain amplitude* $\bar{\varepsilon}^{ampl}$*: Confirmation of the quadratic relationship up to* $\varepsilon^{ampl} \approx 10^{-3}$

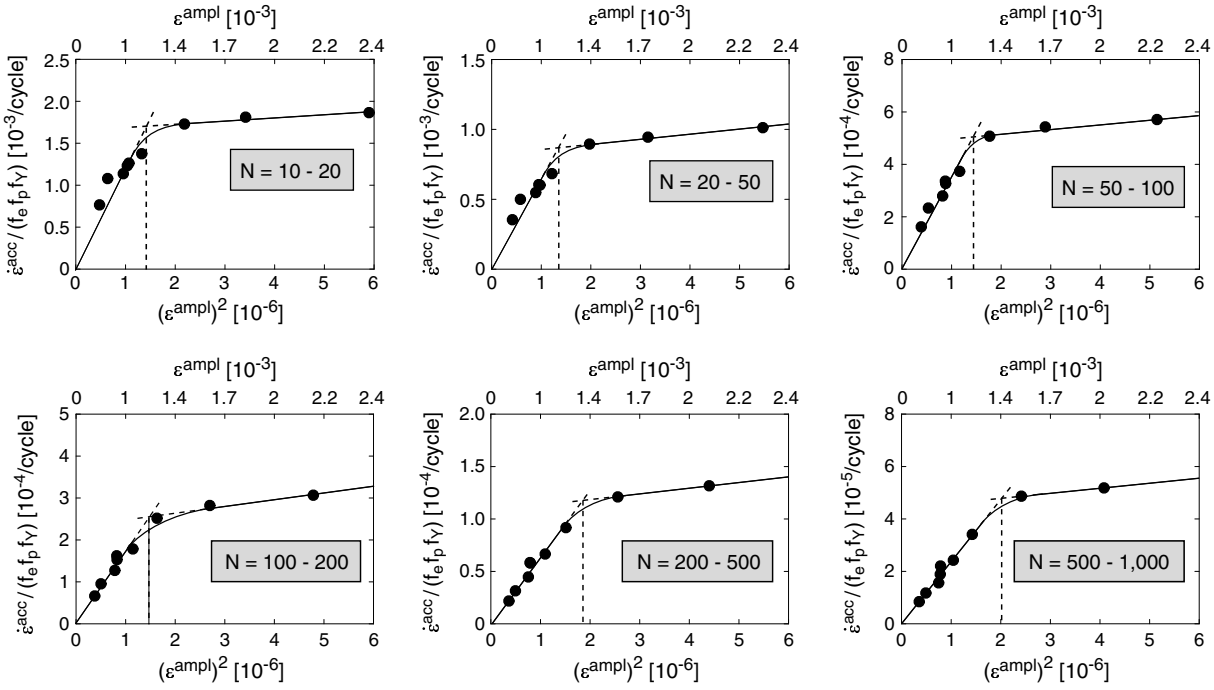

Figure 5.33: *Rate of strain accumulation* $\dot{\varepsilon}^{acc} \approx \Delta\varepsilon^{acc}/\Delta N$ *in dependence on* $(\varepsilon^{ampl})^2$ *for different numbers of cycles*

paths exceed the critical state line in those tests and the sand dilates during loading (Figure 5.34). If one assumes that Equation (5.2) loses its validity if the stress cycles exceed the CSL, the largest strain amplitude for which (5.2) holds depends on the location of the cycles in the stress space.

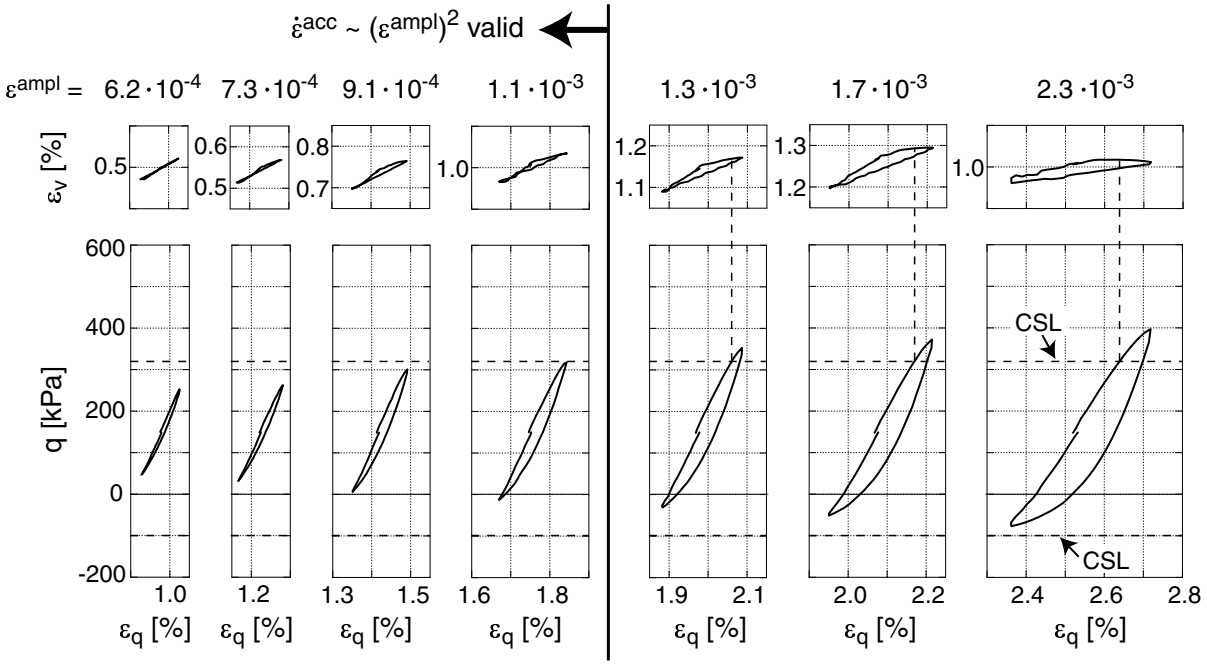

Figure 5.34: *ε_q-q-loops and ε_q-ε_v-loops at $N = 100$ for different strain amplitudes*

Further research is necessary concerning this limit strain amplitude. The accumulation model (Chapter 7) was mainly developed for small strain amplitudes ($\varepsilon^{\text{ampl}} \leq 10^{-3}$). At the moment large strain amplitudes are captured in a simplified manner. For $\varepsilon^{\text{ampl}} > 10^{-3}$ the accumulation rate is set constant. Thus, Equation (5.2) is extended:

$$f_{\text{ampl}} = \begin{cases} \left(\dfrac{\varepsilon^{\text{ampl}}}{\varepsilon^{\text{ampl}}_{\text{ref}}}\right)^2 & \text{for } \varepsilon^{\text{ampl}} \leq 10^{-3} \\ 100 = f(\boldsymbol{\sigma}^{\text{av}}, e?) & \text{for } \varepsilon^{\text{ampl}} > 10^{-3} \end{cases} \tag{5.3}$$

Cycles which temporary fulfill the Coulomb yield criterion need a special treatment. The accumulation rate depends on the time the stress remains on the yield surface (Figure 5.35). Equation (5.3) loses its validity. For large cycles with alternating plastification (Figure 5.35a,b,c), i.e. for cycles which contact the yield surface in the compression the and extension regime of the p-q-plane, the residual strain at the end of each cycle depends on the time the stress remains on the respective part of the yield surface. Despite large amplitudes also stress cycles are possible which cause no accumulation (Figure 5.35c).

However, small stress cycles can lead to large accumulation rates, if they touch the yield surface (Figure 5.35d,e). A decay of the accumulation rate with the number of cycles can only be expected when the yield surface evolves, due to a densification or due to changes of the fabric of the grain skeleton. A numerical treatment of such cycles in an accumulation model is proposed in Section 7.2.5.

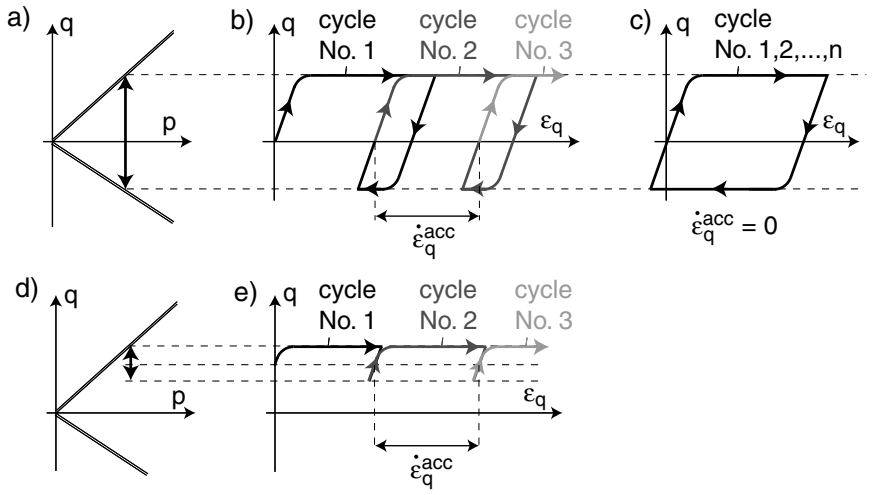

Figure 5.35: *Cycles which temporary fulfill the Coulomb yield criterion: a) to c): large cycles with alternating plastification, d),e) small cycles, which touch the yield surface*

5.2.1.3 Polarization of the cycles

In many explicit accumulation models proposed in the literature (Chapter 6), the shear strain amplitude γ^{ampl} is used as an influencing parameter. The volumetric portion of the strain loop is not considered. In earlier versions (Niemunis et al. [112], Triantafyllidis et al. [163]) of the accumulation model presented in Chapter 7, the strain amplitude was also determined only from the deviatoric portion of the strain loop. The validity of this procedure was checked in cyclic triaxial tests with a simultaneous oscillation of the axial (σ_1) and the lateral stress (σ_3). The application of $\sigma_1(t)$ and $\sigma_3(t)$ without a phase-shift in time results in in-phase cycles. At an average stress with $p^{\mathrm{av}} = 200$ kPa and $\eta^{\mathrm{av}} = 0.5$ different polarizations $0° \le \alpha_{PQ} \le 90°$ with $\tan\alpha_{PQ} = Q^{\mathrm{ampl}}/P^{\mathrm{ampl}}$ in the P-Q-plane were tested. The inclination $\alpha_{PQ} = 54.7°$ corresponds to $\sigma_3 =$ constant. For each polarization four or five tests were performed with amplitudes 20 kPa $\le \sqrt{(P^{\mathrm{ampl}})^2 + (Q^{\mathrm{ampl}})^2} \le 100$ kPa. In Figure 5.36a, the stress cycles are shown in the P-Q-plane and for comparison they are depicted in the p-q-plane in Figure 5.36b.

The resulting strain loops were analyzed with the correction for membrane penetration

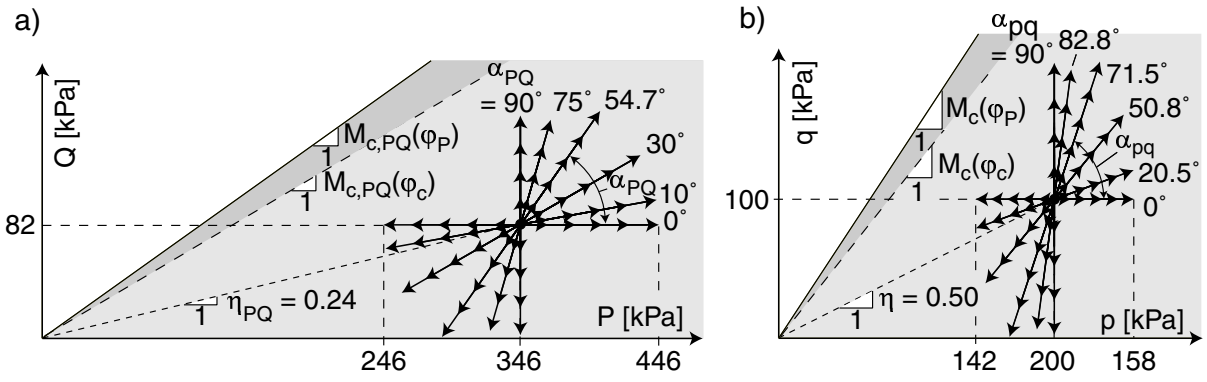

Figure 5.36: *Stress cycles a) in the P-Q-plane and b) in the p-q-plane*

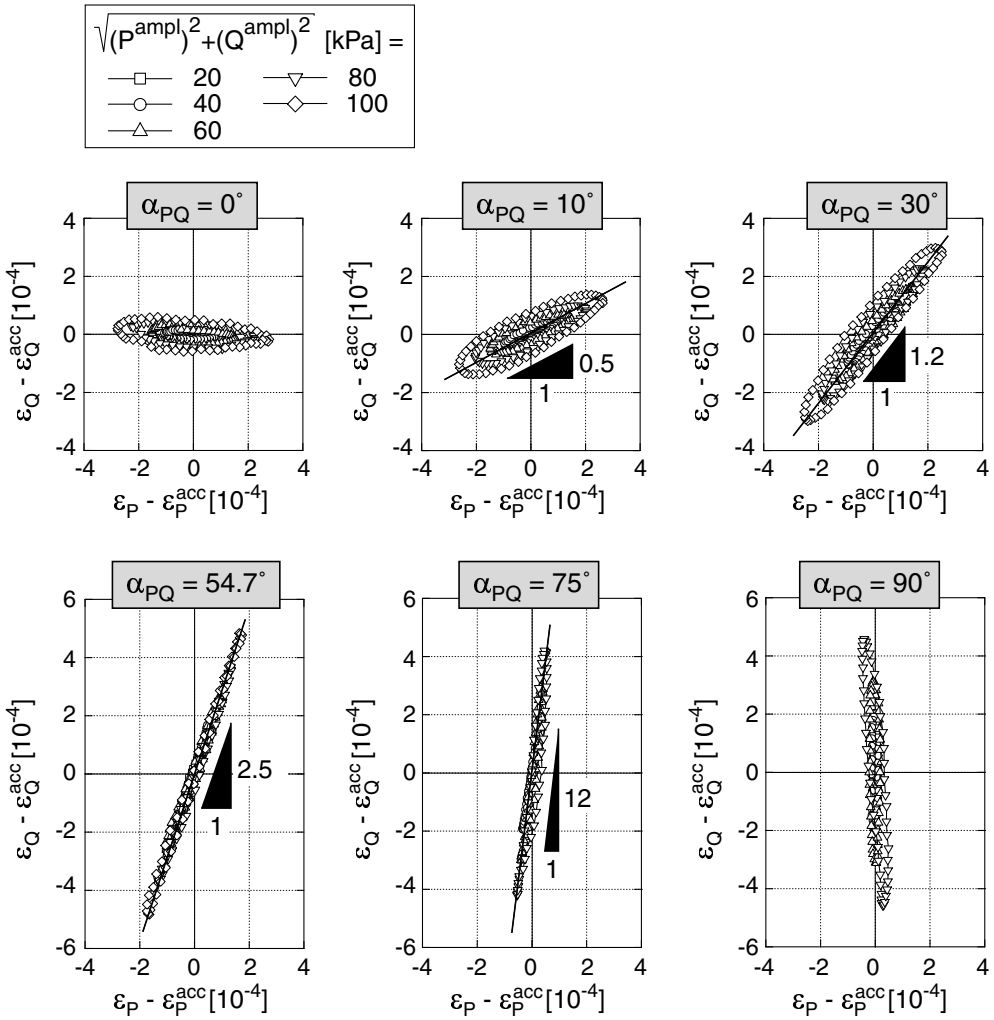

Figure 5.37: *ε_Q-ε_P-strain loops for stress cycles with different inclinations α_{PQ} in the P-Q-plane ($N = 100$)*

being calculated from Equation (4.10). They are summarized in Figure 5.37 for $N = 100$. For stress cycles parallel to the P-axis almost pure volumetric strain loops were obtained. The strain loops were almost pure deviatoric for stress cycles parallel to the Q-axis. Although the stress cycles were perfectly in-phase the resulting strain loops for $\alpha_{PQ} \leq 30°$ enclosed some area in the ε_Q-ε_P-plane.

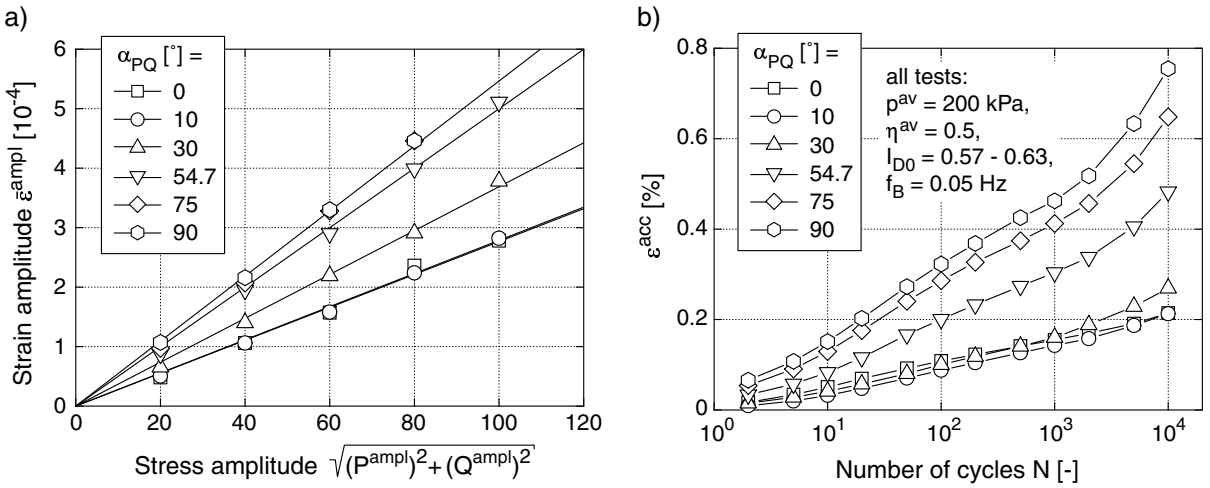

Figure 5.38: *a) Strain amplitudes ε^{ampl} (mean values over 10^4 cycles) as a function of stress amplitude and b) accumulation curves $\varepsilon^{acc}(N)$ for $\sqrt{(P^{ampl})^2 + (Q^{ampl})^2} = 60$ kPa and different polarizations α_{PQ} in the P-Q-plane*

Independent of the polarization α_{PQ} the relationship $\varepsilon^{\text{ampl}} \sim \sqrt{(P^{\text{ampl}})^2 + (Q^{\text{ampl}})^2}$ holds (Figure 5.38a). The secant stiffness of the stress-strain-hysteresis increases with increasing inclination α_{PQ} of the cycles. Accordingly the strain amplitudes decrease with α_{PQ} (Figure 5.38a). At identical values of the stress amplitude $\sqrt{(P^{\text{ampl}})^2 + (Q^{\text{ampl}})^2}$, the strain amplitudes due to deviatoric cycles ($\alpha_{PQ} = 90°$) are twice larger than those caused by isotropic cycles ($\alpha_{PQ} = 0°$).

Accumulation curves $\varepsilon^{\text{acc}}(N)$ for the stress amplitude 60 kPa and different polarizations α_{PQ} are shown in Figure 5.38b. Similar shapes of the curves were measured for the other stress amplitudes. At an identical *stress* amplitude the accumulation rate increases with an increasing deviatoric portion of the stress loop. The linear increase of the curves with $\ln(N)$ (at least up to $N = 2 \cdot 10^3$) is independent of α_{PQ}. Analogously to Figure 5.24, Figure 5.39 contains diagrams presenting the residual strain as a function of the square of the strain amplitude. Each diagram corresponds to a certain polarization α_{PQ}. Figure 5.39 confirms the relationship $\dot{\varepsilon}^{\text{acc}} \sim (\varepsilon^{\text{ampl}})^2$ independently of the direction of the cycles.

In Figure 5.40, the residual strain after 10^4 cycles was normalized with the void ratio

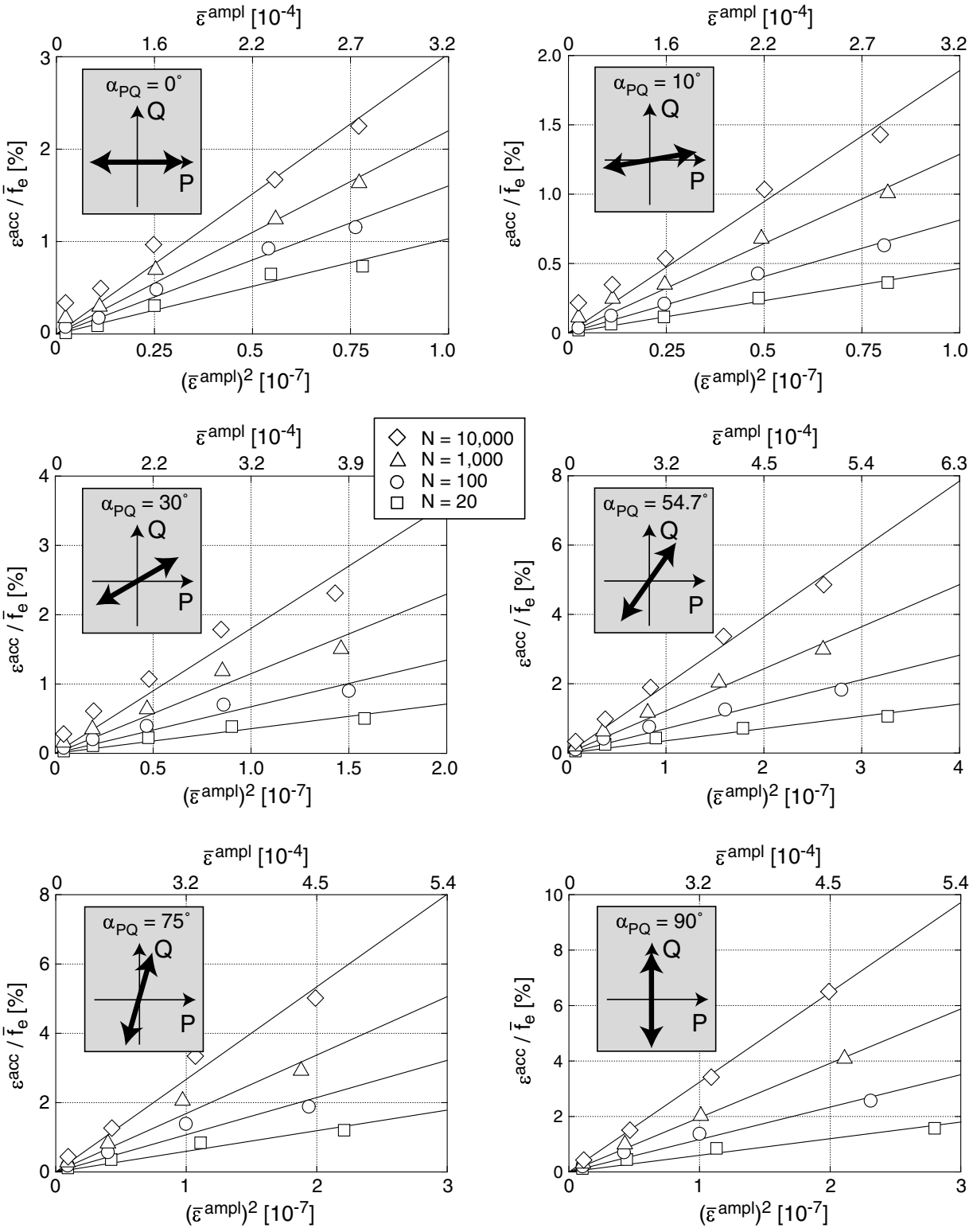

Figure 5.39: *Accumulated strain $\varepsilon^{acc}/\bar{f}_e$ as a function of $(\bar{\varepsilon}^{ampl})^2$ for stress cycles with different inclinations α_{PQ} in the P-Q-plane*

function $\bar{f}_e$ and plotted versus the strain amplitude $\bar{\varepsilon}^{\mathrm{ampl}}$. The data for different polarizations α_{PQ} nearly fall together into a single curve. Thus, for a given strain amplitude $\bar{\varepsilon}^{\mathrm{ampl}}$, the direction of the cycles in the stress or strain space does not significantly influence the accumulation rate. This is confirmed also by the illustration of the accumulation rates in Figure 5.41. From this test series it can be concluded, that not only the deviatoric portion of the strain loop should be used as an input parameter of an explicit accumulation model. $\varepsilon_P^{\mathrm{ampl}}$ and $\varepsilon_Q^{\mathrm{ampl}}$ contribute equally to the accumulation rate. The strain amplitude $\varepsilon^{\mathrm{ampl}}$ should be determined from the full strain loop.

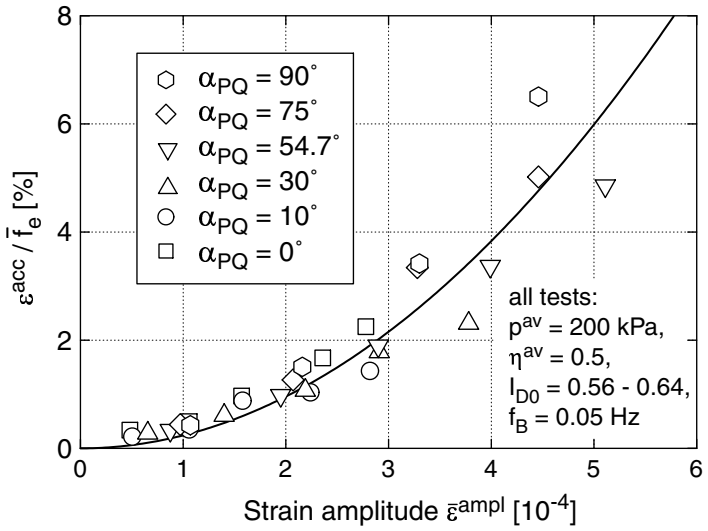

Figure 5.40: *Accumulated strain $\varepsilon^{acc}/\bar{f}_e$ after $N = 10^4$ cycles as a function of the strain amplitude $\bar{\varepsilon}^{ampl}$ for stress cycles with different inclinations α_{PQ} in the P-Q-Ebene*

5.2.1.4 Shape of the cycles

The influence of the shape of the cycles was studied first in the CMDSS device and afterwards in cyclic triaxial tests with elliptic stress cycles in the P-Q-plane.

CMDSS tests

In CMDSS tests, a circular and an uniaxial cyclic shearing with identical amplitude in the γ_{13}-direction (Figure 5.42) were compared. Figure 5.42 shows the accumulation curves $\varepsilon^{\mathrm{acc}}(N)$ during 1,000 cycles in two tests on initially medium dense specimens. The circular cycles cause an approximately twice faster accumulation than the uniaxial cycles.

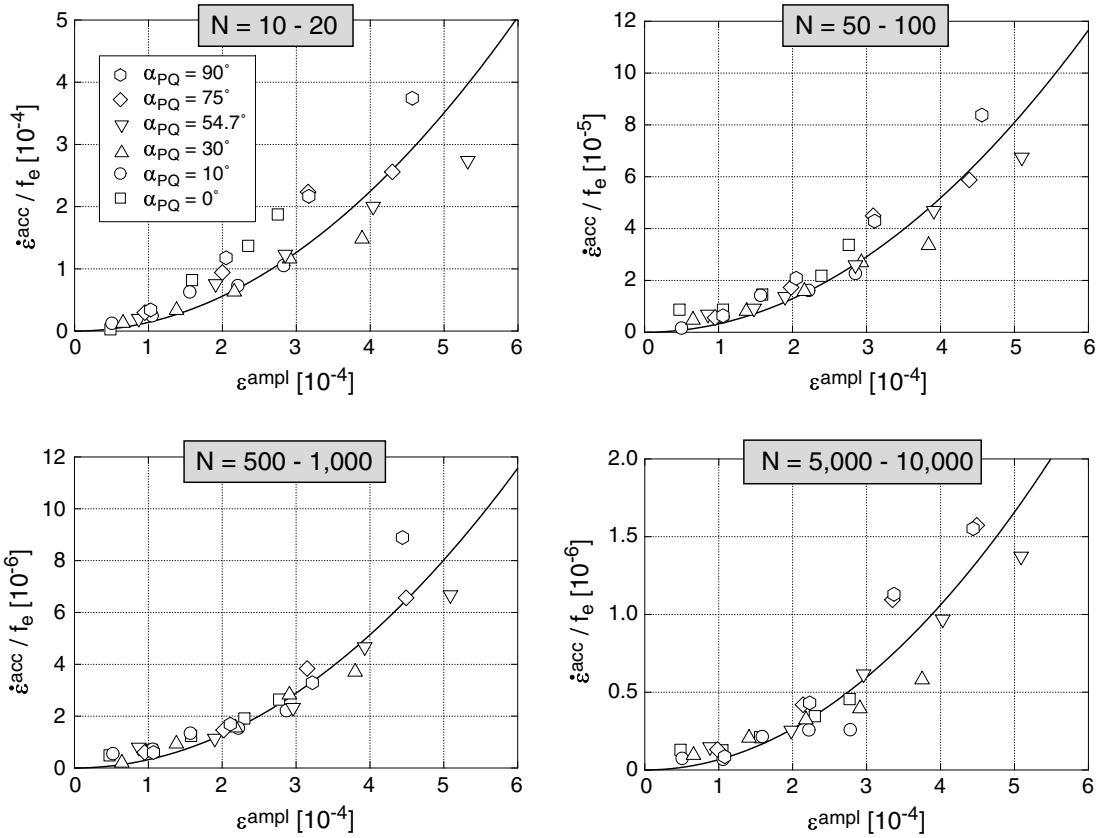

Figure 5.41: *Accumulation rates $\dot{\varepsilon}^{acc}/f_e$ as a function of the strain amplitude ε^{ampl} for stress cycles with different inclinations α_{PQ} in the P-Q-Ebene*

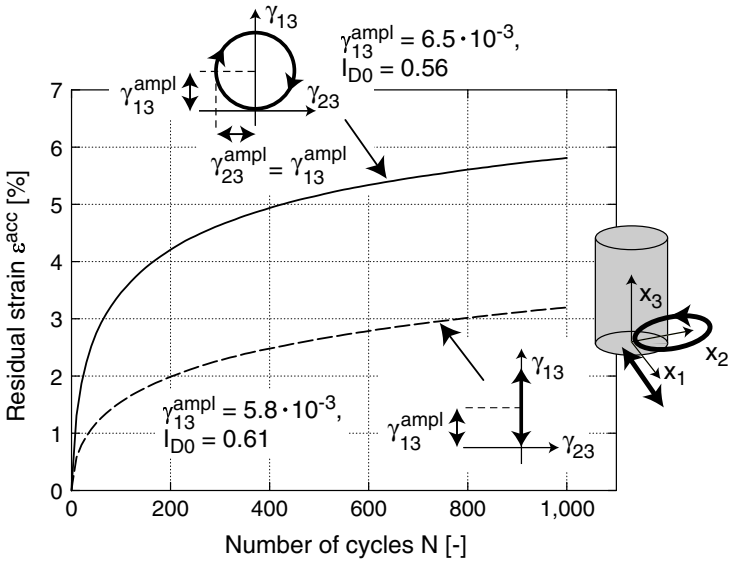

Figure 5.42: *Comparison of circular and uniaxial (1-D) cycles in CMDSS tests*

Tests with different shear strain amplitudes $\gamma_{13}^{\text{ampl}}$ were performed. In Figure 5.43, the accumulated strain after different numbers of cycles is normalized with the void ratio function and plotted as a function of $\gamma_{13}^{\text{ampl}}$. Figure 5.43a presents the tests with uniaxial cycles while Figure 5.43b contains the tests with circular strain paths.

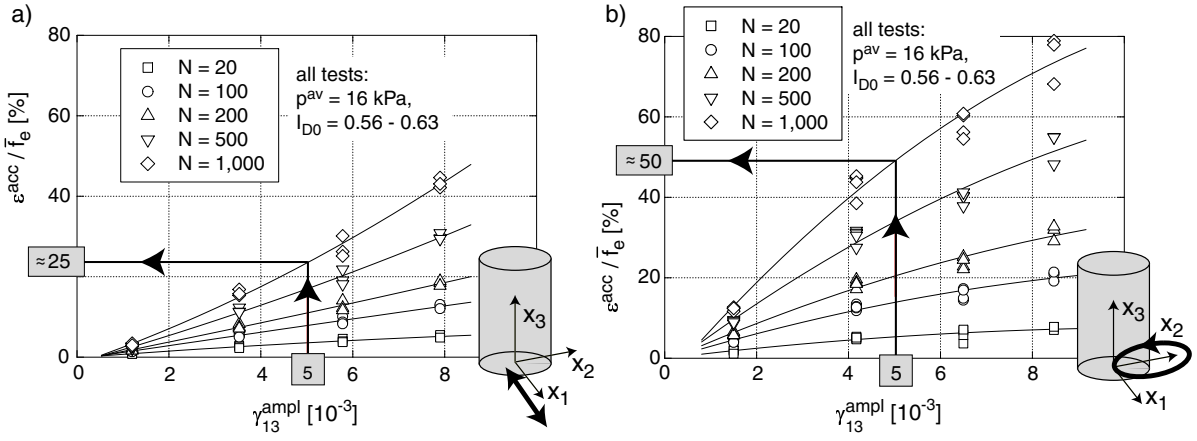

Figure 5.43: *Comparison of the accumulated strain due to a) uniaxial (1-D) and b) circular strain cycles in the CMDSS device*

It can be clearly seen, that circular cycles cause larger residual strains than uniaxial cycles. For the amplitude $\gamma_{13}^{\text{ampl}} = 5 \cdot 10^{-3}$ and $N = 1,000$ the factor 2 is obtained (Figure 5.43). In particular, in Figure 5.43b it is noticeable that the quadratic dependence of the accumulation rate on the shear strain amplitude $\gamma_{13}^{\text{ampl}}$ was not observed in the CMDSS tests. Possible reasons are the large strain amplitudes (see Section 5.2.1.2) and the inhomogeneous strain field (see Section 4.1.2).

Fitting curves to the data in Figure 5.43 (see the solid curves in Figure 5.43) the ratio of the residual strains ε^{acc} due to a circular and an uniaxial cyclic shearing can be obtained. This ratio is illustrated in Figure 5.44a. Figure 5.44b contains an analogous diagram for the accumulation rates $\dot{\varepsilon}^{\text{acc}}$, which are shown in Figure 5.45. A decrease of the ratio with $\gamma_{13}^{\text{ampl}}$ and an increase with N was observed. It averages the value 2, which is in good agreement with the tests of Pyke et al. [122] (Section 3.2.2.5). Also the amplitude definition, which is used in the accumulation model (Chapter 7) delivers the factor 2. This is demonstrated in Section 7.2.1.

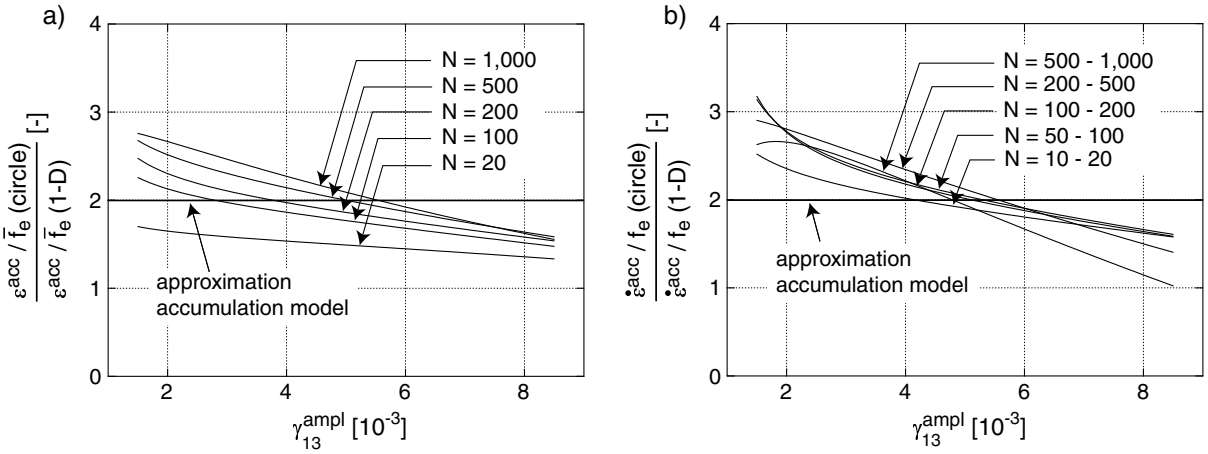

Figure 5.44: *Ratio a) of the residual strains ε^{acc} and b) of the accumulation rates $\dot{\varepsilon}^{acc}$ for circular and uniaxial (1-D) cycles in the CMDSS device*

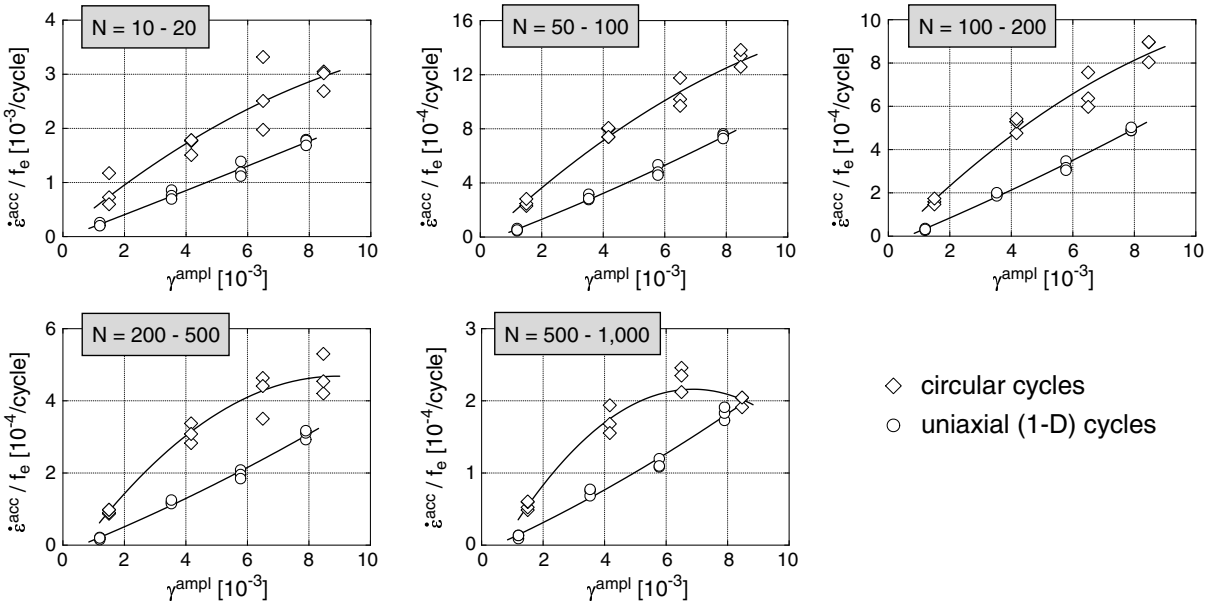

Figure 5.45: *Comparison of the accumulation rates $\dot{\varepsilon}^{acc}$ due to circular and uniaxial (1-D) cyclic shearings in the CMDSS device*

Cyclic triaxial tests

In the cyclic triaxial tests, the axial (σ_1) and the lateral (σ_3) stress were cyclically varied with a phase-shift in time resulting in elliptic stress loops in the P-Q-plane. The cycles were tested on initially medium dense specimens at an average stress (centre of the ellipse in the stress space) with $p^{av} = 200$ kPa and $\eta^{av} = 0.5$. A first impression of the location of

the cycles in the P-Q-plane and for comparison also in the p-q-plane can be gathered from Figure 5.46. The stress paths were chosen under consideration of a sufficient distance to the critical state line.

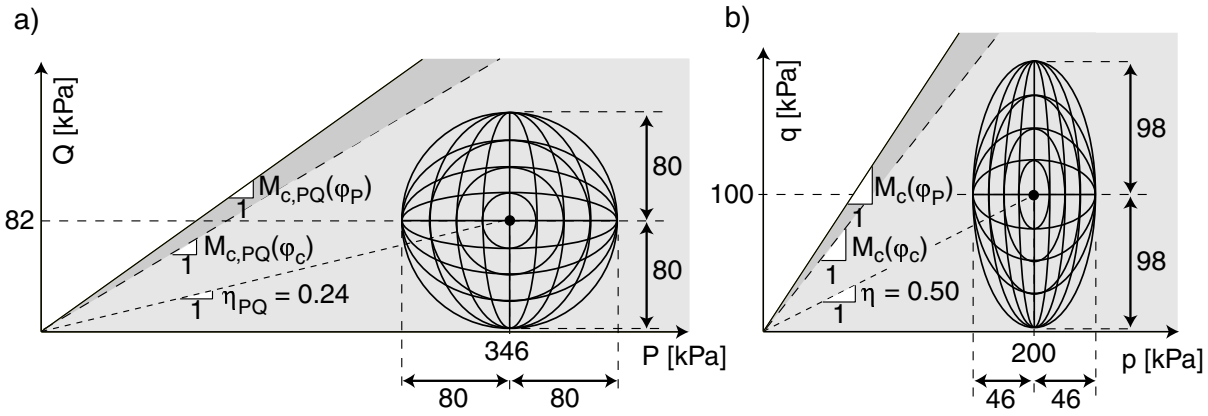

Figure 5.46: *Elliptic stress cycles a) in the P-Q-plane and b) in the p-q-plane*

The *measured* stress paths in the P-Q-plane and the ε_P-ε_Q-strain loops are presented in the left part of Figure 5.47. The tests Nos. 5 and 9 were taken from the test series on the influence of the polarization of the cycles (Section 5.2.1.3). Again, the strain loops were evaluated using Equation (4.10) for the membrane penetration. Circular P-Q-cycles led to slightly inclined nearly elliptic ε_P-ε_Q-strain loops with a considerably longer axis in the ε_Q-direction. In the following, referring to Figure 5.48, the longer axis of the ε_P-ε_Q-ellipse is denoted by $2R_2$ and the shorter one by $2R_1$. In Figure 5.48, the ratio R_1/R_2 (the "ovality" of the strain loops) is plotted as a function of the ratio of the amplitudes $P^{\mathrm{ampl}}/Q^{\mathrm{ampl}}$. With increasing ratio $P^{\mathrm{ampl}}/Q^{\mathrm{ampl}}$ also the ovality of the strain loops increases. At $P^{\mathrm{ampl}}/Q^{\mathrm{ampl}} = 3$ the loops are perfectly round. For larger values of $P^{\mathrm{ampl}}/Q^{\mathrm{ampl}}$ (here only for test No. 10) the larger axis of the strain loop lies in the ε_P-direction.

The accumulation curves $\varepsilon^{\mathrm{acc}}(N)$ of the tests are given in the right part of Figure 5.47. In the tests of series No. 1 (Figure 5.47a) with circular P-Q-stress cycles, the ratios $0.3 \leq R_1/R_2 \leq 0.37$ of the four strain loops were similar. Larger strain loops led to larger accumulation rates. However, inferences on the influence of the shape of the cycles on $\dot{\varepsilon}^{\mathrm{acc}}$ cannot be deduced yet from this series. In the test series No. 2 (Figure 5.47b) with Q^{ampl} = 80 kPa and $P^{\mathrm{ampl}} \leq Q^{\mathrm{ampl}}$ similar values of R_2 and ratios $0.08 \leq R_1/R_2 \leq 0.30$ were measured. The accumulation runs faster with increasing R_1. Due to the small values of R_1/R_2 and the quadratic dependence of the accumulation rate on the strain amplitude, the differences in R_1/R_2 led to only moderate differences in the accumulation rates. In

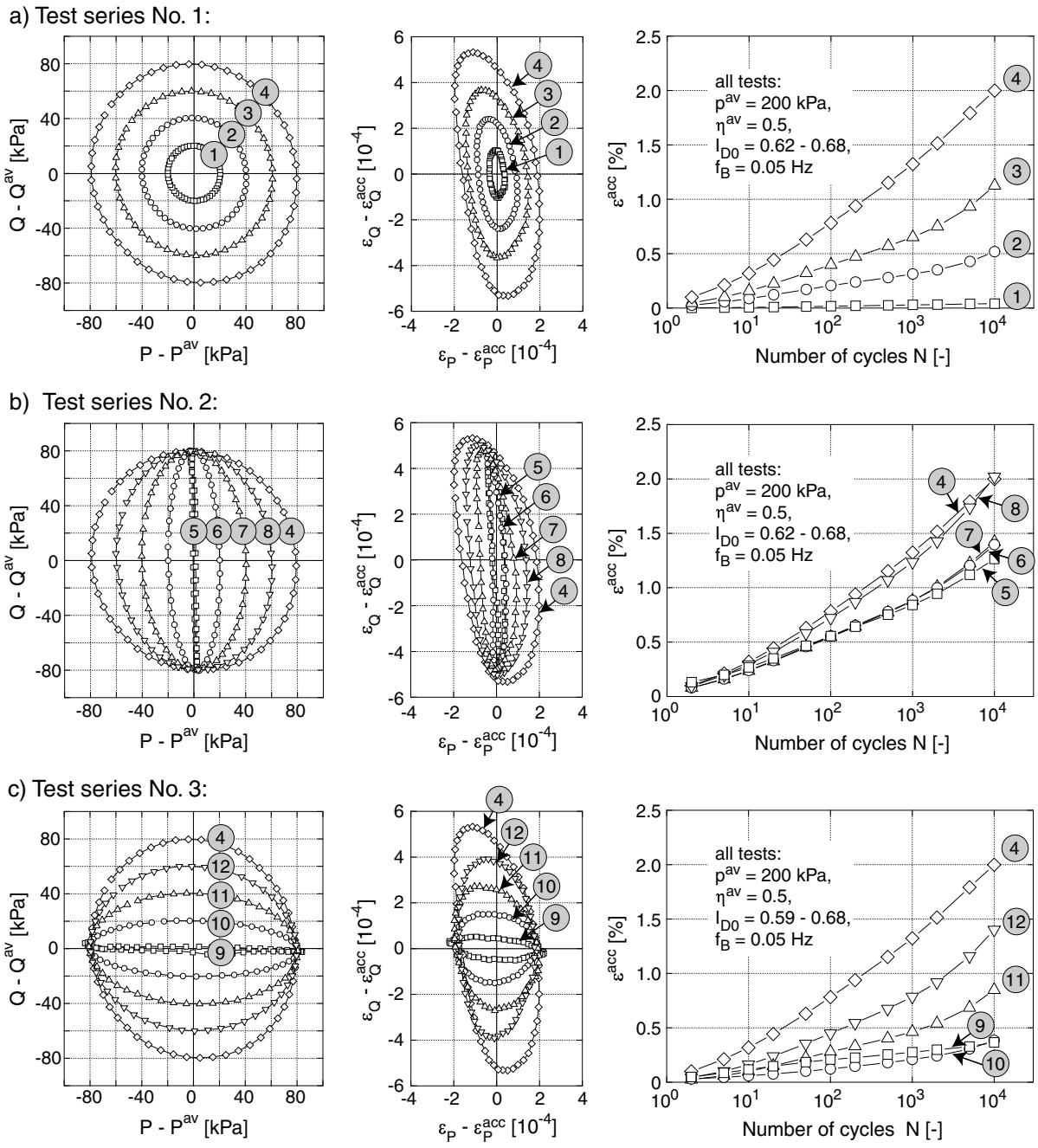

Figure 5.47: *P-Q-stress paths, ε_P-ε_Q-strain loops and accumulation curves $\varepsilon^{acc}(N)$ in cyclic triaxial tests with elliptic stress cycles in the P-Q-plane*

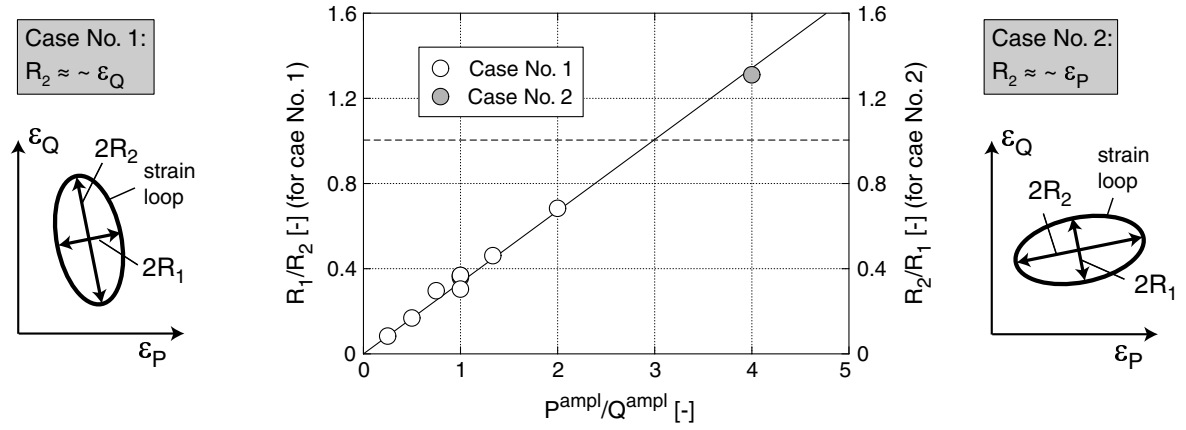

Figure 5.48: *"Ovality" R_1/R_2 of the strain loops in dependence on the amplitude ratio P^{ampl}/Q^{ampl}*

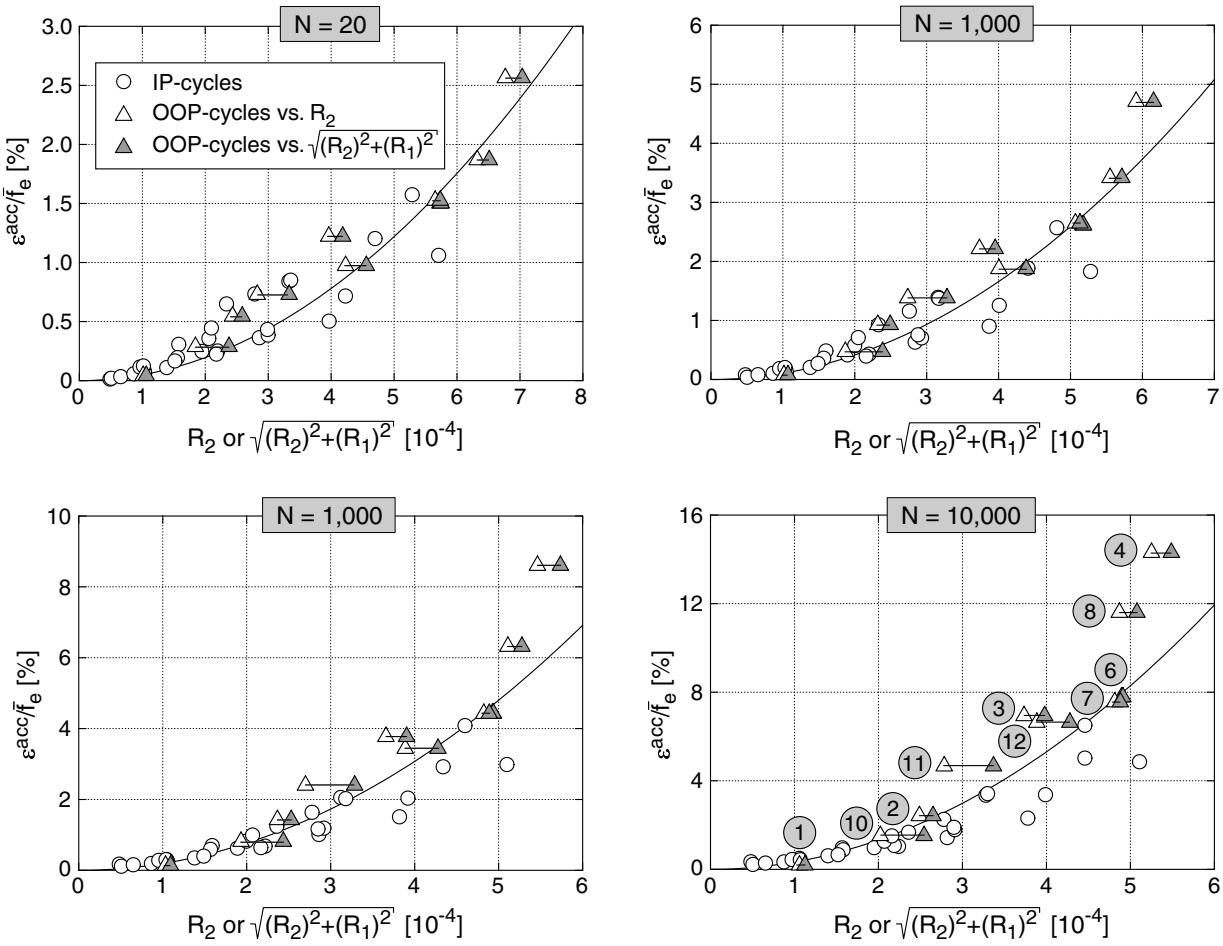

Figure 5.49: *Residual strain $\varepsilon^{acc}/\bar{f}_e$ as a function of R_2 and $\sqrt{(R_2)^2 + (R_1)^2}$, respectively: comparison of IP- and OOP-cycles*

the third test series (Figure 5.47c) with $P^{\mathrm{ampl}} = 80$ kPa and $Q^{\mathrm{ampl}} \leq P^{\mathrm{ampl}}$ the amplitude in the ε_P-direction was almost identical in the five tests. The ratio of the axes of the strain loop took values $0.3 \leq R_1/R_2 \leq 0.76$. With increasing extension of the strain loops in the ε_Q-direction $\dot{\varepsilon}^{\mathrm{acc}}$ increased.

In Figure 5.49, the residual strains in the tests with OOP- and IP-stress cycles (the latter ones were taken from Section 5.2.1.3) are compared. For the IP-stress cycles $\varepsilon^{\mathrm{ampl}} = R_2$ holds (if one neglects the slight ovality of the corresponding strain loops). For elliptic strain cycles the definition of the multiaxial strain amplitude presented in Section 7.2.1 delivers:

$$\varepsilon^{\mathrm{ampl}} = \sqrt{(R_2)^2 + (R_1)^2} \tag{5.4}$$

In Figure 5.49, the residual strain due to the OOP-stress cycles was plotted versus R_2 (white triangles) *and* versus $\varepsilon^{\mathrm{ampl}}$ from Equation (5.4) (gray triangles). The diagram for $N = 10^4$ in Figure 5.47 shows the corresponding number of the test. Generally, the difference between R_2 and $\varepsilon^{\mathrm{ampl}}$ from Equation (5.4) is not large since in most of the tests the ratio R_1/R_2 did not exceed 0.3. The residual strains due to the OOP-stress cycles which were plotted as a function of R_2 are mostly larger than those in the IP-tests with identical values of R_2. This demonstrates, that $\dot{\varepsilon}^{\mathrm{acc}}$ increases with increasing ovality of the strain loop. The definition of the strain amplitude in Equation (5.4) "shifts" the data points in Figure 5.49 to the right (e.g. see the data points for test No. 11 with $R_1/R_2 = 0.68$). Therefore, they coincide better with the data points of the IP-tests. The accumulation rates of the IP- and the OOP-cycles can then be described by a unique relationship $\dot{\varepsilon}^{\mathrm{acc}} \sim (\varepsilon^{\mathrm{ampl}})^2$ (see the solid curve in Figure 5.49). On the basis of Figure 5.49, Equation (5.4) seems appropriate to describe the amplitudes of OOP-strain loops (although there are some discrepancies for tests Nos. 4 and 8 at larger numbers of cycles). This statement should be confirmed in future by further tests with larger ratios R_1/R_2.

5.2.1.5 Circulation

The circulation of the strain cycles does not influence the accumulation rate. Figure 5.50 presents the accumulation curve in a CMDSS tests with a change of the circulation from "clockwise" to "counterclockwise" after approx. 500 cycles. No effect of this change on the accumulation rate could be detected.

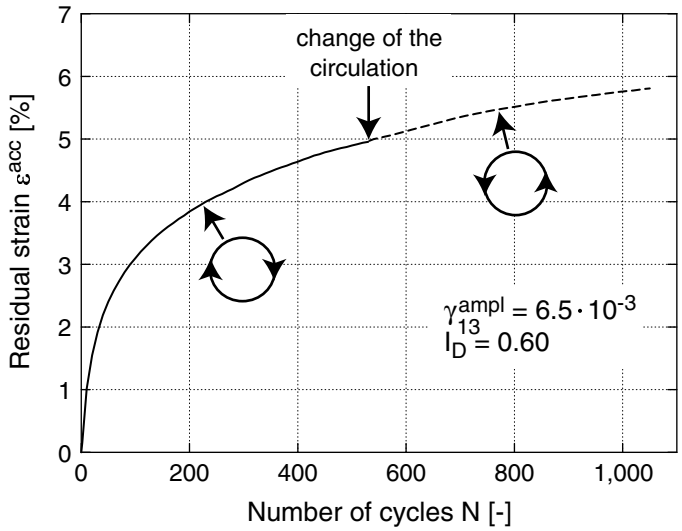

Figure 5.50: *No influence of a change of the circulation in a CMDSS test with a circular cyclic shearing*

5.2.2 Influence of polarization changes

A change of the polarization of the cycles causes a temporary increase of the accumulation rate. This can be clearly demonstrated by CMDSS tests with a sudden 90°-change of the direction of cyclic shearing. Figure 5.51 compares tests with and without a polarization change after 1,000 cycles. The increase of the accumulation rate after the change of the shearing direction is obvious. This effect of a polarization change decays during the following 1,000 cycles. It is independent of the initial density.

In the accumulation model (Chapter 7), the temporary increase of the accumulation rate due to a change of the polarization is captured by the function f_π:

$$f_\pi \;=\; 1 + C_{\pi 1}\,(1 - \cos\alpha) \tag{5.5}$$

Its value depends on the angle α between the actual polarization and the polarization during the previous cycles, which is memorized weighted in a variable $\boldsymbol{\pi}$ called "back polarization". The functionality of f_π and $\boldsymbol{\pi}$ is explained in more detail in Section 7.2.2. If in a CMDSS test the polarization is not changed, $\cos\alpha = 1$ and $f_\pi = 1$ hold. Directly after a change of the polarization by 90°, $\cos\alpha = 0$ and $f_\pi = 1 + C_{\pi 1}$ is valid. From a CMDSS test with a sudden 90°-change of the polarization after $N = N_{\mathrm{cp}}$ cycles, the course of f_π with N can be obtained as the ratio of the accumulation rate $\dot{\varepsilon}^{\mathrm{acc}}$ in this test and $\dot{\varepsilon}^{\mathrm{acc}}$ in a similar test without such a change (Figure 5.52a,b). The material constant $C_{\pi 1}$ is the difference between f_π directly before and f_π directly after the polarization change, i.e. it can be determined from $C_{\pi 1} = f_\pi(N = N_{\mathrm{cp}}) - 1$. The curves $f_\pi(N - N_{\mathrm{cp}})$

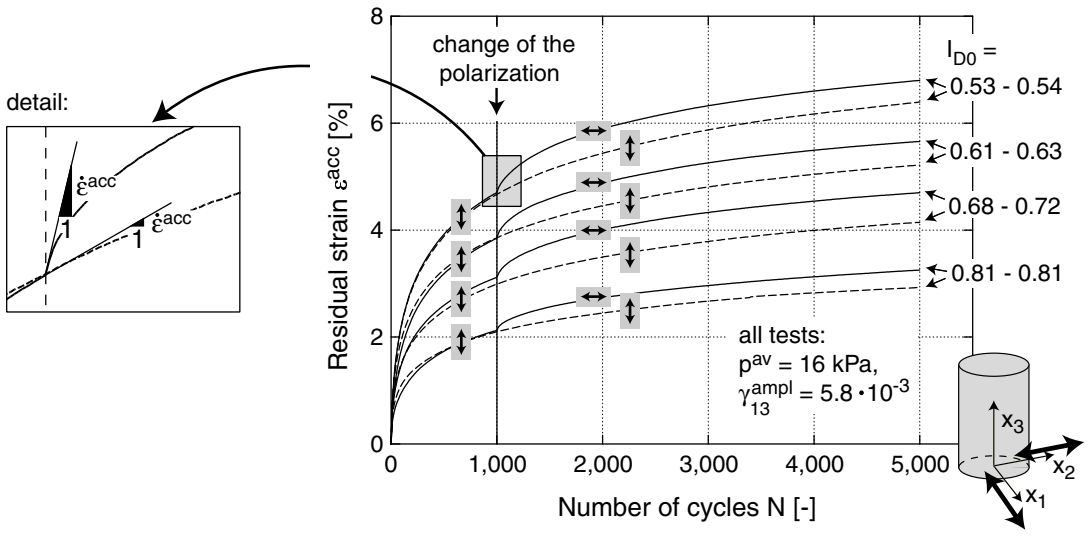

Figure 5.51: *Temporary increase of the accumulation rate due to a change of the polarization*

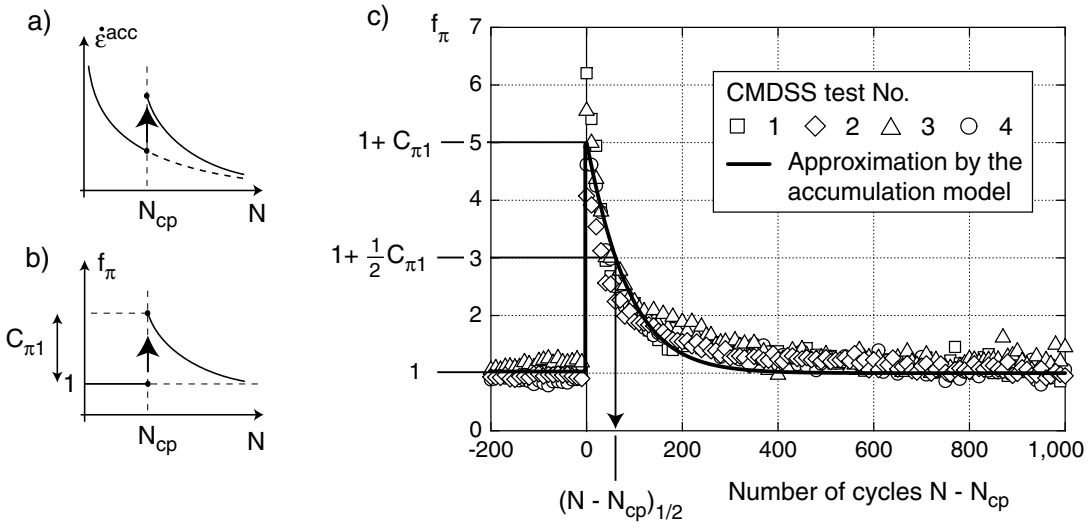

Figure 5.52: *Decay of the temporary increase of the accumulation rate after a 90°-change of the polarization*

for the four tests shown in Figure 5.51 are presented in Figure 5.52c. From the four tests $f_\pi(N = N_{\mathrm{cp}}) = 5.0$ and therefore $C_{\pi 1} = 4.0$ were determined as mean values. The decay of f_π with N after a polarization change is captured by the evolution equation of the angle α, which describes an adaption of the "back polarization" towards the actual polarization (Section 7.2.2):

$$\dot{\alpha} \;=\; -C_{\pi 2}\alpha(\varepsilon^{\mathrm{ampl}})^2 \tag{5.6}$$

The decay is governed by a second material constant $C_{\pi 2}$. It can be determined from the

number of cycles $(N - N_{cp})_{1/2}$ for which the factor f_π takes the value $1 + 0.5C_{\pi 1}$ (Figure 5.52c):

$$C_{\pi 2} = \frac{\ln(3/2)}{(\varepsilon^{ampl})^2 \, (N - N_{cp})_{1/2}} \tag{5.7}$$

The number of cycles $(N - N_{cp})_{1/2}$ can be seen as a kind of "half-life" of the polarization effect. For the four tests in Figure 5.52c, $C_{\pi 2} = 200$ was obtained.

The strain amplitude ε^{ampl} in Equation (5.6) was not tested experimentally yet. It results from the consideration, that the adaption should run faster with increasing amplitude. The quadratic dependence follows Equation (5.2). The course $f_\pi(N - N_{cp})$, predicted by Equations (5.5) and (5.6) with $C_{\pi 1} = 4.0$ and $C_{\pi 2} = 200$, is plotted as the solid curve in Figure 5.52c. It approximates the test data well.

5.2.3 Influence of the void ratio / relative density

The influence of the void ratio was studied in tests with different initial void ratios $0.58 \leq e_0 \leq 0.80$ ($0.24 \leq I_{D0} \leq 0.99$), but with identical stresses ($p^{av} = 200$ kPa, $\eta^{av} = 0.75$, $q^{ampl} = 60$ kPa). Figure 5.53 presents the q-ε_q-hystereses in the first cycle and the residual strains at the end of this cycle. Due to the smaller stiffness during first loading, these residual strains increase with the initial void ratio e_0.

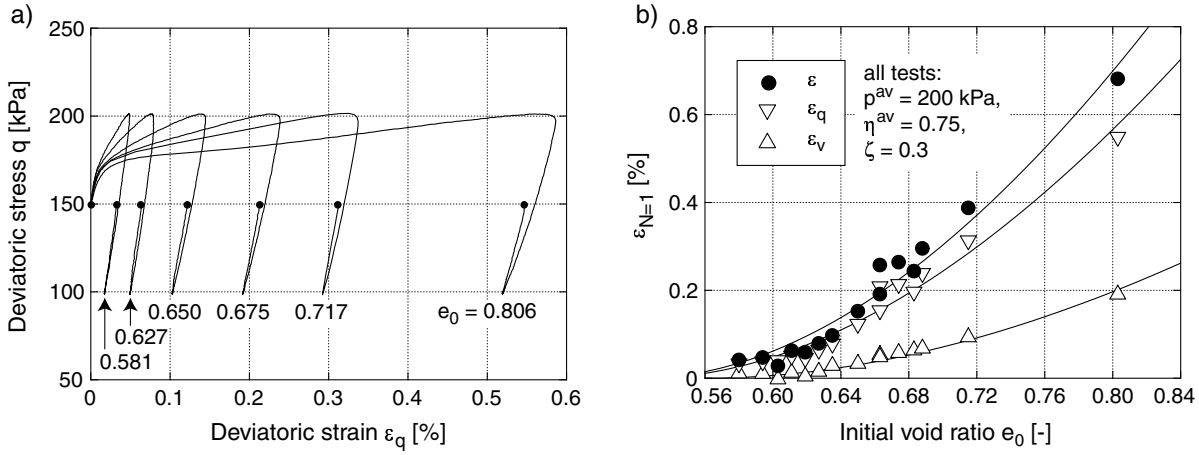

Figure 5.53: *First cycle: a) q-ε_q-hystereses, b) residual strains as a function of the initial void ratio*

Due to the decrease of the secant stiffness of the stress-strain-hysteresis with void ratio (Section 3.3), the constant stress amplitude $q^{ampl} = 60$ kPa leads to an increase of the

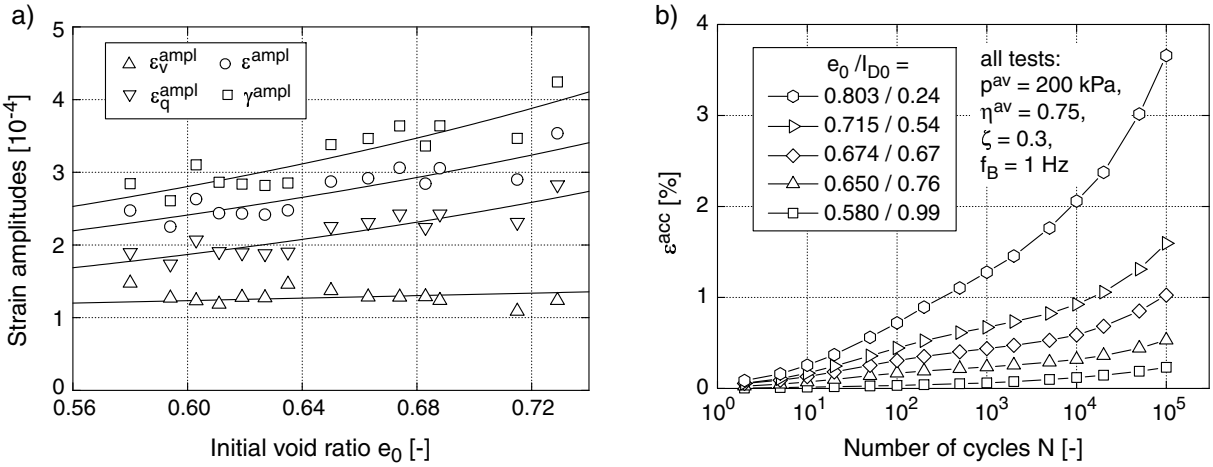

Figure 5.54: *a) Strain amplitudes as a function of the initial void ratio e (mean values over 10^5 cycles), b) Selected curves $\varepsilon^{acc}(N)$*

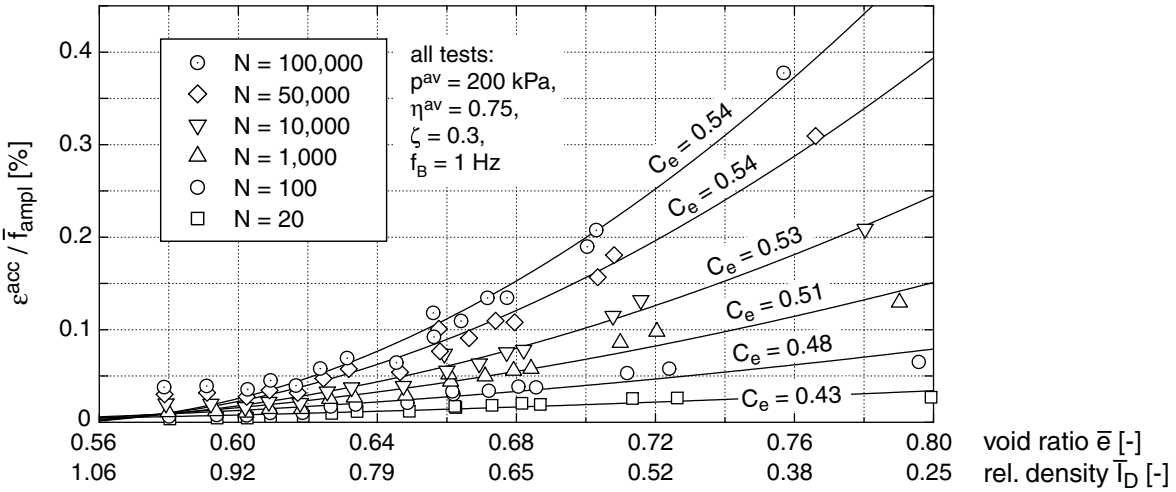

Figure 5.55: *Accumulated strain $\varepsilon^{acc}/\bar{f}_{ampl}$ in dependence on void ratio e*

strain amplitudes with increasing e_0 (Figure 5.54a). Selected accumulation curves $\varepsilon^{\mathrm{acc}}(N)$ are presented in Figure 5.54b. The accumulation rate increases with increasing void ratio. In Figure 5.55 the residual strains, normalized by f_{ampl}, are illustrated as a function of the average void ratio $\bar{e} = (\int_1^N e(N)\ \mathrm{d}N)/N$. The increase of $\varepsilon^{\mathrm{acc}}/\bar{f}^{\mathrm{ampl}}$ with $\bar{e}$ is similar to the curves of Hain [42] and Marr & Christian [94] shown in Figures 3.22 and 3.23. In the accumulation model (Chapter 7) the relationship $\dot{\varepsilon}^{\mathrm{acc}}(e)$ is described by a hyperbolic function:

$$f_e \;=\; \frac{(C_e - e)^2}{1+e}\ \frac{1+e_{\mathrm{ref}}}{(C_e - e_{\mathrm{ref}})^2} \tag{5.8}$$

In Equation (5.8) $e_{\mathrm{ref}} = e_{\max} = 0.874$ is a reference void ratio for which $f_e = 1$ holds. C_e is

a material constant and the void ratio for which the accumulation rate vanishes ($f_e = 0$, "asymptotic" void ratio).

Equation (5.8) was fitted to the data in Figure 5.55. The determined values of C_e are given at the respective curves (solid lines in Figure 5.55). C_e is (irrespective the data for small numbers of cycles) approximately independent of N. For larger numbers of cycles, the approximation delivered $C_e = 0.54$ which corresponds to 94 % of $e_{\min}$ obtained from the standard test procedure of DIN 18126. The void ratio $e_{\min}$ of DIN 18126 is only a convention. As it is known (Section 3.2.2.7), a cyclic loading may lead to larger densities.

Also the analysis of the accumulation rates (Figure 5.56) and the densification rates (Figure 5.57) for different numbers of cycles confirmed Equation (5.8) and the limit void ratio $C_e \approx 0.54$. The densification rates show a larger scatter than the accumulation rates (see also the scatter of the direction of accumulation in Figure 5.13b). Thus, the curve fitting in Figure 5.56 is thought to be more reliable than the approximation in Figure 5.57.

Equation (5.8) overestimates the measured data for large initial densities $I_{D0} > 0.9$ (Figure 5.55). The approximately constant accumulation rates for $I_{D0} > 0.9$ may be due to a thin loose zone at the top of the specimen resulting from the preparation procedure (flattening of the surface of the pluviated sample).

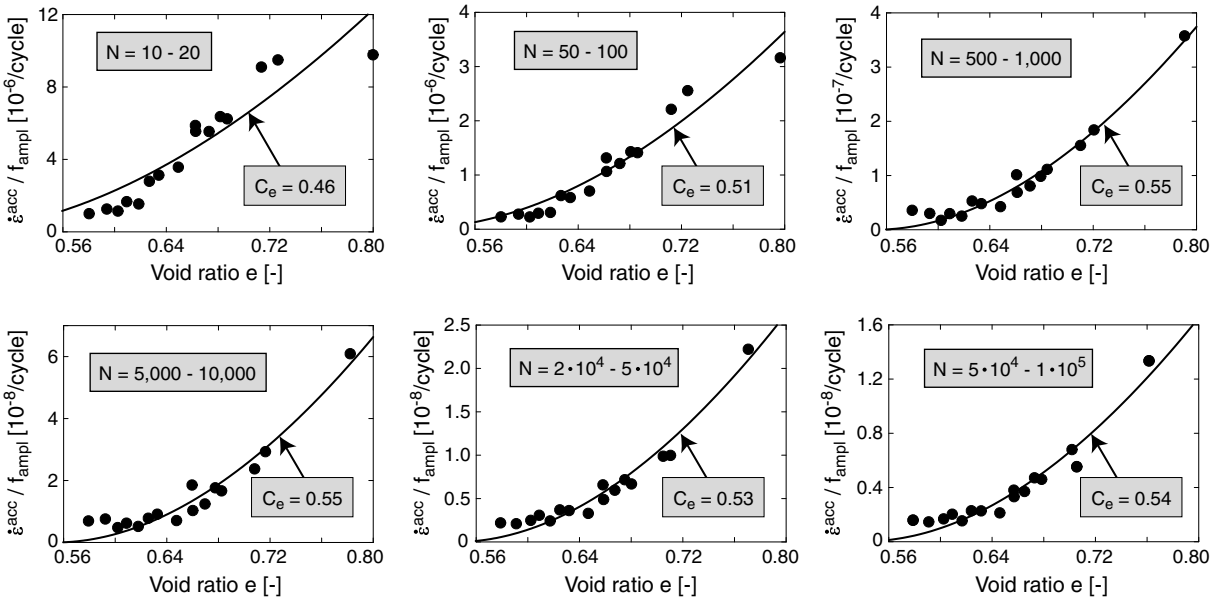

Figure 5.56: *Accumulation rate* $\dot{\varepsilon}^{acc} \approx \Delta\varepsilon^{acc}/\Delta N$ *in dependence on the void ratio* e *for different numbers of cycles*

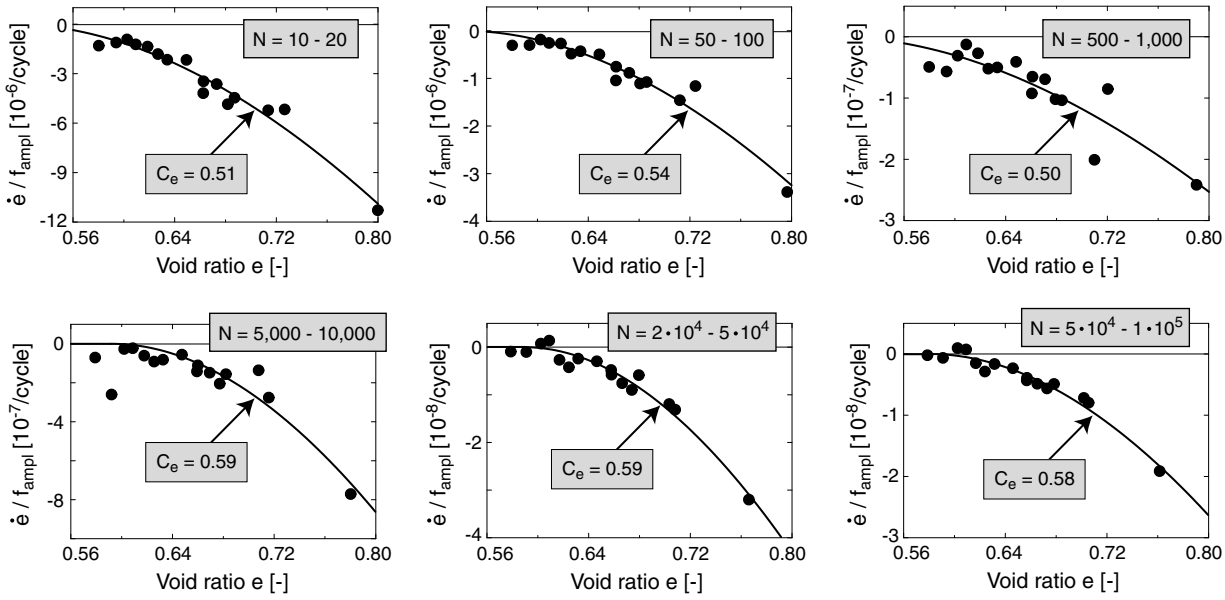

Figure 5.57: *Densification rate $\dot{e} \approx \Delta e/\Delta N$ in dependence on the void ratio e for different numbers of cycles*

5.2.4 Influence of the average stress

5.2.4.1 Influence of the average mean pressure p^{av}

Triaxial compression

The dependence of the intensity of accumulation on the average mean pressure was studied in six tests with 50 kPa $\leq p^{\mathrm{av}} \leq$ 300 kPa. The average stress ratio $\eta^{\mathrm{av}} = 0.75$ and the amplitude ratio $\zeta = q^{\mathrm{ampl}}/p^{\mathrm{av}} = 0.3$ were kept constant (see the scheme of the stress paths in Figure 5.58). The initial densities lay within $0.61 \leq I_{D0} \leq 0.69$.

Figure 5.59a shows the q-ε_q-hystereses in the first cycle. The volumetric, deviatoric and total strains remaining after this cycle increase under-proportional with p^{av} (Figure 5.59b). This is due to the dependence of the stiffness during first loading (first quarter of the first cycle) on p and q and the increase of the stress amplitude q^{ampl} with p^{av} (see the scheme in Figure 5.59a).

In Figure 5.60a the mean values of the strain amplitudes over 10^5 cycles are plotted versus p^{av}. The condition $\zeta = q^{\mathrm{ampl}}/p^{\mathrm{av}} =$ constant implies an increase of the strain amplitudes with an increasing average mean pressure due to the under-linear relationship between the secant stiffness and p^{av}. From the shear strain amplitudes $\gamma^{\mathrm{ampl}}(p^{\mathrm{av}})$, an exponent $n = 0.75$ can be determined for the pressure-dependence of the secant shear modulus $G_{\mathrm{hyst}} \sim (p^{\mathrm{av}})^n$.

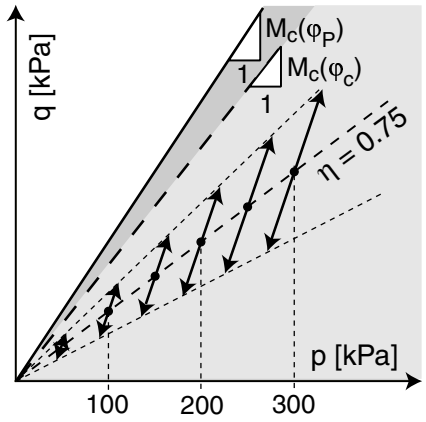

Figure 5.58: *Stress cycles in the tests on the influence of* p^{av}

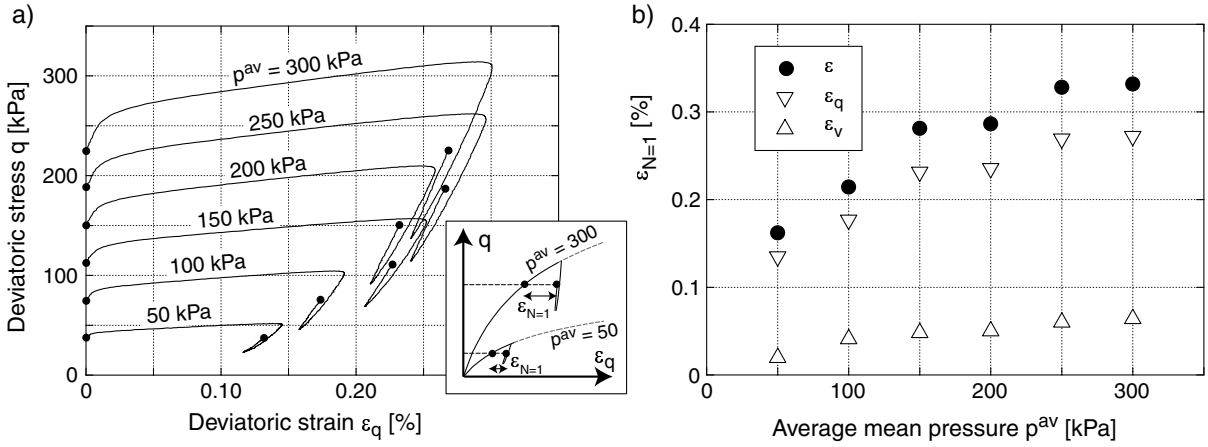

Figure 5.59: *First cycle: a)* q-ε_q*-hystereses, b) residual strains as a function of the average mean pressure* p^{av}

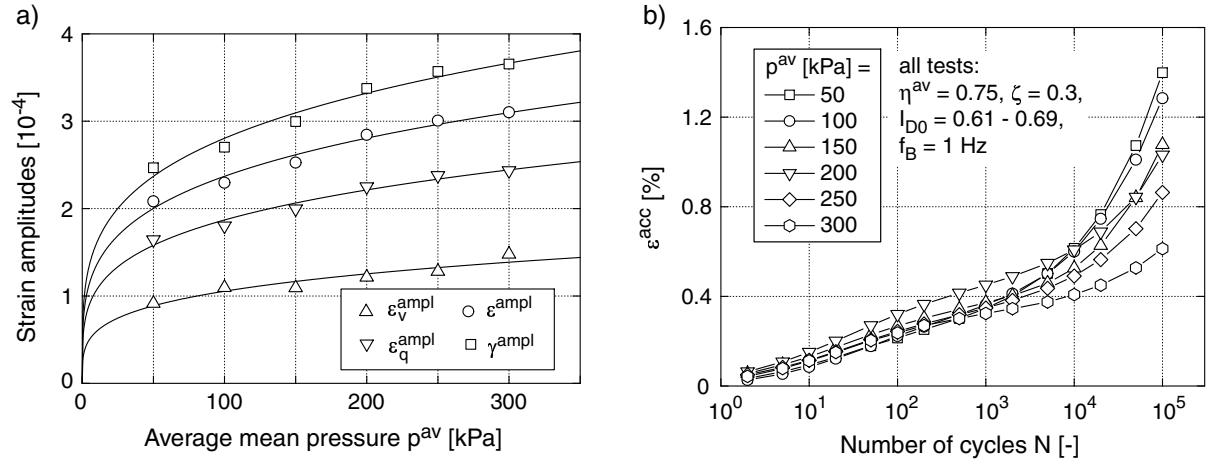

Figure 5.60: *a) Increase of the strain amplitudes with* p^{av} *at* q^{ampl}/p^{av} = *constant, b) accumulation curves* $\varepsilon^{acc}(N)$

Figure 5.60b presents the accumulation curves $\varepsilon^{\mathrm{acc}}(N)$ in the tests. Up to $N = 10^4$ hardly any dependence of the residual strain on p^{av} is noticeable, but for $N > 10^4$ the curves diverge. Larger values of $\varepsilon^{\mathrm{acc}}$ were measured for the smaller pressures. However, it has to be considered that in the tests with the smaller average mean pressures the strain amplitudes were smaller. In Figure 5.61 the accumulated strain after different numbers of cycles was normalized with $\bar{f}_{\mathrm{ampl}}$ und $\bar{f}_e$ and plotted versus the average mean pressure p^{av}. The normalized residual strain decreases exponentially with p^{av}. Therefore, the function

$$f_p \;=\; \exp\left[-C_p\,\left(\frac{p^{\mathrm{av}}}{p_{\mathrm{ref}}}-1\right)\right] \tag{5.9}$$

with the reference pressure $p_{\mathrm{ref}} = p_{\mathrm{atm}} = 100$ kPa and the material constant C_p is used in the accumulation model (Chapter 7). The solid lines in Figure 5.61 and the constants C_p annotated close to them resulted from a fitting of Equation (5.9) to the measured data for different numbers of cycles. Apparantly C_p increases with N, i.e. the pressure-dependence of the intensity of accumulation increases with the number of cycles. In cyclic simple shear tests with small numbers of cycles (Silver & Seed [151], Youd [188], Sawicki & Świdziński [133], see Section 3.2.2.6) no influence of the average stress could be detected. Beside the general disadvantages of this test type (see Section 4.1.2), this may be due to the less pronounced dependence $\dot{\varepsilon}^{\mathrm{acc}}(p^{\mathrm{av}})$ at small numbers of cycles ($N < 1,000$, Figure 5.61).

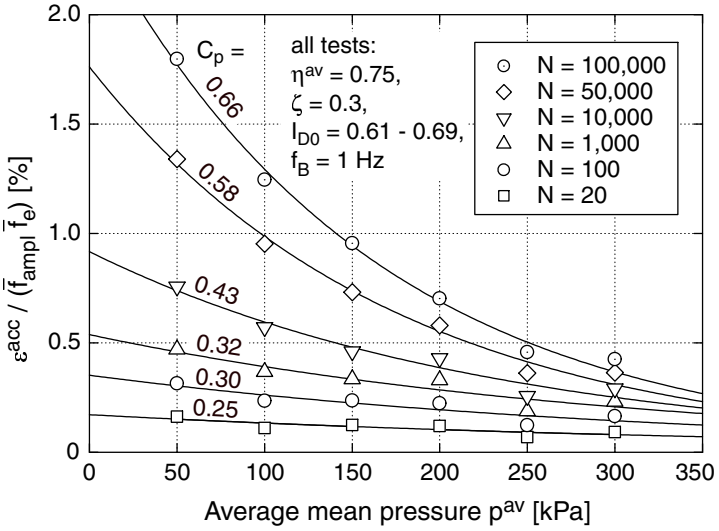

Figure 5.61: *Accumulated strain $\varepsilon^{\mathrm{acc}}/(\bar{f}_{\mathrm{ampl}}\bar{f}_e)$ in dependence on p^{av}*

In order to keep the accumulation model as simple as possible and the number of material constants manageable, the N-dependence of C_p is neglected and a mean value $C_p = 0.43$ is set into approach. Figure 5.62 makes clear that the loss of model accuracy is small. In comparison to Figure 5.61, the measured data was freed from the influences of the average

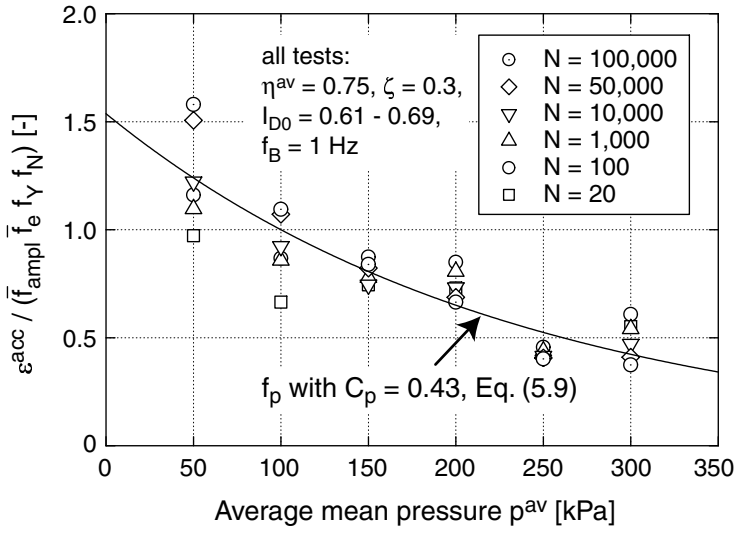

Figure 5.62: *Accumulated strain* $\varepsilon^{acc}/(\bar{f}_{ampl}\bar{f}_e f_Y f_N)$ *in dependence on* p^{av}

stress ratio (division by f_Y, see Section 5.2.4.2) and the number of cycles (division by f_N, see Section 5.2.6) in Figure 5.62. Figure 5.62 shows the acceptable deviation of the test data from the approximation given by Equation (5.9).

Figure 5.63 presents the accumulation rates for different numbers of cycles. The exponential decrease of $\dot{\varepsilon}^{acc}$ with p^{av} and the increase of C_p with N is obvious. Since the direction of accumulation does not depend on p^{av} (Section 5.1), similar conclusions can be drawn for the densification rates $\dot{e}$ in Figure 5.64.

In oder to study the validity of Equation (5.9) for average stress ratios $\eta^{av} \neq 0.75$, supplementary tests with $p^{av} = 100$, 200 und 300 kPa and average stress ratios $0.25 \leq \eta^{av} \leq 1.313$ were performed. The average stresses of these tests are depicted as black points in Figure 5.65. The initial densities of the tests lay within $0.57 \leq I_{D0} \leq 0.69$.

In Figure 5.66 the residual strains after different numbers of cycles were normalized with $\bar{f}_{ampl}$ and $\bar{f}_e$ and plotted over a p^{av}-$\bar{Y}^{av}$-plane. Independently of N and the average stress ratio $\bar{Y}^{av}$, an increase of the residual strains with decreasing average mean pressure p^{av} could be observed. The increase of the accumulation rate with $\bar{Y}^{av}$ is discussed in Section 5.2.4.2.

Figure 5.67 repeats Figure 5.61 for $\eta^{av} = 0.75$ and presents analogous diagrams for the five other tested average stress ratios. The exponential function (5.9) could be fitted to the measured data for all tested average stress ratios. In Figure 5.67, the determined constants C_p are given at the respective curve. For all tested values of η^{av} the constant C_p increases with N. The largest values of C_p were obtained for $\eta^{av} = 0.75$. The pressure-dependence is less pronounced for lower and larger average stress ratios. At small average

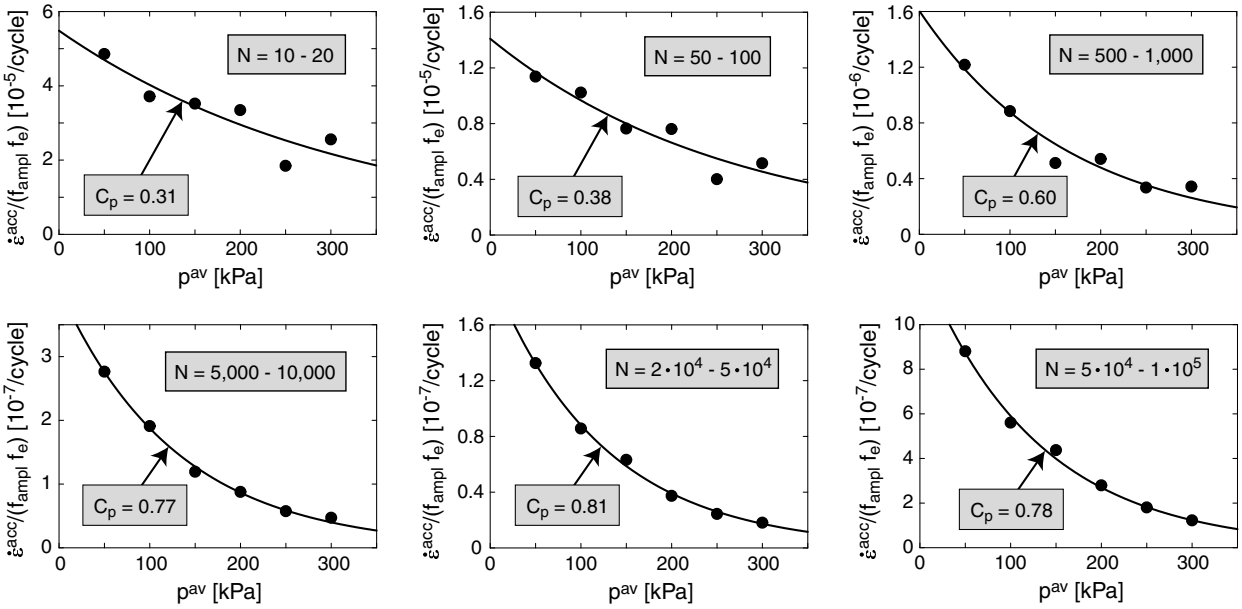

Figure 5.63: *Accumulation rate* $\dot{\varepsilon}^{acc} \approx \Delta\varepsilon^{acc}/\Delta N$ *in dependence on the average mean pressure* p^{av} *for different numbers of cycles*

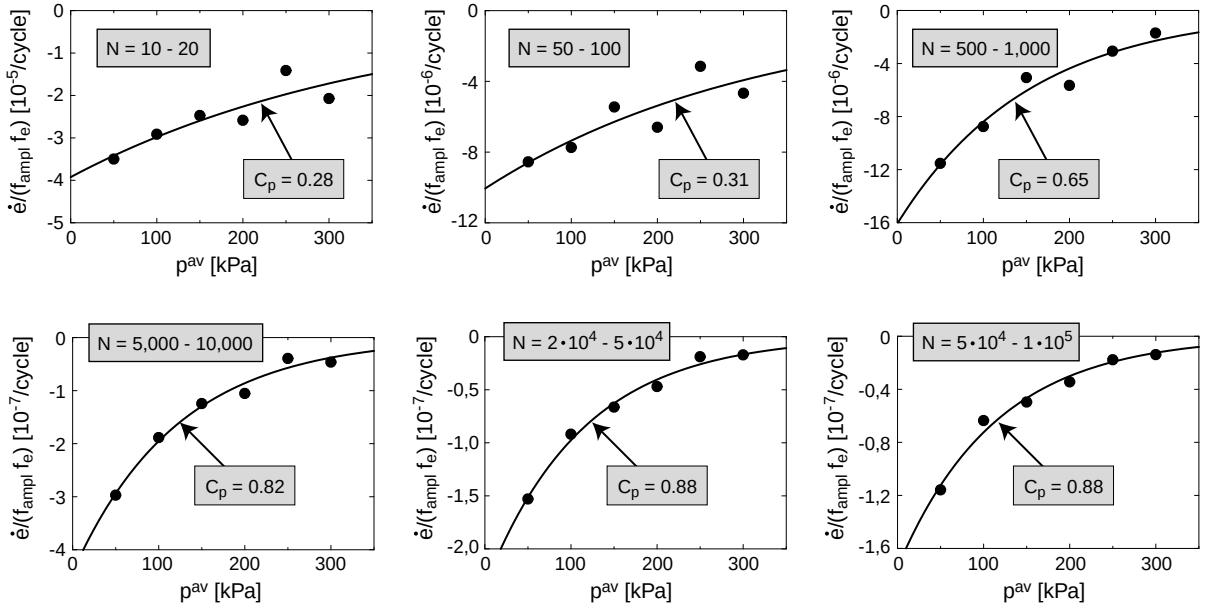

Figure 5.64: *Densification rate* $\dot{e} \approx \Delta e/\Delta N$ *in dependence on the average mean pressure* p^{av} *for different numbers of cycles*

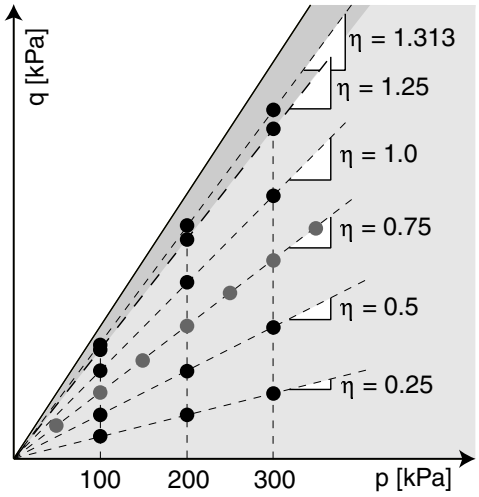

Figure 5.65: *Average stresses in supplementary tests on f_p with different average stress ratios η^{av}*

stress ratios $\eta^{av} \leq 0.5$ and low numbers of cycles $N \leq 100$ hardly any p^{av}-dependence of $\dot{\varepsilon}^{acc}$ could be detected (for some curves even negative values of C_p were determined).

In Figure 5.68 a presentation analogously to Figure 5.62 was chosen, i.e. the residual strains were also normalized with f_Y and f_N and compared with the approximation by Equation (5.9). Equation (5.9) describes best the important case $\eta^{av} = 0.75$ ($K_0 = 0.5$). For other average stress ratios it may lead to an overestimation of the accumulation rate, in particular for small pressures and low numbers of cycles. For larger numbers of cycles (e.g. $N = 10^5$) Equation (5.9) fits well independently of η^{av}. Due to this reason $C_p = 0.43$ is kept as a material constant independently of η^{av}.

Triaxial extension

The dependence of the accumulation rate on the average mean pressure was further studied for the case of triaxial extension ($\eta^{av} = -0.5$). A scheme of the stress cycles at 50 kPa $\leq p^{av} \leq$ 300 kPa and with $\zeta = 0.2$ is given in Figure 5.69.

Analogously to Figure 5.60a, Figure 5.70a shows the increase of the strain amplitudes with the average mean pressure p^{av}. The exponent of the stress-dependence of the secant shear modulus $G_{hyst} \sim (p^{av})^n$ was determined as $n = 0.53$, i.e. smaller than for triaxial compression ($n = 0.75$). For 100 kPa $\leq p^{av} \leq$ 300 kPa the normalized residual strains in Figure 5.70b can be also described by Equation (5.9) (see the solid curves resulting from a curve-fitting). Also for $\eta^{av} = -0.5$ the constant C_p increases with N. The constants C_p are similar to the values determined for triaxial compression and small average stress

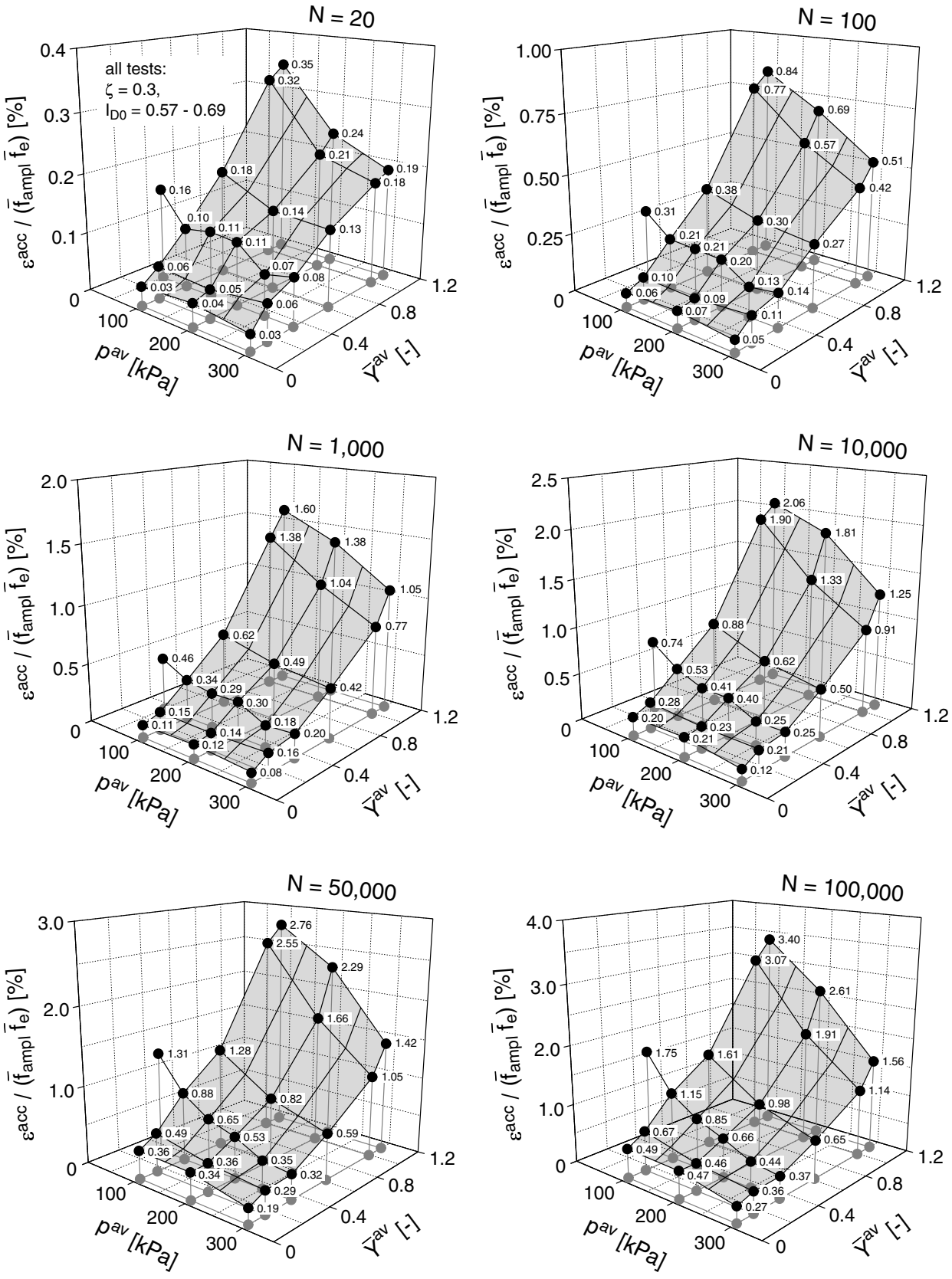

Figure 5.66: *Accumulated strain* $\varepsilon^{acc}/(\bar{f}_{ampl}\bar{f}_e)$ *over a* p^{av}-$\bar{Y}^{av}$-*plane*

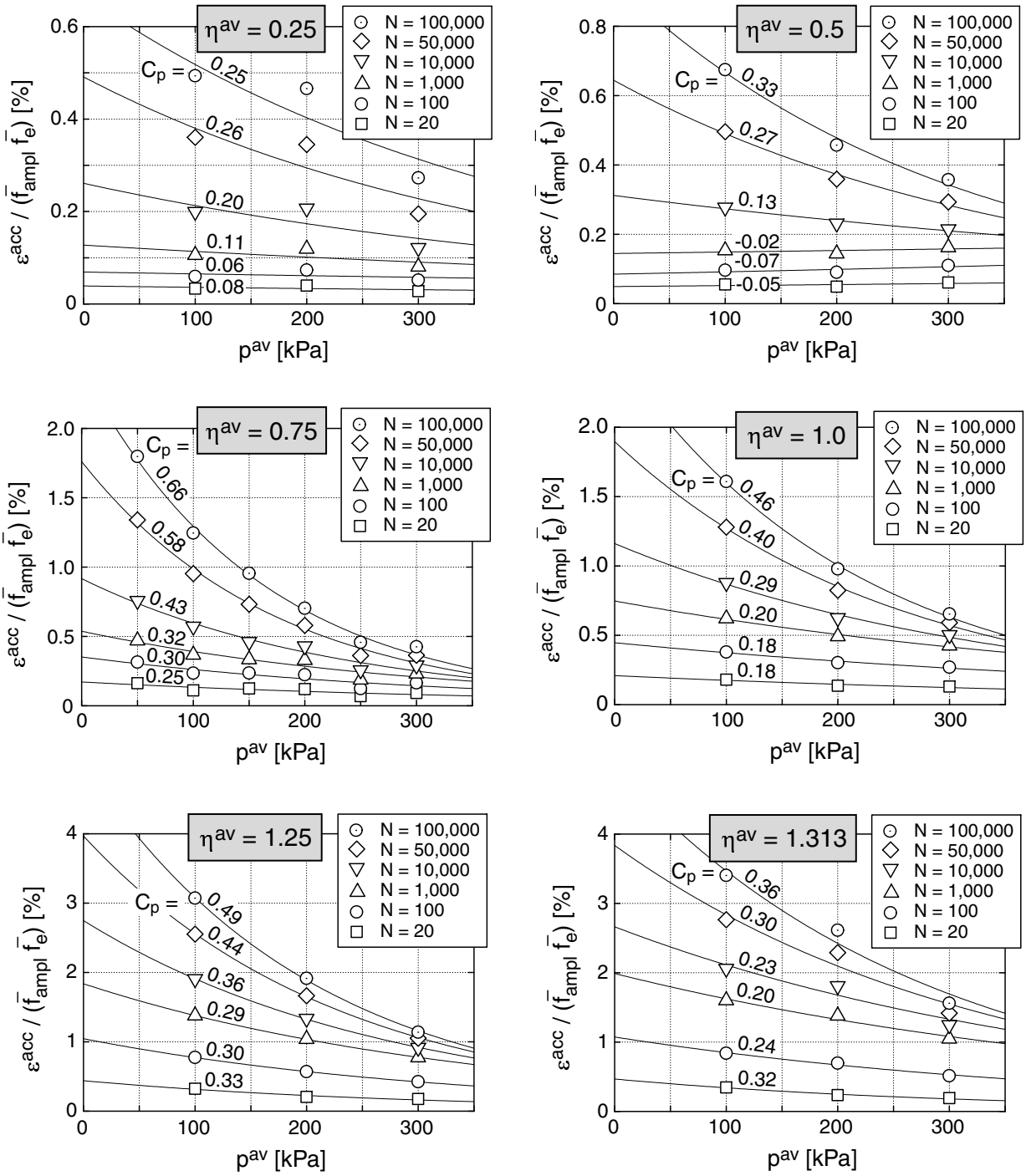

Figure 5.67: *Accumulated strain* $\varepsilon^{acc}/(\bar{f}_{ampl}\bar{f}_e)$ *as a function of the average mean pressure* p^{av} *for different average stress ratios* η^{av}

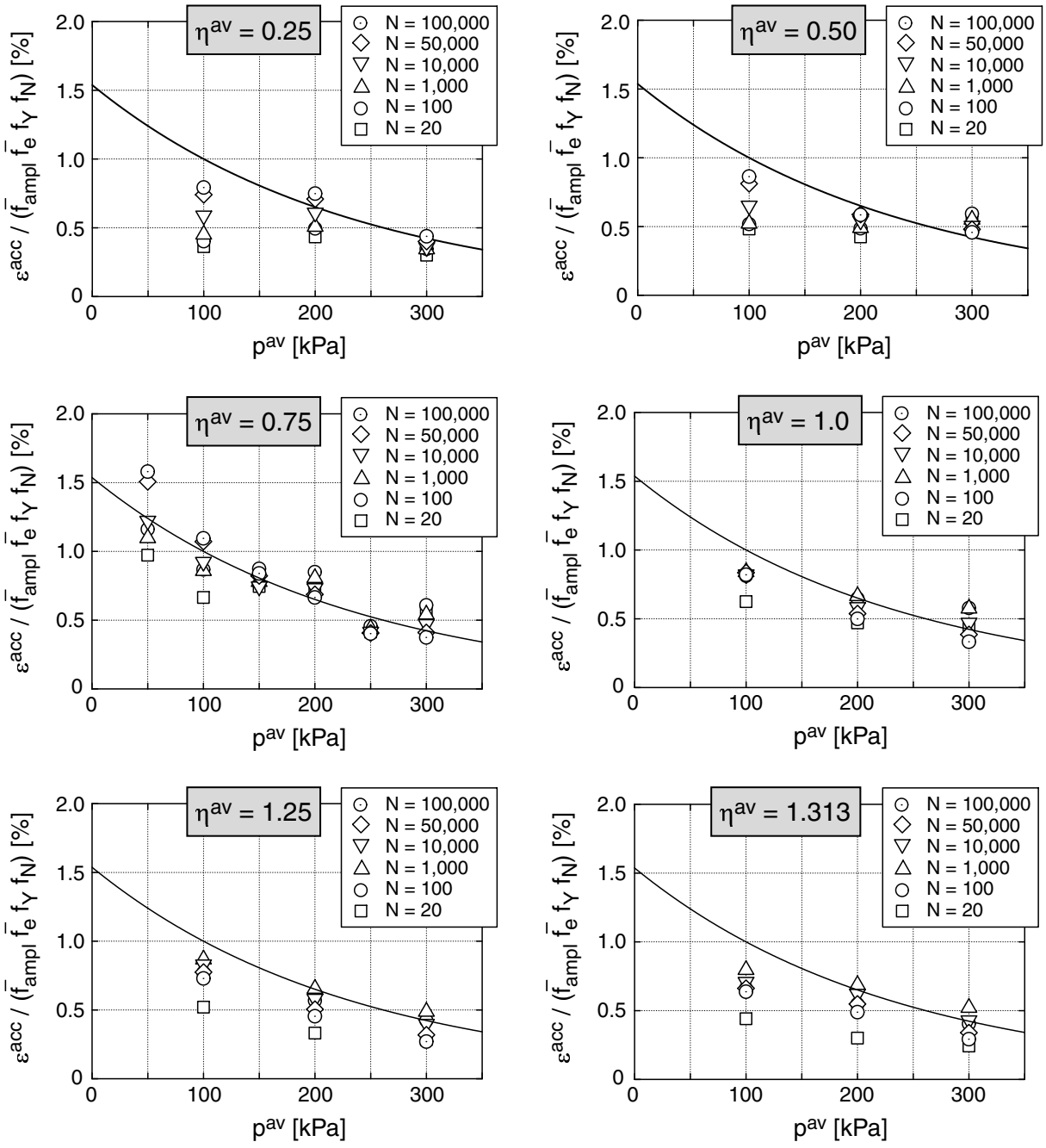

Figure 5.68: *Accumulated strain* $\varepsilon^{acc}/(\bar{f}_{ampl}\bar{f}_e f_Y f_N)$ *as a function of the average mean pressure* p^{av} *for different average stress ratios* η^{av}

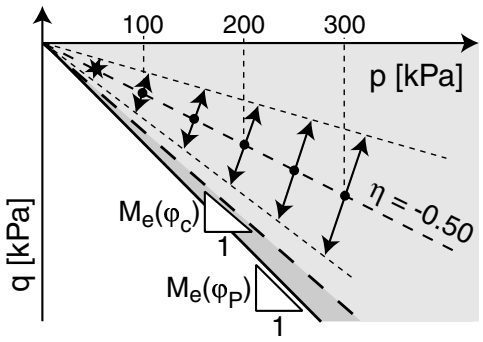

Figure 5.69: *Stress cycles in tests on f_p with triaxial extension*

ratios (Figure 5.67). From Figure 5.69 it can be seen, that in the test with $p^{\mathrm{av}} = 50$ kPa an accumulation rate was measured, which was larger than expected. The test was repeated and similar results were obtained. These rates are not described by Equation (5.9). Thus, the test with $p^{\mathrm{av}} = 50$ kPa was excluded from the determination of the constants C_p given in Figure 5.70. A more detailed study on the accumulation rate at small pressures $p^{\mathrm{av}} \leq 50$ kPa (for triaxial compression and extension) is planned for the future.

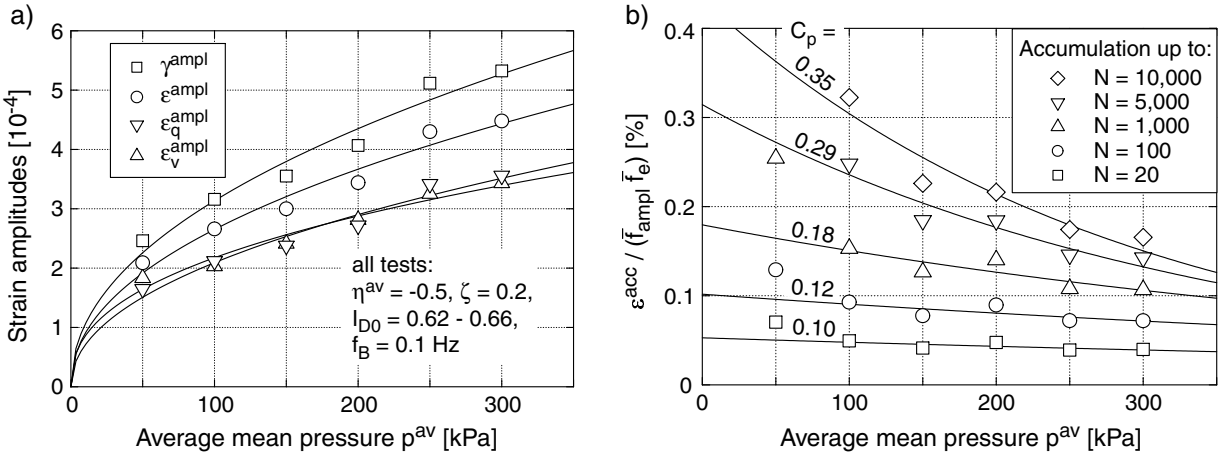

Figure 5.70: *Influence of the average mean pressure p^{av} on strain accumulation in tests with triaxial extension ($\eta^{\mathrm{av}} = -0.5$): a) strain amplitudes, b) residual strains*

Isolines of identical accumulation rates in the pressure-void ratio-diagram

By means of Equations (5.8) and (5.9) isolines with identical accumulation rates in the e-$\ln(p)$-diagram can be drawn. An example with $N = 1,000$, $\varepsilon^{\mathrm{ampl}} = 3 \cdot 10^{-4}$ and $\eta^{\mathrm{av}} = 0.75$ is given in Figure 5.71a.

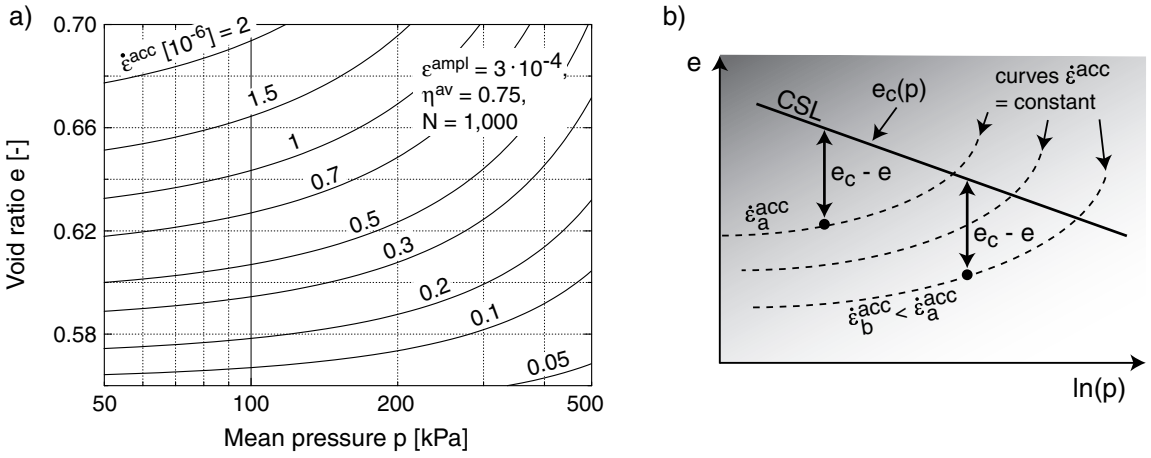

Figure 5.71: *a) Isolines with $\dot{\varepsilon}^{acc}$ = constant in the pressure-void ratio-diagram, b) The accumulation rate is not controlled by the distance $e - e_c$ to the CSL*

The curves $\dot{\varepsilon}^{\mathrm{acc}}$ = constant increase with $\ln(p)$, i.e. their inclination is opposite to the inclination of the critical state line $e_c(p)$, Figure 5.71b. Hence, it can be concluded that the intensity of accumulation under cyclic loading *cannot* be described by the distance $e - e_c$ to the CSL. The scheme in Figure 5.71b makes clear, that two points in the e-$\ln(p)$-diagram can have different accumulation rates although their distance $e - e_c$ to the CSL is identical. Thus, in the accumulation model the influence of barotropy and pyknotropy is expressed by two separate functions f_p and f_e.

Remarks on the pressure-dependence of the secant stiffness

The pressure-dependence of the secant stiffness $G_{\mathrm{hyst}} \sim p^n$ was also studied in RC tests. The curves of the secant shear modulus G_{hyst} with the shear strain amplitude γ^{ampl} were measured for four different isotropic stresses 50 kPa $\leq p \leq$ 400 kPa (Figure 5.72a). If one considers the shear modulus normalized with its maximum value $G_{\mathrm{hyst},0} = G_{\mathrm{dyn}}$ at small strain amplitudes, the ratio $G_{\mathrm{hyst}}/G_{\mathrm{hyst},0}$ decreases faster with γ^{ampl} for smaller pressures compared to larger ones (Wichtmann & Triantafyllidis [180]). If for a certain shear strain amplitude γ^{ampl} the shear moduli G_{hyst} are taken from Figure 5.72a and plotted versus p, the diagram in Figure 5.72b is obtained. A fitting of $G_{\mathrm{hyst}} \sim p^n$ to the measured data revealed that the exponent n increases with increasing shear strain amplitude. For $\gamma^{\mathrm{ampl}} = 10^{-6}$ an exponent $n = 0.45$ and for $\gamma^{\mathrm{ampl}} = 3 \cdot 10^{-4}$ a value $n = 0.60$ was determined. The dependence $n(\gamma^{\mathrm{ampl}})$ is responsible for the larger exponents n measured in cyclic triaxial tests compared to measurements with small strain amplitudes (RC test, wave propagation, Wichtmann & Triantafyllidis [183, 184, 180]). Beside the strain amplitude, also the average stress ratio η^{av} influences n ($n = 0.53$ for $\eta^{\mathrm{av}} = -0.5$ and $n = 0.75$

for $\eta^{av} = 0.75$). Further RC tests on specimens with different initial void ratios and a stepwise increase of the mean pressure 50 kPa $\leq p \leq$ 400 kPa revealed that the void ratio does not influence the exponent n (Figure 5.73).

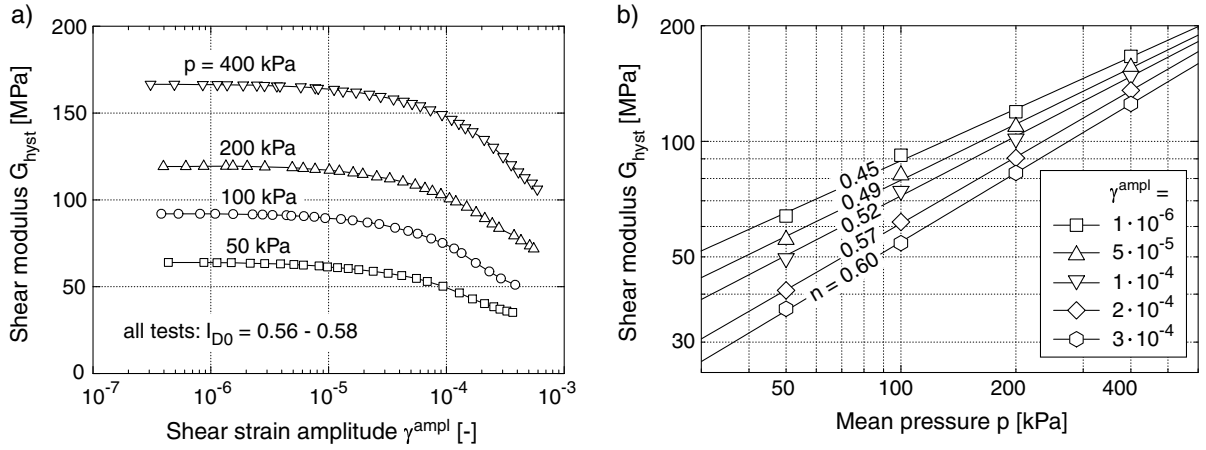

Figure 5.72: *RC tests: a) curves $G_{hyst}(\gamma^{ampl})$ for four different pressures p, b) stress-dependence $G_{hyst}(p)$ for different shear strain amplitudes γ^{ampl}*

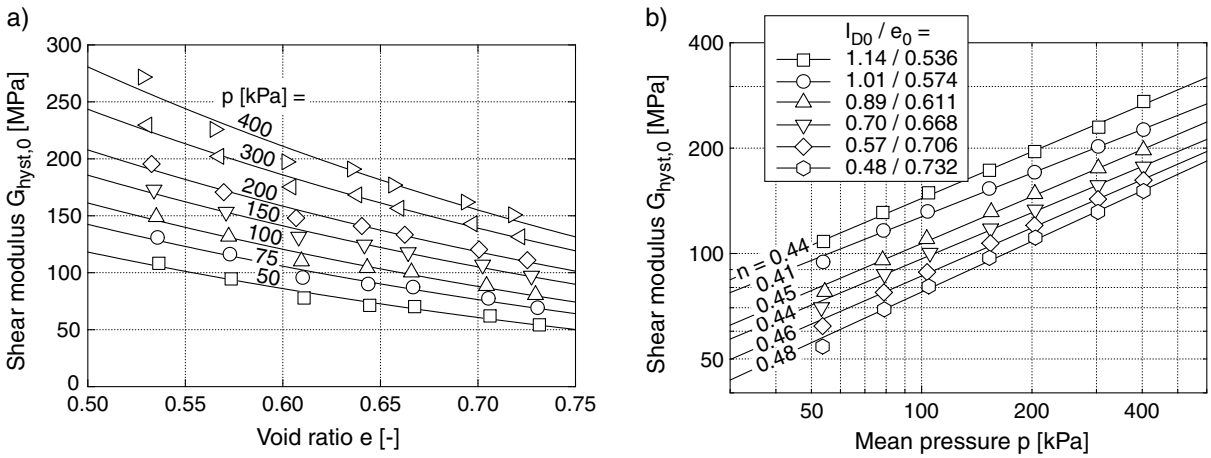

Figure 5.73: *RC tests: a) $G_{hyst,0}(e)$ for seven different mean pressures, b) stress-dependence $G_{hyst}(p)$ for different void ratios*

5.2.4.2 Influence of the average stress ratio η^{av} or $\bar{Y}^{av}$

Triaxial compression

The influence of the average stress ratio on cyclic densification was first studied in eleven tests with $0.375 \leq \eta^{av} \leq 1.375$ ($0.088 \leq \bar{Y}^{av} \leq 1.243$), $p^{av} = 200$ kPa and $\zeta = 0.3$. A scheme of the stress cycles is given in Figure 5.74.

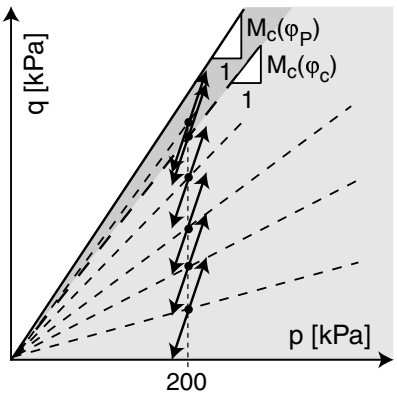

Figure 5.74: *Stress cycles in the tests with different stress ratios* η^{av}

The stress-strain hystereses in the first cycle are shown in Figure 5.75a. With increasing stress ratio η^{av}, the residual deviatoric strain increases due to the decrease of the stiffness during first loading. Large deformations occur in particular for $\eta^{av} \geq 1$ (corresponds to $\eta^{max} \geq 1.3$ at $q^{max} = q^{av} + q^{ampl}$). For the stress cycles with $\eta^{av} \geq 1.125$ ($\bar{Y}^{av} \geq 0.79$), a dilatation of the sand remains at the end of the first cycle (Figure 5.75b).

The strain amplitudes slightly decrease with η^{av} (Figure 5.76a). The accumulation curves in Figure 5.76b demonstrate that the accumulation rate increases with increasing average stress ratio. In Figure 5.77 the residual strains after different numbers of cycles were normalized with $\bar{f}_{ampl}$ and $\bar{f}_e$ and plotted as a function of the average stress ratio $\bar{Y}^{av}$. The residual strains increase exponentially with $\bar{Y}^{av}$. In the accumulation model (Chapter 7), this dependence of the accumulation rate on the average stress ratio is captured by the factor

$$f_Y \;=\; \exp\left(C_Y\, \bar{Y}^{av}\right), \tag{5.10}$$

wherein C_Y is a material constant. Equation (5.10) was fitted to the measured data. The constants C_Y are given at the respective curves in Figure 5.77. Irrespective of the data for $N = 20$ ($C_Y = 1.4$), the constant C_Y varies only slightly with the number of cycles ($1.8 \leq C_Y \leq 2.1$). For the tested sand a mean value of $C_Y = 2.0$ was set into approach.

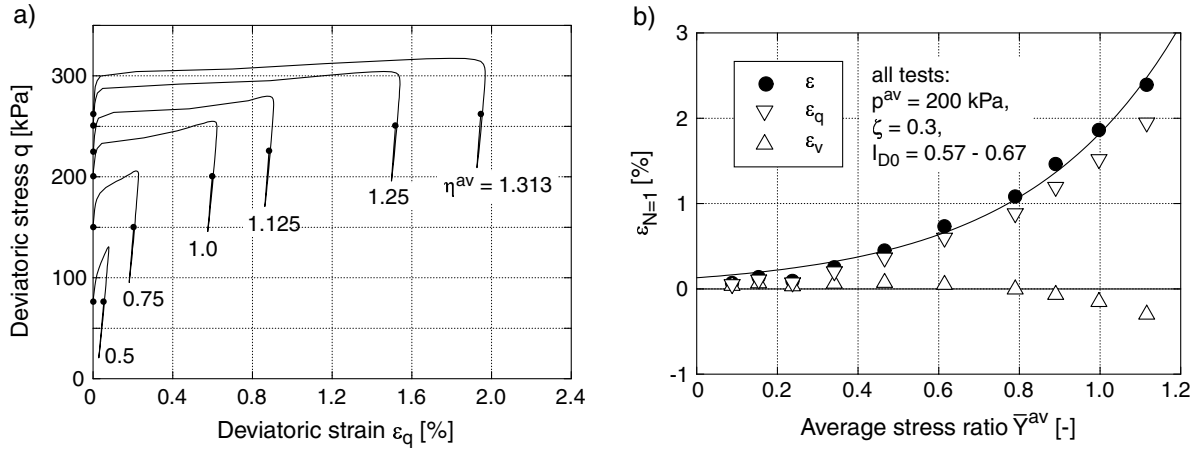

Figure 5.75: *First cycle: a) q-ε_q hystereses, b) residual strains as a function of the average stress ratio $\bar{Y}^{av}$*

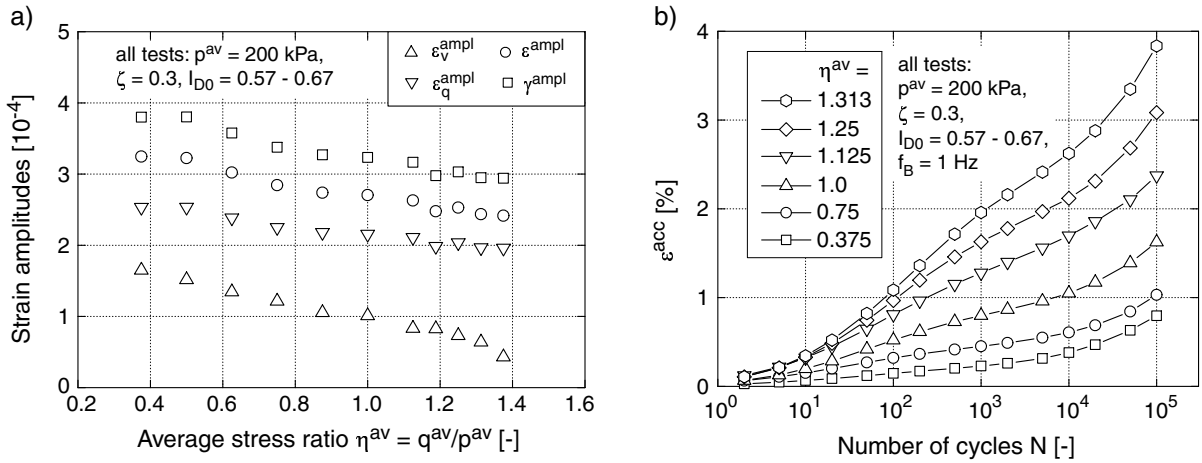

Figure 5.76: *a) Decrease of the strain amplitudes with η^{av} for q^{ampl} = constant (mean values over 10^5 cycles), b) accumulation curves $\varepsilon^{acc}(N)$*

In the test with $\eta^{\mathrm{av}} = 1.375$, the stress cycles touched the failure line (peak shear strength). These cycles corresponded to the case presented in Figure 5.35d,e. The resulting large accumulation rates ($\varepsilon^{\mathrm{acc}} = 20\%$ after 10^5 cycles) cannot be described by Equation (5.10). For these cycles the remarks in Section 7.2.5 apply.

The accumulation rates $\dot{\varepsilon}^{\mathrm{acc}}$ for different numbers of cycles in Figure 5.78 confirm Equation (5.10). The variation of C_Y with N ($1.4 \leq C_Y \leq 2.6$) is somewhat larger than in the analysis of the residual strains (Figure 5.77). However, the value of $C_Y = 2.0$ seems feasible also from Figure 5.78.

While the measured densification rates $\dot{e}$ for different numbers of cycles are depicted in Figure 5.79, Figure 5.80 shows the curve $\dot{e}(\bar{Y}^{\mathrm{av}})$ predicted by the accumulation model

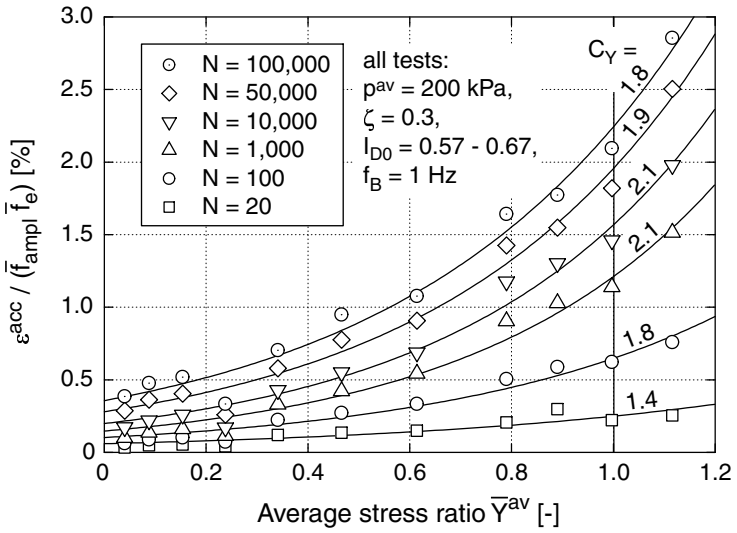

Figure 5.77: *Accumulated strain in dependence on the average stress ratio* $\bar{Y}^{av}$

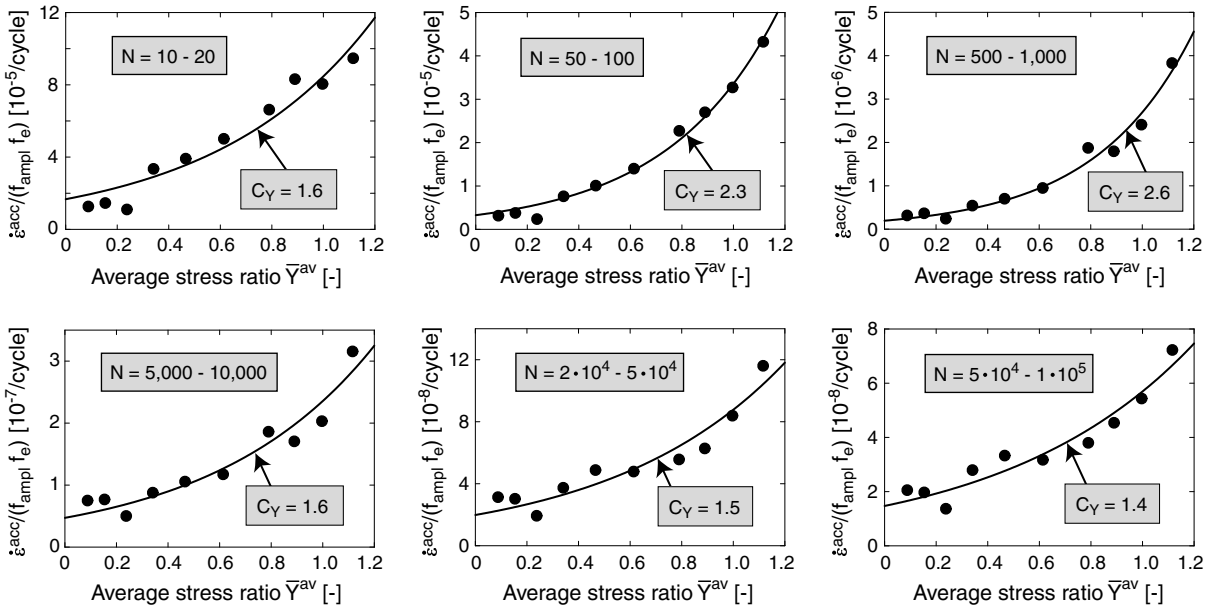

Figure 5.78: *Accumulation rate* $\dot{\varepsilon}^{acc} \approx \Delta\varepsilon^{acc}/\Delta N$ *in dependence on the average stress ratio* $\bar{Y}^{av}$ *for different numbers of cycles*

for typical boundary conditions of a test. The curve in Figure 5.80 was generated for $N = 1,000$, but its shape is independent of N. In order to create the curve $\dot{e}(\bar{Y}^{\mathrm{av}})$ in Figure 5.80, the flow rule of the modified Cam Clay model was used (see Section 5.1). The relationship $\dot{e} \sim 1/\sqrt{3/(2\omega^2) + 1/3}\ f_Y$ holds, i.e. the densification rate vanishes on the CSL ($\bar{Y}^{\mathrm{av}} = 1$). In congruence with the remarks in Section 5.1, Figure 5.79 shows that $\dot{e}(\bar{Y}^{\mathrm{av}} = 1) = 0$ is valid only for small numbers of cycles (i.e. for $N = 10 - 20$) and that the stress ratio corresponding to $\dot{e} = 0$ increases with increasing N. The shape of

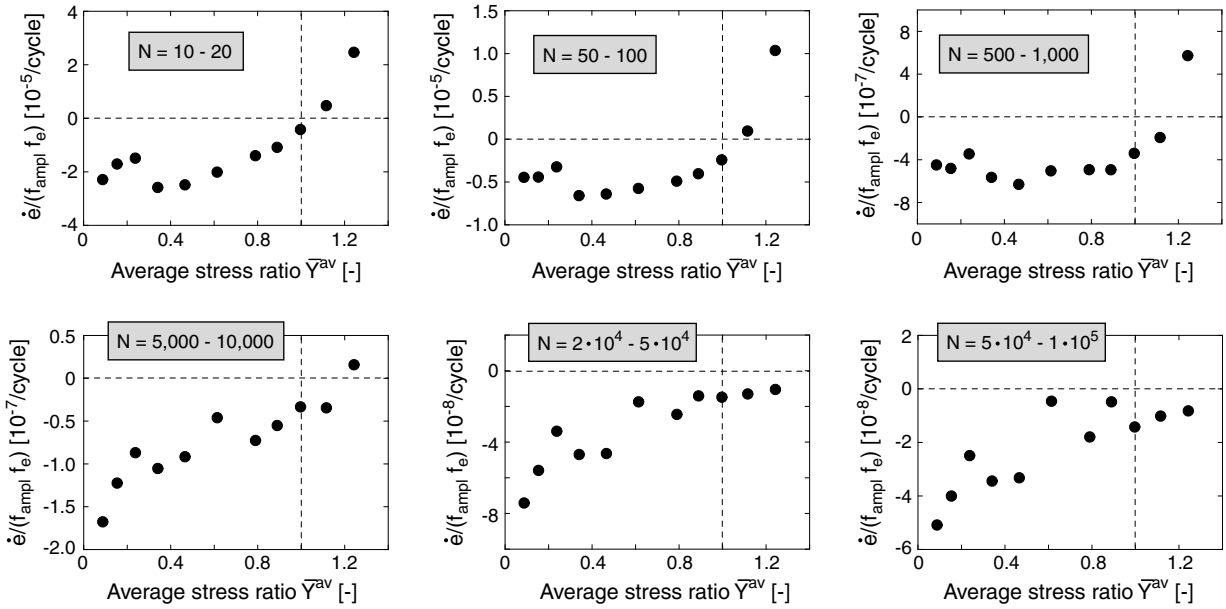

Figure 5.79: *Densification rate* $\dot{e} \approx \Delta e/\Delta N$ *in dependence on the average stress ratio* $\bar{Y}^{av}$ *for different numbers of cycles*

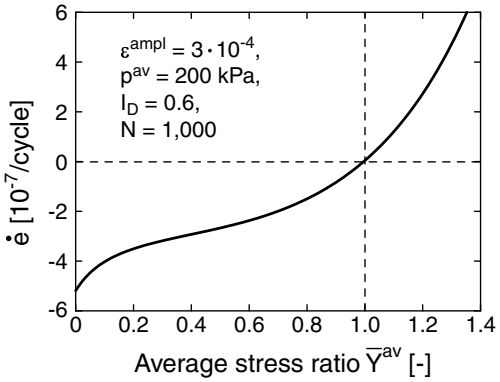

Figure 5.80: *Densification rate* $\dot{e}(\bar{Y}^{av})$ *predicted by the accumulation model*

the curve in Figure 5.80 can be also found in Figure 5.79 (see e.g $N = 5.000 - 10.000$).

Diagrams for $p^{av} = 100$ kPa and $p^{av} = 300$ kPa analogously to Figure 5.77 (see the average stresses of the corresponding tests in Figure 5.65) are given in Figure 5.81. As for $p^{av} = 200$ kPa, Equation (5.10) could be fitted well to the test data resulting in similar values of the constant C_Y ($1.6 \leq C_Y \leq 2.1$ for $p^{av} = 100$ kPa and $1.2 \leq C_Y \leq 2.0$ for $p^{av} = 300$ kPa). Equation (5.10) with $C_Y = 2.0$ seems applicable independent of p^{av}.

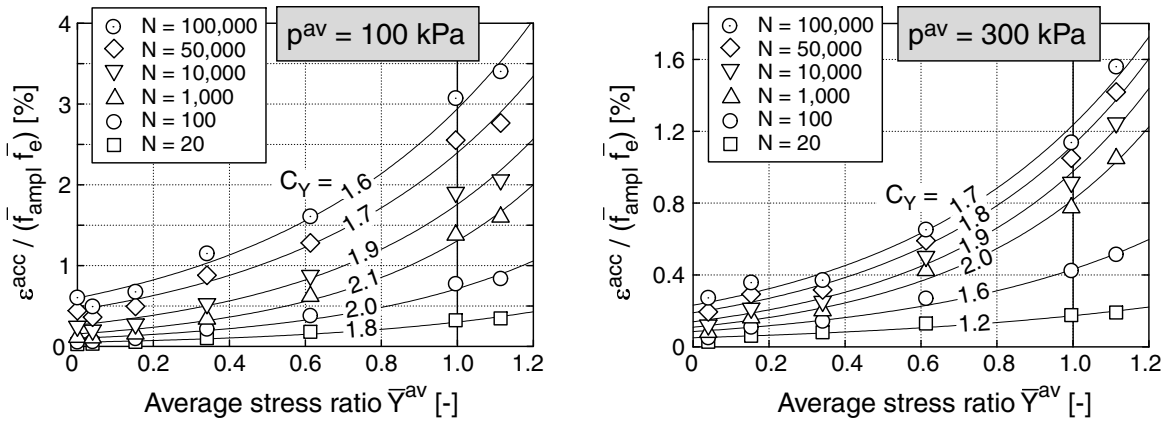

Figure 5.81: *Normalized accumulated strain in dependence on the average stress ratio* $\bar{Y}^{av}$ *for* $p^{av} = 100$ *kPa and* $p^{av} = 300$ *kPa*

Triaxial extension

In order to check the applicability of Equation (5.10) to the case of triaxial extension, the stress cycles shown schematically in Figure 5.82 were tested ($p^{av} = 200$ kPa, $-0.88 \leq \eta^{av} \leq 0$). Due to the smaller distance of the average stress to the failure line, smaller amplitude ratios $\zeta = q^{ampl}/p^{av} = 0.2$ were chosen compared to the tests with triaxial compression. In the tests with η^{av} = -0.75 and η^{av} = -0.88 the amplitude ratio was even reduced to $\zeta = 0.1$ and $\zeta = 0.05$, respectively. The tests with triaxial extension were supplemented by tests with triaxial compression ($p^{av} = 200$ kPa, $0.25 \leq \eta^{av} \leq 1.25$) and $\zeta = 0.2$.

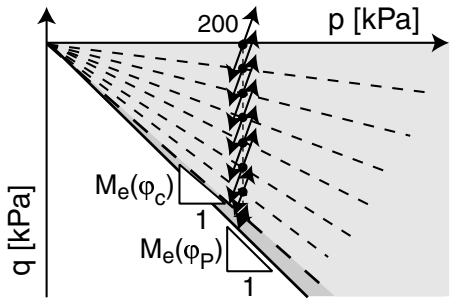

Figure 5.82: *Stress cycles in tests on* f_Y *with triaxial extension*

Figure 5.83 presents the strain amplitudes as a function of η^{av} in the tests with $\zeta = 0.2$. For triaxial extension, the strain amplitudes increase with $|\eta^{av}|$ while they decrease with $|\eta^{av}|$ for triaxial compression (see also Figure 5.76a). While for $\eta^{av} \geq 0$ the deviatoric strain amplitudes are significantly larger than the volumetric ones, the difference of these

amplitudes decays with decreasing η^{av}. For $\eta^{av} < -0.2$ the amplitudes ε_q^{ampl} and ε_v^{ampl} are almost identical. The strain amplitudes in Figure 5.83 reveal, that for the tested stress amplitudes the secant stiffness of the stress-strain-hysteresis strongly depends on the average stress ratio η^{av}. For small strain amplitudes ($\gamma^{ampl} \leq 10^{-6}$) the dependence $G_{hyst,0}(\eta^{av})$ or $E_{s,hyst,0}(\eta^{av})$, respectively, is less pronounced (Wichtmann & Triantafyllidis [184]).

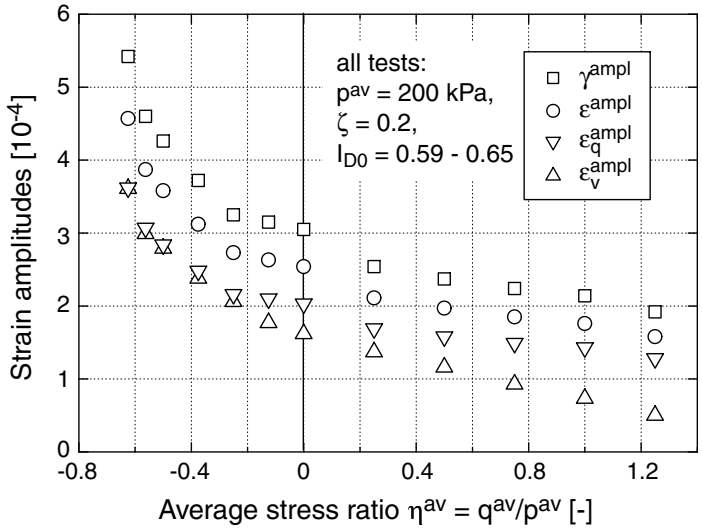

Figure 5.83: *Strain amplitudes in the tests on f_Y with triaxial extension*

The residual strains ε^{acc} normalized with $\bar{f}_{ampl}$ and $\bar{f}_e$ are shown as a function of η^{av} in Figure 5.84. As in the case $\eta^{av} > 0$ the residual strains increase with increasing amount of the average stress ratio $|\eta^{av}|$ also for $\eta^{av} < 0$. However, the shape of the curves $\varepsilon^{acc}(|\eta^{av}|)$ is different for triaxial compression and extension, i.e. $\dot{\varepsilon}^{acc}(-\eta^{av}) \neq \dot{\varepsilon}^{acc}(\eta^{av})$ holds.

In Figure 5.85 the residual strains are plotted as a function of η^{av}. For $\bar{Y}^{av} \geq 0$, again Equation (5.10) could be fitted to the test data resulting in material constants $1.5 \leq C_Y \leq 2.0$. The application of Equation (5.10) with $C_Y = 2.0$ to the tests with $\eta^{av} < 0$ overestimates the accumulation rate (in Figure 5.85 this is shown by the dashed line for $N = 10^4$). For a more precise description of the tests with triaxial extension, the following modification of Equation (5.10) can be used:

$$f_Y = \exp\left[C_{Y1}\,(\bar{Y}^{av})^{C_{Y2}}\right] \tag{5.11}$$

A fitting of Equation (5.11) to the tests with $\eta^{av} \leq 0$ (solid lines in Figure 5.85 for $\eta^{av} \leq 0$) led to $1.2 \leq C_{Y1} \leq 1.3$ and $2.3 \leq C_{Y2} \leq 2.7$. Thus, the following material constants are

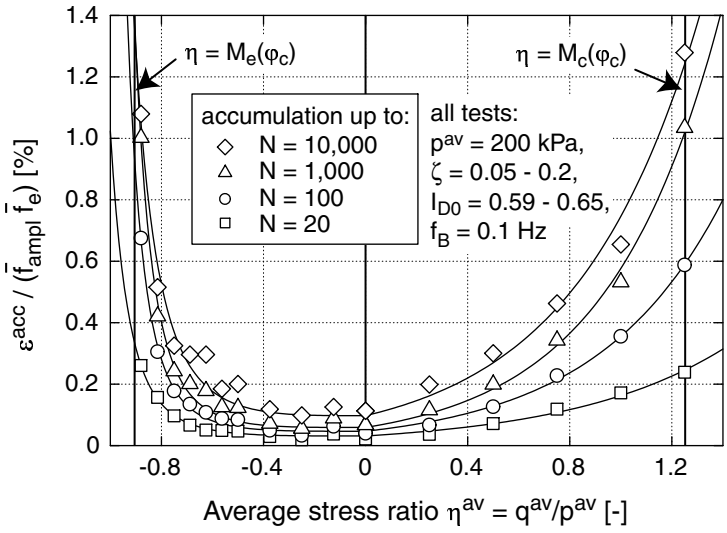

Figure 5.84: *Comparison of the curves $\varepsilon^{acc}(\eta^{av})$ for $\eta^{av} \leq 0$ and $\eta^{av} \geq 0$*

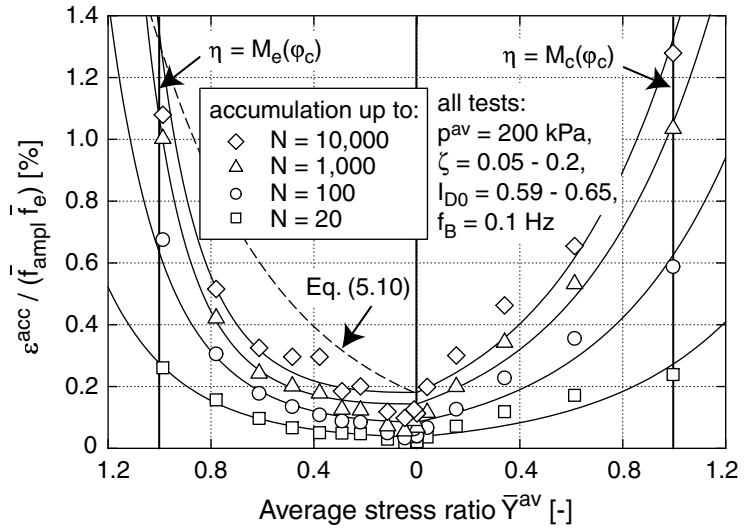

Figure 5.85: *Comparison of the curves $\varepsilon^{acc}(\bar{Y}^{av})$ for $\eta^{av} \leq 0$ and $\eta^{av} \geq 0$*

proposed:

$$C_{Y1} = \begin{cases} 2.0 & \text{for} \quad \eta^{\text{av}} \geq 0 \\ 1.25 & \text{for} \quad \eta^{\text{av}} < 0 \end{cases}$$

$$C_{Y2} = \begin{cases} 1.0 & \text{for} \quad \eta^{\text{av}} \geq 0 \\ 2.5 & \text{for} \quad \eta^{\text{av}} < 0 \end{cases}$$

However, also Equation (5.11) cannot prevent an overestimation of the accumulation rate at small average stress ratios with cyclic extension ($0 \leq \bar{Y}^{\text{av}} \leq 0.2$).

The following hypothesis could explain the difference of the accumulation rates in the

tests with triaxial compression and extension. It is based on the assumption that a static preloading reduces the accumulation rate. If a specimen has sustained an isotropic static preloading, its accumulation rate at the beginning of cyclic loading is lower than the rate of a freshly pluviated specimen despite identical stresses and void ratios. Preloading surfaces can be determined experimentally e.g. by the measurement of acoustic emissions (Oda & Iwashita [115]). In the p-q-plane, such preloading surfaces are similar to the curves drawn with grey colour in Figure 5.86. In all cyclic tests first the stress was isotropically increased to $p = \sigma_3^{av}$. After that, the axial stress was increased (triaxial compression) or decreased (triaxial extension) to reach σ_1^{av}. In the case of an average stress with cyclic compression, the stress cycles were preceded by the monotonic stress path $0 \rightarrow 1 \rightarrow 2$ (Figure 5.86), in the case of triaxial extension by $0 \rightarrow 3 \rightarrow 4$. In Figure 5.86 it can be seen, that the cyclic loading is applied in an "over-consolidated" condition for small average stress ratios with triaxial extension (dashed line). This could explain the lower accumulation rates compared to analogous stress ratios with triaxial compression. For larger average stress ratios with triaxial extension the average stress is "normally consolidated" and the accumulation rates are identical to the ones for triaxial compression. Experiments presented in Section 5.2.8 contradict this hypothesis since (for cycles with $\boldsymbol{\sigma}^{av}$ on the p-axis) only a slight reduction of the accumulation rate due to an isotropic monotonic preloading could be detected.

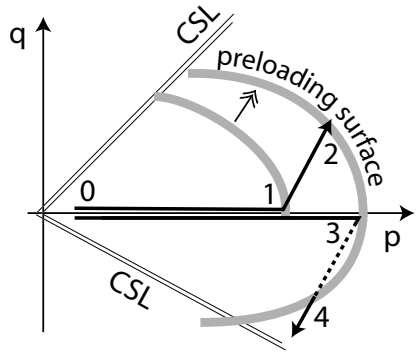

Figure 5.86: *Preloading surface and monotonic stress paths for reaching $\boldsymbol{\sigma}^{av}$ in tests with triaxial compression (path $0 \rightarrow 1 \rightarrow 2$) and triaxial extension (path $0 \rightarrow 3 \rightarrow 4$)*

The difference of the accumulation rates for triaxial compression and extension could also be due to an influence of the direction of deposition in comparison to the direction of the maximum and the minimum principal stresses. In the tests with triaxial compression, the maximum principal stress was acting parallel to the direction of deposition while both directions were perpendicular for triaxial extension. The influence of the direction of

deposition and the polarization of cyclic loading will be studied more detailed in future.

Isolines of identical accumulation rates in the p-q-plane

Figure 5.87 presents isolines of identical accumulation rates in the p-q-plane. In Figure 5.87a the curves $\dot{\varepsilon}^{acc}$ = constant were generated using Equations (5.9) and (5.10). In Figure 5.87b, Equation (5.10) was replaced by its modified form (5.11). In both cases the curves with an identical intensity of accumulation run parallelly to the limit lines in a wide range of the p-q-plane.

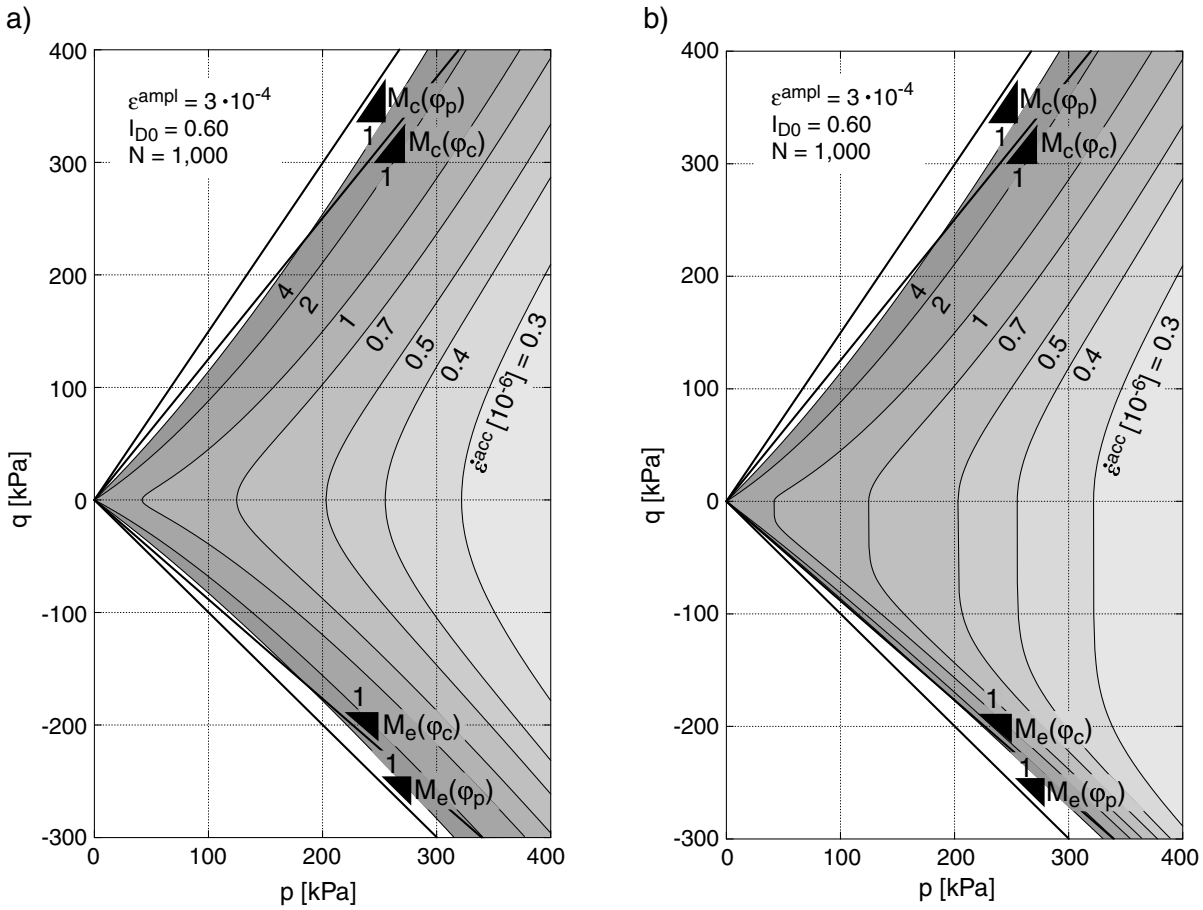

Figure 5.87: *Isolines of identical accumulation rates $\dot{\varepsilon}^{acc}$ in the p-q-plane: a) generated from Equations (5.9) and (5.10), b) generated from Equations (5.9) and (5.11)*

5.2.5 Influence of the loading frequency

The influence of the loading frequency f_B was studied in six tests with identical stresses ($p^{\mathrm{av}} = 200$ kPa, $\eta^{\mathrm{av}} = 0.75$, $q^{\mathrm{ampl}} = 60$ kPa) and similar initial densities $0.50 \leq I_{D0} \leq 0.60$ but different loading frequencies 0.05 Hz $\leq f_B \leq$ 2 Hz. For the tested range, the elastic component of strain is independent of f_B (Figure 5.88).

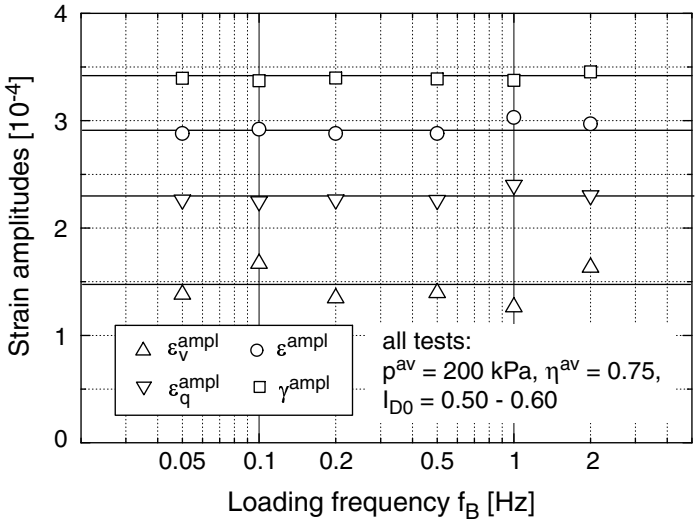

Figure 5.88: *Strain amplitudes in dependence on the loading frequency f_B (mean values over 10^5 cycles)*

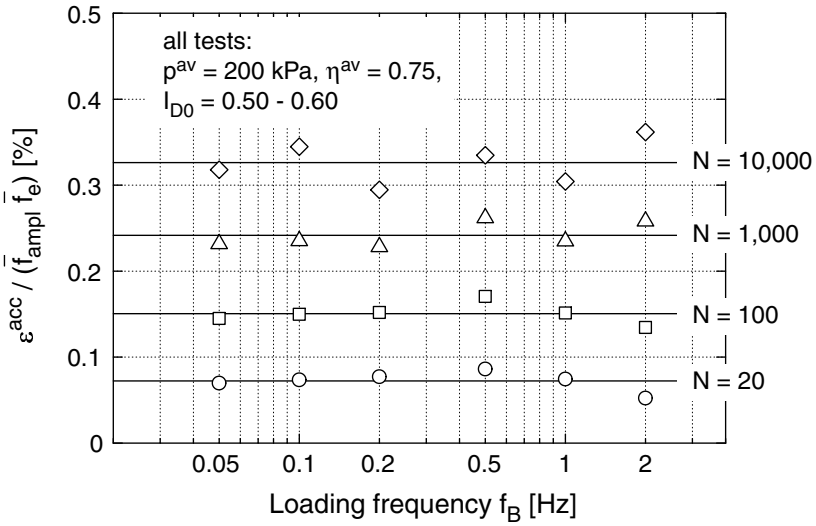

Figure 5.89: *Accumulated strain $\varepsilon^{acc}/(\bar{f}_{ampl}\bar{f}_e)$ as a function of the loading frequency f_B*

In Figure 5.89, the residual strains after different numbers of cycles were normalized with $\bar{f}_{\text{ampl}}$ and $\bar{f}_e$ and plotted as a function of f_B. No systematic influence of the loading frequency on the development of the residual strains could be detected. The same conclusion can be drawn from the presentations of the accumulation rates $\dot{\varepsilon}^{\text{acc}}$ and the densification rates $\dot{e}$ in Figures 5.90 and 5.91. This observation coincides with several studies in the literature (Youd [188], Shenton [149], Kokusho et al. [77], Section 3.2.2.8) but contradicts the measurements of Kempfert et al. [71].

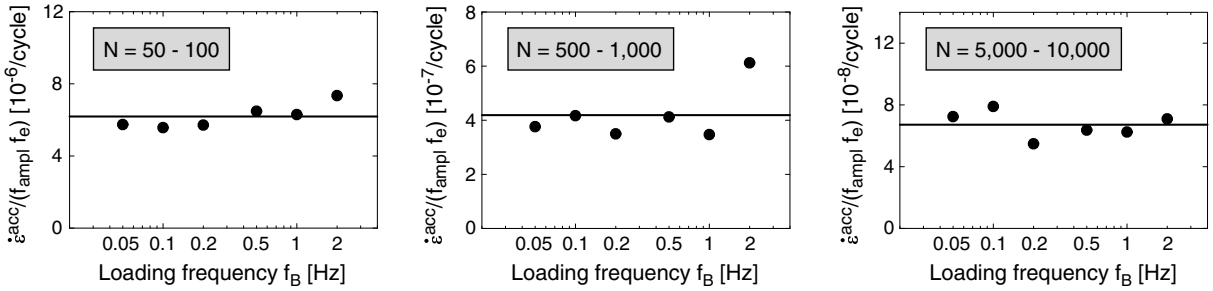

Figure 5.90: *Rate of strain accumulation* $\dot{\varepsilon}^{acc} \approx \Delta\varepsilon^{acc}/\Delta N$ *in dependence on the loading frequency* f_B

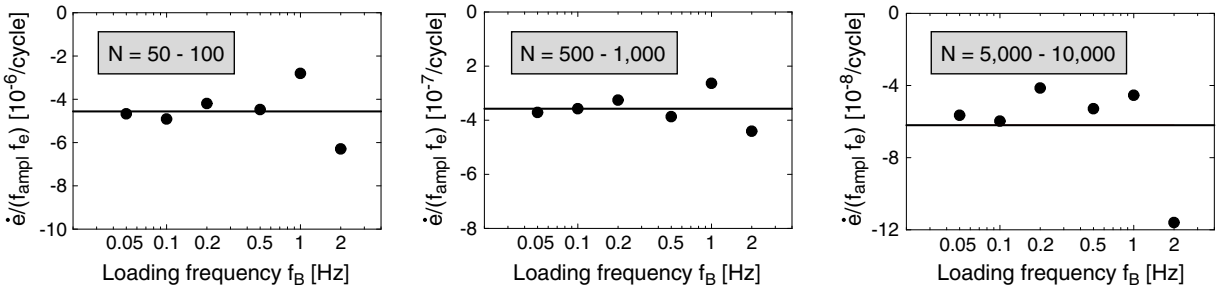

Figure 5.91: *Densification rate* $\dot{e} \approx \Delta e/\Delta N$ *in dependence on the loading frequency* f_B

5.2.6 Influence of the number of cycles and the historiotropy

If the accumulation curves $\varepsilon^{\text{acc}}(N)$ are normalized with the functions f_{ampl}, f_p, f_Y, f_e und f_π, the curves fall together into a band (Figure 5.92). Figure 5.92 contains the accumulation curves of the four test series which were performed in order to determine the functions f_{ampl} (Figure 5.23), f_e (Figure 5.55), f_p (Figure 5.61) and f_Y (Figure 5.77). For the triaxial tests $f_\pi = 1$ holds. Up to $N = 10^4$, the accumulation curves run proportional to the logarithm of the number of cycles. For larger numbers of cycles, the residual strains

increase faster than with $\ln(N)$. Possibly the logarithmic portion of the curves $\varepsilon^{\mathrm{acc}}(N)$ can be attributed to a re-arrangement of the grains while the over-logarithmic component may be due to an abrasion at the particle contacts (see e.g. Katzenbach & Festag [70]).

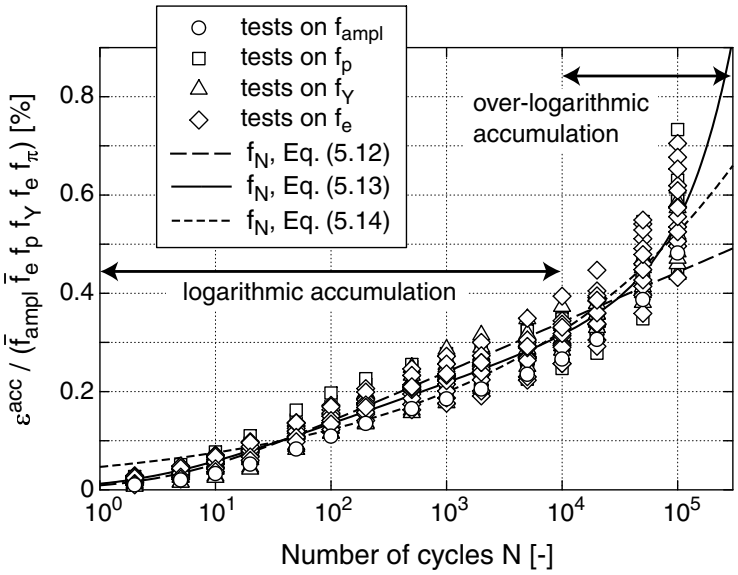

Figure 5.92: *Normalized accumulation curves* $\varepsilon^{\mathrm{acc}}(N)/(\bar{f}_{ampl}\bar{f}_e f_p f_Y f_\pi)$*, fitting of several functions* f_N

In the literature, several functions are used to approximate the curves $\varepsilon^{\mathrm{acc}}(N)$ (Section 3.2.2.1). A logarithmic function

$$f_N = C_{N1}\ln(1 + C_{N2}N) \tag{5.12}$$

can be considered as well as a function consisting of a logarithmic and a linear part

$$f_N = C_{N1}\left[\ln(1 + C_{N2}N) + C_{N3}N\right]. \tag{5.13}$$

Also a power law

$$f_N = C_{N1}N^{C_{N2}}. \tag{5.14}$$

is widely used in the literature. Equations (5.12) to (5.14) were fitted to the test data in Figure 5.92 (see the solid or dashed curves). The determined material constants C_{N1} to C_{N3} are given in Table 5.1 (rows for the tests with $N_{\max} = 10^5$). Figure 5.93 presents the normalized accumulation rates in a diagram with double-logarithmic scale. The rates $\dot{f}_N = \partial f_N/\partial N$ calculated from Equations (5.12) to (5.14) with the constants of Table 5.1 were also drawn in Figure 5.93.

Function f_N	$N_{\max}$	C_{N1}	C_{N2}	C_{N3}
$C_{N1}\ln(1+C_{N2}N)$	10^5	$4.4 \cdot 10^{-4}$	0.23	-
	$2 \cdot 10^6$	not meaningful		
$C_{N1}\left[\ln(1+C_{N2}N)+C_{N3}N\right]$	10^5	$3.6 \cdot 10^{-4}$	0.41	$4.6 \cdot 10^{-5}$
	$2 \cdot 10^6$	$4.7 \cdot 10^{-4}$	0.16	$1.4 \cdot 10^{-5}$
$C_{N1}N^{C_{N2}}$	10^5	$4.7 \cdot 10^{-4}$	0.21	-
	$2 \cdot 10^6$	$4.9 \cdot 10^{-5}$	0.41	-

Table 5.1: Possible functions f_N and their material constants C_{Ni}

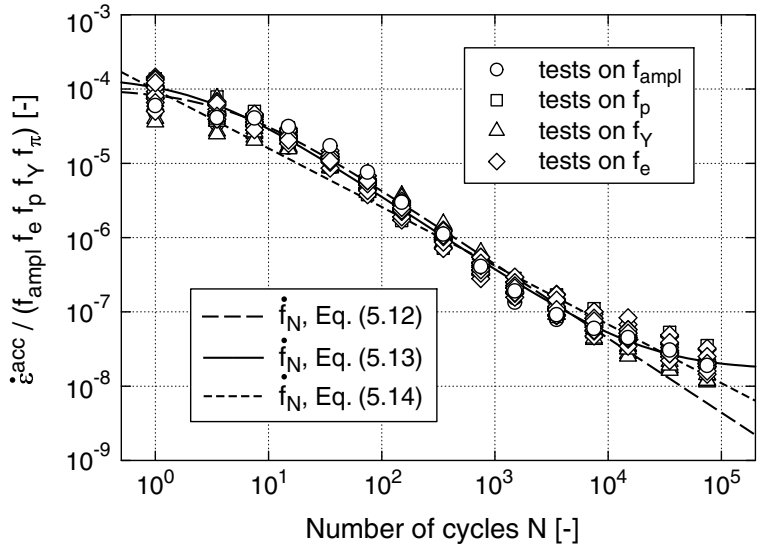

Figure 5.93: *Comparison of the measured accumulation rates $\dot{\varepsilon}^{acc}$ normalized by f_{ampl}, f_e, f_p, f_Y and f_π with the rate form of Equations (5.12), (5.13) and (5.14)*

Equation (5.13) delivers the best approximation of the test data. Due to the linear portion of the function also the over-logarithmic accumulation for $N > 10^4$ can be described. In that range, the logarithmic equation (5.12) underestimates the accumulation rate. The power law (5.14) also gives an acceptable approximation.

Also two long-term tests with $2 \cdot 10^6$ load cycles were performed. The corresponding accumulation curves and the rates are depicted in Figure 5.94. The over-logarithmic course of the accumulation curves continues for $N > 10^5$. In Figure 5.94, also the curves resulting from Equations (5.12) to (5.14), with the material constants determined from Figure 5.92, were drawn. Obviously, Equation (5.13) delivers slightly too large rates for $N > 10^5$. The power law (5.14) and in particular the logarithmic equation (5.12) predict

a too slow accumulation. By fitting Equation (5.13) to the long-term tests alone one obtains modified constants (see the rows for $N_{\max} = 2 \cdot 10^6$ in Table 5.1) and a better approximation of the test data for $N > 10^5$. For the power law in Equation (5.14) such a procedure is of minor success since the better description of the accumulation rates for $N > 10^5$ enforces a bad prediction for $N < 10^5$. A fitting of Equation (5.12) to the long-term tests is not possible. Eventually, a bilinear approximation similar to that of Helm et al. [49] (Section 3.2.2.1) is applicable.

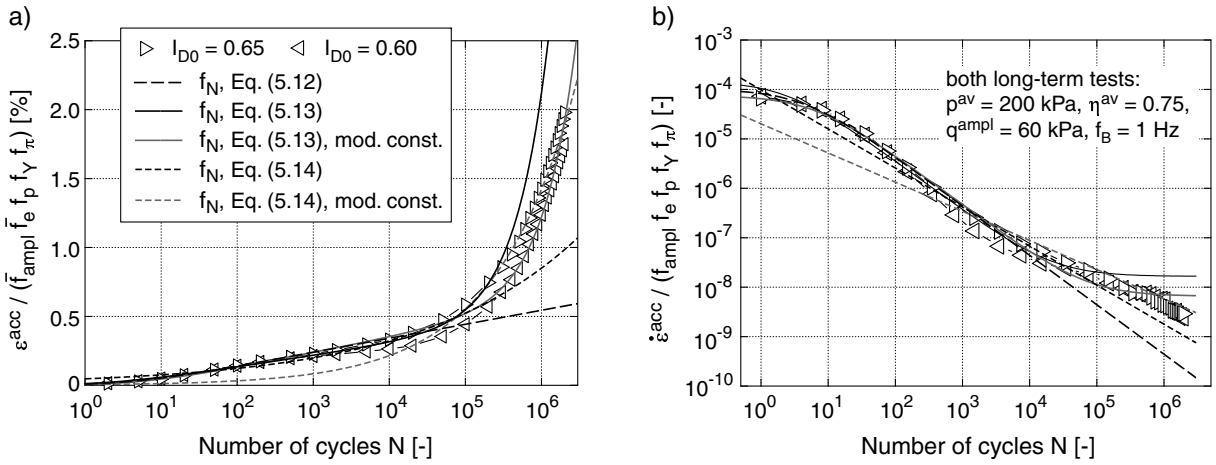

Figure 5.94: *a) Normalized accumulation curves $\varepsilon^{acc}(N)/(\bar{f}_{ampl}\bar{f}_e f_p f_Y f_\pi)$ and b) normalized accumulation rates $\dot{\varepsilon}^{acc}(N)/(f_{ampl}f_e f_p f_Y f_\pi)$ in two tests with $2 \cdot 10^6$ cycles*

The accumulation model presented in Chapter 7 uses Equation (5.13) or its rate form, respectively

$$\dot{f}_N = \underbrace{\frac{C_{N1}C_{N2}}{1 + C_{N2}N}}_{\dot{f}_N^A} + \underbrace{C_{N1}C_{N3}}_{\dot{f}_N^B} \tag{5.15}$$

since this equation delivers the best approximation of the test data. Equation (5.15) consists of a portion $\dot{f}_N^A$, which depends on the number of cycles, and a component $\dot{f}_N^B$, which is independent of N. Since $\dot{f}_N^B$ does not depend on N, this part may be seen as a "basic rate" of accumulation. It may mainly result from abrasion at the grain contacts. The part $\dot{f}_N^A$ decays with N. This decrease of the accumulation rate with the number of cycles may be primarily attributed to a rearrangement of the grains. Thus, the component $\dot{f}_N^A$ is also denoted as the "structural" accumulation rate.

For large numbers of cycles after a decay of the portion $\dot{f}_N^A$, Equation (5.15) predicts an accumulation rate $\dot{f}_N^B = C_{N1}C_{N3}$ which is almost independent of N. A further reduction of the rate $\dot{\varepsilon}^{acc}$ with N can only take place due to a decrease of the strain amplitude

(f_{ampl}) and the void ratio (f_e) resulting from compaction. However, the rates in Figure 5.94b for $N > 10^5$ seem not to approximate a lower bound. Since only two tests were performed so far, the data for $N > 10^5$ are limited. In the future, the necessity, to modify Equation (5.15) for $N > 10^5$ could arise from further long-term tests with $N_{\max} > 10^5$.

The number of cycles N alone is not a suitable state variable for the historiotropy since it contains no information on the intensity of the cycles in the past. This intensity significantly governs the further accumulation. A package with e.g. 10^6 cycles with an evanescent amplitude (e.g. $\varepsilon^{\text{ampl}} < 10^{-6}$) must not influence the accumulation during a subsequent package with larger amplitudes (e.g. $\varepsilon^{\text{ampl}} = 5 \cdot 10^{-4}$). However, in the case of Equation (5.15), the first package has a large impact on the accumulation during the second package, since the number of cycles N is counted independently of the amplitude of the cycles.

Ideally a (tensorial) state variable for the historiotropy should describe the fabric of the grain skeleton. However, test methods delivering sufficient information to formulate such a fabric tensor are missing yet (see some experiments presented by Triantafyllidis & Niemunis [165]). Thus, in the accumulation model a phenomenological description of the historiotropy by a scalar variable is used. This variable should weight the number of cycles with their amplitude.

Sawicki & Świdziński [133, 134] proposed the variable $\tilde{N} = \int (\gamma^{\text{ampl}})^2 \, \mathrm{d}N$ as a measure of the historiotropy. $\tilde{N}$ is based on observations, that the curves $\varepsilon_v^{\text{acc}}(\tilde{N})$ in cyclic simple shear tests with different shear strain amplitudes γ^{ampl} fell together (see Section 3.2.2.2 and Figure 3.13). For the accumulation curves measured in cyclic triaxial tests and shown in Figure 5.23, a diagram $\varepsilon^{\text{acc}}(\tilde{N})$ was generated (Figure 5.95). The curves of the tests with different amplitudes did *not* coincide. Thus, in the accumulation model $\tilde{N}$ could not be chosen as a measure of the historiotropy.

Instead of $\tilde{N}$, the state variable g^A was introduced, which also weights the number of cycles N with the corresponding amplitude $\varepsilon^{\text{ampl}}$. Only the N-dependent portion $\dot{f}_N^A$ of the accumulation rate was taken into account in the formulation of g^A:

$$g^A = \int f_{\text{ampl}} \; \dot{f}_N^A \, \mathrm{d}N \tag{5.16}$$

Replacing the number of cycles N in the term for $\dot{f}_N^A$ in Equation (5.15) by g^A one obtains the rate $\dot{f}_N^A$ as a function of g^A:

$$\dot{f}_N^A \;\; = \;\; C_{N1} C_{N2} \exp\left(- \frac{g^A}{C_{N1} \; f_{\text{ampl}}} \right) \tag{5.17}$$

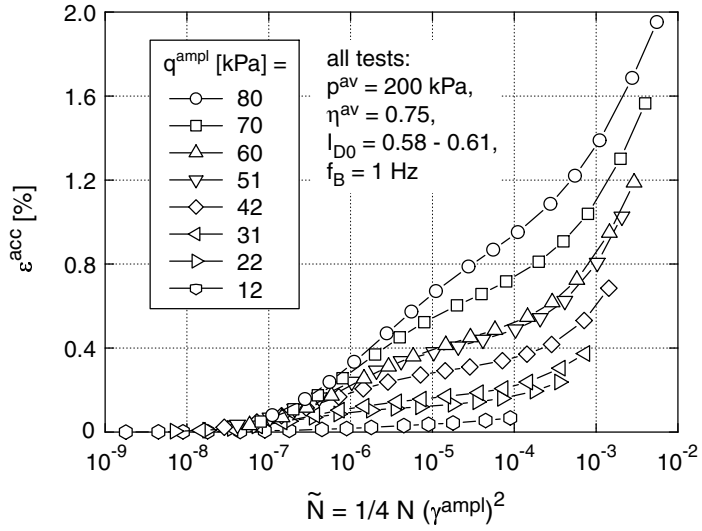

Figure 5.95: *Accumulation curves* $\varepsilon^{acc}(\tilde{N})$ *with* $\tilde{N} = \frac{1}{4}\int(\gamma^{ampl})^2\, dN$*: Falsification of the "common compaction curve" of Sawicki & Świdziński [133, 134] by the own cyclic triaxial tests*

By using Equations (5.16) and (5.17), the accumulation curves in Figure 5.92 are still described correctly, because Equation (5.13) is fulfilled for the special case $\varepsilon^{\mathrm{ampl}} = \text{constant}$. A package of cycles with vanishing amplitudes does not influence the accumulation during subsequent larger cycles since at the beginning of these cycles still $g^A \approx 0$ holds. In Section 7.2.6 it is demonstrated that the accumulation curves in tests with packages of cycles with different amplitudes (Section 5.2.7) can be well described by Equations (5.16) and (5.17).

The large influence of the historiotropy on the accumulation rate becomes clear from the void ratio curves $e(N)$ in Figure 5.96. In the three triaxial tests, the specimens were prepared with slightly different initial void ratios e_0 and afterwards loaded with identical stresses. If one considers a state with an identical void ratio (see the horizontal line in Figure 5.96), the densification rates $\dot{e}$ in the three tests differ strongly despite identical stresses and void ratio. The freshly pluviated specimen exhibits a significantly larger densification rate than a specimen preloaded by 40,000 cycles.

Thus, for a prediction of the accumulation in situ the knowledge of void ratio and average stress is not sufficient. An information about the historiotropy of the soil is needed. The phenomenological variable g^A cannot be measured directly in situ but has to be estimated by correlations. Chapter 9 deals with the problem of the determination of g^A in situ.

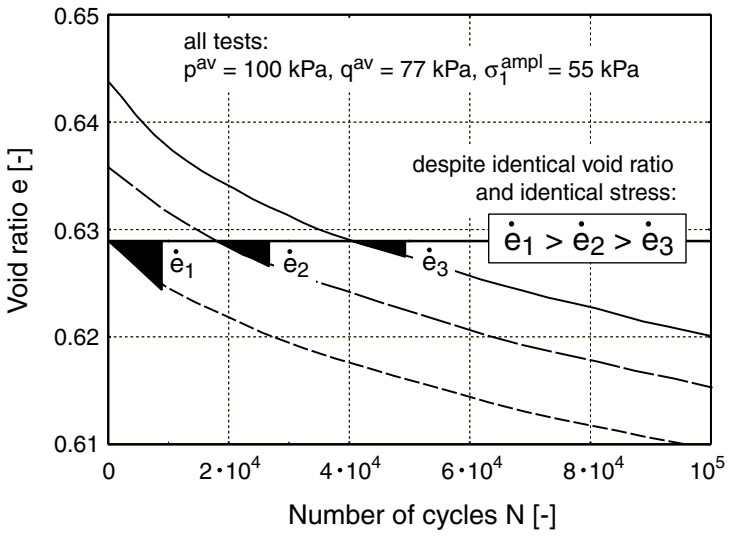

Figure 5.96: *Influence of the historiotropy on the densification rate $\dot{e} = \partial e/\partial N$: cyclic triaxial tests with slightly different initial void ratios e_0*

5.2.7 Random cyclic loading, packages of cycles and the effect of their sequence

In practice, the amplitude of cyclic loading is constant only in special cases (e.g. machine foundations). In the case of traffic routes the amplitudes vary due to the different weights of the vehicles. Also in the case of cyclic loading induced by wind or waves the amplitude fluctuates. Such random cyclic loadings cannot be calculated with an explicit accumulation model since $\varepsilon^{\mathrm{ampl}} =$ constant during a definite number of cycles is a requirement for its applicability. However, by means of stochastic methods, an irregular cyclic loading can be replaced by packages of cycles each with a constant amplitude (Figure 5.97). These packages can then be handled by the explicit model. The question arises, if the sequence of the packages influences the final value of the residual strain.

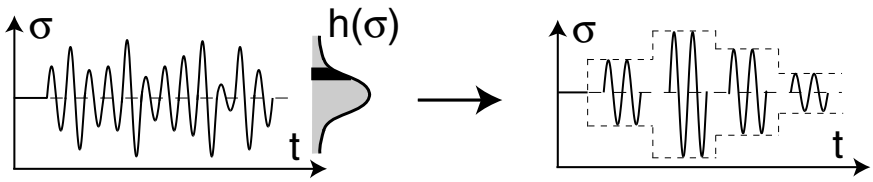

Figure 5.97: *Replacing a random cyclic loading by packages of cycles each with a constant amplitude*

This question was studied in six cyclic triaxial tests on initially medium dense specimens. In each test the average stress was $p^{\mathrm{av}} = 200$ kPa and $\eta^{\mathrm{av}} = 0.75$. Four packages each with 25,000 cycles were applied in succession. The sequence of the amplitudes $q^{\mathrm{ampl}} = 20$, 40, 60 and 80 kPa was varied. An overall view of the tested sequences is given in Figure 5.98.

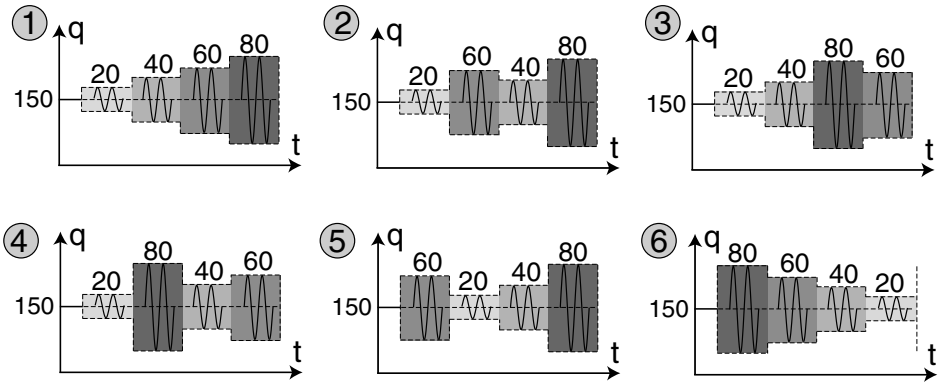

Figure 5.98: *Tested sequences of the amplitudes q^{ampl} = 20, 40, 60 and 80 kPa*

Figure 5.99 presents the q-ε_1-hystereses of the six tests. The diagram 5.99d with the test $20 \rightarrow 80 \rightarrow 40 \rightarrow 60$ makes clear, that a package with small cycles (here $q^{\mathrm{ampl}} = 20$ kPa) increases the stiffness during a subsequent monotonic loading (in this case an increased stiffness was observed until a deviatoric stress $q \approx q^{\mathrm{av}} + 3q^{\mathrm{ampl}} = 210$ kPa was reached). In that part of the stress-strain path, the stiffness during monotonic loading is approximately identical with the secant stiffness during the previous cycles. This increase of stiffness reduces dramatically the residual strain in the first cycle of a subsequent package with larger amplitudes (here $q^{\mathrm{ampl}} = 80$ kPa). Thus, the residual strains in the first cycles of each package are very small for a sequence $20 \rightarrow 40 \rightarrow 60 \rightarrow 80$ (Figure 5.99a). The earlier the packages with large amplitudes are applied the larger are the residual deformations in their first cycles.

Figure 5.100 shows the curves of the strain amplitudes with N in the two tests with the sequences $20 \rightarrow 40 \rightarrow 60 \rightarrow 80$ and $80 \rightarrow 60 \rightarrow 40 \rightarrow 20$. For larger stress amplitudes $q^{\mathrm{ampl}} \geq 60$ kPa a decrease of the strain amplitude $\varepsilon^{\mathrm{ampl}}$ with N at the beginning of a package could be observed only, if no larger amplitude q^{ampl} than the actual one was applied in the previous packages.

In Figure 5.101a, the development of the residual strain $\varepsilon^{\mathrm{acc}}$ including the strain in the first cycles is depicted. The residual strain at the end of the fourth package was the larger, the earlier the packages with $q^{\mathrm{ampl}} \geq 60$ kPa were applied. This can be attributed to the larger residual strains in the first cycles (Figure 5.99). If one subtracts the strains

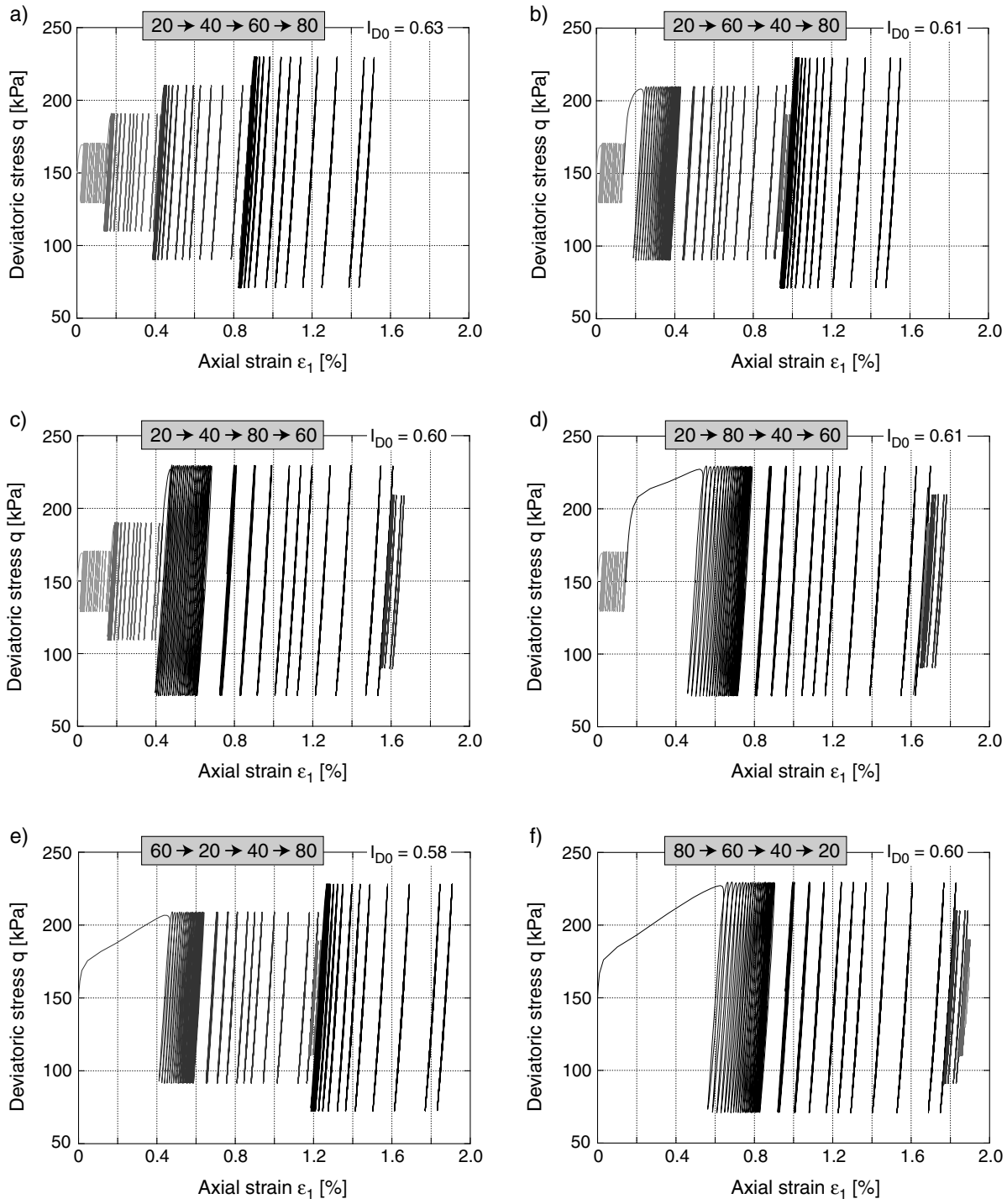

Figure 5.99: *q-ε_1-hystereses in six tests with packages of cycles with amplitudes q^{ampl} = 20, 40, 60 and 80 kPa in different sequences (p^{av} = 200 kPa, η^{av} = 0.75, f_B = 0.25 Hz)*

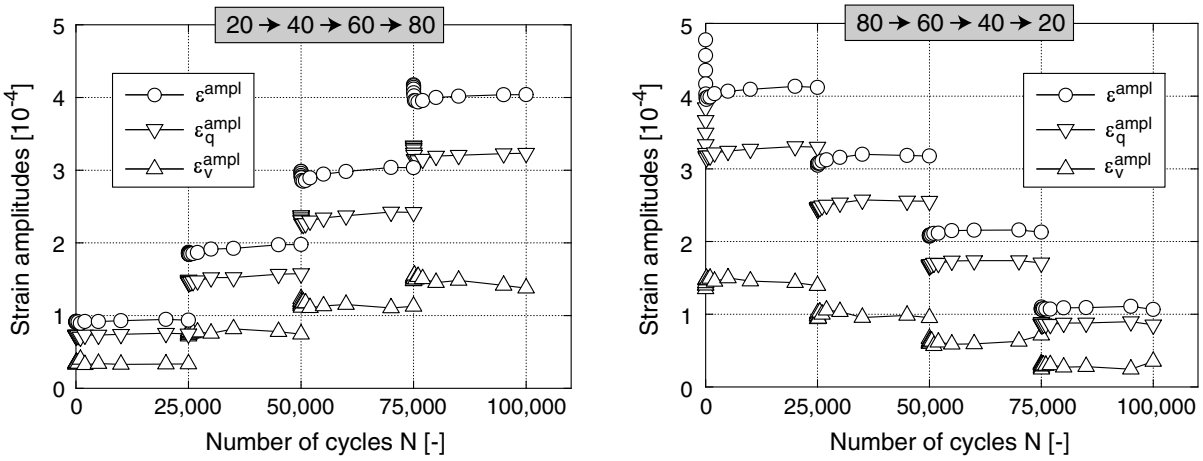

Figure 5.100: *Strain amplitudes as a function of the number of cycles N in two tests with packages of cycles with different sequences (p^{av} = 200 kPa, η^{av} = 0.75, f_B = 0.25 Hz)*

in the first cycles of each package, Figure 5.101b is obtained. In Figure 5.101b the strain accumulation runs the faster the later the packages with the large amplitudes are applied. The slower accumulation in the tests with an early application of the large amplitudes can be explained with the larger densification in the first cycles. This causes smaller void ratios and thus smaller accumulation rates at the beginning of the subsequent cycles.

In general, from Figure 5.101 it can be concluded, that the difference of the residual strains at the end of the tests due to a different sequence of the packages is only moderate. This observations coincides with the tests of Kaggwa et al. [69] (for small numbers of cycles $N_{\max} = 50$ per package, Section 3.2.2.10). Thus, as long the polarization of the cycles is constant, the Miner's rule [96] (Section 3.2.2.10) is approximately applicable to sand. If in a FE calculation with an explicit accumulation model a random cyclic loading is replaced by packages of cycles each with a constant amplitude (Figure 5.97), the influence of the sequence of these packages on the final value of the residual deformation can be neglected.

Further tests with packages of cycles were presented by Wichtmann et al. [177] and Canbolat [16].

5.2.8 Influence of a static (monotonic) preloading

Six cyclic triaxial tests were performed to study, if beside a *cyclic* preloading also a *monotonic* preloading affects the accumulation rate under cyclic loading. Starting from p = 50 kPa, the stress was increased along a line in the p-q-plane with an inclination $\eta = 0$ (p-axis) or η = 0.75 (corresponds to K_0 = 0.5) towards a preloading pressure p_{preload}. After a period of 5 minutes the stress was reduced along the same stress path towards p^{av}

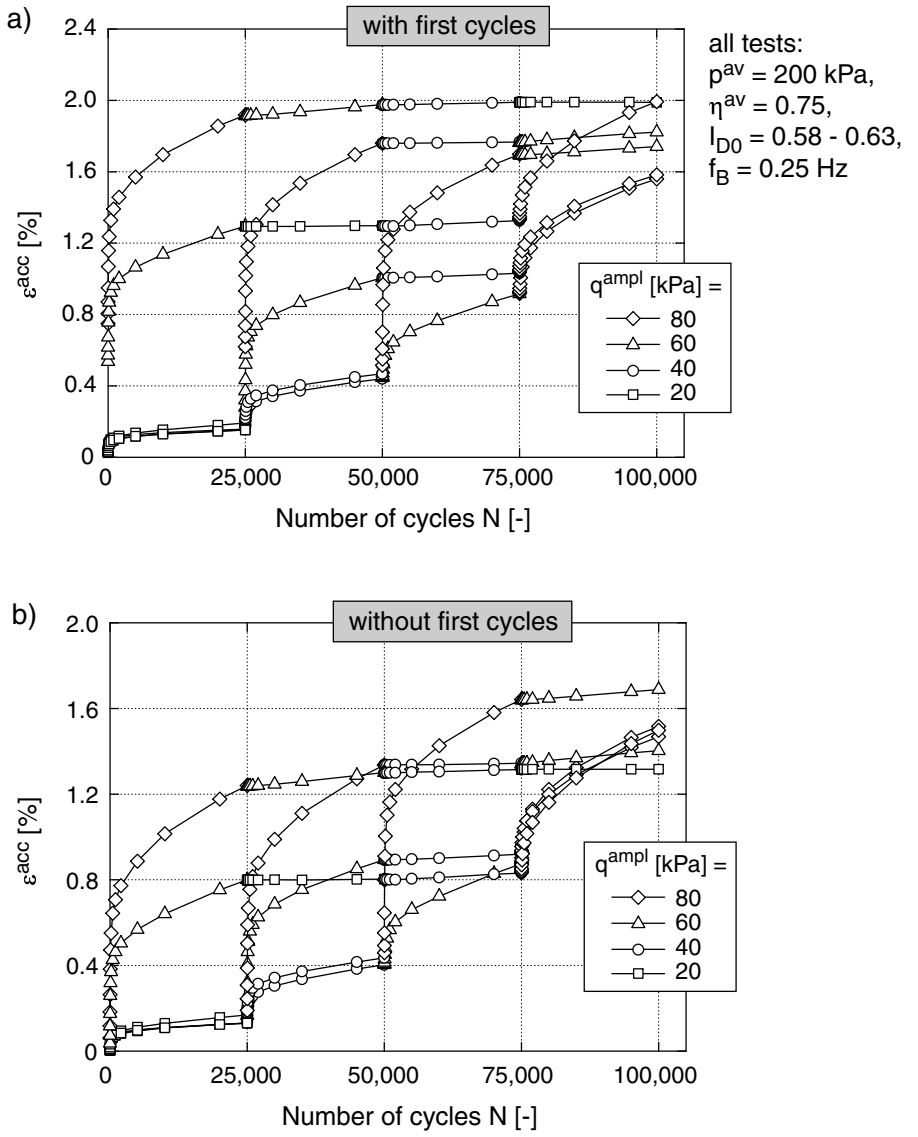

Figure 5.101: *Accumulation curves $\varepsilon^{acc}(N)$: a) with and b) without the residual strains in the first cycles, six tests with packages of cycles with amplitudes q^{ampl} = 20, 40, 60 and 80 kPa in different sequences*

= 100 kPa. At $p^{av} = 100$ kPa and $\eta^{av} = 0$ or $\eta^{av} = 0.75$, 10^4 cycles with $q^{ampl} = 50$ kPa were applied. Preloading pressures $p_{preload} = 100$ (no monotonic preloading), 200 and 300 kPa were tested. A breakage of the grains could not be expected for these pressures. The volumetric ($\varepsilon_{v,preload}$) and the deviatoric ($\varepsilon_{q,preload}$) strains, which remained in the material after the monotonic preloading, are given in the legends of Figure 5.102.

Figure 5.102 shows the accumulation curves $\varepsilon^{acc}(N)$ after the monotonic preloading in the six tests. In both cases, the isotropic (Figure 5.102a) and the K_0-preloading (Figure 5.102b), the curves $\varepsilon^{acc}(N)$ of the non-preloaded specimens and the specimens preloaded

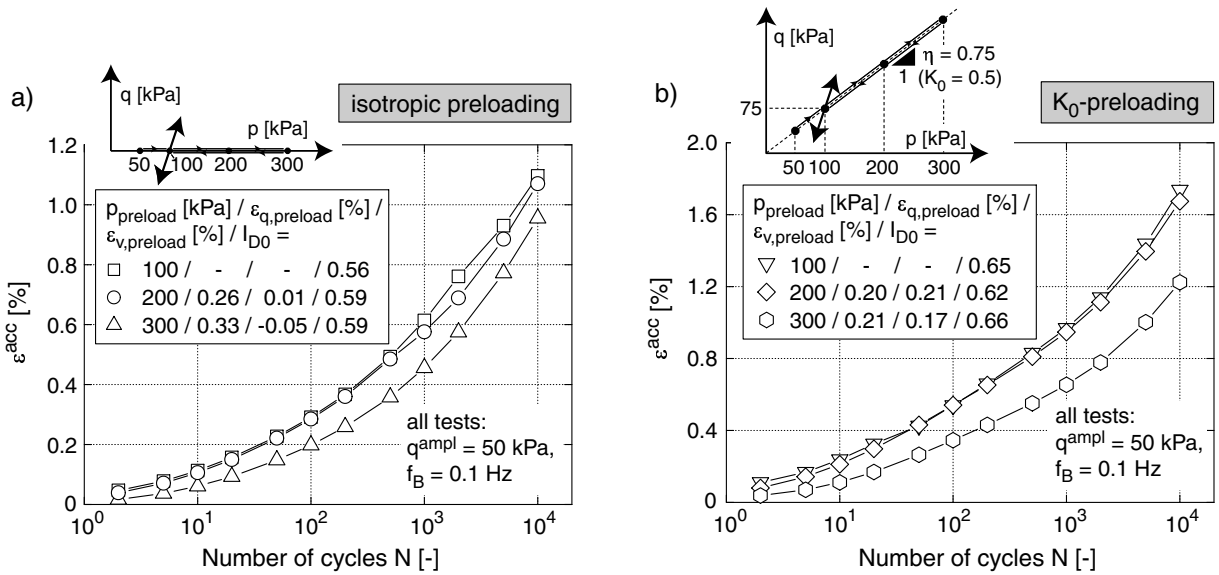

Figure 5.102: *Accumulation curves $\varepsilon^{acc}(N)$ after a) monotonic isotropic preloading and b) monotonic K_0-preloading*

with $p_{\mathrm{preload}} = 200$ kPa do hardly differ. The accumulation rates in the tests with p_{preload} = 300 kPa were slightly lower compared to the tests with $p_{\mathrm{preload}} = 100$ and 200 kPa. The similar initial densities I_{D0} given in Figure 5.102 allow the conclusion, that the reduction of the accumulation rate for larger preloading pressures p_{preload} cannot be attributed to smaller initial void ratios after preloading. A change of the fabric of the grain skeleton is more likely.

However, the accumulation rate is much less affected by a monotonic preloading than by a cyclic one. Eventually, the polarization of the monotonic preloading in comparison to the direction of the cycles is of importance. Additional tests with an identical polarization of the stress path during monotonic preloading and the stress path during the cycles would be interesting. A more significant reduction of $\dot{\varepsilon}^{\mathrm{acc}}$ due to the monotonic preloading may be observed in that case.

5.2.9 Influence of the grain size distribution curve

The tests presented in the previous Sections 5.2.1 to 5.2.8 were all performed on the poorly graded sand with the grain size distribution curve No. 3 ($d_{50} = 0.55$ mm, $U = d_{60}/d_{10} = 1.8$) referring to Figure 4.14. These tests were supplemented by experiments on sand with the grain size distribution curves Nos. 2 and 5 (Figures 4.14 and 4.15), which have a similar non-uniformity index $1.4 \leq U \leq 1.8$ but different mean grain diameters 0.35 mm $\leq d_{50} \leq$ 1.45 mm. In further tests also sand with the well-graded grain size

distribution curve No. 7 ($U = 4.5$, $d_{50} = 0.52$ mm, Figures 4.14 and 4.15) was cyclically loaded. The mean grain diameters of the grain size distribution curves Nos. 7 and 3 are similar. Analogously to the tests described in Section 5.2.1.1, eight further tests were performed on each of the sands Nos. 2, 5 and 7. The average stress was kept constant ($p^{\mathrm{av}} = 200$ kPa, $\eta^{\mathrm{av}} = 0.75$) and the stress amplitude (13 kPa $\leq q^{\mathrm{ampl}} \leq$ 87 kPa) was varied.

In analogy to Figure 5.22, Figure 5.103 presents the curves $\varepsilon^{\mathrm{ampl}}(N)$ and the amplitudes $\varepsilon_v^{\mathrm{ampl}}$, $\varepsilon_q^{\mathrm{ampl}}$, $\varepsilon^{\mathrm{ampl}}$ and γ^{ampl} (mean values over 10^5 cycles) as a function of the stress amplitude q^{ampl}. Similar to sand No. 3, a decrease of the strain amplitude in the range $N \leq 100$ was measured for the sands Nos. 2 and 7. In the tests on the coarse sand No. 5 $\varepsilon^{\mathrm{ampl}}$ remained almost constant during 10^5 cycles. This can be explained with the larger secant stiffness of the stress-strain-hysteresis of sand No. 5, resulting in smaller strain amplitudes. The strain amplitude in the test with $q^{\mathrm{ampl}} = 77$ kPa e.g. amounted only to $\varepsilon^{\mathrm{ampl}} \approx 3 \cdot 10^{-4}$. For similar strain amplitudes, an almost constant course of $\varepsilon^{\mathrm{ampl}}$ with N was measured also for the sands Nos. 2, 3 and 7. The linear relationship between the stress amplitude q^{ampl} and the strain amplitudes $\varepsilon_v^{\mathrm{ampl}}$, $\varepsilon_q^{\mathrm{ampl}}$, $\varepsilon^{\mathrm{ampl}}$ and γ^{ampl} is valid independently of the grain size distribution curve (Figure 5.103b,d,f).

A comparison of the strain amplitudes $\varepsilon^{\mathrm{ampl}}$, measured for the four tested grain size distributions, is given in Figure 5.104a. For an identical stress amplitude q^{ampl} and $I_D \approx$ constant the smallest strain amplitudes were measured for sand No. 5 ($d_{50} = 1.45$ mm), followed by sand No. 3 ($d_{50} = 0.55$ mm) and sand No. 2 ($d_{50} = 0.35$ mm). Thus, the secant stiffness increases with the mean grain diameter d_{50} for $I_D \approx$ constant (but: $e \neq$ constant). The lower initial densities in the tests on sand No. 3 ($0.58 \leq I_{D0} \leq 0.61$) in comparison to the experiments on sands Nos. 2, 5 and 7 ($0.62 \leq I_{D0} \leq 0.72$) should be considered. The strain amplitudes of the well-graded sand No. 7 lay only slightly above those of sand No. 2.

For $N = 1$, the secant shear modulus $G_{\mathrm{hyst}} = \tau^{\mathrm{ampl}}/\gamma^{\mathrm{ampl}} = q^{\mathrm{ampl}}/(2\gamma^{\mathrm{ampl}})$ was determined. In Figure 5.104b it is plotted versus the shear strain amplitude. The values of the cyclic triaxial tests are compared with curves from RC tests ($p = 200$ kPa and similar initial densities). The congruence of the results from RC tests and cyclic triaxial tests is satisfactory for the sands Nos. 2, 3 and 7. The deviations are larger for sand No. 5, whereas both types of tests show the same tendency, i.e. the largest stiffness for sand No. 5. Here specimens with $I_D \approx$ constant were considered. However, it is well-known, that the secant stiffness of the stress-strain-hysteresis correlates with the void ratio e rather than with I_D. Remarks on the dependence of the secant stiffness on the grain size distribution curve at $e =$ constant follow in Section 5.2.9.1.

The increase of the residual strain $\varepsilon^{\mathrm{acc}}$ with the number of cycles N for the four tested

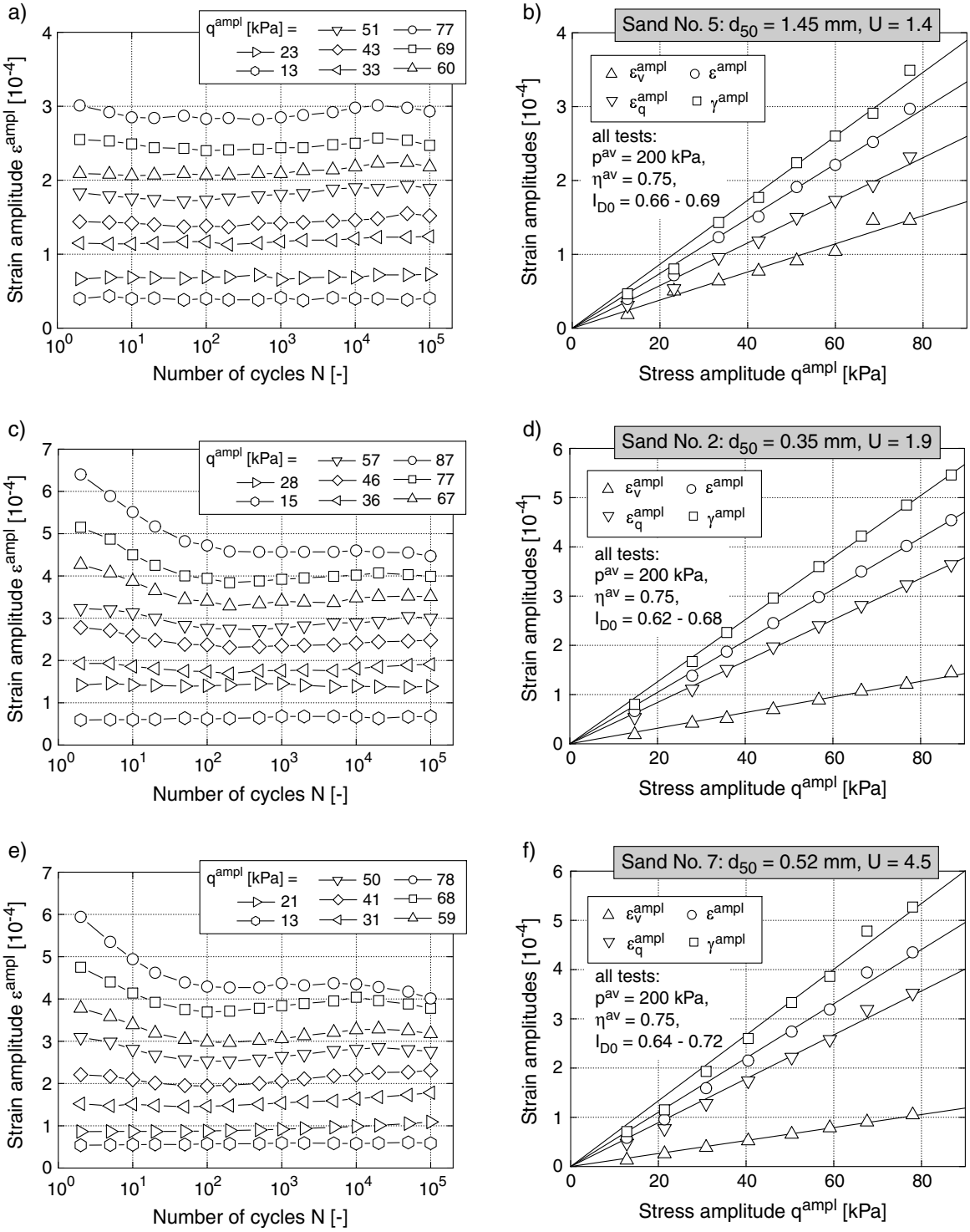

Figure 5.103: *Development of the strain amplitude ε^{ampl} with the number of cycles N and mean values of the strain amplitudes over 10^5 cycles as a function of the stress amplitude for sands Nos. 2, 5 and 7*

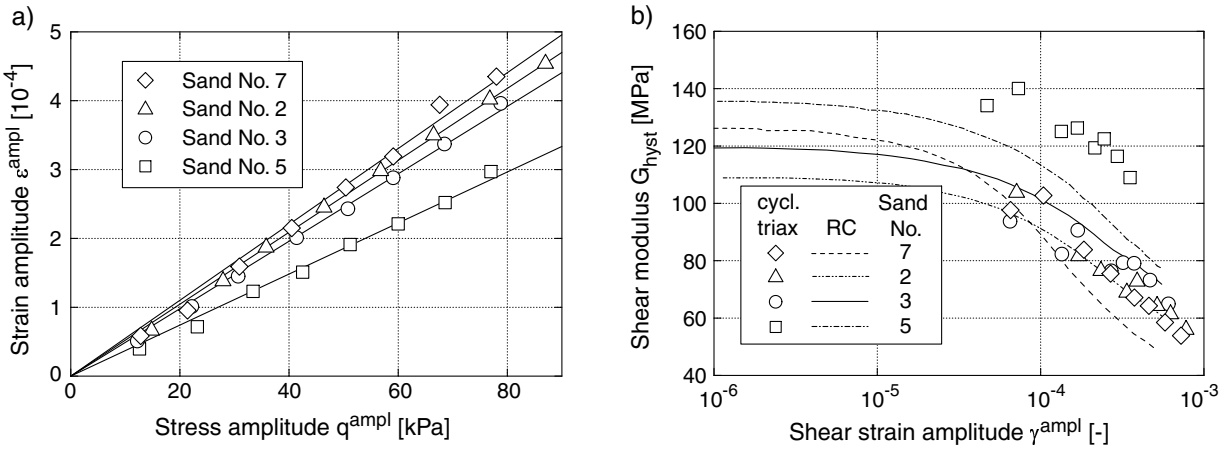

Figure 5.104: *a) Comparison of the strain amplitudes $\varepsilon^{ampl}(q^{ampl})$ and b) the secant shear stiffness $G_{hyst}(\gamma^{ampl})$ for the four tested grain size distributions*

sands is depicted in Figure 5.105. Diagram 5.105b repeats Figure 5.23 for sand No. 3 in order to facilitate comparison. As expected, the accumulation of residual deformations runs faster with increasing stress amplitude for all tested grain size distribution curves. However, the shape of the curves $\varepsilon^{acc}(N)$ (function f_N) is different.

The accumulation rate is significantly influenced by the grain size distribution curve. Figure 5.106a compares the residual strains of the poorly-graded sands Nos. 2, 3 and 5 ($1.4 \leq U \leq 1.9$) in tests with similar initial densities and strain amplitudes. The accumulation rate decreases with increasing mean grain diameter d_{50}. After $N = 10^5$ cycles, the residual strain of sand No. 2 ($d_{50} = 0.35$ mm) was approx. 1.3 times larger than that of sand No. 3 ($d_{50} = 0.55$ mm) and approx. 3 times larger than for sand No. 5 ($d_{50} = 1.45$ mm). Figure 5.106b compares the residual strains of the sands Nos. 3 and 7 with a similar mean grain diameter (0.52 mm $\leq d_{50} \leq 0.55$ mm). The accumulation rate increases significantly with the non-uniformity index U of the grain size distribution curve. After $N = 10^5$ cycles, the residual strain of the well-graded sand No. 7 ($U = 4.5$) was approx. 6 times larger than for the poorly-graded sand No. 3 ($U = 1.8$). The smaller grains serve as a kind of "ball bearing" for the larger ones. This facilitates a re-distribution of the grains.

Until now, no sufficient amount of data for the sands Nos. 2, 5 and 7 is available in order to determine the constants of the functions f_e, f_p, f_Y and f_N. For this reason, the accumulated strains in Figure 5.106 were not normalized with $\bar{f}_e$ in order to consider the different densification rates. Such normalization would even amplify the discrepancy between the accumulation rates of the four tested sands.

The observed increase of the accumulation rate with decreasing mean grain diameter d_{50}

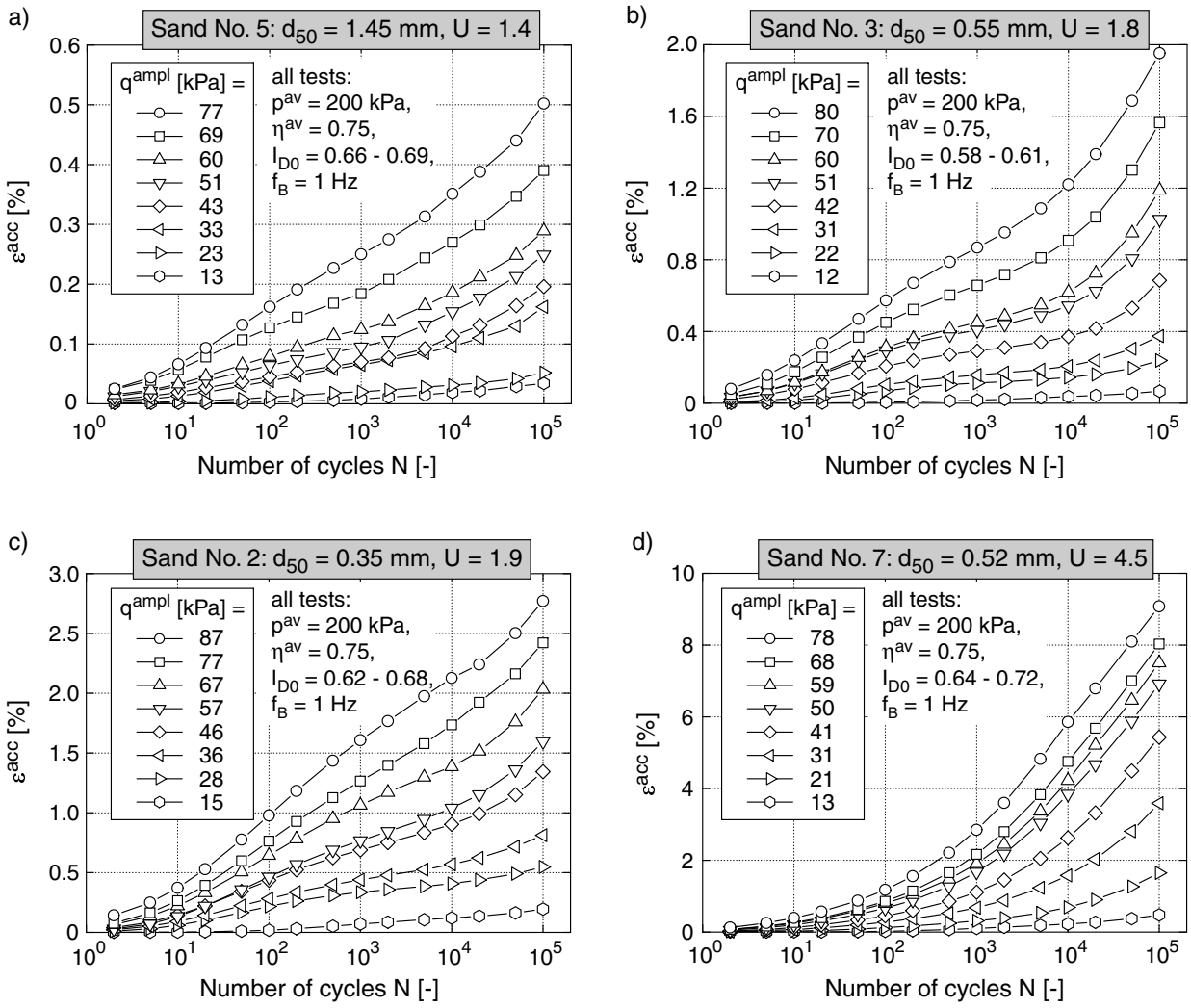

Figure 5.105: *Accumulation curves $\varepsilon^{acc}(N)$ for the four tested grain size distribution curves*

confirms several reports in the literature (Section 3.2.2.12). The increase of $\dot{\varepsilon}^{\mathrm{acc}}$ with the non-uniformity index U of the grain size distribution curve supports in-situ observations during vibratory compaction. According to practical experience for a similar induced energy, a well-graded sand can be compacted easier than a poorly-graded one.

The influence of the grain size distribution curve, the grain shape and the content of fines (the latter two influences were not tested up to now) are considered in the accumulation model (Chapter 7) by using different sets of material constants. The tests presented in this section are part of a larger (not yet completed) test series with the aim to determine the material constants for sands with different grain characteristics. An attempt will be made to correlate the material constants with the grain characteristics or the granulometric properties. Eventually, some constants are even independent of the granulometry or can

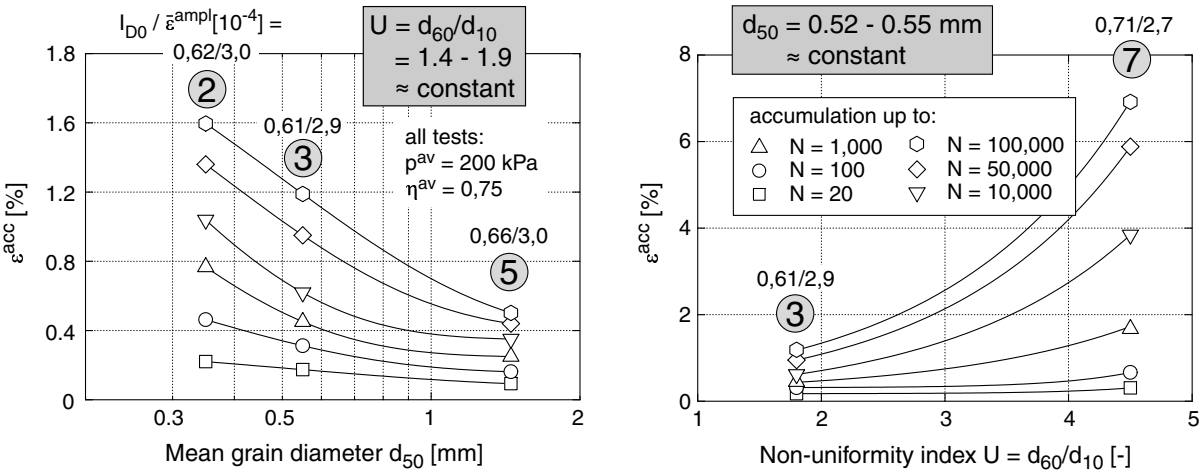

Figure 5.106: *Dependence of the accumulated strain on a) the mean grain diameter d_{50} and b) the non-uniformity index $U = d_{60}/d_{10}$: tests with similar values of I_{D0} and $\bar{\varepsilon}^{ampl}$*

be correlated with index parameters (e.g. C_e with $e_{\min}$ according to DIN 18126). For the future, a determination of a set of material constants with as few tests as possible is desirable.

5.2.9.1 Remarks on the dependence of the secant stiffness on the grain size distribution curve

The cyclic triaxial tests were accompanied by RC tests with material having the seven grain size distribution curves shown in Figures 4.14 and 4.15. The influence of the granulometry on the secant stiffness of the stress-strain-hysteresis was studied. In Figure 5.107a, the secant shear modulus at small strains $G_{\text{hyst},0}$ is plotted versus the void ratio e for soils Nos. 1, 3, 6 and 7 and $p = 100$ kPa. The shear moduli of the poorly-graded soils Nos. 1, 3 and 6 ($1.3 \leq U \leq 1.8$) agree well. They are not affected by the strongly different mean grain diameters (0.15 mm $\leq d_{50} \leq$ 4.4 mm). At an identical void ratio, the shear moduli of the well-graded sand No. 7 ($U = 4.5$) are only half as large as the values of the poorly-graded soils. The shear moduli of the well-graded sand are strongly overestimated by Equation (3.5). The test results agree well with observations of Iwasaki & Tatsuoka [67] (Section 3.3, Figure 3.34).

For all poorly-graded soils the exponent n of the relationship $G_{\text{hyst},0} \sim p^n$ was determined to $0.40 \leq n \leq 0.46$ (Figure 5.107b), i.e. n is almost independent of d_{50}. In the case of the well-graded sand No. 7, the secant shear modulus increased faster with increasing pressure ($n = 0.55$). Furthermore, the decrease of G_{hyst} with the shear strain amplitude γ^{ampl} was faster for the well-graded sand No. 7 than for the poorly-graded soils (Wichtmann &

Triantafyllidis [181]).

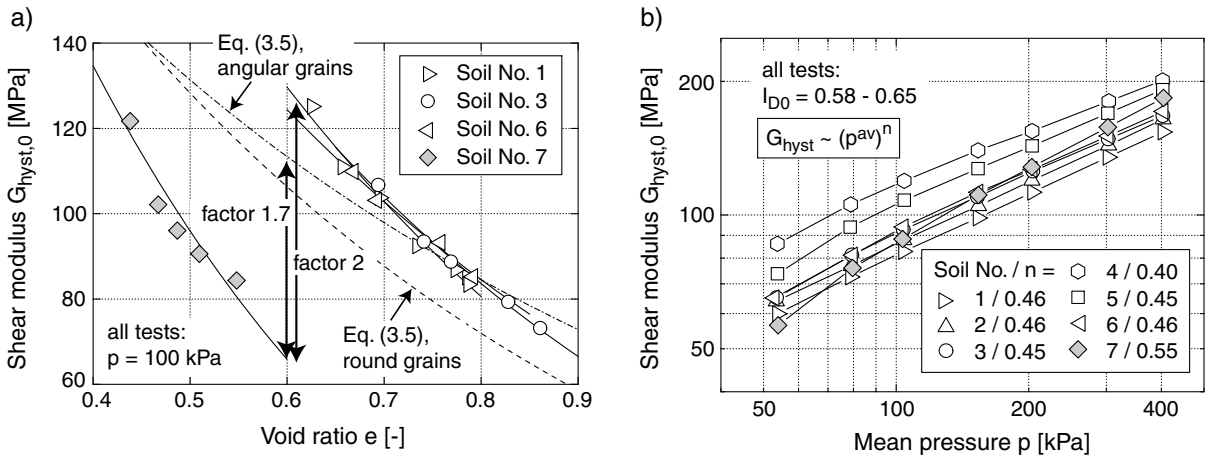

Figure 5.107: *Secant shear modulus $G_{hyst,0}$ for granular soils with different grain size distributions: a) curves $G_{hyst,0}(e)$, b) curves $G_{hyst,0}(p)$*

Chapter 6

Discussion of explicit accumulation models in the literature

In the following, four explicit accumulation models for non-cohesive soils under cyclic loading proposed in the literature are presented and discussed. The first one is the model of Sawicki & Świdziński [133, 134] which served as the origin of the development of the model to be presented in Chapter 7. After that, the model of Bouckovalas et al. [11] is reviewed, which in the authors's opinion (despite some shortcomings) is the completest accumulation model in the literature so far. Some aspects of the model in [11] can be also found in the model in Chapter 7. The model of Marr & Christian [94] is presented since it is cited in the literature several times. The model of Gotschol [35, 36], another model recently developed in Germany is also discussed. Other models (e.g. Güttler [41], Diyaljee & Raymond [26], Kaggwa et al. [69]) are considered in the final judgement in Section 6.2, but not discussed in detail. The models are appraised with respect to the correct and complete description of the material behaviour which was observed in the element tests in the literature (Chapter 3) and in the own experiments (Chapter 5).

6.1 Presentation and discussion of the models

6.1.1 Model of Sawicki & Świdziński

Sawicki & Świdziński [133, 134] formulated a model describing the densification of sand under cyclic shearing. The model is based on the so-called common compaction curve

$$\Phi(\tilde{N}) \;=\; C_1 \;\ln(1 + C_2\tilde{N}) \tag{6.1}$$

(see Section 3.2.2.2) with the state variable "compaction" $\Phi = \Delta n/n_0$ (n: porosity), the number of cycles weighted by the amplitude

$$\tilde{N} \;=\; \int J \; \mathrm{d}N \;=\; \int \frac{1}{2} \; \|{\boldsymbol{\varepsilon}_{\mathrm{ampl}}}^*\|^2 \; \mathrm{d}N \;=\; \frac{1}{4}(\gamma^{\mathrm{ampl}})^2 N \tag{6.2}$$

and the material constants C_1 and C_2. In Equation (6.2), the tensor $\boldsymbol{\varepsilon}^{\mathrm{ampl}}$ contains the amplitudes of the particular strain components, i.e. $\varepsilon_{ij}^{\mathrm{ampl}} = (\varepsilon_{ij})^{\mathrm{ampl}}$ holds. The latter transformation in Equation (6.2) is valid for the case of cyclic simple shear tests with a constant shear strain amplitude γ^{ampl}, which were performed by Sawicki & Świdziński [133, 134]. The compaction rate $\dot{\Phi} = \partial\Phi/\partial N$ is obtained from Equation (6.1):

$$\dot{\Phi} \;=\; \frac{C_1 C_2 J}{1 + C_2 \tilde{N}} \;=\; C_1 C_2 J \exp\left(-\Phi/C_1\right) \tag{6.3}$$

The model of Sawicki & Świdziński is based on tests with a relatively low number of cycles ($N < 10^3$). A major deficit of the model is, that only the volumetric accumulation but not the deviatoric one is described. The volumetric portion ($\varepsilon_v^{\mathrm{ampl}}$) and the shape of the strain loop (OOP-cycles) are not considered. A dependence of the accumulation rate on the average stress is not included in this model. The influence of the void ratio is considered only via different constants C_1 and C_2. Beneficial (see Section 5.2.6) is the usage of a measure of the historiotropy which weights the number of cycles with their amplitudes. However, in Figure 5.95 it was demonstrated that the state variable $\tilde{N}$ does not correctly describe the accumulation in cyclic triaxial tests with a large number of cycles.

6.1.2 Model of Bouckovalas et al.

The model of Bouckovalas et al. [11] describes both, the accumulation of volumetric and the accumulation of deviatoric strains. For the corresponding rates the following equations were proposed:

$$\dot{\varepsilon}_v^{\mathrm{acc}} \;=\; A \; (2\gamma^{\mathrm{ampl}})^a \; I^c \; f \tag{6.4}$$

$$\dot{\varepsilon}_q^{\mathrm{acc}} \;=\; \pm B \; (\eta^{\mathrm{av}}/2)^b \; (2\gamma^{\mathrm{ampl}})^a \; I^c \tag{6.5}$$

In Equation (6.5) the positive sign is valid for $\eta^{\mathrm{av}} \geq 0$ and the negative one for $\eta^{\mathrm{av}} < 0$. A, B, a, b and c are material constants. The dependence of the accumulation rates on the historiotropy is expressed by the state variable

$$I \;=\; \int_0^N [2\gamma^{\mathrm{ampl}}(N)]^a \; N^c \; \mathrm{d}N \tag{6.6}$$

For cycles with a constant shear strain amplitude, the rates are proportional to $N^{c(c+1)}$. The parameter f in Equation (6.4) is stress-dependent. It takes the value 1 on the p-axis and is zero on the critical state line.

The model of Bouckovalas & Whitman [11] predicts the cyclic flow rule correctly: $\dot{\varepsilon}_v^{\mathrm{acc}}$ vanishes on the critical state line while $\dot{\varepsilon}_q^{\mathrm{acc}}$ becomes zero at $\eta^{\mathrm{av}} = 0$. A power law is used for the dependence of the accumulation rates on the number of cycles. The prediction of an increase of $\dot{\varepsilon}^{\mathrm{acc}}$ with increasing amount of the average stress ratio $|\eta^{\mathrm{av}}|$ coincides with the own experimental results. The model uses a state variable for the historiotropy which considers also the amplitude of the cycles. The constant $a = 3$ is chosen in [11], i.e. the model delivers a too strong amplitude-dependence $\dot{\varepsilon}^{\mathrm{acc}} \sim (\varepsilon^{\mathrm{ampl}})^3$ compared to $\dot{\varepsilon}^{\mathrm{acc}} \sim (\varepsilon^{\mathrm{ampl}})^2$ measured in own tests. The volumetric portion ($\varepsilon_v^{\mathrm{ampl}}$) and the shape of the strain loop are not considered. Also the influences of the average mean pressure and the void ratio are not captured. The rather bad documentation of the model in [11] has to be criticized. The mathematical definition of the factor f remains vague. The material constant $c = -1.5$ given in [11] leads to complex values of I^c.

6.1.3 Model of Marr & Christian

The model of Marr & Christian [94] describes the accumulation of the volumetric and the vertical strain with the power laws

$$\dot{\varepsilon}_v^{\mathrm{acc}} = \eta^{*\mathrm{av}}\, C_v\, D_v\, {N_e}^{D_v - 1} \qquad \dot{\varepsilon}_1^{\mathrm{acc}} = \eta^{*\mathrm{av}}\, C_1\, D_1\, {N_e}^{D_1 - 1}, \tag{6.7}$$

wherein the strain at $N = 1$ is the one at the end of the first cycle. Marr & Christian [94] described the state of stress by $p^* = (\sigma_1 + \sigma_3)/2$, $q^* = (\sigma_1 - \sigma_3)/2$, $\eta^* = q^*/p^*$ and $\zeta^* = q^{*\mathrm{ampl}}/p^{*\mathrm{av}}$. In Equation (6.7) C_v, D_v, C_1 and D_1 are material constants. A weighted number of cycles N_e is defined as

$$N_e = N\, C_n\, C_\zeta\, C_p \tag{6.8}$$

The factors C_n, C_ζ and C_p consider the influence of the initial porosity n_0, the stress amplitude and the average mean pressure:

$$C_n = 10^{\frac{n_0 - n_{\mathrm{ref}}}{d}} \qquad C_\zeta = 10^{\frac{\zeta^* - \zeta^*_{\mathrm{ref}}}{a}} \qquad C_p = 10^{\frac{p^{*\mathrm{av}} - p^*_{\mathrm{ref}}}{b}} \tag{6.9}$$

These factors are based on n_0-N-, ζ^*-N- and $p^{*\mathrm{av}}$-N-diagrams which show curves $\varepsilon_v^{\mathrm{acc}} =$ constant or $\varepsilon_1^{\mathrm{acc}} =$ constant, respectively. Such diagrams are presented in Figure 3.20c,d for $p^{*\mathrm{av}}$. The material constants a, b and d conform to the inclination of these curves. Different constants have to be chosen for $\dot{\varepsilon}_v^{\mathrm{acc}}$ and $\dot{\varepsilon}_1^{\mathrm{acc}}$, i.e. N_e is not identical for the

volumetric and the axial strain. Instead of the strain amplitude the model uses the stress amplitude as an input parameter. An equivalent number of cycles N_{eq} is used to describe packages of cycles. Prior to the calculation of the next package of cycles with a definite amplitude, the cycles in the past are converted into N_{eq} cycles with the actual amplitude.

Since equations for $\dot{\varepsilon}_v^{\mathrm{acc}}$ and $\dot{\varepsilon}_1^{\mathrm{acc}}$ are given, the deviatoric rate $\dot{\varepsilon}_q^{\mathrm{acc}}$ can be determined. The different sets of material constants for the volumetric and the axial rate resulting in different values of the weighted number of cycles N_e seem not to make much sense. The prediction of a vanishing accumulation rate for an isotropic average stress ($\eta^{\mathrm{av}} = 0$) is obviously false, although the model captures the increase of the accumulation rate with the average stress ratio η^{av}. The cyclic flow rule is described erroneously (increase of $\dot{\varepsilon}_v^{\mathrm{acc}}$ with η^{av}). The increase of the accumulation rate with increasing stress amplitude and increasing initial porosity is captured. The predicted acceleration of accumulation with increasing average mean pressure appears doubtful regarding the own experimental results. The consideration of the historiotropy by using an equivalent number of cycles (see also the model of Kaggwa et al. [69]) is cumbersome.

6.1.4 Model of Gotschol

The model of Gotschol [35, 36] was developed for the prediction of deformations in the subsoil of railways. The model describes the accumulation of vertical strains for the special case of a cyclic loading with a constant lateral stress σ_3 and a vertical stress which oscillates between $\sigma_1 = \sigma_3$ and $\sigma_1 = \sigma_3 + 2\sigma_1^{\mathrm{ampl}}$. The residual vertical strain is described by a power law ($N = 1$: end of the first cycle):

$$\varepsilon_1^{\mathrm{acc}}(N) \;=\; \varepsilon_1^{\mathrm{acc}}(N=1)\; N^{\alpha} \tag{6.10}$$

The residual strain after N cycles depends on the strain in the first cycle. For $\varepsilon_1^{\mathrm{acc}}(N = 1)$ and the factor α the following functional dependencies were formulated (M = mineralogy):

$$\varepsilon_1^{\mathrm{acc}}(N=1) \;=\; f(f_B, X, \sigma_3, e, M) \qquad\qquad \alpha \;=\; f(f_B, X, \sigma_3, M) \tag{6.11}$$

The relative complex equations of $\varepsilon_1^{\mathrm{acc}}(N = 1)$ and α are not repeated here, they are given e.g. in [35]. The stress amplitude is described by a "cyclic-dynamic stress ratio" $X = 2\sigma_1^{\mathrm{ampl}}/q_f$, wherein q_f is the deviatoric failure stress for monotonic loading. Beside an increase of the stress amplitude, an increase of X means also an increase of p^{av} and q^{av}. For the system of equations given by (6.11), a total of 21 material constants were introduced. However, their values are neither given in [35] nor in [36]. Beside the plastic strains, the elastic portion of deformation is described by a similar system of equations.

The extrapolation of the accumulation rates in the subsequent cycles out of the first cycle was used by several authors to describe element or model tests (e.g. Diyaljee & Raymond [26], Hettler [52, 53]). In situ the soil has sustained a cyclic preloading, i.e. the cyclic loading does not start with the "first cycle". Thus, a model or settlement law of the shape (6.10) should be formulated consistently. If the residual strain between the cycles N_a and N_b is searched for, it should be of no importance, if the calculation extrapolates this strain from the first cycle or from cycle No. N_a. For all models of type (6.10) proposed in the literature, this condition is not fulfilled (Niemunis & Wichtmann [108]).

The model of Gotschol [35, 36] predicts only the accumulation of the vertical strain. Only the special case of uniaxial cycles with a minimum stress on the p-axis is described. The coupling of the stress amplitude with the average stress in the variable X can be seen as a disadvantage with respect to a generalization of the model. Within the models presented in this chapter, the model of Gotschol [35, 36] is the only one which considers an influence of the loading frequency f_B in its constitutive relations. This contradicts most of the experimental work in the literature (Section 3.2.2.8) and also the own test results (Section 5.2.5). Furthermore, the number of material constants is large compared to other models.

6.2 Comparison of the models and conclusion

Finally, in Table 6.2 the four presented accumulation models of Sawicki & Świdziński [133, 134], Bouckovalas et al. [11], Marr & Christian [94] and Gotschol [35, 36] and additionally the models of Güttler [41], Diyaljee & Raymond [26] and Kaggwa et al. [69] are compared. The assessment criteria are the prediction of the volumetric ($\dot{\varepsilon}_v^{\mathrm{acc}}$) *and* the deviatoric ($\dot{\varepsilon}_q^{\mathrm{acc}}$) strain rate, the description of the cyclic flow rule, the correct consideration of the main influencing parameters and the usage of a meaningful state variable for the historiotropy. A correct material description is denoted by "+" and a partially correct or cumbersome one is indicated by "○". For a false description or a non-consideration of an aspect or an influencing parameter "-" is used. If an assessment could not be made, due to missing material constants or due to the fact that the model was developed for a special case only, this is denoted by "*". Furthermore, Table 6.2 summarizes which type of element test was used to establish the explicit equations (DT = drained triaxial test, SS: simple shear test) and how many cycles were applied in these tests.

While several models deliver equations for the deviatoric *and* the volumetric rate, the cyclic flow rule is described correctly only by the model of Bouckovalas et al. [11]. The volumetric portion of the strain loop and the shape of the cycles are considered by none of

the seven models. Also none of the models captures the influence of the state variables void ratio and average stress as it was observed in the tests documented in Sections 5.2.3 and 5.2.4. Mostly the historiotropy is captured by the number of cycles N or a cumbersome equivalent number of cycles. The variable $\tilde{N}$ proposed by Sawicki & Świdziński [133, 134] was disproved in own experiments. In the case of the historiotropic variable defined by Bouckovalas et al. [11], the given material constants irritate and thus no assessment could be made.

The assessment of the models yet proposed in the literature in Table 6.2 makes clear that a need for an explicit model exists which delivers the accumulation rates of the volumetric *and* the deviatoric strain, which describes the cyclic flow rule and considers correctly all relevant influencing parameters. The accumulation model presented in Chapter 7 has this aim. It was developed on the basis of the element tests presented in Chapter 5.

Criteria		Model						
		Sawicki & Świdziński [133, 134]	Bouckovalas et al. [11]	Marr & Christian [94]	Gotschol [35, 36]	Kaggwa et al. [69]	Güttler [41]	Diyaljee & Raymond [26]
Description of $\dot{\varepsilon}_v^{\mathrm{acc}}$ and $\dot{\varepsilon}_q^{\mathrm{acc}}$		-	+	+	-	+	+	-
cyclic flow rule		-	+	-	-	-	-	-
N-dependence: $\varepsilon^{\mathrm{acc}} \sim$		$\ln(1+c\tilde{N})$	N^c	N^c	N^c	N^c	$1+c\log(N)$	N^c
Consideration of the influencing parameters	$\varepsilon_q^{\mathrm{ampl}}$, γ^{ampl}	+	+	+	+	+	+	+
	$\varepsilon_v^{\mathrm{ampl}}$	-	-	-	-	-	-	-
	shape of $\boldsymbol{\varepsilon}(t)$	-	-	-	-	-	-	-
	e	-	-	+	+	-	-	-
	p^{av}	-	-	-	*	-	*	*
	η^{av}	-	+	+	*	-	*	*
	f_B	+	+	+	-	+	+	+
State variable for historiotropy		∘	*	∘	-	∘	-	-
Basis of the model		SS	DT	DT	DT	DT	DT	DT
max. number of tested cycles		10^3	*	10^4	10^6	150	10^5	10^5

Table 6.1: Assessment of several explicit accumulation models in the literature (+ captured correctly , ∘ captured partially correctly or cumbersome, - not captured or false, * not clear)

Chapter 7

Bochum accumulation model for sand under cyclic loading

7.1 History of the model

The explicit accumulation model developed in Bochum since 1999 originated from the model of Sawicki & Świdziński [133, 134] (Section 6.1.1). In order to consider the accumulation of the deviatoric strain, Niemunis [104] extended the model by the hypoplastic flow rule. The experimental evidence of this flow rule under cyclic loading was delivered several years later by the tests of this work (Section 5.1).

The first of the test results, presented in Section 5.2, revealed that the historiotropic variable $\tilde{N}$ proposed by Sawicki & Świdziński [133, 134] had to be abandoned. Some additional influencing parameters (average stress, void ratio) had to be considered. Niemunis et al. [112] replaced the function (6.1) by a multiplicative approach with the functions f_{ampl}, f_N, f_e, f_p, f_Y and f_π. This approach is discussed in the following chapter. A first mathematical formulation of the function f_π and the evolution of the so-called *back polarization* $\boldsymbol{\pi}$ was presented by Niemunis et al. [112] and used in some other publications (Triantafyllidis et al. [163], Wichtmann et al. [176], Niemunis et al. [110]). Recently (Niemunis et al. [111]), this formulation was replaced by a more elegant one, which is explained in Section 7.2.2. While first $\tilde{N}$ (Niemunis [104]) and later only N (Niemunis et al. [112]) were used to describe the historiotropy, the variable g^A was introduced by Niemunis et al. [110].

In order to capture multidimensional strain loops, a tensorial definition of a multiaxial amplitude was developed by Niemunis [105]. This definition is further explained in Section 7.2.1. In first publications of the model (Niemunis et al. [110], Triantafyllidis et al. [163])

the strain amplitude $\varepsilon^{\text{ampl}}$ was determined from the deviatoric portion of the strain loop only. From the tests presented in Section 5.2.1.3 *without* a consideration of membrane penetration it was concluded, that deviatoric cycles cause larger accumulation rates than volumetric cycles. Thus, the strain loop was scaled by a factor C_{ampl} in the volumetric direction (Wichtmann et al. [176], Niemunis et al. [110]). This scaling was abandoned after having analyzed the tests *with* a consideration of membrane penetration (Section 5.2.1.3), i.e. actually $\varepsilon^{\text{ampl}}$ is determined from the full, non-scaled strain loop (Niemunis et al. [111]).

The need for extending Equation (1.1) by a plastic strain rate $\mathbf{D}^{\text{pl}}$ was recognized by Niemunis et al. [111].

7.2 Bochum accumulation model

The basic structure of the accumulation model is similar to that of viscoplastic models. The number of cycles N is used instead of time t. The general stress - strain - relationship extends Equation (1.1) and reads

$$\mathring{\mathbf{T}} = \mathsf{E} : (\mathbf{D} - \mathbf{D}^{\text{acc}} - \mathbf{D}^{\text{pl}}) \tag{7.1}$$

Therein $\mathring{\mathbf{T}}$ is the Jaumann stress rate, E a stress-dependent elastic stiffness (Section 7.2.3), $\mathbf{D}$ the strain rate, $\mathbf{D}^{\text{acc}}$ the given accumulation rate and $\mathbf{D}^{\text{pl}}$ the rate of plastic strain (Section 7.2.4).

The rate of strain accumulation $\mathbf{D}^{\text{acc}}$ is calculated as a product of a scalar intensity of accumulation D^{acc} and a tensorial direction of accumulation $\mathbf{m}$ ("flow rule"):

$$\begin{aligned} \mathbf{D}^{\text{acc}} \;=\; D^{\text{acc}}\,\mathbf{m} \;&=\; f_{\text{ampl}}\;\dot{f}_N\;f_e\;f_p\;f_Y\;f_\pi\;\mathbf{m} \\ &=\; (\underbrace{f_{\text{ampl}}\;\dot{f}_N^{\,A}}_{\dot{g}^A} + \underbrace{f_{\text{ampl}}\;\dot{f}_N^{\,B}}_{\dot{g}^B})\;f_e\;f_p\;f_Y\;f_\pi\;\mathbf{m} \end{aligned} \tag{7.2}$$

The intensity of accumulation D^{acc} is composed of seven multiplicative functions. The experimental basis of these functions was discussed in Section 5.2. They consider the following influences:

f_{ampl}:	strain amplitude $\varepsilon^{\text{ampl}}$
$\dot{f}_N^A$:	historiotropy
	(number of previous cycles N weighted by their amplitude $\varepsilon^{\text{ampl}}$)
$\dot{f}_N^B$:	basic rate of accumulation, independent of N
f_e:	void ratio e

Function	Material constants		
		Sand 3	ZFS
$f_{\text{ampl}} = \begin{cases} \left(\dfrac{\varepsilon^{\text{ampl}}}{\varepsilon^{\text{ampl}}_{\text{ref}}}\right)^2 & \text{for } \varepsilon^{\text{ampl}} \leq 10^{-3} \\ 100 & \text{for } \varepsilon^{\text{ampl}} > 10^{-3} \end{cases}$	$\varepsilon^{\text{ampl}}_{\text{ref}}$	10^{-4}	10^{-4}
$\dot{f}^A_N = C_{N1} C_{N2} \exp\left(-\dfrac{g^A}{C_{N1} f_{\text{ampl}}}\right)$	C_{N1}	$3.6 \cdot 10^{-4}$	$1.1 \cdot 10^{-3}$
$\dot{f}^B_N = C_{N1} C_{N3}$	C_{N2}	0.43	0.38
$\dot{f}_N = \dot{f}^A_N + \dot{f}^B_N$	C_{N3}	$5.0 \cdot 10^{-5}$	$5.3 \cdot 10^{-5}$
$f_p = \exp\left[-C_p \left(\dfrac{p^{\text{av}}}{p_{\text{ref}}} - 1\right)\right]$	C_p	0.43	0.43
	p_{ref}	100 kPa	100 kPa
$f_Y = \exp\left(C_Y \, \bar{Y}^{\text{av}}\right)$	C_Y	2.0	2.0
$f_e = \dfrac{(C_e - e)^2}{1 + e} \dfrac{1 + e_{\text{ref}}}{(C_e - e_{\text{ref}})^2}$	C_e	0.54	0.51
	e_{ref}	0.874	0.908
$f_\pi = 1 + C_{\pi 1} \, (1 - \cos\alpha) \quad \cos\alpha = \vec{\mathsf{A}}_\varepsilon :: \boldsymbol{\pi}$	$C_{\pi 1}$	4.0	4.0
$\dot{\alpha} = -C_{\pi 2} \alpha (\varepsilon^{\text{ampl}})^2 \quad \boldsymbol{\pi}_{\text{neu}} = \mathcal{R} :: \boldsymbol{\pi}$	$C_{\pi 2}$	200	200

Table 7.1: Summary of the functions, reference quantities and material constants for the medium coarse to coarse sand with the grain size distribution curve No. 3 (Figure 4.14) and the fine sand (CFS) used in the centrifuge model test of Helm et al. [49]

f_p: average mean pressure p^{av}
f_Y: average stress ratio η^{av} or $\bar{Y}^{\text{av}}$
f_π: polarization changes

The functions and their reference quantities are summarized in Table 7.1. Table 7.1 also contains the material constants C_i for the medium coarse to coarse sand with the grain size distribution curve No. 3 referring to Figure 4.14. The determination of these constants was discussed in Section 5.2. Another column in Table 7.1 gives the set of material constants for the fine sand ("CFS" for centrifuge fine sand), which was used in the centrifuge model test of Helm et al. [49] (Section 3.4.1.2). This model test was re-calculated by means of the FEM (Section 8.2.1). The functions f_{ampl}, f_e, f_p, f_Y, f_N and $\dot{f}_N$ are illustrated in Figure 7.1, using the constants of sand No. 3.

In the accumulation model the influence of the shape of the strain loop on the accumu-

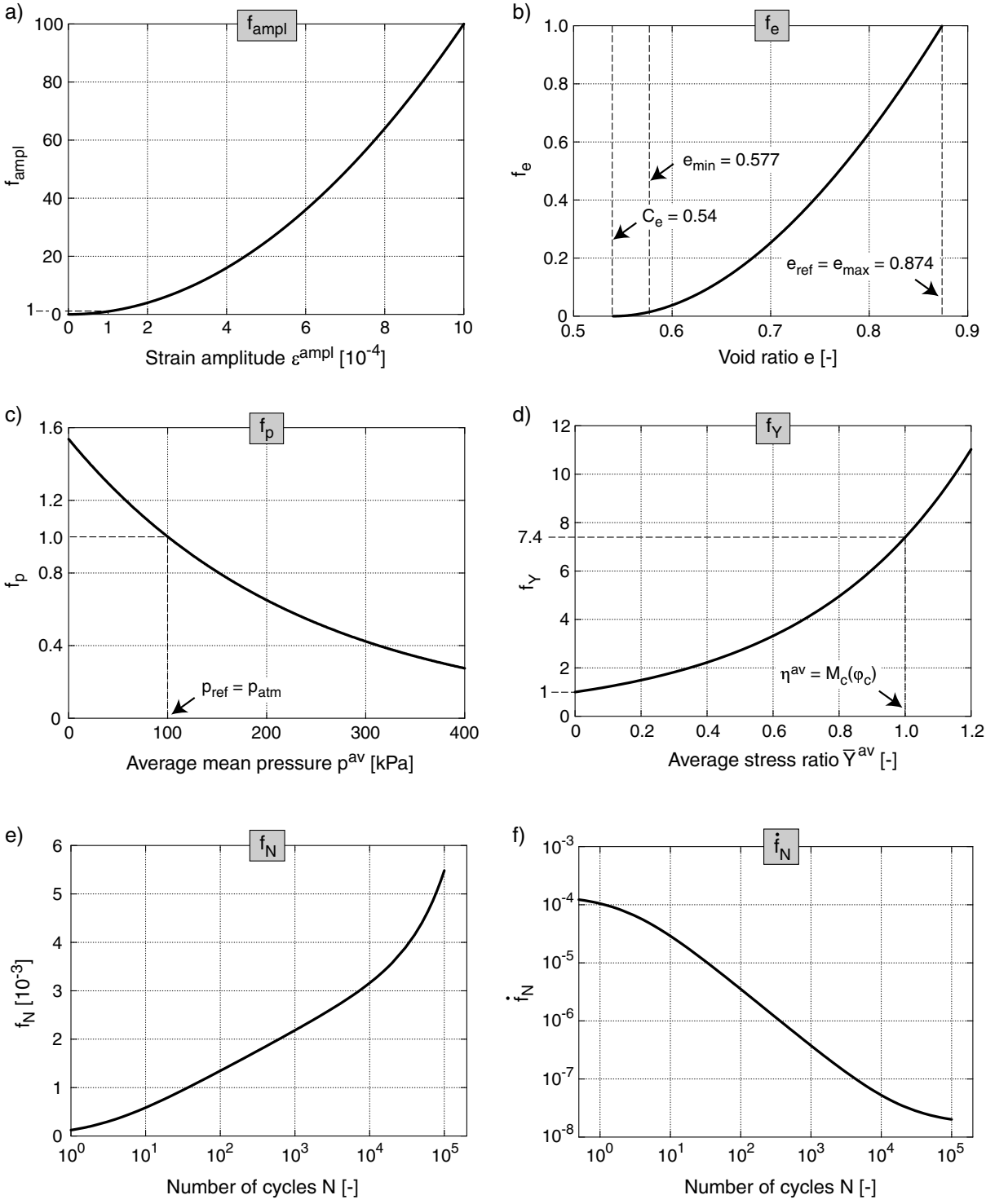

Figure 7.1: *Illustration of the functions of the explicit accumulation model for sand No. 3 (Figure 4.14): a) $f_{ampl}(\varepsilon^{ampl})$, b) $f_e(e)$, c) $f_p(p^{av})$, d) $f_Y(\bar{Y}^{av})$, e) $f_N(N)$, f) $\dot{f}_N(N)$*

lation rate is captured by a tensorial definition of the strain amplitude A_ε (in general a fourth-order tensor, Niemunis [105]), which is explained in Section 7.2.1 for the two-dimensional case. The scalar measure

$$\varepsilon^{\mathrm{ampl}} \;=\; \|\mathsf{A}_\varepsilon\| \tag{7.3}$$

enters the amplitude function f_{ampl}. As will be shown in Section 7.2.1, for the special case of one-dimensional (in-phase) strain cycles $\varepsilon^{\mathrm{ampl}}$ from Equation (7.3) is identical with the classical definition of the amplitude $\varepsilon^{\mathrm{ampl}} = (\varepsilon^{\max} - \varepsilon^{\min})/2$.

In Section 5.2.2 it was demonstrated, that a change of the polarization leads to a temporary increase of the accumulation rate. In order to consider this effect, the accumulation model uses the polarization of the strain amplitude

$$\vec{\mathsf{A}}_\varepsilon \;=\; \frac{\mathsf{A}_\varepsilon}{\|\mathsf{A}_\varepsilon\|}. \tag{7.4}$$

The polarization during the previous cycles is memorized in the so-called "back polarization" tensor $\boldsymbol{\pi}$. The most recent cycles are weighted stronger than cycles further back in the past. In the case of a change of the polarization the accumulation rate is increased by the function f_π. The function f_π depends on the angle α which is included by the actual polarization $\vec{\mathsf{A}}_\varepsilon$ and the "back polarization" $\boldsymbol{\pi}$. An explanation of the functionality of $\vec{\mathsf{A}}_\varepsilon$, $\boldsymbol{\pi}$ and f_π for the two-dimensional case is given in Section 7.2.2.

As a variable for the historiotropy (so-called "cyclic preloading") referring to the comments in Section 5.2.6

$$g^A \;=\; \int f_{\mathrm{ampl}}\; \dot{f}_N{}^A \,\mathrm{d}N \tag{7.5}$$

is used, i.e. beside the number of cycles in the past also their amplitude is considered.

In Section 5.1 it was shown, that the direction of accumulation $\mathbf{m}$ depends only on the average stress ratio $\eta^{\mathrm{av}} = q^{\mathrm{av}}/p^{\mathrm{av}}$ and that it can be well approximated by the flow rules of the modified Cam Clay model and the hypoplastic model. The hypoplastic flow rule is given in Section 7.3. In the calculations presented in Chapter 8, the flow rule of the modified Cam Clay model was used. This flow rule reads

$$\mathbf{m} \;=\; \frac{-\frac{1}{3}\left(p - \frac{q^2}{M^2 p}\right)\mathbf{1} + \frac{3}{M^2}\mathbf{T}^*}{\left\|-\frac{1}{3}\left(p - \frac{q^2}{M^2 p}\right)\mathbf{1} + \frac{3}{M^2}\mathbf{T}^*\right\|}\,, \tag{7.6}$$

wherein $M = F\ (6\sin\varphi_c)/(3-\sin\varphi_c)$ holds. For the special case of triaxial compression and for isotropic stresses the factor F takes the value 1. For triaxial extension it declines

with decreasing stress ratio $\eta = q/p$:

$$F = \begin{cases} 1 & \text{for } \eta \geq 0 \\ 1 + \eta/3 & \text{for } \eta < 0 \end{cases} \tag{7.7}$$

On the critical state line for triaxial extension $F = (3 - \sin\varphi_c)/(3 + \sin\varphi_c)$ is valid. A general form of F will be given in Section 7.3.1. From Equation (7.6) the ratio Ω of the volumetric and the deviatoric accumulation rate can be obtained:

$$\Omega = -\frac{D_v^{\text{acc}}}{D_q^{\text{acc}}} = -\sqrt{\frac{3}{2}}\,\frac{\text{tr}\,(\mathbf{m})}{\|\mathbf{m}^*\|} = \sqrt{\frac{3}{2}}\,\frac{p(M^2-\eta^2)}{3\|\mathbf{T}^*\|} \overset{\text{triax}}{=} \frac{M^2-\eta^2}{2\eta} \tag{7.8}$$

7.2.1 Definition of the strain amplitude

The tensorial definition of the strain amplitude A_ε (in general a fourth-order tensor, Niemunis [105]) considers that in general the strain loop penetrates several dimensions of the strain space. The influence of the shape of the strain loop on the accumulation rate (Section 5.2.1.4) is captured by A_ε. In this section, the definition is explained for the two-dimensional case. The full tensorial definition is given in Appendix III.

From an implicit calculation of the second cycle or a control cycle, the strain loop in each integration point is obtained as a sequence of discrete strain points $\boldsymbol{\epsilon}_k$, $k = 1, ..., M$ (Figure 7.2). First, the two points of the strain loop with the largest distance have to be selected. In the case of the loop illustrated in Figure 7.2 these are the points 5 and 11. Their distance is denoted by $2R^{(2)}$ (the $\sqcup^{(2)}$ stands for two-dimensional). The direction of a straight line through these two points is described by the unit vector $\vec{\mathbf{r}}^{(2)}$. It is of no importance which of the two possible opposite directions is chosen for $\vec{\mathbf{r}}^{(2)}$. In a second step, the strain loop is projected onto a straight line perpendicularly to the direction $\vec{\mathbf{r}}^{(2)}$. The span $2R^{(1)}$ and the direction $\vec{\mathbf{r}}^{(1)}$ of the projected loop are determined.

In order to describe the two-dimensional case, a second-order amplitude tensor $\mathbf{A}_\varepsilon$ is sufficient. It is calculated from the half spans $R^{(i)}$ and the directions $\vec{\mathbf{r}}^{(i)}$:

$$\begin{aligned} \mathbf{A}_\varepsilon &= \sum_{i=1}^{2} R^{(i)}\ \vec{\mathbf{r}}^{(i)} \otimes \vec{\mathbf{r}}^{(i)} \\ &= R^{(1)}\ \vec{\mathbf{r}}^{(1)} \otimes \vec{\mathbf{r}}^{(1)} + R^{(2)}\ \vec{\mathbf{r}}^{(2)} \otimes \vec{\mathbf{r}}^{(2)} \end{aligned} \tag{7.9}$$

Since the orientation of the strain loop in the strain space is of no importance (Section 5.2.1.3), the ε_1^+-ε_2^+ coordinate system in Figure 7.2 can be used for the directions $\vec{\mathbf{r}}^{(i)}$. From Equation (7.9) one obtains:

$$\mathbf{A}_\varepsilon = R^{(1)} \begin{pmatrix} 1 \\ 0 \end{pmatrix} \otimes \begin{pmatrix} 1 \\ 0 \end{pmatrix} + R^{(2)} \begin{pmatrix} 0 \\ 1 \end{pmatrix} \otimes \begin{pmatrix} 0 \\ 1 \end{pmatrix} = \begin{pmatrix} R^{(1)} & 0 \\ 0 & R^{(2)} \end{pmatrix} \tag{7.10}$$

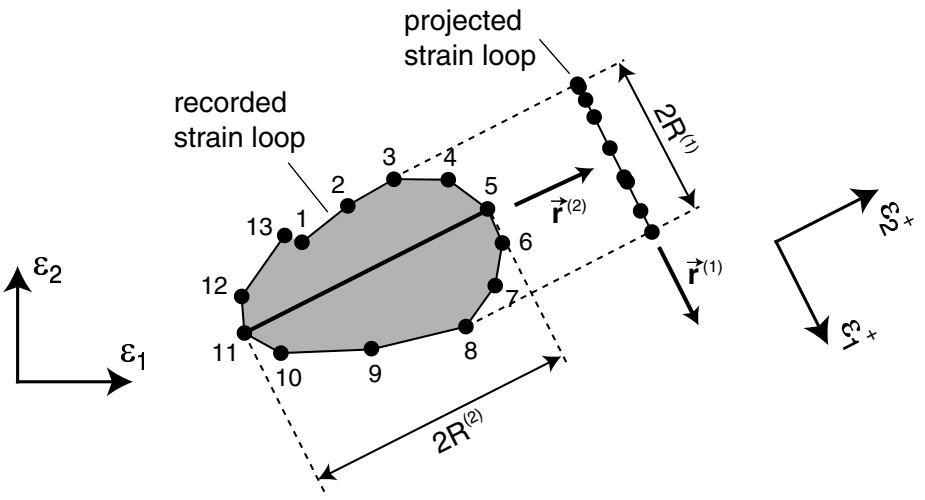

Figure 7.2: *Strain amplitude* A_ε *for the two-dimensional case: Determination of* $R^{(2)}$ *and* $\vec{\mathbf{r}}^{(2)}$ *from the original loop and* $R^{(1)}$ *and* $\vec{\mathbf{r}}^{(1)}$ *from the projection of this loop*

and referring to Equation (7.3) the scalar measure is

$$\varepsilon^{\mathrm{ampl}} = \|\mathbf{A}_\varepsilon\| \;=\; \sqrt{\left(R^{(1)}\right)^2 + \left(R^{(2)}\right)^2} \tag{7.11}$$

In the following, the special cases of an uniaxial cycle (span $2R$, Figure 7.3a) and a circular strain loop (radius R, Figure 7.3b) are discussed. In the case of the 1-D cycle $R^{(2)} = R$ and $R^{(1)} = 0$ holds. Thus $\varepsilon^{\mathrm{ampl}} = R$ follows from Equation (7.11). Therefore, for uniaxial cycles, the amplitude definition given by Equations (7.3) and (7.9) is identical to the classical definition of the amplitude. For circular cycles with $R^{(2)} = R^{(1)} = R$ the strain amplitude is $\varepsilon^{\mathrm{ampl}} = \sqrt{2}R$. Thus, for the circular loops a $\sqrt{2}$ times larger strain amplitude is obtained compared to the uniaxial cycles with the same maximum span. If one considers the quadratic dependence of the accumulation rate on the strain amplitude, $\dot{\varepsilon}^{\mathrm{acc}} \sim (\varepsilon^{\mathrm{ampl}})^2$, the accumulation model delivers a twice larger accumulation rate for circular cycles than for uniaxial ones. This is in good agreement with the results of the experiments presented in Section 5.2.1.4.

If several sources of cyclic loading are acting simultaneously, complex strain loops may result from different polarizations and frequencies of the cycles. A procedure for the determination of the strain amplitude in such cases is proposed by Niemunis et al. [111].

7.2.2 Back Polarization

In the following the functionality of

$$f_\pi \;=\; 1 + C_{\pi 1}\,(1 - \cos\alpha) \tag{7.12}$$

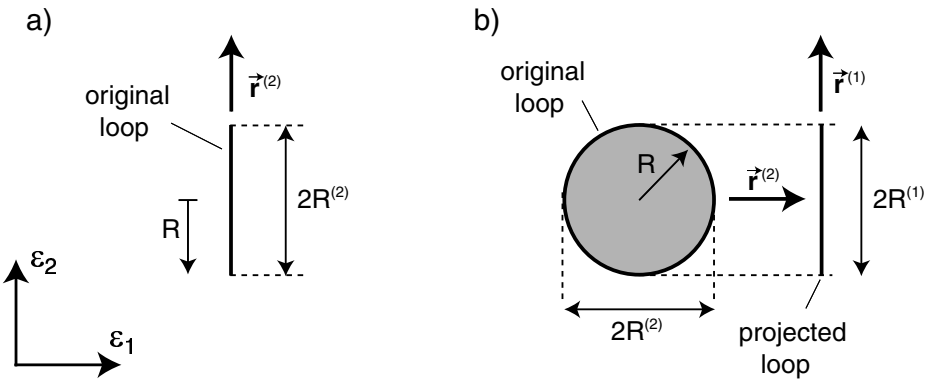

Figure 7.3: *Evaluation of the strain amplitude* A_ε *for a) uniaxial (1-D) cycles and b) circular strain loops*

and the variable *back polarization* for the description of the effect of polarization changes is explained for the two-dimensional case. Appendix III contains a corresponding description in full tensor notation. First, the case of two subsequent packages "a" and "b" of cycles with an identical polarization, but different amplitudes is considered (Figure 7.4a). In the first package, the amplitude $\mathbf{A}_\varepsilon$ and the polarization $\vec{\mathbf{A}}_\varepsilon$ are:

$$\mathbf{A}_\varepsilon^a \;=\; R_a \begin{pmatrix} 1 & 0 \\ 0 & 0 \end{pmatrix} \qquad \vec{\mathbf{A}}_\varepsilon^a \;=\; \begin{pmatrix} 1 & 0 \\ 0 & 0 \end{pmatrix} \tag{7.13}$$

If a sufficient number of cycles with the amplitude $\mathbf{A}_\varepsilon^a$ were applied, then $\boldsymbol{\pi} = \vec{\mathbf{A}}_\varepsilon^a$ holds at the beginning of the second package. In the second package, the amplitude and the polarization read

$$\mathbf{A}_\varepsilon^b \;=\; R_b \begin{pmatrix} 1 & 0 \\ 0 & 0 \end{pmatrix} \qquad \vec{\mathbf{A}}_\varepsilon^b \;=\; \begin{pmatrix} 1 & 0 \\ 0 & 0 \end{pmatrix} \;, \tag{7.14}$$

i.e. $\vec{\mathbf{A}}_\varepsilon^b = \vec{\mathbf{A}}_\varepsilon^a = \boldsymbol{\pi}$ is valid. At the beginning of the second package of cycles, the angle α between the actual polarization $\vec{\mathbf{A}}_\varepsilon^b$ and the "back polarization" $\boldsymbol{\pi}$ is

$$\cos\alpha \;=\; \boldsymbol{\pi} : \vec{\mathbf{A}}_\varepsilon^b \;=\; 1 \;. \tag{7.15}$$

From Equation (7.12) $f_\pi = 1$ follows, i.e. the accumulation rate is *not* increased due to the change from package "a" to package "b".

The next case considers, that the direction of the cycles in package "b" is rotated by 90° in the ε_1-ε_2-plane in comparison to package "a" (Bild 7.4b). For package "a" Equation (7.13) still holds. For package "b" one obtains:

$$\mathbf{A}_\varepsilon^b \;=\; R_b \begin{pmatrix} 0 & 0 \\ 0 & 1 \end{pmatrix} \qquad \vec{\mathbf{A}}_\varepsilon^b \;=\; \begin{pmatrix} 0 & 0 \\ 0 & 1 \end{pmatrix} \tag{7.16}$$

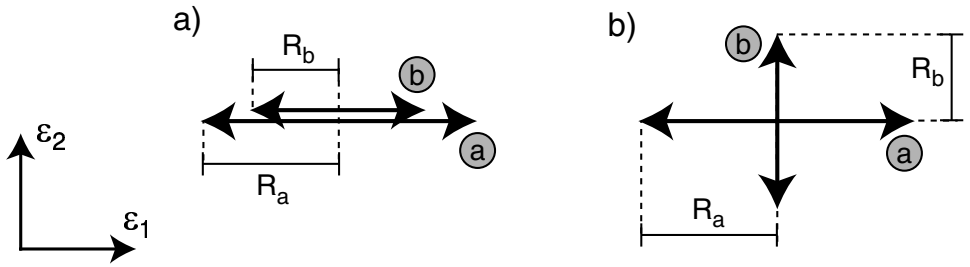

Figure 7.4: *Packages of cycles a) with and b) without a change of the polarization*

At the beginning of package "b" $\boldsymbol{\pi} = \vec{\mathbf{A}}_{\varepsilon}^{a}$ and thus

$$\cos\alpha \;=\; \boldsymbol{\pi} : \vec{\mathbf{A}}_{\varepsilon}^{b} \;=\; 0 \tag{7.17}$$

holds. From Equation (7.12) $f_\pi = 1 + C_{\pi 1}$ follows. Thus, due to the 90°-change of the polarization, the accumulation rate is immediately increased by the factor $1 + C_{\pi 1}$.

The temporary effect of the polarization change, i.e. the decay of f_π during the subsequent cycles with $\vec{\mathbf{A}}_{\varepsilon}^{b}$ is described by an asymptotic adaption of $\boldsymbol{\pi}$ with N to the new polarization $\vec{\mathbf{A}}_{\varepsilon}^{b}$. Niemunis et al. [111] proposed the evolution of the angle α to be:

$$\dot{\alpha} = -C_{\pi 2}\alpha(\varepsilon^{\mathrm{ampl}})^2 \tag{7.18}$$

In order to rotate the tensor $\boldsymbol{\pi}$ by an angle $\Delta\alpha = \dot{\alpha}\Delta N$ (Figure 7.5), the rotational operator R is used. For the two-dimensional case described here, R must be a fourth-order tensor. In the general case ($\vec{\mathbf{A}}_{\varepsilon}$ and $\boldsymbol{\pi}$ are fourth-order tensors), $\mathcal{R}$ is an eight-order tensor. The general formulation of $\mathcal{R}$ can be found in Appendix III. The determination of the material constants $C_{\pi 1}$ and $C_{\pi 2}$ was explained in Section 5.2.2.

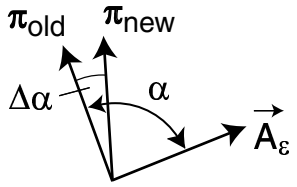

Figure 7.5: *Adaption of $\boldsymbol{\pi}$ to the actual polarization $\vec{\mathbf{A}}_{\varepsilon}$*

The question arises from which initial value $\boldsymbol{\pi}_0$ a calculation should start. It is conceivable to prescribe a polarization along a certain direction $\vec{\mathbf{r}}$ (e.g. the direction of deposition if the cyclic loading in the past resulted from sedimentation and erosion processes):

$$\boldsymbol{\pi}_0 \;=\; \vec{\mathbf{r}} \otimes \vec{\mathbf{r}} \tag{7.19}$$

For a chaotic initial state (no preference for a certain direction)

$$\boldsymbol{\pi}_0 \;=\; \boldsymbol{\pi}^{\mathrm{iso}} \;=\; \frac{1}{3}\mathbf{1} \tag{7.20}$$

(Niemunis et al. [111]) with the unit tensor $\mathbf{1}$ can be set into approach.

7.2.3 Elastic stiffness E

The elastic stiffness E in Equation (7.1) connects the accumulation of strain with the accumulation of stress. In FE calculations with $\mathring{\mathbf{T}} \approx \mathbf{0}$ and thus $\mathbf{D} \approx \mathbf{D}^{\mathrm{acc}}$ the influence of E on the results is low. This is the case e.g. for the cyclically loaded shallow foundations (Section 8.2). In those calculations, a simple isotropic stiffness

$$\mathsf{E} \;=\; \lambda\, \mathbf{1} \otimes \mathbf{1} + 2\,\mu\, \mathsf{I} \tag{7.21}$$

was used with the Lamé constants $\lambda = E\nu/(1+\nu)/(1-2\nu)$ and $\mu = G = E/2/(1+\nu)$, the identity tensor $I_{ijkl} = 0.5(\delta_{ik}\delta_{jl} + \delta_{il}\delta_{jk})$, the Poisson's ratio $\nu = 0.2$ and the pressure-dependent Young modulus $E = 300\ p$. If an accumulation of stress ($\mathring{\mathbf{T}} \neq \mathbf{0}$) is expected (e.g. a build-up of excess pore pressure in the undrained case or a change of the normal stresses on the shaft of a pile), the appropriate choice of E is decisive for the quality of the numerical prediction. Niemunis et al. [113] chose an anisotropic *small strain*-stiffness measured by Kuwano et al. [80] in order to calculate an undrained cyclic loading. The calculations of the piles in Section 8.3 were performed with Equation (7.21) using $\nu = 0.2$ and the pressure- and void ratio-dependent shear modulus G from Equation (3.5) with the constants $A = 39.7$, $a = 1.46$ and $n = 0.46$ (Wichtmann & Triantafyllidis [183]). It has to be annotated, that it is not clear yet, if a *small strain*-stiffness can be set into approach for E in Equation (7.1). Eventually, also the linear stiffness L of the hypoplastic model (Section 7.3.1) is applicable. Further experimental effort is needed to clarify this question.

7.2.4 Plastic strain rate $\mathbf{D}^{\mathrm{pl}}$

In the following, the need for the plastic strain rate $\mathbf{D}^{\mathrm{pl}}$ in Equation (7.1) is explained. The equation

$$\mathring{\mathbf{T}} = \mathsf{E} : (\mathbf{D} - \mathbf{D}^{\mathrm{acc}}) \tag{7.22}$$

is sufficient in the homogeneous case (e.g. in a calculation of an element test). In the extreme case $\mathbf{D} = \mathbf{0}$, the stress rate resulting from $\mathbf{D}^{\mathrm{acc}}$ is inverse proportional to the flow

rule, i.e. $\mathring{\mathbf{T}} \sim -\mathbf{m}$. Since on the yield surface the flow rule $\mathbf{m}$ always points outside, the stress cannot leave the Coulomb pyramid.

However, in FE calculations with non-homogeneous conditions, Equation (7.22) can lead to stresses outside the admissible range. Exemplary, this is explained by means of the FE mesh with nine elements in Figure 7.6a. Displacements of the boundaries are prevented. The initial stress is isotropic. Due to cyclic loading (its cause is not discussed here), the accumulation rate is $\mathbf{D}^{\mathrm{acc}} \neq \mathbf{0}$ in the eight outer elements. Since the average stress is isotropic, these elements contract. The element in the middle of the FE mesh is not subjected to cyclic loading and thus, $\mathbf{D}^{\mathrm{acc}} = \mathbf{0}$ holds. However, due to the deformations of the neighboured elements, it experiences a strain rate $\mathbf{D} > \mathbf{0}$ (extension of the element). In the equilibrium iteration, Equation (7.22) can be fulfilled only by a change of stress $\mathring{\mathbf{T}} = \mathsf{E} : \mathbf{D}$. The stress gets more positive and can leave the Coulomb pyramid (in this case $p = -\mathrm{tr}\,(\mathbf{T})/3$ can get negative). However, in a non-cohesive soil such stresses are physically not possible. The constitutive equation must restrict the stress not to leave the admissible range.

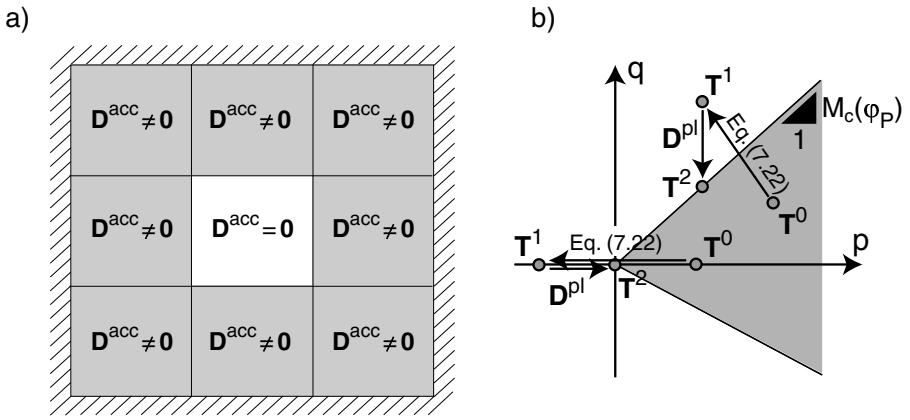

Figure 7.6: *a) The large strain rate* $\mathbf{D}$ *in the element in the middle despite* $\mathbf{D}^{acc} = \mathbf{0}$ *due to deformations of the neighboured elements makes the plastic strain rate* $\mathbf{D}^{pl}$ *indispensable, b) Equation (7.22) may push the stress from* $\mathbf{T}^0$ *to* $\mathbf{T}^1$ *outside the Coulomb pyramid (in the case of the example in part a along the p-axis), the plastic strain rate* $\mathbf{D}^{pl}$ *projects the stress back to the yield surface (*$\mathbf{T}^2$*)*

This can be achieved by extending Equation (7.22) with a plastic strain rate $\mathbf{D}^{\mathrm{pl}}$. The practical realization of $\mathbf{D}^{\mathrm{pl}}$ is identical with the procedure of elasto-plasticity. Stresses which leave the admissible range due to Equation (7.22) are projected back to the yield surface (Figure 7.6b). The associated flow rule of Matsuoka & Nakai [95] is used for this

purpose. The stiffness E is replaced by

$$\mathsf{E}^{\mathrm{ep}} = \mathsf{E} - \frac{\mathsf{E} : \mathbf{m} \otimes \mathbf{m} : \mathsf{E}}{K + \mathbf{m} : \mathsf{E} : \mathbf{m}} \tag{7.23}$$

with the flow rule $\mathbf{m}$ and the hardening modulus K. Thus, Equation (7.22) is transformed to Equation (7.1):

$$\mathring{\mathbf{T}} = \mathsf{E} : (\mathbf{D} - \mathbf{D}^{\mathrm{acc}}) - \underbrace{\frac{\mathsf{E} : \mathbf{m} \otimes \mathbf{m} : \mathsf{E}}{K + \mathbf{m} : \mathsf{E} : \mathbf{m}} : (\mathbf{D} - \mathbf{D}^{\mathrm{acc}})}_{\mathsf{E} : \mathbf{D}^{\mathrm{pl}}} \tag{7.24}$$

In the calculations of shallow foundations under cyclic loading (Section 8.2), the plastic strain rate $\mathbf{D}^{\mathrm{pl}}$ is needed e.g. in elements at the soil surface next to the foundation. In these elements, the strain amplitudes are low (i.e. $\mathbf{D}^{\mathrm{acc}} \approx \mathbf{0}$). However, these elements experience a larger $\mathbf{D}$ due to the deformation of the neighboured elements which lay beneath the edge of the foundation.

7.2.5 Cycles which touch the yield surface

Explicit accumulation models are usually developed for cycles with small strain amplitudes $\varepsilon^{\mathrm{ampl}} \leq 10^{-3}$. However, cycles which temporarily fulfill the Coulomb yield condition (Figure 5.35) may occur in single elements. At the moment, no special treatment of these cycles is implemented. For the future it is planned, to control during the implicit (recording) cycle, if the stress reaches the yield surface. In this case, the accumulation rate $\mathbf{D}^{\mathrm{acc}}$ is not calculated from Equation (7.2) but it is set equal to the residual strain generated by the implicit cycle.

7.2.6 Validation of the accumulation model

The accumulation model was validated by a re-calculation of the cyclic triaxial tests of the four main series (influence of the amplitude, of the void ratio, the average mean pressure and the average stress ratio). The strain amplitude (mean value $\bar{\varepsilon}^{\mathrm{ampl}}$ over 10^5 cycles or measured curve $\varepsilon^{\mathrm{ampl}}(N)$) and the initial void ratio e_0 of the respective test were prescribed. In this subsection due to lack of space, only six calculations are presented for each test series.

Figure 7.7 contains re-calculations of the tests with different stress amplitudes 12 kPa $\leq q^{\mathrm{ampl}} \leq$ 80 kPa at $p^{\mathrm{av}} = 200$ kPa, $\eta^{\mathrm{av}} = 0.75$ on initially medium dense specimens. The diagrams specify the difference $\Delta\varepsilon^{\mathrm{acc}}$ between the residual strains after 10^5 cycles in

the test and in the calculation (with $\bar{\varepsilon}^{\mathrm{ampl}}$). Their difference in percent is denoted as Δ. The accumulation curves $\varepsilon^{\mathrm{acc}}(N)$ calculated with $\bar{\varepsilon}^{\mathrm{ampl}}$ and $\varepsilon^{\mathrm{ampl}}(N)$ do not differ much in Figure 7.7 and in the following illustrations. The prognosis of the residual strains of the tests with amplitudes $q^{\mathrm{ampl}} \leq 70$ kPa is good. The deviations $\Delta\varepsilon^{\mathrm{acc}}$ are relatively small. In the tests with small amplitudes ($q^{\mathrm{ampl}} \leq 22$ kPa) the difference in percent is larger, due to the small residual strain. However, for a settlement prognosis, this is of minor importance. The largest difference between test and re-calculation was detected for $q^{\mathrm{ampl}} = 80$ kPa. From Figure 5.25 it could already be seen, that the approximation by the function f_{ampl} overestimates the accumulation rates in this test.

Figure 7.8 presents the re-calculation of the tests with different initial densities $0.24 \leq I_{D0} \leq 0.94$ and identical average and cyclic stresses ($p^{\mathrm{av}} = 200$ kPa, $\eta^{\mathrm{av}} = 0.75$, $q^{\mathrm{ampl}} = 60$ kPa). Larger differences in percent between test and re-calculation are present only for large initial densities $I_{D0} > 0.9$. This was already addressed in Section 5.2.3. The deviations do not exceed $\Delta\varepsilon^{\mathrm{acc}} = 0.18\%$ for any of the initial densities.

The re-calculation of the tests with different average mean pressures 50 kPa $\leq p^{\mathrm{av}} \leq 300$ kPa ($\eta^{\mathrm{av}} = 0.75$, $\zeta = q^{\mathrm{ampl}}/p^{\mathrm{av}} = 0.3$, medium dense initial density) is shown in Figure 7.9. The N-dependence was disregarded in the function f_p. For the small pressures (e.g. $p^{\mathrm{av}} = 50$ kPa), this leads to calculated curves which, compared with the measured curves, run steeper for small numbers of cycles and more flat for larger values of N. At large pressures (e.g. $p^{\mathrm{av}} = 300$ kPa) this is vice versa. The best approximation is achieved for the test with $p^{\mathrm{av}} = 200$ kPa. The largest deviation in percent was obtained for the test with $p^{\mathrm{av}} = 250$ kPa. This is due to the scatter of the experimental data which could already be seen in Figure 5.61.

The satisfactory prognosis of the explicit equations for the tests with different average stress ratios $0.25 \leq \eta^{\mathrm{av}} \leq 1.313$ ($p^{\mathrm{av}} = 200$ kPa, $q^{\mathrm{ampl}} = 60$ kPa, medium dense initial density) is illustrated in Figure 7.10.

Figure 7.11 presents the re-calculation of the tests with packages of cycles and thus checks the historiotropic variable g^A. Once again, the accumulation rates predicted for $q^{\mathrm{ampl}} = 80$ kPa are slightly too large. Despite this, the variable g^A reproduces well the change of the accumulation rate due to a change of the load amplitude, considering the prior cyclic loading. The calculated accumulation curves follow the experimentally determined curves $\varepsilon^{\mathrm{acc}}(N)$ well.

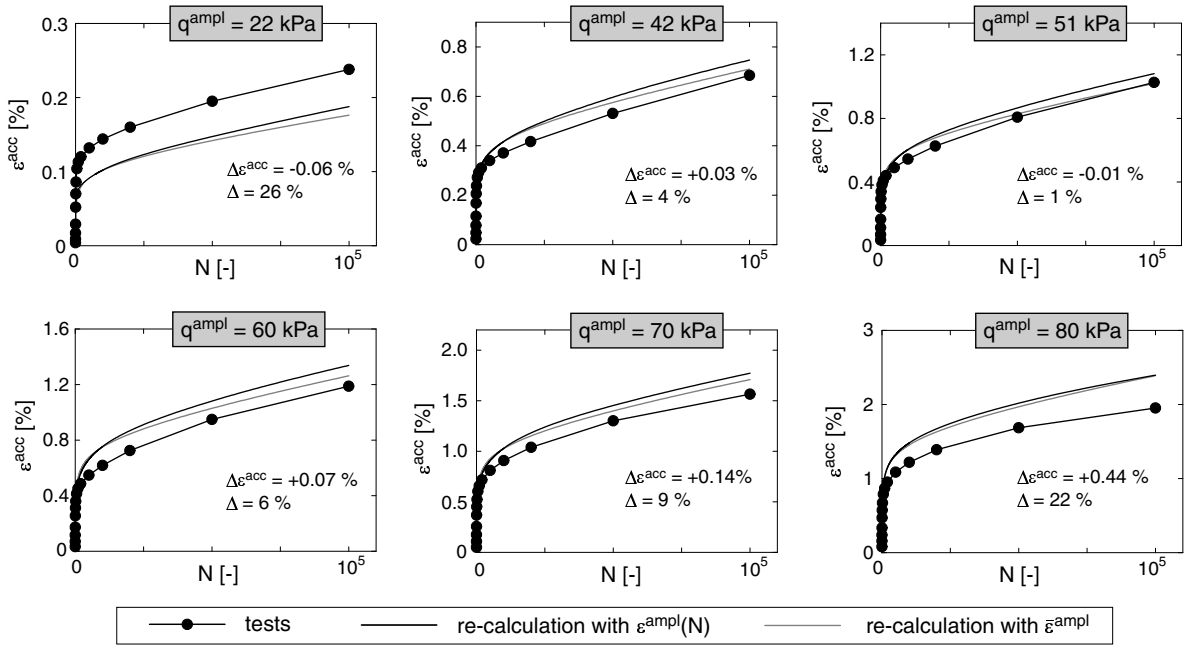

Figure 7.7: *Validation of the accumulation model: re-calculation of cyclic triaxial tests with different stress amplitudes* q^{ampl} *(*$p^{av} = 200$ *kPa,* $\eta^{av} = 0.75$*,* $0.58 \leq I_{D0} \leq 0.61$*)*

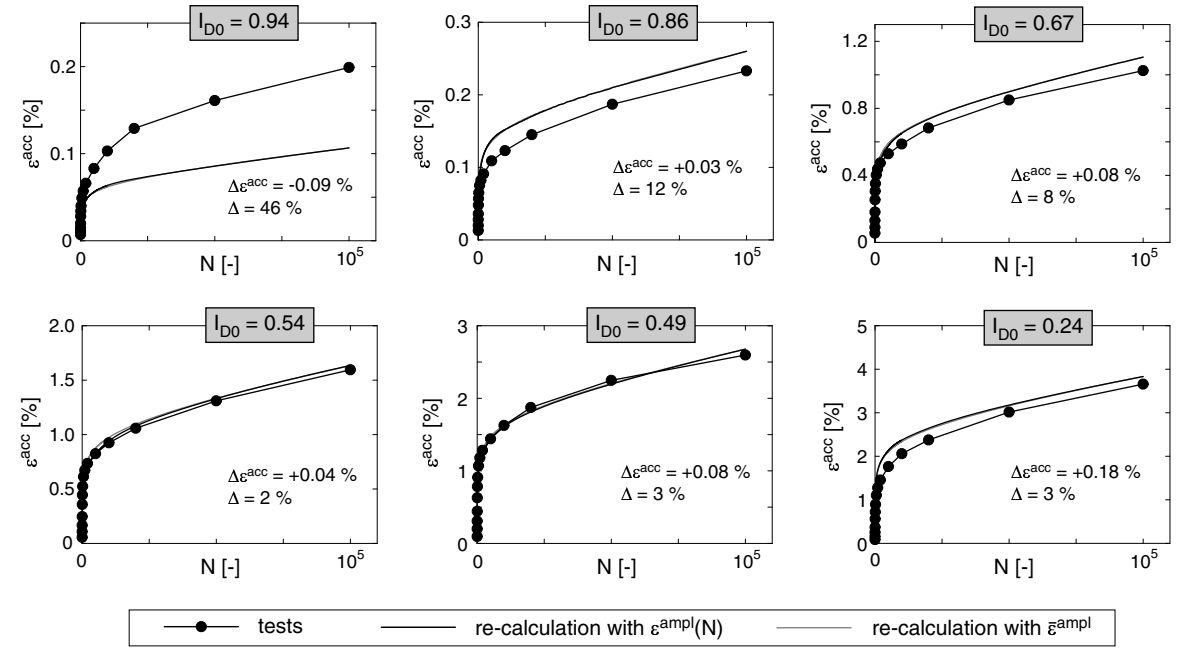

Figure 7.8: *Validation of the accumulation model: re-calculation of cyclic triaxial tests with different initial densities* I_{D0} *(*$p^{av} = 200$ *kPa,* $\eta^{av} = 0.75$*,* $q^{ampl} = 60$ *kPa)*

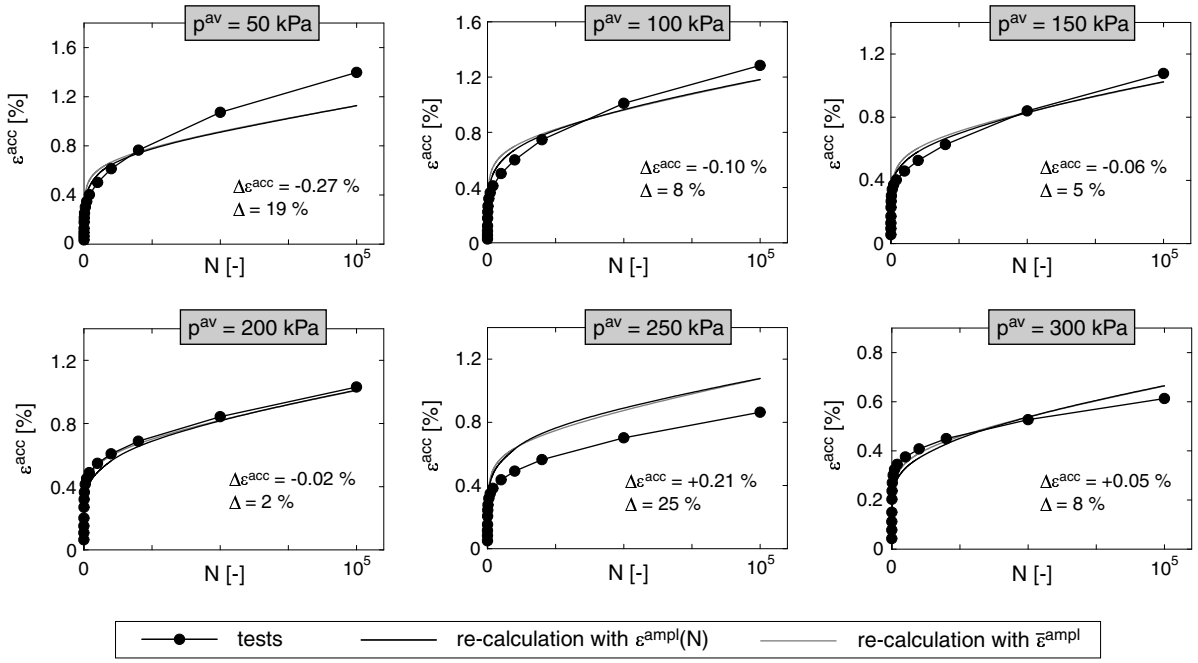

Figure 7.9: *Validation of the accumulation model: re-calculation of cyclic triaxial tests with different average mean pressures* p^{av} *(*$\eta^{av} = 0.75$, $\zeta = q^{ampl}/p^{av} = 0.3$, $0.61 \leq I_{D0} \leq 0.69$*)*

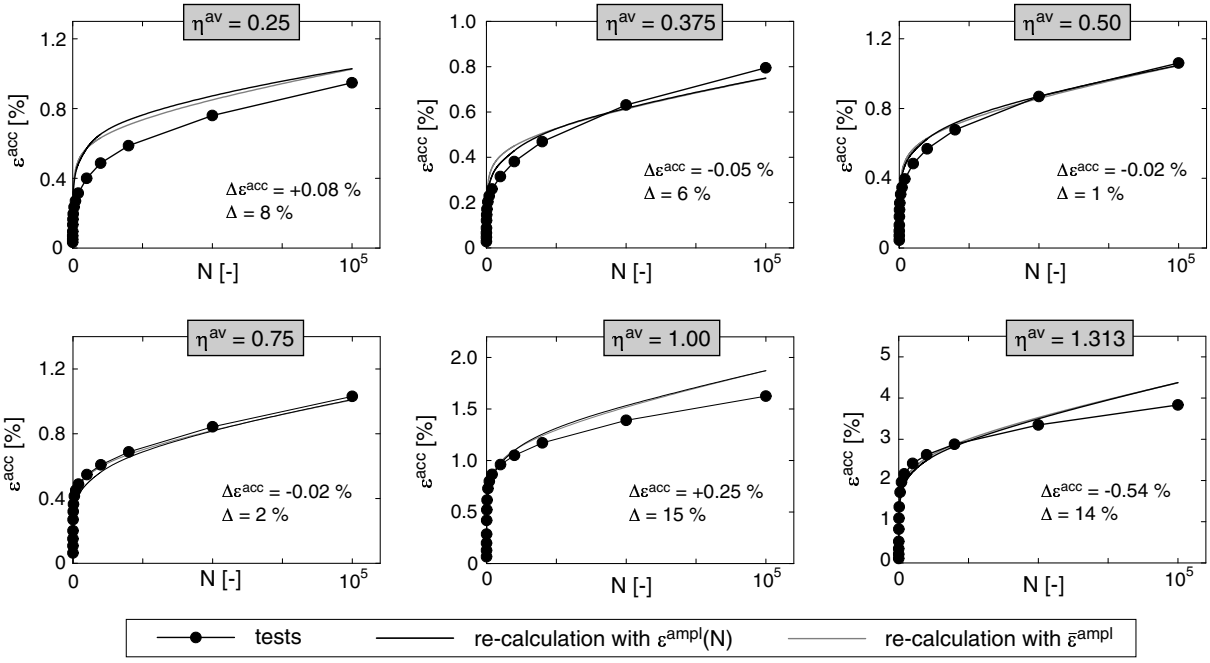

Figure 7.10: *Validation of the accumulation model: re-calculation of cyclic triaxial tests with different average stress ratios* η^{av} *(*$p^{av} = 200$ *kPa*, $q^{ampl} = 60$ *kPa*, $0.57 \leq I_{D0} \leq 0.67$*)*

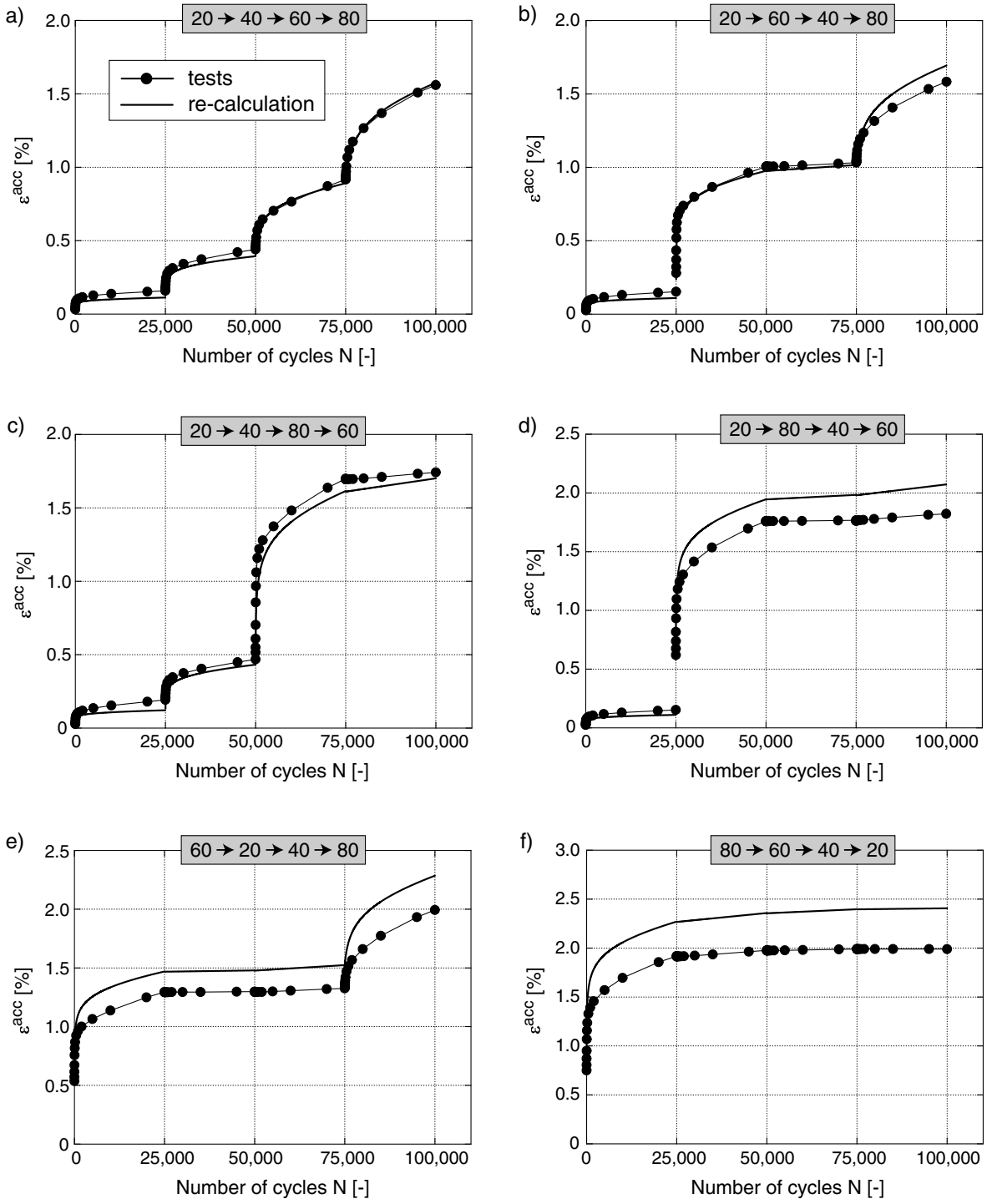

Figure 7.11: *Validation of the accumulation model: re-calculation of cyclic triaxial tests with packages of cycles with amplitudes q^{ampl} = 20, 40, 60 and 80 kPa in different sequences (p^{av} = 200 kPa, η^{av} = 0.75, $0.58 \leq I_{D0} \leq 0.63$)*

7.3 Model for the implicit cycles: Hypoplastic model with intergranular strain

In the FE calculations presented in Chapter 8, the hypoplastic material model (Kolymbas [78], Gudehus [38], von Wolffersdorff [172]) with the extension of the intergranular strain (Niemunis & Herle [106]) was used for the implicit calculation steps, i.e. for the initial equilibrium, the first two cycles and the control cycles. The model is described in the following and its prognosis of the material behaviour is studied.

7.3.1 Basic version of the hypoplastic model

7.3.1.1 Original version according to von Wolffersdorff

The general form of the hypoplastic model reads:

$$\mathring{\mathbf{T}} \;=\; \mathsf{L} : \mathbf{D} \;+\; \mathbf{N}\,\|\mathbf{D}\| \;=\; \underbrace{\left(\mathsf{L} \;+\; \mathbf{N}\,\frac{\mathbf{D}}{\|\mathbf{D}\|}\right)}_{\mathsf{M}} : \mathbf{D} \tag{7.25}$$

Therein $\mathring{\mathbf{T}}$ is the Jaumann stress rate and $\mathbf{D}$ is the strain rate. Here contrary to $\mathbf{D}$ in Equation (7.1) "rate" means a derivative with respect to time and not with respect to the number of cycles. L and $\mathbf{N}$ are the fourth-order linear and the second-order nonlinear stiffness tensor. For sand they can be calculated referring to von Wolffersdorff [172] from:

$$\mathsf{L} \;=\; f_b\; f_e\; \frac{1}{\hat{\mathbf{T}} : \hat{\mathbf{T}}}\; \left(F^2\; \mathsf{I} \;+\; a^2\; \hat{\mathbf{T}}\hat{\mathbf{T}}\right) \tag{7.26}$$

$$\mathbf{N} \;=\; f_b\; f_e\; f_d\; \frac{F\; a}{\hat{\mathbf{T}} : \hat{\mathbf{T}}}\; \left(\hat{\mathbf{T}} + \hat{\mathbf{T}}^*\right) \tag{7.27}$$

Therein $\hat{\mathbf{T}} = \mathbf{T}/\mathrm{tr}\,\mathbf{T}$ is a dimensionless stress and $I_{ijkl} = 0.5(\delta_{ik}\delta_{jl} + \delta_{il}\delta_{jk})$ is an identity tensor. The parameters a and F in Equations (7.26) and (7.27) describe the failure criterion in the deviatoric plane (failure criterion of Matusoka & Nakai [95], Figure 7.12a):

$$a \;=\; \frac{\sqrt{3}\;(3 - \sin\varphi_c)}{2\;\sqrt{2}\;\sin\varphi_c} \tag{7.28}$$

$$F \;=\; \sqrt{\frac{1}{8}\;\tan^2\psi \;+\; \frac{2 - \tan^2\psi}{2 + \sqrt{2}\;\tan\psi\;\cos(3\theta)}} \;-\; \frac{1}{2\;\sqrt{2}}\;\tan\psi \tag{7.29}$$

$$\tan\psi \;=\; \sqrt{3}\;\|\hat{\mathbf{T}}^*\| \tag{7.30}$$

$$\cos(3\theta) \;=\; -\sqrt{6}\;\mathrm{tr}\left(\hat{\mathbf{T}}^* \cdot \hat{\mathbf{T}}^* \cdot \hat{\mathbf{T}}^*\right) / \left[\hat{\mathbf{T}}^* : \hat{\mathbf{T}}^*\right]^{\frac{3}{2}} \tag{7.31}$$

φ_c is the critical friction angle. The angles ψ and θ describe the position of $\mathbf{T}$ in the stress space (Figure 7.12b).

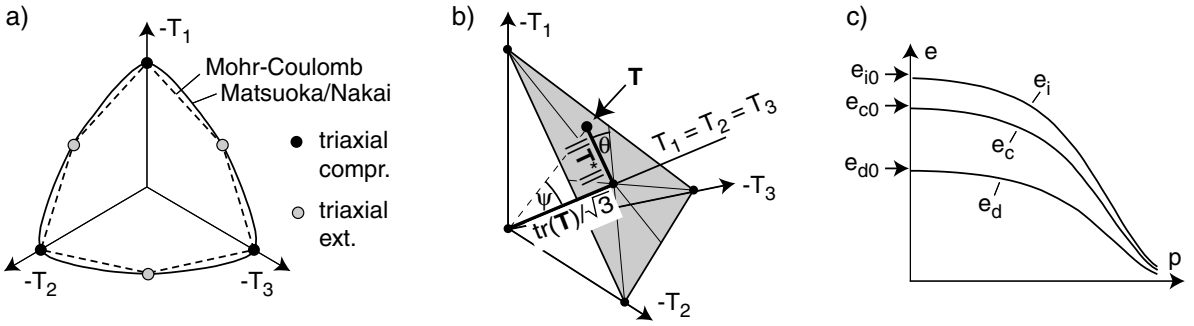

Figure 7.12: *a) Failure criterion of Matusoka & Nakai [95], b) Geometric interpretation of the angles ψ and θ, c) Reduction of void ratio e with mean pressure p after Equation (7.35)*

The factors f_b, f_e and f_d consider the influence of pressure (barotropy) and density (pyknotropy) on stiffness:

$$f_d = \left(\frac{e - e_d}{e_c - e_d}\right)^{\alpha} \tag{7.32}$$

$$f_e = \left(\frac{e_c}{e}\right)^{\beta} \tag{7.33}$$

$$f_b = \left(\frac{e_{i0}}{e_{c0}}\right)^{\beta} \frac{h_s}{n} \frac{1 + e_i}{e_i} \left(\frac{3p}{h_s}\right)^{1-n} \left[3 + a^2 - a\sqrt{3}\left(\frac{e_{i0} - e_{d0}}{e_{c0} - e_{d0}}\right)^{\alpha}\right]^{-1} \tag{7.34}$$

Therein α, β, h_s (granular hardness) and n are material constants. The void ratios e_d, e_c and e_i correspond to the densest, the critical and the loosest possible state. With increasing mean pressure p they decrease affine to each other according to Equation (7.35) after Bauer [7] (Figure 7.12c):

$$\frac{e_i}{e_{i0}} = \frac{e_c}{e_{c0}} = \frac{e_d}{e_{d0}} = \exp\left[-\left(\frac{3p}{h_s}\right)^{n}\right] \tag{7.35}$$

In Equation (7.35) the index "0" in e_{i0}, e_{c0} and e_{d0} corresponds to the stress-free state ($p = 0$). The hypoplastic flow rule can be calculated from

$$\mathbf{m} = -\frac{\mathsf{L}^{-1} : \mathbf{N}}{\|\mathsf{L}^{-1} : \mathbf{N}\|} = -\frac{f_1(\hat{\mathbf{T}} + \hat{\mathbf{T}}^*) + f_2\hat{\mathbf{T}}}{\|f_1(\hat{\mathbf{T}} + \hat{\mathbf{T}}^*) + f_2\hat{\mathbf{T}}\|} \tag{7.36}$$

with $f_1 = F^2 + a^2\ \hat{\mathbf{T}} : \hat{\mathbf{T}}$ and $f_2 = -a^2\ \hat{\mathbf{T}} : (\hat{\mathbf{T}} + \hat{\mathbf{T}}^*)$. For the triaxial case (axial stress

$\sigma_1 = -T_1$, lateral stress $\sigma_3 = -T_3$), the scalar measure Ω is

$$\Omega \;=\; -\frac{D_v^{\rm acc}}{D_q^{\rm acc}} \;=\; -\sqrt{\frac{3}{2}}\,\frac{{\rm tr}\,(\mathbf{m})}{\|\mathbf{m}^*\|} \;\overset{\rm triax}{=}\; \frac{9}{2}\,\frac{f_1+f_2}{2f_1+f_2}\,\frac{1}{\eta} \tag{7.37}$$

with

$$f_1 \;=\; F + a^2\,\frac{{T_1}^2+2{T_3}^2}{(T_1+2T_3)^2} \quad \text{and} \quad f_2 \;=\; -\,a^2\,\frac{5{T_1}^2-4T_1T_3+8{T_3}^2}{3(T_1+2T_3)^2} \tag{7.38}$$

If the factor f_d after Equation (7.32) is applied some deformation paths may lead to an under-shooting of the lower bound e_d of the void ratio (Niemunis et al. [107]). In order to prevent this, Niemunis et al. [107] modified the factor f_d for $e < e_c$:

$$f_d \;=\; \left(\frac{e-e_d}{e_c-e_d}\right)^{\alpha} + \left[1-\left(\frac{e-e_d}{e_c-e_d}\right)^{\alpha}\right]^{z}\;\bar{f}_d \tag{7.39}$$

$$\bar{f}_d \;=\; -\frac{{M_e}^{(d)}\;(1+e)\;\sqrt{3}+{M_T}^{(d)}\;f_b\;f_e\;\sqrt{3}\;(3+a^2)}{{M_T}^{(d)}\;f_b\;f_e\;3a} \tag{7.40}$$

$${M_T}^{(d)} \;=\; -\frac{e_d}{h_s}\;n\;\left(\frac{3p}{h_s}\right)^{n-1} \qquad\qquad {M_e}^{(d)} \;=\; 1 \tag{7.41}$$

${M_T}^{(d)}$ and ${M_e}^{(d)}$ are the components of a vector perpendicular to the yield surface. The exponent $z = 5$ delivers an improved numerical stability.

7.3.1.2 Modified version with increased shear stiffness

Niemunis [105] demonstrated that the original version of the hypoplastic model presented in Section 7.3.1.1 exhibits a too low shear stiffness for the case of shear deformations near the p-axis. In a re-calculation of a cyclic undrained shearing, a much too fast build-up of pore water pressure was obtained (Figure 7.13). The extension of the intergranular strain presented in Section 7.3.2 cannot solve this problem [105].

In order to improve the constitutive equation Niemunis [105] proposed a modification of the shear stiffness. The Poisson's ratio ν was introduced as another material constant (original version: $\nu = 0.38$ is too large). The modified stiffness tensor L_n reads:

$$\mathsf{L}_n \;=\; \mathsf{L} \;+\; f_b\;f_e\;\frac{1}{\hat{\mathbf{T}}:\hat{\mathbf{T}}}\;\left[\frac{\left(1+\frac{a^2}{3}+\frac{a}{\sqrt{3}}\right)(1-2\nu)}{1+\nu}-1\right]\;(\mathsf{I}-\frac{1}{3}\;\mathbf{1}\otimes\mathbf{1}). \tag{7.42}$$

The flow rule given in Equation (7.36) was maintained. Thus, the nonlinear stiffness $\mathbf{N}$ had to be adapted:

$$\mathbf{N}_n \;=\; \mathsf{L}_n : (\mathsf{L}^{-1} : \mathbf{N}) \tag{7.43}$$

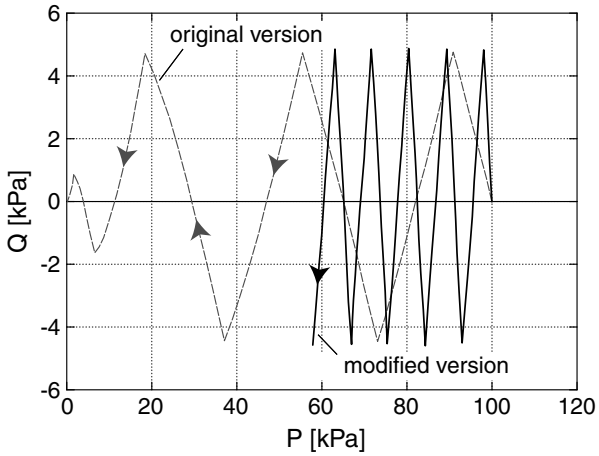

Figure 7.13: *Calculation of an undrained cyclic loading with the original version (OV) and the modified version (MV) of the hypoplastic material model, after Niemunis [105]*

This version of the hypoplastic model with increased shear stiffness is referred to as the "modified version" (MV). The description "original version" (OV) refers to the version of the model described in Section 7.3.1.1.

7.3.1.3 Material constants

For the hypoplastic model, eight material constants φ_c, h_s, n, e_{d0}, e_{c0}, e_{i0}, α and β have to be determined. The corresponding procedure for the OV, using standard laboratory tests (Herle [50]), is explained in the following. Concerning details and alternative methods see [50].

- The critical friction angle φ_c can be determined from undrained triaxial tests or cone pluviation tests. In the cone pluviation test, φ_c is the inclination of the cone.
- The granular hardness h_s and the exponent n describe the decrease of the void ratios e_i, e_c, e_d and e with increasing mean pressure p (Figure 7.12c). The constants are obtained from tests with a proportional compression, e.g. an oedometric compression. Equation (7.35) is fitted to the measured curves $e(p)$ (Figure 4.19a). The initial void ratio of the tests should be chosen ideally in the range $e_{c0} \leq e_0 \leq e_{i0}$. However, $e_0 = e_{\max}$ is thought to be a satisfactory initial state (Herle [50]).
- After Herle [50], the asymptotic void ratios at $p = 0$ can be estimated from $e_{i0} \approx 1.15\ e_{\max}$, $e_{c0} \approx e_{\max}$ and $e_{d0} \approx e_{\min}$.
- The constant α controls the influence of the density on the peak friction angle φ_P. In order to determine α, tests with triaxial compression are performed on initially

dense specimens. From the stress ratio $K_P = T_1/T_3$ at the peak of the curves $q(\varepsilon_1)$ and the corresponding void ratios e, e_c and e_d the constant α can be calculated:

$$\alpha = \frac{1}{\ln r_e} \ln \left[6 \frac{(K_P+2)^2 + a^2 \; K_P \; (K_P - 1 - \tan\nu_p)}{a \; (5K_P - 2) \; (K_P + 2) \; \sqrt{4 + 2 \; (1 + \tan\nu_P)^2}} \right] \quad (7.44)$$

with a from Equation (7.28), the pressure-referenced relative density $r_e = (e - e_d)/(e_c - e_d)$ and

$$\tan\nu_P = 2 \frac{(K_P - 4) + A \; K_P \; (5K_P - 2)}{(5K_P - 2) \; (1 + 2A)} - 1 \quad (7.45)$$

$$A = \frac{a^2}{(K_P + 2)^2} \left[1 - \frac{K_P(4 - K_P)}{5K_P - 2} \right] \quad (7.46)$$

- The constant β effects an increase of the stress rate $\mathring{\mathbf{T}}$ with increasing density of the specimens at $\mathbf{D}$ = constant. It can be obtained from oedometric tests on specimens with different initial densities (e.g. the tests on loose sand for h_s and n can be supplemented by tests on dense sand, Figure 4.19b). For a certain pressure p the void ratio e and the constrained modulus $E_s = \Delta T_1/\Delta\epsilon_1$ are determined. T_1 is the vertical stress corresponding to p and ϵ_1 is the logarithmic vertical strain. If the two different densities are identified by $\sqcup_I$ and $\sqcup_{II}$, the constant β is calculated from:

$$\beta = \frac{\ln \left(\frac{E_{sII}}{E_{sI}} \; \frac{m_I - n_I \; f_{dI}}{m_{II} - n_{II} \; f_{dII}} \right)}{\ln \left(\frac{e_I}{e_{II}} \right)} \quad (7.47)$$

$$\text{with} \quad m = \frac{(1 + 2K_0)^2 + a^2}{1 + 2{K_0}^2} \quad \text{and} \quad n = \frac{a \; (5 - 2K_0)(1 + 2K_0)}{3(1 + 2{K_0}^2)} \; . \quad (7.48)$$

The coefficient of lateral pressure can be obtained from the Jaky formula $K_0 = 1 - \sin\varphi_P$.

Following this procedure, the hypoplastic material constants of the OV were determined for the medium coarse to coarse sand No. 3 (Figure 4.14) using the test results presented in Chapter 4.3 (set of constants I in Table 7.2). Similar tests (not shown in this work) were performed in order to determine the constants of the centrifuge fine sand (set of constants III in Table 7.2).

For the modified version (MV) with increased shear stiffness, Niemunis [105] proposed the modified stiffness tensors but not an adaption of the material constants. If the constants of the OV determined after Herle [50] or following the list given above were used also for the

Material constant	Sand 3		CFS		
	OV	MV	OV	MV	
Set of constants	I	II	III	IV	V
ν	(0.38)	0.2	(0.38)	0.2	0.2
φ_c [°]	31.2	31.2	32.8	32.8	32.8
h_s [MPa]	591	30	5580	150	150
n	0.50	0.65	0.30	0.40	0.40
e_{d0}	0.577	0.577	0.575	0.575	0.575
e_{c0}	0.874	0.874	0.908	0.908	0.908
e_{i0}	1.005	1.005	1.044	1.044	1.044
α	0.12	0.20	0.12	0.12	0.12
β	1.0	1.0	1.6	1.0	1.0
R	10^{-4}	10^{-4}	10^{-4}	10^{-4}	10^{-4}
m_R	2.9	3.8	3.0	3.9	5.5
m_T	1.45	1.9	1.5	1.85	2.0
χ	6.0	6.0	6.0	6.0	6.0
β_r	0.2	0.2	0.2	0.2	0.2

Table 7.2: Summary of the material constants of the hypoplastic model and the intergranular strain for sand No. 3 referring to Figure 4.14 and the centrifuge fine sand (CFS)

MV, the stiffness would be strongly overestimated. At the moment, the material constants of the MV are chosen from a re-calculation of q-ε_1-curves from monotonic drained triaxial tests. The constants are varied, until the test data is reproduced well. It should be annotated, that the constants h_s and n determined this way in combination with Equation (7.35) do not longer describe the curves $e(p)$ in oedometric tests on specimens prepared with the maximum void ratio. Table 7.2 summarizes the constants of the MV for sand No. 3 (set of constants II) and the centrifuge fine sand (sets of constants IV/V)

7.3.1.4 Check of the model prediction

The prognosis of the material behaviour by the OV and the MV of the hypoplastic model was checked in re-calculations of drained monotonic triaxial tests. The test results were

already presented in Figures 4.16 and 4.17. For the re-calculation of the element tests the Fortran program "UMA" (author: A. Niemunis) was used. This program simulates a calculation in a single integration point. In Figures 7.14 and 7.15, the measured and calculated curves $q(\varepsilon_1)$ and $\varepsilon_v(\varepsilon_1)$ are compared.

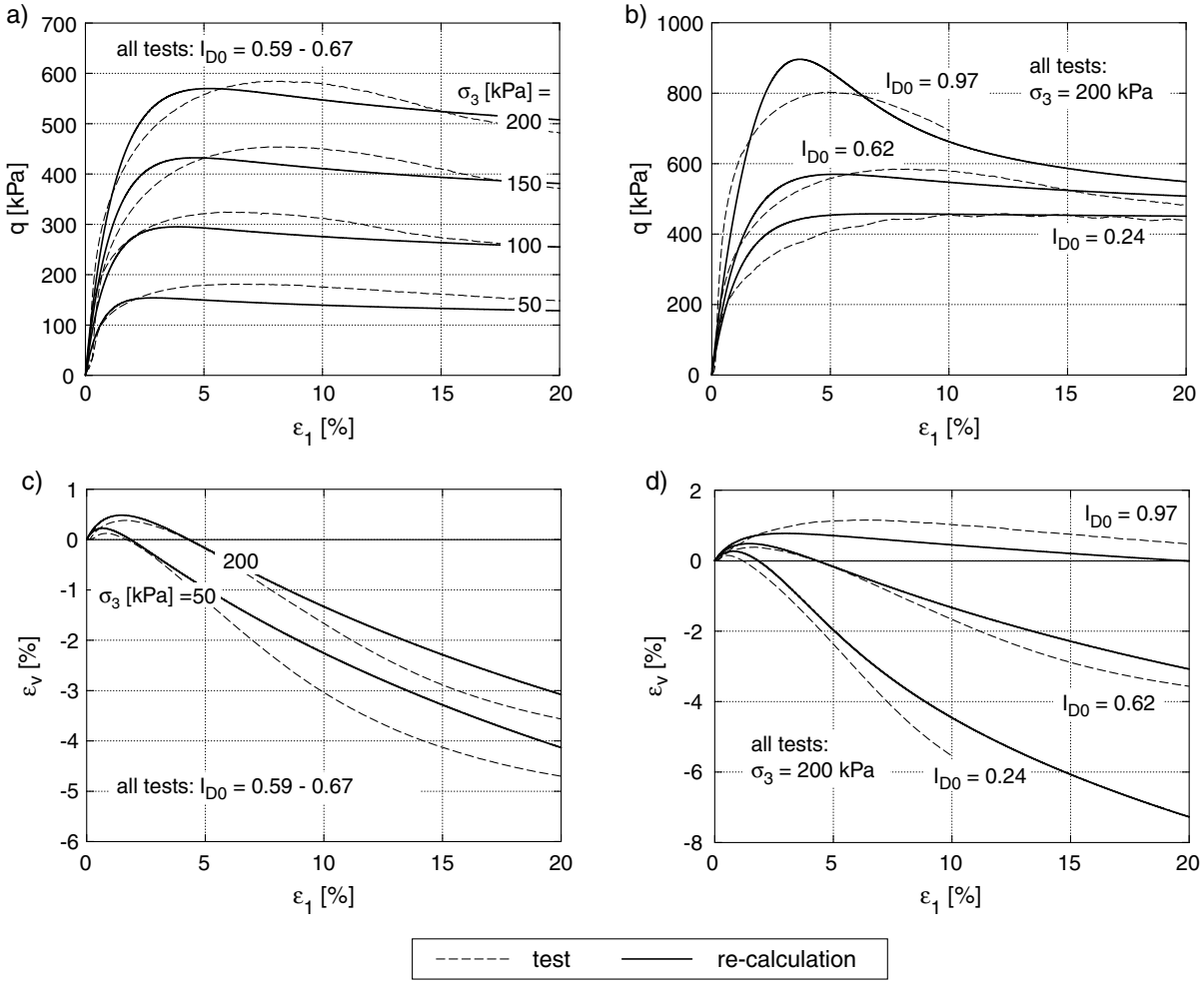

Figure 7.14: *Re-calculation of drained monotonic triaxial tests with the OV of the hypoplastic model and set of constants I in Table 7.2*

The curves in Figure 7.14 were obtained from calculations with the OV and the set of constants I referring to Table 7.2. The congruence of the calculated and measured curves is not perfect, but acceptable. Generally, the calculated curves $q(\varepsilon_1)$ reach the peak value at too small strains. The shear strength is overestimated for large densities.

The curves in Figure 7.15 were generated in calculations with the MV and the set of constants II referring to Table 7.2. While the curves $q(\varepsilon_1)$ hardly differ from the curves received with the OV, the contractancy is overestimated by the MV.

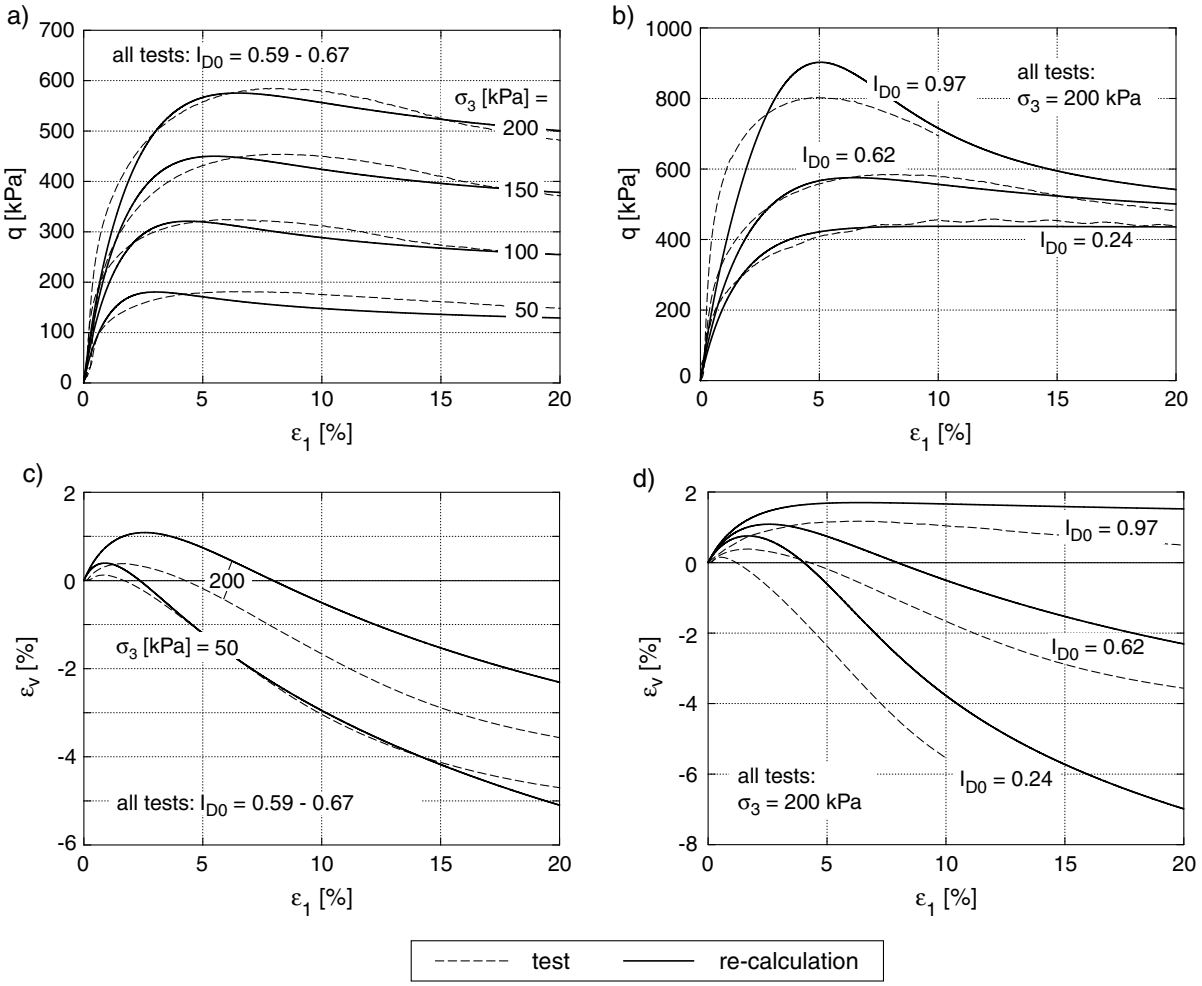

Figure 7.15: *Re-calculation of drained monotonic triaxial tests with the OV of the hypoplastic model and set of constants II in Table 7.2*

A deficit of the original version of the hypoplastic model according to von Wolffersdorff [172] is the too small shear stiffness near the p-axis. The modified version with an increased shear stiffness proposed by Niemunis [105] overestimates the contractancy. Furthermore, no simple procedure for the determination of the material constants from standard laboratory tests exists so far for the MV. The constants h_s and n lose their original meaning. The advantages of both versions (OV and MV) should be combined in order to obtain a powerful hypoplastic material formulation. At present, corresponding efforts are undertaken in Bochum.

7.3.2 Extension by the intergranular strain

7.3.2.1 Motivation and mathematical formulation

Cyclic processes cannot be calculated correctly with the basic version of the hypoplastic model presented in Section 7.3.1. The increase of the stiffness, due to a change of the strain path, is not reproduced adequately. Thus, with each stress cycle an unrealistic large strain remains in the material ("Ratcheting", Figure 7.16).

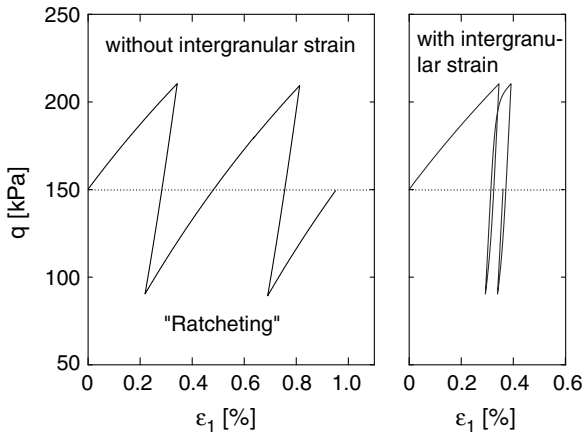

Figure 7.16: *q-ε_1-curves in cyclic triaxial tests without and with intergranular strain*

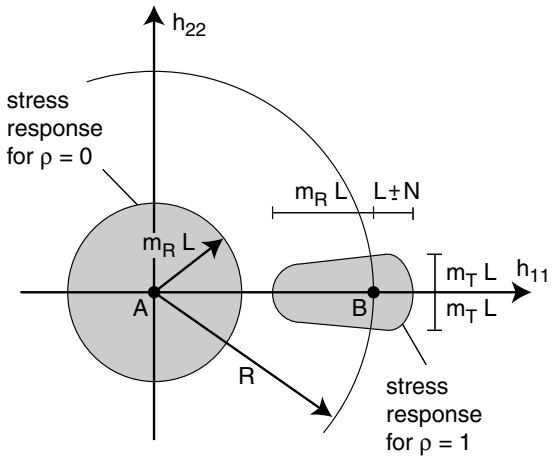

Figure 7.17: *Modification of the stiffness by m_R and m_T for $\varrho = 0$ and $\varrho = 1$, after Niemunis [105]*

In order to eliminate this deficit and to consider the path-dependence of the stiffness, Niemunis & Herle [106] introduced the state variable "intergranular strain" $\mathbf{h}$, which memorizes the last part of the previous strain path. At most, $\|\mathbf{h}\|$ can take the value R (material constant). A measure of the mobilization of the intergranular strain is

$$\rho \;=\; \frac{\|\mathbf{h}\|}{R}. \tag{7.49}$$

Depending on the angle between the actual strain rate $\mathbf{D}$ and the direction of the intergranular strain $\vec{\mathbf{h}} = \mathbf{h}/\|\mathbf{h}\|$ the stiffness M in Equation (7.25) is increased:

$$\mathsf{M} = [\rho^\chi\, m_T + (1-\rho^\chi)\, m_R]\;\mathsf{L} + \begin{cases} \rho^\chi(1-m_T)\mathsf{L} : \vec{\mathbf{h}}\vec{\mathbf{h}} + \rho^\chi\, \mathbf{N}\vec{\mathbf{h}} & \text{for } \vec{\mathbf{h}} : \mathbf{D} > 0 \\ \rho^\chi(m_R - m_T)\mathsf{L} : \vec{\mathbf{h}}\vec{\mathbf{h}} & \text{for } \vec{\mathbf{h}} : \mathbf{D} \le 0 \end{cases} \tag{7.50}$$

In Equation (7.50) m_T, m_R and χ are material constants. In the following, the functionality of Equation (7.50) is demonstrated for the case of plane strain. Corresponding stress

response envelopes are illustrated in Figure 7.17 for the special cases $\varrho = 0$ (intergranular strain = zero) and $\varrho = 1$ (intergranular strain fully mobilized). For a soil without a preloading ($\varrho = 0$), independently of the direction of loading, the linear stiffness increased by m_R is used ($\mathsf{M} = m_R\ \mathsf{L}$). Also for a fully mobilized intergranular strain ($\varrho = 1$) and a return of the strain path the stiffness takes the maximum value $\mathsf{M} = m_R\ \mathsf{L}$. In the case of a rotation of the strain path by 90° at $\varrho = 1$, the linear stiffness L is multiplied by the factor m_T ($\mathsf{M} = m_T\ \mathsf{L}$). In all these cases, the nonlinear stiffness $\mathbf{N}$ remains unconsidered. Between $\varrho = 0$ and $\varrho = 1$, the stiffness is interpolated. For a loading with $\varrho = 1$ and $\mathbf{D} \sim \vec{\mathbf{h}}$ the stiffness reads $\mathsf{M} = \mathsf{L} + \mathbf{N}\ \mathbf{D}/\|\mathbf{D}\|$, i.e. it is identical with the stiffness for monotonic deformation paths given in Equation (7.25). The equation of evolution for the objective rate of the intergranular strain $\mathring{\mathbf{h}}$ is:

$$\mathring{\mathbf{h}} = \begin{cases} (\mathsf{I} - \vec{\mathbf{h}}\vec{\mathbf{h}}\varrho^{\beta_r}) : \mathbf{D} & \text{for} \quad \vec{\mathbf{h}} : \mathbf{D} > 0 \\ \mathbf{D} & \text{for} \quad \vec{\mathbf{h}} : \mathbf{D} \leq 0 \end{cases} \tag{7.51}$$

Therein β_r is another material constant.

7.3.2.2 Material constants

The extension of the hypoplastic model by the intergranular strain requires the determination of the five material constants R, m_R, m_T, χ and β_r. A possible procedure was described by Niemunis & Herle [106]. In this work, an alternative way was chosen. The constants were obtained from a fitting to the strain amplitudes measured in cyclic triaxial tests.

First, by means of Figure 7.18, a general problem of the present formulation of the intergranular strain and the choice of the material constants is discussed. Figure 7.18 presents the calculation of a triaxial test. At a constant lateral stress $\sigma_3 = 150$ kPa starting from the isotropic state the deviatoric stress was increased to $q = 250$ kPa. After that, two cycles were applied, each with the maximum deviatoric stress $q^{\max} = 250$ kPa and the minimum one $q^{\min} = 250$ kPa - $2q^{\text{ampl}}$. Finally, the deviatoric stress was increased to $q = 350$ kPa. The q-ε_1-curves for the amplitudes $q^{\text{ampl}} = 20$, 40, 60 and 80 kPa are given in Figure 7.18. The constants of the intergranular strain were chosen in such way that a realistic prediction of the q-ε_1-curve was achieved for $q^{\text{ampl}} = 60$ kPa (Figure 7.18c). Realistic prediction means slightly hysteretic q-ε_1-curves during the cycles, a small residual strain at the end of the cycles and a stiffness during the continued loading ($q > 250$ kPa), which is identical with the stiffness of the first loading towards $q = 250$ kPa before the first cycle (a possible increase of the stiffness due to the cycles (Figure 5.99) is disregarded here). For the smaller amplitudes $q^{\text{ampl}} = 20$ and 40 kPa, the same set of material constants

causes an overshooting of the stress path when the loading was continued after the second cycle ($q > 250$ kPa), i.e. the transition from the stiffness of reloading to the stiffness of continued (first) loading occurs too late (at a too large deviatoric stress). For the largest amplitude $q^{\mathrm{ampl}} = 80$ kPa, this transition occurs too early which results in an unrealistic ratcheting.

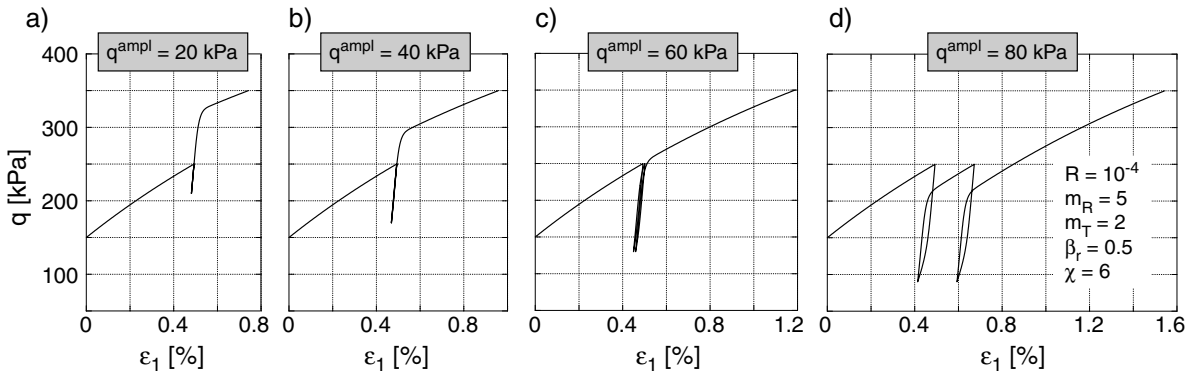

Figure 7.18: *Calculation of a triaxial test with two interposed cycles*

In a FE calculation of a boundary value problem with cyclic and subsequent monotonic loading (e.g. calculation of packages of cycles with different average stresses, Canbolat [16]), the stress amplitude is different in each integration point. However, with a certain set of constants of the intergranular strain, the stress-strain behaviour can be predicted correctly only for *one* amplitude $q_{\mathrm{ref}}^{\mathrm{ampl}}$. This implies the following disadvantages:

- In integration points with $q^{\mathrm{ampl}} < q_{\mathrm{ref}}^{\mathrm{ampl}}$, the deformation path during the monotonic loading following the cycles is calculated incorrectly. A too stiff material behaviour is predicted.
- In integration points with $q^{\mathrm{ampl}} > q_{\mathrm{ref}}^{\mathrm{ampl}}$, the ratcheting leads to an overestimation of the strain amplitude and thus to too large accumulation rates in the explicit calculation.

Eventually, as proposed by Niemunis (Section 4.3.7 in [105]), the described problem can be solved by a coupling of multiple intergranular strains. Future effort on this field is indispensable for realistic FE predictions.

In the FE calculations presented in Chapter 8, a cyclic loading without a subsequent monotonic loading or a change of the average value of the external load during the cycles is considered. In this case it can be accepted if the stress path during a monotonic loading after the cycles would overshoot. A ratcheting for large amplitudes can be avoided by

choosing large values for the constants R and χ and a small one for β_r. Then the stress-strain loops are hardly hysteretic. At least for amplitudes $q^{\text{ampl}} \leq 80$ kPa this coincides with test results presented in Section 5.2.1.1. The inclination of the hystereses and thus the secant stiffness can be adjusted via the constant m_R (Figure 7.19). m_R is chosen in such way, that the strain amplitudes measured in the experiments are reproduced.

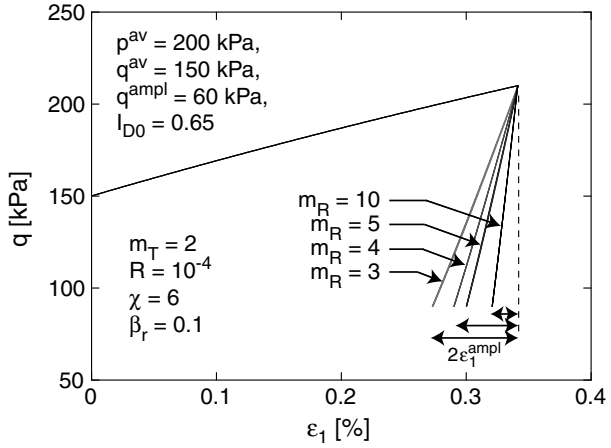

Figure 7.19: *Different strain amplitudes ε_1^{ampl} due to a variation of the material constant m_R*

The residual strain remaining at the end of each cycle is not predicted realistically by this choice of the material constants of the intergranular strain since unloading and reloading are almost elastic. However, the implicit cycles (second cycle and control cycles) are primarily calculated to estimate the strain amplitude. A realistic prediction of the accumulation is not necessary, since this is the task of the explicit accumulation model. The residual strains in a cycle N_i calculated implicitly can be ignored, i.e. the subsequent explicit calculation of the residual strains may start from the beginning of cycle N_i.

The constants of the intergranular strain for sand No. 3 (Figure 4.14) were determined by fitting the data of the cyclic triaxial tests with uniaxial stress cycles and different stress amplitudes q^{ampl} (presented in Section 5.2.1.1). In a re-calculation of the first two cycles of the tests with the Fortran program UMA (see Section 7.3.1.4) $R = 10^{-4}$, $\chi = 6.0$ and $\beta_r = 0.2$ were chosen and m_R was varied until the strain amplitudes $\varepsilon^{\text{ampl}}$ measured in the tests could be reproduced. Figure 7.20a presents the q-ε_1-curves of the re-calculation for different amplitudes q^{ampl}. In Figure 7.20b, the calculated strain amplitudes $\varepsilon^{\text{ampl}}$ (determined from the second cycle) are compared with the values determined experimentally (mean values over 10^5 cycles). Since in the cyclic triaxial tests the stress path is rotated by 180° in the extrems of $q(t)$, the material constant m_T does not influence the

calculation. It was set to $m_T = 0.5\ m_R$. Table 7.2 summarizes the determined sets of constants for sand No. 3 and the centrifuge fine sand. The set of constant V is further addressed in Section 8.2.1.

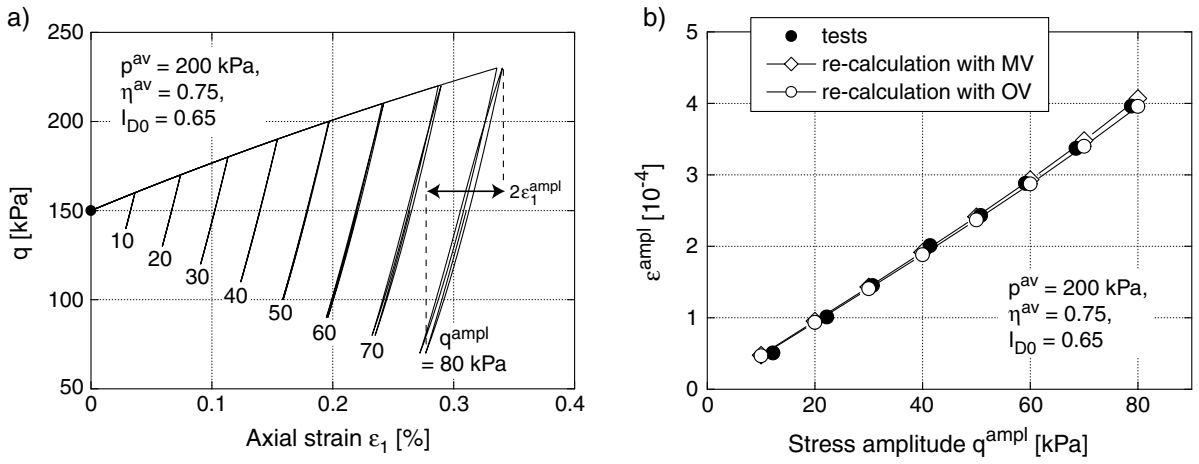

Figure 7.20: *a) Calculated q-ε_1-loops for different stress amplitudes q^{ampl}, b) Determination of the material constants of the intergranular strain from a comparison of the calculated strain amplitudes ε^{ampl} with those measured in the cyclic triaxial tests*

7.3.2.3 Check of the model prediction

From Figure 7.20b it becomes clear, that the linear increase of the strain amplitude $\varepsilon^{\mathrm{ampl}}$ with the stress amplitude q^{ampl}, which was measured in the tests, is reproduced well by the constitutive equations and the sets of constants in Table 7.2. In a similar manner also the first two cycles of the triaxial tests with a variation of the initial density I_{D0} (Section 5.2.3), the average mean pressure p^{av} (Section 5.2.4.1) and the average stress ratio η^{av} (Section 5.2.4.2) were re-calculated. The q-ε_1-curves and an illustration of the strain amplitude $\varepsilon^{\mathrm{ampl}}$ as a function of the respective varied parameter are given in Figure 7.21.

The increase of the strain amplitude with the void ratio (Figure 7.21b) and the decrease of $\varepsilon^{\mathrm{ampl}}$ with η^{av} (Figure 7.21f) is reproduced correctly. The increase of the strain amplitude with increasing average mean pressure for $\zeta = q^{\mathrm{ampl}}/p^{\mathrm{av}} = \text{constant}$ is overestimated (Figure 7.21d). While in the tests $G_{\mathrm{hyst}} \sim (p^{\mathrm{av}})^{0.75}$ was measured, the calculations with the OV (set of constants I in Table 7.2) deliver $G_{\mathrm{hyst}} \sim (p^{\mathrm{av}})^{0.47}$. For the MV (set of constants II in Table 7.2) even $G_{\mathrm{hyst}} \sim (p^{\mathrm{av}})^{0.29}$ is obtained due to the larger value of the material constant n of the hypoplastic model.

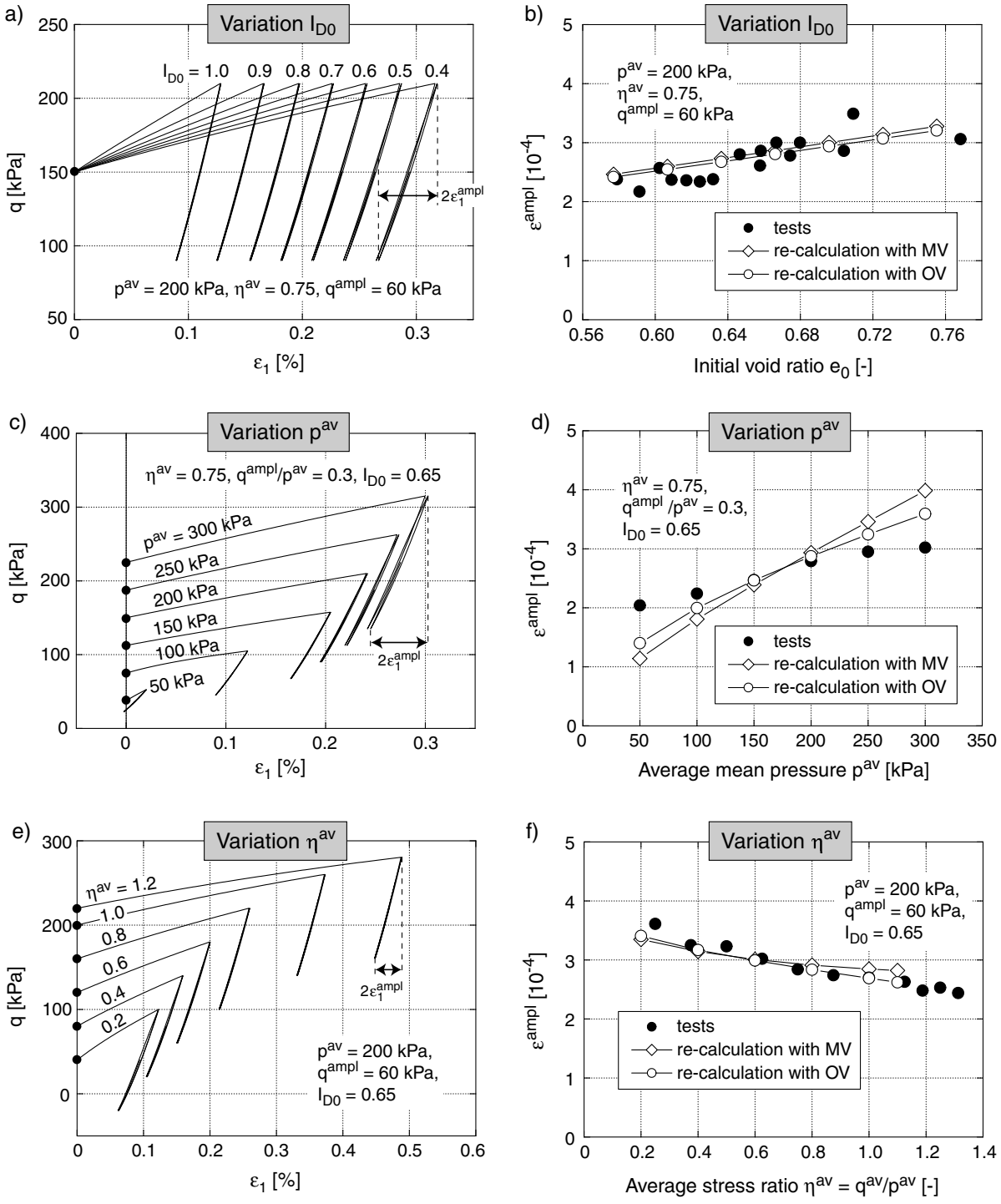

Figure 7.21: *Re-calculation of the first two cycles of the triaxial tests with different initial densities I_{D0}, average mean pressures p^{av} and average stress ratios η^{av}: stress-strain hystereses (calculated with the MV) and strain amplitudes ε^{ampl}*

Another problem becomes clear if the curves of the volumetric strain with the deviatoric stress in Figure 7.22 are considered. In the calculations with the OV (Figure 7.22a) a contractancy was obtained during unloading. This is definitely false. Calculations with the MV (Figure 7.22b) delivered more realistic q-ε_v-hystereses with a dilatancy during unloading.

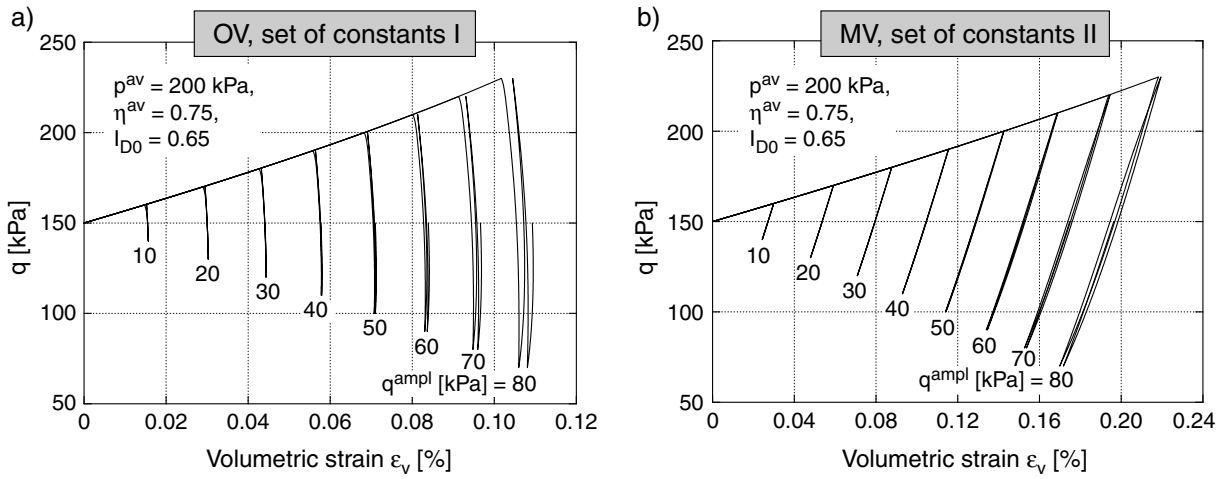

Figure 7.22: *q-ε_v-hystereses for different stress amplitudes q^{ampl}, calculated a) with the OV and set of constants I in Table 7.2 and b) with the MV and set of constants II in Table 7.2*

Figure 7.23 demonstrates by means of calculations with the MV and the set of constants II in Table 7.2, that the fitting of the material constants to the test data of the amplitudes of the total strain $\varepsilon^{\mathrm{ampl}}(q^{\mathrm{ampl}})$ leads to a slight underestimation of the deviatoric strain amplitudes $\varepsilon_q^{\mathrm{ampl}}(q^{\mathrm{ampl}})$. The volumetric strain amplitudes $\varepsilon_v^{\mathrm{ampl}}(q^{\mathrm{ampl}})$ are overestimated. Since $\dot{\varepsilon}^{\mathrm{acc}} \sim (\varepsilon^{\mathrm{ampl}})^2$ holds, the latter is of minor importance as long as the total strain amplitudes $\varepsilon^{\mathrm{ampl}}$ are predicted correctly.

In Section 5.2.4.1 it was demonstrated by means of RC test data, that the exponent k of the pressure-dependent shear stiffness $G_{\mathrm{hyst}} \sim (p^{\mathrm{av}})^k$ (here the exponent is denoted as k in order to distinguish it from the hypoplastic material constant n) increases with the shear strain amplitude γ^{ampl}. In calculations with different average mean pressures p^{av} and ratios $\zeta = q^{\mathrm{ampl}}/p^{\mathrm{av}}$ it was checked, if these experimental observations are reproduced by the constitutive equations. Figure 7.24 shows calculations with the OV and the set of constants I in Table 7.2. The calculations did not agree with the test data. Even a slight decrease of the exponent k with increasing amplitude was obtained. Similar results were attained with the MV.

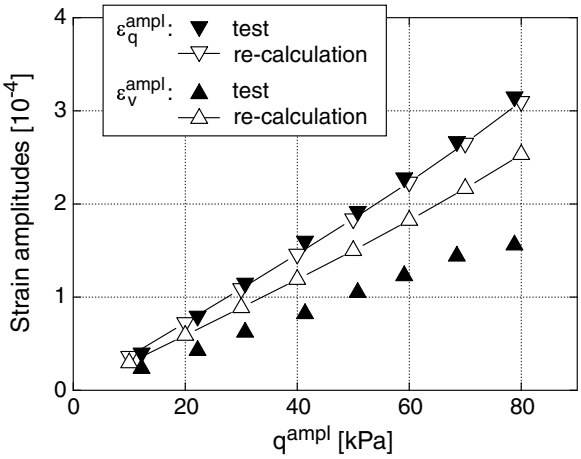

Figure 7.23: *Comparison of the calculated and measured strain amplitudes* $\varepsilon_q^{ampl}(q^{ampl})$ *and* $\varepsilon_v^{ampl}(q^{ampl})$*, calculations with the MV and set of constants II in Table 7.2*

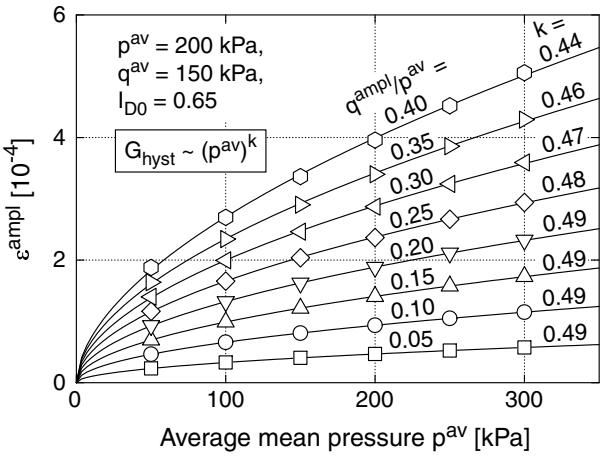

Figure 7.24: *Dependence* $\varepsilon^{ampl}(p^{av})$ *or* $G_{hyst} \sim (p^{av})^k$ *for different stress ratios* $\zeta = q^{ampl}/p^{av}$*, calculations with the OV and set of constants I in Table 7.2*

For a reliable prediction of settlements with an explicit accumulation model, the accurate estimation of the strain amplitude in the implicit cycles is of high importance. The remarks in this section reveal that the recent formulation of the intergranular strain has to be improved. This should be one of the aspects of the continuation of this work.

Since the q-ε_v-hystereses are described more realistically, the modified version (MV) of the hypoplastic model was preferred in the FE calculations presented in Chapter 8.

Chapter 8

FE calculations with the accumulation model

8.1 Implementation

The accumulation model presented in Chapter 7 was implemented into the FE program ABAQUS as a Subroutine UMAT for user-defined materials. This work was done by A. Niemunis.

8.1.1 Modes of the material routine

The UMAT distinguishes three modes of operation:

1. Implicit mode:
   The program control is forwarded to a subroutine, in which the hypoplastic model with the extension by the intergranular strain is implemented. The implementation of hypoplasticity is discussed by Niemunis (Section 4.1.3 in [105]). This mode is used to calculate the initial equilibrium and the first cycle.

2. Recording mode:
   Also the recording mode calls the subroutine with the hypoplastic model. During the calculation, characteristic states of strain are memorized according to selected criteria (Section 8.1.2). From the recorded strain loop the strain amplitude $\varepsilon^{\mathrm{ampl}}$ is determined at the beginning of the pseudo-creep mode. The recording mode is used for the calculation of the second cycle and for control cycles.

3. Pseudo-creep mode:
   In this mode the explicit calculation of accumulation according to Equation (7.1) is carried out. Prior to the first increment in this mode the strain amplitude $\varepsilon^{\text{ampl}}$ has to be determined.

The UMAT identifies the appropriate mode for the respective step by the step number specified in the input file. Exemplary, in Figure 8.1 the assignment of calculation steps and program modes is given for the calculation of a cyclically loaded shallow foundation.

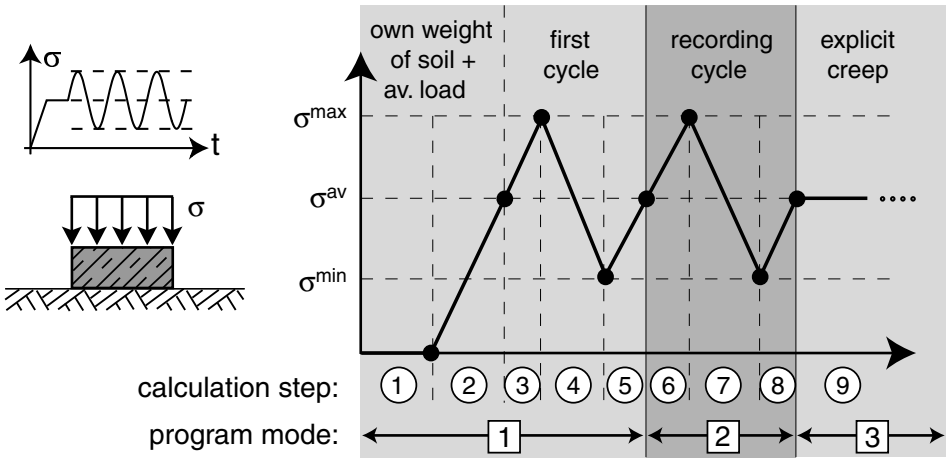

Figure 8.1: *Assignment of calculation steps and program modes for the calculation of a cyclically loaded shallow foundation*

8.1.2 Recording of states of strain in the recording mode

In order to minimize the memory requirements of a calculation, only characteristic points of the strain loop are memorized in the recording mode. From these strain points the amplitude $\varepsilon^{\text{ampl}}$ is determined at the beginning of the pseudo-creep mode (Figure 8.2). Beside the initial strain at the beginning of the implicit cycle, further points are recorded which fulfill certain criteria. These criteria are

- the change of the direction of the strain path by a certain minimum angle $\beta_{\min}$ and
- a certain distance $r_{\min}$ to the latest recorded point.

The procedure is explained by means of Figure 8.2. Let $\boldsymbol{\varepsilon}^l$ be the latest recorded strain point, $\boldsymbol{\varepsilon}^a$ the actual strain, $\boldsymbol{\varepsilon}^d = \boldsymbol{\varepsilon}^a - \boldsymbol{\varepsilon}^l$ the difference of both strain points and $\Delta\boldsymbol{\varepsilon}$ the strain increment from $\boldsymbol{\varepsilon}^a$ to the next strain point. Using the directions

$$\vec{\boldsymbol{\varepsilon}}^d = \frac{\boldsymbol{\varepsilon}^d}{\|\boldsymbol{\varepsilon}^d\|} \quad \text{and} \quad \vec{\Delta\boldsymbol{\varepsilon}} = \frac{\Delta\boldsymbol{\varepsilon}}{\|\Delta\boldsymbol{\varepsilon}\|} \tag{8.1}$$

and the angle between both directions

$$\beta \;=\; \arccos(\vec{\boldsymbol{\varepsilon}^d} : \vec{\Delta\boldsymbol{\varepsilon}}) \tag{8.2}$$

the strain point $\boldsymbol{\varepsilon}^a$ is recorded if both following criteria are simultaneously fulfilled:

$$\beta \;\geq\; \beta_{\min} \quad \text{and} \quad \|\boldsymbol{\varepsilon}^d\| \;\geq\; r_{\min}$$

The more stringent the criteria $\beta_{\min}$ and $r_{\min}$ are chosen, the larger are the number of recorded strain points and thus the memory requirements and the numerical effort during the calculation of $\varepsilon^{\text{ampl}}$. If the criteria are chosen too weak, the strain loop is not captured sufficiently. Section 8.2.3.2 deals with the appropriate choice of $\beta_{\min}$ and $r_{\min}$.

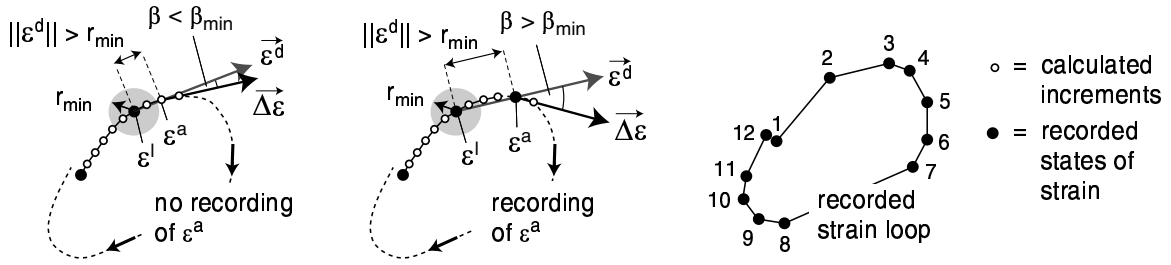

Figure 8.2: *Recording of characteristic points of the strain loop if the criteria* $\beta \geq \beta_{\min}$ *and* $\|\boldsymbol{\varepsilon}^d\| = \|\boldsymbol{\varepsilon}^a - \boldsymbol{\varepsilon}^l\| \geq r_{\min}$ *are fulfilled*

8.2 FE calculation of shallow foundations under cyclic loading

First, the re-calculation of the centrifuge model test of Helm et al. [49] (strip foundation under cyclic loading, Section 3.4.1.2) is presented in Section 8.2.1. After that, the same set of material constants was used to calculate boundary conditions deviating from the centrifuge model test. The influence of several parameters on the accumulation of settlements was studied (Section 8.2.2). Furthermore, in Section 8.2.3 some technical aspects of an FE calculation with an explicit accumulation model (control cycles, recording criteria, fineness of the FE mesh, boundaries of discretisation) are discussed.

8.2.1 Re-calculation of the centrifuge model test of Helm et al.

8.2.1.1 Material constants

In the centrifuge model test of Helm et al. [49] a poorly-graded fine sand (centrifuge fine sand (CFS), $d_{50} = 0.21$ mm, $U = d_{60}/d_{10} = 2.0$, $\varrho_s = 2.66$ g/cm^3) was used. Its grain size distribution curve is given in Figure 1 in [49]. The model test documented in [49] was performed on charge 942d of the sand, while in this work the material constants were determined using charge 942e ($e_{\min} = 0.575$, $e_{\max} = 0.908$).

The hypoplastic material constants of the sand were determined according to the procedure described in Section 7.3.1.3. They are summarized in Table 7.2. The material constants of the intergranular strain were first identified from a fitting to the strain amplitudes measured in cyclic triaxial tests (Section 7.3.2.2, set of constants IV in Table 7.2). However, the re-calculation of the cyclically loaded foundation presented in the following exhibited, that this set of material constants overestimates the measured settlement amplitudes ($s^{\text{ampl}} = 1.3$ mm in contrary to the experimental value $s^{\text{ampl}} \approx 0.8$ mm). For this reason, the constants m_R and m_T were corrected upwards and the set of constants V referring to Table 7.2 was used in all following calculations.

The material constants of the CFS for the accumulation model were determined in cyclic triaxial tests. The validity of the functions f_p and f_Y with $C_p = 0.43$ and $C_Y = 2.0$ was assumed. The constants C_e, C_{N1}, C_{N2} and C_{N3} could be derived from six tests with different stress amplitudes and initial densities (Figure 8.3). The determined set of constants was summarized in Table 7.1. In the tests on the CFS ($d_{50} = 0.21$ mm) significantly larger accumulation rates were measured than in the tests on the medium coarse to coarse sand No. 3 ($d_{50} = 0.55$ mm) presented in Chapter 5. Thus, the conclusions of Section 5.2.9 concerning the influence of the mean grain diameter were confirmed.

8.2.1.2 Boundary conditions of the FE calculation and discretisation

The centrifuge model test was re-calculated with following boundary conditions:

- Strip foundation, therefore calculation as a problem with plane deformations
- Dimensions of the test container: width 18.1 m, height 7.3 m (prototype). Using the symmetry only half of the soil was discretised (9.05 m × 7.3 m, Figure 8.4).
- Foundation: width $b = 1.0$ m, height $h = 0.6$ m, depth of embedding $t = 0$ m
- Material of the foundation: aluminium with weight $\gamma = 27$ kN/m^3, $E = 25.000$ MPa and $\nu = 0.3$

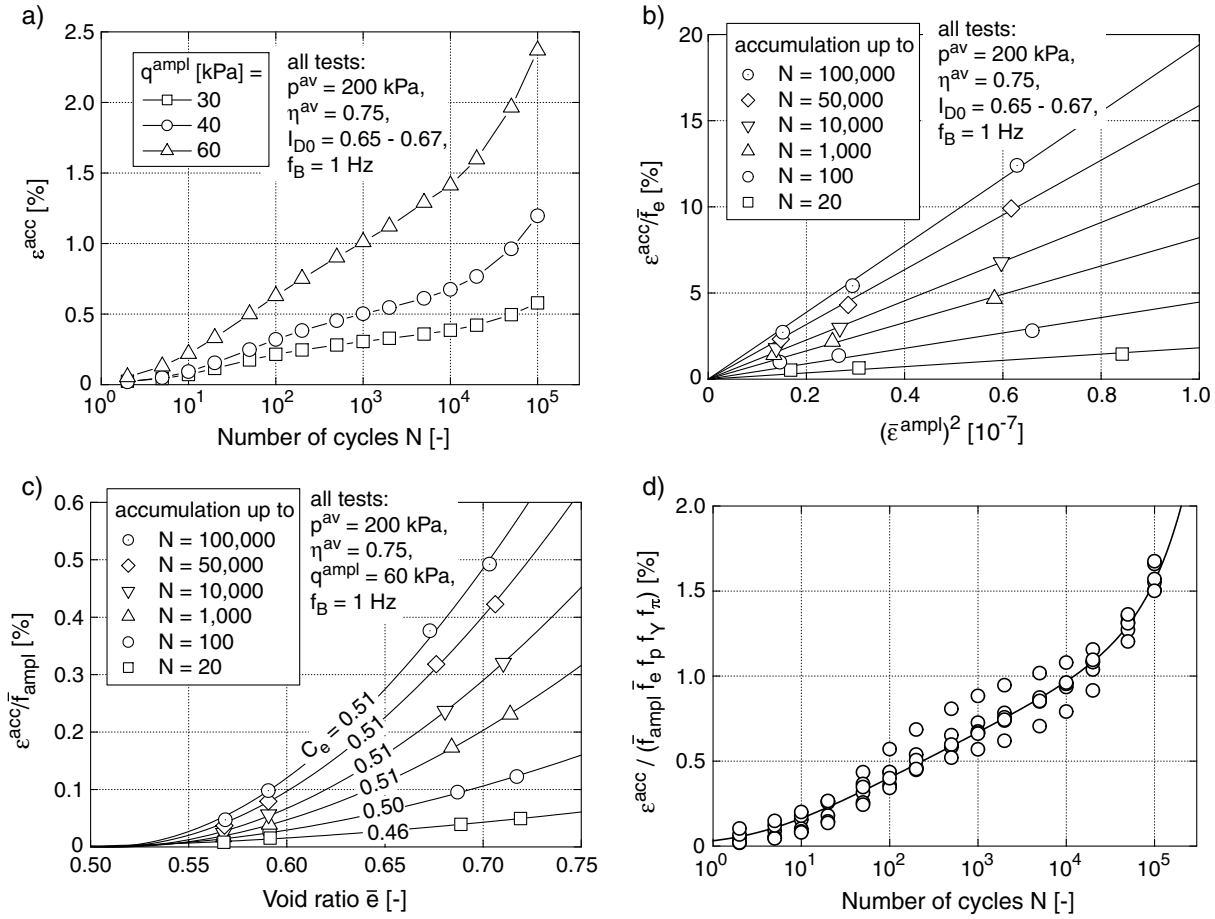

Figure 8.3: *Determination of the material constants of the accumulation model in cyclic triaxial tests on CFS: a) curves $\varepsilon^{acc}(N)$, b) confirmation of function f_{ampl}, c) function f_e, d) function f_N*

- Coefficient of friction in the contact between foundation and soil:
  $\mu = \tan(2/3\varphi_P) = \tan(2/3 \cdot 38°) = 0.47$
- Average load $\sigma^{av} = 89$ kPa, amplitude $\sigma^{ampl} = 75$ kPa (determined from the stress-settlement-hystereses in Figure 3.40b)
- Freshly pluviated sand, i.e. $g_0^A = 0$
- Initial density $I_{D0} = 0.9$
- Coefficient of lateral pressure $K_0 = 1 - \sin(\varphi_P) = 1 - \sin(38°) = 0.38$
- Initial value of the intergranular strain: component in the vertical direction $h_{11} = R$ due to pluviation, all other components zero
- Initial value of back polarization $\boldsymbol{\pi}$: A vertical polarization stemming from pluviation is assumed, i.e. the calculation starts with $f_\pi = 1$

The FE discretisation with four-nodal CPE4 elements (linear shape functions, full integration) is depicted in Figure 8.4. Remarks on the influence of the fineness of the mesh and the element type follow in Section 8.2.3.

As the results from the centrifuge model test, the curve of the residual settlement with the number of cycles (Figure 8.5) and the settlement amplitude $s^{\mathrm{ampl}} \approx 0.8$ mm (from the stress-settlement-hystereses in Figure 3.40b) are obtained. In Figure 8.5, the settlement in the model test does not contain the settlement due to the self-weight of the foundation. In the centrifuge model test, a settlement of 2.4 cm remained after the first cycle. After 10^5 cycles, a settlement of 7.3 cm was measured.

8.2.1.3 Results

Figure 8.5 presents the good congruence of the settlement curves $s(N)$ in the re-calculation and in the centrifuge model test. The settlement due to the self-weight of the foundation (approx. 0.4 cm) was subtracted from the settlements in the re-calculation. The implicit model predicts a slightly larger settlement ($s = 2.8$ cm) than it was measured in the model test ($s = 2.4$ cm). The amplitude of settlement in the re-calculation amounted $s^{\mathrm{ampl}} = 0.86$ mm. Thus, it was somewhat larger than the experimental value ($s^{\mathrm{ampl}} \approx 0.8$ mm). The calculated settlement after 10^5 cycles ($s = 6.8$ cm) lay slightly below the final settlement in the model test ($s = 7.3$ cm). The fields of the strain amplitude $\varepsilon^{\mathrm{ampl}}$ and the vertical displacement (including the settlement due to the self-weight of the foundation) are shown in Figure 8.6. It has to be critically annotated, that in contrary to the observations in the centrifuge model test (Figure 3.40c), a bulging of the soil surface beneath the foundation was not obtained in the FE calculation (Figure 8.6b). Some discrepancies between the FE results and the model test may result from general disadvantages of centrifuge model tests (e.g. parasitic vibrations).

8.2.2 Settlement prognoses for other boundary conditions

With the set of material constants of the fine sand (set of constants V in Table 7.2), settlement prognoses for the strip foundation under cyclic loading were established for boundary conditions, which deviate from those of the centrifuge model test of Helm et al. [49]. The variables of the soil (initial density I_{D0}, coefficient of lateral earth pressure K_0, historiotropic variable g_0^A), the loading of the foundation (average value σ^{av}, amplitude σ^{ampl}) and the geometry of the foundation (depth of embedding t, width b) were varied. Beside the strip foundation also the influence of the shape of the foundation was studied in calculations of shallow foundations with a quadratic or circular cross section.

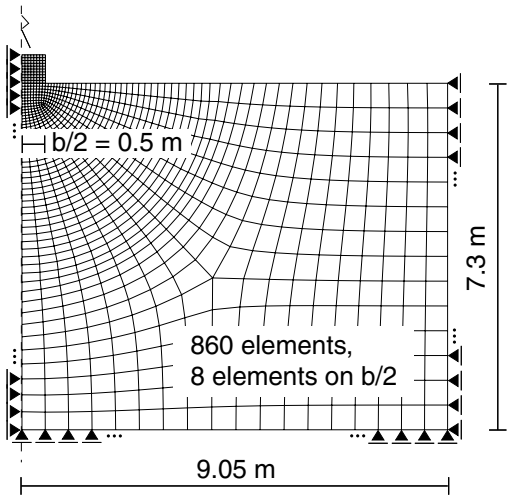

Figure 8.4: *FE discretisation considering the symmetry*

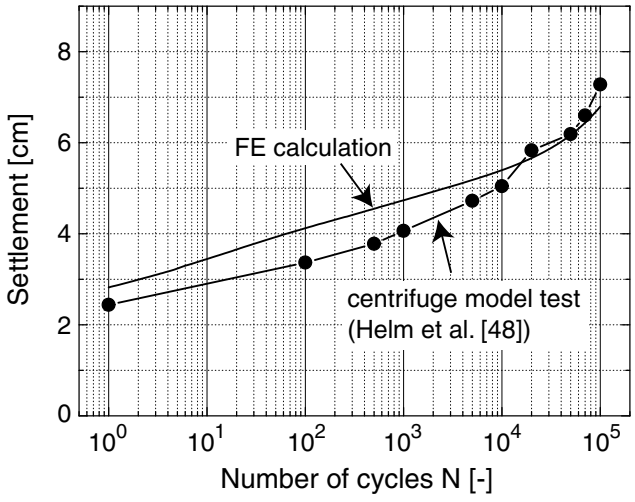

Figure 8.5: *Comparison of the settlement curves $s(N)$ in the model test and in the FE calculation*

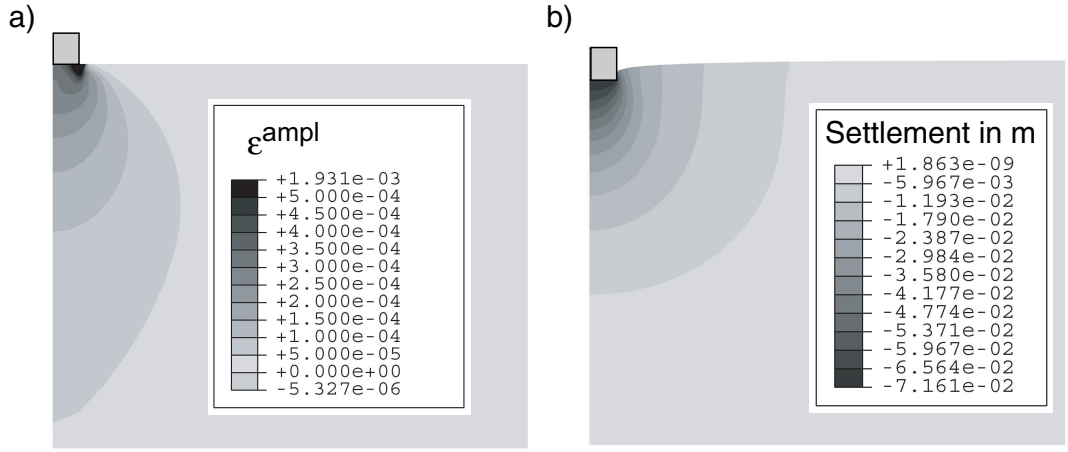

Figure 8.6: *Fields a) of the strain amplitude ε^{ampl} and b) of the vertical displacement*

8.2.2.1 Influence of the initial density

The initial density was varied within $0.5 \leq I_{D0} \leq 0.9$ in five calculations. Accordingly, the weight of the soil and thus the initial vertical stress were different. The coefficient of lateral earth pressure $K_0 = 0.38$ was kept constant (and not varied according to $K_0 = 1 - \sin(\varphi_P)$) in order to study exclusively the influence of the density. As expected, Figure 8.7 shows an increase of the settlement in the first cycle and the accumulation of settlements during the subsequent cycles with decreasing initial density. The latter is due to the void ratio-dependence of the accumulation rate ($\rightarrow$ increase of the function f_e of the accumulation model with e). Another reason is the increase of the amplitudes of strain or settlement

with decreasing I_{D0} (Figure 8.7, → larger f_{ampl}).

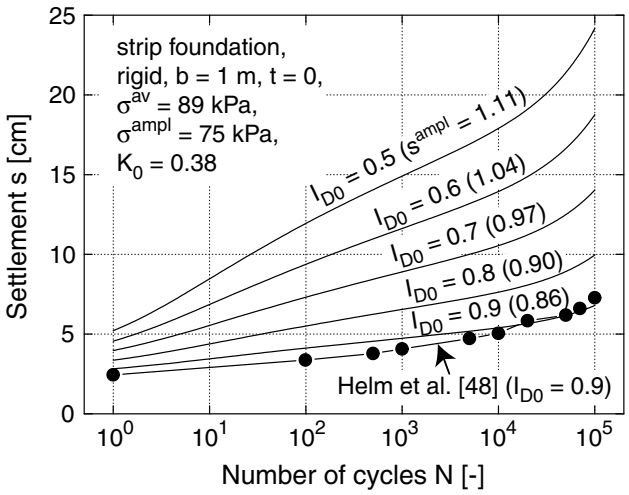

Figure 8.7: *Influence of the initial density I_{D0} on the accumulation of settlements*

8.2.2.2 Influence of the coefficient of lateral earth pressure

Coefficients of lateral earth pressure $0.2 \leq K_0 \leq 1.0$ were tested in five calculations. Figure 8.8 shows the decrease of the static settlements and the rates of settlement during cyclic loading with increasing K_0. Since the vertical stresses due to the self-weight of the soil remain constant, the lower rates can be attributed to an increase of the average mean pressure (→ smaller f_p) and a reduction of the deviatoric stress q and thus the stress ratio $\eta = q/p$ (→ smaller f_Y). Also the smaller settlement or strain amplitudes for the larger coefficients K_0 (→ smaller f_{ampl}) play a role. However, with decreasing stress ratio η^{av} also the volumetric portion of the accumulation rate (densification) grows and the rate of shear deformation declines. According to the Jaky formula $K_0 = 1 - \sin(\varphi_P)$, the reduction of the peak friction angle φ_P with decreasing I_D and the corresponding increase of K_0 lead to a reduction of the accumulation rate. This moderately counteracts the increase of the accumulation rate with decreasing initial density (Figure 8.7).

8.2.2.3 Influence of the historiotropy

Figure 8.9 makes clear, that the initial value of the historiotropic variable g_0^A significantly influences the settlement curves. For large initial values of g_0^A the portion $\dot{f}_N^A$ of the accumulation rate (see Table 7.1), which depends on the historiotropic variable, becomes negligible. The basic rate $\dot{f}_N^B$, which is independent of N or g^A, becomes dominant. The

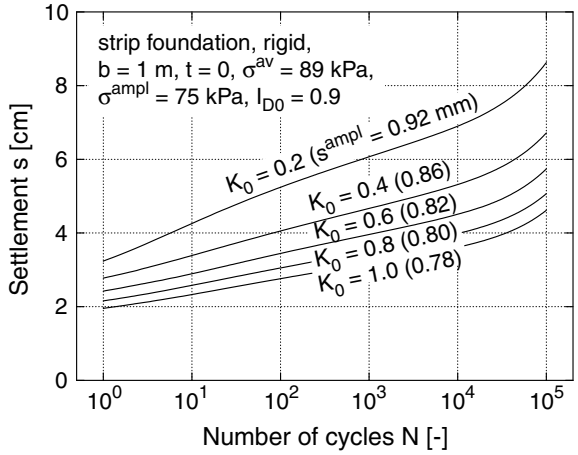

Figure 8.8: *Influence of the coefficient of lateral earth pressure K_0 on the accumulation of settlements*

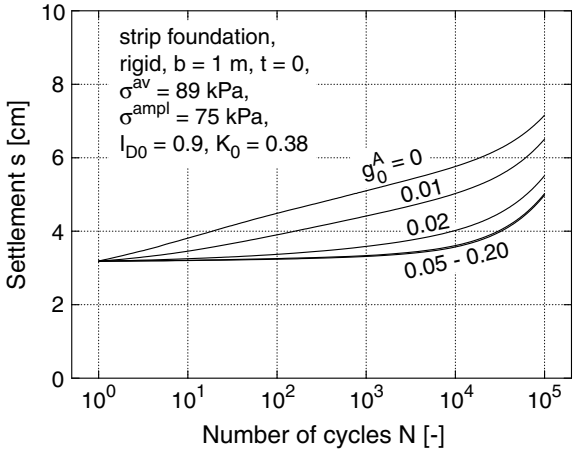

Figure 8.9: *Influence of the historiotropic variable g_0^A on the accumulation of settlements*

settlement s then increases almost linearly with N. In a diagram with semi-logarithmic scale (Figure 8.9) bent curves are obtained. Thus, the shape of the curves measured in situ depends strongly on the historiotropy of the soil.

8.2.2.4 Influence of the loading

Figure 8.10 presents calculations, in which the load, analogously to the tests of Hettler ([52, 53, 54], Section 3.4.1.1), oscillated between $\sigma^{\min} = 0$ and different maximum values $\sigma^{\max}$. From Figure 8.10a the increase of the settlement after the first cycle, the amplitude of settlement s^{ampl} and the rate of settlement in the subsequent cycles with increasing $\sigma^{\max}$ is obvious. Figure 8.10b confirms (at least approximately) the observations of Hettler, that the curves $s(N)$ are parallel in the double-logarithmic scale (compare Figure 3.37).

Figure 8.11 contains FE calculations with different average values 50 kPa $\leq \sigma^{\text{av}} \leq$ 200 kPa and amplitude ratios $0.25 \leq \sigma^{\text{ampl}}/\sigma^{\text{av}} \leq 1.0$. In Figure 8.11a the total residual settlement after 10^5 cycles is depicted. In Figure 8.11b the settlement at the end of the first cycle $s_{\text{stat}} + s_1$ was subtracted. The increase of the accumulation of settlement with the square of the amplitude ratio $\sigma^{\text{ampl}}/\sigma^{\text{av}}$ for σ^{av} = constant, which was already reported by Holzlöhner ([56], Section 3.4.1.1) and could also be derived from the tests of Laue ([82], Figure 3.39b), is confirmed by the data in Figure 8.11b. The main reason is the almost linear increase of the strain amplitude (compare s^{ampl}) with σ^{ampl} and the quadratic amplitude-dependence of the accumulation rate ($\rightarrow$ function f_{ampl}). Furthermore, Figure 8.11 shows, that for a constant amplitude ratio $\sigma^{\text{ampl}}/\sigma^{\text{av}}$ the rate of accumulation increases with increasing average load σ^{av}. This also agrees with observations of Holzlöhner

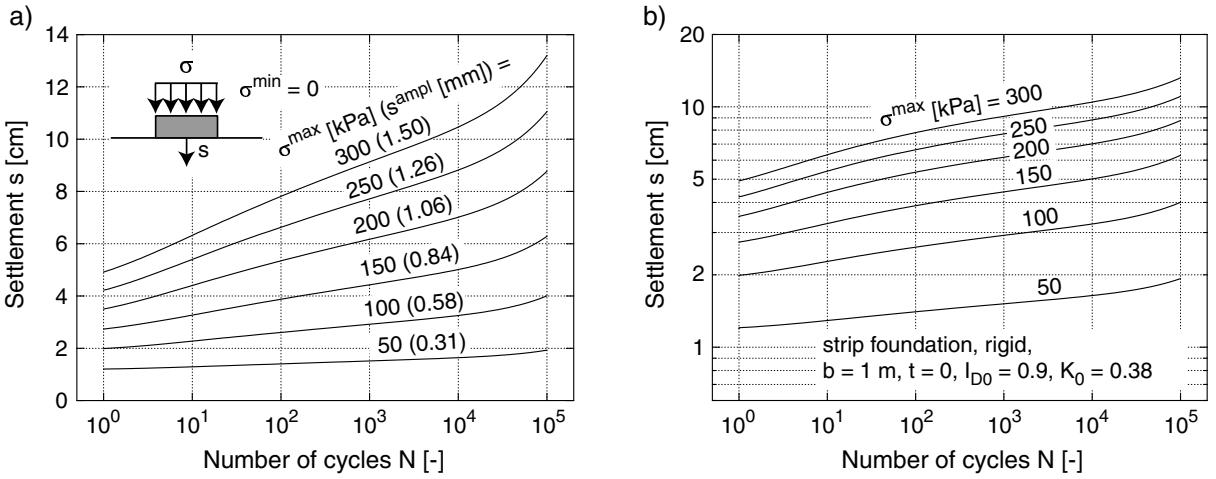

Figure 8.10: *Settlement curves for a loading with* $\sigma^{\min} = 0$ *and different values of* $\sigma^{\max}$, *illustration in a) semi- and b) double-logarithmic scale*

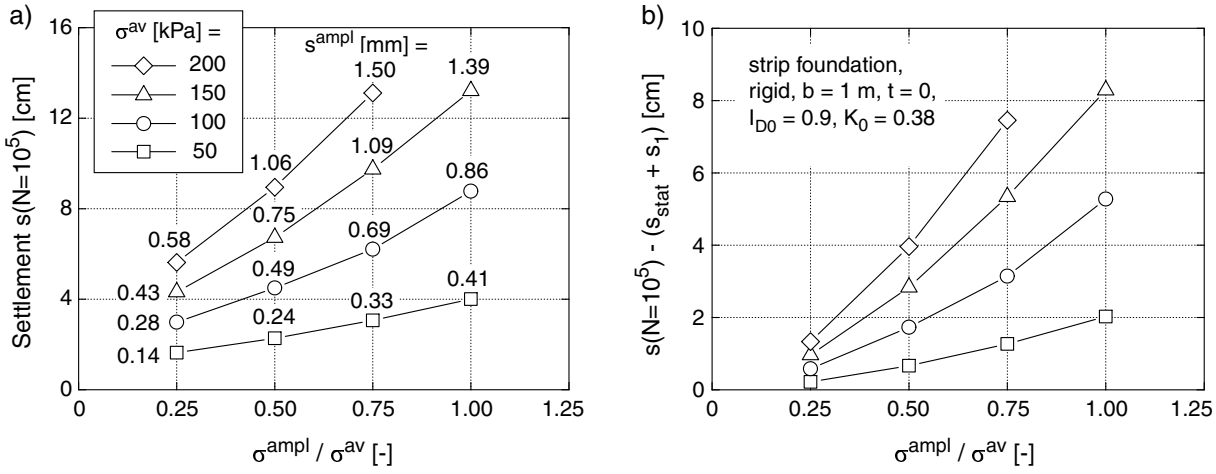

Figure 8.11: *Settlements under cyclic loading with different average values* σ^{av} *and amplitude ratios* $\sigma^{ampl}/\sigma^{av}$*: a) total strain after* 10^5 *cycles, b) accumulated settlement during the cycles with* $N > 1$

[56] and Laue [82]. It is caused by larger strain amplitudes (compare $s^{\mathrm{ampl}} \rightarrow$ larger f_{ampl}) and larger stress ratios $\eta^{\mathrm{av}} = q^{\mathrm{av}}/p^{\mathrm{av}}$ ($\rightarrow$ larger f_Y, but also smaller volumetric component of $\mathbf{m}$). The increase of the average mean pressure, which results in a reduction of the rate of accumulation ($\rightarrow$ smaller f_p), counteracts.

In Figure 8.12, calculations with identical amplitudes σ^{ampl} (and not $\sigma^{\mathrm{ampl}}/\sigma^{\mathrm{av}} = \text{constant}$) and different average loads 50 kPa $\leq \sigma^{\mathrm{av}} \leq$ 200 kPa are compared. For $\sigma^{\mathrm{ampl}} = \text{constant}$ the residual settlement after 10^5 cycles increases with σ^{av} (Figure 8.12a). However, this is due to the larger deformations during the monotonic loading up to the maximum load

whereas the rate of settlement accumulation during the subsequent cycles decreases with σ^{av} (Figure 8.12b). This can be attributed to a reduction of the strain amplitude with σ^{av} due to the stress-dependence of the stiffness (compare $s^{\mathrm{ampl}} \rightarrow$ smaller f_{ampl}).

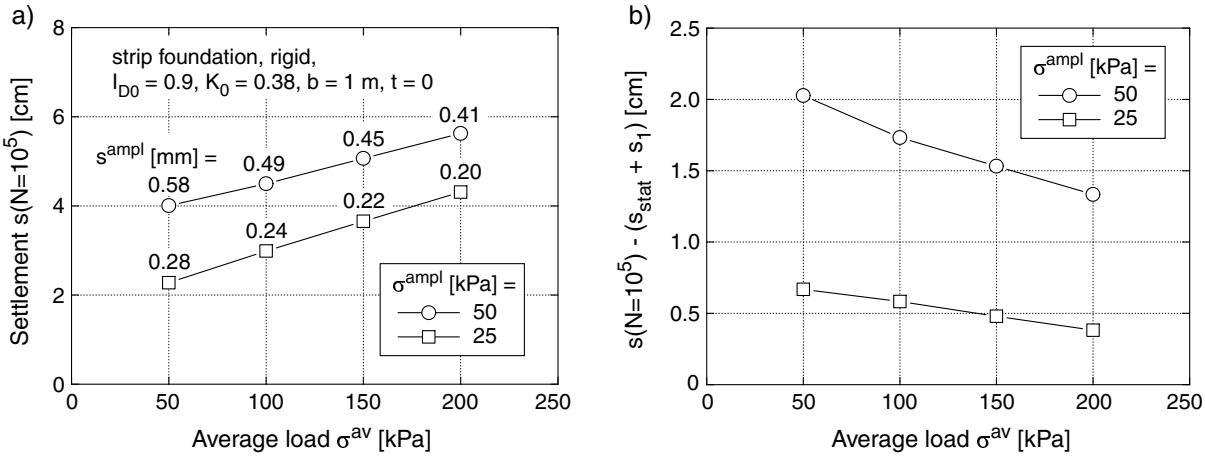

Figure 8.12: *Settlements under cyclic loading with different average values σ^{av} and amplitudes σ^{ampl} = 25 kPa or 50 kPa: a) total settlement after 10^5 cycles, b) accumulated settlement during the cycles with $N > 1$*

8.2.2.5 Influence of the depth of embedding

Figure 8.13a presents FE results for strip foundations with different depths of embedding 0 m $\leq t \leq$ 4 m. In these calculations, the soil was discretised up to a depth of 15 m below the surface. In this way an influence of a too small distance between the base of the foundation and the lower model boundary should be prevented.

For an identical loading ($\sigma^{\mathrm{av}} = 200$ kPa, $\sigma^{\mathrm{ampl}} = 150$ kPa, Figure 8.13a), the settlement after the first cycle and the amplitude of settlement s^{ampl} decrease with increasing depth of embedding. During the subsequent cycles, the accumulation of settlements is smaller with increasing depth of embedding (Figure 8.13a). This is partly caused by the decrease of the strain amplitudes with t (compare $s^{\mathrm{ampl}} \rightarrow$ smaller f_{ampl}). Another reason is the larger stress in the soil below the base of the foundation resulting from the self-weight of the foundation and the soil beside the foundation ($\rightarrow$ smaller f_p).

In the calculations presented in Figure 8.13b, the ratio of the stress in the base of the foundation (including the self-weight σ^{SW} of the foundation) $\sigma^{\mathrm{SW}} + \sigma^{\mathrm{av}}$ and the bearing capacity σ^{BC} was kept constant. Also the same amplitude ratio $\sigma^{\mathrm{ampl}}/(\sigma^{\mathrm{SW}} + \sigma^{\mathrm{av}})$ was chosen in each calculation. The values of σ^{BC} were computed according to DIN 4017.

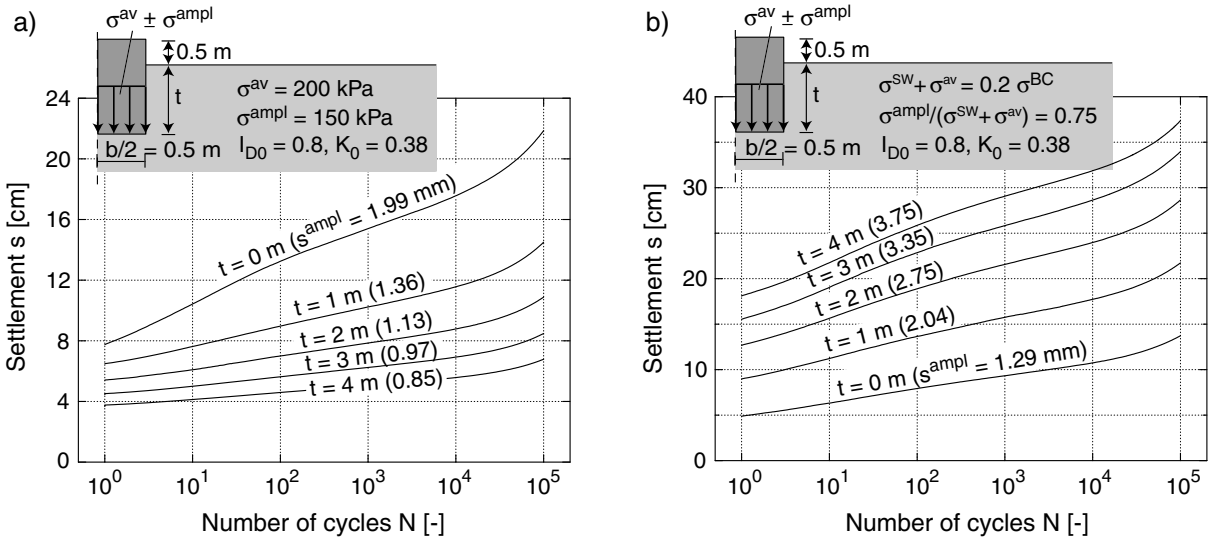

Figure 8.13: *Influence of the depth of embedding t for a)* $\sigma^{av} = 200$ *kPa and* $\sigma^{ampl} = 150$ *kPa, b)* $(\sigma^{SW} + \sigma^{av})/\sigma^{BC} = 0.2$ *and* $\sigma^{ampl}/(\sigma^{av} + \sigma^{SW}) = 0.75$

t [m]	0	1	2	3	4
σ^{BC} [kPa]	625	1442	2258	3075	3891

Table 8.1: Bearing capacity for different depths of embedding t according to DIN 4017

They are summarized in Table 8.1. Under such loading, the accumulation of settlement runs faster with increasing depth of embedding (Figure 8.13b). The effect of the larger strain amplitudes (compare $s^{\mathrm{ampl}} \rightarrow$ larger f_{ampl}) and the larger stress ratios $\eta^{\mathrm{av}} = q^{\mathrm{av}}/p^{\mathrm{av}}$ (due to the increase of $\sigma^{\mathrm{av}} \rightarrow$ larger f_Y, but smaller volumetric component of $\mathbf{m}$) prevails over the influence of the larger average mean pressure ($\rightarrow$ smaller f_p). Due to the increase of $\sigma^{\max} = \sigma^{\mathrm{av}} + \sigma^{\mathrm{ampl}}$, the settlements after the first cycle increase with t anyway. Laue [82] reported a smaller accumulation of settlements with increasing depth of embedding at constant values of $\sigma^{\mathrm{av}}/\sigma^{\mathrm{BC}}$ and $\sigma^{\mathrm{ampl}}/\sigma^{\mathrm{av}}$. This could not be confirmed by the FE calculations.

8.2.2.6 Influence of the width of the foundation

The influence of the width of the strip foundation for identical soil pressures becomes clear from Figure 8.14. In the FE calculations, the width of the foundation was varied in the range 1 m $\leq b \leq$ 4 m. For an identical loading $\sigma^{\mathrm{av}} \pm \sigma^{\mathrm{ampl}}$, the settlement at the end of the first cycle, the amplitude of settlement s^{ampl} and the rate of settlement accumulation during the subsequent cycles grow with increasing b. For identical soil pressures,

Raymond & El Komos ([126], Section 3.4.1.1) observed a decrease of the accumulated settlements with increasing width of the foundation. As expected, these findings could not be confirmed by the FE calculations. If the settlements are plotted versus the width of the foundation and a double-logarithmic scale is used (Figure 8.14b), linear curves are obtained for the settlement at the end of the first cycle $s_{\text{stat}} + s_1$ and (approximately) also for the final settlement $s(N = 10^5)$, i.e. $s \sim b^n$ holds. For $s_{\text{stat}} + s_1$ an exponent $n = 0.53$ was determined, which coincides with the proposal $s \sim \sqrt{b}$ in the literature (Burland et al. [15], Holzlöhner [57]). For $s(N = 10^5)$ the smaller exponent $n = 0.41$ was obtained, since the rate of settlement during the cycles with $N > 1$ increases less strongly with increasing b than the settlement $s_{\text{stat}} + s_1$ (Figure 8.14b).

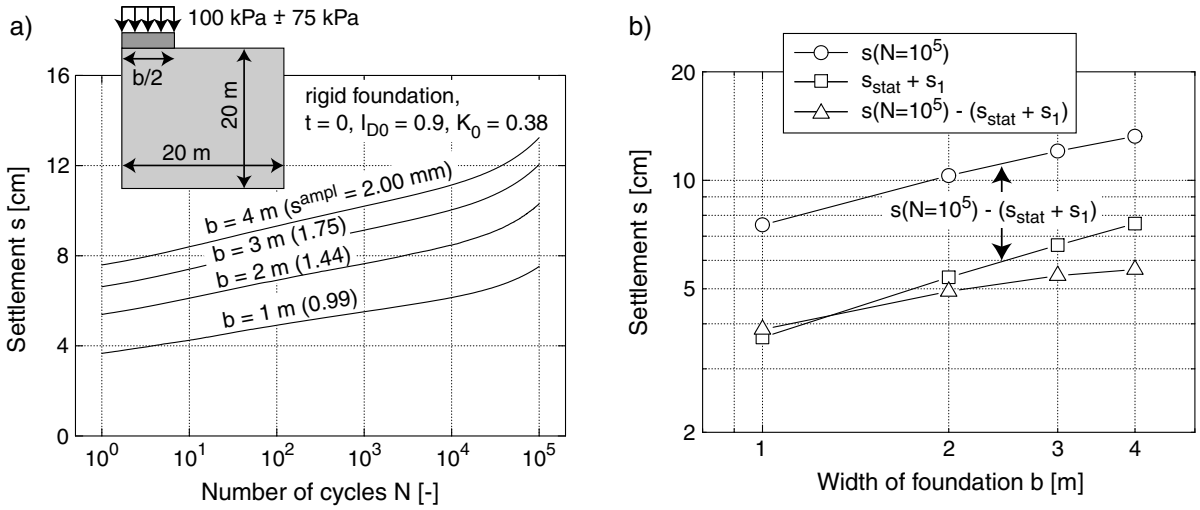

Figure 8.14: *Influence of the width b of the strip foundation for identical soil pressures*

From Figure 8.14 it can be seen, that a doubling of the amplitude of settlement s^{ampl} due to an increase of the width of the foundation b from 1 m to 4 m does not lead to a four times ($\rightarrow$ square function f_{ampl}) larger accumulated settlement. This can be explained with the distribution of the strain amplitude $\varepsilon^{\text{ampl}}$ in the half space. The strain amplitudes directly below the foundation are almost identical for $b = 1$ m and $b = 4$ m. However, the decay of $\varepsilon^{\text{ampl}}$ with the depth becomes slower with increasing width of the foundation due to the larger penetration of the load. This leads to larger settlement amplitudes, but due to $\dot{\varepsilon}^{\text{acc}} \sim (\varepsilon^{\text{ampl}})^2$, the effect on the accumulation rate is less pronounced. Niemunis et al. [109] already pointed out that, concerning the resulting settlements, a static loading has a larger range than a cyclic loading.

Next, the case, that a uniform load of a certain magnitude composed of a static (F^{av}) and a cyclic portion (F^{ampl}) has to be carried by a strip foundation, is considered (Figure 8.15).

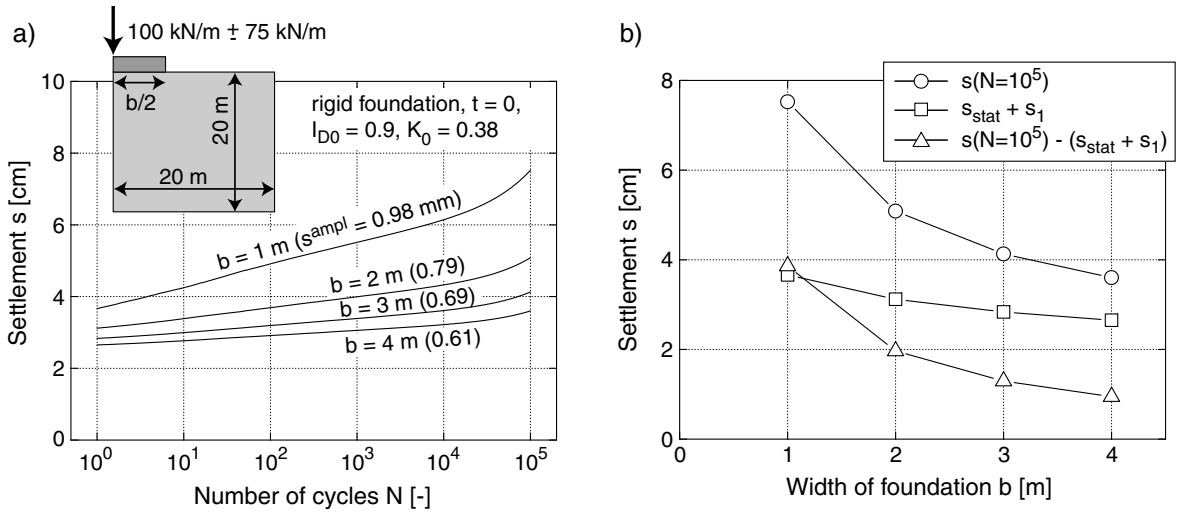

Figure 8.15: *Influence of the width b of the strip foundation for a constant uniform load*

An increase of the width of the foundation reduces much more effectively the settlements resulting from cyclic loading than those due to static loading, i.e. the settlements during the cycles with $N > 1$ decay much faster with increasing b than the settlements $s_{\text{stat}} + s_1$ (Figure 8.15b). Though the average soil pressure is lower for the larger widths of the foundation ($\rightarrow$ larger f_p), the simultaneous decrease of the strain amplitude due to smaller stress amplitudes has much more effect on the settlement rate (due to $\dot{\varepsilon}^{\text{acc}} \sim (\varepsilon^{\text{ampl}})^2$).

8.2.2.7 Summary of the FE parametric studies on strip foundations

Table 8.2 summarizes the effect of the parameters varied in the FE calculations on the settlement after the first cycle $s_{\text{stat}} + s_1$, the amplitude of settlement s^{ampl}, the settlements during the subsequent cycles $s(N = 10^5) - (s_{\text{stat}} + s_1)$ and the total residual settlement $s(N = 10^5)$ after 10^5 cycles. The effect of an increase ($\uparrow$) of the respective parameter on the settlements ($\uparrow$: increase, $\downarrow$: reduction) is indicated.

If a given uniform load $F^{\text{av}} \pm F^{\text{ampl}}$ has to be carried by a strip foundation and the geometry is fixed (e.g. standardized statics), the settlements resulting from the cyclic loading can be reduced by a vibratory compaction of the soil. This causes an increased density I_{D0} but also induces a cyclic preloading g_0^A and eventually an increase of the coefficient of lateral earth pressure K_0. All three effects lead to a decrease of the rate of accumulation. If the geometry of the foundation is variable, the depth of embedding or the width of the foundation can be enlarged. The increase of the width of the foundation reduces much more effectively the settlements due to cyclic loading than those due to static loading. If only the cyclic portion of the load F^{ampl} is fixed (e.g. in the case of wind

Varied parameter	Constant parameter	s_{stat} $+s_1$	s^{ampl}	$s(N=10^5)$ $-(s_{\text{stat}}+s_1)$	$s(N=10^5)$
$I_{D0}\uparrow$	$\sigma^{\text{av}}, \sigma^{\text{ampl}}, b, t, K_0, g_0^A$	$\downarrow$	$\downarrow$	$\downarrow$	$\downarrow$
$\sigma^{\max}\uparrow$	$\sigma^{\min}=0, b, t, I_{D0}, K_0, g_0^A$	$\uparrow$	$\uparrow$	$\uparrow$	$\uparrow$
$\sigma^{\text{ampl}}/\sigma^{\text{av}}\uparrow$	$\sigma^{\text{av}}, b, t, I_{D0}, K_0, g_0^A$	$\uparrow$	$\uparrow$	$\uparrow$	$\uparrow$
$\sigma^{\text{av}}\uparrow$	$\sigma^{\text{ampl}}/\sigma^{\text{av}}, b, t, I_{D0}, K_0, g_0^A$	$\uparrow$	$\uparrow$	$\uparrow$	$\uparrow$
$\sigma^{\text{av}}\uparrow$	$\sigma^{\text{ampl}}, b, t, I_{D0}, K_0, g_0^A$	$\uparrow$	$\downarrow$	$\downarrow$	$\uparrow$
$b\uparrow$	$\sigma^{\text{av}}, \sigma^{\text{ampl}}, t, I_{D0}, K_0, g_0^A$	$\uparrow$	$\uparrow$	$\uparrow$	$\uparrow$
$b\uparrow$	$F^{\text{av}}, F^{\text{ampl}}, t, I_{D0}, K_0, g_0^A$	$\downarrow$	$\downarrow$	$\downarrow$	$\downarrow$
$t\uparrow$	$\sigma^{\text{av}}, \sigma^{\text{ampl}}, b, I_{D0}, K_0, g_0^A$	$\downarrow$	$\downarrow$	$\downarrow$	$\downarrow$
$t\uparrow$	$\sigma^{\text{av}}/\sigma^{\text{BC}}, \sigma^{\text{ampl}}/\sigma^{\text{av}}, b, I_{D0}, K_0, g_0^A$	$\uparrow$	$\uparrow$	$\uparrow$	$\uparrow$
$K_0\uparrow$	$\sigma^{\text{av}}, \sigma^{\text{ampl}}, b, t, I_{D0}, g_0^A$	$\downarrow$	$\downarrow$	$\downarrow$	$\downarrow$
$g_0^A\uparrow$	$\sigma^{\text{av}}, \sigma^{\text{ampl}}, b, t, I_{D0}, K_0$	-	-	$\downarrow$	$\downarrow$

Table 8.2: Summary of the results of the FE calculations on strip foundations under cyclic loading: influence of several parameters on the settlements

or wave loads) and the geometry of the rising construction has to be designed, it should be considered, that for F^{ampl} = constant a larger self-weight of the building (larger F^{av}) leads to larger settlements from the static load. In contrary, the settlements during the cyclic loading are smaller with increasing F^{av}.

8.2.2.8 Influence of the shape of the foundation

Beside the strip foundations discussed above also single foundations with a circular and a quadratic cross section were calculated. Figure 8.16 shows the settlement curves in the FE calculations with a three-dimensional discretization of the boundary value problem (element type C3D8).

For a constant area of the foundation, the shape of the cross-section is of minor importance. The settlements of the quadratic foundation are slightly lower than those for the circular one (in particular during the implicit calculation of the first two cycles). This can be explained by the larger portion of the external load, which is transmitted to the soil via shear stresses along the depth of embedding (perimeter of a square = $\sqrt{4/\pi}$ × perimeter of a circle). Thus, smaller soil pressures result at the base of the foundation. The circular

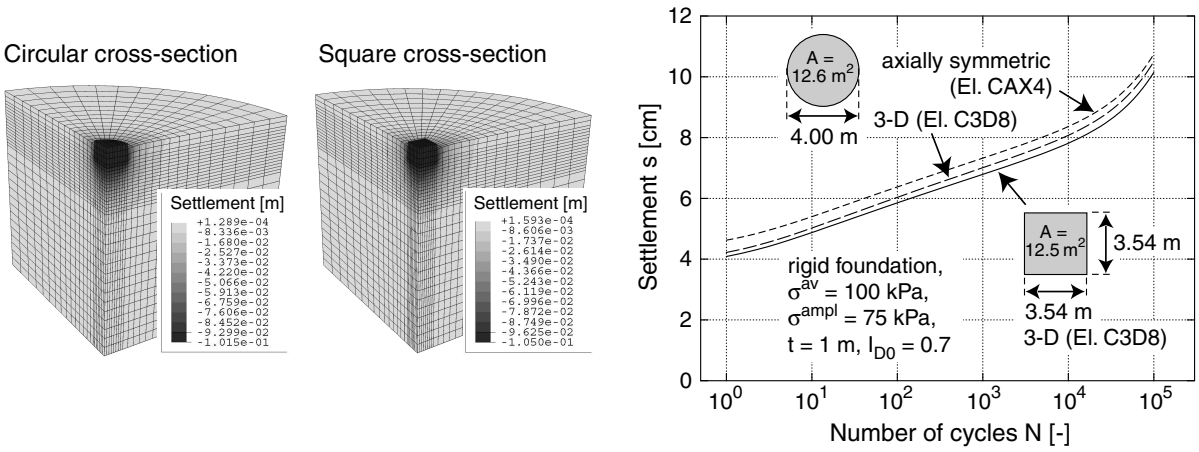

Figure 8.16: *Comparison of the settlements of foundations with a circular and a quadratic cross-section but identical area*

foundation can also be calculated as an axisymmetric problem (element type CAX4). The differences in the settlement curves of the axisymmetric and the 3D calculation (Figure 8.16) are probably due to a slightly different discretisation.

8.2.3 Technical remarks

8.2.3.1 Control cycles

Implicitly calculated control cycles can be interposed into the FE calculation in order to update the field of the strain amplitude. This field may change due to a densification or a re-distribution of stress. The effect of control cycles was studied for the strip foundation and different initial densities $0.3 \leq I_{D0} \leq 0.9$. In Figure 8.17 the results of calculations with control cycles after $N = 10$, 10^2, 10^3 and 10^4 cycles are compared with the settlement curves from calculations without control cycles. The control cycles reduce the amplitudes and the settlements only for loose soil ($I_{D0} \leq 0.5$). However, also for $I_{D0} = 0.3$ the improvement of the solution (reduction of the settlement at $N = 10^5$) amounts only 5 % with respect to the settlement without control cycles. In contrast, a significantly larger numerical effort (factor 3 to 4 in the case of four control cycles) is necessary. Thus, the benefit of control cycles for simple boundary value problems is questionable. However, control cycles may have advantages for more complex boundary value problems with a larger re-distribution of stress.

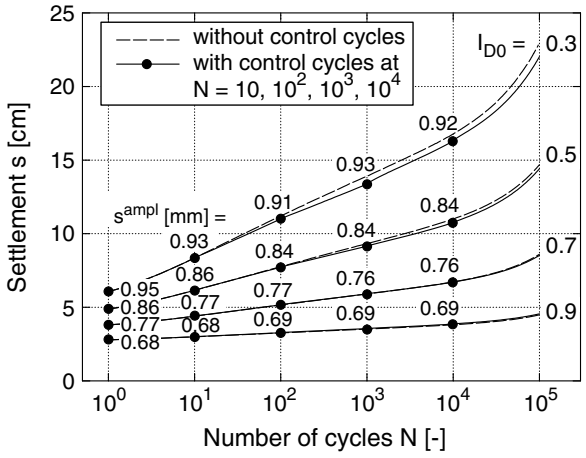

Figure 8.17: *Comparison of calculations with and without control cycles for different initial densities (b = 1 m, t = 1 m, $K_0 = 0.38$, σ^{av} = 100 kPa, σ^{ampl} = 75 kPa)*

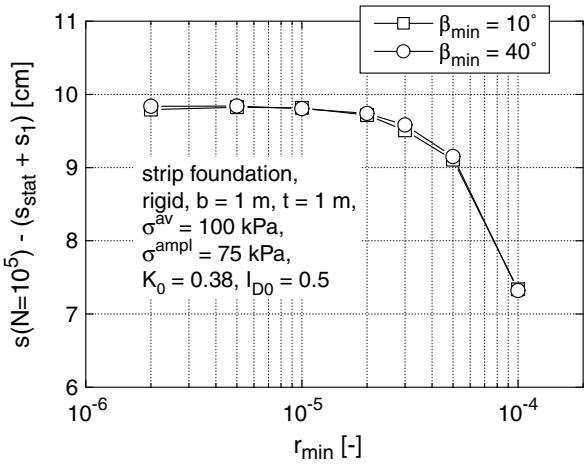

Figure 8.18: *Influence of the criteria $\beta_{\min}$ and $r_{\min}$ for the recording of characteristic points of the strain loop on the settlements in the cycles $N > 1$*

8.2.3.2 Criteria $\beta_{\min}$ and $r_{\min}$ for the recording of strain points

The criteria $\beta_{\min}$ and $r_{\min}$ specify which states of strain are memorized during the implicit calculation in the recording mode (Section 8.1.2). In FE calculations of the cyclically loaded strip foundation, the values were varied in the range $10° \leq \beta_{\min} \leq 40°$ and $2{\cdot}10^{-6} \leq r_{\min} \leq 10^{-4}$. The aim of these calculations was to find out, how weak the criteria $\beta_{\min}$ and $r_{\min}$ can be chosen without losing much accuracy of the solution. Figure 8.18 presents the residual settlements after $N = 10^5$ cycles. Since the strain loops of this boundary value problem are almost one-dimensional (in-phase) and thus the strain path has only two inflexion points, the choice of the angle $\beta_{\min}$ does hardly influence the calculation (Figure 8.18). In the range $r_{\min} \leq 10^{-5}$ the choice of $r_{\min}$ does not affect the accumulation of settlement. If a larger value of $r_{\min}$ is chosen, only the initial point is recorded for strain loops with an amplitude smaller than $r_{\min}$ and thus the amplitude is calculated as $\varepsilon^{\text{ampl}} = 0$. For this reason, the residual settlement is reduced with increasing $r_{\min}$. On the basis of Figure 8.18, the usage of $\beta_{\min} = 10°$ and $r_{\min} \leq 10^{-5}$ is recommended.

8.2.3.3 Element type

Niemunis et al. [111] suggested to use eight-nodal finite elements with reduced integration (four integration points, element type CPE8R) in order to keep the unintentional accumulation of self-stresses in an element during the explicit calculation small. However, in

the case of the considered boundary value problem and the chosen discretisation (mesh according to Figure 8.4) comparative calculations with CPE4 (linear shape functions, full integration), CPE8 (quadratic shape functions, full integration) and CPE8R elements did reveal no influence of the element type on the settlements (Figure 8.19). The usage of CPE4 elements is thus thought to be sufficient.

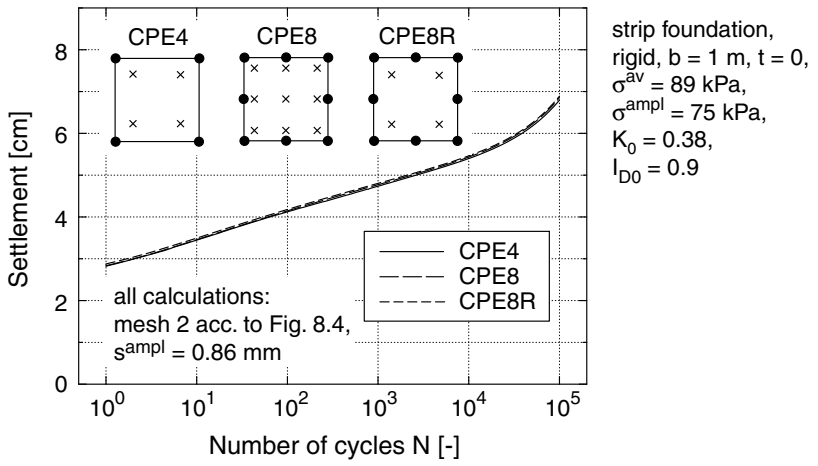

Figure 8.19: *Influence of the element type on the FE calculation*

8.2.3.4 Mesh dependence

In addition to the mesh shown in Figure 8.4, also a finer discretisation with 16 elements under the half width of the foundation and two coarser meshes with 4 or 2 elements on the length $b/2$ were tested (Figure 8.20a). The results of the calculations are illustrated in Figure 8.20b. They reveal that the meshes Nos. 1, 2 and 3 with 16, 8 or 4 elements on $b/2$ deliver similar amplitudes of settlement s^{ampl} and curves $s(N)$. For the coarsest mesh (2 elements on $b/2$) a smaller settlement amplitude and lower residual settlements were obtained. Thus, a discretisation with 4 elements on the length $b/2$ is sufficient. Adequate fine discretisations with rectangular elements delivered the same results as the discretisations 1 to 4 in Figure 8.20a with the shape of spider webs. Therefore, they are equivalent but easier to generate.

8.2.3.5 Region to be discretised in the case of a half space with infinite dimensions

Due to the square dependence of the rate of accumulation on the strain amplitude, the settlements resulting from a cyclic loading decay faster with depth than the settlements

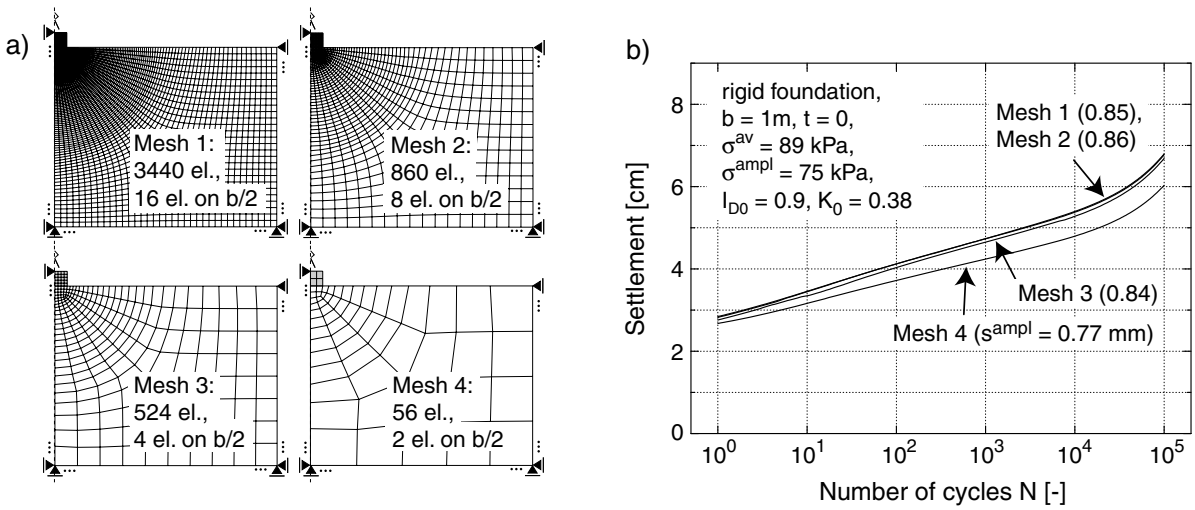

Figure 8.20: *Influence of the fineness of the mesh on the FE calculation*

due to static loads (see also Section 8.4). Thus, the static loading is decisive concerning the boundaries of the discretised area. This could be confirmed in calculations (not shown here) of the strip foundation with different dimensions of the discretized region of the soil. Concerning the boundaries of discretisation, respective recommendations for monotonic loads can be adopted.

8.3 FE calculation of a pile under cyclic axial loading

In FE calculations of a drilled pile (diameter $d = 1$ m, length $l = 20$ m) under cyclic axial loading, the development of the settlements and the stresses was studied. The sand had an initial density of $I_{D0} = 0.7$ and the historiotropic variable was $g_0^A = 0$.

The pile and the surrounding soil were discretised as an axisymmetric problem with CAX4 elements (Figure 8.21). 100 elements were arranged along the shaft of the pile. Four elements were located under its bottom. In the contact between soil and pile, friction contacts were used. Shear stresses can be transmitted by these contacts up to $\tau = \mu\ \sigma_N$ (σ_N: normal stress on the contact). Larger shear stresses cause sliding. The coefficient of friction is treated as a constant. At present, a possible degradation of μ with the number of cycles N (e.g. due to a breakage of grains in the contact) cannot be considered. A respective extension by a user-defined contact with an implementation of a dependence $\mu(N)$ (Subroutine UINTER in ABAQUS) is planned for the future. The calculations were performed with a coefficient of friction $\mu = \tan(\varphi/2) = \tan(38°/2) = 0.34$. For drilled

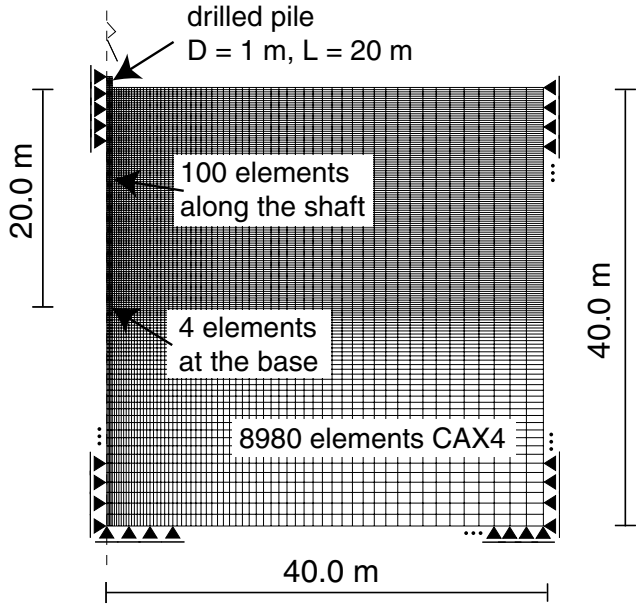

Figure 8.21: *FE discretisation of the drilled pile as an axially symmetric problem*

piles, this value is realistic due to the production process. Comparative calculations were performed with a higher coefficient of friction $\mu = \tan(\varphi) = 0.78$. The MV of the hypoplastic model with the set of constants V in Table 7.2 was used.

First, the load-settlement-curves $s(F)$ for the two coefficients of friction were generated by calculating a monotonic loading of the pile. The curves are shown in Figure 8.22. According to DIN 4014, the bearing capacity was defined as the load at a settlement-to-diameter ratio of $s/d = 0.1$. For $\mu = 0.34$ a bearing capacity of $Q_{l,c} = 3.5$ MN and for $\mu = 0.78$ a value of $Q_{l,c} = 5.9$ MN was determined.

The pile under cyclic axial loading was calculated with the minimum and maximum loads summarized in Table 8.3. For both coefficients of friction μ calculations with a minimum load $F^{\min} = 0,1\ Q_{l,c}$ and maximum loads $F^{\max} = 0.4\ Q_{l,c}$ or $0.7\ Q_{l,c}$ were conducted. Furthermore, calculations with identical minimum and maximum loads ($F^{\min} = 0.60$ MN, $F^{\max} = 2.36$ MN or 4.12 MN) were performed.

A typical field of the strain amplitude $\varepsilon^{\text{ampl}}$ (calculation No. 3) is shown in Figure 8.23a. The larger strain amplitudes concentrate within a small zone along the shaft and below the base of the pile. The settlements after 10^5 cycles are depicted in Figure 8.23b.

The development of the settlement with increasing number of cycles is presented in Figure 8.24. As expected, for $F^{\min}$ = constant, the settlement after the first cycle and the settlement rates during the subsequent cycles increase with increasing maximum load $F^{\max}$. Furthermore, for identical absolute values of $F^{\min}$ and $F^{\max}$, an increase of the

Coefficient of friction μ		0.34				0.78	
Calculation No.		1	2	3	4	5	6
Minimum load	$F^{\min}/Q_{l,c}$	0.10	0.10	0.17	0.17	0.10	0.10
	$F^{\min}$ [MN]	0.35	0.35	0.60	0.60	0.60	0.60
Maximum load	$F^{\max}/Q_{l,c}$	0.40	0.70	0.67	1.17	0.40	0.70
	$F^{\max}$ [MN]	1.41	2.47	2.36	4.12	2.36	4.12

Table 8.3: FE calculations of a drilled pile under cyclic axial loading

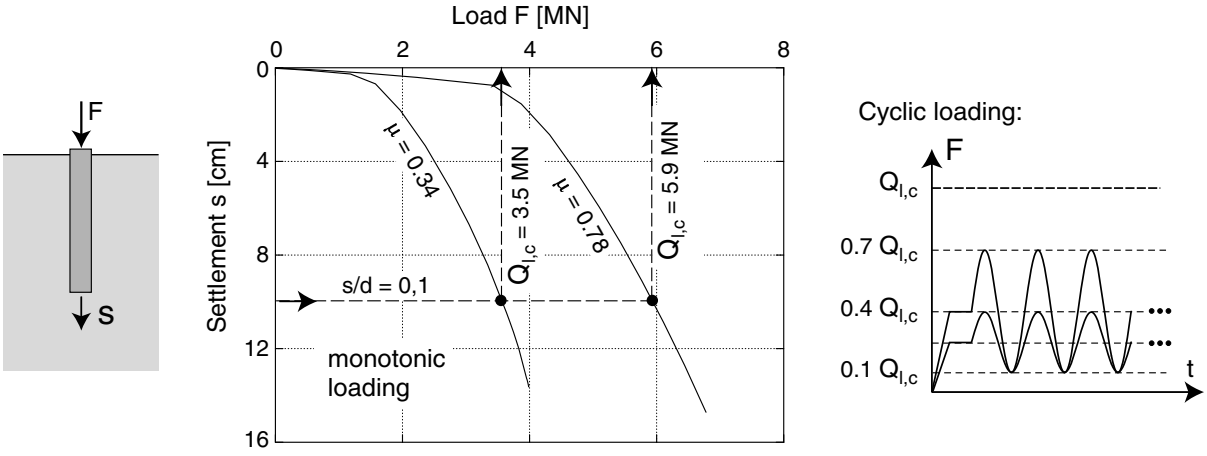

Figure 8.22: *Load-settlement-curves for coefficients of friction $\mu = 0.34$ and $\mu = 0.78$ resulting from a FE calculation of a monotonic pile loading; defining the cyclic loading*

settlement with a decreasing coefficient of friction μ could be detected (compare Figure 8.24a for $\mu = 0.34$ and Figure 8.24b for $\mu = 0.78$). The increase of $\dot{s}$ with decreasing coefficient of friction μ is due to a larger portion of the external load which is carried by the base of the pile. This causes larger strain amplitudes below the base of the pile, which manifests itself in larger amplitudes of settlement. If for different coefficients of friction μ the ratios $F^{\min}/Q_{l,c}$ and $F^{\max}/Q_{l,c}$ are identical, the residual strains after the first cycle, the amplitudes of settlement and the settlements after 10^5 cycles do not differ much (Figure 8.24).

Figure 8.25 confirms observations in model tests in the literature (Section 3.4.2), that the normal stress σ_N on the pile shaft decreases during cyclic loading. For a constant minimum load this reduction of σ_N with N runs the faster the larger the maximum load is chosen (compare Figures 8.25a and 8.25b). After a large number of cycles an almost constant distribution of the normal stress with depth establishes (Figure 8.25b). In Figure 8.25b the strong fluctuation of σ_N over depth for the larger numbers of cycles is probably

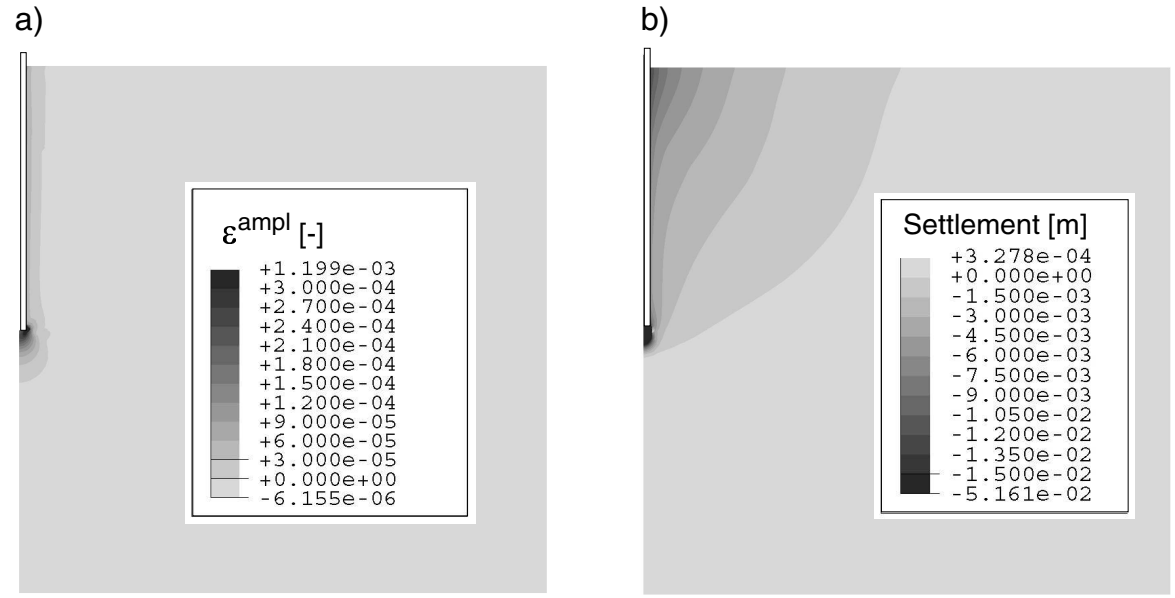

Figure 8.23: *Fields a) of the strain amplitude ε^{ampl} and b) of the vertical displacement after 10^5 cycles (calculation No. 3 referring to Table 8.3)*

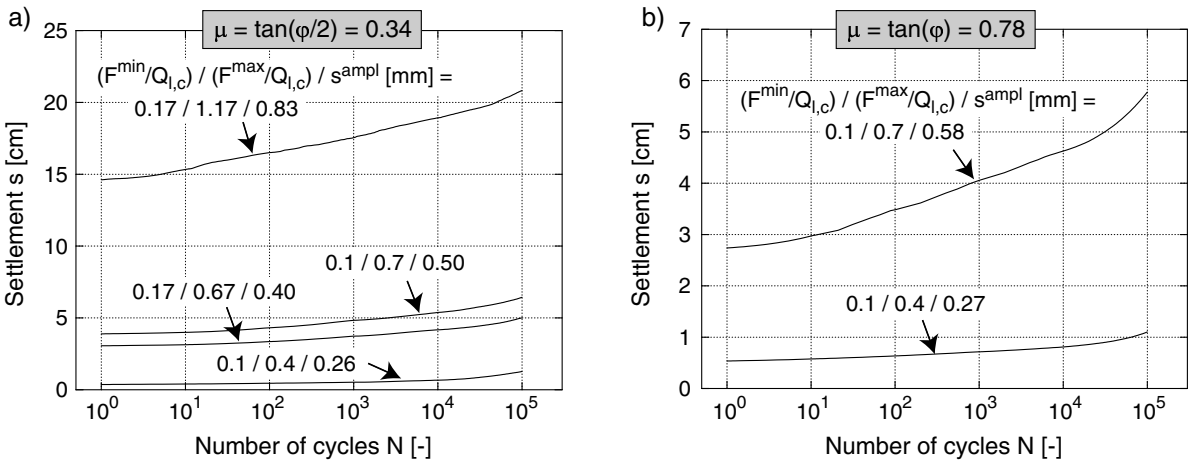

Figure 8.24: *Settlement of the pile for different loadings and coefficients of friction μ*

due to numerical reasons.

The development of the shear stresses carried by the pile shaft and the normal stresses in the contact at the pile base during the first two cycles calculated implicitly is illustrated in Figure 8.26 (for calculation No. 3 referring to Table 8.3). The self-weight of the pile causes initially small shear stresses (state 1 in Figure 8.26a). When the loading is raised to F^{av}, the maximum possible shear stress $\tau = \mu\ \sigma_N$ (compare σ_N in Figure 8.25a) is mobilized almost along the whole length of the pile (state No. 2 in Figure 8.26). The subsequent additional loading from F^{av} to F^{max} cannot be carried by shaft friction. It

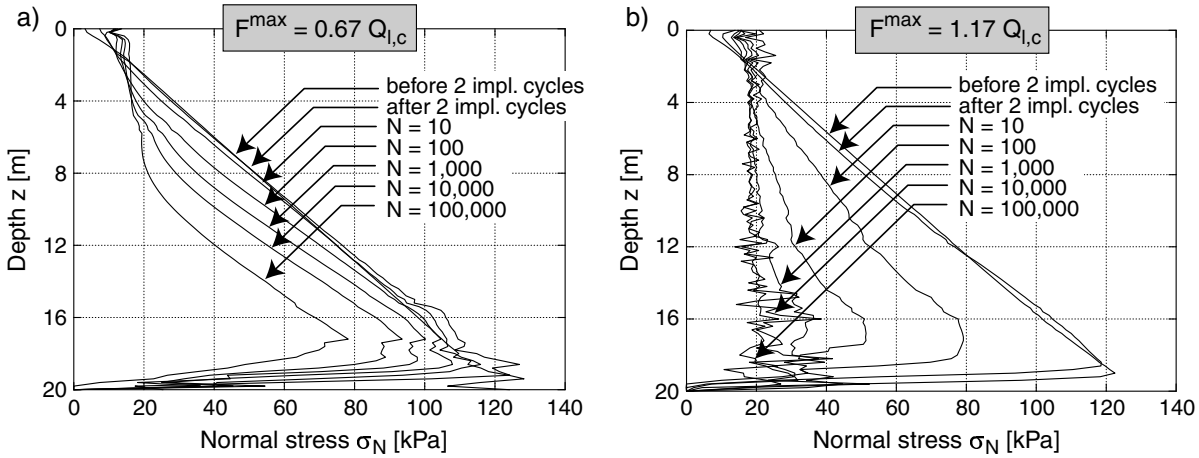

Figure 8.25: *Development of the distribution of the normal stresses σ_N on the pile shaft for $F^{\min} = 0.17\ \sigma_l$ and two different maximum loads $F^{\max}$ (calculations Nos. 3 and 4 referring to Table 8.3 with $\mu = 0.34$)*

leads to a significant increase of the base pressure (Figure 8.26b, state No. 3). The following unloading to $F^{\min}$ results in negative shaft friction in the upper half of the pile (state No. 4 in Figure 8.26). When the average load F^{av} has been reached again (state No. 5 in Figure 8.26), the shear stresses are considerably smaller and the base pressure is significantly larger than at F^{av} prior to the application of the first cycle. In the second cycle (states Nos. 6 to 8 in Figure 8.26), from which the strain amplitude is gained, the distributions of stress do hardly change compared to the corresponding states of the first cycle.

The decrease of the shear stresses carried by the pile shaft and the increase of the base pressure resulting from the implicit calculation are almost completely reversed in the explicit calculation of the first 10 cycles (Figure 8.27). During the subsequent cycles $N \geq 10$, similar to several model tests in the literature (Section 3.4.2, see e.g. Figure 3.43a after Le Kouby et al. [83]), a decrease of the shear stresses carried by the pile shaft and an increase of the base pressure with the number of cycles could be determined (Figure 8.27). Due to the development of the normal stresses σ_N acting on the pile shaft (Figure 8.25), a constant distribution of shear stress over depth establishes with increasing number of cycles. In Figure 8.27a this can be clearly seen for the upper 8 m of the pile. Such homogenisation of the profile $\tau(z)$ has already been reported by Schwarz [138] (see Figure 3.45).

The change of the stresses on the pile, i.e. the decrease of the shear stresses acting on the pile shaft and the increase of the base pressure with the number of cycles N becomes even clearer from Figure 8.28c. Figure 8.28c shows the development of the resulting forces

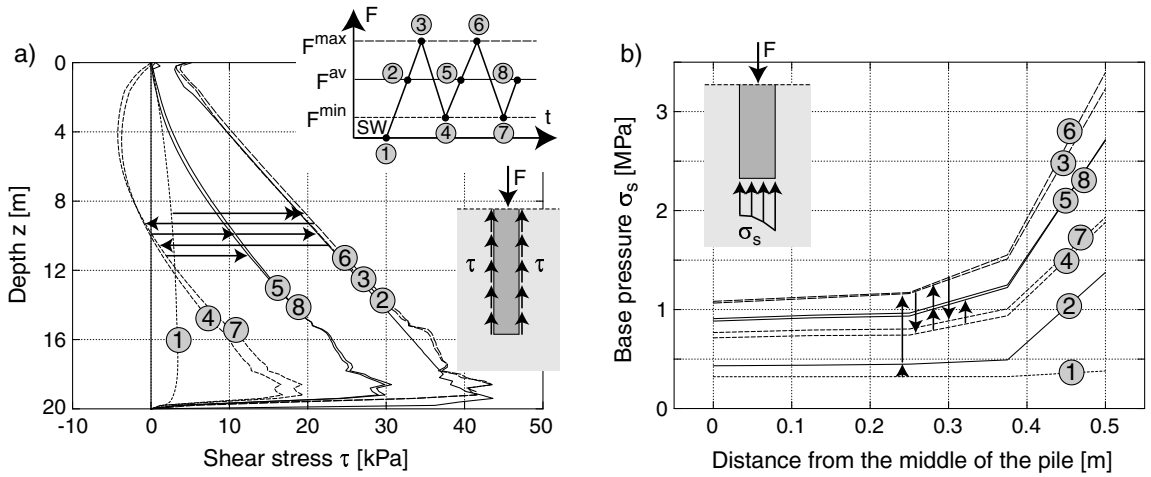

Figure 8.26: *Development of a) the shear stresses acting on the pile shaft and b) the base pressures during the implicit calculation of the first two cycles (calculation No. 3 referring to Table 8.3)*

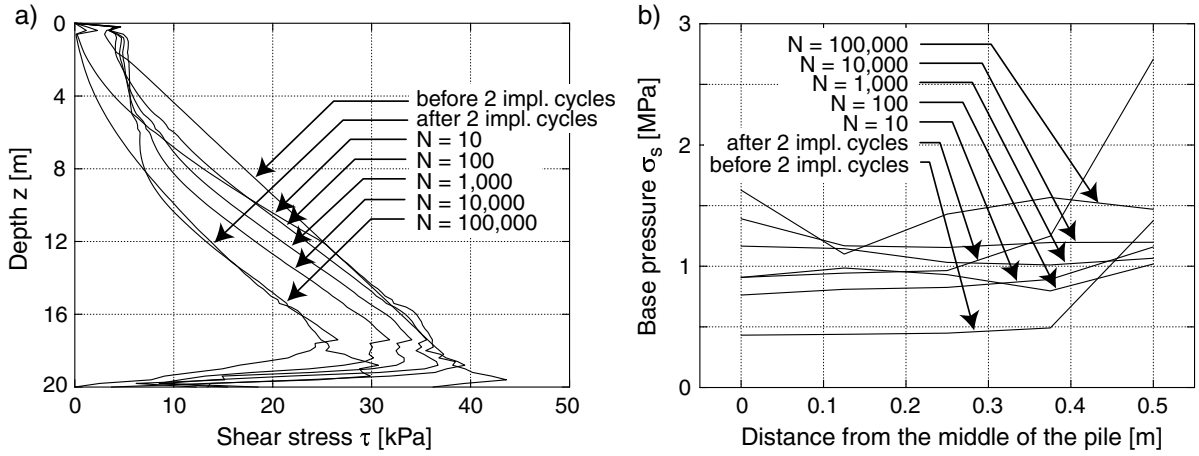

Figure 8.27: *Development of a) the shear stresses acting on the pile shaft and b) the base pressures during* 10^5 *cycles in the explicit calculation (No. 3 referring to Table 8.3)*

of the shear stresses acting on the pile shaft and the base pressure as a function of N for calculation No. 3. The other diagrams in Figure 8.28 contain analogous illustrations for the five other calculations. For the larger load amplitudes ($F^{\max} \geq 0.67\ Q_{l,c}$, Figure 8.28b,c,d,f) an increase of the resulting force of the base pressure with increasing number of cycles N was always observed while the resulting force of the shear stresses carried by the pile shaft decreased simultaneously. Another behaviour could be detected for the smaller amplitudes ($F^{\max} = 0.4\ Q_{l,c}$). In the case of the coefficient of friction $\mu = 0.78$ (Figure 8.28e), the shear stresses acting on the pile shaft increased with N while the base pressure declined. With increasing number of cycles N the portion of the external

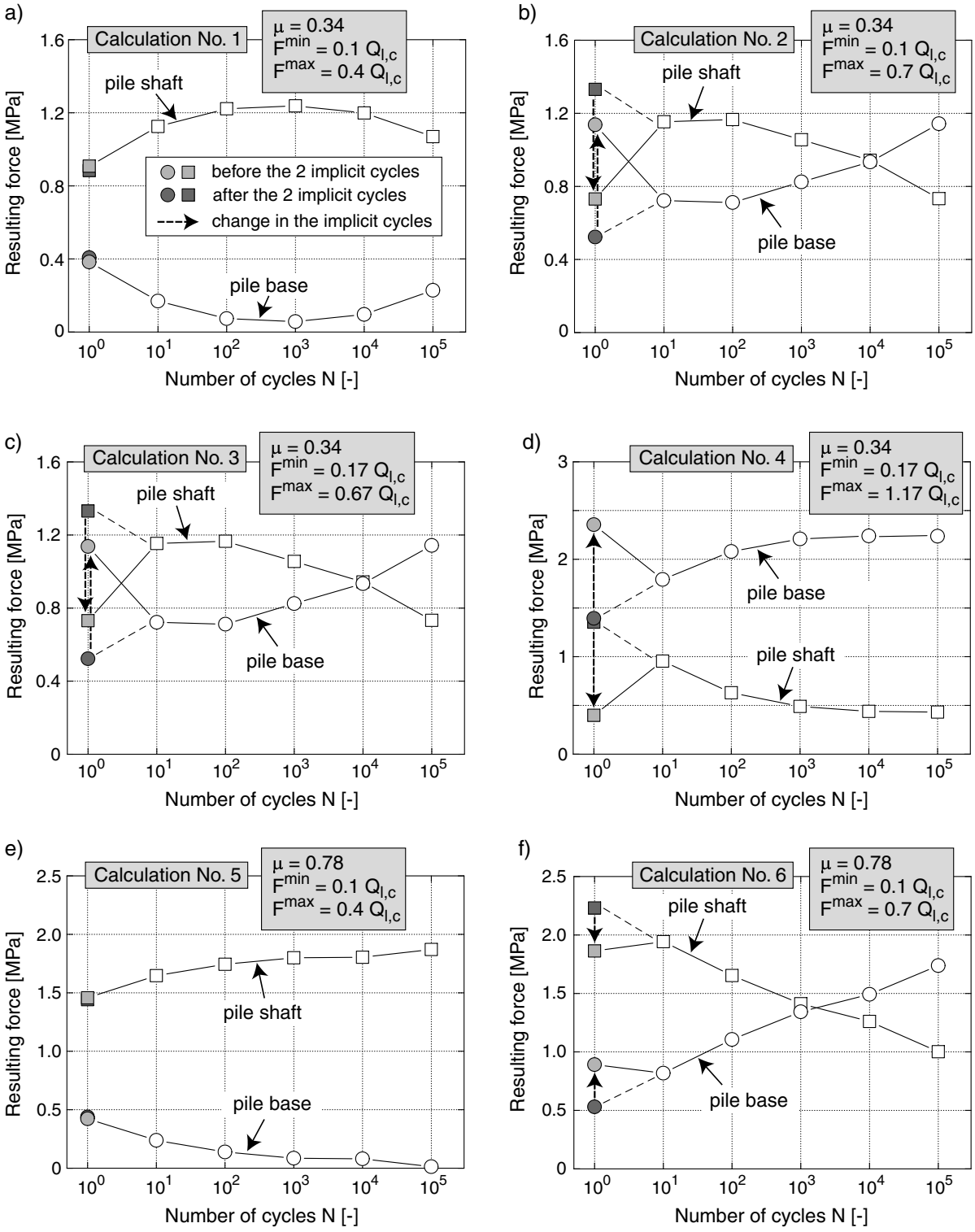

Figure 8.28: *Development of the resulting forces of the shear stress acting on the shaft pile and the base pressure with the number of cycles N*

load carried by shaft friction (especially in the lower quarter of the pile) increased and the portion carried by the base decreased. For $\mu = 0.4$ (Figure 8.28a), an increase of the shear stresses acting on the pile shaft and an accompanying decrease of the base pressure was also observed up to $N = 10^3$. However, this tendency was reversed for larger numbers of cycles. The calculations in Figure 8.28 reveal, that the development of the stresses acting on a pile under cyclic axial loading depends on the magnitude of the load amplitude and the coefficient of friction in the contact pile - soil.

In general, it has to be annotated that the rate of stress accumulation depends on the choice of the elastic stiffness E in Equation (7.1). Respective remarks were given in Section 7.2.3.

8.4 Other applications of the accumulation model

The accumulation model was used to calculate other boundary value problems, which are briefly summarized in the following. Details can be read in the respective publications (Niemunis et al. [109], Niemunis et al. [113]) or diploma theses (Keßler [72], Canbolat [16]).

Niemunis et al. [109] calculated the differential settlements of two neighboured foundations. The spatial distribution of the void ratio $e(\mathbf{x})$ was stochastically generated (with three different correlation lengths). 30 different fields $e(\mathbf{x})$ (see an example in Figure 8.29a) were tested. Let s_l and s_r be the settlements of the left and the right foundation, respectively (Figure 8.29a). The differential settlement $\Delta s = |s_l - s_r|$ was divided by the mean value of the settlement $\bar{s} = (s_l + s_r)/2$. The related differential settlement $(\Delta s/\bar{s})_{\text{stat}}$ due to the static loading up to σ^{av} was compared to the additional differential settlement $(\Delta s/\bar{s})_{\text{cyc}}$ during the subsequent 10^5 cycles. Independently of the correlation length it was detected, that the differential settlement stemming from the cyclic loading $(\Delta s/\bar{s})_{\text{cyc}}$ was approximately three times larger than that resulting from static loading $(\Delta s/\bar{s})_{\text{stat}}$ (Figure 8.29b). This can be attributed to the fact that the settlement due to monotonic loading is proportional to the load, while the accumulation rate under cyclic loading is proportional to the square of the strain amplitude, i.e. approximately proportional to the square of the load. Therefore, the cyclic loading has a smaller range than the monotonic loading. In the larger range of the monotonic loading a compensation of inhomogeneities of the field $e(\mathbf{x})$ is more likely than in the smaller range of the cyclic loading near the foundation. The correlations given in Figure 8.29b could be practically used in order to estimate the differential settlement due to cyclic loading from the differential settlements

during the application of the static loads (e.g. during the construction process, due to the increase of the self-weight).

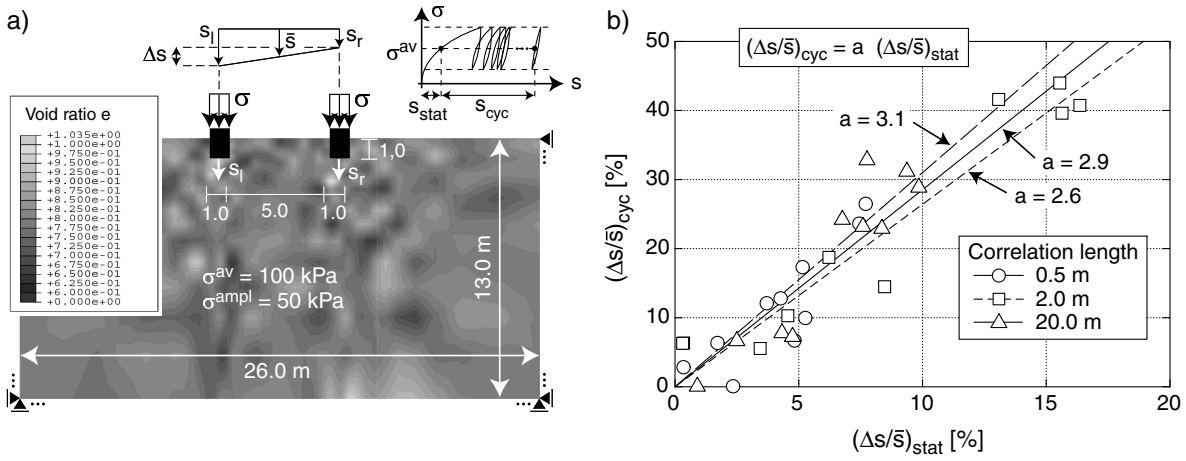

Figure 8.29: *FE calculations with stochastically fluctuating fields of the initial void ratio: a) example of a field $e(\mathbf{x})$, b) differential settlement due to cyclic loading as a function of the differential settlement due to static loading*

Keßler [72] used the accumulation model to simulate a vibratory compaction in a certain depth (the pulling-out of the vibrator was not modelled yet) for different initial densities and frequencies (Figure 8.30). In that case, the implicit steps were calculated dynamically. Canbolat [16] determined the settlements of the abutment of a bridge (so called "Hünxer Brücke" leading over the Wesel-Datteln waterway) under 50 years of traffic loading. The traffic loads were modelled using the concept for packages of cycles mentioned in Section 5.2.7.

The accumulation model was also used by Niemunis et al. [113] for the prognosis of excess pore water pressures and settlements of a water-saturated sand layer under earthquake loading. This problem was studied using the Finite Difference Method. A special numerical strategy was tested (Figure 8.32). The fast processes (propagation of shear wave) were decoupled from the slow processes (accumulation of the mean value of excess pore water pressure) for one period T of the harmonic excitation of the rock bed.

The dynamic calculation of the shear wave propagation in the sand layer during the first period T of excitation was performed with "frozen" values of the slowly changing variables $\boldsymbol{\sigma}'^{\mathrm{av}}$ (average effective stress), u^{av} (average excess pore water pressure) and e^{av} (average void ratio). At the end of the period, the change of $\boldsymbol{\sigma}'^{\mathrm{av}}$, u^{av} and e^{av} during T was calculated by means of the accumulation model and the strain amplitude received from the dynamic calculation. Afterwards, the values were again modified in a calculation

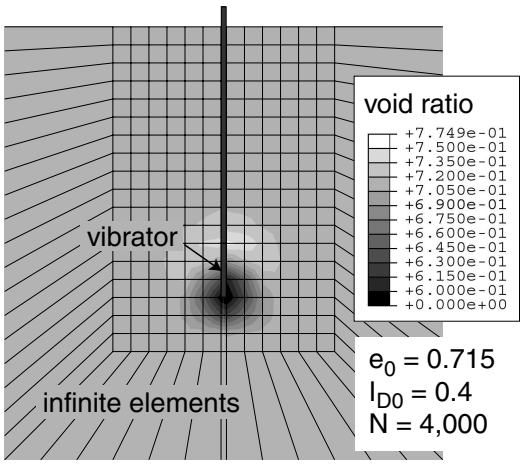

Figure 8.30: *FE calculation of a vibratory compaction after Keßler [72]*

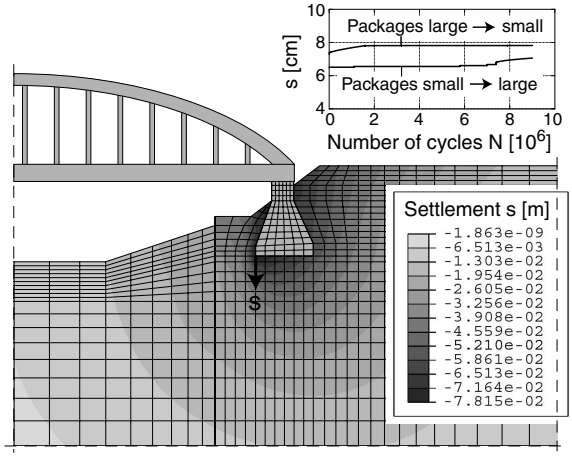

Figure 8.31: *FE calculation of the settlements of a bridge after Canbolat [16]*

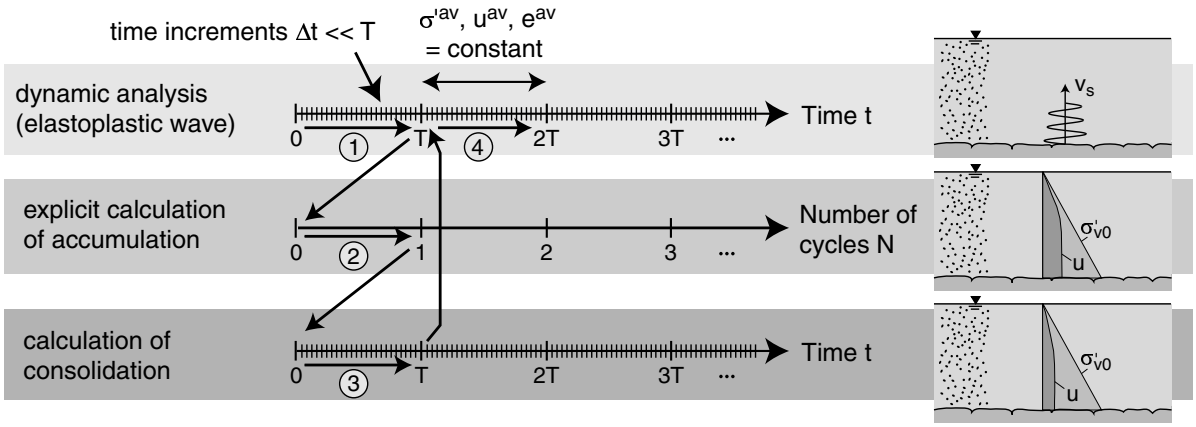

Figure 8.32: *Numerical strategy in a calculation of the pore water pressure accumulation in a water-saturated sand layer under earthquake loading after Niemunis et al. [113]*

of the dissipation of the pore water pressure during T (consolidation). The dynamic calculation of the wave propagation during the second period of excitation followed using the modified values of $\boldsymbol{\sigma}'^{\mathrm{av}}$, u^{av} and e^{av}, and so on. The introduction of special boundary conditions lead to a reflection of the shear wave at liquefied layers. Figure 8.33 presents the distributions of the shear strain γ, the shear strain amplitude γ^{ampl} and the excess pore water pressure u^{av} with depth z for certain numbers N of the calculated periods T. Concerning details of the calculations it is referred to [113] or the corresponding oral presentation [114]. A validation of the results by a comparison with in-situ measurements has still to be done. It has to be critically remarked, that the shear strain amplitudes mostly exceed $\gamma^{\mathrm{ampl}} = 10^{-3}$ (Figure 8.33). Thus, the amplitudes lay in a range, which, apart from the experiments presented in Section 5.2.1.2, was scarcely tested up to now.

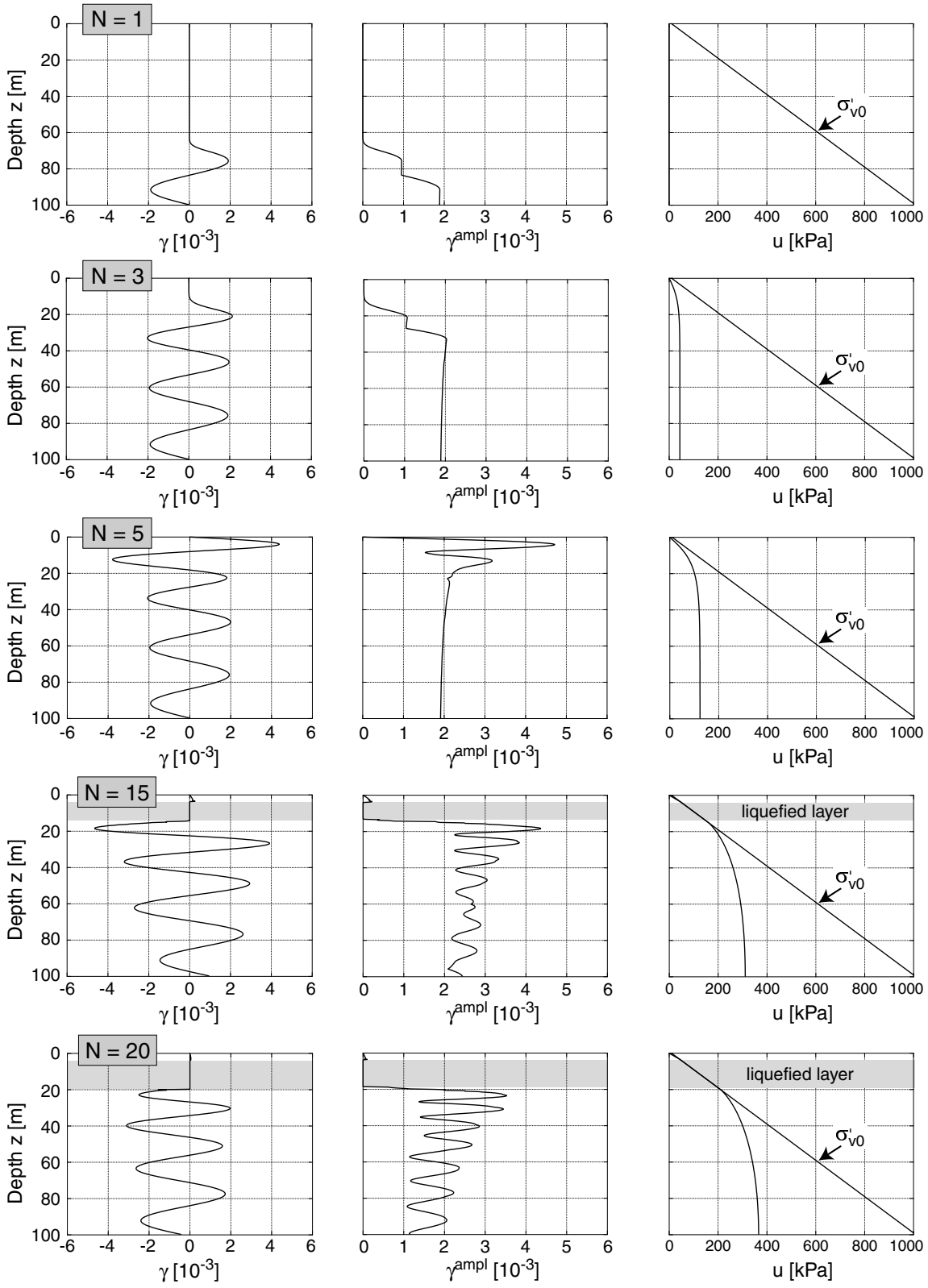

Figure 8.33: *Calculation of an earthquake with a displacement amplitude u^{ampl} = 1 cm in a depth z = 100 m: propagation of the shear wave, strain amplitudes γ^{ampl} and profile of excess pore water pressure u with depth after Niemunis et al. [113, 114]*

Chapter 9

Determination of the historiotropic variable g_0^A in situ

In Section 5.2.6 it was demonstrated, that the rate of accumulation depends not only on the state variables void ratio and stress, but also on the historiotropy (also called "cyclic preloading"), i.e. the fabric of the grain skeleton (arrangement of the contacts, orientation of the contact normals, coordination number, fluctuation of stress). In the laboratory depending on the method of specimen preparation, a certain initial fabric of the soil skeleton is generated. It is changed by a subsequent cyclic loading. The accumulation rates measured in the laboratory correspond to this special initial fabric.

The fabric of the soil skeleton of a non-cohesive soil in situ results from its sedimentation and the subsequent cyclic and monotonic loading history. A historiotropy may result e.g. from seismic activity, from the sedimentation and erosion of superposed layers or from oscillating ground water levels. Aging phenomena may cause changes of the particle contacts (e.g. cementation, improvement of interlocking). In general, the fabric of the soil in situ is unknown and cannot be directly measured.

In the accumulation model described in Chapter 7, fabric effects are summarized in the scalar historiotropic variable g^A. For the freshly pluviated sample in the laboratory the initial value is $g_0^A = 0$. Normally, this is not the case for an in-situ soil. Thus, for a prognosis of accumulation beside an information about void ratio and stress the initial value g_0^A is required. Since g^A is a phenomenological variable, it cannot be measured directly but has to be determined by means of correlations. In this work, a possible correlation of g_0^A with the P- and the S-wave velocity was studied. This correlation was disproved by the experiments presented in Section 9.1. Furthermore, a correlation between g_0^A and the liquefaction resistance was established (Section 9.2). The practical application

of this correlation needs further studies. Other ideas for a determination of g_0^A are given in Section 9.3.

9.1 Correlation of the historiotropy with dynamic soil properties

9.1.1 Motivation

The measurement of wave velocities in laboratory specimens was already discussed in Sections 3.3 and 4.1.4. In situ wave velocities can be determined by means of seismic measurements (e.g. cross-hole measurements). The idea was, to collect information about the historiotropic variable g_0^A from in-situ measurements of the wave velocities.

The secant shear modulus at small strains $G_{\text{hyst},0}$ is correlated with the S-wave velocity via Equation (3.7). It was reported on an increase of $G_{\text{hyst},0}$ of non-cohesive soils due to cyclic loading several times in the literature. Figure 9.1 shows respective RC tests on hollow cylinder specimens performed by Drnevich & Richart [27]. In comparison to a freshly pluviated sample they found an increase of $G_{\text{hyst},0}$ by up to 300 % due to $2.2 \cdot 10^7$ strain cycles. An increase of $G_{\text{hyst},0}$ due to cyclic loading was pointed out also by Richart [127] and Shen et al. [148]. However, contradictory to those studies several other researchers reported, that the secant stiffness at small strains is hardly influenced by a cyclic loading or by the fabric of the grain skeleton (method of sample preparation) (Alarcon-Guzman et al. [4], Tatsuoka et al. [157], Lo Presti et al. [90], Teachavoransinskun et al. [159], Li & Yang [88]). A discussion of these contradictory publications is given by Wichtmann & Triantafyllidis [183].

Micromechanical considerations support an increase of the dynamic stiffness due to a regular cyclic loading. As demonstrated in the following, this increase can result from a change of the geometry of the grain contacts or a reduction of the spatial stress fluctuation. The stiffness E and the elastic energy W_e of an elastic contact of two ideal spheres with identical radii R under the axial force F were derived by Hertz [51]:

$$E = \frac{3}{2} \left[\frac{2\bar{G}}{3(1-\bar{\nu})} \right]^{\frac{2}{3}} \sigma^{\frac{1}{3}} \tag{9.1}$$

$$W_e = \frac{4^{\frac{8}{3}}}{5} \left[\frac{3(1-\bar{\nu})}{8\bar{G}} \right]^{\frac{2}{3}} R^{\frac{4}{3}} \sigma^{\frac{5}{3}} \tag{9.2}$$

with the shear modulus $\bar{G}$ and the Poisson's ratio $\bar{\nu}$ of the sphere material. $\sigma = F/D^2$ is the stress in the axial direction. Goddard [33] developed formulas for the stiffness and

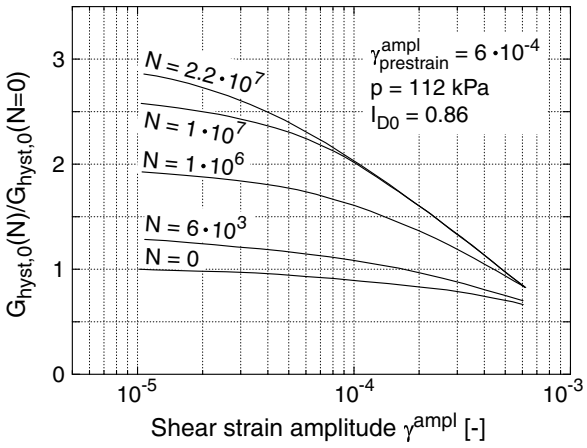

Figure 9.1: *Increase of the shear stiffness $G_{hyst,0}$ due to a dynamic torsional loading, RC tests of Drnevich & Richart [27]*

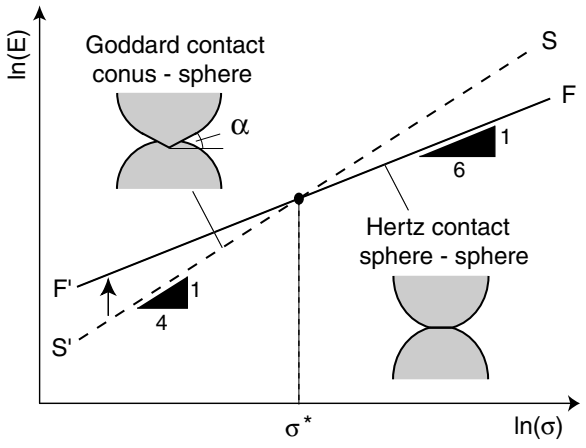

Figure 9.2: *Comparison of the stiffnesses of a Hertz contact (sphere - sphere) and a Goddard contact (conus - sphere)*

the energy of a contact of a sphere and a conus (inclination angle α, see Figure 9.2):

$$E = \left(\frac{\bar{G}}{1-\bar{\nu}}\right)^{\frac{1}{2}} \left(\frac{6}{\pi\alpha}\right)^{\frac{1}{2}} \sigma^{\frac{1}{2}} \tag{9.3}$$

$$W_e = \frac{4^{\frac{3}{2}}}{3} \left[\frac{3(1-\bar{\nu})}{8\bar{G}}\right]^{\frac{1}{2}} (\pi\alpha)^{\frac{1}{2}} R^3 \sigma^{\frac{3}{2}} \tag{9.4}$$

Goddard assumed Equation (9.3) to be valid for stresses σ, which do not exceed a transition stress σ^*. σ^* can be derived from setting equal Equations (9.1) and (9.3). It is strongly dependent on α:

$$\sigma^* = \frac{1}{96} \frac{\bar{G}}{1-\bar{\nu}} \pi^3 \alpha^3 \tag{9.5}$$

For $\sigma > \sigma^*$ Equation (9.1) holds. This relationship is schematically shown in Figure 9.2. The line F'-F results from Equation (9.1) and S'-S corresponds to Equation (9.3). Goddard thought of Figure 9.2 as a kind of "thermodynamic" phase diagram. The curve F'-F (contact sphere - sphere) represents a stable and the curve S'-S (contact conus - sphere) a metastable phase. Due to abrasion or a re-orientation of the grains, a vibration of the grain skeleton may lead to a replacement of "weak" contacts of the type conus - sphere by stiffer Hertz contacts (see the vertical arrow in Figure 9.2).

An increase of the stiffness can be also expected due to a reduction of the spatial fluctuation of stress. This is made clear using the simple example of four ideal spheres shown in Figure 9.3 (Triantafyllidis & Niemunis [165]). In case I the total external force $2F$ is carried by a single column of grains. In case II it is equally distributed on both grain

columns. If Hertz contacts are assumed, the ratio of the stiffnesses is $E_{II}/E_I = 2^{\frac{2}{3}} = 1.58$ and for the elastic energies $W_{eII}/W_{eI} = 2^{-\frac{2}{3}} = 0.63$ holds. If one assumes that the grain skeleton intends to reach a state of minimum energy, a cyclic loading should homogenize the stress field and thus lead to a larger stiffness. A detailed study of the energy in a particle assembly for different stress fluctuations using the "q-model" of Coppersmith [24] was documented by Triantafyllidis & Niemunis [165]. It has to be critically annotated, that in cyclic oedometric tests with a recording of the grain impressions at the base of the specimens by means of a special foil, a homogenization of the stress field due to cyclic loading could not be verified (Humme [59]).

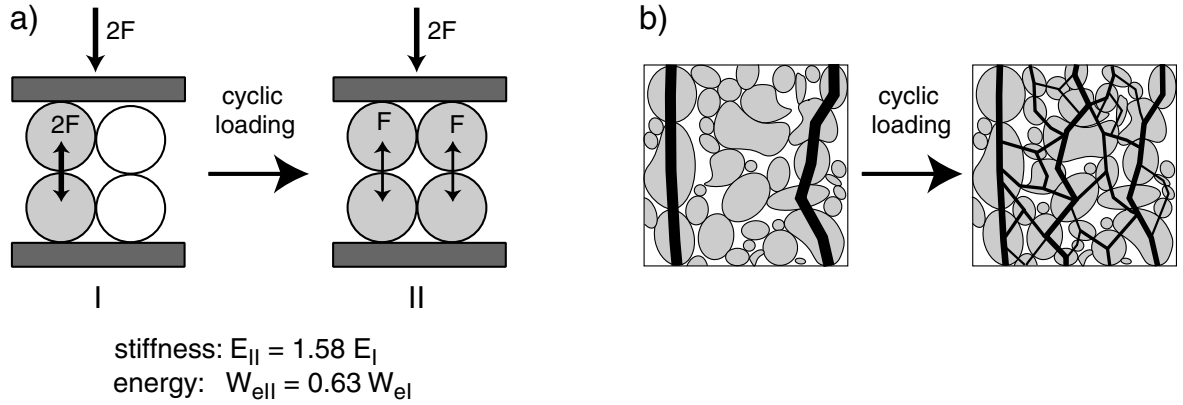

Figure 9.3: *Increase of the stiffness and decrease of the elastic energy due to a homogenization of the stress field (reduction of stress fluctuation)*

9.1.2 Laboratory tests

A possible correlation of the historiotropy with dynamic soil properties was studied in several test series. RC tests on cyclically preloaded specimens as well as cyclic triaxial tests with a measurement of P- and S-wave velocities were performed.

9.1.2.1 RC tests on specimens after a cyclic axial preloading

In a first test series (Wichtmann [175]), specimens of a fine sand ($d_{50} = 0.12$ mm, $U = d_{60}/d_{10} = 1.6$) were subjected to a cyclic axial preloading in a load press (Figure 9.4). While the lateral stress $\sigma_3 = 65$ kPa was generated by vacuum, the deviatoric stress was oscillating between $q^{\min} = 0$ and $q^{\max} = 130$ kPa. The resulting strain amplitudes were $\varepsilon_1^{\text{ampl}} \approx 7 \cdot 10^{-4}$. The number of preloading cycles was varied. After preloading the

specimens were built into the RC device and the curves $G_{\mathrm{hyst}}(\gamma^{\mathrm{ampl}})$ and $D(\gamma^{\mathrm{ampl}})$ were measured at a mean pressure of $p = 100$ kPa. Figure 9.4 compares the shear moduli $G_{\mathrm{hyst},0}$ of the preloaded and the non-preloaded specimens. Despite some scatter of the data no clear correlation between cyclic preloading and $G_{\mathrm{hyst},0}$ could be detected. Neither were the curves $G_{\mathrm{hyst}}(\gamma^{\mathrm{ampl}})/G_{\mathrm{hyst},0}$ and $D(\gamma^{\mathrm{ampl}})$ influenced by the historiotropy [175].

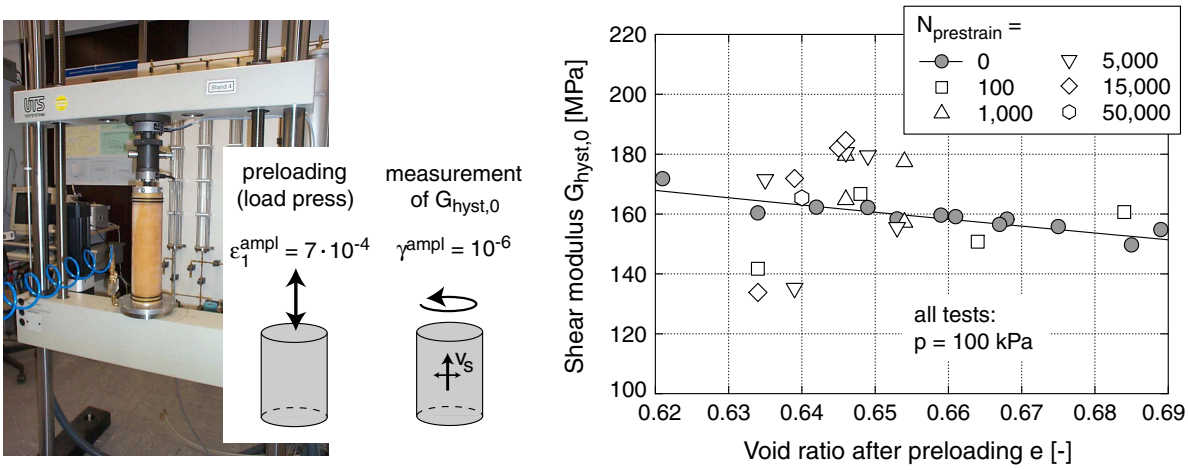

Figure 9.4: *Shear moduli $G_{hyst,0}$ after a cyclic axial preloading*

Having finished this test series, the question, if the polarization of the testing wave in comparison to the polarization of the preloading is of importance, arose. In the tests presented in Figure 9.4, the specimens were preloaded in the axial direction while the testing wave measured in the RC device was horizontally polarized. Thus, in the next test series it was studied, if the historiotropy can be better correlated with a testing wave with identical polarization.

9.1.2.2 RC tests with dynamic torsional preloading (small amplitudes)

In a second test series, specimens with a full cross-section were subjected to a dynamic torsional preloading in the RC device. In these tests, the direction of preloading and the polarization of the testing wave were identical. The shear strain amplitude was increased to a value $\gamma^{\mathrm{ampl}}_{\mathrm{prestrain}}$ (Figure 9.5) and a definite number of strain cycles was applied. After certain numbers of cycles a temporary reduction of the amplitude towards $\gamma^{\mathrm{ampl}} \approx 10^{-6}$ was undertaken in order to measure the shear modulus $G_{\mathrm{hyst},0}$. After having reached the maximum number of cycles of the test and after having measured $G_{\mathrm{hyst},0}$, the curves $G_{\mathrm{hyst}}(\gamma^{\mathrm{ampl}})$ and $D(\gamma^{\mathrm{ampl}})$ were determined also for $\gamma^{\mathrm{ampl}} > \gamma^{\mathrm{ampl}}_{\mathrm{prestrain}}$.

Figure 9.5 shows an example of a test result. After the first reduction of the shear strain

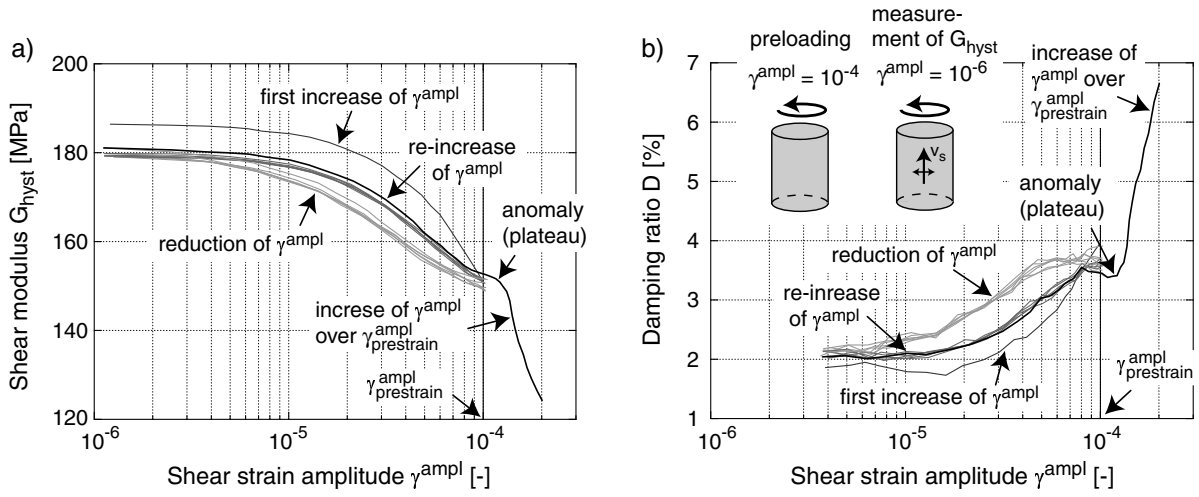

Figure 9.5: *Anomalies in the curves a) $G_{hyst}(\gamma^{ampl})$ and b) $D(\gamma^{ampl})$ at $\gamma^{ampl}_{prestrain} = 10^{-4}$ due to a dynamic torsional preloading, test with $N_{prestrain} = 3 \cdot 10^6$, $I_{D0} = 0.64$ and $p = 200$ kPa*

amplitude to $\gamma^{\mathrm{ampl}} \approx 10^{-6}$ the shear modulus $G_{\mathrm{hyst},0}$ lay slightly below the initial value of the freshly pluviated specimen. During the following $N_{\mathrm{prestrain}} = 3 \cdot 10^6$ cycles $G_{\mathrm{hyst},0}$ remained almost constant. This is confirmed also by Figure 9.6 for tests on fine and medium coarse sand with different maximum numbers of cycles $N_{\mathrm{prestrain}}$. The curves $G_{\mathrm{hyst}}(\gamma^{\mathrm{ampl}})$ and $D(\gamma^{\mathrm{ampl}})$ measured after preloading show an anomaly at $\gamma^{\mathrm{ampl}}_{\mathrm{prestrain}}$ (Figure 9.5). Some kind of plateau develops in both curves with the preloading cycles. Similar test results were already reported by Li et al. [88, 87, 86]. Schanzmann [136] (see also Wichtmann et al. [179]) proposed a method to quantify these anomalies. He demonstrated that the magnitude of the plateaus increases with the intensity of preloading, i.e. with $N_{\mathrm{prestrain}}$ and $\gamma^{\mathrm{ampl}}_{\mathrm{prestrain}}$. Furthermore, Wichtmann et al. [179] showed that for an application of several packages of cycles with different amplitudes $\gamma^{\mathrm{ampl}}_{\mathrm{prestrain}}$ the sequence of the packages influences the development of the plateaus. However, a utilization of the correlation of the historiotropy with the anomalies in the curves $G_{\mathrm{hyst}}(\gamma^{\mathrm{ampl}})$ and $D(\gamma^{\mathrm{ampl}})$ is difficult, since these curves cannot be measured in situ. Furthermore, changes of the stress blur these signs of the historiotropy (Wichtmann & Triantafyllidis [183]).

9.1.2.3 RC tests on hollow cylinder specimens after a cyclic torsional preloading (large amplitudes)

The small changes of $G_{\mathrm{hyst},0}$ in the tests presented in the preceding section could be due to the small preloading amplitudes $\gamma^{\mathrm{ampl}}_{\mathrm{prestrain}} \leq 10^{-4}$ or due to the inhomogeneous distribution of the shear strain amplitude over the cross-section of the specimen. However, tests similar

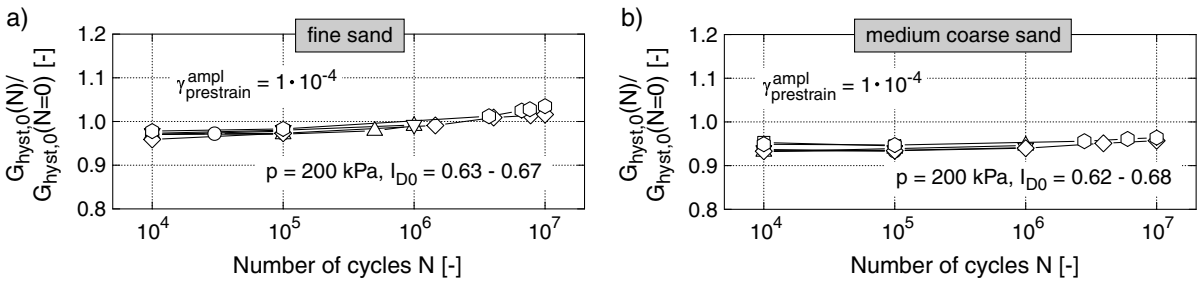

Figure 9.6: *Development of the shear modulus $G_{hyst,0}$ with the number of cycles due to a dynamic torsional loading in the RC device, tests on a) a fine sand and b) a medium coarse sand*

to those in Section 9.1.2.2 on hollow cylinder specimens (more homogeneous distribution of γ^{ampl} over the cross-section of the specimen) exhibited similar results as the tests on full cylinder specimens (Wichtmann & Triantafyllidis [183]). Thus, an influence of the homogeneity of the distribution of γ^{ampl} can be excluded.

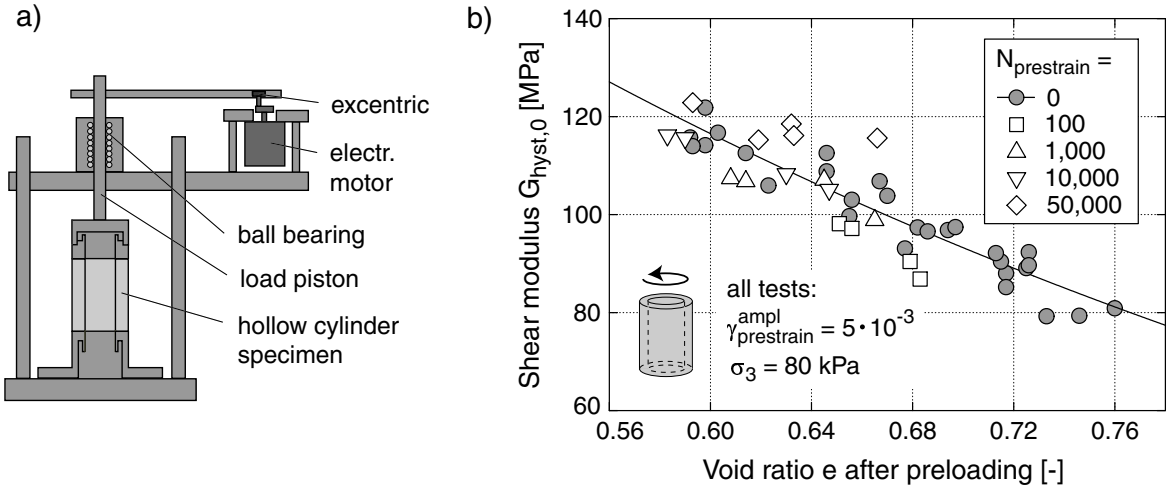

Figure 9.7: *a) Device for the application of a cyclic torsional preloading with large amplitudes on hollow cylinder specimens, b) Shear moduli $G_{hyst,0}$ of hollow cylinder specimens after cyclic torsional preloading with large strain amplitudes*

The hypothesis that the strain amplitudes in the previous tests were too small was checked in another test series on hollow cylinder specimens. The specimens were subjected to a cyclic torsional preloading in a special device (Figure 9.7a). Large amplitudes ($10^{-3} \leq \gamma^{\mathrm{ampl}}_{\mathrm{prestrain}} \leq 10^{-2}$) were applied with a loading frequency of $f_B = 0.5$ Hz. Different numbers of preloading cycles $N_{\mathrm{prestrain}}$ were chosen. After preloading, the specimens were tested in the RC device. Figure 9.7b shows exemplary the results of the tests with

$\gamma_{\text{prestrain}}^{\text{ampl}} = 5 \cdot 10^{-3}$ (the results for the other tested amplitudes are given by Wichtmann & Triantafyllidis [183]). Despite the large amplitudes, the shear modulus $G_{\text{hyst},0}$ was only moderately affected by the cyclic preloading. Analogously to Figures 9.5 and 9.6, the specimens preloaded with $N_{\text{prestrain}} = 100$ exhibited a smaller shear modulus compared to the non-preloaded specimens. With increasing number of cycles $N_{\text{prestrain}}$ the values of $G_{\text{hyst},0}$ increased. For $N_{\text{prestrain}} = 50{,}000$ all values lay above those of the non-preloaded specimens. However, relating to the stiffness of the non-preloaded specimens, the increase of $G_{\text{hyst},0}$ amounts 20 % in maximum. Thus, the correlation of the historiotropy with $G_{\text{hyst},0}$ is too weak in order to utilize it for practical purposes.

9.1.2.4 Cyclic triaxial tests with a measurement of P- and S-waves

Beside the RC tests also cyclic triaxial tests with σ_3 = constant were performed. The oscillation of the axial stress σ_1 was interrupted after definite numbers of cycles in order to measure the compressional and shear wave velocities at the average stress $\boldsymbol{\sigma}^{\text{av}}$. In this case, the P-wave and the cyclic preloading had an identical polarization.

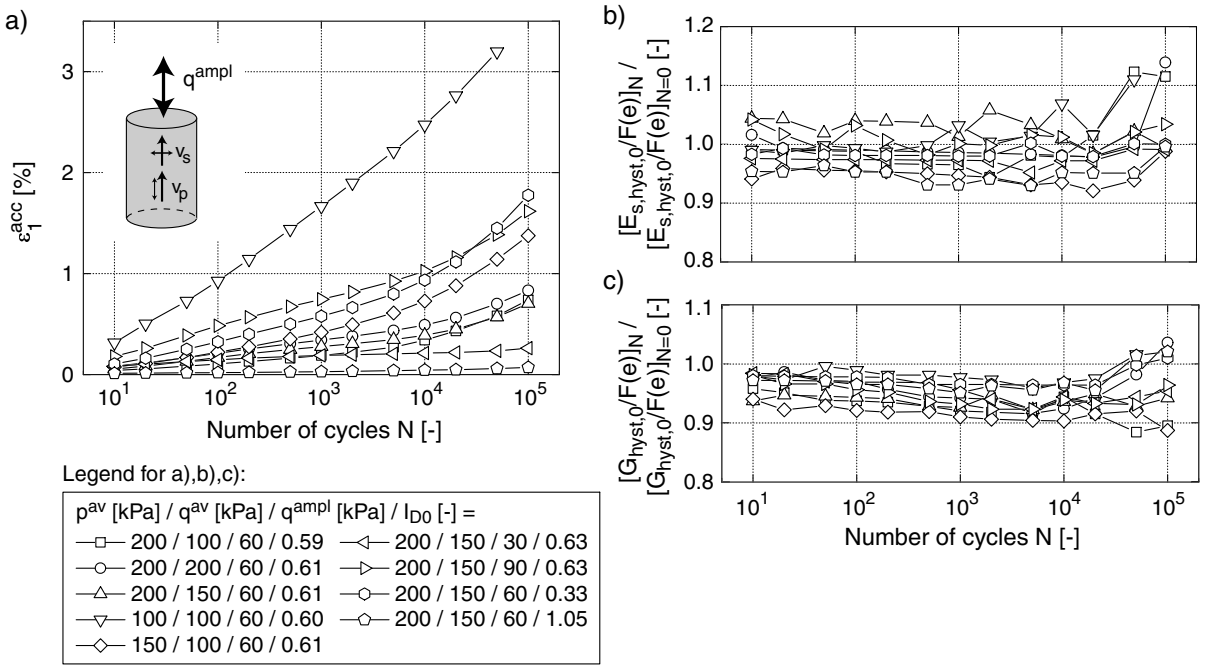

Figure 9.8: *Development of the stiffnesses $E_{s,hyst,0}$ and $G_{hyst,0}$ with the number of cycles in cyclic triaxial tests with different average stresses, stress amplitudes and initial densities (the curves were freed from the influence of the void ratio)*

The average stress $\boldsymbol{\sigma}^{\mathrm{av}}$, the stress amplitude q^{ampl} and the initial density I_{D0} were varied from test to test. Although a significant accumulation of residual strains occurred in some tests (Figure 9.8a shows the axial strain $\varepsilon_1^{\mathrm{acc}}$), hardly any changes of the stiffnesses $E_{s,\mathrm{hyst},0}$ (Figure 9.8b) and $G_{\mathrm{hyst},0}$ (Figure 9.8c) could be observed. The curves in Figures 9.8b and 9.8c were freed from the stiffness increase due to densification by a normalization with the void ratio function $F(e) = (a-e)^2/(1+e)$ according to Equation (3.5) with $a = 1.46$ for $G_{\mathrm{hyst},0}$ und $a = 2.36$ for $E_{s,\mathrm{hyst},0}$ (Wichtmann & Triantafyllidis [184]). Thus, the P-wave is similarly unsensitive to the historiotropy as the S-wave.

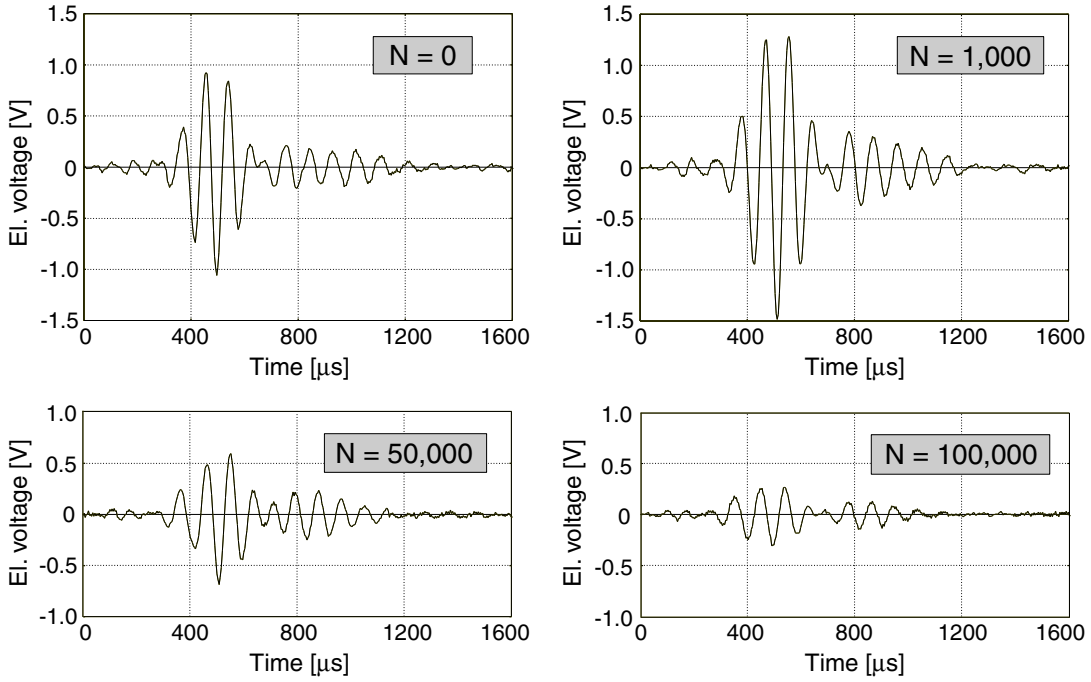

Figure 9.9: *Change of the intensity of the received signal with the number of cycles for a constant intensity of the transmitted impulse (cyclic triaxial tests, measurements with bender elements)*

In the case of the measurements of the S wave, a change of the intensity of the received signal with the number of cycles attracted attention, although the amplitude of the transmitted signal was kept constant. These observations were made for both the shear plate (SP) and the bender element (BE). Figure 9.9 exemplarily presents the results of a test, in which the signal intensity increased up to $N \approx 1,000$ and was strongly reduced afterwards. In contrast, the measurements of the P-wave with the compression element (CE) exhibited no change of the signal intensity. A detailed description of this topic is given by Triantafyllidis et al. [166]. The reduction of the signal intensity could be due to an increase of material damping as a result of cyclic loading (e.g. due to an increase of the

number of particle contacts). However, also a change of the bedding of the piezoelectric elements in the surrounding grains could be responsible. The latter one is more likely, since in the RC tests (Sections 9.1.2.1 to 9.1.2.3) no significant change of the damping ratio could be detected.

9.1.3 Assessment of the correlation

The test series presented in the preceding sections demonstrated that a correlation of the historiotropy with the dynamic soil properties, in particular the wave velocities or the dynamic stiffnesses, does not exist or is at least not clear enough for practical purposes. Thus, the tests of Drnevich & Richart [27] were disproved and also the micromechanical considerations (Section 9.1.1) could not be confirmed. Furthermore, a correlation of the historiotropy with the material damping is rather unlikely. However, this should be clarified in future.

9.2 Correlation of cyclic preloading with the liquefaction resistance

9.2.1 Motivation

In Section 3.2.2.9 it was shown, that a cyclic preloading or the fabric of the grain skeleton influence the liquefaction resistance of a non-cohesive soil. Furthermore, many diagrams in the literature correlate the liquefaction resistance with sounding resistances. Correlation diagrams as those in Figure 9.10 after Robertson & Wride [129] are established on the basis of observations if a soil has liquefied during an earthquake of a certain magnitude or not. With the estimated intensity of cyclic loading τ^{ampl}/p_0 and sounding resistances *before* the earthquake a borderline can be found, above which a liquefaction is likely while it will probably not occur below this line. Correlation diagrams were established e.g. by Seed et al. [141, 140, 139] for SPT soundings ("standard penetration test") and by Robertson & Campanella [128] and Robertson & Wride [129] for CPT soundings ("cone penetration test"). Other citations are given by Wichtmann et al. [178].

9.2.2 Laboratory tests

The aim of the tests presented in the following was to establish a correlation between the historiotropy g^A and the liquefaction resistance. In a second step, correlations of the

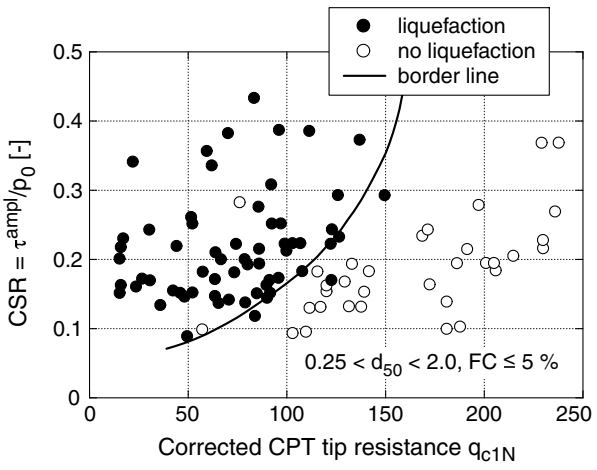

Figure 9.10: *Estimation of the liquefaction resistance from the tip resistance of CPT soundings for an earthquake of magnitude 7.5 (= 15 equivalent cycles) after Robertson & Wride [129]*

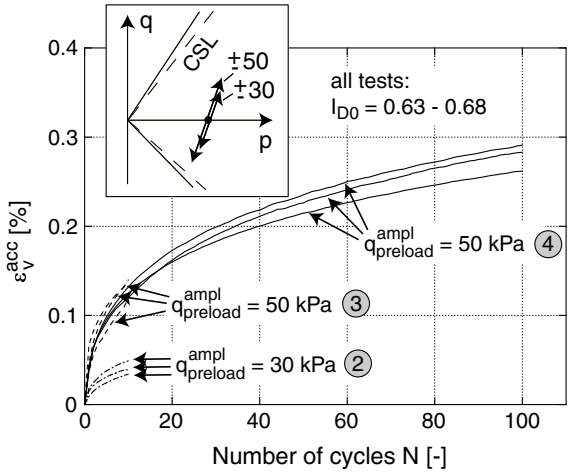

Figure 9.11: *Accumulation curves $\varepsilon_v^{acc}(N)$ during drained cyclic preloading*

liquefaction resistance with sounding resistances could be used in order to determine g_0^A in situ. Undrained cyclic triaxial tests were performed on specimens, which were previously subjected to a drained cyclic preloading. Four different intensities of cyclic preloading (number of cycles $0 \leq N_{\text{preload}} \leq 100$ and stress amplitudes 30 kPa $\leq q_{\text{preload}}^{\text{ampl}} \leq$ 50 kPa) were tested (Table 9.1).

Cyclic preloading No.	1	2	3	4
$q_{\text{preload}}^{\text{ampl}}$ [kPa]	-	30	50	50
N_{preload} [-]	0	10	10	100

Table 9.1: Tested cyclic preloadings

The specimens were prepared with initial densities $0.63 \leq I_{D0} \leq 0.68$ and consolidated under isotropic stresses with $p_0 = 100$ kPa. A drained cyclic preloading with $p^{\text{av}} = 100$ kPa, $q^{\text{av}} = 0$, $\sigma_3 =$ constant and a stress-controlled cyclic variation of the axial stress followed. The stress amplitudes $q_{\text{preload}}^{\text{ampl}} = 30$ kPa and $q_{\text{preload}}^{\text{ampl}} = 50$ kPa led to strain amplitudes $\varepsilon^{\text{ampl}} \approx 3.1 \cdot 10^{-4}$ and $\varepsilon^{\text{ampl}} \approx 5.8 \cdot 10^{-4}$, respectively. Since the average stress lay on the p-axis, a pure volumetric accumulation of strain took place ($\dot{\varepsilon}_q^{\text{acc}} = 0$, see Figure 6 in [178]). Typical accumulation curves for the volumetric strain $\varepsilon_v^{\text{acc}}(N)$ in the

preloading phase are depicted in Figure 9.11.

After the application of the drained cyclic preloading, the drainage of the specimens was closed and the cyclic loading was continued without drainage. While the total lateral stress remained constant, the axial stress was cyclically varied with an amplitude q^{ampl}. For each of the four tested cyclic preloadings several tests with different amplitudes q^{ampl} during the undrained cyclic loading were performed. In the analysis of the undrained cyclic loading, the effective stresses are denoted by $\sqcup'$ in the following.

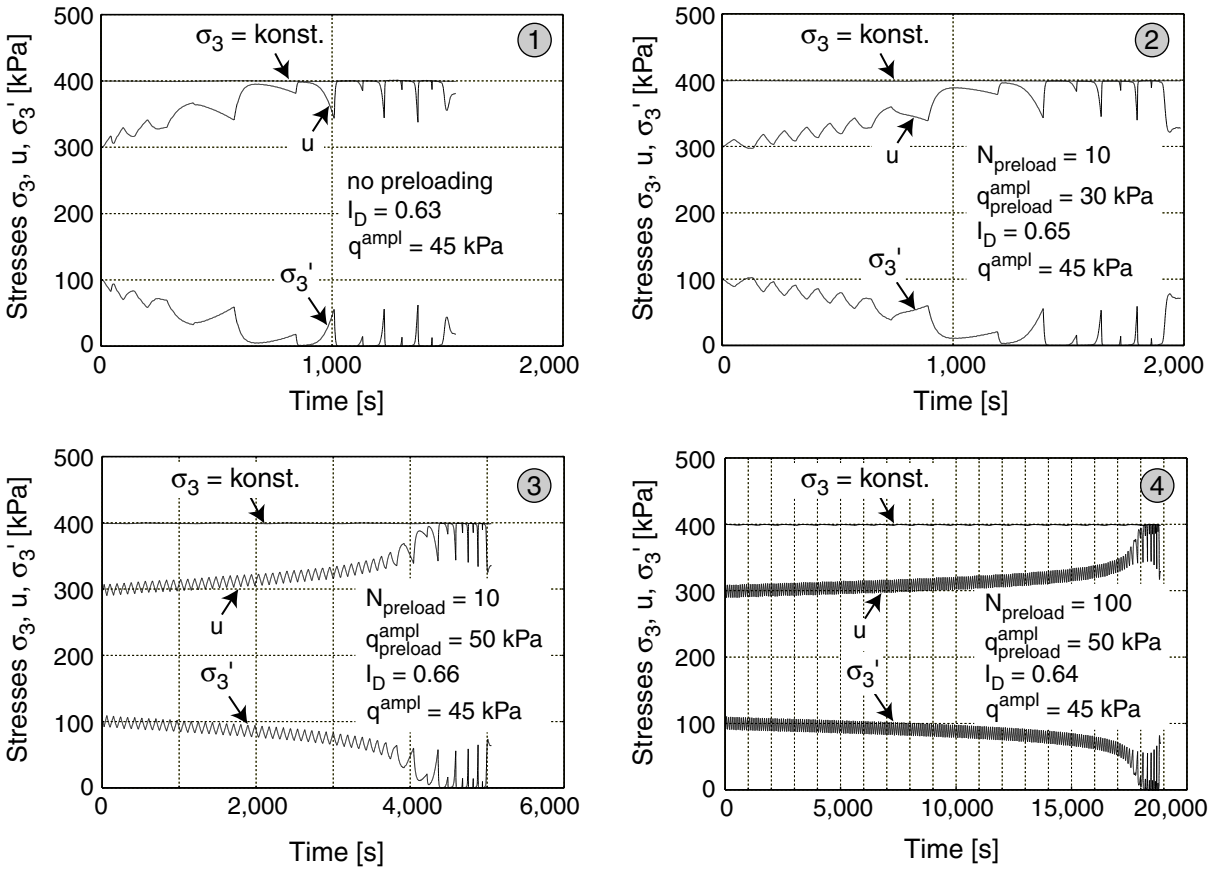

Figure 9.12: *Development of the pore water pressure u and the effective lateral stress σ_3' during undrained cyclic loading in four tests on specimens with different drained cyclic preloadings (all tests: $q^{\mathrm{ampl}} = 45$ kPa)*

Figure 9.12 shows the increase of the pore water pressure u during the undrained cyclic loading in four tests with different cyclic preloadings but identical amplitudes $q^{\mathrm{ampl}} = 45$ kPa in the test phase without drainage. The *initial* liquefaction was defined as the state when $u = \sigma_3$ and thus $\sigma_3' = 0$ was reached for the first time. The initial liquefaction was followed by a phase with cyclic mobility. An increase of the intensity of cyclic preloading

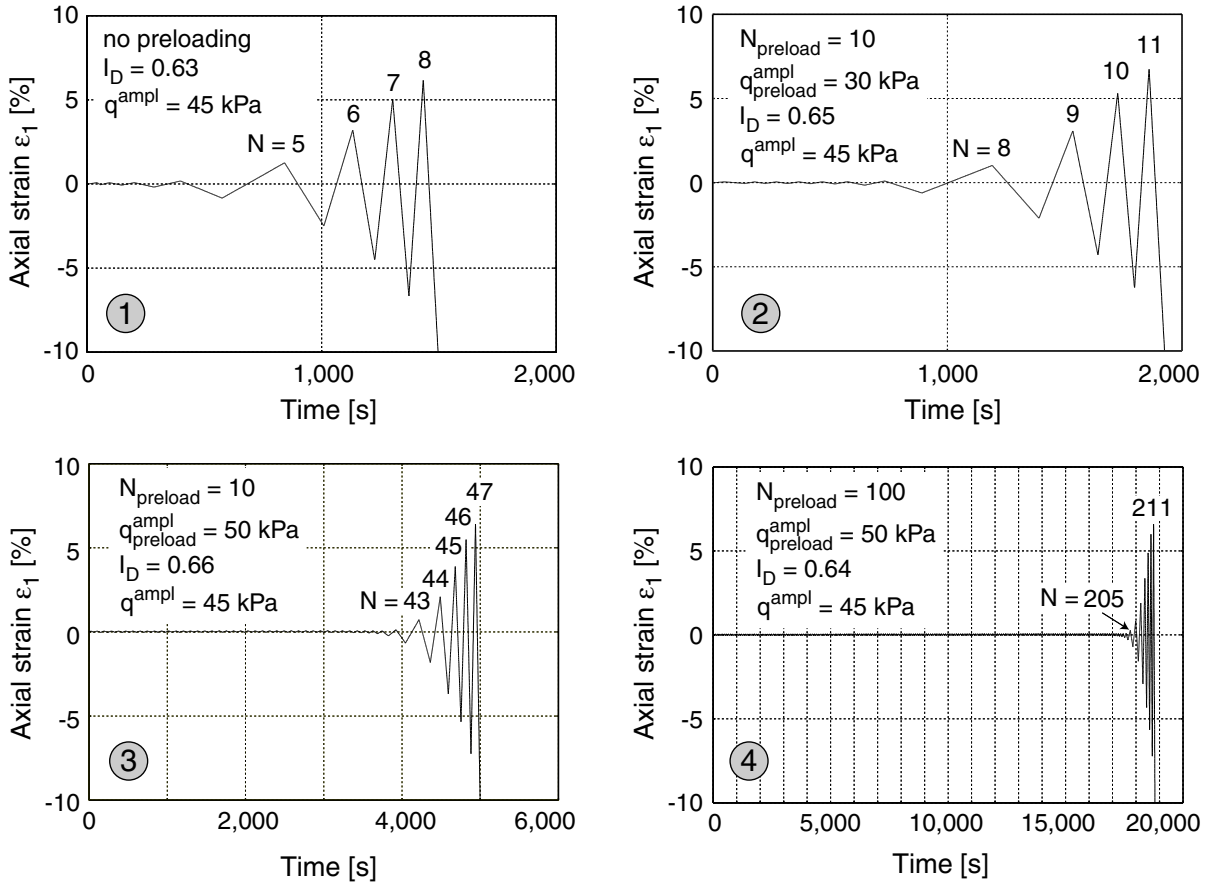

Figure 9.13: *Development of the axial strain ε_1 during undrained cyclic loading in four tests on specimens with different drained cyclic preloadings (all tests: q^{ampl} = 45 kPa)*

(in the amplitude or in the number of cycles) reduced the rate of pore water pressure accumulation $\dot{u} = \partial u / \partial N$ and as a result, more cycles were needed to reach initial liquefaction. The freshly pluviated specimen attained $u = \sigma_3$ for the first time after approx. 5 cycles, while the specimen preloaded with $q^{\mathrm{ampl}}_{\mathrm{preload}} = 30$ kPa and $N_{\mathrm{preload}} = 10$ liquefied after 8 cycles. The preloading with $q^{\mathrm{ampl}}_{\mathrm{preload}} = 50$ kPa and $N_{\mathrm{preload}} = 10$ delayed the initial liquefaction to occur after 43 cycles and in the case of the preloading with $q^{\mathrm{ampl}}_{\mathrm{preload}} = 50$ kPa and $N_{\mathrm{preload}} = 100$ even 205 cycles were needed.

While the amplitude of the axial strain $\varepsilon_1^{\mathrm{ampl}}$ remained small during the first cycles, it increased strongly during the cycle which led to initial liquefaction (Figure 9.13). In the following, $\varepsilon_1^{\mathrm{ampl}}$ increased with each cycle. The strain cycles were approximately symmetrically to $\varepsilon_1 = 0$, i.e. in each cycle $|\varepsilon_1^{\mathrm{min}}| \approx |\varepsilon_1^{\mathrm{max}}|$ was valid. From Figure 9.13 it becomes clear, that independently of cyclic preloading the so-called "*full* liquefaction" (defined as the time when a double amplitude of the axial strain of $2\varepsilon_1^{\mathrm{ampl}} = 10$ % was reached) and the failure of the specimen occured within four or five cycles after the initial

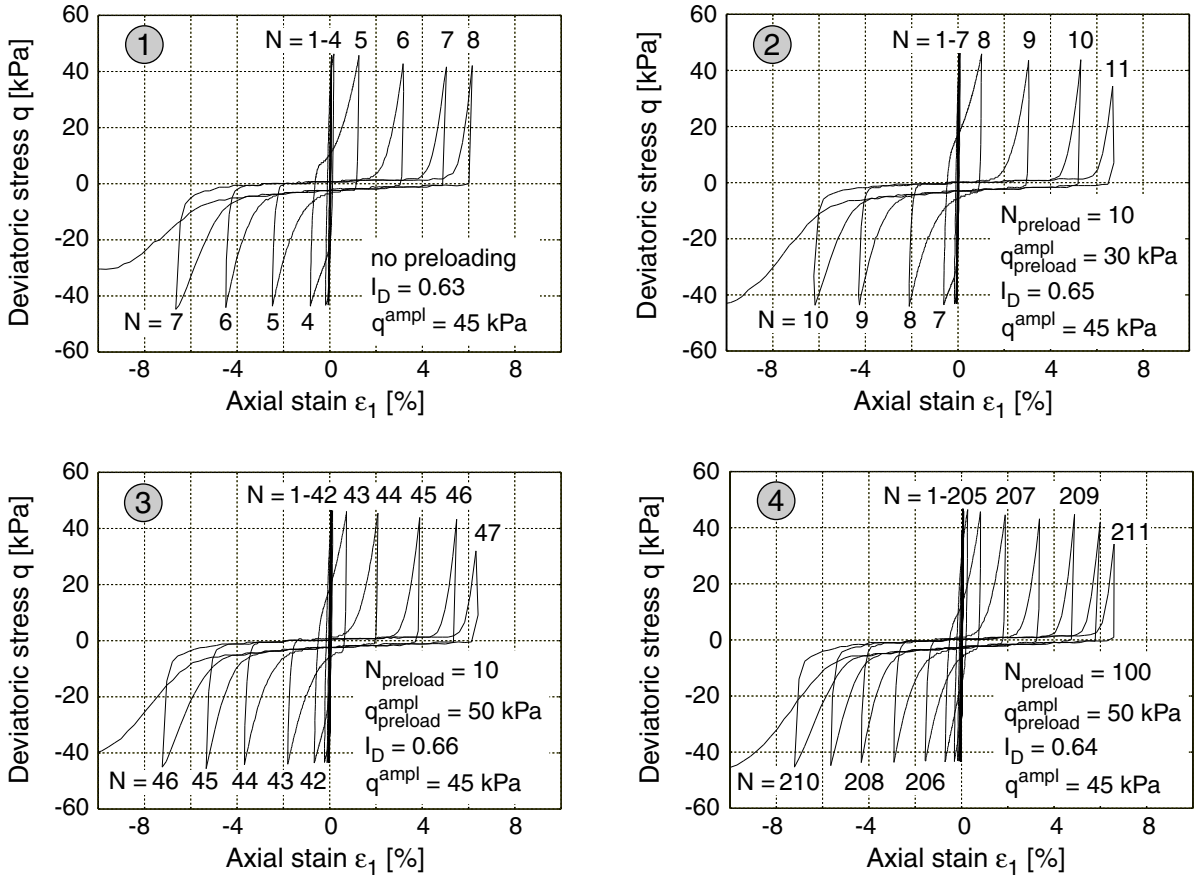

Figure 9.14: *Stress-strain-hystereses for different numbers of cycles N during undrained cyclic loading in four tests on specimens with different drained cyclic preloadings (all tests: $q^{ampl} = 45$ kPa)*

liquefaction. The specimens always failed on the extension side of the p-q-plane.

Figure 9.14 presents the q-ε_1-hystereses and in Figure 9.15 the effective stress paths in the p-q-plane are given. Despite the fact that the cyclic preloading increased the number of cycles necessary to reach liquefaction, no principal differences could be detected in the shape of the hystereses or the course of the stress paths. Similar stress paths and hystereses were observed in undrained cyclic triaxial tests by other authors (e.g. Hyodo et al. [61, 62, 60]).

In Figure 9.16, the amplitude ratio $CSR = q^{\mathrm{ampl}}/(2p_0)$ was plotted for each test versus the number of cycles N necessary to cause full liquefaction ($2\varepsilon_1^{\mathrm{ampl}} = 10$ %). Figure 9.16 makes clear, that for a certain cyclic preloading larger stress amplitudes q^{ampl} in the test phase without drainage cause an earlier liquefaction of the specimens. The cyclic preloading shifts the curves $CSR(N)$ in the direction of the upper right corner, i.e. it leads to a significant increase of the liquefaction resistance. For a freshly pluviated and non-

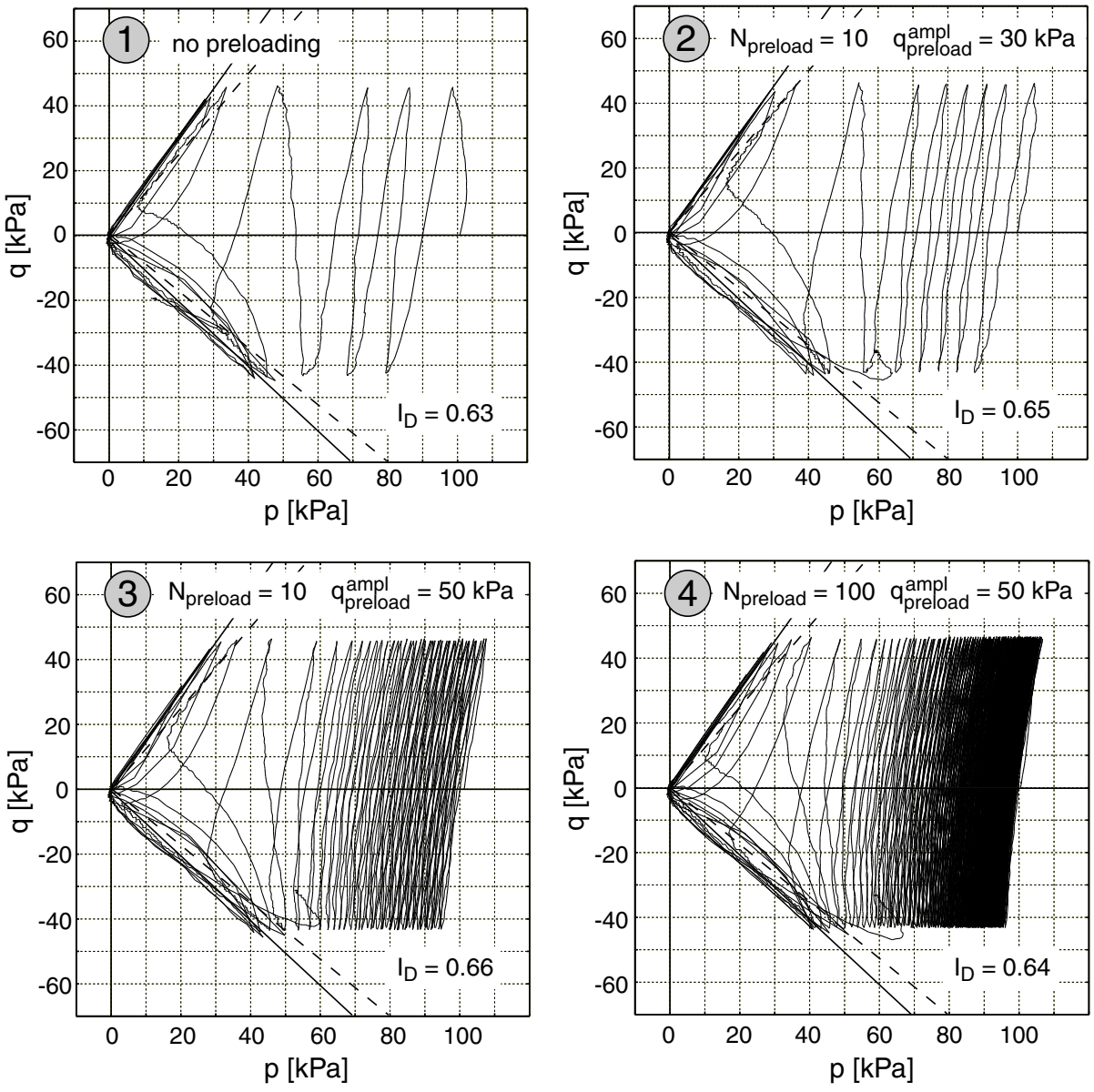

Figure 9.15: *Stress paths in the p-q-plane during undrained cyclic loading in four tests on specimens with different drained cyclic preloadings (all tests: $q^{ampl} = 45$ kPa)*

preloaded specimen, the full liquefaction in 15 cycles (earthquake magnitude $M = 7.5$) is reached with an amplitude ratio $CSR_{N=15} = 0.189$. For the cyclic preloadings Nos. 2, 3 and 4, this value amounts $CSR_{N=15} = 0.208$, $CSR_{N=15} = 0.259$ and $CSR_{N=15} = 0.295$, respectively.

The historiotropic variable g_0^A was calculated according to Equation (5.16) for the different cyclic preloadings. In Figure 9.17, the amplitude ratio $CSR_{N=15}$ is plotted versus g_0^A.

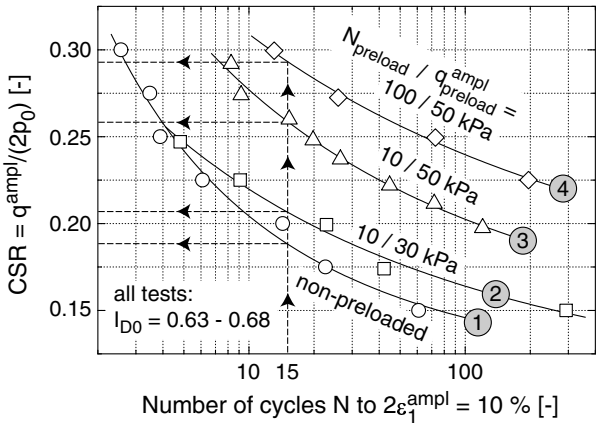

Figure 9.16: *Relationship between the amplitude ratio $CSR = q^{ampl}/(2p_0)$ and the number of cycles N necessary to reach full liquefaction ($2\varepsilon_1^{ampl} = 10$ %) for different cyclic preloadings*

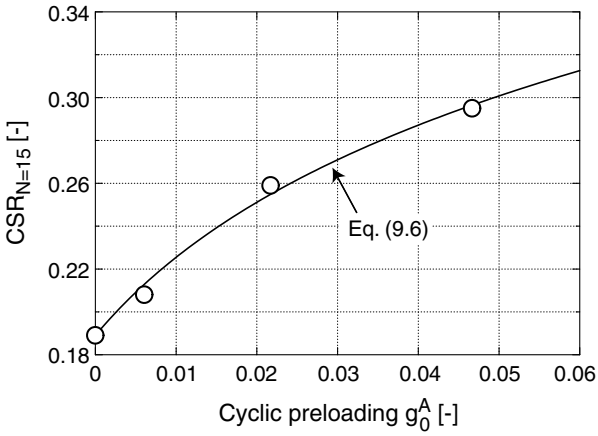

Figure 9.17: *Amplitude ratio $CSR_{N=15}$ necessary to cause a full liquefaction in 15 cycles as a function of cyclic preloading g_0^A*

$CSR_{N=15}$ increases with g_0^A according to

$$CSR_{N=15} \;=\; CSR_{N=15,0}\;\left[1 + C_{g1}\ln\left(1 + C_{g2}\;g_0^A\right)\right] \tag{9.6}$$

with the material constants $C_{g1} = 0.46$ and $C_{g2} = 51.6$. $CSR_{N=15,0} = 0.189$ is the amplitude ratio for the reference state $g_0^A = 0$ and an average void ratio of the tests of $e_{\mathrm{ref}} = 0.681$ ($I_D = 0.65$).

9.2.3 Practical application of the correlation

A possible practical application of the correlation of g_0^A with the liquefaction resistance is described in the following. Having performed SPT or CPT soundings in situ, a profile with depth of $CSR_{N=15}$ can be obtained from correlations as those in Figure 9.10. An example of such a profile is given in Figure 9.18. If correlation diagrams between sounding resistances and $CSR_{N=15}$ do not exist (e.g. in regions with no or little seismic activity), a correlation appropriate for the given grain size distribution has to be chosen from the literature.

From a few tests on disturbed specimens, a curve $CSR(N)$ similar to curve No. 1 in Figure 9.16 (non-preloaded specimens) is established and $CSR_{N=15,0}$ is determined. The tests should be performed with the in-situ density. However, if the density strongly fluctuates it may be more reasonable to determine $CSR_{N=15,0}$ for a constant reference void ratio e_{ref}

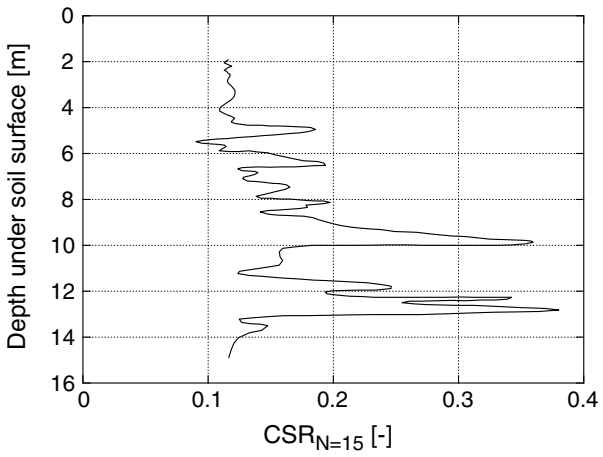

Figure 9.18: *Example of a profile $CSR_{N=15}(z)$ after Robertson & Campanella [128]*

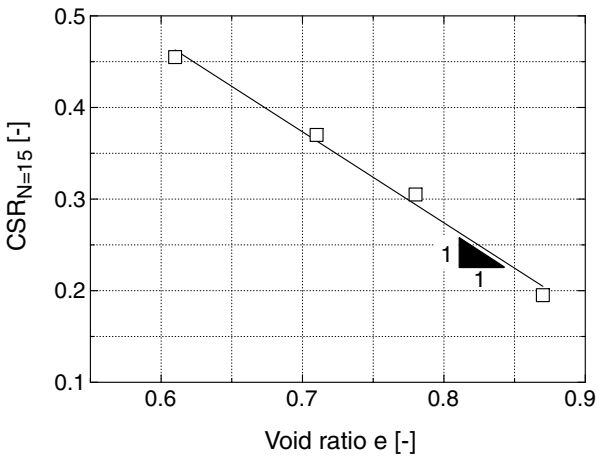

Figure 9.19: *$CSR_{N=15}$ as a function of the void ratio e after Seed & Lee [143]*

and to introduce a void ratio function $f(e)$ with $f(e) = 1$ for $e = e_{\text{ref}}$. It has to be proven, if Equation (5.8) obtained from drained tests can be set into approach. From the data of undrained tests performed by Seed & Lee [143] e.g. $f(e) = 1 + e_{\text{ref}} - e$ results (Figure 9.19). Assuming the validity of Equation (9.6), independently of the grain characteristics of the sand (this also has to be proven in future), the initial value g_0^A can be determined from

$$g_0^A(z) = \frac{1}{C_{g2}} \left\{ \exp\left[\frac{1}{C_{g1}} \left(\frac{CSR_{N=15}(z)}{CSR_{N=15,0}\ f(e)} - 1 \right) \right] - 1 \right\} \tag{9.7}$$

Equation (9.7) neglects (similar to Seed & Lee [143]) the influence of the stress on the liquefaction resistance. The sounding resistances also increase due to an aging of the soil. Following the procedure described above, aging effects are treated equivalent to a cyclic preloading. However, this can be legitimated by the decrease of the accumulation rate due to aging effects (Section 3.2.2.11). Another problem of the proposed method is, that the profile of density with depth $I_D(z)$ cannot be determined by means of correlations of the sounding resistance with I_D (see e.g. supplementary sheet 1 of DIN 4094). The reason for this is, that the procedure is based on the assumption that the sounding resistances depend not only on density but also on the cyclic preloading of the soil. A determination of I_D by means of sampling seems to be possible.

Considering the disadvantages and uncertainties of the proposed procedure, further research is necessary concerning its practical application.

9.3 Determination of the historiotropy with test loadings

A determination of the historiotropic variable g_0^A of an in-situ soil may be possible also by means of test loadings on the soil surface. Quasi-static cyclic loadings have only a small penetration. Dynamic test loadings should be preferred, since they cause a wave propagation in the soil and thus also deeper layers are cyclically sheared. Triantafyllidis et al. [164] e.g. discussed a dynamic test loading using a vibrator (Figure 9.20a) on a temporary foundation. More practically and economically meaningful is a transportable device. Figure 9.20b presents a test device which already exists at the institute in Bochum. A repeated loading of the soil by single impulses is achieved by a weight which is lifted up and afterwards dropped down. At the moment, the device is in the test phase. Independently of the used method (vibrator or falling weight), the amplitude of the settlement (e.g. by acceleration transducers) and the development of the settlement with the number of cycles (e.g. by geodetic methods or by a grid with displacement transducers) have to be measured. If the state variables and the material constants of the soil are known, g_0^A can be obtained from an FE calculation of the boundary value problem of the test loading. Eventually, direct correlation diagrams between the rate of settlement accumulation in the test loading and g_0^A can be established. In either case the influence of the ground water has to be analysed. The capillarity above the ground water level reduces the accumulation rate. Furthermore, the wave generated by the dynamic loading is reflected at the ground water level.

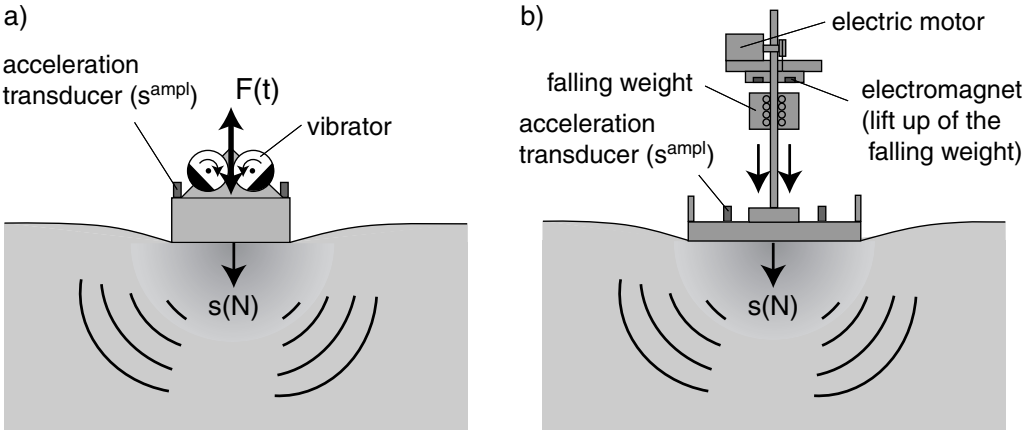

Figure 9.20: *Determination of the historiotropy g_0^A from a dynamic test loading generated a) by means of a vibrator and b) by means of a falling weight*

Due to their limited penetration, test loadings at the soil surface can deliver the historiotropy only for the upper soil layers. At the moment, no information is available how strongly g_0^A varies with depth z. If this variation is large, the determination of a profile $g_0^A(z)$ is desirable, in particular in the case of settlement prognoses for deep foundations. Such a profile could be received from cyclic pressuremeter tests, which were recently performed by Dupla & Canou [28] in a small scale in a calibration chamber. The principle of the pressuremeter traces back to Ménard. It is based on the lateral expansion of a cylindrical excavation in the soil over a certain depth. Usually, pressuremeter tests with a monotonic expansion of the excavation are applied in order to determine the stress-deformation-behaviour and the bearing capacity of the soil. Pressuremeter tests can be interpreted well by theories of the expansion of excavations (e.g. Baguelin et al. [6], Hughes et al. [58], Cudmani [25]). An undrained cyclic loading of a cylindrical excavation was studied experimentally by Schwab & Dormieux [137].

In tests with different initial densities and cycles under drained conditions, Dupla & Canou [28] measured the development of the volumetric strain of the excavation $\varepsilon_{v,\mathrm{cav}}^{\mathrm{acc}}$ with the number of cycles N. Figure 9.21a shows a typical curve $\varepsilon_{v,\mathrm{cav}}^{\mathrm{acc}}(N)$. Furthermore, in undrained cyclic triaxial tests on the same sand similar initial densities were tested. Thus, for different stress amplitudes a correlation between the number of cycles necessary to reach liquefaction and the expansion of the excavation $\varepsilon_{v,\mathrm{cav}}^{\mathrm{acc}}(N = 50)$ after 50 cycles could be established (Figure 9.21b).

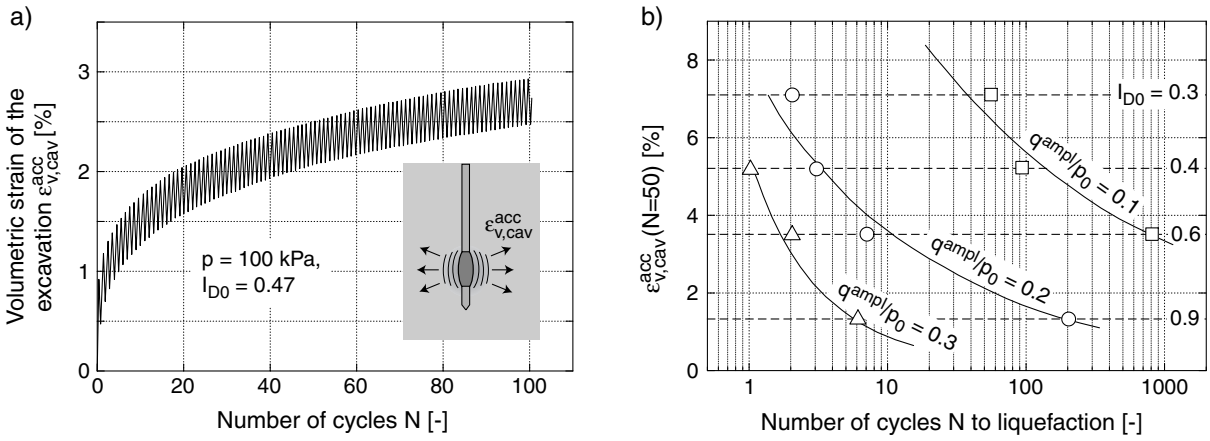

Figure 9.21: *Cyclic pressuremeter tests of Dupla & Canou [28]: a) Increase of the volumetric strain of the excavation $\varepsilon_{v,cav}^{acc}$ with the number of cycles N, b) correlation of $\varepsilon_{v,cav}^{acc}(N = 50)$ with the number of cycles necessary to reach liquefaction in undrained cyclic triaxial tests*

The experimental determination of correlation diagrams between the expansion of the

excavation after a definite number of load cycles with a predefined amplitude of pressure on the one side and the historiotropic variable g_0^A on the other side seems to be viable. Such correlations would have to be established for different grain size distribution curves, densities and stresses. During the sounding in situ, an excavation would be cyclically expanded in several depths (e.g. a test every 1 m) and by means of the correlations a profile $g_0^A(z)$ can be obtained.

However, it has to be proven in which distance to the pressuremeter probe the soil is disturbed due to the penetration of the probe. Furthermore, the range of the cyclic expansion has to be checked. It has to be clarified how strongly the change of the fabric of the grain skeleton near the probe affects the accumulation curves. For poorly draining soils, i.e. soils with a low permeability, it would be longsome to choose such a low frequency that no pore pressure would be built up or to wait the consolidation after each cycle. In this case the loading can be applied faster, i.e. partly drained or almost undrained, if the build-up of pore water pressures is measured at the probe with respective transducers. The sum of the effects of the pore water pressure accumulation and $\varepsilon_{v,\mathrm{cav}}^{\mathrm{acc}}$ can be considered as a measure of volumetric accumulation.

Chapter 10

Summary and outlook

10.1 Summary

A cyclic loading often leads to an accumulation of residual deformations in the soil. The resulting differential settlements or tiltings may endanger the serviceability of a foundation. Thus, a class A prediction is desirable. For such prognoses, an explicit accumulation model was developed in Bochum. It is based on numerous cyclic triaxial tests and cyclic multidimensional simple shear tests on a medium coarse to coarse quartz sand with subangular grains.

The main findings of the element tests with cylindrical compression or extension concerning the direction of accumulation $\varepsilon_v^{\mathrm{acc}}/\varepsilon_q^{\mathrm{acc}}$ ("cyclic flow rule") were:

- The direction of accumulation depends almost exclusively on the average stress ratio $\eta^{\mathrm{av}} = q^{\mathrm{av}}/p^{\mathrm{av}}$. At an isotropic average stress ($\eta^{\mathrm{av}} = 0$), a pure volumetric accumulation ($\dot{\varepsilon}_q^{\mathrm{acc}} = 0$) takes place. On the critical state lines ($\eta^{\mathrm{av}} = M_c(\varphi_c)$ for triaxial compression and $\eta^{\mathrm{av}} = M_e(\varphi_c)$ for triaxial extension) only the deviatoric strains accumulate ($\dot{\varepsilon}_v^{\mathrm{acc}} = 0$). At average stresses laying between the critical state lines in the p-q-plane, small cycles lead to a compaction of the material. For average stresses with $\eta^{\mathrm{av}} < M_e(\varphi_c)$ and $\eta^{\mathrm{av}} > M_c(\varphi_c)$, a dilative material behaviour was observed.
- The direction of accumulation is not influenced by the average mean pressure p^{av}, the stress or strain loop (span, polarization, shape), the void ratio, the loading frequency, the monotonic preloading and the grain size distribution curve.
- A slight increase of the volumetric portion of the direction of accumulation with the number of cycles N was measured. Simultaneously, the stress ratio $\eta^{\mathrm{av}}(\dot{\varepsilon}_v^{\mathrm{acc}} = 0)$ evolved with N towards larger amounts $|\eta^{\mathrm{av}}|$.

- The direction of accumulation under cyclic loading can be well described by flow rules for monotonic loading (e.g. modified Cam Clay model, hypoplasticity).

Referring to the intensity of accumulation $\dot{\varepsilon}^{\mathrm{acc}} = \sqrt{\dot{\varepsilon}_1^{\mathrm{acc}} + 2\dot{\varepsilon}_3^{\mathrm{acc}}}$, the following results were obtained:

- In triaxial tests with a constant average stress, $\sigma_3 =$ constant and an oscillation of the axial stress in the range 10 kPa $\leq \sigma_1^{\mathrm{ampl}} \leq$ 80 kPa (resulting in small strain amplitudes $\varepsilon^{\mathrm{ampl}} < 10^{-3}$) it was observed, that the accumulation rate $\dot{\varepsilon}^{\mathrm{acc}}$ is proportional to the square of the strain amplitude, i.e. $\dot{\varepsilon}^{\mathrm{acc}} \sim (\varepsilon^{\mathrm{ampl}})^2$ holds.
- Tests with larger strain amplitudes ($\varepsilon^{\mathrm{ampl}} > 10^{-3}$) revealed that this quadratic relationship loses its validity when the stress cycles exceed the critical state line.
- If among σ_1 also the lateral stress σ_3 is cyclically varied and if both stress components oscillate without a phase shift in time, stress cycles along a straight line with a certain inclination in the p-q-plane are obtained. For a given strain amplitude $\varepsilon^{\mathrm{ampl}}$, the accumulation rate $\dot{\varepsilon}^{\mathrm{acc}}$ is independent of the inclination of the cycles.
- In simple shear tests it was observed that circular strain loops cause twice larger accumulation rates than one-dimensional strain loops with an identical maximum span. Thus, the shape of the strain loop strongly influences the accumulation rate.
- A simple shear test, in which the circulation was changed from "clockwise" to "counterclockwise", demonstrated that the circulation of the strain loop is unimportant for $\dot{\varepsilon}^{\mathrm{acc}}$.
- In further simple shear tests a temporary increase of the accumulation rate was measured due to a sudden change of the polarization (i.e. the direction) of the cycles.
- Triaxial tests with identical stresses but different initial void ratios confirmed that the accumulation rate increases with the void ratio e. The relationship $\dot{\varepsilon}^{\mathrm{acc}}(e)$ can be described by a hyperbolic function. The zero-crossing of this function corresponds to the void ratio for which the accumulation rate vanishes ($\dot{\varepsilon}^{\mathrm{acc}} = 0$). The void ratio $e(\dot{\varepsilon}^{\mathrm{acc}} = 0)$ is smaller than the minimum void ratio e_{min} from the standard procedure of DIN 18126.
- From triaxial tests with different average mean pressures 50 kPa $\leq p^{\mathrm{av}} \leq$ 300 kPa (at a constant average stress ratio η^{av}) it could be concluded that for a given void ratio and a given strain amplitude, the accumulation rate $\dot{\varepsilon}^{\mathrm{acc}}$ decreases with increasing p^{av}. The dependence $\dot{\varepsilon}^{\mathrm{acc}}(p^{\mathrm{av}})$ can be described by an exponential function. However, the pressure-dependence $\dot{\varepsilon}^{\mathrm{acc}}(p^{\mathrm{av}})$ increases with the number of cycles N.

- Tests with p^{av} = constant but different average stress ratios $0.375 \leq \eta^{\mathrm{av}} \leq 1.375$ showed, that the accumulation rate increases with increasing average stress ratio. The relationship $\dot{\varepsilon}^{\mathrm{acc}}(\eta^{\mathrm{av}})$ can be captured by an exponential function. Also for triaxial extension ($\eta^{\mathrm{av}} < 0$), an increase of the accumulation rate with $|\eta^{\mathrm{av}}|$ was measured.
- In the tested range 0.05 Hz $\leq f_B \leq$ 2 Hz, the loading frequency f_B did not influence the accumulation rate.
- In the triaxial tests on a medium coarse to coarse sand, the increase of the residual strain with the number of cycles N was proportional to $\ln(N)$ up to $N = 10^4$. For larger numbers of cycles, over-logarithmical curves $\varepsilon^{\mathrm{acc}}(N)$ were obtained, probably due to abrasion at the particle contacts. Tests on different sands revealed that the shape of the curves $\varepsilon^{\mathrm{acc}}(N)$ depends also on the grain size distribution curve.
- For an identical void ratio e and an identical average stress $\boldsymbol{\sigma}^{\mathrm{av}}$, different accumulation rates were measured depending on the historiotropy (cyclic preloading), i.e. depending on the fabric of the grain skeleton. A strong historiotropy significantly reduces the accumulation rate.
- If the soil is loaded by packages of cycles with different amplitudes (but with a constant polarization), the sequence of the packages plays a minor role concerning the residual strain at the end of the test. Thus, as long as the polarization of the cycles is constant, the Miner's rule [96] is applicable to sand in a first approximation.
- The influence of a monotonic preloading (an isotropic and a K_0-preloading were tested) is much less pronounced than the effect of a cyclic preloading.
- Also the grain size distribution curve influences significantly the accumulation rate. Four different sands (0.35 mm $\leq d_{50} \leq$ 1.45 mm and $1.4 \leq U = d_{60}/d_{10} \leq 4.5$) were tested in cyclic triaxial tests. For identical strain amplitudes and relative densities, fine-grained non-cohesive soils densify much faster than coarse soils, i.e. $\dot{\varepsilon}^{\mathrm{acc}}$ increases with decreasing mean grain diameter d_{50}. The largest accumulation rates were measured for a well-graded soil, i.e. $\dot{\varepsilon}^{\mathrm{acc}}$ increases with the non-uniformity index U.

The Bochum accumulation model describes the experimentally observed dependencies in a material formulation which is similar to viscoplastic models. The number of cycles N is used instead of time t. The accumulation rate $\dot{\boldsymbol{\varepsilon}}^{\mathrm{acc}}$ is calculated as a product of a tensorial direction of accumulation $\mathbf{m}$ (flow rule) and several factors, each considering one individual influencing parameter. For the description of multidimensional strain loops (consideration of the shape of the strain loop), a special tensorial definition of the strain amplitude is used. The polarization of the previous cycles is memorized in a variable

called "back polarization". An additional factor describes the temporary increase of the accumulation rate due to polarization changes. The historiotropic variable g^A weights the number of the cycles in the past with their amplitude. The accumulation model needs eight material constants, which, at present, are available for a medium coarse to coarse sand and partly also for a fine sand.

By means of the Finite Element Method and the accumulation model, a centrifuge model test of Helm et al. [49] (strip foundation under cyclic loading) was re-calculated and a good agreement of the settlement curves of the model test and the re-calculation could be achieved. Furthermore, parametric studies on cyclically loaded shallow foundations were performed. The variables of the soil (initial density I_{D0}, coefficient of lateral earth pressure K_0, historiotropic variable g_0^A), the loading of the foundation (average value F^{av}, amplitude F^{ampl}) and the geometry of the foundation (depth of embedding t, width b) were varied. If a strip foundation carries a cyclic load $F^{\mathrm{av}} \pm F^{\mathrm{ampl}}$, the rate of settlement decreases

- with increasing initial density I_{D0},
- with increasing coefficient of lateral earth pressure K_0,
- with increasing historiotropy g_0^A,
- with decreasing load amplitude F^{ampl} while the average load F^{av} is kept constant,
- with increasing average load F^{av} while the amplitude F^{ampl} is kept constant,
- with increasing depth of embedding t and
- with increasing width of the foundation b.

For a given cyclic portion F^{ampl}, a reduction of the rate of settlement can be achieved by a pre-compaction of the soil ($I_{D0} \uparrow, g_0^A \uparrow, K_0 \uparrow$), by choosing a larger self-weight of the building ($F^{\mathrm{av}} \uparrow$) or (if possible) by an increase of the width of the foundation (much more effective than for static loads) or an increase of the depth of embedding. As another boundary value problem, a pile under cyclic axial loading was calculated. The development of the settlements and the stresses acting on the pile was studied in dependence on the pile loading.

For a prediction of the settlement, the determination of the historiotropic variable g_0^A of the in-situ soil is of primary importance. The historiotropy cannot be measured directly but has to be determined from correlations. The laboratory tests in this work demonstrate, that a correlation of g_0^A with dynamic soil properties (wave velocities, material damping) is not viable. A correlation of g_0^A with the liquefaction resistance could be established. A practical application of this correlation using soundings is proposed.

10.2 Outlook

The present work could answer several questions concerning the material behaviour of non-cohesive soils under cyclic loading. However, the need for further research on some aspects of this wide topic became clear. Further cyclic element tests are necessary to improve the explicit equations:

- Correlation of the material constants of the accumulation model with the characteristics of the grains (d_{50}, $U = d_{60}/d_{10}$, grain shape and roughness). The use of correlations shall allow the determination of a set of material constants of the accumulation model with only a few tests.
- Tests with large strain amplitudes $\varepsilon^{\mathrm{ampl}} > 10^{-3}$ in order to develop a procedure for the handling of such cycles in an explicit calculation. This is of importance especially for the application of the model on problems with large strain amplitudes (e.g. vibratory compaction, earthquakes).
- Study of the accumulation rate at small stresses ($p^{\mathrm{av}} < 50$ kPa)
- Tests on $\dot{\boldsymbol{\varepsilon}}^{\mathrm{acc}}$ for large numbers of cycles $N > 10^5$
- Additional tests on the influence of a monotonic preloading and eventually also on the influence of aging effects on $\dot{\boldsymbol{\varepsilon}}^{\mathrm{acc}}$

In the accumulation model, the elastic stiffness E connects the accumulation of stress with the accumulation of strain. The value of E is especially important in such applications, where a non-negligible accumulation of stress takes place (e.g. piles under cyclic loading). The correct choice of E has to be studied in more detail in future.

The correct prediction of the strain amplitudes in the implicit cycles is of major importance for the prognosis of accumulation with an explicit model. In this work, the hypoplastic model with the intergranular strain was used. The studies in this work reveal that improvements concerning the hypoplastic model and in particular the formulation of the intergranular strain are necessary.

An efficient method to determine the historiotropy g_0^A in situ has to be developed. The practical application of the correlation of g_0^A with the liquefaction resistance has to be checked. Furthermore, the applicability of dynamic test loadings on the soil surface and the suitability of cyclic pressuremeter soundings for the determination of g_0^A has to be proven. An alternative way could be the determination of g_0^A by means of measurements of acoustic emissions.

Furthermore, the development of explicit relations for the cyclic behaviour of cohesive soils is desirable.

Bibliography

[1] *Empfehlungen des Arbeitskreises 1.4 "Baugrunddynamik" der Deutschen Gesellschaft für Geotechnik e.V. (DGGT)*, 2001.

[2] S.S. Afifi and Jr. Richart, F.E. Stress-history effects on shear modulus of soils. *Soils and Foundations*, 13(1):77–95, 1973.

[3] S.S. Afifi and R.D. Woods. Long-term pressure effects on shear modulus of soils. *Journal of the Soil Mechanics and Foundations Division, ASCE*, 97(SM10):1445–1460, 1971.

[4] A. Alarcon-Guzman, J.L. Chameau, G.A. Leonardos, and J.D. Frost. Shear modulus and cyclic undrained behavior of sands. *Soils and Foundations*, 29(4):105–119, 1989.

[5] R. Arulnathan, R.W. Boulanger, and M.F. Riemer. Analysis of bender elements tests. *Geotechnical and Geological Engineering*, 21(2):120–131, 1998.

[6] F. Baguelin, J.F. Jézéquel, and D.H. Shield. The pressuremeter and foundation engineering. Series on Rock and Soil Mechanics, Trans Tech Publications, 617, 1978.

[7] E. Bauer. Calibration of a comprehensive constitutive equation for granular materials. *Soils and Foundations*, 36:13–26, 1996.

[8] C.D.P. Baxter. *An experimental study on the aging of sands.* PhD thesis, Faculty of the Virginia Polytechnic Institute and State University, July 1999.

[9] R. Bellotti, M. Jamiolkowski, D.C.F. Lo Presti, and D.A. O'Neill. Anisotropy of small strain stiffness in Ticino sand. *Géotechnique*, 46(1):115–131, 1996.

[10] L. Bjerrum and A. Landva. Direct simple shears tests on a norwegian quick clay. *Géotechnique*, 16(1):2–20, 1966.

[11] G. Bouckovalas, R.V. Whitman, and W.A. Marr. Permanent displacement of sand with cyclic loading. *Journal of Geotechnical Engineering, ASCE*, 110(11):1606–1623, 1984.

[12] G.M. Brignoli, M. Gotti, and K.H. II. Stokoe. Measurement of shear waves in laboratory specimens by means of piezoelectric transducers. *Geotechnical and Geological Engineering*, 19(4):384–397, 1996.

[13] M. Budhu. Nonuniformities imposed by simple shear apparatus. *Canadian Geotechnical Journal*, 20:125–137, 1984.

[14] M. Budhu and A. Britto. Numerical analysis of soils in simple shear devices. *Soils and Foundations*, 27(2):31–41, 1987.

[15] J.B. Burland, B.B. Broms, and V.F.B. de Mello. Behaviour of foundations and structures. In *Proc. 9th ICSMFE, Tokio*, volume 2, pages 495–546, 1977.

[16] H. Canbolat. Setzungsakkumulation infolge von Zyklenpaketen mit variierender Amplitude und Reihenfolge. Diplomarbeit am Lehrstuhl für Grundbau und Bodenmechanik, Ruhr-Universität Bochum, 2005.

[17] G. Castro and S.J. Poulos. Factors affecting liquefaction and cyclic mobility. *Journal of the Geotechnical Engineering Division, ASCE*, 103(GT6):501–516, 1977.

[18] J.L. Chaboche. Constitutive equations for cyclic plasticity and cyclic viscoplasticity. *International Journal of Plasticity*, 5:247–302, 1989.

[19] J.L. Chaboche. Modelling of ratchetting: evaluation of various approaches. *European Journal of Mechanics*, 13(4):501–781, 1994.

[20] S.-F. Chan and T.-H. Hanna. Repeated loading on single piles in sand. *Journal of the Geotechnical Engineering Division, ASCE*, 106(GT2):171–188, 1980.

[21] C.S. Chang and R.V. Whitman. Drained permanent deformation of sand due to cyclic loading. *Journal of Geotechnical Engineering, ASCE*, 114(10):1164–1180, 1988.

[22] L.-K. Chien, Y.-N. Oh, and C.-H. Chang. Effects of fines content on liquefaction strength and dynamic settlement of reclaimed soil. *Canadian Geotechnical Journal*, 39:254–265, 2002.

[23] C. Choi and P. Arduino. Behavioral characteristics of gravelly soils under general cyclic loading conditions. In T. Triantafyllidis, editor, *Cyclic behaviour of soils and liquefaction phenomena, Proc. of CBS04*, pages 115–122. Balkema, 2004.

[24] S.N. Coppersmith, C.-H. Liu, S. Majumdar, O. Narayan, and T.A. Witten. A model for force fluctuations in bead packs. *Physical Review E.*, 53:4673–4685, 1996.

[25] R.O. Cudmani. Statische, alternierende und dynamische Penetration in nichtbindige Böden. Dissertation, Veröffentlichungen des Institutes für Bodenmechanik und Felsmechanik der Universität Fridericiana in Karlsruhe, Heft 152, 2001.

[26] V.A. Diyaljee and G.P. Raymond. Repetitive load deformation of cohesionless soil. *Journal of the Geotechnical Engineering Division, ASCE*, 108(GT10):1215–1229, 1982.

[27] V.P. Drnevich and F.E. Richart. Dynamic prestraining of dry sand. *Journal of the Soil Mechanics and Foundations Division, ASCE*, 96(SM2):453–467, 1970.

[28] J.-C. Dupla and J. Canou. Cyclic pressuremeter loading and liquefaction properties of sands. *Soils and Foundations*, 43(2):17–31, 2003.

[29] R. Dyvik and C. Madshus. Laboratory measurements of $G_{\max}$ using bender elements. Technical report, ASCE Convention, Detroit, Michigan, 1985.

[30] M.D. Evans and S. Zhou. Liquefaction behavior of sand-gravel composites. *Journal of Geotechnical Engineering, ASCE*, 121(3):287–298, 1995.

[31] W.D.L. Finn, P.L. Bransby, and D.J. Pickering. Effect of strain history on liquefaction of sand. *Journal of the Soil Mechanics and Foundations Division, ASCE*, 96(SM6):1917–1934, 1970.

[32] S. Frydman, J.G. Zeitlen, and I. Alpan. The membrane effect in triaxial testing on granular soils. *Journal of Testing and Evaluation*, 1(1):37–41, 1973.

[33] J.D. Goddard. Nonlinear elasticity and pressure-dependent wave speeds in granular media. *Proceedings of the Royal Society London*, 430:105–131, 1990.

[34] M. Goldscheider and G. Gudehus. Einige bodenmechanische Probleme bei Küsten- und Offshore-Bauwerken. In *Vorträge zur Baugrundtagung 1976*. DGEG, 1976.

[35] A. Gotschol. Veränderlich elastisches und plastisches Verhalten nichtbindiger Böden und Schotter unter zyklisch-dynamischer Beanspruchung. Dissertation, Universität Gh Kassel, 2002.

[36] A. Gotschol and H.-G. Kempfert. Zyklisch viskoelastisch-viskoplastischer Stoffansatz nichtbindiger Böden und Schotter. *Bautechnik*, 81(4):279–285, 2004.

[37] N. Gruber, H.-W. Koreck, and P. Schwarz. Beiträge zum Tragverhalten axial zyklisch belasteter Pfähle. Schriftenreihe des Lehrstuhls und Prüfamtes für Grundbau, Bodenmechanik und Felsmechanik der TU München, Heft 5, 1985.

[38] G. Gudehus. A comprehensive constitutive equation for granular materials. *Soils and Foundations*, 36:1–12, 1996.

[39] G. Gudehus. Nichtlineare Bodendynamik in der Geotechnik. In *Vorträge der Baugrundtagung 2000 in Hannover*, pages 263–270. DGGT, 2000.

[40] G. Gudehus, I. Loukachev, and N. Pralle. Inelastic behaviour of grain skeletons with propagation of plane shear waves. In Kishino, editor, *Powders and Grains*, pages 125–128. Swets & Zeitlinger, Lisse, 2001.

[41] U. Güttler. Beurteilung des Steifigkeits- und Nachverdichtungsverhaltens von ungebundenen Mineralstoffen. Schriftenreihe des Instituts für Grundbau, Wasserwesen und Verkehrswesen, Heft 8, 1984.

[42] S.J. Hain. An application of cyclic triaxial testing to field model test. In *International Symposium on Soils under cyclic and transient loading*, pages 23–31, Januar 1980. Swansea.

[43] B.O. Hardin and W.L. Black. Sand stiffness under various triaxial stresses. *Journal of the Soil Mechanics and Foundations Division, ASCE*, 92(SM2):27–42, 1966.

[44] B.O. Hardin and V.P. Drnevich. Shear modulus and damping in soils: design equations and curves. *Journal of the Soil Mechanics and Foundations Division, ASCE*, 98(SM7):667–692, 1972.

[45] B.O. Hardin and F.E. Richart Jr. Elastic wave velocities in granular soils. *Journal of the Soil Mechanics and Foundations Division, ASCE*, 89(SM1):33–65, 1963.

[46] M. Hatanaka, Y. Suzuki, T. Kawasaki, and M. Endo. Cyclic undrained shear properties of high quality undisturbed Tokyo gravel. *Soils and Foundations*, 28(4):57–68, 1988.

[47] H.-J. Heller. Bauwerkssetzungen bei sandigem Untergrund infolge von Erschütterungen durch Bahnverkehr. *Baumaschine und Bautechnik*, 35(2):56–61, 1981.

[48] H.-J. Heller. Setzungen von Kranbahnstützen infolge von Lastwechseln bei sandigem Untergrund. *Bautechnik*, 72:11–19, 1995.

[49] J. Helm, J. Laue, and Th. Triantafyllidis. Untersuchungen an der RUB zur Verformungsentwicklung von Böden unter zyklischen Belastungen. In *Beiträge zum Workshop: Boden unter fast zyklischer Belastung: Erfahrungen und Forschungsergebnisse, Veröffentlichungen des Institutes für Grundbau und Bodenmechanik, Ruhr-Universität Bochum, Heft Nr. 32*, pages 201–222, 2000.

[50] I. Herle. Hypoplastizität und Granulometrie einfacher Korngerüste. Promotion, Institut für Bodenmechanik und Felsmechanik der Universität Fridericiana in Karlsruhe, Heft Nr. 142, 1997.

[51] H. Hertz. Über die Berührung fester elastischer Körper. *Journal reine und angewandte Mathematik*, 92:156–171, 1881.

[52] A. Hettler. Verschiebungen starrer und elastischer Gründungskörper in Sand bei monotoner und zyklischer Belastung. Institut für Boden- und Felsmechanik der Universität Karlsruhe, Heft Nr. 90, 1981.

[53] A. Hettler. Verschiebungen von lotrecht mittig belasteten Einzelfundamenten und horizontal belasteten Pfählen in Sand unter Schwellast. *Der Bauingenieur*, 59:351–355, 1984.

[54] A. Hettler. Gründungskörper mit zyklischer Belastung in Sand und 1g-Modelltechnik. In *Beiträge zum Workshop: Boden unter fast zyklischer Belastung: Erfahrungen und Forschungsergebnisse*, pages 59–75, 2000. Veröffentlichungen des Institutes für Grundbau und Bodenmechanik, Ruhr-Universität Bochum, Heft Nr. 32.

[55] A. Hettler and G. Gudehus. A pressure dependent correction for displacement results from 1g model tests with sand. *Géotechnique*, 35(4):497–510, 1985.

[56] U. Holzlöhner. Bleibende Setzung von Fundamenten infolge dynamischer Last. *Bautechnik*, 55:150–154, 1978.

[57] U. Holzlöhner. Settlement of shallow foundations on sand. *Soils and Foundations*, 24(4):58–70, 1984.

[58] J.M.O. Hughes, C.P. Wroth, and D. Windle. The pressuremeter tests in sands. *Géotechnique*, 27(4):455–472, 1977.

[59] B. Humme. Struktur von granularen Medien und deren Änderung infolge zyklischer Belastung. Diplomarbeit am Lehrstuhl für Grundbau und Bodenmechanik, Ruhr-Universität Bochum, 1999.

[60] M. Hyodo, A.F.L. Hyde, N. Aramaki, and Y. Nakata. Undrained monotonic and cyclic shear behaviour of sand under low and high confining stresses. *Soils and Foundations*, 42(3):63–76, 2002.

[61] M. Hyodo, H. Murata, N. Yasufuku, and T. Fujii. Undrained cyclic shear strength and residual shear strain of saturated sand by cyclic triaxial tests. *Soils and Foundations*, 31(3):60–76, 1991.

[62] M. Hyodo, H. Tanimizu, N. Yasufuku, and H. Murata. Undrained cyclic and monotonic triaxial behaviour of saturated loose sand. *Soils and Foundations*, 34(1):19–32, 1994.

[63] K. Ishihara and S. Okada. Effects of stress history on cyclic behavior of sands. *Soils and Foundations*, 18(4):31–45, 1978.

[64] K. Ishihara and S. Okada. Effects of large preshearing on cyclic behavior of sand. *Soils and Foundations*, 22(3):109–125, 1982.

[65] K. Ishihara and F Yamazaki. Cyclic simple shear tests on saturated sand in multidirectional loading. *Soils and Foundations*, 20(1):45–59, 1980.

[66] K. Ishihara and S. Yasuda. Sand liquefaction in hollow cylinder torsion under irregular excitation. *Soils and Foundations*, 15(1):29–45, 1975.

[67] T. Iwasaki and F. Tatsuoka. Effects of grain size and grading on dynamic shear moduli of sands. *Soils and Foundations*, 17(3):19–35, 1977.

[68] T. Iwasaki, F. Tatsuoka, and Y. Takagi. Shear moduli of sands under cyclic torsional shear loading. *Soils and Foundations*, 18(1):39–56, 1978.

[69] W.S. Kaggwa, J.R. Booker, and J.P. Carter. Residual strains in calcareous sand due to irregular cyclic loading. *Journal of Geotechnical Engineering, ASCE*, 117(2):201–218, 1991.

[70] R. Katzenbach and G. Festag. Material behaviour of dry sand under cyclic loading. In T. Triantafyllidis, editor, *Cyclic behaviour of soils and liquefaction phenomena, Proc. of CBS04*, pages 153–158. Balkema, 2004.

[71] H.G. Kempfert, A. Gotschol, and T. Stöcker. Kombiniert zyklische und dynamische Elementversuche zur Beschreibung des Kurz- und Langzeitverhaltens von Schotter und granularen Böden. Technical Report 32, 2000. Beiträge zum Workshop: Boden unter fast zyklischer Belastung: Erfahrungen und Forschungsergebnisse, S. 241-254.

[72] S. Keßler. Simulation von Rütteldruckverdichtungsmaßnahmen. Diplomarbeit am Lehrstuhl für Grundbau und Bodenmechanik, Ruhr-Universität Bochum, 2004.

[73] M. Kiekbusch and B. Schuppener. Membrane penetration and its effects on pore pressure. *Journal of the Geotechnical Engineering Division, ASCE*, 103(GT11):1267–1279, 1977.

[74] W. Kjellman. Testing the shear strength of clay in sweden. *Géotechnique*, 2(3):225–232, 1951.

[75] G. Klein. Bodendynamik und Erdbeben. In Ulrich (eds.) Smoltczyk, editor, *Grundbautaschenbuch*, pages 443–495, 2001.

[76] H.Y. Ko and R.F. Scott. Deformation of sand in hydrostatic compression. *Journal of the Soil Mechanics and Foundations Division, ASCE*, 93(SM3):137–156, 1967.

[77] T. Kokusho, T. Hara, and R. Hiraoka. Undrained shear strength of granular soils with different particle gradations. *Journal of Geotechnical and Geoenvironmental Engineering, ASCE*, 130(6):621–629, 2004.

[78] D. Kolymbas. An outline of hypoplasticity. *Archive of Applied Mechanics*, 61:143–151, 1991.

[79] S.L. Kramer and N. Sivaneswaran. Measurement and analysis of membrane penetration. Technical Report 30, University of Washington, Seattle, 1988. Soil Engineering Research Report.

[80] R. Kuwano, T.M. Connolly, and R.J. Jardine. Anisotropic stiffness measurements in a stress-path triaxial cell. *Geotechnical and Geological Engineering*, 23(2):141–157, 2000.

[81] R.S. Ladd. Specimen preparation and liquefaction of sands. *Journal of the Geotechnical Engineering Division, ASCE*, 100(GT10):1180–1184, 1974.

[82] J. Laue. Zur Setzung von Flachfundamenten auf Sand unter wiederholten Lastereignissen. Dissertation, Veröffentlichungen des Institutes für Grundbau und Bodenmechanik, Ruhr-Universität Bochum, Heft Nr. 25, 1996.

[83] A. Le Kouby, J. Canou, and J.C. Dupla. Behaviour of model piles subjected to cyclic axial loading. In Triantafyllidis, editor, *Cyclic Behaviour of Soils and Liquefaction Phenomena, Proc. of CBS04, Bochum*, pages 159–166. Balkema, 31 March - 02 April 2004.

[84] K.L. Lee and H.B. Seed. Cyclic stress conditions causing liquefaction of sand. *Journal of the Soil Mechanics and Foundations Division, ASCE*, 93(SM1):47–70, 1967.

[85] R.W. Lentz and G.Y. Baladi. Simplified procedure to characterize permanent strain in sand subjected to cyclic loading. In *International Symposium on soils under cyclic and transient loading*, pages 89–95, Januar 1980.

[86] X.S. Li and Z.Y. Cai. Effects of low-number previbration cycles on dynamic properties of dry sand. *Journal of Geotechnical and Geoenvironmental Engineering, ASCE*, 125(11):979–987, 1999.

[87] X.S. Li and W.L. Yang. Effects of vibration history on modulus and damping of dry sand. *Journal of Geotechnical and Geoenvironmental Engineering, ASCE*, 124(11):1071–1081, 1998.

[88] X.S. Li, W.L. Yang, C.K. Chen, and W.C. Wang. Energy-injecting virtual mass resonant column system. *Journal of Geotechnical and Geoenvironmental Engineering, ASCE*, 124(5):428–438, 1998.

[89] S-C.R. Lo, J. Chu, and I.K. Lee. A technique for reducing membrane penetration and bedding errors. *Geotechnical and Geological Engineering*, 12(4):311–316, 1989.

[90] D.C.F. Lo Presti, O. Pallara, R. Lancellotta, M. Armandi, and R. Maniscalco. Monotonic and cyclic loading behaviour of two sands at small strains. *Geotechnical and Geological Engineering*, (4):409–424, 1993.

[91] M.P. Luong. Mechanical aspects and thermal effects of cohesionless soils under cyclic and transient loading. In *Proc. IUTAM Conf. on Deformation and Failure of Granular materials, Delft*, pages 239–246, 1982.

[92] J. Malkus. Untersuchung des Bodenverhaltens im Kontaktbereich zyklisch axial belasteter zylindrischer Gründungselemente. In *Beiträge zum Workshop: Boden unter fast zyklischer Belastung: Erfahrungen und Forschungsergebnisse*, pages 93–108, 2000. Veröffentlichungen des Institutes für Grundbau und Bodenmechanik, Ruhr-Universität Bochum, Heft Nr. 32.

[93] K. Mallwitz and U. Holzlöhner. Verfahren zur Ermittlung der Setzung von Fundamenten infolge zyklischer Beanspruchung. *Bautechnik*, 73:175–186, 1996.

[94] W.A. Marr and J.T. Christian. Permanent displacements due to cyclic wave loading. *Journal of the Geotechnical Engineering Division, ASCE*, 107(GT8):1129–1149, 1981.

[95] H. Matsuoka and T. Nakai. A new failure for soils in three-dimensional stresses. In *Deformation and Failure of Granular Materials*, pages 253–263, 1982. Proc. IUTAM Symp. in Delft.

[96] M. Miner. Cumulative damage in fatigue. *Transactions of the American Society of Mechanical Engineering*, 67:A159–A164, 1945.

[97] Z. Mróz, V.A. Norris, and O.C. Zienkiewicz. An anisotropic hardening model for soils and its application to cyclic loading. *International Journal For Numerical And Analytical Methods in Geomechanics*, 2:203–221, 1978.

[98] J.P. Mulilis, C.K. Chan, and H.B. Seed. The effects of method of sample preparation on the cyclic stress-strain behavior of sands. Technical Report EERC 75-18, Earthquake Engineering Research Center, University of California, Berkeley, 1975.

[99] J.P. Mulilis, H.B. Seed, C.K. Chan, J.K. Mitchell, and K. Arulanandan. Effects of sample preparation on sand liquefaction. *Journal of the Geotechnical Engineering Division, ASCE*, 103(GT2):91–108, 1977.

[100] S. Nemat-Nasser and K. Takahashi. Liquefaction and densification of sand. *Journal of Geotechnical Engineering, ASCE*, 110(9):1291–1306, 1984.

[101] P.L. Newland and B.H. Allely. Volume changes during drained triaxial tests on granular materials. *Géotechnique*, 7:17–34, 1957.

[102] P.L. Newland and B.H. Allely. Volume changes during undrained triaxial tests on saturated dilatent granular materials. *Géotechnique*, 9:174–182, 1959.

[103] P.G. Nicholson, R.B. Seed, and H.A. Anwar. Elimination of membrane compliance in undrained triaxial testing. I. Measurement and evaluation. *Canadian Geotechnical Journal*, 30:727–738, 1993.

[104] A. Niemunis. Akkumulation der Verformung infolge zyklischer Belastung - numerische Strategien. In *Beiträge zum Workshop: Boden unter fast zyklischer Belastung: Erfahrungen und Forschungsergebnisse, Veröffentlichungen des Institutes für Grundbau und Bodenmechanik, Ruhr-Universität Bochum, Heft Nr. 32*, pages 1–20, 2000.

[105] A. Niemunis. Extended hypoplastic models for soils. Habilitation, Veröffentlichungen des Institutes für Grundbau und Bodenmechanik, Ruhr-Universität Bochum, Heft Nr. 34, 2003. available from `www.pg.gda.pl/~aniem/an-liter.html`.

[106] A. Niemunis and I. Herle. Hypoplastic model for cohesionless soils with elastic strain range. *Mechanics of Cohesive-Frictional Materials*, 2:279–299, 1997.

[107] A. Niemunis, C. Karcher, and T. Theile. An averaging procedure for layered materials. *International Journal For Numerical And Analytical Methods in Geomechanics*, 24:837–851, 2000.

[108] A. Niemunis and T. Wichtmann. Zuschrift zum Beitrag "Zyklisch visko-elastisch-viskoplastischer Stoffansatz nichtbindiger Böden und Schotter von A. Gotschol und H.-G. Kempfert. *Bautechnik*, 82(1):57–59, 2005.

[109] A. Niemunis, T. Wichtmann, Y. Petryna, and Th. Triantafyllidis. Stochastic modelling of settlements due to cyclic loading for soil-structure interaction. In *9th International Conference on Structural Safety and Reliability, ICOSSAR 2005, Rom*, 2005.

[110] A. Niemunis, T. Wichtmann, and T. Triantafyllidis. Explicit accumulation model for cyclic loading. In Triantafyllidis, editor, *Cyclic Behaviour of Soils and Liquefaction Phenomena, Proc. of CBS04, Bochum*, pages 65–76. Balkema, 31 March - 02 April 2004.

[111] A. Niemunis, T. Wichtmann, and T. Triantafyllidis. A high-cycle accumulation model for sand. *Computers and Geotechnics*, 32(4):245–263, 2005.

[112] A. Niemunis, T. Wichtmann, and Th. Triantafyllidis. Compaction of freshly pluviated granulates under uniaxial and multiaxial cyclic loading. In *XIIIth European Conference On Soil Mechanics and Geotechnical Engineering: Geotechnical problems with man-made and man-influenced grounds*, pages 855–860, August 2003. Prag.

[113] A. Niemunis, T. Wichtmann, and Th. Triantafyllidis. Settlements and pore pressure generation in sand during earthquakes - physical phenomena and their 1-d description. In *5th International Conference on Earthquake Resistant Engineering Structures, ERES 2005, Skiathos (Greece)*, pages 13–22, 2005.

[114] A. Niemunis, T. Wichtmann, and Th. Triantafyllidis. Settlements and pore pressure generation in sand during earthquakes - physical phenomena and their 1-D description. Vortrag, 5th International Conference on Earthquake Resistant Engineering Structures, ERES 2005, Skiathos (Greece), available from `www.gub.rub.de/mitarbeiter/torsten_wichtmann.htm`, 2005.

[115] M. Oda and K. Iwashita. *Mechanics of Granular Materials*. Balkema, Rotterdam, 1999.

[116] M. Oda, K. Kawamoto, K. Suzuki, H. Fujimori, and M. Sato. Microstructural interpretation on reliquefaction of saturated granular soils under cyclic loading. *Journal of Geotechnical and Geoenvironmental Engineering, ASCE*, 127(5):416–423, 2001.

[117] D. Porcino, G. Ciccìù, and V.N. Ghionna. Laboratory investigation of the undrained cyclic behaviour of a natural coarse sand from undisturbed and reconstituted samples. In T. Triantafyllidis, editor, *Cyclic Behaviour of Soils and Liquefaction Phenomena, Proc. of CBS04*, pages 187–192. Balkema, Rotterdam, 2004.

[118] H.G. Poulos. Cyclic axial response of single pile. *Journal of the Geotechnical Engineering Division, ASCE*, 107:41–58, 1981.

[119] H.G. Poulos. Cyclic stability diagram for axially loaded piles in sand. *Journal of the Geotechnical Engineering Division, ASCE*, 114(GT 8):877–895, 1988.

[120] H.G. Poulos. Cyclic axial loading analysis of piles in sand. *Journal of Geotechnical Engineering, ASCE*, 115:836–852, 1989.

[121] T.B.S. Pradhan, F. Tatsuoka, and Y. Sato. Experimental stress-dilatancy relations of sand subjected to cyclic loading. *Soils and Foundations*, 29(1):45–64, 1989.

[122] R. Pyke, H.B. Seed, and C.K. Chan. Settlement of sands under multidirectional shaking. *Journal of the Geotechnical Engineering Division, ASCE*, 101(GT4):379–398, 1975.

[123] X. Quian, D.H. Gray, and R.D. Woods. Voids and granulometry: effects on shear modulus of unsaturated sands. *Journal of Geotechnical Engineering, ASCE*, 119(2):295–314, 1993.

[124] M. Raffel, C. Willert, and J. Kompenhans. *Particle image velocimetry*. Springer Verlag, 1998.

[125] V.S. Raju and S.K. Sadasivian. Membrane penetration in triaxial tests on sand. *Journal of the Geotechnical Engineering Division, ASCE*, 100(GT4):482–489, 1974.

[126] G.P. Raymond and F. El Komos. Repeated load testing of a model plane strain footing. *Canadian Geotechnical Journal*, 15:190–201, 1978.

[127] F.E.Jr. Richart, J.R.Jr. Hall, and R.D. Woods. *Vibrations of Soils and Foundations*. Prentice-Hall, Englewood Cliffs, New Jersey, 1970.

[128] P.K. Robertson and R.G. Campanella. Liquefaction potential of sands using the cone penetration test. *Journal of Geotechnical Engineering, ASCE*, 22(3):298–307, 1985.

[129] P.K. Robertson and C.E. Wride. Evaluating cyclic liquefaction potential using the cone penetration test. *Canadian Geotechnical Journal*, 35:442–459, 1998.

[130] S.K. Roesler. Anisotropic shear modulus due to stress anisotropy. *Journal of the Geotechnical Engineering Division, ASCE*, 105(GT7):871–880, 1979.

[131] I. Sanchez-Salinero, J.M. Roesset, and K.H.II. Stokoe. Analytical studies of body wave propagation and attenuation. Technical Report GR86-15, University of Texas, Austin, 1986.

[132] S. Savidis, F. Rackwitz, T. Richter, J. Rhner, and N. Schneider. Verhalten von Pfählen in wassergesättigten Sanden unter zyklischen Horizontallasten. *Der Bauingenieur*, 79(9):383–385, 2004.

[133] A. Sawicki and W. Świdziński. Compaction curve as one of basic characteristics of granular soils. In E. Flavigny and D. Cordary, editors, *4th Colloque Franco-Polonais de Mechanique des Sols Appliquee*, volume 1, pages 103–115, 1987. Grenoble.

[134] A. Sawicki and W. Świdziński. Mechanics of a sandy subsoil subjected to cyclic loadings. *International Journal For Numerical And Analytical Methods in Geomechanics*, 13:511–529, 1989.

[135] A. Sawicki, W. Świdziński, and B. Zadroga. Settlement of shallow foundations due to cyclic vertical force. *Soils and Foundations*, 38(1):35–43, 1998.

[136] F. Schanzmann. Veränderung der dynamischen Steifigkeit und Dämfpung von Sand infolge zyklischer Belastung. Diplomarbeit am Lehrstuhl für Grundbau und Bodenmechanik, Ruhr-Universität Bochum, 2001.

[137] E. Schwab and L. Dormieux. Liquefaction due to expansion of a cylindrical cavity. In *Proc. of 11th ICSMFE, San Francisco*, volume 2, pages 1049–1054, 1985.

[138] P. Schwarz. Beitrag zum Tragverhalten von Verpresspfählen unter axialer zyklischer Belastung. Dissertation, Schriftenreihe des Lehrstuhls und Prüfamtes für Grundbau, Bodenmechanik und Felsmechanik der TU München, 2002.

[139] H.B. Seed. Soil liquefaction and cyclic mobility evaluation for level ground during earthquakes. *Journal of the Geotechnical Engineering Division, ASCE*, 105(GT2):201–255, 1979.

[140] H.B. Seed, I. Arango, and C.K. Chan. Evaluation of soil liquefaction potential during earthquakes. Technical Report EERC 75-28, Earthquake Engineering Research Center, University of California, 1975.

[141] H.B. Seed and I.M. Idriss. Simplified procedure for evaluating soil liquefaction potential. *Journal of the Soil Mechanics and Foundations Division, ASCE*, 97(SM9):1249–1273, 1971.

[142] H.B. Seed, I.M. Idriss, F. Makdisi, and N. Banerjee. Representation of irregular stress time histories by equivalent uniform stress series in liquefaction analyses. Technical Report EERC 75-29, Univ. of California, Berkeley, Calif, 1975.

[143] H.B. Seed and K.L. Lee. Studies of liquefaction of sands under cyclic loading conditions. Technical Report TE-65-65, Dept. of Civil Engineering, University of California, Berkeley, 1965.

[144] H.B. Seed, K. Mori, and C.K. Chan. Influence of seismic history on liquefaction of sands. *Journal of the Geotechnical Engineering Division, ASCE*, 103(GT4):257–270, 1977.

[145] R.B. Seed, H.A. Anwar, and P.G. Nicholson. Evaluation and mitigation of membrane compliance effects in undrained testing of saturated soils. Technical Report SU/GT/89-01, Stanford University, 1989.

[146] R.B. Seed, S.R. Lee, and H.-L. Jong. Penetration and liquefaction resistances: prior seismic history effects. *Journal of Geotechnical Engineering, ASCE*, 114(6):691–697, 1988.

[147] Y. Shamoto, M. Sato, and J.-M. Zhang. Simplified estimation of earthquake-induced settlements in saturated sand deposits. *Soils and Foundations*, 36(1):39–50, 1996.

[148] C.K. Shen, X.S. Li, and Y.Z. Gu. Microcomputer based free torsional vibration test. *Journal of Geotechnical Engineering, ASCE*, 111(8):971–986, 1985.

[149] M.J. Shenton. Deformation of Railway Ballast under repeated loading conditions. Railroad track mechanics and technology. *Pergamon Press*, pages 405–425, 1978.

[150] M.L. Silver and H.B. Seed. Deformation characteristics of sands under cyclic loading. *Journal of the Soil Mechanics and Foundations Division, ASCE*, 97(SM8):1081–1098, 1971.

[151] M.L. Silver and H.B. Seed. Volume changes in sands during cyclic loading. *Journal of the Soil Mechanics and Foundations Division, ASCE*, 97(SM9):1171–1182, 1971.

[152] T. Staupe. Setzungsverhalten von Einzelpfählen unter zyklischer Belastung. Diplomarbeit, Lehrstuhl für Grundbau und Bodenmechanik, Ruhr-Universität Bochum, November 1997.

[153] A.S.J. Suiker. Static and cyclic loading experiments on non-cohesive granular materials. Technical Report 1-99-DUT-1, TU Delft, 1999.

[154] T. Suzuki and S. Toki. Effects of preshearing on liquefaction characteristics of saturated sand subjected to cyclic loading. *Soils and Foundations*, 24(2):16–28, 1984.

[155] M. Sweeney and M.D. Lambson. Long term settlements of storage tanks on sand. In *X. ECSMFE, Florence*, volume 2, pages 587–591, 1991.

[156] J. Swinianski and A. Sawicki. A model of soil pile interaction owing to cyclic loading. *Canadian Geotechnical Journal*, 28(1):11–19, 1991.

[157] F. Tatsuoka, T. Iwasaki, S. Yoshida, S. Fukushima, and H. Sudo. Shear modulus and damping by drained tests on clean sand specimen reconstituted by various methods. *Soils and Foundations*, 19(1):39–54, 1979.

[158] F. Tatsuoka, S. Maeda, K. Ochi, and S. Fujii. Prediction of cyclic undrained strength of sand subjected to irregular loadings. *Soils and Foundations*, 26(2):73–89, 1986.

[159] S. Teachavoransinskun, F. Tatsuoka, and D.C.F. Lo Presti. Effects of cyclic prestraining on dilatancy characteristics and liquefaction of sand. In Shibuya, Mitachi, and Miura, editors, *Pre-failure deformation of geomaterials*, pages 75–80, 1994.

[160] D.H. Timmerman and T.H. Wu. Behavior of dry sands under cyclic loading. *Journal of the Soil Mechanics and Foundations Division, ASCE*, 95(SM4):1097–1112, 1969.

[161] K. Tokimatsu and Y. Hosaka. Effects of sample disturbance on dynamic properties of sand. *Soils and Foundations*, 26(1):53–64, 1986.

[162] T. Triantafyllidis. Bodenverflüssigung infolge zyklischer Belastung. *Geolex*, (3):1–16, 2003.

[163] T. Triantafyllidis, T. Wichtmann, and A. Niemunis. Explicit accumulation model for granular materials under multiaxial cyclic loading. In *Advances in Scattering and Biomechanical Engineering, Proc. of the Sixth Int. Workshop, Tsepelovo, Greece, 18-21 September*, pages 394–405. World Scientific, 2003.

[164] T. Triantafyllidis, T. Wichtmann, and A. Niemunis. On the determination of cyclic strain history. In Triantafyllidis, editor, *Cyclic Behaviour of Soils and Liquefaction Phenomena, Proc. of CBS04, Bochum*, pages 321–332. Balkema, 31 March - 02 April 2004.

[165] Th. Triantafyllidis and A. Niemunis. Offene Fragen zur Modellierung des zyklischen Verhaltens von nichtbindigen Böden. In *Beiträge zum Workshop: Boden unter fast zyklischer Belastung: Erfahrungen und Forschungsergebnisse, Veröffentlichungen des Institutes für Grundbau und Bodenmechanik, Ruhr-Universität Bochum, Heft Nr. 32*, pages 109–134, 2000.

[166] Th. Triantafyllidis, T. Wichtmann, and A. Niemunis. Analytische und Numerische Studien zum Effekt der Mikrostruktur auf das Antwortverhalten elastischer Körper und Strukturen. Zwischenbericht zum IKYDA - DAAD - Projekt, 2003.

[167] Th. Triantafyllidis, T. Wichtmann, and A. Niemunis. Analytische und Numerische Studien zum Effekt der Mikrostruktur auf das Antwortverhalten elastischer Körper und Strukturen. Abschlussbericht zum IKYDA - DAAD - Projekt, Förderperiode 2003 - 2004, Februar 2005.

[168] J.G. Trofimenkov and L.G. Mariupolskii. Screw piles used for mast and tower foundations. In *Proc. of 6. ICSMFE, Montreal*, volume 2, pages 328–332.

[169] Y.P. Vaid and D. Negussey. Relative density of pluviated sand samples. *Soils and Foundations*, 24(2):101–105, 1984.

[170] K.C. Valanis and C.F. Lee. Endochronic theory of cyclic plasticity with applications. *Journal of Applied Mechanics*, 51:367–374, 1984.

[171] G. Viggiani and J.H. Atkinson. Interpretation of bender elements tests. *Géotechnique*, 45(1):149–154, 1995.

[172] P.-A. von Wolffersdorff. A hypoplastic relation for granular materials with a predefined limit state surface. *Mechanics of Cohesive-Frictional Materials*, 1:251–271, 1996.

[173] P.-A. von Wolffersdorff and R. Schwab. Schleuse Uelzen I - Hypoplastische Finite-Elemente-Analyse von zyklischen Vorgängen. *Bautechnik*, 78(11):771–782, 2001.

[174] M. Vucetic, G. Lanzo, and M. Doroudian. Damping at small strains in cyclic simple shear test. *Journal of Geotechnical and Geoenvironmental Engineering, ASCE*, 124(7):585–594, 1998.

[175] T. Wichtmann. Prognose der Verdichtbarkeit des Sandes infolge zyklischer Belastung. Diplomarbeit am Lehrstuhl für Grundbau und Bodenmechanik, Ruhr-Universität Bochum, Dezember 2000.

[176] T. Wichtmann, A. Niemunis, and T. Triantafyllidis. The effect of volumetric and out-of-phase cyclic loading on strain accumulation. In Triantafyllidis, editor, *Cyclic Behaviour of Soils and Liquefaction Phenomena, Proc. of CBS04, Bochum*, pages 247–256. Balkema, 31 March - 02 April 2004.

[177] T. Wichtmann, A. Niemunis, and T. Triantafyllidis. Setzungsakkumulation in nichtbindigen Böden unter hochzyklischer Belastung. *Bautechnik*, 82(1):18–27, 2005.

[178] T. Wichtmann, A. Niemunis, T. Triantafyllidis, and M. Poblete. Correlation of cyclic preloading with the liquefaction resistance. *Soil Dynamics and Earthquake Engineering*, 25(12):923–932, 2005.

[179] T. Wichtmann, T. Sonntag, and T. Triantafyllidis. Über das Erinnerungsvermögen von Sand unter zyklischer Belastung. *Bautechnik*, 78(12):852–865, 2001.

[180] T. Wichtmann and T. Triantafyllidis. Dynamische Steifigkeit und Dämpfung von Sand bei kleinen Dehnungen. *Bautechnik*, 82(4):236–246, 2005.

[181] T. Wichtmann and T. Triantafyllidis. Über den Einfluss der Kornverteilungskurve auf das dynamische und das kumulative Verhalten nichtbindiger Böden. *Bautechnik*, 82(6):378–386, 2005.

[182] T. Wichtmann and Th. Triantafyllidis. Über die Korrelation der ödometrischen und der dynamischen Steifigkeit nichtbindiger Böden. *Bautechnik*. (zur Veröffentlichung eingereicht).

[183] T. Wichtmann and Th. Triantafyllidis. Influence of a cyclic and dynamic loading history on dynamic properties of dry sand, part I: cyclic and dynamic torsional prestraining. *Soil Dynamics and Earthquake Engineering*, 24(2):127–147, 2004.

[184] T. Wichtmann and Th. Triantafyllidis. Influence of a cyclic and dynamic loading history on dynamic properties of dry sand, part II: cyclic axial preloading. *Soil Dynamics and Earthquake Engineering*, 24(11):789–803, 2004.

[185] R.T. Wong, H.B. Seed, and C.K. Chan. Cyclic loading liquefaction of gravely soils. *Journal of the Geotechnical Engineering Division, ASCE*, 101(6):571–583, 1975.

[186] S. Wu, D.H. Gray, and F.E. Richart Jr. Capillary effects on dynamic modulus of sands and silts. *Journal of Geotechnical Engineering, ASCE*, 110(9):1188–1203, 1984.

[187] Y. Yamada and K. Ishihara. Yielding of loose sand in three-dimensional stress conditions. *Soils and Foundations*, 22(3):15–31, 1982.

[188] T.L. Youd. Compaction of sands by repeated shear straining. *Journal of the Soil Mechanics and Foundations Division, ASCE*, 98(SM7):709–725, 1972.

[189] P. Yu and F.E. Richart Jr. Stress ratio effects on shear modulus of dry sands. *Journal of Geotechnical Engineering, ASCE*, 110(3):331–345, 1984.

Appendix I

Notation

The tensorial notation is used as well as the index notation. For scalar variables, characters with normal letters (e.g. e, N) are used while second-order tensors are denoted by fat (e.g. $\mathbf{T}$, $\mathbf{D}$), fourth-order tensors by sans-serif (e.g. L, I) and eighth-order tensors by caligraphical (e.g. $\mathcal{R}$) characters. The notation of several tensor products is given in Table I.1 exemplary for the two tensors $\mathbf{A}$ and $\mathbf{B}$.

Product	Tensorial notation	Index notation	Result
dyadic product	$\mathbf{A} \otimes \mathbf{B}$	$A_{ij}\ B_{kl}$	fourth-order tensor
single contraction	$\mathbf{A} \cdot \mathbf{B}$	$A_{ik}\ B_{kj}$	second-order tensor
double contraction	$\mathbf{A} : \mathbf{B}$	$A_{kl}\ B_{kl}$	scalar
quadruple contraction	$\mathbf{A} :: \mathbf{B}$	$A_{klmn}\ B_{klmn}$	scalar

Table I.1: Tensor products

The Euclidean norm is defined (here exemplary for the second-order tensor $\mathbf{A}$) as

$$\|\mathbf{A}\| \;=\; \sqrt{\mathbf{A} : \mathbf{A}} \;\hat{=}\; \sqrt{A_{kl}\ A_{kl}} \tag{I.1}$$

The trace of a tensor is calculated from the sum of the elements on its primary diagonal, i.e.:

$$\mathrm{tr}\,(\mathbf{A}) \;\hat{=}\; A_{kk} \;=\; A_{11} + A_{22} + A_{33} \tag{I.2}$$

The deviator of a tensor $\mathbf{A}$ is

$$\mathbf{A}^* \;=\; \mathbf{A} - \frac{1}{3}\,\mathrm{tr}\,(\mathbf{A})\ \mathbf{1} \tag{I.3}$$

wherein $\mathbf{1} \mathrel{\hat{=}} \delta_{ij}$ is an identity tensor. The Kronecker symbol δ_{ij} means

$$\delta_{ij} = \begin{cases} 1 & \text{for} \quad i = j \\ 0 & \text{for} \quad i \neq j \end{cases} \tag{I.4}$$

A normalization is denoted by an arrow above the respective symbol

$$\vec{\mathbf{A}} = \frac{\mathbf{A}}{\|\mathbf{A}\|} \tag{I.5}$$

and a division by the trace of the tensor is identified by a roof:

$$\hat{\mathbf{A}} = \frac{\mathbf{A}}{\mathrm{tr}\,(\mathbf{A})} \tag{I.6}$$

Appendix II

Tensorial generalization of several definitions in Chapter 2

In Chapter 2, the definitions were shown for the triaxial case. Here, they are given in full tensor notation. The Roscoe invariants of the Cauchy stress tensor $\boldsymbol{\sigma} = -\mathbf{T}$ read:

$$p = \operatorname{tr}\boldsymbol{\sigma}/3 \tag{II.1}$$

$$q = \sqrt{3/2}\ \|\boldsymbol{\sigma}^*\| \tag{II.2}$$

The basic invariants of $\boldsymbol{\sigma}$ are:

$$I_1 = -(\sigma_{11} + \sigma_{22} + \sigma_{33}) \tag{II.3}$$

$$I_2 = {\sigma_{12}}^2 + {\sigma_{13}}^2 - \sigma_{11}\sigma_{22} + {\sigma_{23}}^2 - \sigma_{11}\sigma_{33} - \sigma_{22}\sigma_{33} \tag{II.4}$$

$$I_3 = {\sigma_{13}}^2\sigma_{22} - 2\sigma_{12}\sigma_{13}\sigma_{23} + \sigma_{11}{\sigma_{23}}^2 + {\sigma_{12}}^2\sigma_{33} - \sigma_{11}\sigma_{22}\sigma_{33} \tag{II.5}$$

The basic invariants of the stress deviator are defined as follows:

$$J_2 = (\boldsymbol{\sigma}^* : \boldsymbol{\sigma}^*)/2 \tag{II.6}$$

$$J_3 = \det(\boldsymbol{\sigma}^*) \tag{II.7}$$

The octahedral shear stress is:

$$\tau_{\mathrm{oct}} = (\boldsymbol{\sigma}^* : \boldsymbol{\sigma}^*)/\sqrt{3} \tag{II.8}$$

The invariants of the strain tensor $\boldsymbol{\varepsilon}$ (volumetric strain ε_v, deviatoric strain ε_q) read:

$$\varepsilon_v = \operatorname{tr}\boldsymbol{\varepsilon} \tag{II.9}$$

$$\varepsilon_q = \sqrt{2/3}\ \|\boldsymbol{\varepsilon}^*\| \tag{II.10}$$

The total strain is:

$$\varepsilon \;=\; \|\boldsymbol{\varepsilon}\| \tag{II.11}$$

The shear strain can be calculated from:

$$\gamma = \sqrt{3/2}\;\|\boldsymbol{\varepsilon}^*\| \tag{II.12}$$

The tensorial rate of strain accumulation can be written as a product of the scalar intensity of accumulation $\dot{\varepsilon}^{\mathrm{acc}} = ||\dot{\boldsymbol{\varepsilon}}^{\mathrm{acc}}||$ and the direction of accumulation $\mathbf{m} = \dot{\boldsymbol{\varepsilon}}^{\mathrm{acc}}/||\dot{\boldsymbol{\varepsilon}}^{\mathrm{acc}}||$:

$$\dot{\boldsymbol{\varepsilon}}^{\mathrm{acc}} \;=\; \dot{\varepsilon}^{\mathrm{acc}}\;\mathbf{m} \tag{II.13}$$

Figure II.1 shows a respective illustration in the $\dot{\varepsilon}_P^{\mathrm{acc}}$-$\dot{\varepsilon}_Q^{\mathrm{acc}}$-plane. The intensity of accumulation is identical with the length of the vector, the direction of accumulation describes its inclination.

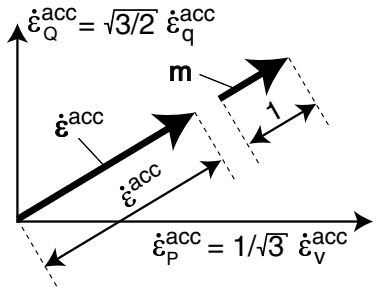

Figure II.1: *Multiplicative description of the accumulation rate* $\dot{\boldsymbol{\varepsilon}}^{acc} = \dot{\varepsilon}^{acc}\;\mathbf{m}$

Appendix III

General, tensorial notation of the amplitude and the back polarization

Amplitude definition

From the implicit calculation of the second cycle or a control cycle, in each integration point the strain loop is available as a series of discrete strain points $\boldsymbol{\varepsilon}_k$, $k = 1, ..., M$ each with six independent components. The following scheme describes the practical realization of the determination of the amplitude A_ε:

1. Determination of the two strain points of the loop which have the largest distance, calculation of their distance $2R^{(6)}$ and the direction $\vec{\mathbf{r}}^{(6)}$ (unit tensor) of a straight line through these points. It does not matter which of both possible opposite directions is chosen.

2. Projection of the loop on the (hyper)plane perpendicular to $\vec{\mathbf{r}}^{(6)}$. The result is the projected loop with the strain points $\boldsymbol{\varepsilon}^{(5)}$:

$$\boldsymbol{\varepsilon}^{(5)} = \boldsymbol{\varepsilon}^{(6)} - \vec{\mathbf{r}}^{(6)} : \boldsymbol{\varepsilon}^{(6)} \vec{\mathbf{r}}^{(6)} \tag{III.1}$$

3. Determination of the two strain points of the projected loop with the largest distance, calculation of this distance $2R^{(5)}$ and the corresponding direction $\vec{\mathbf{r}}^{(5)}$.

4. Repetition of steps 2 and 3 for the dimensions (4) to (1). This procedure can be stopped before the dimension (1) is reached, if the span of the projected loop $2R^{(i)}$ is smaller than a certain percentage (e.g. 10 %) of the span $2R^{(6)}$. This way, up to six spans $2R^{(i)}$ and directions $\vec{\mathbf{r}}^{(i)}$ are obtained. The directions of projection are

mutually perpendicular, i.e. $\vec{\mathbf{r}}^{(i)} : \vec{\mathbf{r}}^{(j)} = 1$ for $i = j$ and $\vec{\mathbf{r}}^{(i)} : \vec{\mathbf{r}}^{(j)} = 0$ for $i \neq j$ holds with $i, j = 1, ..., 6$.

5. Finally, the fourth order tensor of the strain amplitude A_ε is calculated from the sum of the dyadic products of the directions $\vec{\mathbf{r}}^{(i)} \otimes \vec{\mathbf{r}}^{(i)}$ weighted with the respective half spans $R^{(i)}$:

$$\mathsf{A}_\varepsilon = \sum_{i=1}^{6} R^{(i)} \ \vec{\mathbf{r}}^{(i)} \otimes \vec{\mathbf{r}}^{(i)} \tag{III.2}$$

Back Polarization

Let us consider two subsequent packages "a" and "b" with an identical polarization ($\vec{\mathsf{A}}_\varepsilon^a = \vec{\mathsf{A}}_\varepsilon^b$). Assuming $\boldsymbol{\pi} = \vec{\mathsf{A}}_\varepsilon^a$ at the change from package "a" to "b", the angle between $\boldsymbol{\pi}$ and $\vec{\mathsf{A}}_\varepsilon^b$ is

$$\cos\alpha \ = \ \vec{\mathsf{A}}_\varepsilon^b :: \boldsymbol{\pi} \ = \ 1 \tag{III.3}$$

and $f_\pi = 1$ follows from Equation (7.12). If the polarizations of the two packages of cycles are mutually perpendicular ($\vec{\mathsf{A}}_\varepsilon^a :: \vec{\mathsf{A}}_\varepsilon^b = 0$) one obtains

$$\cos\alpha \ = \ \vec{\mathsf{A}}_\varepsilon^b :: \boldsymbol{\pi} \ = \ 0 \tag{III.4}$$

and Equation (7.12) delivers $f_\pi = 1 + C_{\pi 1}$. The angle α evolves according to Equation (7.18). In order to rotate the tensor $\boldsymbol{\pi}$ by the angle $\Delta\alpha = \dot{\alpha}\Delta N$ (Figure 7.5) the eighth-order tensor $\mathcal{R}$ is used (Niemunis et al. [111]):

$$\boldsymbol{\pi}_{\text{new}} \ = \ \mathcal{R} :: \boldsymbol{\pi}_{\text{old}} \tag{III.5}$$

$$\mathcal{R} \ = \ (\cos\Delta\alpha - 1)\ (\vec{\boldsymbol{\mu}} \otimes \vec{\boldsymbol{\mu}} + \vec{\boldsymbol{\nu}} \otimes \vec{\boldsymbol{\nu}}) + \sin\Delta\alpha\ (\vec{\boldsymbol{\nu}} \otimes \vec{\boldsymbol{\mu}} - \vec{\boldsymbol{\mu}} \otimes \vec{\boldsymbol{\nu}}) + \mathsf{I} \tag{III.6}$$

with $\boldsymbol{\mu} = \vec{\mathsf{A}}_\varepsilon + \boldsymbol{\pi}$ and $\boldsymbol{\nu} = \vec{\mathsf{A}}_\varepsilon - \boldsymbol{\pi}$ and the fourth-order identity tensor $I_{ijkl} = 0.5(\delta_{ik}\delta_{jl} + \delta_{il}\delta_{jk})$. In the general case, Equation (7.20) for the initial value of $\boldsymbol{\pi}$ for a fully chaotical state (no preference for any direction) is replaced by (Niemunis et al. [111])

$$\boldsymbol{\pi}_0 \ = \ \boldsymbol{\pi}^{\text{iso}} \ = \ \frac{1}{3}\mathsf{J} \tag{III.7}$$

with the identity tensor $J_{ijkl} = \delta_{ik}\delta_{jl}$.

SCHRIFTENREIHE DES LEHRSTUHLS FÜR GRUNDBAU UND BODENMECHANIK DER RUHR-UNIVERSITÄT BOCHUM

Herausgeber: H.L. Jessberger

Heft Nr.		
1	(1979)	**Hans Ludwig Jessberger** Grundbau und Bodenmechanik an der Ruhr-Universität Bochum
2	(1978)	**Joachim Klein** Nichtlineares Kriechen von künstlich gefrorenem Emschermergel
3	(1979)	**Heinz-Joachim Gödecke** Die Dynamische Intensivverdichtung wenig wasserdurchlässiger Böden
4	(1979)	**Poul V. Lade** Three Dimensional Stress-Strain Behaviour and Modeling of Soils
5	(1979)	**Roland Pusch** Creep of soils
6	(1979)	**Norbert Diekmann** Zeitabhängiges, nichtlineares Spannungs-Verformungsverhalten von gefrorenem Schluff unter triaxialer Belastung
7	(1979)	**Rudolf Dörr** Zeitabhängiges Setzungsverhalten von Gründungen in Schnee, Firn und Eis der Antarktis am Beispiel der deutschen Georg-von-Neumayer- und Filchner-Station
8	(1984)	**Ulrich Güttler** Beurteilung des Steifigkeits- und Nachverdichtungsverhaltens von ungebundenen Mineralstoffen
9	(1986)	**Peter Jordan** Einfluß der Belastungsfrequenz und der partiellen Entwässerungsmöglichkeiten auf die Verflüssigung von Feinsand
10	(1986)	**Eugen Makowski** Modellierung der künstlichen Bodenvereisung im grundwasserdurchströmten Untergrund mit der Methode der finiten Elemente
11	(1986)	**Reinhard A. Beine** Verdichtungswirkung der Fallmasse auf Lastausbreitung in nichtbindigem Boden bei der Dynamischen Intensivverdichtung
12	(1986)	**Wolfgang Ebel** Einfluß des Spannungspfades auf das Spannungs-Verformungsverhalten von gefrorenem Schluff im Hinblick auf die Berechnung von Gefrierschächten

13 (1987) **Uwe Stoffers**
Berechnungen und Zentrifugen-Modellversuche zur Verformungsabhängigkeit der Ausbaubeanspruchung von Tunnelausbauten in Lockergestein

14 (1988) **Gerhard Thiel**
Steifigkeit und Dämpfung von wassergesättigtem Feinsand unter Erdbebenbelastung

15 (1991) **Mahmud Taher**
Tragverhalten von Pfahl-Platten-Gründungen im bindigen Baugrund, Berechnungsmodelle und Zentrifugen-Modellversuche

16 (1992) **Rainer Scherbeck**
Geotechnisches Verhalten mineralischer Deponieabdichtungsschichten bei ungleichförmiger Verformungswirkung

17 (1992) **Martin M. Bizialiele**
Torsional Cyclic Loading Response of a Single Pile in Sand

18 (1993) **Michael Kotthaus**
Zum Tragverhalten von horizontal belasteten Pfahlreihen aus langen Pfählen in Sand

19 (1993) **Ulrich Mann**
Stofftransport durch mineralische Deponieabdichtungen: Versuchsmethodik und Berechnungsverfahren

20 (1992) **Festschrift anläßlich des 60. Geburtstages von Prof. Dr.-Ing. H. L. Jessberger**
20 Jahre Grundbau und Bodenmechanik an der Ruhr-Universität Bochum

21 (1993) **Stephan Demmert**
Analyse des Emissionsverhaltens einer Kombinationsabdichtung im Rahmen der Risikobetrachtung von Abfalldeponien

22 (1994) **Diethard König**
Beanspruchung von Tunnel- und Schachtausbauten in kohäsionslosem Lockergestein unter Berücksichtigung der Verformung im Boden

23 (1995) **Thomas Neteler**
Bewertungsmodell für die nutzungsbezogene Auswahl von Verfahren zur Altlastensanierung

24 (1995) **Ralph Kockel**
Scherfestigkeit von Mischabfall im Hinblick auf die Standsicherheit von Deponien

25 (1996) **Jan Laue**
Zur Setzung von Flachfundamenten auf Sand unter wiederholten Lastereignissen

26	(1996)	**Gunnar Heibrock** Zur Rißbildung durch Austrocknung in mineralischen Abdichtungsschichten an der Basis von Deponien
27	(1996)	**Thomas Siemer** Zentrifugen-Modellversuche zur dynamischen Wechselwirkung zwischen Bauwerken und Baugrund infolge stoßartiger Belastung
28	(1996)	**Viswanadham V. S. Bhamidipati** Geosynthetic Reinforced Mineral Sealing Layers of Landfills
29	(1997)	**Frank Trappmann** Abschätzung von technischem Risiko und Energiebedarf bei Sanierungsmaßnahmen für Altlasten
30	(1997)	**André Schürmann** Zum Erddruck auf unverankerte flexible Verbauwände
31	(1997)	**Jessberger, H. L. (Herausgeber)** Environment Geotechnics, Report of ISSMGE Technical Committee TC 5 on Environmental Geotechnics (www.gub.ruhr-uni-bochum.de/tc5)

Herausgeber: Th. Triantafyllidis

Heft Nr.

32	(2000)	**Triantafyllidis, Th. (Herausgeber)** Workshop "Boden unter fast zyklischer Belastung: Erfahrung und Forschungsergebnisse". Bochum April 2000
33	(2002)	**Christof Gehle** Bruch- und Scherverhalten von Gesteinstrennflächen mit dazwischenliegenden Materialbrücken
34	(2003)	**Andrzej Niemunis** Extended hypoplastic models for soils
35	(2004)	**Christiane Hof** Über das Verpressankertragverhalten unter kalklösendem Kohlensäureangriff
36	(2004)	**René Schäfer** Einfluss der Herstellungsmethode auf das Verformungsverhalten von Schlitzwänden in weichen bindigen Böden
37	(2005)	**Henning Wolf** Zur Scherfugenbänderung granularer Materialien unter Extensionsbeanspruchung

38 (2005) **Torsten Wichtmann**
Explicit accumulation model for non-cohesive soils under cyclic loading